Edited by
M-L. Saboungi, D. S. Newman,
K. Johnson, and D. Inman
FIFTH INTERNATIONAL SYMPOSIUM

MOLTEN SALTS

PV 86-1

PROCEEDINGS OF THE FIFTH INTERNATIONAL SYMPOSIUM ON

MOLTEN SALTS

Edited by

Marie-Louise Saboungi
Chemical Technology Division
Argonne National Laboratory
Argonne, Illinois

David S. Newman
Department of Chemistry
Bowling Green State University
Bowling Green, Ohio

Keith Johnson
Department of Chemistry
University of Regina
Regina, Saskatchewan, Canada

Douglas Inman
Department of Metallurgy and
and Materials Science
Imperial College
London, England

PHYSICAL ELECTROCHEMISTRY AND HIGH TEMPERATURE MATERIALS DIVISIONS

Proceedings Volume 86-1

THE ELECTROCHEMICAL SOCIETY, INC., 10 South Main St., Pennington, NJ 08534-2896

PROCEEDINGS OF THE FIFTH INTERNATIONAL
SYMPOSIUM ON

MOLTEN SALTS

Edited by

Marie-Louise Saboungi
Chemical Technology Division
Argonne National Laboratory
Argonne, Illinois

Keith Johnson
Department of Chemistry
University of Regina
Regina, Saskatchewan, Canada

David S. Newman
Department of Chemistry
Bowling Green State University
Bowling Green, Ohio

Douglas Inman
Department of Metallurgy and
and Materials Science
Imperial College
London, England

PHYSICAL ELECTROCHEMISTRY AND HIGH TEMPERATURE MATERIALS DIVISIONS

Proceedings Volume 86-1

HE ELECTROCHEMICAL SOCIETY, INC., 10 South Main St., Pennington, NJ 08534-2896

Library of Congress Catalog Number 86-80323
Printed in the United States of America

DOI: 10.1149/198601.0iiiPV

PREFACE

The Fifth International Symposium on Molten Salts was held at the 168th Meeting of the Electrochemical Society, October 13–18, 1985, in Las Vegas, Nevada. The Physical Electrochemistry Division and the High-Temperature Division of the Electrochemical Society cosponsored this Symposium. Additional funding was generously provided by the Aluminum Company of America.

The Proceedings are dedicated to the memory of Dr. Warren Grimes whose strong leadership of the chemistry project associated with the molten salt reactor at the Oak Ridge National Laboratory was a major factor in the recognition of the technological importance of molten salts. The subsequent growth of many fundamental and applied research activities in this field has led to the sophisticated scientific foundation we have today.

The papers presented at this Symposium cover a variety of topics ranging from fundamental studies to applications in numerous technologies. Electrochemical research on room temperature haloaluminates—a class of molten salts with many potential technological applications—was well represented. The large number of papers presented at this Symposium indicates that the state of molten salt research is healthy and diversified. (Not all of the papers scheduled in the program were included in this volume.) Use of modern state-of-the-art techniques and supercomputers is becoming more frequent and has revealed new dimensions in the understanding of basic fundamental properties and mechanisms in ionic molten media.

I am especially grateful to Drs. Noel Jarrett and Warren Haupin of the Aluminum Company of America for their enthusiastic interest and support of the Symposium. I would like to express my appreciation to Drs. M. Blander, R. Kumar, N. Q. Minh, V. A. Maroni, G. Mamantov, J. R. Selman, and L. A. Curtiss for reviewing some of the Proceedings papers. The contributions of the session chairmen and vice-chairmen, i.e., Drs. M. Blander, S. Biggin, K. Johnson, D. Newman, J. R. Selman, V. A. Maroni, D. Inman, H. C. Gaur, N. Jarrett, G. P. Smith, G. Mamantov, C. L. Hussey, E. J. Cairns, E. Dewing, J. S. Wilkes, Y. Ito and S. von Winbush, are appreciated. I sincerely thank Profs. R. Osteryoung and W. Worrell for their helpful suggestions. It is my pleasure to acknowledge Mr. V. H. Branneky and Mrs. Sarah Kilfoyle of the Electrochemical Society for their invaluable cooperation. Finally, these Proceedings would have read less smoothly without the voluminous editorial input of Mr. J. Harmon (Argonne National Laboratory).

Marie-Louise Saboungi
December, 1985

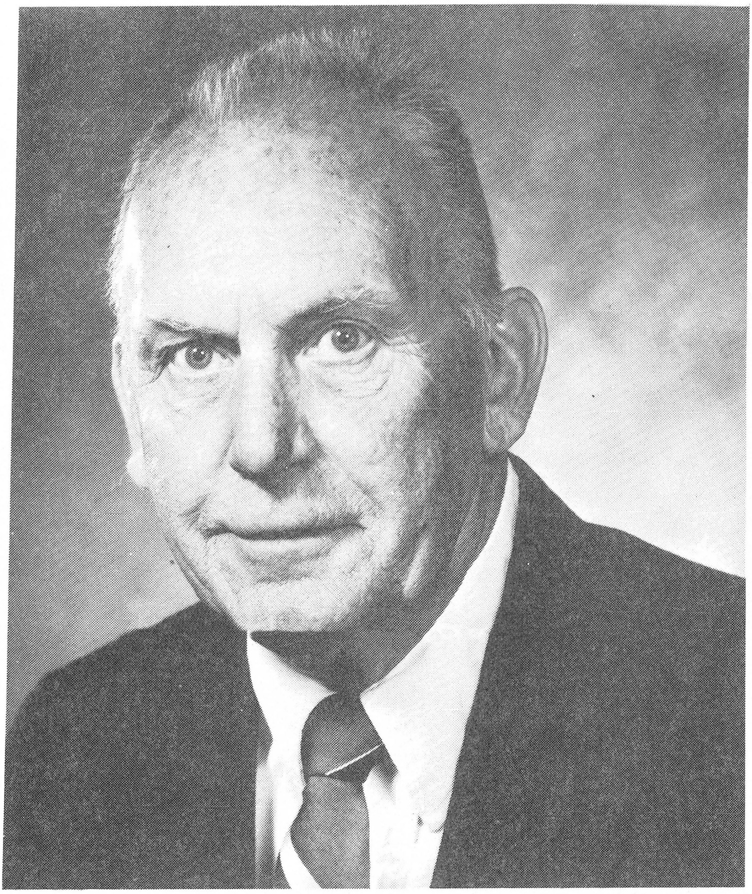

To the memory of

WARREN GRIMES

November 16, 1919 - July 26, 1985

TABLE OF CONTENTS

DOI: 10.1149/198601.0001PV

ELECTRON LOCALIZATION AND METAL-NONMETAL TRANSITION IN ALKALI-METAL/ALKALI-HALIDE SOLUTIONS

W. Freyland
Physikalische Chemie, Universität Marburg
D-3550 Marburg, Germany

Dedicated to Professor Dr. E. U. Franck
on the occasion of his sixty-fifth birthday

ABSTRACT

This paper reviews recent results from spectroscopic experiments which give strong evidence that electron localization by F-center or polaronic states occurs in non-metallic alali-metal/alkali-halide melts. Spectroscopic and thermodynamic measurements indicate that, with increasing metal concentrations, aggregation of localized states occurs and leads to the formation of stable diamagnetic F-center dimers or bipolarons. This is discussed for the example of $Na_x(NaBr)_{1-x}$ solutions. The experimental characterization of the metal-nonmetal transition region is critically analyzed. It is shown that the electronic transition occurs at lower metal concentrations than the critical point of some alkali-metal/alkali-halide solutions. The correlation between electron localization and thermodynamic phase separation is qualitatively discussed.

I. INTRODUCTION

In recent years metal-molten salt solutions have attracted renewed attention, motivated by the interest in metal-nonmetal (M-NM) transitions in various disordered systems - for recent reviews see (1) and (2). Alkali-metal/alkali-halide (M-MX) solutions are relatively simple systems. They exhibit complete ionization in condensed phase and form true solutions, as has been shown by the work of Bredig and coworkers (3). At elevated temperatures they exhibit a continuous transformation from an ionic to a metallic liquid. A characteristic of the phase behavior of some M-MX solutions (3) is the occurrence of a critical point of liquid-liquid immiscibility with consolute temperatures in the range of 634°C (Rb-RbI) to 1180°C (Na-NaF). In experimental investigations, the high chemical reactivities at these temperatures together with increased vapor pressures of the metal require new high-temperature techniques.

In the discussion of the M-NM transition in M-MX solutions a central question concerns the nature of the metal valence electrons in salt-rich solutions. Different types of localized electronic states have been discussed in the literature (1) (2). We shall confine ourselves here to a brief description of recent results from spectroscopic experiments, which clearly show that liquid F-center or polaronic states form in the nonmetallic solutions. With increasing metal concentrations, interaction between localized states and aggregation of F-centers become important, probably in the form of dimers (the F'- or F_2-center analogue) or bipolarons. Approaching the M-NM transition region, the possibility of small metal clusters has been conjectured (4). On the basis of new information from spectroscopic and thermodynamic measurements, the dimer-F-center equilibrium will be discussed in some detail for the example of $Na_x(NaBr)_{1-x}$. In the second section of the paper we will focus on the question: where in the phase region can we identify the transition? Changes in the electronic structure in relation with the phase behavior will briefly be discussed.

II. ELECTRON LOCALIZATION IN M-MX SOLUTIONS

A EVIDENCE FOR LIQUID F-CENTERS

In an analysis of the phase diagrams of liquid M-MX solutions Pitzer (5) first suggested that electron solvation similar to crystalline F-centers might occur, i.e. an electron might occupy the site of an anion vacancy. Clear experimental confirmation of this type of electron localization in concentrated solutions up to several mole percent metal has recently been obtained from NMR (6), ESR (4) and optical absorption measurements (7) in various M-MX systems.

The main optical evidence for liquid F-centers is summarized in Fig. 1, where the energy E_m of the maximum of the optical absorption band (F-band) in various M-MX systems is plotted versus the sum of ionic radii at a constant reduced temperature. The dependence of the optical excitation on the salt matrix is obvious. In the crystalline case this relation presents the optical characteristic of F-centers, known as the Mollwo-Ivey relation. It also holds in the liquid state and a best fit of the data in Fig. 1 yields (7)

$$E_m = 13(r_+ + r_-)^{-2.0},$$

where E_m is in eV and $(r_+ + r_-)$ is in Å-units. In comparison to the crystalline F-center, the liquid E_m-values are shifted to lower energies; this shift is due to changes in the local structure and thus the Madelung energy on melting (see also (8), (9)).

The ESR-spectra observed in different solutions of excess metal in eutectic salt mixtures give additional evidence for the liquid F-center model. First, the spectra do not change if different metals are dissolved in the same salt. This demonstrates that the metal valence electron is solvated according to

$$M_s \rightarrow M_s^+ + e_s^-$$

i.e. the metal does not go in solution in atomic-like states M_s. A second characteristic of the ESR-spectra is the systematic shift of the resonance position with varying salt matrix measured by the g-factor shift $\Delta g = g_e - g$, where g_e is the free electron g-factor. In general, Δg is determined by the spin-orbit coupling constant ξ and a characteristic excitation energy ΔE, i.e.

$$\Delta g \propto \xi/\Delta E.$$

As ξ scales with the atomic number N, one expects an increased shift with increasing N of the salt cation or anion. This trend is demonstrated by the results given in table 1, which also show the strong similarity with the g-factor of crystalline F-centers. In a first approximation the g-factor for F-centers in mixed crystals should lie between the corresponding values of the pure crystals.

TABLE 1: g-factors of F-center resonances observed in liquid alkali-metal/eutectic alkali-halide mixtures compared with corresponding crystalline data from the literature (25)

liquid MX-M soln	g-factor	crystal	g-factor
(Na,K)Cl-Rb or Na	1.995±0.002	NaCl	1.9978±0.0003
x = 0.04		KCl	1.9958±0.0001
(Na,Rb)Cl-Na	1.988±0.002	NaCl	1.9978±0.0003
x = 0.04		RbCl	1.9804±0.0006
(Na,Rb)I-Na	1.948±0.002	NaI	
x = 0.025		RbI	1.9494±0.0006

The NMR gives information on the structure and dynamics of excess electrons in M-MX solutions. Assuming Curie-type paramagnetism for the electrons, the hyperfine field can be determined from the measured chemical shift. From the magnitude of the fields Warren et al.(5) conclude that it is too low to be explained by atomic or multi-site localized states, but is consistent with F-center analogue states. A valuable insight into the dynamics is obtained from measurements of the nuclear spin relaxation rate. From this localization, times of the electron of the order of 10^{-12} sec have been deduced, which is comparable to the lifetime of ionic configurations in the liquid. For further details of this aspect, see the article by Warren in these proceedings.

A theoretical description of electron solvation in molten KCl has recently been reported by Parrinello and Rahman (9). Employing the methods of constant pressure molecular dynamics and treating the electron by the Feynman path integral method, they found that the electron is selftrapped in a cation shell with an average coordination number of 4-metal ions; the electron density is spatially well localized (less smeared out than in the case of the solid); the binding energy is about 4 eV and is comparable to the potential energy per ion in the bulk salt. The authors add at the end of their paper that for two electrons, they may localize in the same cation solvation shell, i.e., the coulomb repulsion may be compensated by the strong lattice relaxation energy.

B F-CENTER-DIMER EQUILIBRIUM

With increasing metal concentrations and reducing average separation between F-centers, strong interactions between localized states become important. The concentration dependence of the static magnetic susceptibilities (4) in various M-MX solutions indicates that diamagnetic spin paired centers are formed so that an equilibrium between F-centers and aggregated centers must be considered. This is also indicated by the concentration and temperature dependence of the optical spectra. Fig. 2 shows the optical absorption of $Na_x(NaBr)_{1-x}$ in the range $0.005 \leq x \leq 0.042$ at constant temperature (10); the total absorption has been deconvoluted into two bands, an F-band at 1.42 eV and a dimer band at 2 eV. At low concentrations these two bands are clearly separated in the original extinction curves (10). With increasing temperature at constant x, the intensity of the dimer band decreases in proportion to the increase of the F-band, indicating a dissociation equilibrium dimer $\rightleftarrows$ F-center. From the optical energy of 2 eV of the dimer band, it is not likely that this excitation can be assigned to such diamagnetic species as M^- or M_2; for the former, typical absorption energies of 1.5 to 1.8 eV have been found in different polar solvents (11).

A quantitative analysis of this equilibrium in $Na_x(NaBr)_{1-x}$ was recently obtained on the basis of exact sodium activity measurements (12) using the EMF technique of Egan (13). For the interpretation of these results the following thermodynamic model has been applied. At low sodium activities anion vacancies and electrons are assumed to be the major defects; with increasing metal concentrations, F-centers and F-center dimers or dielectrons--two F-centers attached or two electrons in the same anion vacancy--take over. From the corresponding chemical equilibrium equations together with the ionization and dissociation equilibria for F-centers and dimers, a relation between the metal mole fraction and the metal activity is derived--for details see the original paper (12). The important point of this model is that it yields the separate equilibrium constants from a fit of the activity relation to the measured activities. In this way a link is made between the concentration and temperature dependencies of the thermodynamic and the electronic properties. The model allows a prediction of the concentration of F-centers and aggregated localized species like dimers and explains spectroscopic and transport measurements quantitatively. An example is given in Fig. 3, where the ratio of the number of F-centers and dimers calculated from the thermodynamic model is compared with the corresponding result determined from the F-band and dimer band intensities of Fig.2. The agreement between these independent results is good.

Little is known yet about the thermal stabilities, the binding energies of aggregated localized states. The temperature dependence of the ESR in (Na,Rb)Cl melts yields a dissociation enthalpy of about 0.5 eV (4). The optical absorption measurements of $K_x(KCl)_{1-x}$ give values around 0.3 eV, changing with composition (14). New measurements of the temperature coefficient of the electrical conductivity in the $K_x(KCl)_{1-x}$ (15) are consistent with these energies, which is indicated by the maximum in the apparent activation energy ΔE_σ as plotted in Fig.4. Both the thermodynamic calculations (12) and the detailed analysis of the NMR results (6) show that the electronic conductivity is dominated by a diffusive transport of F-centers. From the NMR correlation times it is inferred that the activation energy of the electronic mobility is that of the diffusion of ions. Therefore the maximum in ΔE_σ should be related with the dissociation energy of aggregated centers like dimers. It is interesting to note that, in $Na_x(NaBr)_{1-x}$, $\Delta E\sigma$ seems to approach a maximum of about 0.5 eV (15), whereas in the $Cs_x(CsX)_{1-x}$ systems no maximum of $\Delta E\sigma$ is observed (16).

III. EXPERIMENTAL CHARACTERIZATION OF THE M-NM TRANSITION REGION

In the fluid phase changes in the electronic structure are smeared out by the high thermal energy kT. Thus, many electronic properties show a smooth change as a function of composition and do not allow a simple division into metallic and nonmetallic ranges. As a first clue the behavior of the electrical conductivity is often used. For monovalent metals the nearly free electron theory of Ziman (17) predicts a negative temperature coefficient of the electrical conductivity, $\partial \ln\sigma/\partial T < 0$, in agreement with experiment. In Fig.4 we present new measurements of $\sigma(x,T)$ for liquid $K_x(KCl)_{1-x}$ (15). A change of sign of $\partial \ln\sigma/\partial T$ occurs near $x = 0.25$. Within the nearly free electron picture this marks the lower limit of the metallic weak scattering transport regime. From this criterion the onset of electron localization in $K_x(KCl)_{1-x}$ should take place for $x < 0.25$. At this point the calculations of Morgan et al.(18) are of special interest. Using the theory of $2K_F$ scattering, they predict that localization in liquid $K_x(KX)_{1-x}$ should occur for $x = 0.15$.

Consistent with the conclusions drawn from the transport properties is the behavior of the static magnetic susceptibilities of various M-MX systems which are presented in Fig.5. Here the ratio of the mole susceptibility of dissolved metal, $\chi_m(M)$, and of bulk metal at the same temperature is plotted versus metal mole fraction x (19). In the evaluation of $\chi_m(M)$ from the total measured susceptibilities of the solutions, the assumption is made that the ionic susceptibilities of the core electrons do not change on mixing. From the data of Fig.5 it is clear that the metallic bulk susceptibility of $K_x(KCl)_{1-x}$ is approached near $x \sim 0.2$.

From the nonmetallic side the transition is characterized by a strong enhancement of the dielectric susceptibility (20). First measurements of the refractive index in the infrared spectral region indicate the beginning of a polarization catastrophe approaching the transition. The existing data on $K_x(KCl)_{1-x}$ for temperatures around 850°C yield for the dielectric anomaly a concentration of $x = 0.15 \pm 0.05$. For a more precise determination of this limit, further measurements nearer to the transition are necessary which are in preparation using an ellipsometric technique.

On the basis of the present experimental information, we may conclude, at least for the $K_x(KCl)_{1-x}$ system, that the composition of the M-NM transition lies in the range $x = 0.1$ to 0.2 for temperatures above the critical temperature of $T_c = 790^oC$ (K-KCl). As the consolute composition of $K_x(KCl)_{1-x}$ is $x_c = 0.4$ (3), a direct correlation between the thermodynamic critical point and the M-NM transition does not appear. Chieux et al.(21) have studied in detail the critical behavior of the concentration fluctuations by small angle neutron scattering in K-KBr. They find that the critical fluctuations are well described by a tri-dimensional Ising model. As they state, this is coherent with the fact that the miscibility gap occurs almost entirely within the metallic concentration regime. This is in contrast to the observations made in metal-ammonia solutions where the critical indices are of mean field type and the electronic transition seems to be connected with the thermodynamic phase transition.

For the general problem of M-NM transitions in disordered systems, different mechanisms have been invoked to describe the change in the electronic structure - for a detailed discussion see Mott (22). In the case of M-MX solutions, the self-trapping of electrons (polaronic states) and the effect of electron-electron correlation leading possibly to doubly occupied states are manifested in some of the electronic properties. It is not clear yet if higher aggregated localized states form. The concept of a percolation transition may apply. A first indication of aggregation in the form of small metal clusters was reported in the ESR experiments (4). Further information on this question may be obtained, possibly, from a more detailed investigation of the structural and dielectric properties.

Another unsolved problem concerns the correlation between the transformation in the electronic structure approaching the M-NM transition from the nonmetallic side and the macroscopic thermodynamic behavior. It seems that the occurrence of a miscibility gap is connected with the formation of stable aggregated localized states. A first indication for this is given in Fig.6. Here the ratio of the number of F-centers and excess metal atoms is plotted for $Na_x(NaBr)_{1-x}$ in comparison with $Cs_x(CsCl)_{1-x}$ as determined from the optical spectra. As the absolute concentration of F-centers cannot be determined unambiguously from the optical data, the ratio has been normalized to 1 at the lowest metal concentration. However, this comparison shows that, in the Cs-system, F-centers prevail at low metal concentrations, whereas in the Na-system dimers are important from the beginning. The latter solutions have a wide miscibility gap the former show no liquid-liquid phase separation. Possibly the existence and magnitude of the miscibility gap are related to the formation and thermal stability of aggregated localized states. This suggestion would explain the phase separation in the nonmetallic solutions and the trend in the phase diagrams going from the Na- to the Cs-systems. A similar proposal was recently given by Warren et al.(6) based on the dynamics of localized states as derived from NMR.

ACKNOWLEDGEMENT

The author would like to thank J.Egan and W.W.Warren, Jr., with whom he has discussed some aspects of this subject. Financial support in part by the Deutsche Forschungsgemeinschaft and the Fonds der Chemischen Industrie is gratefully acknowledged.

REFERENCES

(1) N.H.Nachtrieb, in: Adv.Chem.Physics, eds. I.Prigogine and S.A. Rice, 1975 (Wiley Interscience, New York)

(2) W.W.Warren,Jr., in: The Metallic and the Non-Metallic States of Matter, eds. P.P.Edwards and C.N.R.Rao, 1985 (Taylor and Francis, London)

(3) M.A.Bredig, in: Molten Salt Chemistry, ed. M.Blander, 1964 (Interscience, New York)

(4) N.Nicoloso and W.Freyland, J.Phys.Chem. 87 (1983) 1997

(5) K.S.Pitzer, J.Am.Chem.Soc. 84 (1962) 2025

(6) W.W.Warren,Jr., S.Sotier and G.F.Brennert, Phys.Rev.Lett. 50 (1983) 1505; Phys.Rev.B 30 (1984) 65

(7) W.Freyland, K.Garbade, H.Heyer and E.Pfeiffer, J.Phys.Chem. 88 (1984) 3745

(8) G.Senatore, M.Parrinello and M.P.Tosi, Phil.Mag.B 41 (1980) 595

(9) M.Parrinello and A.Rahman, J.Chem.Phys. 80 (1984) 860

(10) K.Garbade, Diplome Thesis, Universität Marburg, 1983

(11) J.W.Fletcher and W.A.Sneddon, Discuss.Faraday Soc. 63 (1978) 18

(12) J.J.Egan and W.Freyland, Ber.Bunsenges.Phys.Chem. 89 (1985) 381

(13) J.J.Egan, High Temp.Science 19 (1985) 111

(14) E.Pfeiffer, Diplome Thesis, Universität Marburg, 1982

(15) D.Nattland, Diplome Thesis, Universität Marburg, 1983 and D.Nattland and W.Freyland, to be published

(16) S.Sotier, H.Ehm and F.Maidl, J.Non-Crystalline Solids 61-62 (1984) 95

(17) J.M.Ziman, Phil.Mag. 6 (1961) 1013

(18) G.J.Morgan, R.Gilbert and B.J.Hickey, J.Phys.F: Met.Phys. 15 (1985) 2171

(19) N.Nicoloso and W.Freyland, Z.Physik.Chemie, Neue Folge 135 (1983) 39

(20) W.Freyland, K.Garbade and E.Pfeiffer, Phys.Rev.Lett. 51 (1983) 1304

(21) P.Chieux, P.Damay, J.Dupuy and J.F.Jal, J.Phys.Chem. 84 (1980) 1211

(22) N.F.Mott, Metal-Insulator Transition, 1974 (Taylor and Francis, London)

(23) W.Schmitt and U.Schindewolf, Ber.Bunsenges.Phys.Chem. 81 (1977) 584

(24) H.R.Bronstein and M.A.Bredig, J.Am.Chem.Soc. 80 (1958) 2077

(25) D.Schmid, Phys.Status Solidi 18 (1966) 653.

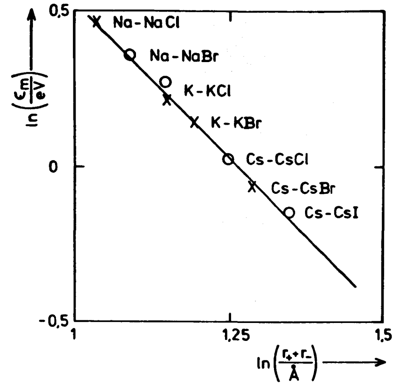

Fig.1. Energy of F-band maximum vs. the sum of ionic radii in dilute (x, ref.(23)) and concentrated (o, ref.(7)) nonmetallic M-MX solutions; the E_m-values are for the same reduced temperature of T/T_m = 1.08 (7).

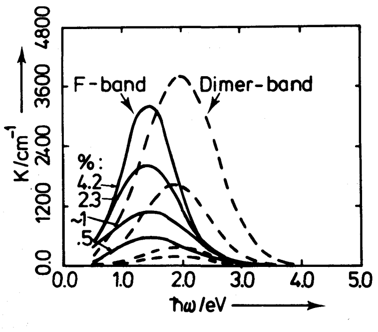

Fig.2. Optical absorption constant K vs. photon energy in liquid $Na_x(NaBr)_{1-x}$; drawn are the deconvoluted spectra of F-band and dimer-band for different compositions in mole % (10).

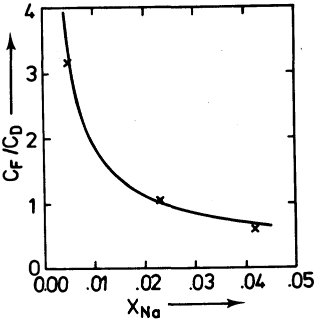

Fig.3. Ratio of F-center/dimer concentrations in liquid $Na_x(NaBr)_{1-x}$; (+) optical results, (—) thermodynamic model (12).

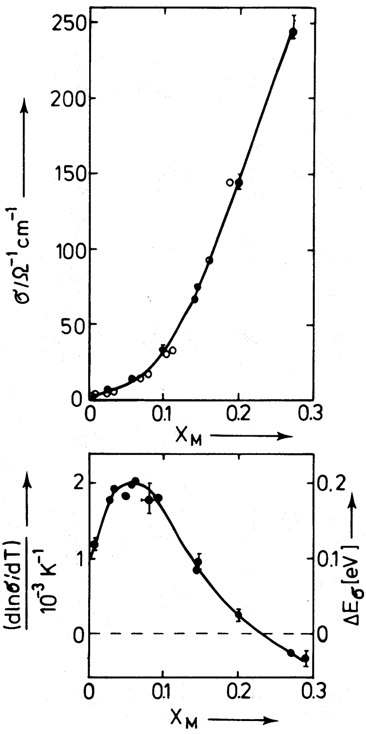

Fig. 4. Electrical conductivity, σ, and temperature coefficient, $\partial \ln\sigma/\partial T$, vs. mole fraction, x, in liquid $K_x(KCl)_{1-x}$; (o) points in the $\sigma(x_M)$ plot are from ref. (24), the full points and the $\partial \ln\sigma/\partial T$-data are from ref. (15).

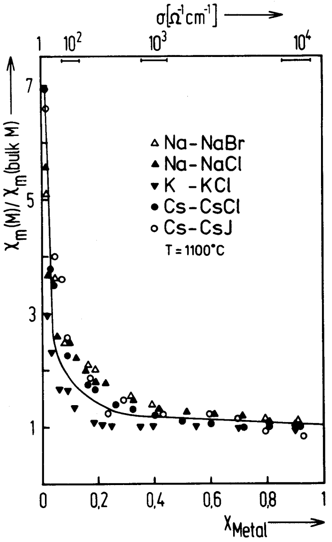

Fig.5. Ratio of molar magnetic susceptibility of dissolved metal, $\chi_m(M)$, and of bulk metal, $\chi_m(\text{bulk M})$, versus metal mole fraction in various M-MX solutions at 1100°C. The upper scale gives a rough indication of the different conductivity ranges.

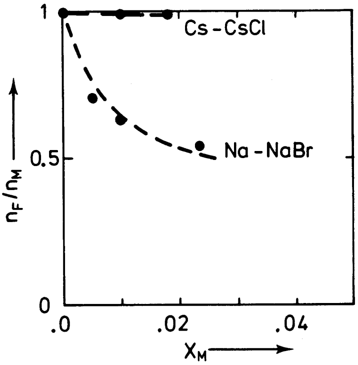

Fig.6. Relative change of F-center concentration, n_F/n_M, vs. metal mole fraction in Cs-CsCl and Na-NaBr; n_M is the number density of excess metal.

DOI: 10.1149/198601.0012PV

DYNAMICS OF LOCALIZED ELECTRONS IN METAL-MOLTEN SALT SOLUTIONS

W. W. Warren, Jr.

AT&T Bell Laboratories
Murray Hill, New Jersey 07974

The properties of electrons in molten salts are reviewed with special emphasis on the dynamics of electrons in alkali halides. Lattice polarization effects (polarons) are of great importance for the binding of electrons in F-center analogues and for the stability of hole centers. The latter may determine the recombination times for electrons studied by optical transient absorption. A simple non-activated model of transport by localized electrons is outlined.

I. INTRODUCTION

Understanding the behavior of electrons introduced into the highly coulombic structure of a molten salt presents a continuing challenge. Among the various methods of introducing excess electrons, the best known is the addition of metal to form a metal-molten salt solution. Many metals form such solutions and in some cases metal solubility is so high that homogeneous solutions can be formed over the full range of concentration up to the pure metal. Relatively low electron concentrations may be achieved without addition of metal by direct injection from a cathode or by ultraviolet irradiation.

The structure of the states occupied by low concentrations of excess electrons together with their transport characteristics are problems of central importance. After considerable and longstanding controversy it has been established during the last few years that the electrons are invariably localized rather than forming some kind of dilute metal (1). However, the forms of the localized states differ markedly among different classes of molten salt. In the alkali halides, for example, the states are closely analogous to the F-centers in which excess electrons localize in alkali halide crystals. In addition, there is evidence in these salts for spin-paired two-electron species such as M^-, M_2, paired or doubly occupied F-centers, etc. (2,3) In polyvalent metals, two-electron species in the form of lower valence ions frequently dominate. The formation of Bi^+ in the bismuth trihalides Bi-BiX_3 is an example of this type of localized state.

My concern in this paper is mainly with the time-dependent properties of electrons in the alkali halides. The static structure of the F-center analogues in these salts is now reasonably well established, at least at low electron concentrations. However dynamic properties of the electrons present some apparent inconsistencies which have not yet been addressed in a comprehensive manner. I will discuss the available experimental results, including nuclear magnetic resonance and picosecond transient optical absorption, and will describe a simple picture relating the observed lifetimes of localized electronic states to electronic transport.

II. PROPERTIES OF ELECTRONS IN ALKALI HALIDES

Perhaps the most direct demonstration of the localization phenomenon is provided by measurements of the hyperfine correlation time in nuclear magnetic resonance. The rate for longitudinal relaxation of nuclear spins interacting with unpaired electrons is

$$1/T_1 = \omega_i^2 \tau_e \tag{1}$$

where ω_i is a frequency characterizing the strength of the magnetic hyperfine coupling and τ_e is a correlation time for the rapid local field fluctuations. For mobile electrons τ_e is essentially the association time for a particular electron-ion pair.

The concentration dependence of the hyperfine correlation time in Cs-CsI solutions is shown in Fig. 1 for the full range of concentrations (4). From a value of about 10^{-15} s typical of electron-ion interactions in a metal, τ_e increases dramatically with decreasing cesium content reaching a value of about 2×10^{-12} s for concentrations around 1%. In this limit the electron-ion correlation time τ_e is comparable with the ion-ion correlation time τ_i estimated from the diffusion coefficient. Thus the electrons are localized in the vicinity of particular ions only as long as is permitted by fluctuations of the liquid structure itself.

Excess electrons localized in molten alkali halides are responsible for strong optical absorption bands in the red or near infrared. The spectrum of K-KCl shown in Fig. 2 is typical (5). The similarity of these bands to F-bands observed in the crystalline state made plausible Pitzer's suggestion (6) of the F-center model for electrons in the liquid. In this model the electron is solvated by cations and roughly fulfills the role of an anion in the strongly charge-ordered structure. The magnitudes of the magnetic hyperfine fields felt by neighboring ions are in excellent agreement with this model (2,7). Further support has come from recent path integral-molecular dynamics calculations (8) which show the electron solvated by roughly four neighboring cations. Finally, Senatore et al. (9) calculated the trend of the optical absorption energy through the family of alkali halides using a spherical approximation for the F-center potential and they obtained good agreement with experiment.

Several experiments provide information on the dynamics of the excess electrons. NMR relaxation, already mentioned, shows that electrons interact with neighboring ions for times comparable with ion-ion interaction times. The electrical conductivity, however, shows that the average mobility of the electrons greatly exceeds that of the ions. Addition of excess metal produces an electronic contribution to the conductivity on the order of 1 $(\Omega \mathrm{cm})^{-1}$/percent excess metal (1,10). This corresponds to an average electronic mobility $\mu_e \simeq 10^{-1}$ cm^2/Vs. The ionic mobility μ_i is of the order of 10^{-3} cm^2/Vs. Thus the electrons move rapidly from one localized state to another, spending a small fraction of the time moving much more rapidly than the ions. Yet another time scale is introduced by recent electron spin resonance (ESR) studies. Nicoloso and Freyland (11) observed ESR signals in several solutions of excess metal in eutectic alkali halide mixtures. The ESR lines, which they attribute to F-center analogues, are very narrow (5-10 G) implying spin lifetimes $\tau_s \gtrsim 10^{-8}$ s.

We have recently undertaken a series of picosecond transient absorption studies with the hope of gaining an additional perspective on electron dynamics in alkali halides (12). These experiments utilize a pulsed YAG laser which produces pulses of 30-50 ps width at 1064 nm. In the experiment, a fourth-harmonic pulse (266 nm) creates an initial population of electron-hole pairs by two photon absorption. The absorption due to localized electrons is probed with the 1064 nm fundamental. The excitation and probe energies are compared with the absorption spectrum of K-KCl in Fig. 2. In preliminary experiments, an excitation of roughly 10^{18} photons/cm^3 yielded a 25% reduction in transmission at 1064 nm. Under the assumption that the short-time absorption spectrum near 1 eV is the same as shown in Fig. 2, we estimate that a density $n_F \sim 10^{17}$ cm^{-3} of F-center analogues is created in the irradiated portion of the sample. Our observation that the induced absorption develops in less than 100 ps is consistent with a previous report of transient absorption at 532 nm in KCl at a single delay time of 46 ps (13). We found that the induced absorption persists with no detectable change out to at least 1 ns. Thus the recombination time exceeds by at least one order of magnitude the estimated mean time ($\sim$ 100 ps) between electron-hole collisions at a density of 10^{17} cm^{-3}.

The various time-dependent properties discussed above raise several problems concerning the electron dynamics:

(i) The optical absorption energy $\Delta E_{opt} \sim 1$ eV indicates that the localized electron sits in a potential well whose depth (> 1 eV) greatly exceeds kT ($\sim$ 0.1 eV). A crude estimate of the maximum rate for thermal hopping out of such a well gives $\nu_{hop} \lesssim 10^{14} \exp(-\Delta E_{opt}/\mathrm{kT}) \sim 10^9$ s^{-1}. For a diffusive transport process with mobility

$$\mu = e\,a^2/6\mathrm{kT}\tau, \qquad (2)$$

an enormous mean hopping distance $a \gtrsim 700$Å is required to achieve the observed mobility $\mu = 0.1$ cm^2/Vs with a hopping rate $\nu_{hop} = 1/\tau \lesssim 10^9$ s^{-1}.

(ii) The NMR correlation times τ_e indicate that a given electron-ion configuration is stable for only a few ps. What is the relationship of τ_e to the spin-lifetimes $\tau_s \sim 10^{-8}$ s inferred from the ESR linewidths?

(iii) Why does the recombination time in the transient absorption experiments so greatly exceed the mean collision time with recombination centers?

We will discuss these points in the next section after consideration of lattice relaxation effects (polarons).

III. POLARON EFFECTS

A. Localized Electrons (F-centers)

The importance of lattice polarization around F-centers in crystals is well-known. Compared with an unoccupied vacancy, the distance from an F-center to the first neighbors is contracted by about 10% (14). Because of the looseness of the liquid structure and relative ease with which second neighbors can adapt to movement of the first neighbors, it is reasonable that polarization effects should be larger in molten salts. In fact, the recent numerical work of Parrinello and Rahman (8) yielded a 30% contraction relative to the normal anion-cation distance. This implies a self-trapping effect in which the potential well is deepened substantially by the presence of the electron.

The optical transition, in the Franck-Condon approximation, occurs in a static lattice. In the thermal release of an electron during the transport process, in contrast, ions are free to move. The energy needed to excite an electron out of the static potential well is offset by the large coulomb energy recovered as the neighboring cations expand outward. For the polarization calculated by Parrinello and Rahman, this energy is several electron volts and is comparable with the cohesive energy of the salt. Thus the energy of the final state (electron removed, structure relaxed) is much closer to that of the initial configuration (electron bound, structure polarized) than implied by the static potential well.

It is a simple fact that thermal energies are sufficient to permit diffusion of the ions even though the energy to *remove* an ion is very large. Since the coulomb energies involved are comparable, this suggests a diffusion-controlled mechanism for electron transport as well. The model summarized in Fig. 3 is based on this idea. A localized electron is initially bound in its cage of neighboring cations which are polarized. Now a diffusing anion penetrating this configuration will repel the electron, pushing it onto the cations. In terms of the potential well picture, the presence of an anion weakens the potential, allowing the electron wavefunction to spread (15). This further weakens the potential until the bound state is pushed up into the continuum. Delocalization by this process occurs on the diffusion time scale of a few picoseconds.

The continuum states lie at the bottom of the "conduction band" and are primarily metal s-states. We might expect the mobility in these states to approximate the Ioffe-Regel mobility μ_{IR} in which electrons scatter with a mean free path comparable with the interionic separation (16). The Ioffe-Regel mobility lies in the range 1-5 cm^2/Vs (17). If the NMR correlation times τ_e are used for the lifetimes in the localized states, the magnitude of the conductivity requires that the electrons move 10-20Å before forming a new localized state. If the mobility in the continuum is μ_{IR}, they can cover this distance in a time on the order of 10^{-14} s.

The picture we have described for dilute electron concentrations has much in common with earlier suggestions by Durham and Greenwood (18) and by Littlewood (19). The former authors proposed that a certain fraction of electrons are localized while the conductivity is due to the remainder. Littlewood discussed exchange between localized and delocalized electrons. In the present picture, all the electrons participate in conduction on the picosecond time scale, each spending some very short time in a high mobility state.

There is evidence at higher excess metal concentrations for the presence of additional two-electron states which affect the conductivity significantly (2,3). When such species (M^-, M_2, etc.) are stable for long times with respect to the diffusion-limited structural lifetime, such states effectively remove electrons from the conductivity process. This appears to be the case for systems such as Na-NaX at low temperatures (2). On the other hand, rapid equilibrium between two-electron species and F-center analogues can enhance the average electronic mobility giving a concentration-dependent mobility as is observed, for example, in Cs-CsX solutions (2).

Let us return to the question of the long spin relaxation times implied by the narrow observed ESR lines (11). If these electrons in eutectic hosts are as mobile as those in single salts, they must retain phase memory over a large number of conduction hops. If this were not so and electrons remained in one ionic configuration for 10^{-8}s, they would have to remain in conduction states for several hundred ps to provide the observed conductivity. The initial evidence from transient absorption studies indicates the electrons in conduction states localize more rapidly than this. Thus the observed spin relaxation times require spin-orbit coupling to be sufficiently weak that an electron hop has a low probability ($\sim 10^{-4}$) of producing a spin-flip in the eutectic hosts. Strong spin-orbit coupling in Cs-CsX melts was given as the reason for the absence of observable ESR in those single-salt solutions (11). The possibility that ESR in eutectic hosts is due to a minority of low mobility states in special ionic configurations is an alternative which has yet to be explored.

B. Localized Holes

In order to discuss the recombination dynamics of electrons generated by ultraviolet irradiation, it is necessary to consider the nature of the recombination centers, i.e., the holes. Our knowledge of these states is due in large part to studies of alkali halides (mainly iodides) containing excess halogen. The magnetic properties shown in Fig. 4 illustrate two important differences between the hole and electron states in such solutions. The first point is the strong asymmetry in the magnetic susceptibility (3,20) with respect to stoichiometric CsI. While both excess Cs and excess I introduce paramagnetic contributions, the susceptibility increase per atom of excess I is substantially smaller than the increase per Cs atom. A significant fraction of the excess I therefore forms diamagnetic species. Second, on the scale shown in Fig. 4, there is no increase in the ^{133}Cs nuclear relaxation (4) on the excess I side in contrast with the rapid rise which occurs as Cs is added. This shows that the paramagnetism associated with excess I resides on the I ions and couples only weakly to the Cs nuclei.

In alkali halide crystals, the dominant hole center at low concentrations is the V_k-center, an associated I-I$^-$ pair. The liquid-state counterpart of this simple polaron is the I_2^- molecular ion. The data shown in Fig. 4 as well as optical and ESR studies (20) strongly indicate that this species is responsible for the paramagnetism associated with excess I. The diamagnetic species is believed to I_3^-. The concentration of paramagnetic species increases sharply with increasing temperature as might be expected from the equilibrium

$$I_3^- + I^- = 2I_2^-. \tag{3}$$

In sum, there are two types of recombination centers (X_3^-, X_2^-) which must be considered. Both of them are small species in which the "polaron energy" is represented by the binding energy of the polyhalide ion.

We can now consider the possible recombination reactions in the irradiated pure halides. The two simplest are

$$e^- + X_2^- \rightarrow 2X^- \tag{4}$$

$$2e^- + X_3^- \rightarrow 3X^-. \tag{5}$$

Since both reactions involve dissociation of polyhalides, an activation energy will control the rate of recombination. In addition, reaction (5) is third order and requires simultaneous recombination of two electrons. Both factors act to reduce the recombination rate relative to the frequency of collision between a single electron and a single localized hole.

IV. SUMMARY

Polaron effects in the form of structural polarization around F-center analogues and bonding of polyhalide species play an important role in electron dynamics in molten alkali halides. The energies associated with these effects are many times thermal energies and they help account for the large optical absorption energies, low barrier to electron delocalization and long electron recombination times. I have outlined a qualitative model of electron transport in which electrons are temporarily delocalized by the diffusive motions of ions. Localization times on the order of a few ps alternate with rapid motion to new localization sites. The transport process resembles in many respects a hopping process but no appreciable energy barrier is involved. Compared with the F-center analogues, the polyhalide hole states are more stable and recombination requires formation of an activated complex and dissociation of the species.

ACKNOWLEDGEMENTS

I am indebted to R. Dupree and W. Freyland for valuable discussions of various aspects of the subjects discussed in this paper.

REFERENCES

1. For a recent review, see W. W. Warren, Jr. in *The Metallic and Nonmetallic States of Matter*, edited by P. P. Edwards and C. N. R. Rao (Taylor and Francis, London, 1985).
2. W. W. Warren, Jr., S. Sotier, and G. F. Brennert, Phys. Rev. Lett. *50*, 1505 (1983).
3. M. Nicoloso and W. Freyland, Z. Phys. Chem. *135*, 39 (1983).
4. W. W. Warren, Jr., S. Sotier, and G. F. Brennert, Phys. Rev. B *30*, 65 (1984).
5. W. Freyland, K. Garbade, and E. Pfeiffer, Phys. Rev. Lett. *51*, 1304 (1983).
6. K. S. Pitzer, J. Am. Chem. Soc. *84*, 2025 (1962).
7. W. W. Warren, Jr., and S. Sotier in *Proceedings of the Third International Symposium on Molten Salts*, edited by G. Mamantov, M. Blander, and G. P. Smith (Pennington, Electrochemical Society, 1981), p. 95.
8. M. Parrinello and A. Rahman, J. Chem. Phys. *80*, 860 (1984).
9. G. Senatore, M. Parrinello, and M. P. Tosi, Phil. Mag. *41*, 595 (1980).
10. M. A. Bredig in *Molten Salt Chemistry*, edited by M. Blander (New York, Interscience, 1964), p. 367.
11. M. Nicoloso and W. Freyland, J. Phys. Chem. *87*, 1997 (1983).
12. W. W. Warren, Jr., B. Campbell, and G. F. Brennert (unpublished).
13. R. T. Williams, J. N. Bradford, W. L. Faust, Phys. Rev. B *18*, 7038 (1978).
14. W. B. Fowler in *Physics of Color Centers*, edited by W. B. Fowler (Academic, New York, 1968), p. 99.

15. The tendency for the wave function to spread at energies closer to the continuum may be clearly seen in the excited state charge distributions presented in Ref. 8.

16. A. F. Ioffe and A. R. Regel, Prog. Semiconductors *4*, 237 (1960).

17. N. F. Mott and E. A. Davis, *Electronic Processes in Noncrystalline Materials* (Oxford, Clarendon, 1979).

18. P. J. Durham and D. A. Greenwood, Phil. Mag. *33*, 427 (1976).

19. P. Littlewood, Phys. Rev. B *24*, 1710 (1981).

20. B. Nakowsky, N. Nicoloso, and W. Freyland, Ber. Bunsengesell. Phys. Chem. *88*, 297 (1984).

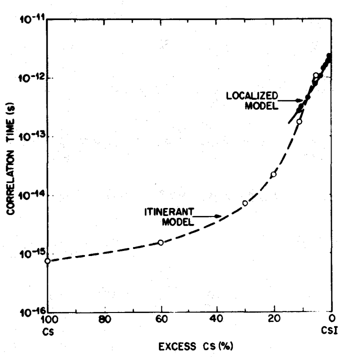

Figure 1. Magnetic hyperfine correlation times for ^{133}Cs nuclei in Cs-CsI solutions (4).

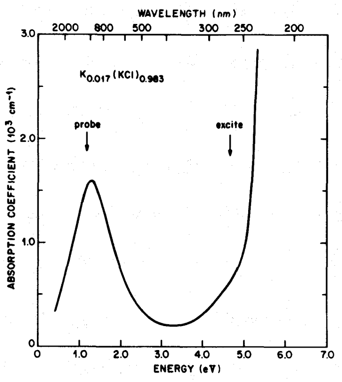

Figure 2. Optical absorption spectrum of $K_{0.017}$ $(KCl)_{0.983}$ solution at 860°C (5). Arrows indicate energies of probe and excitation photons in ps transient absorption measurement (12).

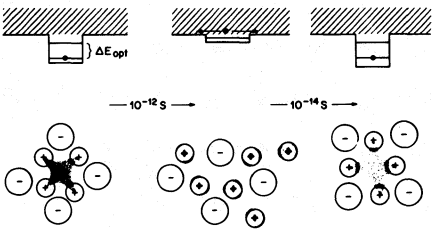

Figure 3. Schematic representation of diffusion-controlled electron transport process in molten alkali halides. Electron intially localized in F-center analogue is delocalized as ionic diffusion destroys favorable configuration. After brief period in high mobility state, electron again forms F-center analogue at new location.

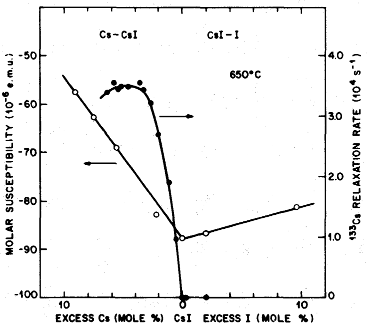

Figure 4. Magnetic properties of excess Cs and I in molten CsI. Open points, molar susceptibility (3,20); closed points ^{133}Cs nuclear spin relaxation rate (4).

DOI: 10.1149/198601.0021PV

CONTRASTING BEHAVIOR OF THE SO_4^{2-} SYMMETRIC RAMAN MODE IN HIGH AND LOW CONDUCTING SULFATES

L. Börjesson and L.M. Torell
Department of Physics
Chalmers University of Technology
S-412 96 Göteborg, Sweden

Raman spectra of fast ion conducting sulfates give evidence for sulfate ion reorientations, whereas no reorientational motion is observed in the low conducting sulfates case. The results suggest that fast ion conducting sulfates, in contrast to low conducting sulfates, are described by rotator phases. New results for high conducting bcc $LiNaSO_4$ and low conducting hexagonal Na_2SO_4 are compared with previous results for fast ion conducting fcc Li_2SO_4 and bcc $LiAgSO_4$. The obtained reorientational time decreases with increasing temperature to a value of $\underset{-}{\sim}1$ ps close to the melting points (848 - 1133 K)of solid electrolytes. The results are typical for plastic materials and in accordance with predictions from molecular simulation studies. Furthermore, if sulfate ion reorientations are coupled to the fast ion diffusion, then the surprisingly large activation energies of cation diffusion may be explained by the also high activation energies of sulfate ion reorientation found in the present study.

INTRODUCTION

A group of solid sulfates with both monovalent and divalent cations shows a high temperature phase of excellent conductivity ($\simeq 1\Omega^{-1}cm^{-1}$)(1). In these materials neutron scattering demonstrates that the fast ion conducting phase is characterized by a high degree of orientational oxygen disorder (2). This, together with a high heat of transition compared to the heat of fusion (3), suggests a premelting process with rapid rotational reordering of the sulfate groups (3). Raman scattering results on some sulfate systems below the phase transition suggest a beginning sulfate rotational motion as the phase transition is approached (4,5). Molecular dynamics simulation studies indicate a sulfate ion rotational time of $\simeq$2 ps in the fast ion conducting phase (6). Recently in this laboratory Raman scattering in fcc Li_2SO_4 and bcc $LiAgSO_4$ shows a component due to sulfate ion reorientation, which could be separated from the spectra by comparing the anisotropic and isotropic spectral bandwiths for the symmetric sulfate internal mode, ν_1, (7). Thus a plastic behavior of some crystals in the high conducting phase is confirmed.

In the present study the fast ion conducting sulfate, bcc $LiNaSO_4$, as well as a low conducting sulfate, hexagonal Na_2SO_4, have been chosen for a Raman investigation of the dynamics of the sulfate ion in the two cases. The conductivity of bcc $LiNaSO_4$ is approximately three orders in magnitude larger than that of Na_2SO_4 at a comparable temperature (8,9,10). Data on the structure, temperature range, heat of transition, conductivity and activation energy for bcc $LiNaSO_4$ and low conducting Na_2SO_4 are shown in Table I together with data on high conducting Li_2SO_4 and $LiAgSO_4$. From the table it can be seen that the hexagonal phase of low conducting Na_2SO_4 covers the temperature ranges of the three high conducting sulfates, which makes comparable studies at corresponding temperatures possible. The aim of the work is to investigate whether a rotator phase is a general characteristic of the fast ion conducting phase or if it is merely a result of the high temperature of these phases. Also, it has been suggested that rotations of the sulfate ions are enhancing cation diffusion and that this mechanism is partly responsible for the high conductivity in the fast ion conducting sulfates (13). Therefore, the temperature dependence of the symmetric mode ν_1 will be analyzed in detail to investigate any possible relation between sulfate ion reorientations and fast ion diffusion.

Previous results for fcc Li_2SO_4 and bcc $LiAgSO_4$ (7) will be summarized together with new data on bcc $LiNaSO_4$ and hexagonal Na_2SO_4.

Table I Heat of solid-solid phase transition, electrical conductivity and activation energy of cation diffusion in three fast ion conducting sulfates and in Na_2SO_4.

		ΔH $(kJ\ kg^{-1})$	σ at 823K $(\Omega^{-1}cm^{-1})$	E (eV)	Ref
Li_2SO_4	fcc: 848-1133K	214	0.86	0.34	3,11,1
$LiNaSO_4$	bcc: 791-883K	17.9	0.93	0.63 (Li^+) 0.64 (Na^+)	12,8,1 1
$LiAgSO_4$	bcc: 728-848K	155	1.17	0.52 (Li^+) 0.52 (Ag^+)	3,11,1 1
Na_2SO_4	hexagonal: 513-1157K	80	$1x10^{-3}$	1.68	3,10

EXPERIMENTAL

Polarized and depolarized Raman spectra were analyzed by a Spex double monochromator model 1403 with holographic gratings (1800 lines mm^{-1}). The spectrometer slits were set to give a measured resolution of 2 cm^{-1}. An Ar^+ laser operating at 488.0 nm was used as a light source. Lock-in technique was employed to minimize the effect of thermal radiation. A high-temperature cell, essentially the same as that described elsewhere (14), controlled the temperature within 1K in the range, 500–1100 K, of investigation. The samples, grown by the Bridgman method, were unoriented and kept in a cylindrical quartz cell (diameter 3 mm). The salts, suprapur Li_2SO_4 and Na_2SO_4, were dried 24 h in a vacuum oven before sample preparation. The crystals were approximately 3 mm long and perfectly transparent.

RESULTS AND DISCUSSION

In the Raman spectra of bcc $LiNaSO_4$ no external modes are present in accordance with the observations by Frech et al (4). In the latter report the external modes were studied in the phase below the high conducting phase and they disappeared at the transition temperature. The four internal sulfate modes, ν_1, ν_2, ν_3 and ν_4, of bcc $LiNaSO_4$ are shown in Fig. 1 as well as a spectrum for hexagonal Na_2SO_4. As can be seen in the figure, the widths of the components of the high conducting $LiNaSO_4$ are broader than those of the corresponding components of low conducting Na_2SO_4. This is in agreement with the observation that the fast ion conducting phase is a phase of significant disorder, and it is a general finding for solid electrolytes (15). The frequency shifts obtained for the internal sulfate modes in $LiNaSO_4$ are given in Table II where previous results for Li_2SO_4 and $LiAgSO_4$ (7) are included for a comparison. The results are mean values over the observed temperature ranges since the frequency decrease with temperature is small and about the same as the accuracy of the peak positions, $\sim 1\ cm^{-1}$ over the temperature range of stability of each crystal. Table II demonstrates the decreasing frequency shift with increasing size of the cation; this has been observed in other systems as well (16).

Table II Raman frequencies of the internal sulfate modes in three fast ion conducting sulfates and in Na_2SO_4

	Li_2SO_4 fcc (a)	$LiNaSO_4$ bcc	$LiAgSO_4$ bcc (a)	Na_2SO_4 hexagonal
ν_1 (cm^{-1})	993	989	970	980
ν_2 (cm^{-1})	455	455	453	454
ν_3 (cm^{-1})	≈1107	≈1110	≈1097	≈1100
ν_4 (cm^{-1})	629	627	614	621

a) Ref. 7

The halfwidth and its temperature dependence on the ν_2 and ν_4 isotropic (polarized) components are about the same as those of the anisotropic (depolarized) components for all studied crystals, see Fig. 1 for the $LiNaSO_4$ case. The halfwidth of the ν_3 mode could not be obtained in the case of the solid electrolytes due to an overlapping with the high intensity ν_1 mode, see Fig. 1. For the ν_1 mode, however, the anisotropic width, Γ_{aniso}, increases more rapidly with temperature than the width of the isotropic component, Γ_{iso}, in the case of the fast ion conducting systems. The observation is an immediate indication of reorientational motion of the sulfate ion with a reorientational time τ determined by

$$\tau^{-1} = 2\pi c\Gamma_R = 2\pi c(\Gamma_{aniso} - \Gamma_{iso}) \qquad (1)$$

where c is the speed of light and Γ_R is the broadening due to a rotational motion. In the simple approximation that vibrational and rotational motions are uncorrelated and that dipole-dipole coupling and collision induced effects may be neglected, Eq. (1) is applicable for a symmetric Raman mode of low depolarization ratio like the ν_1 mode of the present systems. To determine Γ_{aniso} of ν_1, any contribution of ν_3 must be minimized. A Lorentzian was fitted to the ν_3 by using its shape of the high frequency side. ν_3 is then subtracted from the spectrum and the resulting ν_1 is also fitted to a Lorentzian. The isotropic ν_1 mode was also found to be Lorentzian in shape. Results for Γ_{aniso} and Γ_{iso} are shown in Fig. 2.

Table III Reorientational broadening and time due to sulfate ion reorientations in bcc $LiNaSO_4$

T (K)	Γ_R (cm^{-1})	τ ($10^{-12}s$)
806	0.6	8.8
817	0.7	7.6
829	1.7	3.1
841	2.7	2.0
853	2.7	2.0
865	3.0	1.8
876	3.2	1.7
876	4.1	1.2

For $LiNaSO_4$ an increased difference in half-widths is observed, see Fig. 2a and Table III, where Γ_R and the corresponding reorientational time are tabulated. The values are to be compared with the value, 2 ps, reported in a molecular dynamics simulation study of fcc Li_2SO_4 (6). For Li_2SO_4 and $LiAgSO_4$ the previous Raman study (7) also indicated a component due to sulfate ion reorientations, and the reported values of Γ_R are shown in Table IV for the three sulfate crystals at a temperature in the middle of the range of the fast ion conducting phase. In the last column of Table IV τ is compared with the free rotor time, τ_{FR}, defined as

$$\tau_{FR}\ (41^o) = (41^o/360^o) \times 2\pi(I/kT)^{\frac{1}{2}} \qquad (2)$$

where τ_{FR} (41^o) is the time for a free rotor to travel 41^o which is the relevant time for a comparison with τ of Eq. (1) (17). Present values of τ/τ_{FR} are close to the reported value, $\simeq 4$, for free diffusion liquids including some plastic crystals (17). Plastic phases are normally associated with a large heat of transition. This is true for the high conducting sulfates, see Table I, which show values almost more than three times larger than the heat of fusion (3). The elastic constants, reported from a Brillouin scattering study of fcc Li_2SO_4, also give results typical for a plastic material (14,18).

Table IV Reorientational broadening and time compared to the free rotor time in three fast ion conducting crystals

	T (K)	Γ_R (cm^{1})	τ ($10^{-12}s$)	$\tau/\tau_{FR}(41^\circ)$
Li_2SO_4 (a)	993	4.8	1.1	3.8
$LiNaSO_4$	841	2.7	2.0	6.0
$LiAgSO_4$(a)	792	4.5	1.2	3.5

(a) Ref. 7

For low conducting hexagonal Na_2SO_4, however, no excess broadening was found in the corresponding temperature range, see Fig. 2b. Thus, plastic behavior and rotation characteristics seem to be the general attribute of fast ion conducting sulfates and are not due to the high temperature at which these phases of high conductivity exist.

If the transition into the high conducting phase is associated not only with rotational motion of the sulfate ion, as has now been observed, but also with a suggested coupling between the reorientational motion and fast ion diffusion (13), then a similar temperature dependence of the two processes may be expected. To make a comparison we therefore assume an Arrhenius behavior of the reorientational contribution

$$\Gamma_R = Ae^{-E/kT} \qquad (3)$$

where E is the activation energy necessary for reorientations and A is a constant. In Fig. 3 results for $\log\Gamma_R$ are plotted vs. 1/T and previous results of Li_2SO_4 and $LiAgSO_4$ are also included (7). The activation energies obtained for Li_2SO_4, $LiNaSO_4$ and $LiAgSO_4$ are 0.40, 0.86 and 0.72 eV, respectively, which are comparable to the activation energies of cation diffusion (see Table I). In fast ion conducting sulfates the activation energies of cation diffusion are significantly higher than in other solid electrolytes (e.g. in α-AgI the activation energy is only ≈ 0.1 eV (19)). If there is an interaction between sulfate ion reorientation and cation diffusion, then the high values for cation diffusion may be explained by the also high activation energies for sulfate ion reorientations obtained in the present study.

ACKNOWLEDGMENT

We thank Professor A. Lundén for alerting us to this interesting problem and for helpful discussion. Financial support from Wilhelm och Martina Lundgrens Vetenskapsfond, Adlerbertska Forskningsfonden and the Swedish Natural Science Research Council is gratefully acknowledged.

REFERENCES

1. A. Lundén, A. Bengtzelius, R. Kaber, L. Nilsson, K. Schroeder and R. Tärneberg, Solid State Ionics 9/10 (1983) 89.

2. L. Nilsson, Ph.D. thesis, Chalmers University of Technology, Göteborg, Sweden (1981).

3. K. Schroeder and C.A. Sjöblom, High Temp. High Pressures 12 (1980) 327.

4. D. Teeters and R. Frech, Phys.Rev. B, 26 (1982) 5897.

5. R. Frech and E. Cazzanelli, Solid State Ionics 9/10 (1983) 95.

6. R.W. Impey and M.L. Klein, J. Phys.C. 17 (1984) 3941.

7. L. Börjesson and L.M. Torell, Phys. Rev. B (in press)

8. A.-M. Josefson and A. Kvist, Z. Naturforsch. 24a (1969) 466.

9. A. Kvist, A. Bengtzelius and A. Schiraldi, in A.N. Sherwood, A.K. Chadwick, W.M. Muirand and F.L. Swinton (eds), Diffusion Processes 2, 523 (Gordon and Breach, London 1971).

10. M.A. Careem and B.E. Mellander, Solid State Ionics 15, (1985) 327.

11. A. Kvist and A. Lundén, Z, Naturforsch 20a (1965) 235; 22a (1967) 208.

12. A.F. Polishchuk and A.K. Bogdanova, Russ. J. Phys. Chem. 51 (1977) 1195.

13. L. Nilsson, J.O. Thomas and B.C. Tofield, J. Phys. C13 (1980) 6441.

14. R. Aronsson, Ph. D. thesis, Chalmers University of Technology, Göteborg, Sweden (1983).

15. M.J. Delaney and S. Ushioda in Superionic Conductors, ed. M.B. Salamon (Springer, Berlin 1979)

16. M.H. Broker and M.A. Bredig, J. Chem. Phys. 58 (1973) 5319.

17. F.J. Bartoli and T.A. Litovitz, J. Chem. Phys. 56 (1972) 404; 56 (1972) 413.

18. R. Aronsson, H.E.G Knape and L.M. Torell, J. Chem. Phys. 77 (1982) 677.

19. A. Kvist and R. Tärneberg, Z. Naturforsch. 25a (1970) 257.

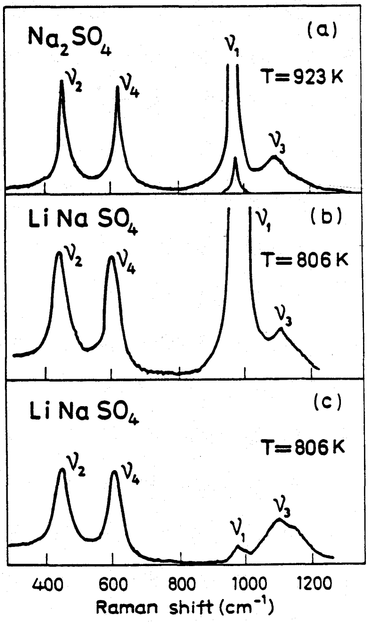

Fig. 1.

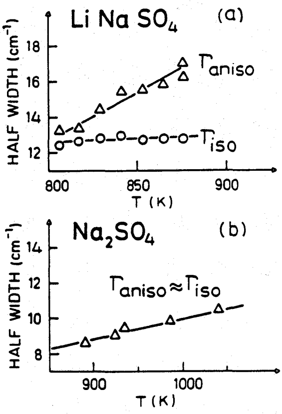

Fig. 2.

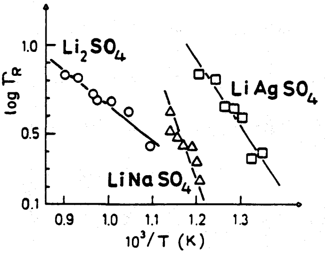

Fig. 3.

Fig. 1. Internal Raman sulfate modes in the
a) isotropic spectrum of Na_2SO_4 at 923 K
b) isotropic and c) anisotropic spectra of $LiNaSO_4$ at 806 K.

Fig. 2. Halfwidth vs temperature for the anisotropic and isotropic components of the symmetric internal sulfate mode ν_1 in
a) high conducting $LiNaSO_4$ and b) low conducting Na_2SO_4.

Fig. 3. Logarithmic plot of the reorientational contribution Γ_R (in cm^{-1}) to the bandwidth of the symmetric internal sulfate mode in three fast ion conducting sulfates.

DOI: 10.1149/198601.0029PV

VISUAL SIMULATION OF MOLTEN Li_2BeF_4 BY MOLECULAR DYNAMICS

Masuhiro Mikami* and Kazuo Furukawa**

*Scientific System Development Dept., Fujitsu Limited,
Shinkamata, Ota-ku, Tokyo, Japan 144.
**Institute of Research and Development, Tokai University,
Hiratsuka, Kanagawa, Japan 259-12.

Abstract

A new computer "visual simulation" which efficiently uses coordinates and velocities to represent structure and ionic motion in liquids is presented. As an initial try, visual simulation using molecular dynamics was applied to molten Li_2BeF_4 and $LiBeF_3$ to clarify the salts' liquid structure and their ionic dynamics. New information about liquid structure and ionic dynamics was obtained from the simulation as follows. There are many clusters such as monomers (BeF_4) and dimers (Be_2F_7) in molten Li_2BeF_4. On the other hand, there is a network structure in molten $LiBeF_3$. The diffusion coefficient of F ions in molten Li_2BeF_4 is larger than that of molten $LiBeF_3$. This is explained by the differences in liquid structure between the two salts.

1. Introduction

It has been 15 years since the application of the results of computer simulation of simple liquids [1] to molten salts has begun. During these 15 years, computer simulations have largely contributed to the development of molten salts chemistry by giving new information and interpretation about structure and transport phenomena in liquids [2] [3].

However, previous computer simulations do not fully utilize their output data, which consists of coordinates and velocities of all the particles in the system. Therefore, in this work, a new computer "visual simulation", which efficiently uses coordinates and velocities to represent structure and ionic motion in liquids is presented.

Previously, limited graphical representations were created, such as stereoscopic figures of liquid structures or trajectory figures of atomic motion projected on a plane by wire frame models. But it was difficult to produce a more realistic animation of structure and ionic motion in a liquid by three dimensional computer graphics with shading and highlights [4] because of limitations in computer technology. Recent developments in computer technology, such as a supercomputer capable of performing hundreds of millions of floating point operations per second (MFLOPS) and high speed graphics technology now enables us to produce these kinds of animated films.

As an initial try, visual simulation using molecular dynamics was applied to molten Li_2BeF_4 and $LiBeF_3$ to clarify the salts' liquid structure and their ionic dynamics.

2. Molecular Dynamics Simulations

Molecular dynamics simulations were performed under the conditions shown in table one. An initial configuration of 150 Li_2BeF_4 molecules (or 210 $LiBeF_3$ molecules) was taken from a crystal structure. The temperature of the system was increased to the desired temperature by making small, random velocity changes during the first 10000 integral time steps in the trajectories, which were then continued for a total of 20ps (20000 integral time steps). The computation time per time step was about 0.48 seconds on the FACOM VP-200 supercomputer (570 MFLOPS). This computation speed was 15 times faster than that of the current fastest general purpose computer, the FACOM M380 (9 MFLOPS).

The forces on the ions were calculated from the Born-Mayer-Huggins function. The parameter of the repulsion term adopted the Busing's values (model 2) which were determined for crystal Li_2BeF_4 [5]. The coulombic force term on ions was calculated using Ewald's summations ($R_{cut}=L/2$, $n<27$, $\alpha \cdot L=6$, where L is the edge length of the cubic box).

3. Visualization of Liquid Structure and Ionic Motion

Liquid structure and ionic motion in the molten Li_2BeF_4 and $LiBeF_3$ was visualized by means of the painter's algorithm and trapezoidal approximation, as well as other high speed graphics techniques incorporating shading and highlights (see [4]), using the three dimensional coordinates of the ions in the cubic box at each integral time step. A snapshot of the liquid structure of molten Li_2BeF_4 is shown in figure one. Video tapes of ionic motion in molten Li_2BeF_4 and $LiBeF_3$ were produced using the computer system described in figure two.

4. Results and Discussion

4.1 Pair Correlation Function

In table two, the first peak positions are shown together with the corresponding experimental values by Vaslow and Narten [6]. Though the peak positions obtained by molecular dynamics are shorter than the experimental ones by 0.03-0.06 angstroms, the agreement between molecular dynamics results the the experimental ones are very good.

In figures three and four, the pair correlation functions for unlike ion pairs and like ion pairs are shown together with their corresponding running coordination numbers. There are no observed differences between the pair correlation functions for unlike pairs for molten Li_2BeF_4 and for $LiBeF_3$. However, in the case of the functions for like ion pairs (F-F pairs, Be-Be pairs), the second peak position of the pair correlation function in Li_2BeF_4 is shifted by 0.02nm to the right. These facts suggest that the liquid structure over a long range for Li_2BeF_4 differs from the structure for $LiBeF_3$.

4.2 Coordination Number

In figure five, the distribution function of the number of F ions located around Be ions with radius R_n (where R_n is the distance where a pair correlation function crosses unity after the first peak, as in table three) is shown. The average value is 3.86 in molten Li_2BeF_4 and 3.85 in molten $LiBeF_3$. The proportion of coordination number 4 is 80 percent for both Li_2BeF_4 and $LiBeF_3$. In figure six, the distribution function of the number of Be ions located around F ions with R_n is shown. The proportion of coordination number 2 is 16% in Li_2BeF_4 and 35% in $LiBeF_3$. The proportion of coordination number 1 is 66% is Li_2BeF_4 and 58% is $LiBeF_3$. These facts suggest that there are monomers (BeF_4) in molten Li_2BeF_4 but that in the case of $LiBeF_3$ a network structure exists.

4.3 Angular Distribution

For a more detailed description of the short-range structure, an angular distribution function [7] is defined as

$$P(\theta) = n(\theta) \,/ \int_0^{\pi} n(\theta) d\theta$$

where $n(\theta)$ is the number of ion pairs located around an ion within R_n at an angle of θ . In figure seven, the angular distribution functions around a Be ion are shown. The angle of F-Be-F distributes sharply about a center of 104 degrees, which is close to the central angle of a regular tetrahedron. This suggests that F ions coordinate around Be ions in a regular tetrahedron arrangement. The angle of Be-Be-Be widely distributes around a center of 100 degrees, which is close to the vertex angle of a pentagon (108 degrees).

4.4 Rings and Clusters

For a more detailed description of the long range structure, topological analysis was performed. The "ring" shown in figure eight is defined as the minimum circle formed by Be-F pairs which are connected with a distance of 0.22nm. For example, a 3-membered ring consists of three Be ions and three F ions. The "cluster" showing in figure nine is defined as an ionic complex that is formed by Be-F pairs also connected within 0.22nm where, in this case, F ions on the outside of the complex connect to only one Be ion.

In table four, the number of rings existing in a basic cell are shown. These numbers were averaged over 150 ensembles at 0.02 picosecond intervals. In molten Li_2BeF_4 the 5-membered ring is most populous. The largest ring is a 30-membered one. There are, in all, about 19 rings in molten $LiBeF_3$. These analyses were confirmed by the use of computer graphics.

In figure 10, pictures of rings existing in molten $LiBeF_3$ are shown. On the other hand, there are few rings in molten Li_2BeF_4. It was observed, by using computer graphics, that the network structure disappears in the case of Li_2BeF_4. In table five, the number of clusters in a basic cell is shown. There are about 14 monomers (BeF_4) and about 5 dimers (Be_2F_7) in molten $LiBeF_3$. However, in molten Li_2BeF_4 there about 40 monomers and 14 dimers, as many as 3 times as in molten $LiBeF_3$.

It was observed that there are many clusters in molten Li_2BeF_4 by computer graphics. In figure 11, pictures of clusters in molten Li_2BeF_4 are shown.

4.5 Diffusion Coefficient

In table six, the diffusion coefficients of each ion at 1120 degrees K, obtained from mean square displacement, are shown together with their corresponding experimental results [8]. The diffusion coefficients in molten Li_2BeF_4 are larger than those for molten $LiBeF_3$. This can be explained from the differences in liquid structure between molten Li_2BeF_4 and $LiBeF_3$. That is, there are network structures in molten $LiBeF_3$, but in molten Li_2BeF_4 there are many clusters but few network structures. To make sure that a small complex of ions moves more easily that a large one, the mean square displacements of Be ions and F ions, which are members of monomers (BeF_4), and one of Be ions and F ions which are not members of monomers were calculated. In figure 12, the mean square displacements of Be ions and F ions in molten $LiBeF_3$ are shown. The displacements of Be and F ions which are members of monomers are larger than ones which are not members of monomers. This proves that a small complex moves more easily than a large complex. In figure 13, the mean square displacements of Be ions and F ions is molten Li_2BeF_4 are shown. Though the displacements of the ions which are monomer members are larger than one which are not, the differences are not remarkable. This is explained from the fact that 30 percent of all Be ions in a basic cell of Li_2BeF_4 are the members of monomers, and network structures are few.

4.6 Relative Velocity Auto Correlation Function

To clarify the ionic dynamics in molten Li_2BeF_4 and $LiBeF_3$, an auto-correlation function of relative velocity (RVAF) between a central ion and ions located around that ion with R_n was calculated.

In figure 14, relative velocity auto-correlation functions for Be-Be pairs are shown. In the same figure, V_r is the relative velocity, V_t is the transverse component of V_r ($V_t = u_r \times V_r$, where u_r is the unit direction vector from a central ion to the surrounding ion), and V_l is the longitudinal component of V_r ($V_l = u_r \cdot V_r$). Though the longitudinal part of the RVAF in molten Li_2BeF_4 vibrates, in its cosine form, with a period of 0.04ps over 0.4ps, $LiBeF_3$ deforms over 0.12ps. This is consistent with the fact that 26 percent of all Be ions in the basic cell of molten Li_2BeF_4 are member of dimers (Be_2F_7). In the case of $LiBeF_3$, 54 percent of all Be ions in the basic cell are members of dimers (Be_2F_7). This suggests that Be_2F_7, with a lifetime over 0.4ps exists in molten Li_2BeF_4, and the dimer vibrates in stretching mode.

In figure 15, RVAFs for Be-F pairs are shown. A remarkable difference between the longitudinal part and the transverse part of the the RVAF is not observed. Their correlation is weaker than that for Be-Be pairs. This suggests that F ions located around Be ions may rotate around the Be ions. To observe such a motion, a videotape of ionic motion was produced using the computer system described in figure one. This video tape will be shown at the 5th International Symposium on Molten Salts.

5. Conclusion

We have presented the first visual simulation of molten salts Li_2BeF_4 and $LiBeF_3$. The information about the liquid structure and dynamics behavior of the salts obtained from the visual simulation was as follows.

(1) There are many clusters such as BeF_4 and Be_2F_7 in molten Li_2BeF_4. 50 percent of all Be ions in the basic cell are members of monomers and dimers.

(2) There are network structures in molten $LiBeF_3$. Five-membered rings comprise the most abundant of these in the basic cell, numbering about six. 60 percent of all Be ions in the basic cell are the members of rings. On the other hand, only 11 percent of all Be ions in the basic cell are members of monomers or dimers.

(3) The diffusion coefficient of F ions in molten Li_2BeF_4 is larger than that for $LiBeF_3$. This is consistent with experimental results and is due to the difference in liquid structure between molten Li_2BeF_4 and $LiBeF_3$.

We think that there are still a few problems to solve, as follows:

(1) It is necessary to refine the pair potential function and its parameters to provide better agreement with experimental results, including a discussion of the failure in the pair potential [9].

(2) It is necessary to develop techniques which more effectively and clearly demonstrate the characteristics of ionic motion in a liquid.

If these problems are resolved, visual simulation can serve to help understand the dynamical behavior and various properties of liquids at any temperature and pressure. For example, the results of this work may be applied to silicates because of the similarity between $MgO-SiO_2$ systems and $LiF-BeF_2$ systems [10].

Acknowledgments

We would like to thank Prof. Isao Okada and Dr. Yoshio Tago for stimulating discussions. We would also like to thank Takamitsu Okada, Douglas M. Lerner, and Mikio Sasaki for producing the animation video tape of ionic motion.

References

[1] A. Rahman: Phys. Rev., 136(1984)A405; L. Verlet: ibid., 159(1967)298.

[2] L. V. Woodcock: Chem. Phys. Letters, 10(1971)257.

[3] J. W. E. Lewis, K. Singer and L. V. Woodcock: J. Chem. Soc. Faraday Trans. II 71(1975)301.

[4] N. Max: Computer Graphics, 13(1979)165.

[5] W. R. Busing: J. Chem. Phys., 57(1972)3008.

[6] F. Vaslow and A. H. Narten: J. Chem. Phys., 59(1973)4949.

[7] I. Okada, et. al.: Chem. Phys. Letters, 100(1983)436.

[8] T. Ohmichi, H. Ohno and K. Furukawa: J. Phys. Chem., 80(1976)1628; H. Ohno, et. al.: J. Chem. Res. (M) 2046, (S) 158 (1978).

[9] K. Furukawa and H. Ohno: Proc. 3rd International Symposium on Molten Salts, Proc. 81-9(1981)36.

[10] K. Furukawa and H. Ohno: Trans. JIM, 19(1978)553.

- Ensemble ------ micro canonical system

- Number of ions in the basic cell
  Li_2BeF_4 --- 1050 ions (300Li, 150Be, 600F)
  $LiBeF_3$ --- 1050 ions (210Li, 210Be, 630F)

- Size of the basic cell

Liquid	Temp/K	L / nm	ρ / g·cm^3
Li_2BeF_4	673	2.31003	2.064
	873	2.34257	1.979
	1120	2.38183	1.874
$LiBeF_3$	828	2.30590	2.009
	873	2.31436	1.987
	1120	2.36315	1.866

L is the edge length of a basic cell.

Table 1 Conditions of Molecular Dynamics simulations.

Pair	Li_2BeF_4 : 828 K	$LiBeF_3$: 673 K
Li-Li	0.296 (----)	0.292 (----)
Be-Be	0.312 (----)	0.308 (----)
F-F	0.252 (0.256*)	0.252 (0.256*)
Li-Be	0.306 (----)	0.310 (----)
Li-F	0.178 (0.185*)	0.180 (0.185*)
Be-F	0.154 (0.158*)	0.156 (0.158*)

Table 2 Mean distances of ion pair in molten Li2BeF4 and LiBeF3.
(*) F.Vaslow and A.H.Narten, J.Chem.Phys., 59 (1973) 4049

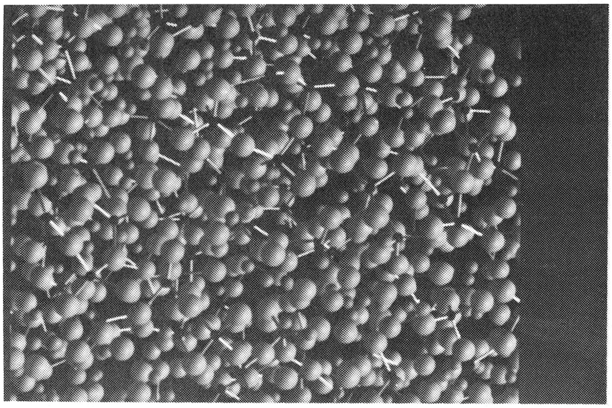

Fig. 1 Snapshot of molten Li2BeF4 by computer graphics ; the small balls are Be ions, the medium ones are Li ions, the big ones are F ions, the sticks join Be ions and F ions where their separation is within 0.22 nm.

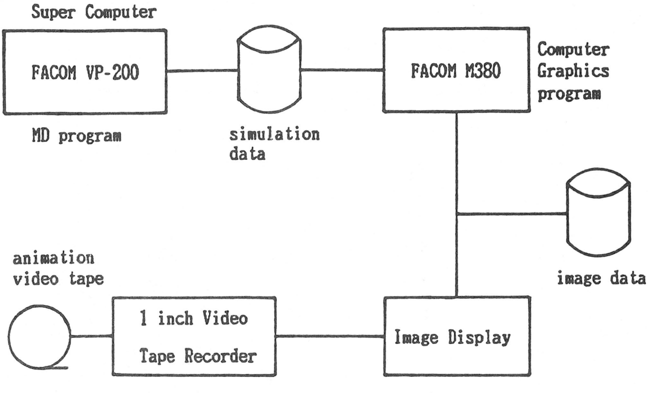

Fig. 2 Computer system configuration for Visual Simulation.

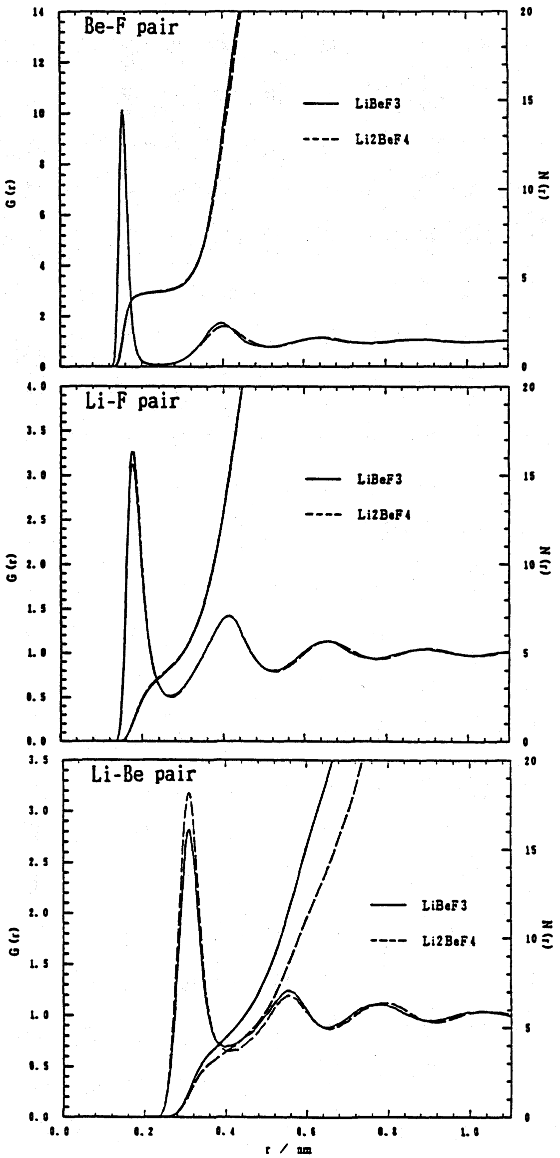

Fig. 3 Pair correlation functions and running coordination numbers of unlike ion pairs in molten Li2BeF4 and LiBeF3.

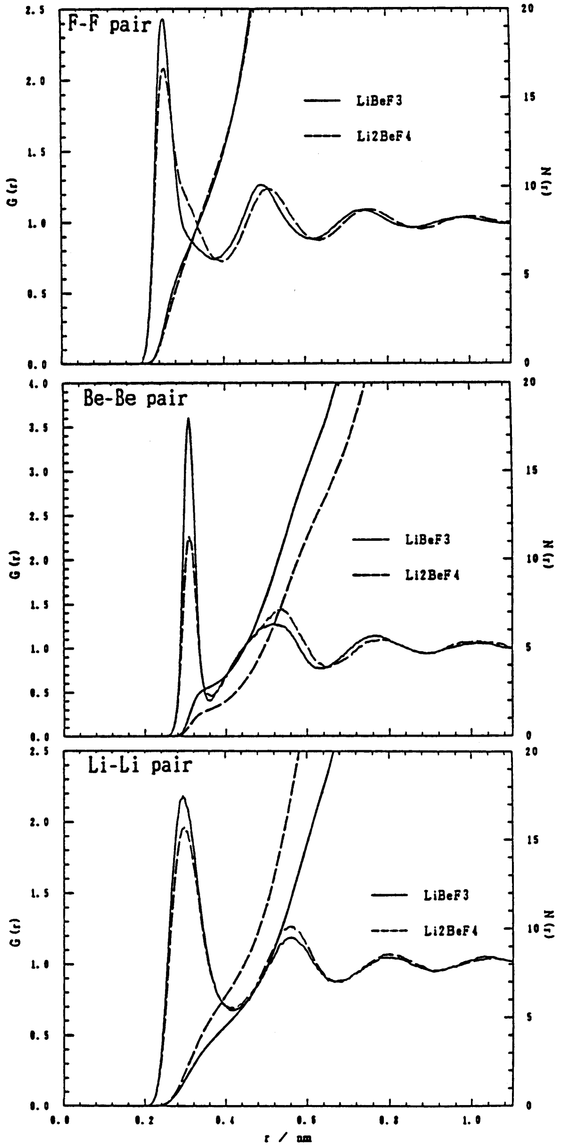

Fig. 4 Pair correlation functions and running coordination numbers of like ion pairs in molten Li2BeF4 and LiBeF3.

ion pair	$LiBeF_3$	Li_2BeF_4
Li-Li	0.365	0.362
Be-Be	0.338	0.337
F-F	0.300	0.328
Li-Be	0.360	0.361
Li-F	0.220	0.221
Be-F	0.187	0.187

Table 3 Upper limit distances (Rn) of nearest neighbor of ion pair.

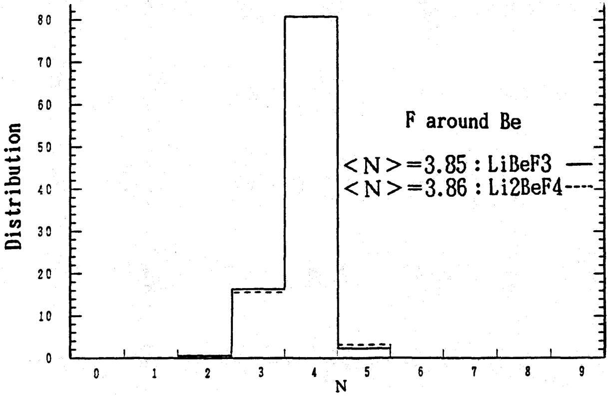

Fig. 5 Distribution functions of the number of F ions located around Be ion within Rn.

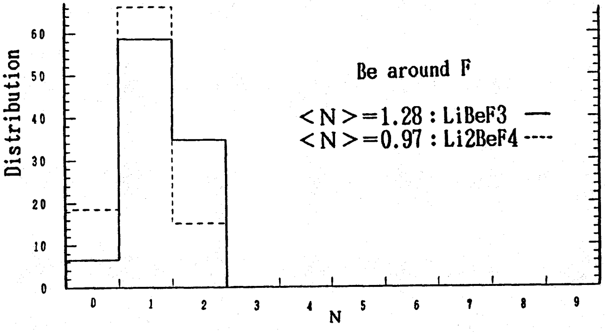

Fig. 6 Distribution functions of the number of Be ions located around F ion within Rn.

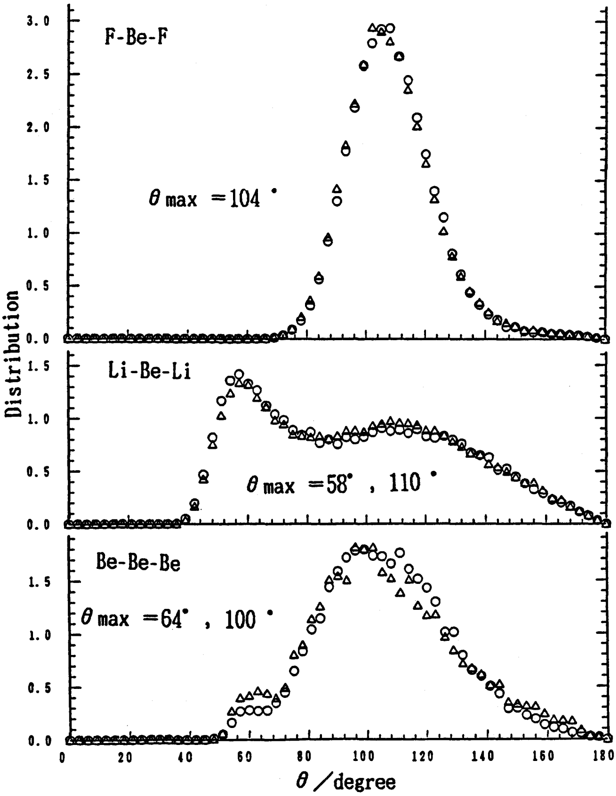

Fig. 7 Distribution function of angle around Be ion
△ : Li_2BeF_4, ○ : $LiBeF_3$

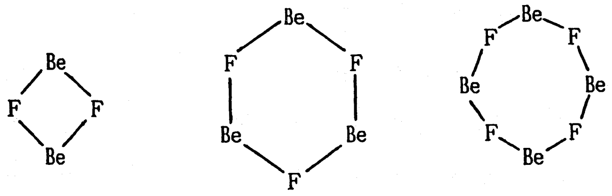

2-membered ring 3-membered ring 4-membered ring

Fig. 8 Rings formed by Be-F pairs which are connected within a distance of 0.22 nm.

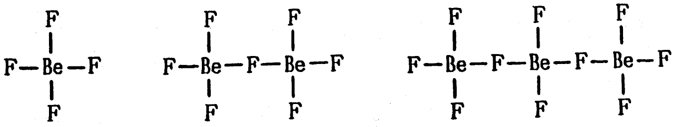

BeF_4 Be_2F_7 Be_3F_{10}

Fig.9 Clusters formed by Be-F pairs connected within 0.22nm where F ions on the outside of the complex connects to only one Be ion.

Kind of Ring	$LiBeF_3$	Li_2BeF_4
2-membered ring	0.36	0.58
3-membered ring	1.48	0.26
4-membered ring	3.24	1.18
5-membered ring	6.02	0.52
6-membered ring	2.44	0.007
7-membered ring	1.48	0.0
8-membered ring	0.63	0.0
9-membered ring	0.78	0.0
total	18.90	2.55

Table 4 The numbers of Rings existing in a basic cell.

Kind of Cluster	$LiBeF_3$	Li_2BeF_4
BeF_4	13.70	39.30
Be_2F_7	4.82	13.70
Be_3F_{10}	2.05	5.14
Be_4F_{13}	0.17	2.68
total	22.50	66.70

Table 5 The numbers of Clusters existing in a basic cell.

Temp.	ion	Li_2BeF_4	$LiBeF_3$
1120 K	Li	$6.1X10^{-9}$	$4.7X10^{-9}$
	Be	$2.6X10^{-9}$	$1.5X10^{-9}$
	F	$3.9X10^{-9}$	$2.4X10^{-9}$
900 K	F (exp.*)	$3.0X10^{-8}$	$3.0X10^{-9}$

* Ref. [8]

Table 6 The diffusion coefficients (m^2s^{-1}) of each ion at 1120 K obtained from their corresponding mean square displacements together with the experimental results at 900 K.

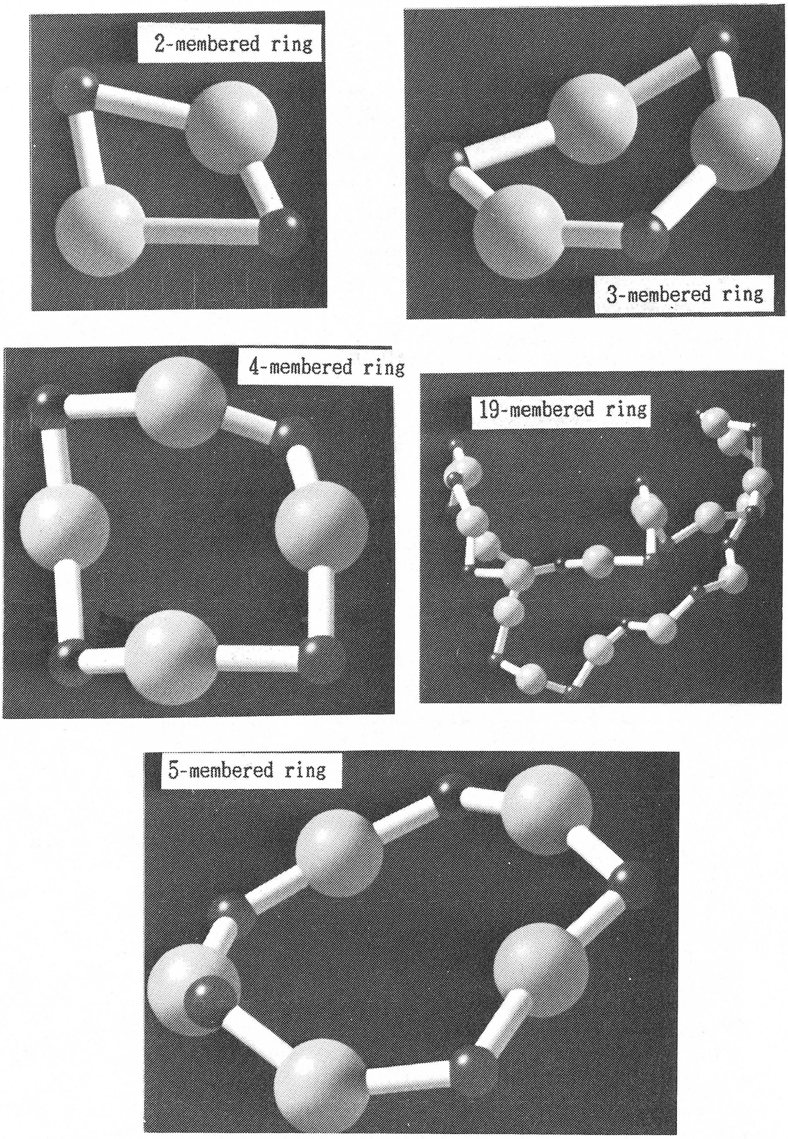

Fig. 10 Pictures of Rings existing in molten LiBeF3 : the small balls are Be ions, the big ones are F ions.

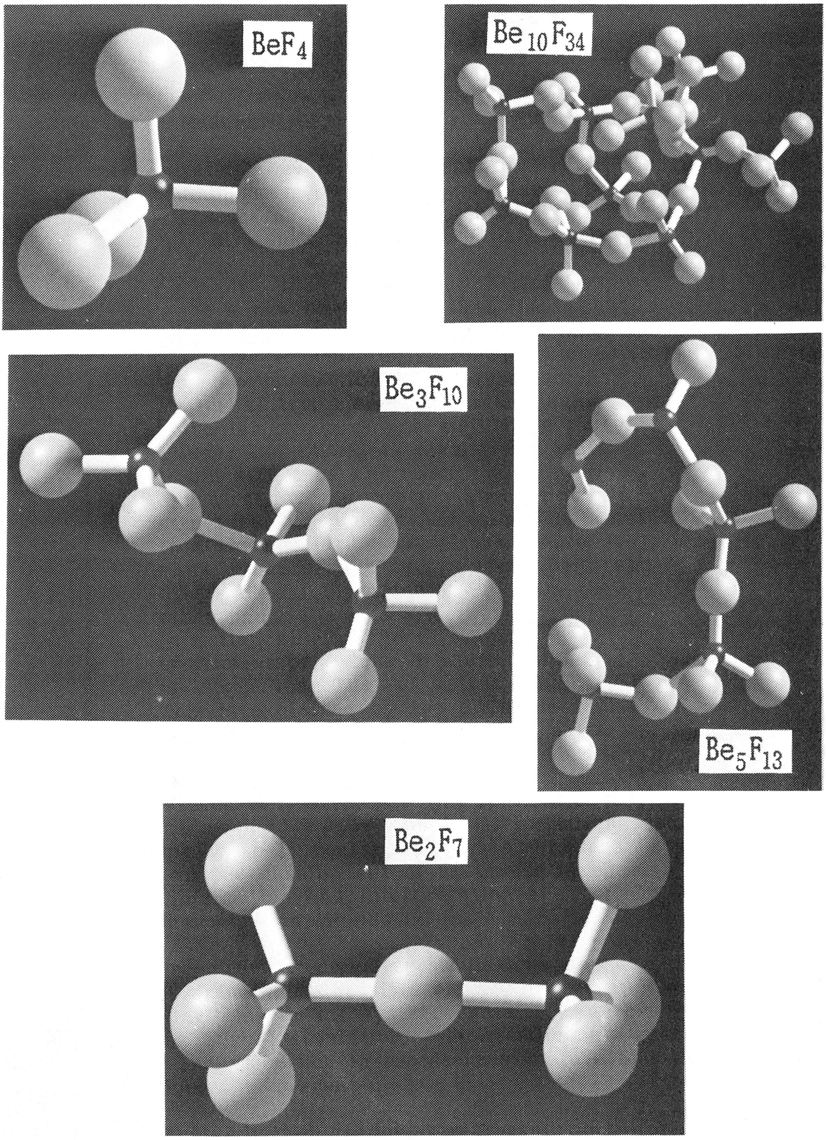

Fig. 11 Pictures of Clusters existing in molten Li2BeF4 : the small balls are Be ions, the big ones are F ions.

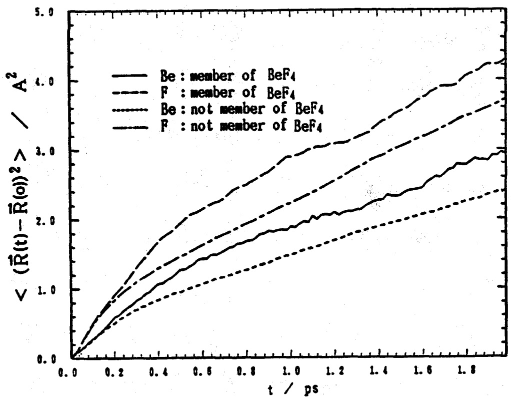

Fig. 12 The mean square displacements of ions in molten LiBeF3.

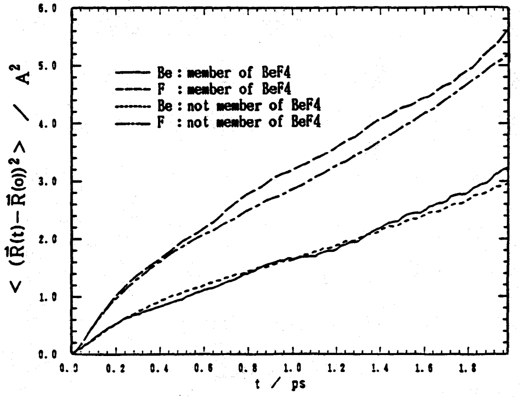

Fig. 13 The mean square displacements of ions in molten Li2BeF4.

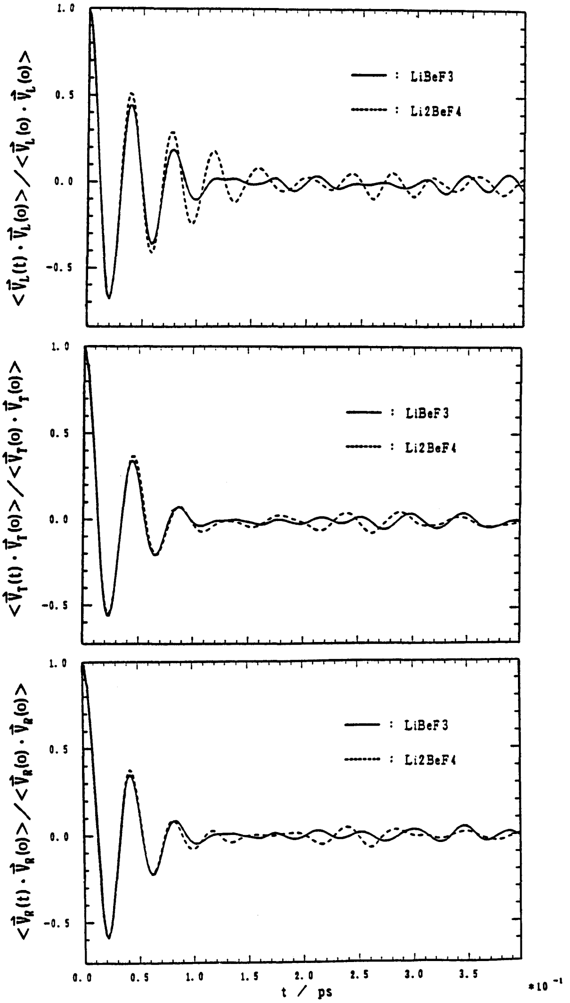

Fig. 14 The relative velocity autocorrelation function for Be-Be pair.

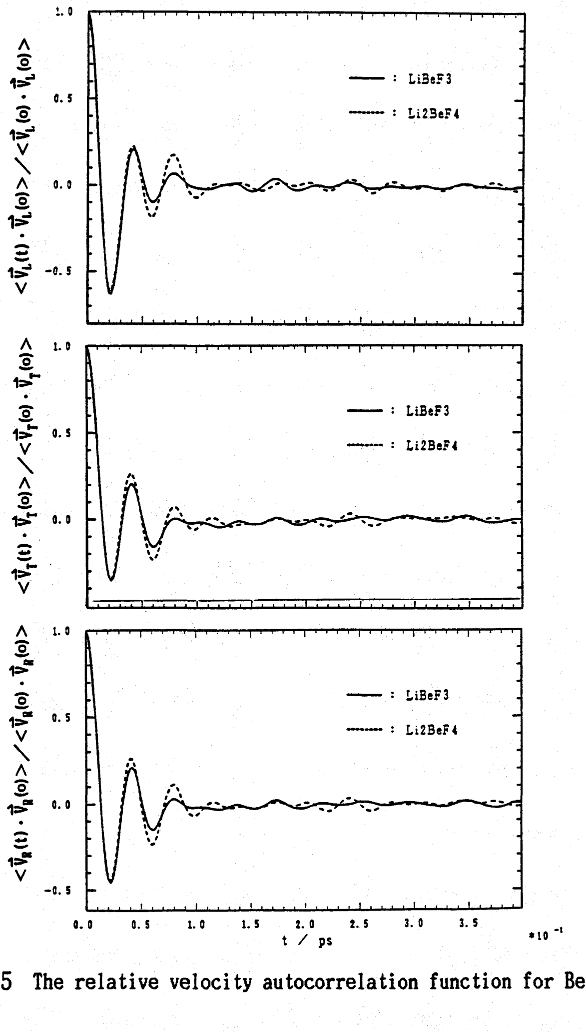

Fig. 15 The relative velocity autocorrelation function for Be-F pair.

DOI: 10.1149/198601.0049PV

FRACTAL DIMENSIONALITIES OF BROWNIAN TRAJECTORIES AND BROWN ISOSETS IN SUPERIONIC AND MOLTEN Ag_2S*

P. Vashishta, I. Ebbsjö,† and R. K. Kalia
Materials Science and Technology Division
Argonne National Laboratory
Argonne, IL 60439

and

S. W. de Leeuw
Department of Physics
Ohio University
Athens, OH 45701

ABSTRACT

Fractal behavior is observed in molecular dynamics simulations of ionic trails and isosets of Brown functions in Ag_2S. For diffusing silver ions in the superionic state and silver and sulfur ions in the molten phase, the Hausdorff dimensionalities are found to have universal values of 2 and 0.5, respectively.

I. INTRODUCTION

Atomic self-motion in fluids is conventionally characterized by the velocity autocorrelation function and the constant of self-diffusion, which are functions of thermodynamic states of the system. Associated with these properties are two universal aspects of single-particle motion which deal with the fractal behavior of ionic trails and isosets of Brown functions. Their Hausdorff dimensionalities are expected to have universal values of 2 and 1/2, respectively (1).

II. COMPUTATIONAL DETAILS

We have investigated the fractal behavior associated with ionic self-motion in the superionic conductor Ag_2S by the molecular dynamics (MD) method. The construction of interionic potential for MD calculations is approached from a phenomenological point of view

---

*This work supported by the U.S. Department of Energy, BES-Materials Sciences, under Contract W-31-109-ENG-38.

and the effective interaction is taken to be

$$V_{ij}(r) = A_{ij}\left(\frac{\sigma_i + \sigma_j}{r}\right)^{n_{ij}} + \frac{Z_i Z_j e^2}{r} - \frac{1}{2}\,\frac{\left(Z_i^2\alpha_j + Z_j^2\alpha_i\right)e^2}{r^4}, \qquad (1)$$

where σ_i, Z_i and α_i are the radii, effective charges, and electronic polarizabilities of ions, respectively. The three terms in Eq. (1) describe the size related ionic repulsion, the Coulomb interaction between ions, and the charge-dipole interaction. We have taken all A_{ij} and n_{ij} to be the same (A_{ij} = A and n_{ij}=n) and the resulting constants in Eq. (1) can be determined from the low-temperature crystal structure, the cohesive energy, and the bulk modulus of Ag_2S (2). Based on earlier calculations on AgI we take n=7. The remaining constants in Eq. (1) are $\alpha_{Ag} = 0$, $\alpha_S = 6.52Å^3$, $Z_{Ag} = 0.45$, $Z_S = -0.90$, $\sigma_{Ag} = 0.61Å$, $\sigma_S = 2.1Å$, and A = 0.01502. Figure 1 shows the potential functions for S-S, Ag-S, and Ag-Ag.

Molecular dynamics calculations were performed on a system of 384 ions (128 S + 256 Ag) at a fixed number density of $5.233\text{x}10^{22}$ cm^{-3}. The long range Coulomb contributions to potential energy and forces were calculated by the Ewald method. At each temperature the system was first thermalized for several thousand MD time steps and then it was run for another 60,000 time steps.

RESULTS

MD calculations in the superionic phase (T = 833K) reveal that the sulfur ions form a stable bcc lattice while the Ag ions diffuse among the tetrahedral (t) and octahedral (o) sites with a diffusion constant of $3.2\text{x}10^{-5}$ cm^2/sec. Figure 2 illustrates the bcc configuration of S ions as well as the tetrahedral (t) and octahedral (o) sites. MD results (2) for the temperature dependence of the diffusion constant of Ag are in excellent agreement with experimental measurements (4).

Figure 3 shows the partial pair-distribution functions $g_{SS}(r)$, $g_{SAg}(r)$ and $g_{AgAg}(r)$ in the superionic phase at T = 833K. The first peak in g_{SS} has a co-ordination of 14 (8+6) whereas the (S,Ag) correlation function peak shows a coordination of 8. Charge neutrality prevails around 5.7Å where g_{AgAg} and g_{SS} have coordinations of 28 and 14, respectively.

X-ray diffuse scattering measurements (3) in the superionic phase reveal anisotropic discs of intensity in the vicinity of wavevector Q_o = (1.6, 1,0). MD calculations with the model potential of Eq. (1) show that this is due, in part, to the diffusive motion of Ag ions between tetrahedral and octahedral sites along [100] channels (2). The agreement between MD results (2) and transport measurements (4) of the diffusion constant of Ag and also between the calculated intensities and x-ray diffuse scattering experiments (3) show the validity of the model potential of Ag_2S.

Fractal behavior of ionic trails is investigated by calculating the length of MD trajectories of Ag and S ions. MD calculations provide the positions of ions at equally spaced time intervals Δt ($= 1\times10^{-14}$ sec) and since Δt is very small, it is assumed that the ions travel in a straight line during the interval Δt. The length of a trajectory, $L(\varepsilon)$, is measured as if with a pair of dividers of length ε and the end correction is included as a fraction of the step distance ε. The trail length $L(\varepsilon)$ is expected to scale as ε^{1-D} where D is the fractal dimension of ionic trails (1).

The isosets of ionic coordinates $x(t)$, $y(t)$ and $z(t)$, called Brown functions, are also expected to display fractal behavior (1). An isoset consists of times $t=\tau_0,\tau_1,\tau_2\ldots$at which $x(t)$ is equal to a given value x_0, and if x_0 is the origin of the coordinate system the instants of time $\{\tau_i\}$ constitute a zeroset. The gaps between successive values of $\{\tau_i\}$, $G_1=\tau_1-\tau_0$, $G_2=\tau_2-\tau_1\ldots G_i=\tau_i-\tau_{i-1}$ are given by a probability function $Pr(G>g)$ for finding a gap G of duration greater than a given value g. The behavior of $Pr(G>g)$ is expected to be (1)

$$P(g) \equiv Pr\ (G>g) \propto g^{-\overline{D}}\ , \tag{2}$$

where $\overline{D}$ is the Hausdorff dimensionality of Brown isosets. It is related to D by the simple relation

$$D = (1 - \overline{D})^{-1}. \tag{3}$$

Results in the superionic phase: The length $L(\varepsilon)$ versus ε for silver trails is shown in Fig. 4(a). Fractal behavior occurs over a large range of step distance, ε, and the slope (i.e., 1-D) of the straight-line segment on the logarithmic plot is found to be equal to -1, which implies that the fractal dimension D=2. The behavior of probability distribution function, $P(g)$, is shown in Fig. 4(b). The slope of the straight-line segment yields 0.5 for the fractal dimension of the Brown isoset of silver. The fractal dimensions D and $\overline{D}$ obey Eq. (3) and are the same as for a simple fluid even though the silver ions diffuse on octahedral and tetrahedral sites of the body-centered sulfur lattice.

Results in the molten phase: Unlike the superionic phase, sulfurs have a finite diffusion and silver and sulfur ions form an isotropic liquid. The variations of $L(\varepsilon)$ with ε for sulfur and silver are shown in Figs. 5(a) and (c). The fractal dimensions of ionic trails for both sulfur and silver ions are calculated to be 2. Since sulfur is doubly charged and has a much larger size, its diffusion coefficient and consequently the trails are smaller than those for silver. This results in slightly poorer statistics for

D. From Figs. 5(b) and (d) for the variation of P(g) with g, we determine $\bar{D}$=0.5 for both sulfur and silver ions. Our results confirm the universality of D and $\bar{D}$.

REFERENCES

1. B. B. Mandelbrot, The Fractal Geometry of Nature (Freeman, San Francisco, 1982).
2. P. Vashishta, I. Ebbsjö, R. Dejus and K. Sköld, J. Phys C 18, L291 (1985); see also A. Rahman and P. Vashishta in Physics of Superionic Conductors, ed. J. W. Perram (Plenum 1983), p. 93.
3. R. J. Cava, R. Reidinger and B. J. Wuensch, J. Solid State Chem. 31, 69 (1980).
4. R. L. Allen and E. J. Moore, J. Phys. Chem. 63, 223 (1959).

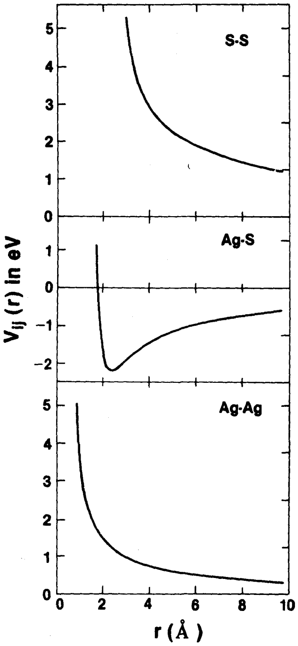

Fig. 1. Pair potentials for S-S, Ag-S, and Ag-Ag used in the MD calculations. The potentials are measured in units of $e^2/\text{Å} = 14.4$ eV.

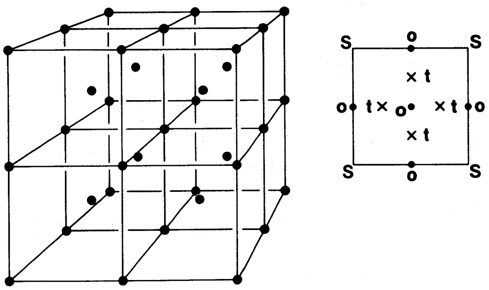

Fig. 2. BCC lattice structure of S ions in the superionic phase of Ag_2S. The silver ions diffuse among the tetrahedral (t) and octahedral (o) sites.

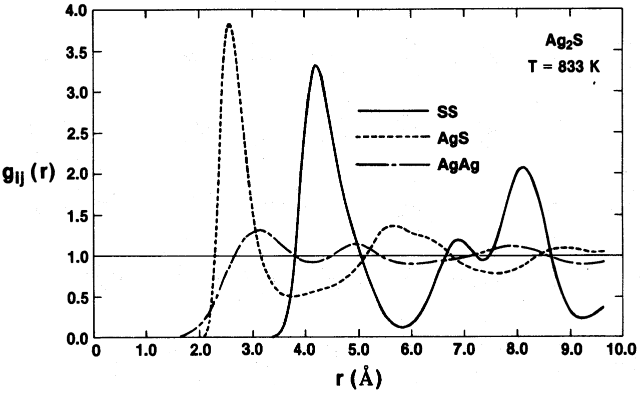

Fig. 3. MD results for partial pair-correlation functions in the superionic phase of Ag_2S. The first peaks of g_{SS} and g_{AgS} have coordinations of 14 and 8 respectively. Coordinations of (28) Ag-Ag and (14) of S-S around 5.7Å imply local charge neutrality at this distance.

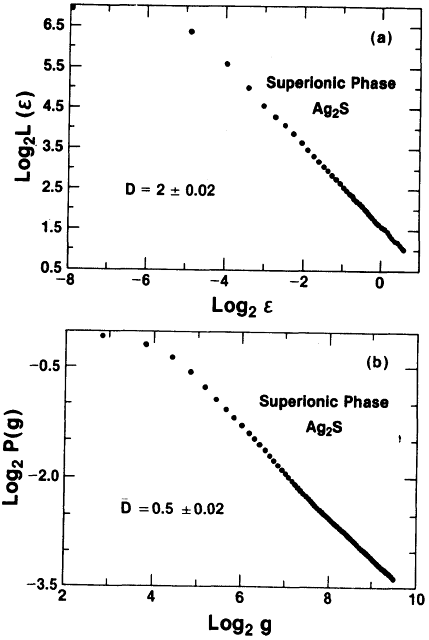

Fig. 4. a) Length dependence of Ag trails as a function of step distance ε in the superionic phase of Ag_2S. The straight line between $\varepsilon=2^{-5}$ to 1 shows that the fractal behavior persists over a large range of ε. The slope of this straight line yields a value of 2 for the fractal dimension of Ag trails.

b) Probability function for gaps in isosets of Ag. The straight-line segment shows a large range over which the fractal behavior is observed and the corresponding slope gives a value of 0.5 for the fractal dimension of Brown isosets of Ag.

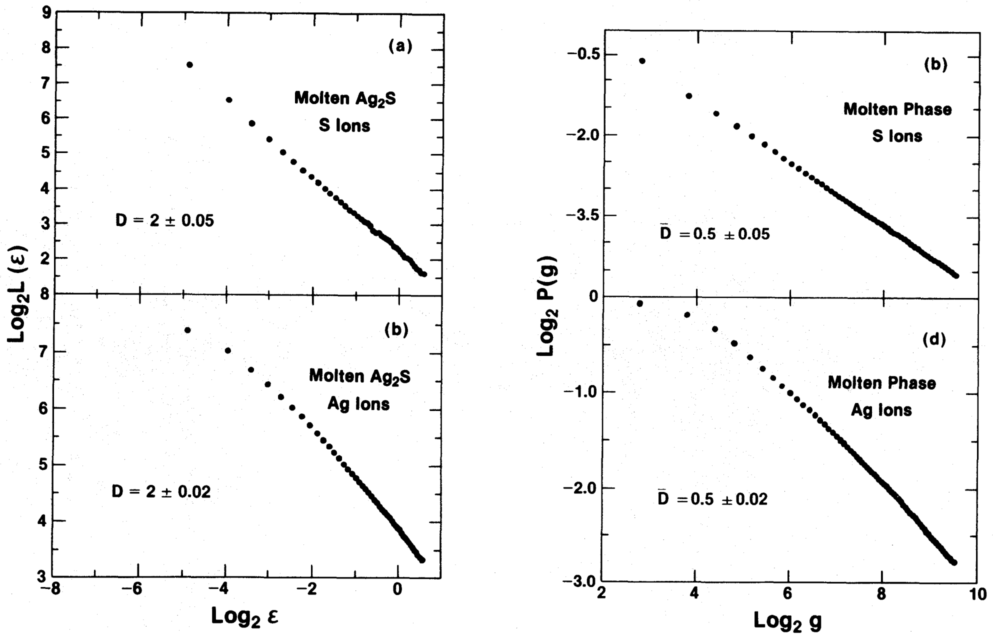

Fig. 5. The length L(ε) of ionic trails of a) sulfur and b) silver as a function of the step distance ε in the molten phase of Ag_2S. The fractal dimensions of trails is found to be 2 for both S and Ag. Figures 5(b) and 5(d) show the behavior of the probability function P(g) for S and Ag. The slopes of the straight-line segments in these logarithmic plots give 0.5 for the fractal dimension of Brown isosets.

DOI: 10.1149/198601.0057PV

NOVEL SIMULATIONS OF MOLTEN SALTS

J.H.R.Clarke

Chemistry Department, University of Manchester Institute of Science and Technology, Manchester M60 1QD U.K.

and

W.Smith

Theory and Computational Science Division, S.E.R.C. Daresbury Laboratory, Warrington WA4 4AD U.K.

ABSTRACT

It has long been assumed that the long range charge ordering in ionic liquids is a direct consequence of the strength and long range of the coulomb interactions. In this paper we demonstrate, using molecular dynamics computer simulation, that short range effective pair (SHREP) potentials can be used to reproduce the structural and transport properties of many molten salts. The thermodynamic properties of the ionic liquids can be obtained rather simply using first order perturbation theory. SHREP potential simulations of molten KCl, $SrCl_2$ and $NaAlCl_4$ generate structures and properties which compare favourably with the results of previous simulations and with experiment.

INTRODUCTION

The main aim of this paper is to demonstrate that the essential structural and dynamic features of molten salts are not a consequence of the long range coulomb interactions. Charge ordering, which was originally discovered by computer simulation studies [1] and which has now been observed in neutron diffraction measurements [2,3,4] as the familiar signature of ionic liquids, is reproduced to good accuracy using short range effective pair (SHREP) potentials with a range of about three ionic diameters. This work extends previous studies of molten potassium chloride [5] to SHREP potential simulations of molten strontium chloride and molten sodium tetrachloroaluminate. Each of these systems has been examined recently using diffraction techniques and also by computer simulation.

The development of an understanding of molten salts at the microscopic level depends on an important mixture of theory and experiment. While detailed experimental data on molten salt structure is now becoming available from neutron and X-ray scattering measurements, development of analytical theories is frustrated by the need to make simplifying and sometimes incorrect assumptions regarding the statistical mechanical behaviour of the system. Success has been limited to calculations on alkali halides using the hypernetted chain (HNC) [6] and mean spherical approximations (MSA) [7].

Computer simulation techniques, both Monte Carlo and molecular dynamics (MD), occupy an important position between theory and experiment. They can provide a complete numerical solution to the classical many body problem while avoiding many unnecessary assumptions. On the one hand they can be employed to evaluate theoretical predictions using simplified but well defined models for the particle interactions. On the other hand the aim can be to reproduce accurately the properties of a particular molten salt and to enhance the interpretation of experimental data. We are thus lead to the real current theoretical challenge - that of providing an accurate desription of particle interactions in a molten salt.

Substantial effort has been expended in the last 10 or 15 years in developing semi-empirical interaction potentials for molten salt simulations. To date all have been firmly based on the Born model in which the dominant interaction is the r^{-1} coulomb term. With few exceptions all these potentials require the use of lattice summation methods, in conjunction with the usual periodic boundary conditions, to overcome the divergence problem of the r^{-1} term. These methods are computationally expensive and impose severe practical limitations on the size of system. There is a variety of experimental evidence, however, which suggests that at long range there is almost complete cancellation of coulomb effects in molten salts. For instance it is possible completely to neglect the reciprocal space sums, which account for long range effects in the Ewald representations of the coulomb potential, without damaging the essential physics of the liquid [8]. These cancellation effects were also found in a recent approximate theoretical treatment of the hard sphere electrolyte [9]. In simulations of molten alkali halides it is found [10] that the force correlations describing the ion dynamics are dominated by contributions from the immediate neighbours. Indeed it was postulated many years ago that coulomb forces have little influence on dynamic properties in molten salts [11].

Aside from this practical evidence there are also theoretical objections to a rigid adherence to the Born model. The total potential energy Φ_T of a system of N interacting particles can be written as follows:

$$\Phi_T(N) = \Phi(2) + \Phi(3) + \Phi(4) + \ldots\ldots\ldots\Phi(N) \qquad \ldots\ldots\ldots(1)$$

where $\Phi(m)$ is the isolated m-body contribution to the total energy. To date it has been usual practise, in both computer simulations and theoretical studies, to assume that 3- and higher-body interactions are sufficiently weak so that their effects can either be neglected or incorporated in an *effective* pairwise additive interaction $\Phi_{eff}(2)$ so that

$$\Phi_T = \Phi_{eff}(2) \qquad \ldots\ldots\ldots(2)$$

While this may be a reasonable assumption for many non-ionic liquids, it would be surprising if the intense particle interactions in a molten salt did not give rise to significant non-pairwise additive effects, especially at short range. The most obvious of these is the first order induction energy due to ion polarisation. Although attempts have been made to take account of this effect by use of the shell model [12] the majority of simulations to date have made use of semi-empirical rigid ion effective pair potentials with parameters fitted using either low temperature crystal data [13] or gas-phase spectroscopic data [14]. If one compares results for simple ionic molten salts such as the alkali halides obtained using these different potentials, the structural differences turn out to be quite small and often within the limits of accuracy of the experimental data available for comparison. It can be regarded as fortuitous, however, that these models should be adequate as effective pair potentials in molten salts.

Simulations employing SHREP potentials are computationally highly efficient, enabling studies of systems containing more than 10000 particles such as are desirable for the simulation of mixtures or interfacial phenomena. Like the parent Born model these potentials are as yet still semi-empirical in basis. Their relative simplicity emphasises, however, the ***minimum*** requirements for the successful simulation of ionic liquids. Essential parameters are the unlike particle separations, r_0, at the respective potential energy minima, the curvatures of the potentials in the region of r_0 and the depths ϵ of the minima. All of these parameters can be obtained from gas phase spectroscopic data. This approach, coupled with more extensive experimental data, may provide a route to the empirical evaluation of specific short range many body interactions.

SHREP POTENTIALS

The idea underlying the use of Short Range Effective Pair potentials is that it is only necessary to consider interactions between *immediate* like and unlike neighbours, beyond which the potentials are smoothly and symmetrically truncated to zero. An important property of ionic interactions that must be retained in the model is the balance, at ***medium*** range, of attractions and repulsions between like and unlike particles respectively. Aside from this the only essential features are the distance parameters r_0 which in the case of unlike particles are the separations at the potential energy minima, and the curvatures of the potentials in the region of near neighbour separations. One particularly simple form of SHREP potential that we have used [5] is

$$E(r) = \epsilon(k,l)\left[A\left(\frac{r_0(k,l)}{r} \right]^n + \chi B \left[\frac{r_0(k,l)}{r}\right]^m\right] \qquad \ldots.(3)$$

where $A = m/(n-m)$, $B = n/(m-n)$. $\epsilon(k,l)$ and $r_0(k,l)$ are energy and distance parameters characterising the interaction between particles of species k and l. The switching parameter χ is set equal to -1 for particles of like charge and $\chi = +1$ for particles of unlike charge. It is convenient to add a term $(ar+b)$ to equation (3), where a and b are constants, in order to provide smooth truncation of the potential at, typically, $3r_0$. This modification has been shown to cause only minor distortions in the form of the potential [5].

The balance of like and unlike particle interactions appears partly (and automatically) in the stoichiometry of the sample but is also determined by the *relative* values of ϵ for the different pair types. It is well recognised that the depth of ion pair potential energy minima are orders of magnitude greater than kT. Consequently the absolute values of ϵ are not critical to the simulation as long as the condition is upheld that $\epsilon >> kT$. A much more important property is the force constant at r_0 (or, for like particles, the curvature of the interaction potential in the region of near neighbours) which for the simple SHREP potential are proportional to ϵ. These features determine the magnitude of structural *fluctuations* which are reflected in the sharpness of peaks in g(r) and the values of dynamic properties such as the diffusion coefficient.

The form of potential in equation (3) was used recently in simulations of molten potassium chloride [5] with n=8 and m=4. It is compared with the corresponding BHM potential in Fig.1. The value of r_0 is the same in both cases and the force constants are also very similar although the depths of the energy minima are quite different. It is important to note that the *ratios* of the unlike and like particle interaction energies are very similar for all distances corresponding to the most probable nearest neighbour separations (see Fig.1).

An alternative approach is to start with the full ionic potential of the Born-Huggins-Mayer form (with or without dispersion energy terms):

$$V(r)= \frac{q_i q_j}{4\pi\epsilon_0 r} + b \exp B(\sigma_i + \sigma_j - r_{ij}) \qquad \ldots(4)$$

and to truncate the long range interactions by multiplying with a function P(r)(a third order polynomial), so that

$$\begin{aligned} E(r) &= V(r) \quad ; \quad r < r_1 \\ E(r) &= V(r)\, P(r) \quad ; \quad r_1 < r < r_C \qquad \ldots\ldots(5) \\ E(r) &= 0 \quad ; \quad r > r_C \end{aligned}$$

and P(r) is chosen to be 1 at r_1, 0 at r_C and dP/dr = 0 at both r_1 and r_C. The simplest procedure is to identify r_1 with r_0.

For the simulations reported here we have used only the SHREP potential formulation given in equation (3).

DETAILS OF COMPUTER SIMULATIONS

Molecular dynamics simulations using the SHREP potentials have been carried out at constant volume on equilibrated samples of 500, 750 or 4000 particles using link cell coding to increase the efficiency of the computations. Equations of motion were integrated using the leapfrog forms of the Verlet algorithm for either constant energy or constant temperature (damped force) dynamics. The time step was $0.5*10^{-14}$ s. Details of the procedure with the simulations has been described elsewhere [5].

The full ionic calculations with the BHM potential were carried out using the program MDIONS from the SERC CCP5 program library. For 512 ions each time step consumed 2.65 s of CPU time on a CDC 7600 computer, compared to 0.8 s for 500 particles and 4.6 s for 4000 particles using the n-m SHREP potentials.

RESULTS AND DISCUSSION

1. *Molten Alkali Halides*

SHREP potential simulations of molten alkali halides are exemplified by the case of potassium chloride . The results at 1300 K preented here are compared with those generated using Born-Huggins-Mayer (BHM) potential with Tosi-Fumi parameters [1]. For the short range part of this potential the values of these parameters are very similar for K^+-Cl^-, K^+ -K^+ and Cl^--Cl^- interactions. To gain simplicity,therefore, the same values of r_0 and ϵ were used for each of the three types of interaction in the SHREP potential. The value of r_0 was 0.2589 nm which is the unlike ion separation at the minimum of the BHM potential. It has already been shown [5] that the main structural features are not very sensitive to ϵ. Its value (0.2 of the depth of the BHM minimum) was chosen so that the force constant (curvature at r_0) was approximately the same as that obtained from spectroscopic data on the gas phase K-Cl ion pair (this is also very close to the value for the BHM potential). The potentials were truncated at $3r_0$.

The partial radial distribution functions generated by the SHREP and BHM potentials are compared in Fig.2 and the indiscriminate (particle-particle) functions are shown in Fig.3. The SHREP potentials are seen to generate 'charge' oscillations remarkably similar to those of the true ionic liquid but nevertheless produce the same ***strong damping*** of particle-particle correlations beyond the second nearest neighbour shell . It should be noted that the 'charge' oscillations occur out to much larger distances than the range of the potential showing that they are clearly a long range manifestation of short range interactions. Observation of these oscillations out to distances of the order $10r_0$ emphasises the advantage of being able to use large samples in the computer simulation. The potential of mean force, $E_m(r)$, on an ion in the BHM liquid can be calculated from the particle-particle distribution function in Fig.3, since

$$E_m(r) = -kT\ln g(r) \quad ....(5)$$

It is clear that $E_m(r)$ decays to zero within three particle diameters, emphasising the dominance of short range interactions.

Charge charge structure factors $S_{QQ}(k)$ were also computed from direct Fourier transforms of the radial distributions. In this representation

$$S_{QQ}(k) = 1/2\{S_{++}(k) + S_{--}(k) - 2S_{+-}(k)\} \quad ....(7)$$

Fig.4 demonstrates the clear similarity between $S_{QQ}(k)$ for the SHREP potential liquid and for the BHM liquid. The sharp main peak (often referred to as the 'coulomb' peak) and strong oscillations are the well established signatures of 'charge ordering' [9]. In a coulomb system overall charge neutrality demands [15] that $S_{QQ}(k) \propto k^2$ as $k \to 0$. As a result of the limited sample size the small k region is not accessible in our simulations. The results for the SHREP potential liquid show that the trend in $S_{QQ}(k)$ is, however, not inconsistent with the above requirement.

It has been shown previously that the thermodynamic properties of the ionic liquid can be calculated from the structure generated by the SHREP potential using first order perturbation theory [5]. In Table I we compare the predicted values of U_{ionic} and p_{ionic} with experimentally measured values and with those obtained for an ionic simulation using the BHM potential. The agreement is extremely good since it is unlikely that the experimentally measured value of the internal energy U is known to better than a few per cent.

Values of the particle self diffusion coefficients computed from plots of the mean squared displacements against time are included in

property	SHREP potential	BHM potential	experiment[a]
$\frac{U_{ionic}}{kJ\ mol^{-1}}$	-594	-609 (-612)	610
$\frac{P_{ionic}}{MPa}$	270±150	250±40 (-290)	0
$\frac{D_m}{10^{-8}\ m^2s^{-1}}$	1.18±0.1	1.16±0.1 (1.3)	1.42

a - G.J.Janz, *Molten Salts Handbook*
(Academic Press, N.Y., 1967)

Table I : Thermodynamic properties and mean ion diffusion coefficients for liquid potassium chloride at 1300 K and 54 cm^3 mol^{-1}. For the SHREP potential simulation U and p were calculated using first order perturbation theory [5].

Table I. The statistical error in the computed values of D and also accuracy of the experimental values is only about ± 10%. Within margin there is excellent agreement between diffusion coefficients computed for the SHREP potential, the ionic simulation and experiment.

Simulations of other alkali chlorides have been made using SHREP potentials of the form in equation (3). The changes in structural features, as compared to KCl, are much the same as has been obtained from previous studies utilising BHM potentials and show good agreement with experimental data on the respective systems. The position of the first peak in the Cl-Cl distribution, for instance, moves very slightly to larger r values as the cation size increases. In molten lithium chloride, as expected [1], the unlike nearest neighbour peak in the radial distribution function sharpens and moves to shorter distances.

So far we have discussed simulations of the bulk properties of molten alkali chlorides. An additional and remarkable demonstration of the successful use of SHREP potentials is found in the simulation of *interfacial* properties of molten potassium chloride. We have previously reported studies of thin films of the ionic liquid confined between rigid planar walls, in a first attempt to simulate the electrode-molten salt interface [16]. Several interesting predictions emerged from these studies. The rigid boundary induces a partially layered structure of the liquid which rapidly decays into the bulk of the liquid and which is very similar in form to that for simple atomic liquids such as argon. This result was compared with that obtained after applying an electric field of 3.6×10^{7} V cm^{-1} across the film. This is the same magnitude of field strength thought to exist near a metal electrode in a molten salt. Interestingly there was *no change* in the overall *particle* density profile although clearly the distribution of anions and cations in the interfacial layers changed in response to the perturbation. This is illustrated in the density profiles shown in Fig.5. The asymmetric distribution of ions is perhaps more clearly revealed in the oscillation of the excess charge, the form of which broadly confirms theoretical predictions [17]. The problem was that we could not be sure that the charge oscillations at the two 'electrodes' were not mutually disturbed by long range coulomb interactions across these very thin films. Recent simulations using a SHREP potential [10] show clearly that this is *not* the case and that the phenomena observed are likely to be reproduced for films of macroscopic thickness.

In Fig.5 we also show the excess 'charge' profile generated for a thin film of liquid in which the particles were made to interact with each other according to the SHREP potential in equation (3) with a truncation range of $3r_o$. They were made to respond to the applied electric field, however, as if they were K^+ and Cl^- ions. Clearly there are no possible direct long range interactions in this system yet the excess charge profile is almost identical to that obtained for the ionic liquid. These striking interfacial phenomena are not, therefore, spurious effects due to the small thickness of the films and are indeed explainable in terms of minor perturbations (induced by the electric field) on *short range* packing effects in the molten salt.

2.*Molten Strontium Chloride*

This liquid was chosen in order to evaluate the use of a SHREP potential for simulating molten salts where the cations and anions have different charge numbers. The experimental structural characteristics of molten strontium chloride [18] have previously been explained in terms of the simple ionic model [3,4] and successful simulations using a Busing potential (very similar to BHM) have been reported [19].

We used the equation (3) form of SHREP potential. Values of ϵ and r_o were taken from gas phase spectroscopic data on the diatom SrCl, so that

$$\epsilon(1,2) = 6.74 \times 10^{-19}\ \mathrm{J}$$
$$r_o(1,2) = 0.267\ \mathrm{nm}$$

To ensure balance of attractions and repulsions at medium range $\epsilon(1,1) = 2.0 \times \epsilon(1,2)$, $\epsilon(2,2) = 0.5 \times \epsilon(1,1)$. The value of r_0 for the like particle interactions is not critical and we have chosen $r_0(1,1) = r_0(2,2) = r_0(1,2)$.

The simulations were performed for a temperature of 1150 K and a constant volume of 61.95 $cm^3\ mol^{-1}$. This volume is the same as that used in the ionic potential simulations [19] and is about 5% larger than the experimental volume at the same temperature. The partial radial distribution functions generated by the SHREP potentials are shown in Fig.6. The same general pattern is observed as for molten potassium chloride although the distribution functions for the Sr and Cl are now quite different. Charge oscillations again clearly persist out to quite long range. Points on this figure show the peak positions obtained in the ionic potential simulations and the agreement is excellent. The structure generated by the SHREP potential shows all the detail observed experimentally for this liquid such as the strong penetration of the first coordination shell by like particles. To emphasise how accurately the SHREP potential reproduces the structure of strontium chloride, in Table II we compare the ionic internal energy (calculated using perturbation theory) with the values from the previous simulation and from experiment. The agreement is extremely good. Calculated diffusion coefficients are also shown for the various models. Values for the SHREP potential liquid actually agree rather better with experiment than do those from the ionic simulation, although this may be fortuitous.

property	SHREP potential	BHM potential [a]	experiment [a]
U_{ionic} / kJ mol^{-1}	-2025	-2036	-2029
D_+	2.9±0.3	0.68	2.2
D_-	6.3±0.5	1.71	4.3

a - data from ref. 19

Table II : Internal energies and diffusion coefficients (in $10^{-9}\ m^2\ s^{-1}$) for liquid strontium chloride at 1150 K and 61.95 $cm^3\ mol^{-1}$. For the SHREP potential simulation U_{ionic} was calculated using first order perturbation theory [5].

Crystalline strontium chloride is an ionic superconductor due to a high mobility of the chloride ions in the lattice. Certainly chloride is far more mobile in the liquid. It has been suggested [20] that this property can be related to the strong damping of g_{ClCl} as compared to g_{SrSr}. (The damping of the former function is particularly noticeable because it shows such distinct *short* range structure). Our data (wnich extend out to nearly $6r_0$) show that this is really a rather small differential effect.

The structural properties of molten strontium chloride are explainable in terms of straightforward ionic interactions. There are several other molten divalent metal chlorides, such as magnesium and zinc chloride, where this is not the case [4]. For instance the results of neutron diffraction experiments show that the most probable separations of positive ion and negative ion near neighbours are very similar, which would certainly not be expected from a simple ionic model (see Fig.6). If these effects are to be explained then it will be necessary to introduce additional short range (perhaps many-body) contributions to the interaction potential.

3. *Molten sodium tetrachloraluminate*

Finally we briefly discuss some preliminary simulations of liquid sodium tetrachloraluminate, $NaAlCl_4$, using a SHREP potential. This material has been examined recently using both X-ray [21] and neutron [22] diffraction techniques. These studies confirm the conclusions of previous spectroscopic observations - namely that there is little dissociation of the tetrahedral $AlCl_4^-$ unit in the liquid. Simulations have also been reported [23] based on an ionic model of interactions between Al^{3+}, Cl^- and Na^+. Since little is known about the short range interactions between these ions, model BHM potentials were employed in order to explore the sensitivity of the melt structure to various parameters. The most important parameter turned out to be the 'size' assigned to the chloride ion. To illustrate just how sensitive the structure was to the value chosen we plot in Fig.7 the ratios of the interaction energies for various particle pairs relative to the Al-Cl energy at the same separation. Marked on this figure are the positions of the nearest neighbour peaks in g(r). The shaded area shows the small difference in the ratio of interactions required to cause a changeover in the melt structure from octahedral to tetrahedral coordination. At a separation corresponding to the first peak in g_{ClCl} this difference is hardly observable on the plot, although the difference in absolute energies is several times kT! Of course it is always possible *a posteriori* to choose parameters to give the correct structure. The much greater challenge to theory is the correct *prediction* of these small details of the interaction potential.

The above discussion shows that the structure adopted by this molten salt mixture is strongly dependent on a very delicate balance between on the one hand Al-Cl (and Na-Cl) unlike particle interactions and on the other hand the Cl-Cl repulsions. Consequently, realistic simulations of this liquid presents a stringent test for SHREP potentials, indeed for any set of potentials.

We have recently performed a SHREP potential simulation using the equation (3) form with $n = 8$, $m = 1$ but with a truncation range of only $3r_0(2,3)$, where we number the species in order Na,Al,Cl. The values used for the most important parameters were:

$$\epsilon(2,3) = 16.0 \times 10^{-19}\ \mathrm{J}$$
$$r_0(2,3) = 0.182\ \mathrm{nm}$$

where the former value is about half the depth of the BHM potential but was chosen so that the force constants were the same. To maintain a close comparison with the ionic simulation the value of $r_0(2,3)$ was identical to that of the BHM potential [23]. Values for all the other parameters were chosen so as to maintain the same ratios as shown in Fig.7 for the potential c discussed by Saboungi Rahman and Blander. It must be stressed that the results are preliminary but they are nevertheless very encouraging. The coordination number for chloride around aluminium was, within the error limits, four and very well defined. Table III shows the positions and heights of the three main peaks in the partial radial distribution functions. There is generally good agreement with the data for the ionic potential.

pair	ht. pos./nm	this work	Saboungi et al ref 23	experiment ref 22
Cl-Cl	h	3.2	3.5	3.0
	r	0.35	0.34	0.35
Al-Cl	h	13	16.5	9.3
	r	0.21	0.21	0.21
Na-Cl	h	4.2	3.8	
	r	0.26	0.27	

Table III : Nearest neighbour peak heights (h) and positions (r in nm) in the partial radial distribution functions obtained from a SHREP potential simulation of molten $NaAlCl_4$ at 500 K.

CONCLUSIONS

Evidence has been presented that the structure and many properties of molten salts are not determined by long range coulomb interactions. It has been shown that simulations of molten salts using SHREP potentials preserve the same essential physics of the liquid as in the case of Born potentials. SHREP potentials are a highly practical alternative for simulation studies. They permit more economic use of computer time and broaden the range of systems that can be examined. One problem in accurately modelling all but the simplest of molten salts, however, is our limited knowledge of the details of short range (repulsive) interactions, especially between *unlike* ions. This limitation applies both to SHREP potentials and to those based on the Born model. There is a clear need for more fundamental work in this area.

REFERENCES

1. L.V.Woodcock and K.Singer,
J.Chem.Soc.Farad. Trans. II, 67, 12 (1971).
L.V.Woodcock, Chem.Phys.Lett.,10, 257 (1971).
2. E.W.J.Mitchell, P.F.J.Poncet and R.J.Stewart, Phil.Mag., 34, 721(1976)
3. S.Biggin and J.E.Enderby, Adv. Molten Salt Chem.,Vol 5 (Ed. G.Mamantov, Elsevier,Amsterdam 1983)
4. J.E.Enderby, Contemp. Phys., 24, 561 (1983)4.
5. J.H.R.Clarke, W.Smith and L.V.Woodcock, J.Chem.Phys.(in press)
6. J.C.Hansen and I.R.McDonald, Phys.Rev.,A11, 2111 (1975)
7. M.Gillan, B.Larsen, M.P.Tosi and N.H.March,
J.Phys. C, 9, 889 (1976).
8. L.V.Woodcock, Adv. Molten Salt Chem., Vol 3 (Ed. J.Braunstein, G.Mamantov and G.P.Smith,Plenum,NY 1975)
9. A.P.Copestake and R.Evans, J.Phys.C, 15, 4961 (1982)
10. J.H.R.Clarke, unpublished data, 1985
11. S.A.Rice, Trans.Farad.Soc., 58, 499 (1962)
12. M.J.L.Sangster and M.Dixon, Adv. Physics, 25, 247 (1976)
13. M.P.Tosi and F.G.Fumi, J.Phys.Chem.Sol., 25, 31 (1964).
14. L.V.Woodcock, J.Chem.Soc.Farad.Trans. 2, 70, 1405 (1974).
15. F.H.Stillinger and R.Lovett, J. Chem. Phys., 48, 3858 (1968)
16. D.M.Heyes and J.H.R.Clarke, J.Chem.Soc.Farad.Trans. 2, 77, 1089 (1981).
17. A.D.Graves and D.Inman, Electroanal.Chem.Interfac.Electrochem., 25, 349 (1970).
18. R.L.McGreevy and E.W.J.Mitchell, J.Phys. C, 15, 5537 (1982).
19. S.W.de Leeuw, Mol.Phys., 36, 103,765 (1978),
20. J.E.Enderby and G.W.Neilson, Adv. Physics, 29, 323 (1980).
21. S.Takahashi, T.Muneta and N. Koura, J.Chem.Soc.Farad.Trans. 2, 81, 1107 (1985).
22. S.Biggin, S.Cummings and J.E.Enderby, private communication.
23. M.L.Saboungi, A.Rahman and M.Blander, J.Chem.Phys., 80, 2141 (1984).

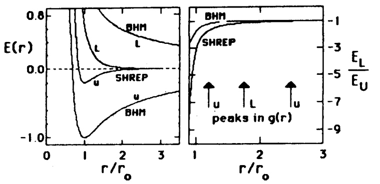

Fig.1: SHREP and BHM interaction potentials for liquid KCl.
u - unlike, L - like particles

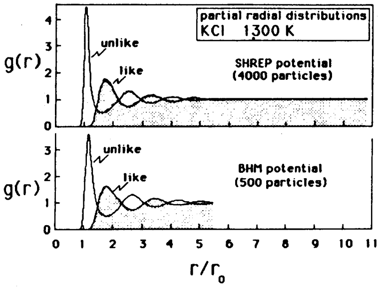

Fig.2: Partial radial distribution functions for model KCl at 1300 K.

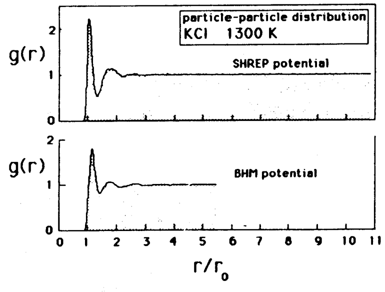

Fig.3: Particle-particle distribution functions for the BHM and SHREP potential liquids at 1300 K.

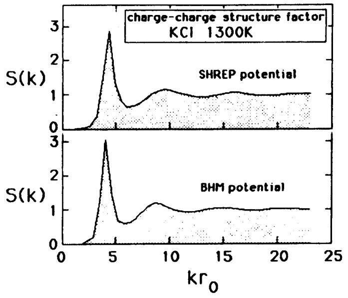

Fig.4: Charge-charge structure factors for the two models of molten KCl at 1300 K.

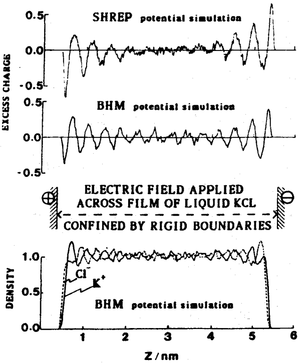

Fig.5: Density and Charge distributions across a thin film of molten KCl at 1050 K constrainedby rigid boundaries and a uniform electric field.

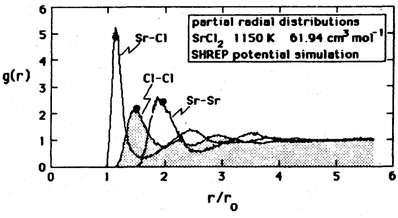

Fig.6: Partial radial distribution functions for strontium chloride. Circles show peak positions for an ionic simulation [19].

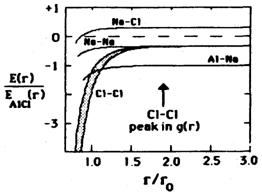

Fig.7: BHM potentials [23] for NaAlCl$_4$. Shown is the ratio of interaction energies and the position of the Cl–Cl nearest neighbour peak. The shaded area shows the difference in interactions giving rise to octahedral and tetrahedral coordination of Cl around Al.

DOI: 10.1149/198601.0071PV

INTUITIVE INTERPRETATION OF SELF-DIFFUSION MECHANISM IN LIQUID ARGON BY MOLECULAR DYNAMICS

Kazuo Furukawa* and Minoru Tanaka**
*Tokai University, Institute of Research and Development,
Hiratsuka, Kanagawa, Japan 259-12
**Tohoku University, Department of Engineering Science
Aramaki, Sendai, Japan 980

ABSTRACT

To get an intuitive understanding of the self-diffusion mechanism in liquids, molecular dynamics simulation analysis was performed on liquid argon composed of 864 atoms just above the melting point. Examining the histograms of root-mean-square displacements at several time intervals, we found a few abnormal fast atom movements, indicating a jump diffusion mechanism. About 20% of the self-diffusion coefficient originates from the jump mechanism, which occurs about 1.25 times per one hundred atomic oscillations; the residual part comes from Brownian-like movement of a cage-forming atomic group composed of an atom and its nearest neighbor atoms.

I. INTRODUCTION

The essential feature of atomic and ionic behavior in several types of liquids, including molten salts, can be understood with an intuitive interpretation of self-diffusion mechanisms. For this purpose, a computer simulation analysis by molecular dynamics of more than several hundred particles is one of the most direct and effective methods, although even the molten alkali halides could not effectively be analyzed by the pair potential approximation (1).

As an initial try, liquid argon just above the melting point was chosen because argon is the simplest monoatomic liquid and has the most reliable information on interatomic forces, which are, to a high degree of accuracy, approximated by a pair potential form. This means a central force approximation can be used and provides an easier condition for the molecular dynamics experiments (2,3). The condition of melting point was chosen as the densest atom-packed state, most significantly characterizing the normal liquid state, even though the rather dense conditions will be present in the super-cooled liquids.

Rahman already tried an ambitious examination of the self-diffusion mechanism in argon by this method (4), where he considered the primary and higher order polyhedra formed by neighbor atoms and their local fluctuations. This idea has some qualitative relation to that of Swalin (5). However, one of the authors had declared that it could not be denied that the jump diffusion might occur by the passage through interstices prepared by the normal fluctuations of local atom-packing density, in the monoatomic liquids including pure metallic liquids (6) and alkali halide melts (7), even near their melting points.

Therefore, several new examinations were performed again, and a realistic diffusion mechanism in liquid argon was revealed.

II. MOLECULAR DYNAMICS CALCULATION OF LIQUID ARGON AT MELTING POINT

The conditions of the calculation are as follows:

(A) the number of argon atoms: 864 particles,

(B) interaction force: Lennard-Jones type 6-12 potential,

$$\phi(r) = 4\epsilon\left((\sigma/r)^{12} - (\sigma/r)^{6}\right)$$

where $\epsilon = 119$ K and $\sigma = 0.34$ nm,

(C) temperature: 87 K, just above melting point
not far from triple point (83.8 K, 1.435 g/cm^3),

(D) density: 1.418 g/cm ^{3},

(E) length of basic cube: 3.43 nm,

(F) time of step for integral with periodic boundary condition: 0.005 psec, and

(G) total integral step: 2500.

III. PHENOMENOLOGICAL ANALYSIS OF SELF-DIFFUSION COEFFICIENT

The phenomenological self-diffusion coefficient, D_{total} was calculated by the conventional method (3) from the following relation with the mean-square displacements $< \{(R(t) - R(t_o)\}^2 >$:

$$W(t) = 1/3 < \{R(t) - R(t_o)\}^2 > \approx 2D_{\mathrm{total}}(t - \tau_o)$$

which was taken from 1.7 x 10^5 samples per 0.005 psec interval for the time of $\tau_o < t < 7.5$ psec.

The delay time, τ_o, in the above was 1.055 psec. D_{total} was 1.96×10^{-5} cm^2/sec, which was sufficiently in agreement with the experimental values (8,9).

It is doubtful that the microscopic self-diffusion coefficient is equivalent to the macroscopically measured one, considering complex semi-microatomic mass movements, for example.

IV. SUBSTANTIAL ANALYSIS OF SELF-DIFFUSION MECHANISM

To get an intuitive understanding of the self-diffusion mechanism of atoms, the following examination was performed using the root-mean-square displacements:

$$\Delta R_i(t_o, \Delta t) = \sqrt{\{(R_i(t_o + \Delta t) - R_i(t_o)\}^2}$$

after several time intervals, Δt, from several initial times, t_o for all 864 atoms.

The histograms of $\Delta R_i(t_o, \Delta t)$ are shown for the intervals of $\Delta t = 0.2$, 0.3, 0.4, 0.5, and 0.6 psec in Fig. 1 and $\Delta t = 0.5$, 1.0, 2.0, 3.0, 4.0, 6.0, and 12.0 psec in Fig. 2. These curves in Figs. 1 and 2 reflect the straight distance of movement from the initital position of each atom after the time interval, Δt, independently of its paths. The curves in Fig. 1 in general look like the natural results after simple random walks. However, in the curves for the intervals longer than 1.0 psec in Fig. 2, abnormally elongated tails near the horizontal axis were found. The position of r_1 shows the nearest neighbor atom distance. These tail parts would originate from some abnormal displacement mechanism, such as "jumping," according to the following two reasons:

(1) Several projection charts were drawn of atomic movements included in the 0.58-nm-thick slab inside the basic cube, presenting the two-dimensional trajectories of about 140 atoms onto the x-y plane. For example, the chart of 0.5-psec interval had shown only small curved trajectories of about 0.03 to 0.1 nm length with no apparent abnormality. However, as shown in Fig. 3(b), the chart of 1.0 psec interval included two or three abnormal trajectories having a nearly straight line and being about 0.3 nm or longer. These long trajectories might be understood as the jump movement of some atoms passing through the side of many irregularly oscillating atoms.

(2) In 1959, an effective structural model (6) of monoatomic liquids, including van der Waals and pure metallic liquids, was proposed. This model suggested a high feasibility of jumping through the interstices of the atom cage formed by an average of 10.8 atoms surrounding an atom, even just above the melting point.

A simplified picture with rigid-sphere atoms is shown in (a), (b), and (c) of Fig. 4, for which a quasi-face-centered-cubic arrangement was used to help the intuitive understanding. Figure 4(a) shows schematically the jump mechanism. In Fig. 4(b), solid-line circles represent the average position determined by the rigid-sphere atoms of effective radii placed in the quasi-(100) plane; if four central atoms were moved to the positions of the dotted-line circles, the other shaded atom would pass through this plane freely. Figure 4(c) shows the side view of the above mechanism. If the shaded atom could move straight for more than about 0.2 nm, there is a high probability that it would jump out of the cage. (The velocity of gas-like free movement is about 0.23 nm/psec at this temperature.)

With the above consideration, the number of atoms that have jumped in the time intervals of $\Delta t = 2, 3, 4$, or 6 psec was estimated from the number of atoms that have moved farther than the threshold distances of 0.22, 0.225, 0.23, or 0.24 nm, respectively, shown by vertical arrows in Fig. 2. The accounted number of "jumped" atoms is shown in Table 1.

The oscillation frequency, ν_m, of atoms near the melting point, T_m, was assumed to be estimated by Lindemann's formula (10):

$$\nu_m = 2.8 \times 10^{12} T_m^{1/2} M^{-1/2} V_m^{-1/3}$$

where M represents the atomic weight and V_m the atomic volume at T_m. In the case of argon, ν_m is 1.335×10^{12} per sec and the oscillation period of atoms is 0.75 psec. From Table 1, the jump frequency is estimated to be 1.25

The self-diffusion coefficient, D_{jump}, as a result of jumping can be calculated (11) from

$$D_{\text{jump}} = 1/6 \text{ (jump frequency) (displacement)}^2$$

The displacement by single jump can, on the average, be considered nearly equal to the mean interatomic distance (0.375 nm). Therefore,

$$D_{\text{jump}} = 1/6(1.335 \times 10^{12} sec^{-1} \times 1.25\%)(0.375 nm)^2 = D_{\text{total}} \times 20\%$$

The residual part of the self-diffusion coefficient will be originated from the Brownian-like movement of an atomic group consisting of a central atom and the surrounding cage atoms:

$$D_{\text{total}} = D_{\text{jump}} + D_{\text{Brownian-like}}$$

The number of cage atoms is estimated to be about 10.8 atoms from the radial distribution function at the melting point (12,6).

From the Langevin's relation of Brownian motion:

$$D_{\text{Brownian-like}} = \tau_o \times kT/M^*$$

where τ_o = 1.055 psec, as shown in Section II, and the effective mass, M^*, is calculated as

$$M^* = 8.10 \times 10^{-22}\text{gr} = 12.2\text{atoms} \times M_{\text{Ar}}$$

This is consistent with the above prediction: $10.8 + 1 = 11.8$ atoms. Although this coincidence may be fortuitous with respect to the above crude estimations, it seems that the essential feature of the self-diffusion mechanism is a little more revealed by the above analysis.

V. CONCLUSION

Using molecular dynamics simulation, the self-diffusion mechanism in liquid argon just above the melting point has been analyzed for a very short time scale. The essential mechanism was divided into two parts. One was the jumping process of an atom passing through its surrounding atom cage, with a jumping frequency of about 1.25 times per one hundred oscillations of the central atom. This process will contribute about 20% to the total self-diffusion coefficient. The second process was a Brownian-like movement of an atom with its cage as a whole (the effective mass of 12.2 Ar atoms).

These approaches for analysis of self-diffusion mechanisms apply to liquid argon at higher temperatures, to pure metallic liquids, and also to ionic liquids starting as molten alkali halides.

REFERENCES

1. K. Furukawa, H. Ohno, Proc. 3rd Int. Symp. Molten Salts 81-9 36 (1981)
2. A. Rahman, Phys. Rev. 136 A405 (1964); L. Verlet, *ibid.* 159 98 (1967)
3. D. Levesque, L. Verlet, *ibid.* A2 2514 (1970)
4. A. Rahman, J. Chem. Phys. 45 2585 (1966)
5. R. A. Swalin, Acta Met. 7 736 (1959); 9 379 (1961)
6. K. Furukawa, Nature 184 1209 (1959); Sci. Rep. RITU A12 368 (1960); Rep. Prog. Phys. 25 395 (1962)
7. K. Furukawa, Elec. Chem. Seminar 1 (1967) (in Japanese); cf. Discuss. Faraday Soc. 32 53 (1962)
8. J. Naghizadeh, S. A. Rice, J. Chem. Phys. 36 2710 (1962)
9. G. Cini-Castagnoli, F. P. Ricci, Nuovo Cim. 15 795 (1965)
10. F. A. Lindemann, Phys. Z. 11 609 (1910)
11. A. Einstein, "An Introduction of the Theory of Brownian Movement," Methuen, 1926
12. N. S. Gingrich, C. W. Tompson, J. Chem. Phys. 36 2398 (1962)

Table 1. Jump probability of atoms in liquid argon near melting point.(87.0K, 1.418gr/cm^3)

time-interval Δt(psec)	threshold distance D (nm)	jumped atoms Nj	$\frac{Nj}{864}$ (%)	$\frac{Nj}{\nu m}$ (%)	
2	>0.22	28.5	3.30	1.24	average: 1.25%
3	>0.225	43.7	5.06	1.26	
4	>0.23	57.9	6.70	1.26	
6	>0.24	87.2	10.09	1.26	

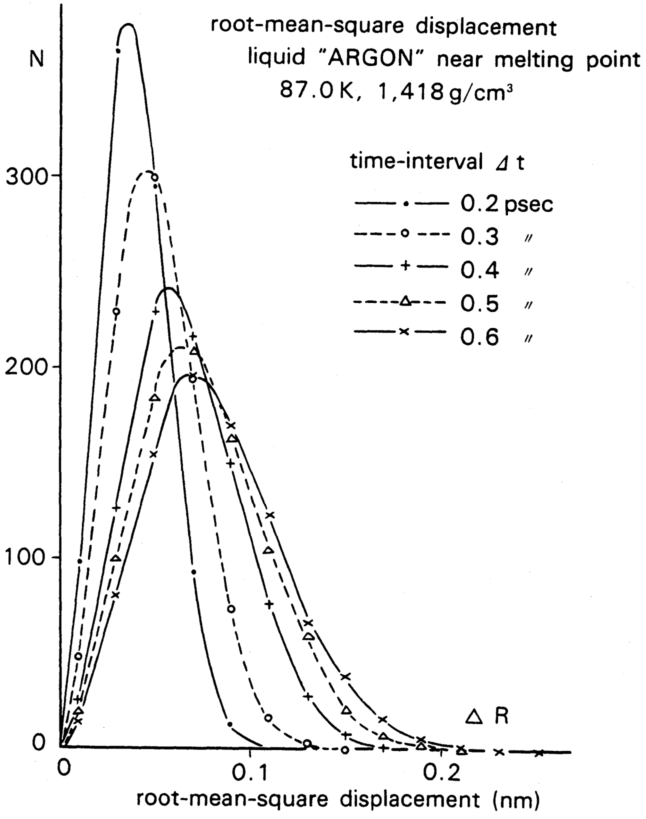

Fig.1 Histogram of root-mean-square displacements at several time intervals in liquid argon.

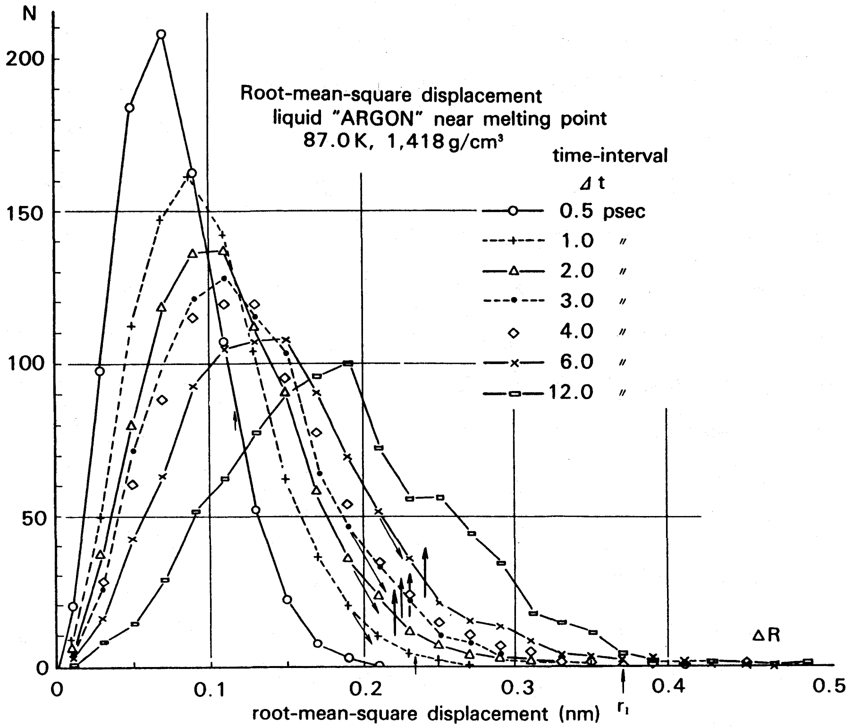

Fig.2 Histogram of root-mean-square displacements at several time intervals in liquid argon.

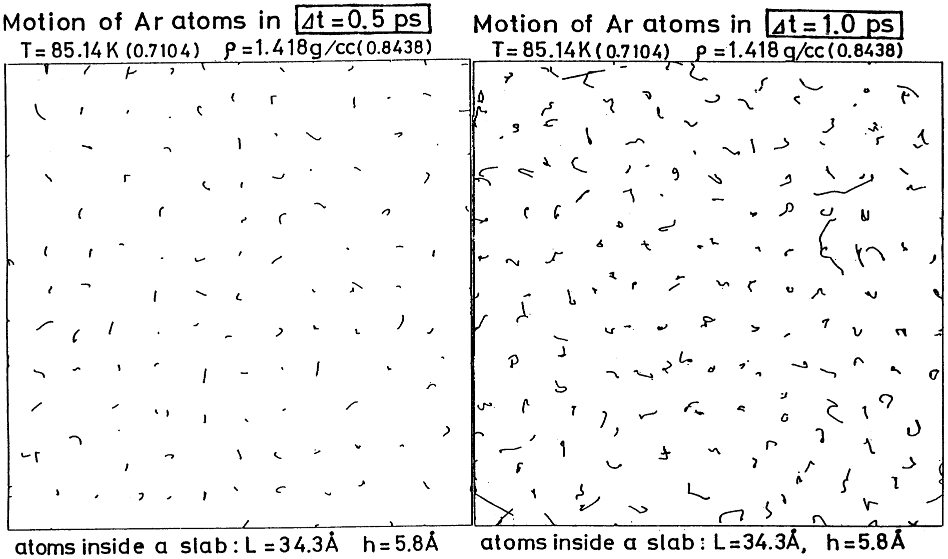

(a) (b)

<u>Fig.3</u> Trajectories of argon atoms inside a slab of 0.58nm thickness in the time intervals of (a) 0.5psec and (b) 1.0psec.

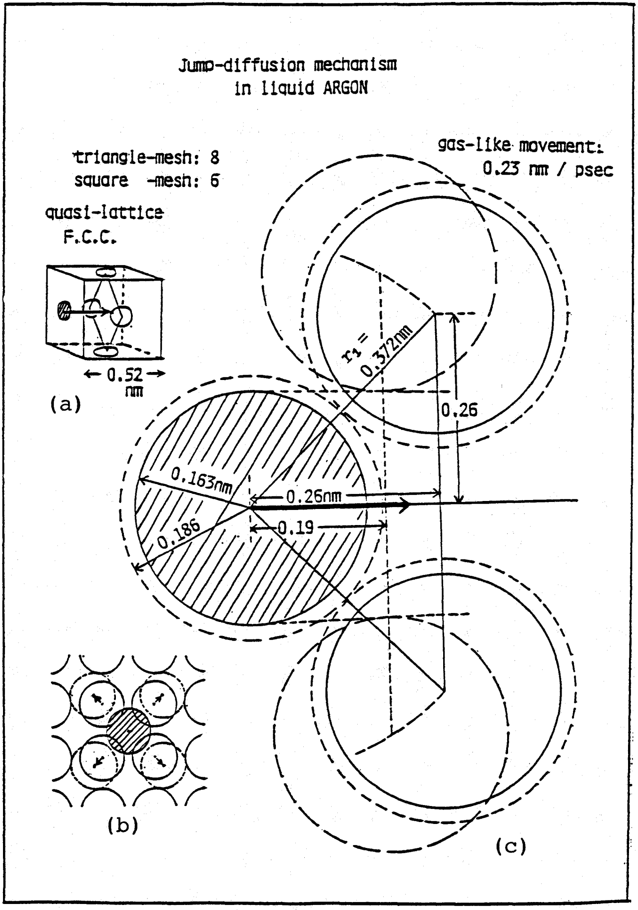

Fig.4 Schematic figures of jump-diffusion mechanism in liquid argon assuming quasi face-center-cubic arrangements.

DOI: 10.1149/198601.0081PV

THE STRUCTURE OF EQUIMOLAR $LiCl-AlCl_3$ MELT BY NEUTRON SCATTERING

S. Biggin[1], S. Cummings[1], J. E. Enderby[1] and M. Blander[2]

[1] H. H. Wills Physics Laboratory
Royal Fort, Tyndall Avenue
Bristol, BS8 1TL, England

[2] Argonne National Laboratory
9700 South Cass Avenue
Argonne, Illinois 60439, USA

ABSTRACT

The structure of $LiAlCl_4$ has been investigated by neutron diffraction of isotopically enriched samples. The lithium contribution to the scattering has been removed by using a "null" scattering sample, of ^6Li and ^7Li. We have derived three partial structure factors $S_{AlAl}(k)$, $S_{ClCl}(k)$ and $S_{AlCl}(k)$ and their Fourier transforms, the partial radial distribution functions (rdf's), $g_{ij}(r)$. The first peaks in $g_{ClCl}(r)$ and $g_{AlCl}(r)$ are at 3.51, and 2.13 Å, respectively. The coordination numbers obtained by integrating to the first minima are about 6, and 4, respectively. As anticipated, the existence of extremely well defined $AlCl_4^-$ tetrahedra has been established, with little if any Al-Cl-Al bridging between tetrahedra in this melt. The results are similar to those predicted from molecular dynamical calculations on model systems.

INTRODUCTION

Ordered or complexing molten salt mixtures have aroused the interest of thermodynamicists and structural chemists alike since the thermodynamic and physical properties of these mixtures have strong compositional dependencies which are not completely understood. There is no statistical mechanical theory for the precise description of binary complexing systems such as $LiF-BeF_2$ or $LiCl-AlCl_3$. In order to deduce useful concepts and theories for such systems, much more information on the structural and thermodynamic characteristics are needed.

With this in mind, we set out to investigate the structure of the melt $LiAlCl_4$, as a first step in the characterization of a particular binary complexing salt pair at different compositions. This type of melt has been central to recent molecular dynamical (MD) studies carried out by Saboungi *et al.*[1] who demonstrate that the structure is a very strong function of interionic potential. We have been able to confirm the expected presence of $AlCl_4^-$ tetrahedra in this melt and to make detailed comparison with MD calculations.

We find broad agreement with the MD results which are based on a simplified Tosi-Fumi potential for a melt analogous to $NaAlCl_4$. The height of the first peak in the measured partial radial distribution function, $g_{AlCl}(r)$, is unusually large. This was not detected in recent X-ray results on this melt [2] which are otherwise consistent with our results. In what follows we describe our neutron diffraction measurements as well as the partial structure factors and radial distribution functions (rdf's) for AlAl, ClCl, and AlCl pairs deduced from the measurements.

EXPERIMENT

The sample parameters pertaining to the experiment are shown in Table 1; the sample temperature was 200°C. As with previous experiments by the group at Bristol,[4] the partial structure factors $S_{\alpha\beta}(k)$ (where $\hbar k$ is the momentum transfer in the scattering process) can be separated from three independent total structure factors, F(k), obtained from at least three samples of a given chemical composition with each sample having a different isotopic composition. F(k) is the quantity obtained directly from a single neutron diffraction experiment on a liquid with a particular isotopic composition.

In the case of $LiAlCl_4$, the Li contribution to the scattering has been removed using null-scattering lithium, a mixture of ^6Li and ^7Li (see Table 1). The melt is then seen by the neutron beam as a simple two species melt, where

$$F(k) = c_{Al}^2 f_{Al}^2[S_{AlAl}(k) - 1] + c_{Cl}^2 f_{Cl}^2[S_{ClCl}(k) - 1] + 2c_{Al}c_{Cl}f_{Al}f_{Cl}[S_{AlCl}(k) - 1]$$

for example

$$F^{nat}(k) = 0.0033[S_{AlAl}(k) - 1] + 0.408[S_{ClCl}(k) - 1] + 0.0734[S_{AlCl}(k) - 1]$$

where c_α is the atomic fraction of species α, f_α is its neutron coherent scattering length, and $S_{\alpha\beta}(k)$ is a partial structure factor. The Fourier transform of F(k) produces the total radial distribution function G(r) using the relation

$$G(r) = \frac{1}{2\pi^2 \rho r}\int_0^\infty k \sin kr F(k) dk.$$

Similarly, the partial structure factors relate to the partial rdf's, $g_{\alpha\beta}(r)$, through

$$g_{\alpha\beta}(r) = 1 + \frac{1}{2\pi^2 \rho r} \int_0^\infty k \sin kr \left[S_{\alpha\beta}(k) - 1 \right] dk$$

where ρ is the ionic number density. To separate out the $S_{\alpha\beta}(k)$, f_{Cl} was changed by isotopic substitution, using ^{nat}Cl, ^{mix}Cl, and ^{37}Cl, where ^{nat}Cl is composed largely of ^{35}Cl, and ^{mix}Cl is a mixture of natural Cl with ^{37}Cl. The parameters for these three compositions are given in Table 1. A natural sample (not containing the null Li) was also investigated. All the measurements were carried out on the D4 diffractometer at the reactor facility of the Institut Laue-Langevin (ILL) in Grenoble, France using a neutron wavelength of 0.7Å.

SAMPLE PREPARATION

Samples of $^oLi^*Cl$ and Al^*Cl_3 were synthesized at Bristol, using Na^*Cl salt as the starting material, where $^*Cl$ denotes an isotope of chlorine. The $Al^{nat}Cl_3$ sample was supplied by Anderson Physics Laboratories (Champaign, Illinois, USA), and the $^oLiAlCl_4$ was prepared at the Argonne National Laboratory. The chloride isotopes were supplied as Na^*Cl, by the Oak Ridge National Laboratory.

Labeled hydrochloric acid was made by cationic exchange using an Amberlite IR 120(H) ion exchange resin as follows:

$$\text{Resin} + H_{(S)} + Na^*Cl_{(aq)} \rightarrow \text{Resin} + Na + H^*Cl_{(aq)}$$

The $^oLi^*Cl$ samples were then produced through the reaction:

$$^oLiOH_{(aq)} + H^*Cl_{(aq)} \rightarrow {}^oLi^*Cl_{(aq)} + H_2O$$

The $^oLi^*Cl$ solutions were dehydrated by gentle heating on a vacuum line. Residual water content was checked by examination of the infrared absorbance at 3440 cm^{-1} of a deuterium oxide (heavy water) solution of the dried salt.

The Al^*Cl_3 salts were produced from Ag^*Cl salt and Al pieces via the following reaction:

$$3AgCl + Al \rightarrow 3Ag + AlCl_3$$

The containment apparatus is shown in Fig. 1.

Ag^*Cl (formed from the Na^*Cl) powder was fused under vacuum in the graphite crucible. Clean dry Al pieces were placed in the side arm of the quartz reaction vessel and the evacuated vessel sealed.

All the aluminum pieces were then tipped into the graphite crucible. The main tube was heated to 700°C–the reaction started when the silver chloride melted (455°C). The aluminum chloride which formed sublimed and was collected in the cooler side arm. After cooling, the side arm containing the Al^*Cl_3 was removed from the main tube, ready for mixing with the $^oLi^*Cl$.

RESULTS

The F(k) for the four $LiAlCl_4$ samples are shown in Fig. 2 and their transforms to G(r) in Fig. 3. The three partial structure factors $S_{AlAl}(k)$, $S_{ClCl}(k)$, and $S_{AlCl}(k)$, and partial rdf's $g_{AlAl}(r)$, $g_{ClCl}(r)$, and $g_{AlCl}(r)$ deduced from the measurements are given in Figs. 4 and 5. MD results for $g_{AlAl}(r)$, $g_{ClCl}(r)$ and $g_{AlCl}(r)$ are also shown for comparison in Fig. 5. We have checked that the $S_{\alpha\beta}(k)$ correctly generate the measured F(k) for all three samples where the lithium contribution was zero. The agreement can be seen in Figs. 2a-c. We summarize the structural parameters in Table 2. Finally, Fig. 6 shows the running coordination number, $n_{\alpha\beta}(r)$, for both the neutron diffraction measurements and the molecular dynamical calculations. The running coordination number is defined as the average number of ions of type β within a radius r from an ion of type α.

DISCUSSION

The Cl-Cl interaction

The $g_{ClCl}(r)$ peak height of 3.0, with a maximum at 3.51Å and a smaller shoulder, peaking at 4.0Å, are consistent with the rdf simulated by using potential c (but are also close to that from potential d with both potentials c and d giving rise to tetrahedral A-X symmetry, where A is a triply charged cation and X is a singly charged anion). The ClCl coordination number, Z_{ClCl}, (the number of Cl atoms within a radius from a particular Cl which is given by the distance to the first minimum in the rdf for the ClCl pair) has a significant uncertainty because of the asymmetry of the peak shape which leads to a strong dependence on the method of evaluation. Comparison of values of Z_{ClCl} obtained using various methods of evaluation, is shown in Table 3. Fig. 6b shows the more informative running coordination number for neutron and MD work, $n_{\alpha\beta}(r)$ and indicates overall agreement. The slightly lower value for the MD work is related to the narrower first peak in the rdf (see Table 4).

The shoulder at about 4.0 – 4.5Å reflects the strong attraction of the highly charged aluminum ion. The Cl^- ions tend to pack tightly about polyvalent cations thus maximizing the number of Cl^- ions around the Al^{3+} ion. Integrating under the curve out to the long r side of the shoulder gives a coordination number of 9–10, see Fig. 6b.

The Al-Cl interaction

As regards the cross term, the $g_{AlCl}(r)$ has the expected narrow first peak at 2.13Å, with a large maximum reaching to 9.3. This falls to very small values before rising again at about 3.7Å. This value of 2.13Å, along with the Cl-Cl separation of 3.51Å, indicates a tetrahedral distribution of Cl^- ions about Al^{3+}

ions ($\sqrt{8/3} = 1.63$, $3.51/2.13$(experiment) $= 1.65 \pm 0.03$). As has been discussed[1], one can consider that the chloride ions are sitting in a deep potential well and are tightly bound. A comparison of the measured and molecular dynamically calculated running coordination numbers $n_{AlCl}(r)$ is shown in Fig. 6c. The value of about 4 for the nearest neighbor coordination number of Al by Cl is consistent with our deduction of the presence of $AlCl_4^-$ tetrahedra. The structureless form of the $g_{AlAl}(r)$ curve suggests that there are very few Al-Cl-Al bridges.

A final point to note is the partial charge cancellation effect when $g_{ClCl}(r)$ and $g_{AlCl}(r)$ are superimposed. This is also evidenced by the corresponding peak and trough in the $S_{ClCl}(k)$ and $S_{AlCl}(k)$, respectively, at about 2.1Å^{-1}.

<u>The Al-Al interaction</u>

If we now consider the $S_{AlAl}(k)$ for the AlAl pair, we see that the S(k) and consequently g(r) are relatively structureless, resembling the Ni-Ni structure factor in aqueous $NiCl_2$ solutions. Isolation of this S(k) and g(r) was very difficult because of the very low weighting in the simultaneous equations being solved, and because of its lack of structure. Consistent with this lack of structure, the equilibrium constant for the reaction

$$2AlCl_4^- \rightleftharpoons Al_2Cl_7^- + Cl^-$$

is known to be so small that essentially no Al-Al pairs should be present at 4.3Å.

The r-space information we obtained merely indicates a curve rising from zero around 4.0Å, increasing to no more than about 1.5 units, and falling back to the $r = \infty$ asymptotic value by about 9Å, results which are not inconsistent with the $g_{AlAl}(r)$ calculated by molecular dynamics.

<u>The Li-Cl interaction</u>

Comparison of our results for $^{nat}LiAl^{nat}Cl_4$, and the $^{o}LiAl^{nat}Cl_4$, in principle, should provide information on the LiCl pair distribution function. Because of the relative insensitivity of the experimental results to this interaction the statistical noise led to ambiguity in the results. Further work with substitution of Li isotopes would be needed to deduce the LiCl pair distribution function.

<u>Other concentrations</u>

Molecular dynamical simulations of more acid melts are under way,[5] and we intend to carry out neutron experiments on more acid mixtures, especially to study the expected increase in the number of Al-Cl-Al bridges.

To complete our experimental work, we should use lithium isotopes to improve the Li-Cl separation, although absorption by ^6Li might well limit our success.

CONCLUSIONS

The $AlCl_4^-$ tetrahedra known to be present in the equimolar melt LiCl-$AlCl_3$ appear to be tightly bound moieties as has been observed in MD simulations. This conclusion follows from the large first peak height in the rdf for AlCl pairs. The partial structure factors of Al-Al, Cl-Cl and Al-Cl have been determined. Reliable information on $g_{LiCl}(r)$ could not be extracted because of statistical noise in the data.

As expected, Al-Cl-Al bridging between tetrahedra was not observed. An increase in bridging is expected with an increase in melt acidity as has been observed in MD calculations.[5] The MD potentials c and d used by Saboungi *et al.* simulate our experimental results reasonably well with potential c being somewhat better. This conclusion was also deduced from X-ray results.[2]

ACKNOWLEDGMENTS

Two of us (SB,SC) would like to acknowledge the financial support of the Science and Engineering Research Council of Great Britain and one of us (MB) acknowledges the support of the Division of Materials Sciences, Office of Basic Energy Sciences of the U. S. Department of Energy. We would also like to thank Mr. P. Gullidge (Bristol) for carrying out the isotopic substitutions, and Mr. J. Settle (ANL) for assistance with sample drying and containment. Thanks are also due to P. Chieux (ILL) for his expert and diligent assistance throughout the experiment.

REFERENCES

1. M.-L. Saboungi, A. Rahman, and M. Blander, J. Chem. Phys., **80** 2141–2150 (1984).
2. S. Takahashi, T. Muneta, N. Koura, and H. Ohno, J. Chem. Soc. Farad. Trans. II, **81** 319–326 (1985).
3. R. A. Carpio, L. A. King, and A. A. Fannin, J. Chem. Eng. Data, **24** 22–24 (1979).
4. S. Biggin, M. Gay, and J. E. Enderby, J. Phys. C: Solid State Phys., **17** 977–985 (1984).
5. M.-L. Saboungi, A. Rahman, and M. Blander, this volume, p. **97**.

Table 1. **Parameters used in the data analysis.**

Temperature (°C)	200					
Density (gcm^{-3})	1.6^3					
Number density (Å^{-3})	0.032					
Cl isotopes	nat	38	mix	all-natural	^{o}Li	^{nat}Li
Scattering cross section (barns atom^{-1})	9.12	1.72	5.42	9.61	1.19	1.4
Absorption cross section (barns atom^{-1})	106.97	86.78	96.88	34.14	507.6	70.5
Aluminum scattering length (x 10^{-12}cm)	0.345	0.345	0.345	0.345	0.345	0.345
^{nat}Li scattering length (x 10^{-12}cm)	−0.203	−0.203	−0.203	−0.203	−0.203	−0.203
Anion scattering length (x 10^{-12}cm)	0.958	0.363	0.660	0.958	--	--

^{o}Li : 0.54 ^{6}Li + 0.46 ^{7}Li

^{nat}Li : 0.075^{6}Li + 0.925^{7}Li

Table 2. ^{o}LiAlCl$_4$ structural parameters. $r_{\alpha\beta}$ is the position of the first peak maximum in $rg_{\alpha\beta}(r)$, or in $g_{\alpha\beta}(r)$, as indicated. The coordination number of β about α is given by $Z_{\alpha\beta}$, using either the method of integrating under the symmetrized first peak in rg(r), *i.e.*, symmetrical distribution in rg(r) is assumed, or the method of integrating to the first minimum in $g_{\alpha\beta}(r)$, as indicated.

	$r_{\alpha\beta}$(Å)		$Z_{\alpha\beta}$	
	rg(r)	g(r)	rg(r)	g(r)
Cl-Cl	3.51 ± 0.03	3.50	4.54 ± 0.8	~6(to 4.1Å)
Al-Cl	2.13 ± 0.03	2.12	3.80 ± 0.4	3.81 ± 0.03
Al-Al	--	4.56	--	--

Table 3. **Comparison of diffraction and computer experimental results for the structural parameters. Ion-ion separation from the first maximum in $g_{\alpha\beta}(r)$ (fm) or symmetrical $rg_{\alpha\beta}(r)$ is given by r(Å) as indicated. Co-ordination number is given as indicated by either integration to first minimum in $g_{\alpha\beta}(r)$, (FM), or integration using symmetrical first peak in $rg_{\alpha\beta}(r)$.**

	molecular dynamics (ref.1)		this work	X-ray diffraction (ref.2)	
	potential c	potential d			
Cl-Cl					
r(Å)	∼3.47 fm	∼3.55 fm	3.51 ± 0.03 rg(r)		3.50 rg(r)
Z	∼3.5 FM	∼4 FM	4.5 ± 0.8 rg(r)	∼6 FM	∼6 rg(r)
Al-Cl					
r(Å)		2.1 - 1.2† fm	2.13 ± 0.03 rg(r)	2.15 rg(r)	
Z	∼4 FM	∼4 FM	3.8 ± 0.4 rg(r)	4.1 rg(r)	

†(defined from experiment)

Table 4. Comparison of the first peak height and full widths at half maximum for $g_{ClCl}(r)$ and $g_{AlCl}(r)$.

	peak height	FWHM
Cl-Cl		
this work	3.0	0.56
MD		
pot c	3.40	0.42
pot d	3.95	0.35
Al-Cl		
this work	9.3	0.34
MD		
pot c	16	0.25
pot d	18.5	0.32

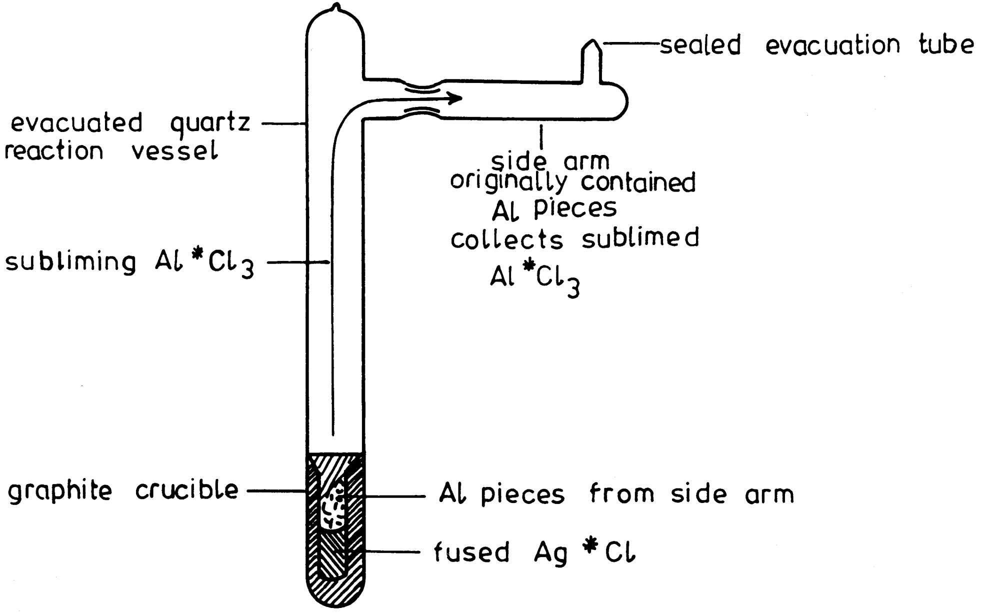

Fig. 1. Experimental setup for $AlCl_3$ powder production. Reaction was carried out at 450°C.

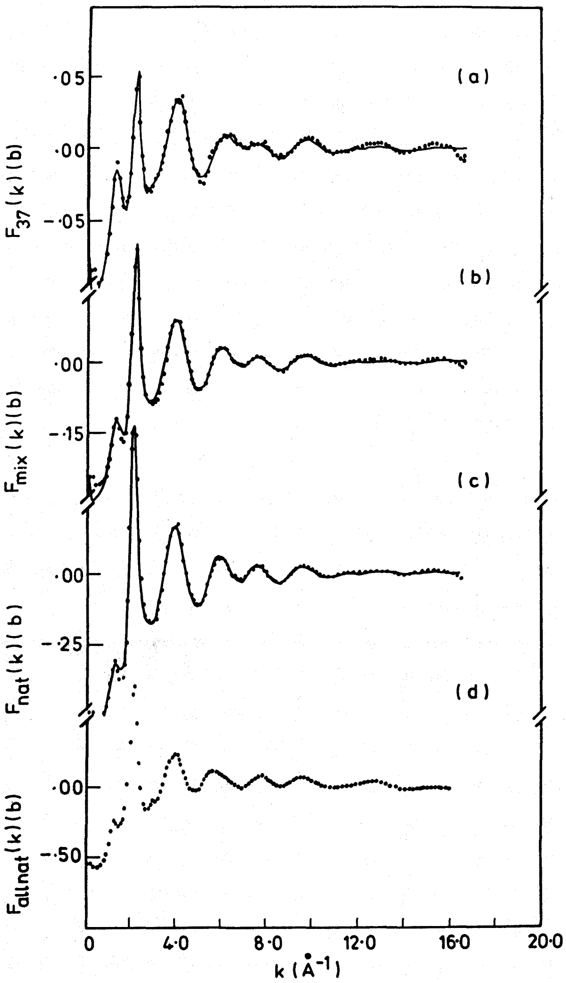

Fig. 2. Total structure factors, F(k), for $LiAlCl_4$, (a) $^{o}LiAl^{37}Cl_4$; (b) $^{o}LiAl^{mix}Cl_4$; (c) $^{o}LiAl^{nat}Cl_4$; (d) $^{nat}LiAl^{nat}Cl_4$. The full curves show the F(k) reconstructed using the $S_{\alpha\beta}(k)$ shown in Fig. 4. The statistical error of an average data point in F(k) is $\leq \pm 0.002$.

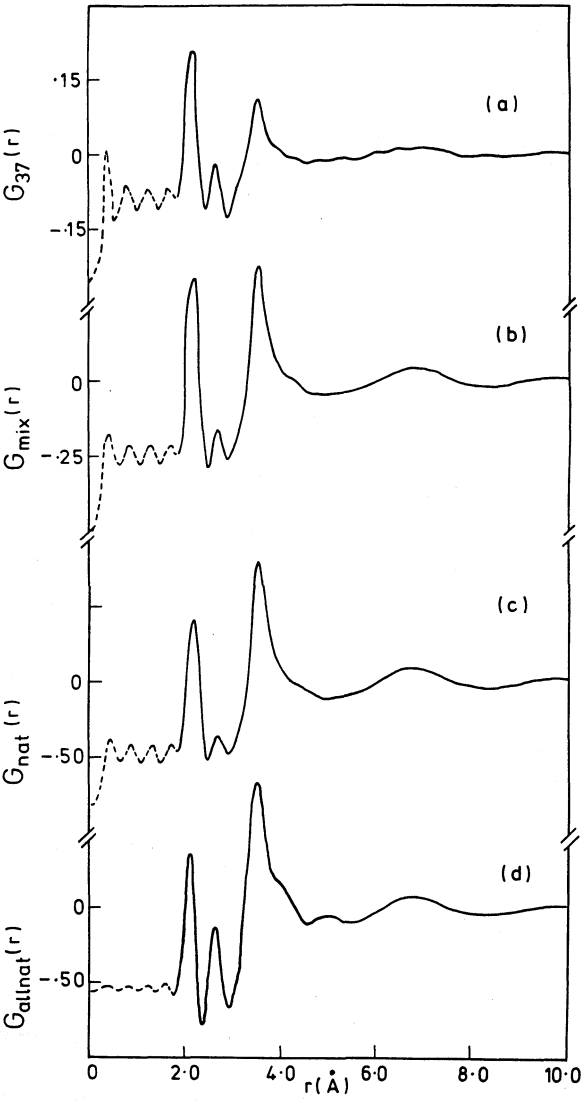

Fig. 3. Total radial distribution functions, G(r), obtained from the F(k) shown in Fig. 2. (a) $^{o}LiAl^{37}Cl_4$; (b) $^{o}LiAl^{mix}Cl_4$; (c) $^{o}LiAl^{nat}Cl_4$; (d) $^{nat}LiAl^{nat}Cl_4$.

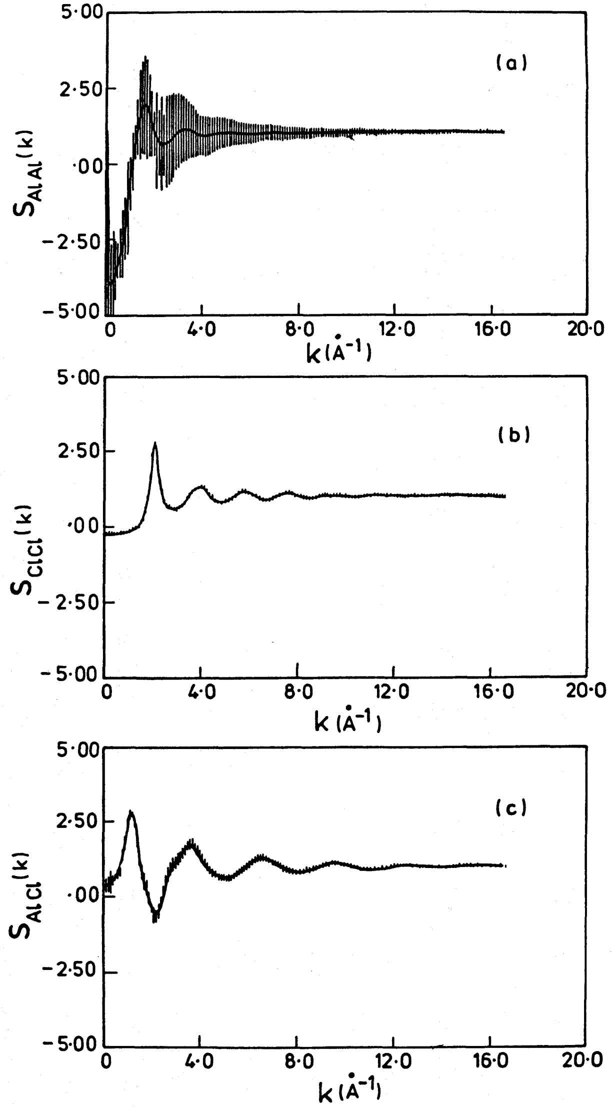

Fig. 4. Partial structure factors, $S_{\alpha\beta}(k)$. (a) $S_{AlAl}(k)$; (b) $S_{ClCl}(k)$; and (c) $S_{AlCl}(k)$.

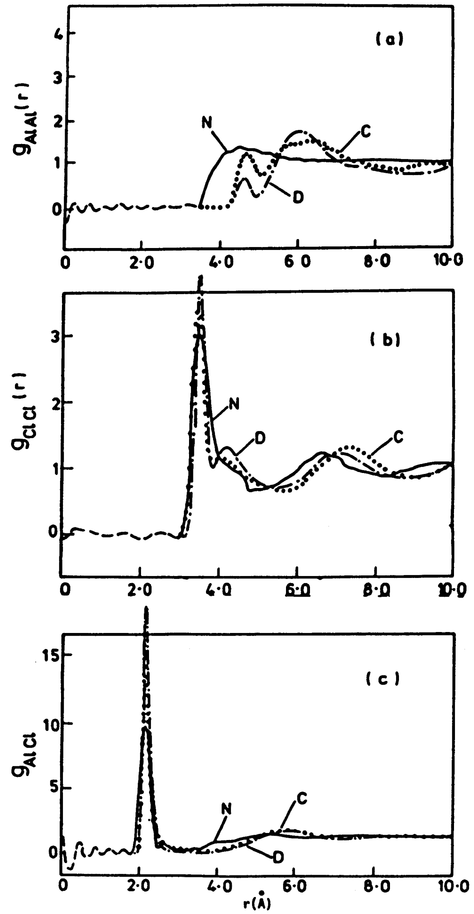

Fig. 5. Partial radial distribution functions, $g_{\alpha\beta}(r)$. (a) $g_{AlAl}(r)$; (b) $g_{ClCl}(r)$; and (c) $g_{AlCl}(r)$. N: neutron experiment; C: MD result, potential c; D: MD result, potential d.

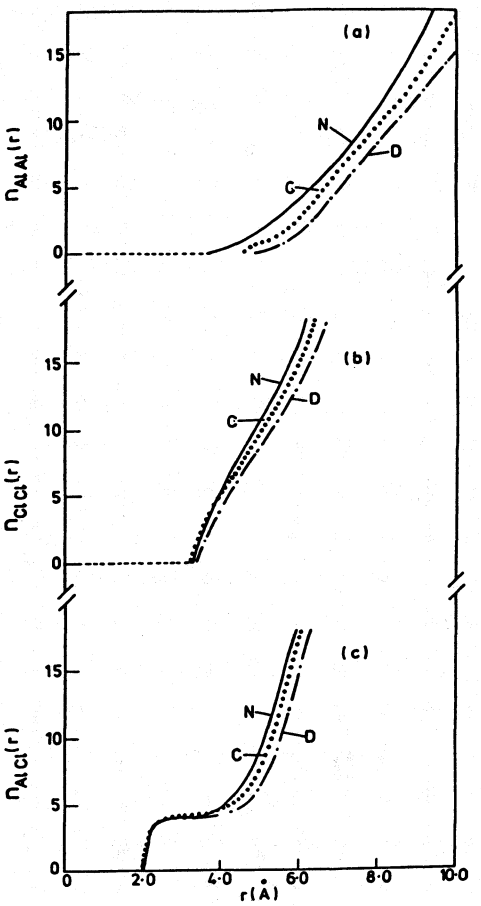

Fig. 6. Dependence of the running coordination numbers on r (a) Al-Al pairs; (b) Cl-Cl pairs; (c) Al-Cl pairs. N: neutron experiment; C: MD result, potential c; D: MD result, potential d.

DOI: 10.1149/198601.0097PV

A MOLECULAR DYNAMICS STUDY OF THE COMPOSITION DEPENDENCE OF ORDERING IN MOLTEN SALT COMPLEXING SOLUTIONS

M.-L. Saboungi, A. Rahman, and M. Blander
Argonne National Laboratory
9700 South Cass Avenue
Argonne, Illinois 60439

ABSTRACT

Analyses of molecular dynamics calculations for MX-AX_3 solutions of different compositions have been completed using two pair potentials. As previously observed, for the large radius ratio of X^-/A^{3+}, tetrahedral coordination of A^{3+} cations by X^- anions is obtained and the structures resemble those of chloroaluminates. For the small radius ratio, octahedral coordination of A^{3+} cations by X^- anions is obtained; however, some of the results defy conventional wisdom with e.g., a new complex species, unexpected stability of A-X-A bridges, and intermediate to long range order even at the M_3AX_6 composition.

INTRODUCTION

The terms complexing and ordering are often used to characterize solution properties of polyvalent halides with alkali halides. In order to develop a deeper understanding as well as theories of complexing, more detail on the structures of such solutions is required than is experimentally available. Molecular dynamics (MD) calculations of complexing systems have been reported[1] for a solution containing M^+, A^{3+}, and X^- ions at a composition corresponding to MAX_4; it was shown that when the interaction potentials between the ions were modified in a systematic fashion, the types of complexing also changed systematically from the case in which A^{3+} cations were octahedrally coordinated by X^- anions to that in which they were tetrahedrally coordinated by X^- anions. In the latter case, a small number of the tetrahedra were connected via a bridging X^- anion; the bridging could be described by the equilibria $2AX_4^- \rightleftarrows A_2X_7^- + X^-$ and $3AX_4^- \rightleftarrows A_3X_{10}^- + 2X^-$. Although these equilibria are similar to those observed in chloroaluminate melts,[2] the computed equilibrium constants were much larger than those determined experimentally. For the case in which A^{3+} ions were octahedrally coordinated, bridging of A^{3+} ions by X^- anions led to a tendency for ordering to distances at least as large as 10 Å; in addition, unexpected triangular configurations of A^{3+} ion triplets were observed. The overall results provided new insights into the phenomenon of "complexing" and were used for comparison with real systems.[1] Similar MD calculations are reported here on the two compositions M_3AX_6 and MA_3X_{10}. Investigation of the variations of structures with composition should provide a better understanding of structures to be expected in real melts. Our calculations provide the possibility of examining detailed structural differences in complexing melts at different compositions.

MOLECULAR DYNAMICS CALCULATIONS

As mentioned above, two additional compositions were studied in the MX–AX_3 system, namely M_3AX_6 composed of 150 M^+ ions, 50 A^{3+} ions and 300 X^- ions; and MA_3X_{10} composed of 35 M^+ ions, 105 A^{3+} ions, and 350 X^- ions. The following potential based on the Tosi–Fumi model[1,3] was used to describe the ionic interactions:

$$u_{ij} = Z_i Z_j e^2/r + B exp[A(\sigma_i + \sigma_j - r)] \qquad (1)$$

where $Z_k e$ is the charge on the k^{th} ion, e is the electron charge, r is the distance between particles, B is 0.19 (10^{-12}) erg, A is 3.155 Å^{-1}, and σ_k is the radius of the k^{th} ion. Four sets of values of σ_k were studied in which the anion/cation radius ratio, σ_X/σ_A was varied while the sums $\sigma_M+\sigma_X$ and $\sigma_A+\sigma_X$ were kept constant. In this paper, we will report results obtained with the two extreme sets of repulsive parameters (Table I). In potential a (or d), the sum of the radii was chosen so that the nearest neighbor interatomic spacings between M^+ and X^- in the melts would be similar to those found in KF (or NaCl) and the interatomic spacings between A^{3+} and X^- would be similar to those in YF_3 (or $AlCl_3$). Molecular dynamics calculations were carried out at temperature in the vicinity of 500 K. Details on the computational techniques have been described elsewhere. [1,4]

Table I. Repulsive parameters for the M^+, A^{3+} and X^- ions for the two pair potentials (Å). α_{XA} is the ratio (σ_X/σ_A).

Potential	σ_M	σ_A	σ_X	α_{XA}
a	1.352	1.372	1.578	1.150
d	1.052	1.072	1.878	1.752

RESULTS AND DISCUSSION

For each pair potential at a given composition, the calculations yielded the radial distribution functions (rdf's, $g_{ij}(r)$), the coordination numbers of a central ion, i, by another ion, j, at a distance r, $N_{ij}(r)$, as well as the angular distribution of selected triplets and the distribution of coordination numbers within a radius fixed by the first minimum in $g_{ij}(r)$ for certain pairs of ionic species. For simplicity, in what follows, the M^+ ion will be labelled as 1, A^{3+} as 2, and X^- as 3.

A. On Radial Distribution Functions and Coordination Numbers

The radial distribution functions which yield the most direct information on structures and complexing are those related to the pairs A–X and A–A, i.e., g_{23} and g_{22}. The g_{23} functions for the three compositions, M_3AX_6, MAX_4,[1] and MA_3X_{10}, exhibit very few differences. (see Figs. 1 and 2 and also Figs 1 and 2 from reference 1). In all melts and for both potentials, the variations of g_{23} with r show a sharp peak at 2.2 Å. Thus the A–X distance is very well defined in all these cases. The coordination numbers under these sharp peaks show an octahedral (∼6) coordination for potential a and a tetrahedral (4.0) coordination for potential d. As we had observed previously in MAX_4, the g_{23} in M_3AX_6 and MA_3X_{10} exhibit narrow steep first peaks at about 2.2 Å which drop to very low values between 3 and 4 Å. Thus, one would expect that an X anion in the first coordination sphere of any given cation will seldom "escape" from that sphere without first entering the coordination sphere of another A cation. This means that a mechanism for such an escape usually requires that an X anion is part of an A–X–A bridge as an intermediate state. Recent neutron diffraction[5] and x-ray scattering[6] studies have shown that the radial distribution function of the pair Al-Cl in tetrachloroaluminate melts have features similar to that calculated by molecular dynamics for a hypothetical MAX_4 ionic melt with tetrahedral coordination of the A^{3+} cation.

A careful examination of g_{22} can provide information on A-X-A bridges which connect pairs of A^{3+} cations and their surrounding coordination spheres. In MAX_4 and in M_3AX_6, for potential a, there is a pronounced peak at 4.5 Å in g_{22} (refer to Fig 1, and Figs 1 and 2 in reference 1). This indicates the presence of a significant number of linear A-X-A bridges for potential a in the two cases mentioned and there is, in fact, a relative absence of independent unconnected AX_6^{3-} moieties. For potential d, for the same two melts, the peak at 4.5 Å becomes an ill defined bump. However in MA_3X_{10} it is present for both a and d. Now the presence of a large peak in g_{22} at double the distance of the first peak in g_{23} must imply the presence of many almost linear A–X–A bridges. Such a peak is present in g_{22} in M_3AX_6 and MAX_4 for potential a but not for d. So far, the following conclusions can be made:

i) For potential a, many A–X–A bridges are present and very few if any

AX_6^{3-} moieties are detected for all three compositions. For example, using triplet correlations, we have calculated[4] that only 3 of the 50 A^{3+} cations are part of an unbridged AX_6^{3-} moiety in M_3AX_6. This result goes counter to commonly held concepts for such melts where a large number of AX_6^{3-} species are usually assumed to be present.

ii) For potential d, A–X–A bridges are present and AX_4^- moieties absent for MA_3X_{10}; but for M_3AX_6 and for MAX_4 there is very little bridging and AX_4^- moieties predominate.

B. Triplet Distribution Functions

The tendency for octahedral coordination of A^{3+} cations with potential a and tetrahedral coordination with potential d can be further justified by results obtained for the angular distributions of ion triplets.[4] In Fig. 3, distributions of X–A–X triplets are plotted versus the cosine of the angle with A as an apex for the two melts. As expected, for potential a there are peaks near $\cos\theta = -1$ and 0 (180° and 90°) consistent with the angles expected in an octahedral configuration. The peaks at $\cos\theta = 0$ are asymmetric and the tails of these peaks (at values of $\cos\theta < 0$) are related to the presence of A^{3+} cations which have coordination numbers less than six (see Table II). For potential a, the A^{3+} cations in MA_3X_{10} have a lower average coordination number than in M_3AX_6; this fact is reflected in a larger tail of the angular distribution of the X–A–X triplets in MA_3X_{10} than for M_3AX_6. Also, for this potential, there is a distribution of the coordination number. For potential d, the coordination number for essentially all A^{3+} cations is 4 for all melts. Consequently, the tail in Fig. 3 for the dashed curves is negligible.

Table II. Distribution of A^{3+} ions according to their coordination by X^- ions within 3.0 Å for the two pair potentials.

a. M_3AX_6

Potential/z	4	5	6	Z_{23}^*
a	0.00	2.81	47.19	5.94
d	50.00	0.00	0.00	4.00

b. MA_3X_{10}

Potential/z	3	4	5	6	Z_{23}^*
a	0.00	1.81	33.64	69.55	5.64
d	0.34	104.61	0.05	0.00	4.00

*Z_{23} is the average coordination number evaluated at the first mimimum in g_{23}.

As we had found for the MAX_4 composition, the A–X–A configurations for most of the melts are close to linear. However, the maximum of the angular distribution of A–X–A triplets (with X as an apex) for M_3AX_6 is at cos $\theta \sim$-0.9 (not at -1); this broad peak includes contributions from angles ranging from 145–160°. For MA_3X_{10}, the maximum of the angular distribution of A–X–A triplets is at $\theta = 0$. These observations suggest that when, there are many bridges which tend to form a three-dimensional network of interconnected A-X-A bridges (as for potential a in MAX_4 and for both the potentials in MA_3X_{10}), the geometric constraints imposed by the network lead to fewer bent and more of the energetically less favorable linear bridges. If this suggestion is correct, the formation of a network would impose a strain energy on the bridge to keep it more linear.

The intermediate to long range order discussed in Ref. (1) can be examined by referring to the angular distribution of A–A–A triplets given in Fig. 4 for potential a. If the A–X–A triplets were linear, and all the A^{3+} octahedrally coordinated by the anions, then the A ions would be octahedrally coordinated by the A cation (*e.g.*, the angular distribution would exhibit sharp peaks at the octahedral angles, 90° and 180°). In a manner similar to MAX_4 (potential a), the A-A-A angular distribution shows the presence of peaks at or near 90° and 180° for M_3AX_6 and for MA_3X_{10} in Fig. 4. These peaks are not sharp, indicating significant distortion from octahedral coordination (with perhaps possible ancillary peaks near 100 – 110°).

In addition, there is a sharp peak at 60°. The relatively large size of this peak together with the presence of a maximum in the angular distribution of A-X-A indicates a possible structural relationship between the formation of A-A-A equilateral triplets and the presence of A-X-A angles near 150°. One can speculate on the types of configurations which might lead to this apparent correlation. One possible idealized structure is a planar hexagonal structure with three X anions which are part of 150° A-X-A triplets alternating with three A cations which are part of 90° X-A-X triplets. (In reality, the structure may not be as symmetric as this where the angles are meant to represent an average of a broad distribution). These observations require confirmation by further calculations and ultimately by experiments.

For potential a, the intermediate range ordering can be detected from the angular distributions of A-A-A triplets, more specifically by the presence of peaks near 180° (Fig. 4). The relative number of these triplets is quite small for M_3AX_6. As a result, a feature such as the small peak in g_{22} near 9 Å for potential a are significantly smaller for M_3AX_6 (Fig. 1) than for MAX_4 (Fig. 2 of Ref. 1) or MA_3X_{10} (Fig. 2).

Of particular interest, are the peaks at or near 90° in the angular distributions of A-A-A triplets of *e.g.*, potential a for M_3AX_6, MAX_4, and MA_3X_{10}. The shape and positions of the peaks for these triplets is commensurate with the shape of the peaks in g_{22} in the vicinity of 6–8 Å. The width and general shape of these peaks is largely a reflection of the angular distribution of A-A-A triplets. Consequently, we see that measured binary (radial) distribution functions could be used to deduce information concerning triplet distribution functions of moderate range.

C. Complexing and Bridging

Up to now, many features of our calculations appear to reproduce experimental observations; however some are unexpected and deserve careful experimental investigations. As noted, the strong coulomb attractions of the X^- anions by the trivalent A^{3+} cations leads to tight packing of the anions in the first coordination shell of the A^{3+} ion. The most clear-cut results of the tight packing are the relatively tall narrow first peaks in g_{23} which drop to very low values between 3 and 4 Å. These are present at all compositions (including MAX_4 discussed in Ref. 1) and for all potentials indicating that their presence is independent of whether the X^- ions are or are not part of an A-X-A bridge. The low values of g_{23} at 3-4 Å imply that there is a constraint on the transport of a nearest neighbor X^- anion away from an A^{3+} cation such that it would usually have to first enter the first coordination shell of another A^{3+} cation and form a bridged A-X-A structure. Thus, in very dilute solutions of AX_3 in MX, the complex ion AX_n^{3-n} would be expected to have a relatively long lifetime.

The strong cation–anion attraction also leads to the maximum number of X^- anions in the first coordination shell of A^{3+} ions which is commensurate with the effective radii of the anions. Thus, the increase in the X^-/A^{3+} radius ratios in going from potential a to d is reflected by a decrease in the average coordination numbers of A^{3+} cations from about 6 to 4.0. The close packing of X^- ions in the first coordination sphere produces complex ions in dilute solutions of AX_3 which, with an increase in the AX_3 concentration, become interconnected by A-X-A bridges to ultimately form a three dimensional network.

The formation of A-X-A bridges can be written in terms of an equilibrium

$$2(A-X) \rightleftarrows (A-X-A) + (X) \qquad (2)$$

where (X) represents an X^- ion which has no A^{3+} cations as nearest neighbors and (A-X-A) denotes a bridged X^- ion which has two A^{3+} cations as nearest neighbors. For potential a, this equilibrium goes much more to the right than for potential d. This can be most simply illustrated for the cases where one has a relatively small number of bridges.

For example, for potential d, the formation constant of a bridged species from an unbridged species, $2AX_4^- \rightleftarrows A_2X_7^- + X^-$ is 4×10^{-2} in M_3AX_6; this value is commensurate with that deduced for MAX_4, 3×10^{-2}.[1] However, the measured value of this constant in a $NaAlCl_4$ melt is of the order of 10^{-7}. The inclusion of polarizability in our calculations is expected to improve the correspondence between the computed and experimental values. In fact, the field intensity at the center of an X^- ion would then be smaller for a bridging than for a non-bridging anion thus decreasing the relative stability of non-bridging anions and the ratio of bridging to non-bridging anions.

For the case of potential a in M_3AX_6, (octahedral coordination of A by X) the formation constant of a bridged species from an unbridged species, $2AX_6^{3-} \rightleftarrows A_2X_{11}^{5-} + X^-$ is estimated to be about 60. This can only be approximated to a factor of about two, because the exact number of "free" $A_2X_{11}^{5-}$ moieties can not be derived from our data due to the relatively large number of A-X-A bridges and species with multiple bridges. In any case, the formation constant of a bridging species is much larger for potential a than for potential d.

Irrespectively of the potential, with a decrease in the MX/AX_3 ratio, the number of A–X–A bridges continues to increase to ultimately form a three dimensional network. The network tends to be somewhat ordered as is evidenced by the angular distributions of A-A-A triplets and the appearance of peaks in g_{22}. For potential a, the order is evident with well-defined peaks in the angular distribution of A-A-A and in g_{22} corresponding to distances between A^{3+} cations at least as large as 9.2 Å. The steric constraints imposed by the octahedral packing of X^- about A^{3+} ions combined with the linearity of the A-X-A bridges, tend to lead to the formation of cubic structures for potential a. The corresponding tendency for tetrahedral structures for potential d is much weaker as evidenced by the shallow flat peak near the tetrahedral angle in the angular distribution of A-A-A triplets and in the broad peaks in g_{22} near 7.8 Å.

CONCLUSIONS

The concept of complexing, therefore, encompasses several kinds of structural effects. First, there is the tendency for a particular coordination number for the polyvalent cation. In dilute solutions this leads to complex ions, AX_n^{3-n}, which are independent moieties dispersed in the solvent. As the concentration of AX_3 increases, these moieties become joined by A-X-A bridges to form larger species until ultimately a three dimensional interconnected network is formed. Such a network can exhibit intermediate to long range order depending on the nature of the network. In our work, this order is clear-cut when a significant fraction of the A^{3+} species are octahedrally coordinated. This order should be a characteristic feature of some complexing systems and can even be present in "neutral" melts (*i.e.*, M_3AX_6 for octahedrally coordinated A^{3+} cations).

In addition to these general characteristics there are notable specific features, the most striking of which is the appearance of triplets of A^{3+} cations for potential a which may be part of a larger structure discussed earlier. The means for detecting such species poses a considerable challenge to experimentalists.

The increase in the relative numbers of bent A-X-A bridges with an increase in the MX/AX_3 ratio for potential a seems to parallel that of A-A-A equilateral triplets. One might speculate on this increase of bent A-X-A bridges as follows. Because of geometric constraints, a three dimensional network of bridged AX_n groups is too rigid to accommodate bent A-X-A bridges. With an increase in the MX/AX_3 ratio the number of A-X-A bridges decreases and the network becomes less stiff. This flexibility permits the assemblage to more readily accommodate somewhat bent A-X-A bridges and enhances the relative probability for the formation of the equilateral A-A-A triplets.

Most important perhaps is that our results provide a basis for the interpretation of structural measurements. Similarities and differences between measurements and our calculations can enhance the structural information provided by experiment and provide many structural details one could not readily deduce from measurements. For example, the height and width of the first peak in g_{23} can be interpreted in terms of the effective pair potentials between ions. Peaks similar to those found in g_{22} for potential a at about 6-8 Å can be used to provide information on triplet distributions. Finally, the MD calculations provide a basis for planning an experimental program.

ACKNOWLEDGMENTS

This work was supported by the U. S. Department of Energy, Office of Basic Energy Sciences. MLS and MB are grateful to Dr. Romesh Kumar for helpful suggestions.

REFERENCES

1. M-L. Saboungi, A. Rahman, and M. Blander, J. Chem. Phys. **80** 2141–50 (1984)
2. L. G. Boxall, H. L. Jones, and R. A. Osteryoung, J. Electrochem. Soc. **120**, 223 (1973); E.W. Dewing, Met. Trans. **12B**, 705 (1981)
3. F. G. Fumi and M. P. Tosi, J. Phys. Chem. Solids **25**, 31 (1964); M. P. Tosi and F. G. Fumi *ibid* **25**, 45 (1964)
4. M. Blander, M.-L. Saboungi and A. Rahman, in preparation
5. S. Biggin, S. Cummings, J. E. Enderby and M. Blander, This volume, p. 81
6. S. Takahashi, T. Muneta, N. Koura and H.Ohno, J. Chem. Soc. Farad. Trans. II **81**, 319 (1985)

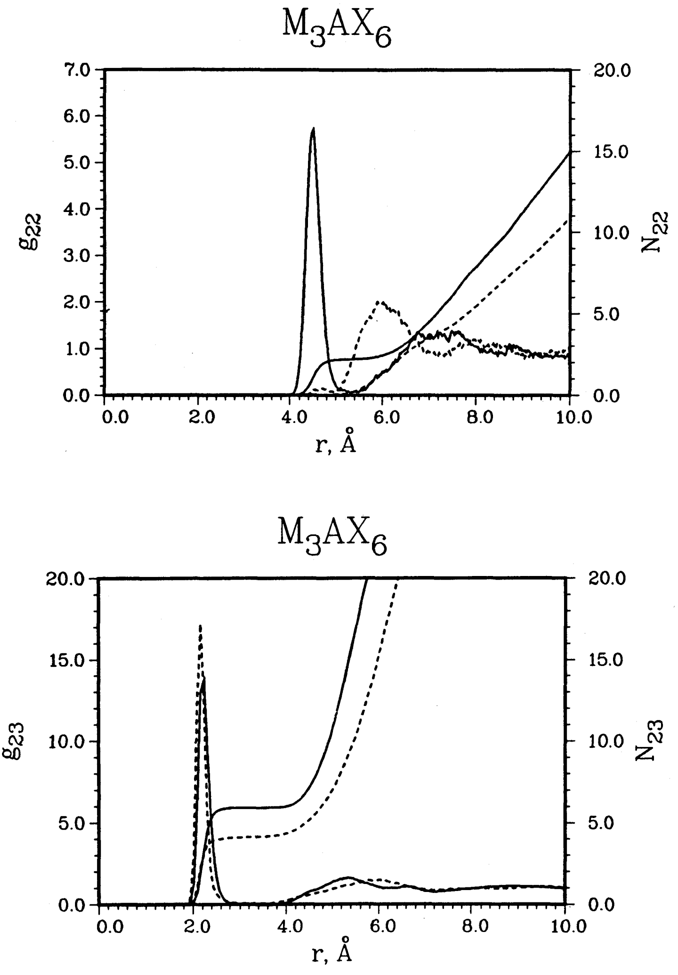

Fig. 1 **Radial distribution functions, $g_{ij}(r)$ and radius dependence of the average coordination numbers, N_{ij} calculated for M_3AX_6 using potential a, (solid line) and potential d, (dashed line).**

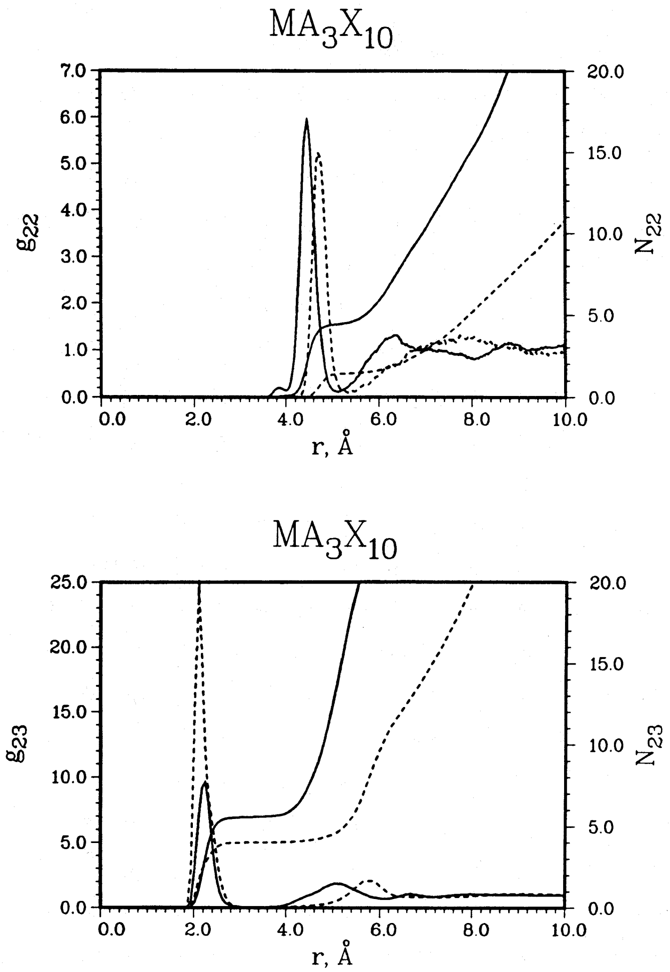

Fig. 2 Radial distribution functions, $g_{ij}(r)$ and radius dependence of the average coordination numbers, N_{ij} calculated for MA_3X_{10} using potential a, (solid line) and potential d, (dashed line).

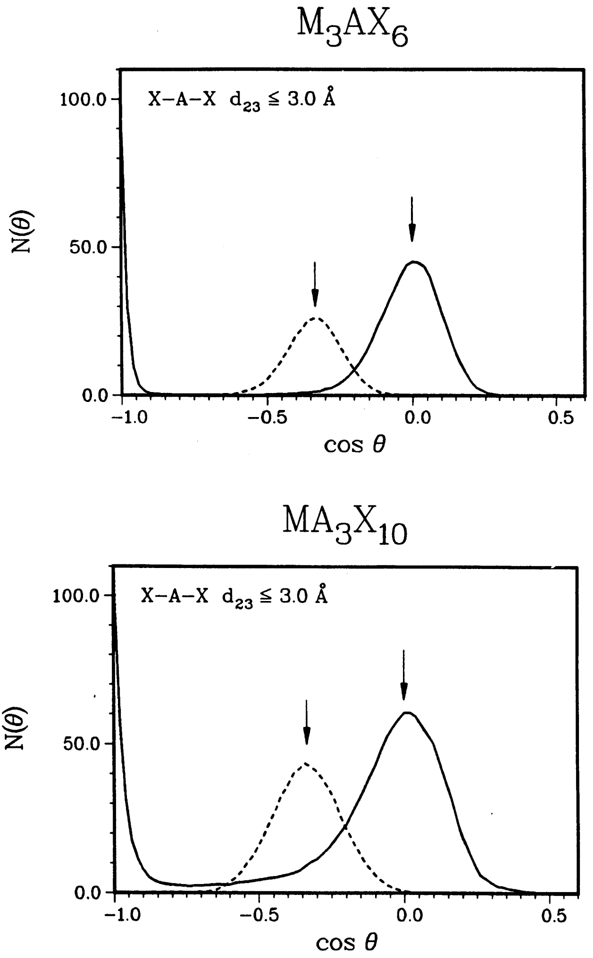

Fig. 3 Angular distribution of the A–X–A triplets for a maximum distance of the A–X pairs of 3.0 Å. Potential a, solid line; potential d, dashed line.

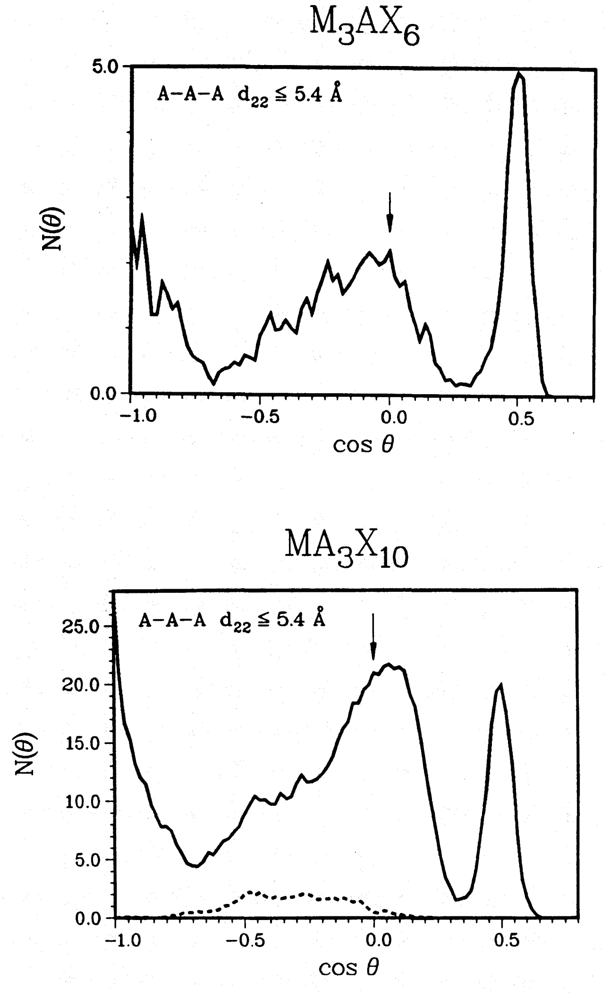

Fig. 4 Angular distribution of the A–A–A triplets for a maximum distance of the A–A pairs of 5.4 Å; potential a, solid line; potential d, dashed line. The arrows indicate the angles at 90° and 60°.

DOI: 10.1149/198601.0109PV

ELECTRODE REACTIONS IN MOLTEN SALTS

D. Inman

Department of Metallurgy and Materials Science,
Imperial College of Science and Technology,
London SW7 2BP, U.K.

ABSTRACT

Many types of electrode reaction occur in molten salts but, relative to aqueous solutions, little is known concerning their kinetics and mechanisms.

After a general survey, detailed attention is given to the cathodic deposition of metals and non-metals from halide and oxy-anionic melts, including the dependence of the structures of the metallic deposits on the corresponding electrochemical parameters.

For liquid metal deposits the very rapid charge transfer steps dominate the behaviour of the overall reaction. This phenomenon is related to the metal-molten salt interfacial structure. For solid metal deposits produced by single step processes, the focus of interest is their nucleation and growth. If these deposits are produced by multistep processes from transition metal ions the chemical complications often obscure the structural phenomena.

Finally, future prospects for high temperature electrode reaction studies are cited and discussed.

INTRODUCTION

It is difficult to provide a short review of such a broad and diverse topic as electrode reactions in molten salts, even if this is restricted to the high-temperature inorganic systems. This paper will therefore comprise an overview of the results and conclusions which have been and will be discussed in more detail elsewhere.

The inorganic molten salts extend from the low-melting nitrates through the ionic and partially ionic halides, to the very high-melting silicates; they can be usefully subdivided into the simple ionic melts, the oxyanionic melts, the polymeric or network melts, the molecular melts and the aqueous melts, although an increasing number of intermediate types such as $AlCl_3$-NaCl, where Lewis acidity (and ionicity) is dependent on composition, are being investigated.

The absence of the complicating influences of an associated liquid such as water might lead us to suppose that atomic events at molten salt/metal (particularly liquid metal) interfaces would be relatively simple. However, the complexity of many molten salt electrode processes in practice due, for example, to the effects of adsorption and coupled chemical reactions along with the difficulties of conducting experiments on these interfaces at high temperatures, have frustrated many of our efforts to gain a better understanding of these phenomena. Nevertheless, understanding of electrode processes in fused salts has increased very rapidly in recent years.

Starting with the Manhattan project in the second world war, much of the modern fundamental work has been stimulated by, and supported because of, the technological applications of molten salts. The increasing diversity of these technological applications does however have its adverse features: although a coherent body of literature is built up over the years if the industrial interest is large and continuous (e.g. in aluminium electrowinning), if it is small and ephemeral then its influence is diversive, at least in regard to our **general fundamental understanding** of electrode processes in molten salts. Thus the end of the molten salt reactor experiment at Oak Ridge can be seen to mark the end of a golden era of molten salt electrochemistry (and chemistry!).

Nevertheless some present or potential technological applications, viz. the electro-extraction and electro-forming of refractory metals and high temperature fuel cells and batteries for energy conversion and storage have generated a considerable body of fundamental information.

Perhaps the biggest improvements over the last thirty years or so have been with regard to electrochemical instrumentation. It is now common to apply the techniques well known to aqueous solution electrochemists to molten salts. Techniques such as chronopotentiometry and, latterly, particularly linear sweep voltammetry, have been very useful in providing us with the "electrochemical spectra" of unknown and perhaps, in the stoichiometric sense, complicated electrode processes.

These techniques however are not very helpful with regard to understanding the kinetics and mechanisms of charge transfer processes proper, and we should not attempt to extract too much information from them in this regard.

Perhaps the most surprising development of recent years is the applicability of many of the concepts of aqueous solution electrode processes to those occurring in molten salts. One can cite such phenomena as the coupling of chemical reactions to charge transfer processes, the (presumed) presence of multi-ionic layers on the solution side of metal-melt interfaces, the adsorption of ions, the occurrence of charge transfer and reaction overpotential, the key importance of Lux-Flood acidity-basicity to electrode reactions in oxyanionic melts, the occurrence of surface film phenomena, the formation of less common species such as O_2^{2-} and O_2^{-} in oxidising media and so on.

In this article, the many types of electrode reaction encountered in molten salts will be listed but in particular the cathodic metal ion/liquid metal reactions in molten halides will be compared with those involving solid metals, and in turn these reactions in halides will be compared and contrasted with processes involving both metals and non-metals, (viz. Pb, Cd and C) in oxyanionic melts. Much of this latter work is very recent and relates to other presentations at this symposium whereas in the former case (solid metals) the interest centres on the dependence of the structures and morphologies of the deposits on the electrochemical parameters of the corresponding reduction processes and on this basis to the electrical control of these processes and their products.

CLASSIFICATION OF ELECTRODE REACTIONS

Many electrode reactions in molten salts, especially metal-metal ion reactions, are subject to mass transfer rate control but it is now recognised that there are several significant exceptions and many slow, i.e. classically irreversible, reactions do occur. Under laboratory conditions mass transfer will generally take place by linear diffusion but in certain circumstances spherical diffusion and convection can augment this process and their effects are difficult to distinguish from kinetic and catalytic complications arising from chemical reactions coupled to charge transfer processes. Also it is sometimes difficult to distinguish the effects of the discharge of adsorbed ions from non-Faradaic multilayer charging, particularly at short times.

The types of cathode process encountered are:

(i) reduction of the solvent cation to a liquid metal product, e.g. Na from NaCl. The processes are complicated by the back reaction in which the metal dissolves in the melt to form electronically conducting solutions.

(ii) reduction of a solute cation to a liquid metal product, e.g. Pb from $PbCl_2$ in NaCl. These processes frequently exhibit adsorptive effects (see below).

(iii) reduction of a solute cation in a single step to a solid metal product, e.g. Ag from AgCl in NaCl, Cr from $CrCl_2$ in LiCl-KCl (see below). These processes frequently exhibit the post-charge transfer complications of deposit nucleation and growth.

(iv) reduction of a solute cation by a multiple step process to a solid metal product (e.g. Ta from TaF_5 in LiF). These can involve the formation of insoluble or soluble intermediate oxidation states which may or may not disproportionate and/or inhibit the thermodynamically predicted overall process. Electro-nucleation and growth processes probably play a part in these processes as well, although this may be obscured by the gross complication of the behaviour of the intermediate oxidation state.

As well as multiple charge transfer steps, the overall process may involve the coupling of the dissociation of complexed precursors to the main charge transfer process (e.g. Mo from $MoCl_3$ in LiCl-KCl).

(v) reduction of an oxy-anion to produce a non-metal (e.g. C from Na_2CO_3 in LiCl-KCl).

(vi) reduction of a dissolved gas (e.g. $\frac{1}{2}O_2 + 2e \rightarrow O^{2-}$) which, superficially, is the simplest of oxygen electrodes but in practice is complicated by the formation of such ions as O_2^{2-} and O_2^-.

(vii) reduction of a solute cation to a soluble product. These may involve metal ions (e.g. $Cr^{3+} + e \rightarrow Cr^{2+}$) or non-metal ions (e.g. $NO_3^- + 2e \rightarrow NO_2^- + O^{2-}$ or $S_2^{2-} + 2e \rightarrow 2S^{2-}$).

The types of anode process encountered are:

(a) oxidation of a solute cation to a soluble product (e.g. $Cr^{2+} - e \rightarrow Cr^{3+}$).

(b) oxidation of an anion to a gaseous product, e.g. $2Cl^- - 2e \rightarrow Cl_2$).

(c) anodic production of a solid film on the electrode surface. Post-charge transfer chemical reactions in oxygen evolution reactions such as $M + \frac{1}{2}O_2 \rightarrow MO$, or direct participation of the metal electrode in the electrode reaction, $M + O^{2-} \rightarrow MO + 2e$, or dissolution-precipitation reactions of the type $M \rightarrow M^{2+} + 2e$ followed by $M^{2+} + O^{2-} \rightarrow MO$, can lead to these solid films.

The anodic production of sulphur can be even more complicated as in this case, in addition to the interaction of the product with the substrate, there is the possibility of sulphur atom/ion catenation parallel to the electrode surface.

CHARGE TRANSFER PROCESSES INVOLVING LIQUID METALS

These processes are generally so rapid (in the steady state mass transfer controls the rate of the overall reaction) so that special relaxation techniques are needed for the measurement of their kinetics. Nagy and his collaborators have recently made several improvements to data collection in this area as in the past many of the techniques have not been applied correctly.(1)Because of this, doubts surround the quantitative significance of many of the published values of, e.g., exchange current density. Nevertheless, on the basis of the data now available, it is possible to develop a qualitative picture of the events taking place at the metal-melt interface. This should form the basis of future quantitative investigations using these improved techniques.

Classical methods for characterising the electrical double ("multi") layer at any metal/electrolyte solution interface involve making measurements of the interfacial tension(2) &/or the interfacial capacitance as functions of applied potential(3). Many studies of this type have been made, particularly by Russian schools, with the following overall conclusions.

The minimum interfacial capacitances for metal/molten salt systems are of the same order of magnitude as those for, e.g., $Hg/H_2O(KCl)$ at 25°C. The interfacial capacitance - applied potential curves are roughly parabolic in shape (at potentials close to the zero charge potential, $E_{q=0}$) with the minimum capacitance at a potential which coincides within experimental error with the potential of the electrocapillary maximum. While the characteristics of the electrical double ("multi") layers, as exemplified by these curves, appear to be largely independent of the nature of the metal phase, the observed capacitances do depend, both in magnitude and in potential response, on the composition of the molten salt phase; the cationic composition of these phases seems to exert the greatest influence.

The general features of the interfacial capacitance/potential plots are as follows:

(a) the profiles are parabolic with minima at $E_{q=0}$ (the zero charge potential);

(b) the zero charge potential for halides is the same for bromides, iodides and chlorides (same cation composition) but changes for the corresponding fluoride melt. C_{min} increases as $Cl^- < Br^- < I^-$;

(c) a marked dependence of the zero charge potential on the cation composition is found (e.g. for the melts LiCl, KCl and CsCl);

(d) C_{min} increases with temperature and the interfacial capacitance/potential profile is very different in the low (~ 673K) and high (1073K) regions.

These comments apply to the alkali metal halides.

This behaviour may be interpreted in terms of an electrical multilayer with the excess charge on the melt side of a liquid metal-molten salt interface distributed across several ionic layers. Various attempts have been made to describe this layer in theoretical terms(4). However, the remarkable changes which occur in the shapes of the capacitance-potential curves as the temperature is raised, and the accompanying rapid increase of capacitance with potential has not been adequately accounted for by these theories. Many years ago, Graves and I tried to separate the charging process from the Faradaic electrode process **instrumentally** by making pulse measurements at very short times (equivalent to measuring the interfacial impedance at very high frequency)(5). In principle, charge rearrangement at the interface has a much shorter time constant than charge transfer **across** the interface. A plot of the multilayer capacitance vs potential plot for liquid lead in LiCl-KCl at low temperature (450°C) is shown in figure 1. Two regions are clearly delineated. At potentials well cathodic to the Nernst potential for Pb/Pb^{2+}, the capacitance-potential plot is a very shallow parabola and in this region, which corresponds to the limiting current region in voltammetry, the concentration of lead ions at the lead metal surface equals zero and the electrode is quasi-ideally polarisable ($i_o \rightarrow 0$). Near to the Nernst potential, the capacitance rises very sharply with electrode potential and the electrode is quasi-ideally reversible ($i_o \longrightarrow \infty$). Some quantitative support for this is shown in figure 2. In this region common data are obtained through varying the electrode potential externally and through poising the electrode potential by the addition of lead chloride. Whether or not there are lead ions present in the bulk melt, their concentration at the electrode surface will be zero in the quasi-ideally polarisable region. The atomic-level model on which this plot is based is that the enhanced capacitances in the quasi-ideally reversible region are adsorption pseudo-capacitances; that is, the discharge and formation of adsorbed metal ions are very rapid processes (high exchange current density) which cannot be distinguished with presently available techniques from the processes of ion rearrangement (normal charging).

Unhappily, there has not been much research activity in this area in recent years (but see (6)). However, the liquid metal/molten salt interface **is** extremely important vis-a-vis the electrowinning of metals such as magnesium and aluminium, so that hopefully there will soon be a resurgence of interest. There is much scope for measurement of this sort over the temperature ranges spanning the melting points of the metals and of course for fast response time measurements allowing the time resolution of these fast interfacial processes.

CHARGE TRANSFER PROCESSES INVOLVING SOLID METALS: SINGLE STEP REDUCTION.

As will be evinced below, gross complications arise when solid metals are deposited via multi-step charge transfer processes. When however, the element concerned only exhibits one oxidation state in solution e.g. Ag^+ , or the element is present in solution in its lowest oxidation state, e.g. Cr^{2+}, then in the absence of these gross complications the phenomena of electro-nucleation and -growth play dominant roles subsequent to the primary charge transfer process.

This may or may not involve the discharge of adsorbed ions, as discussed above, for liquid metals where these subsequent complications are absent.

That electro-nucleation and -growth complications are playing a part is most straightforwardly indicated by initial potential "overshoot" on chronopotentiograms (7). This can be eliminated by predepositing the metal concerned on the foreign substrate used for the working electrode. The (excess) nucleation overpotential which is necessary to effect nucleation is of course analagous to the excess concentration of a supersaturated solution. The phenomena can be studied in a more detailed way by chronoamperometry (that is by studying the current-time relationships obtained at constant applied overpotential) (8). Typical plots of this type are shown in figure 3. After initial charging, the current falls during an induction period and then rises during the subsequent continuous nucleation and growth stage before falling according to the classical diffusion-controlled model when the surface layer is completely formed. That nucleation and growth phemonena are occurring simultaneously during this process is evinced by the plots of I vs $t^{3/2}$ as functions of applied overpotential shown in figure 4. However, the most important result to come out of this work is that the saturated nucleus densities (N_s) on the substrate increase with increasing applied overpotential. A plot of N_s vs η (overpotential) is shown in figure 5 along with the corresponding i (current density) vs overpotential plot (9). It is noteworthy that for high N_s values (high overpotential), the current density (i) is in its limiting region and dendritic growth is very likely to occur.

On the other hand, it can be seen that when the overpotential is low, i is a small fraction of its limiting value, dendritic formation will be very unlikely but the saturation nucleus density will be very low (i.e. the coverage of the substrate by the deposit will be poor). A consideration of these plots led to the idea of a pulsing method to optimise the electroplating of chromium in molten salts. Maximum surface coverage is obtained by applying an initial high overpotential "spike" and this is followed by much lower overpotential growth electrolysis. The success of this process is described elsewhere (10).

CHARGE TRANSFER PROCESSES INVOLVING SOLID METALS: MULTIPLE-STEP REDUCTION/REACTION CONTROL

Several reviews on this topic have appeared in recent years so the present position will only be summarised here (11). There are major differences between the results (mainly for the transition group refractory metals) which have been obtained for fluoride melts and those for chlorides. In the former it is generally possible to reach the metallic state whereas in the latter the formation of insoluble, inhibiting lower oxidation state compounds often constitutes the final reduction stage observed within the available electrochemical window of the solvent. In both types of melt however, reduction to metal etc. from the highest oxidation state ions takes place by several steps.

Electroanalytical techniques such as linear sweep voltammetry and chronopotentiometry are often used to establish the stoichiometries of overall electrochemical reactions and it is this sort of technique which establishes that reduction/oxidation takes place in stages. Furthermore, by suitable analysis of the LSV or chronopotentiometric waves, the "irreversibility" of these waves may be estabished. At high temperatures this probably arises from factors other than slow charge transfer. As initially observed by Mellors and Senderoff, (12) the last step in the sequence of steps leading from a high oxidation state in a fluoride melt to the metal is generally slow (i.e. irreversible and rate-determining). This slow step seems to play an important part in ensuring a dendrite-free deposit by a continuous (i.e. non-pulsed) electrolysis.

Mellors and Senderoff related this slow step to the formation of a sparingly-soluble intermediate oxidation-state compound on the electrode surface. However, in some cases the stoichiometries of the compounds that they proposed are not in accord with those generally accepted. In any event, this matter needs to be looked at again in the light of current knowledge and with the improved techniques (e.g. linear sweep voltammetry) which are now available.

Although evidence has been published to support the premise that the transition (refractory) metal ions form strong complexes in fluoride melts, this does not seem to play a major role in determining the **kinetics** of the overall electrochemical reaction. Certainly the original electroanalytical evidence pointed to diffusion-controlled "first step" reductions. Another contrary indication was that although foreign anions such as chloride in the fluoride melt had a major effect on the form of the metal deposits (and thus presumably on the kinetics of the overall reaction and/or metal deposition step), this was unlikely to be because they displaced fluoride ions from any transition metal fluoride complexes present in the bulk melts. (Complex stability order for transition metal ions: F>> Cl > Br > I (Group A).)

It is tempting to suggest that foreign anions such as chloride adsorb on the electrode (the interface behaves like a soft metal) where they are in a position to inhibit the formation of the vital intermediate lower oxidation state compound. A further point concerns whether the experimental work is correct or whether at least one of the chronopotentiometric steps is due to the reduction of an impurity in the melt. Some of the original work has been reproduced by other authors but of course their results may have been subject to the same artefacts, if they exist(13).

It is probably impossible to arrive at a general explanation of these results and also those obtained in chlorides, and it will be necessary to have recourse to the rather specific chemistry of these elements and their compounds.

Finally, seemingly clear cut evidence for the coupling of a rate-determining chemical reaction to a charge transfer process has been obtained for $MoCl_3$ in molten NaCl - 80 mol % KCl at 1033K(13).Schematically a complex ion which is normally electroinactive itself (at least within the available solvent electrochemical window) dissociates to form an electroactive species O,

viz. $Z \rightleftharpoons O$

and this is followed by the reaction

$$O + ne \rightarrow R$$

where Z represents the complex ion, O the oxidised species and R the reduced species (metal). Experimentally a single chronopotentiometric wave is observed for $MoCl_3$ concentrations $< 2.10^{-2}$M. Although the transition times themselves obeyed Sand's equation, the shifts of $e_{\tau/4}$ (the quarter-wave potential; i.e. that at a quarter of the transition time) with applied current and the slopes of the so-called log plots (e vs log f(t)) suggest an irreversibility having chemical rather than electrochemical origin. Using Vetter's treatment for a homogeneous rate-controlling prior chemical step as a very rough approximation, and identifying the reaction overpotential ηr in this treatment with $e_{\tau/4}$, the following overall reaction pathway was postulated:

$$\left(Mo\right)_2^{6+} \xrightarrow{\text{slow}} 2Mo^{3+} \quad \text{(rds)}$$

$$Mo^{3+} + 3e \rightarrow Mo \quad \text{(fast)}$$

At high Mo(III) concentrations, two chronopotentiometric reduction waves are observed (figure 6). The more cathodic one, which is absent at low concentrations, is shorter than the first. The parameters of this second wave were not consistent with its being due to the reduction of another oxidation state of molybdenum. A higher oxidation state would have produced a new wave at more anodic potentials, while a lower oxidation state would have produced a wave having a larger transition than the initial one and would have been apparent at all concentrations. However, this second wave is certainly due to molybdenum since addition of more $MoCl_3$ causes the transition time of the second wave to increase. Thus this second wave probably corresponds to the direct reduction of a multi (probably di-) nuclear complex to metallic molybdenum. This study provides additional quasi-quantitative support for the earlier observations of Mellors and Senderoff who employed the eutectic melt LiCl-KCl as solvent(14).

CATHODIC CHARGE-TRANSFER PROCESSES IN OXY-ANIONIC MELTS

Some of the difficulties involved in depositing metals from halide melts have been mentioned above. Although the form of the deposit is always a problem (from the point of view of electroplating), the metals themselves are at least inert in these halide solvents although insoluble lower-oxidation-state compounds often inhibit their cathodic electrodeposition.

This is not so in oxyanionic melts where the cathodic activity of the oxyanion often masks the deposition of the metal. Alternatively, the oxidising power of the oxyanion may be sufficient to form an oxide on the metal surface after electrodeposition.

The oxyanion itself of course contains a reducible component (viz. C in CO_3^{2-}, N in NO_3^-, etc.) and it may be possible to electrodeposit the corresponding element by a direct cathodic process.

The question of the electrodeposition of oxidisable metals such as lead and cadmium from molten nitrates has been the subject of controversy since 1983. Until then it had been assumed that although these metals could be directly electrodeposited on, e.g., platinum substrates, they were rapidly oxidised to the corresponding oxides. In 1983 Miles, McManis and Fletcher gave an alternative interpretation to the effect that the oxides were formed directly by the electroreduction of the corresponding nitrato-complexes in molten KNO_3, molten $LiNO_3$ and KNO_3- $LiNO_3$ eutectic (viz. $Pb(NO_3)^+ + 2e \rightarrow PbO + NO_2^-$). This conclusion was based on the absence of anodic waves in linear sweep voltammetry for metal dissolution after the cathodic deposition even at very high scan rates (i.e. to 1000V/s)(15).However, in recent studies on Cd^{2+} and Pb^{2+} in the equimolar $NaNO_3$ - KNO_3 melt at 260°C, we have found evidence (using Hg substrates) of the direct electrodeposition of the corresponding metals using linear sweep voltammetry and chronopotentiometry(16).The important factors in obtaining these results are:

(i) the use of mercury to lower the thermodynamic activity of the primary metallic product;
(ii) the use of high sweep rates; and
(iii) the use of low concentrations of solute.

Certainly on platinum indicator electrodes our **experimental** results were in accord with those of Miles et alia. Some examples of the results obtained for lead ions with mercury electrodes are shown in figures 7 and 8. Even at this low lead concentration the anodic dissolution wave corresponding to lead deposition disappears at the lowest sweep rate (0.02V s^{-1}). For the longer deposition time in this case the concentration of lead at the electrode surface is sufficientfor oxidation to intervene.

As figure 9 shows, the Randles-Sevcik equation is obeyed by the reduction wave and this leads to a $D_{Pb^{2+}}$ value of $2.13.10^{-6}$ cm^2 s^{-1}. Furthermore the plot of anodic peak current vs lead nitrate concentration shown in figure 10 (drawn for a sweep rate of 2.0V s^{-1} and concentrations lower than $10.75.10^{-3}$m. to avoid lead oxidation problems) is a straight line as would be expected if the anodic current is due to the dissolution of lead. Similar results were obtained for cadmium. This work will be published in detail elsewhere but at this stage it appears that it is not necessary to invoke the " reduction of complex" model of Miles et alia to explain the differing results with substrates, sweep rates and concentrations, although it should be emphasised that the results presented here apply strictly to $NaNO_3$-KNO_3 melts at 260°C, and the temptation to generalise should be resisted.

As mentioned above, the oxyanion in these melts contains a reducible component and many authors have concerned themselves with studies of the electroreduction of these anions (17) (18) (19).
We have recently been studying the electrodeposition of carbon from the carbonate ion dissolved in LiCl-KCl-NaCl at 450°C(20).(Earlier work has involved the electrodeposition of carbon from carbonates themselves (21,22) and from carbonate dissolved in NaCl-KCl (23). Tungsten, stainless steel and platinum substrates and cyclic voltammetry and chronopotentiometry were employed in this study. A typical linear sweep voltammogram for the stainless steel substrate is shown in figure 10. The single reduction wave generally observed occurs at e = -1.745V (Pt), -1.90V (stainless steel) and -2.05V (W) with regard to the 0.4M Ag/Ag(I) reference electrode. This corresponds to the process:

$$CO_3^{2-} + 4e \rightarrow C + 3O^{2-}$$

but the wave is irreversible as upon reversal of the sweep scan only a small oxidation peak at about -0.95V was observed. As indicated in figure 12 the cathodic peak current increases linearly with the square root of sweep rate although the plot did not pass through the origin. The details of this investigation will be published elsewhere, but on the basis of the electrochemical results it was possible to devise a method of carbon "plating" by pulse potentiostatic electrolysis.

THE FUTURE

Electrode reactions in molten salts are certainly not as straightforward as was once thought, nor are they easy to investigate experimentally. Nevertheless, the absence of spectacular advances in recent years is perhaps surprising; part of the reason for this is the rather small number of researchers interested in this field, scattered throughout the world and having diverse technological aims. There is not too much scope these days for non mission-orientated research.

The central questions concerning the kinetics and mechanisms of electrode processes are:
(i) what is the nature of the pre-charge transfer state at the electrode surface? (Are we concerned with "bare" ions, complexed ions or adsorbed ions? How does the energy level of this state differ from that of the ion in the bulk state? What is the "geometry" of this

state?)
(ii) what are the individual steps of the charge transfer process proper, what is the reaction pathway within this process and ipso facto, what is the rate-determining step? At the moment we have to admit that we know very little about these central questions in spite of the improvements in the techniques applied, both electrochemical and otherwise, over recent years.

There is prime need now for:
(a) more electrochemical measurements using the full range of modern techniques in a complementary manner in well defined and purified systems. In particular the techniques need to become more diagnostic viz. thin-layer electroanalytical techniques in order to avoid mass transfer complications in studying electrode processes, particularly those involving coupled chemical reactions and ring-disc electrode voltammetry, particularly for studying electrode processes involving soluble intermediates.
(b) more coupling of structural techniques (both in situ and ex situ) with the electrochemical techniques mentioned above(24).For example, in principle soluble intermediates could be studied "spectro-electrochemically" at the rings of ring-disc electrodes using fibre-optics. Insoluble intermediates (and products) are best studied ex situ after **potentiostatic** preparation. Studies of electrocrystallisation phenomena are developing and these are important both from the pure and the applied points of view. An important question concerns the special effects (if any) of using molten salt solvents for this purpose. Another question concerns the effects of adsorbed ions on the initial electro-nucleation step. The correlation of the fundamental electrochemical parameters of a metal deposition process and the properties of the subsequent deposit is of course extremely important in devising new electroplating processes.
(c) finally, the study of other interfaces such as the solid electrolyte-molten salt interface is worthy of attention as well as the related topic of semi-conductor electrodeposition (25) and the semi-conductor-molten salt interface.

REFERENCES

1. J.L. Settle and Z. Nagy, Paper presented at the 165th meeting of the Electrochemical Society, Cincinnati, Ohio, May 1984.

2. M.V. Smirnov and V.P. Stepanov, Proceedings, III Int. Conference on Molten Salt Chemistry, Wroclaw-Karpacz, Poland, May-June, 1979.

3. A.D. Graves and D. Inman, J. Electronal. Chem., 25, 357 (1970).

4. R.R. Dogonadze and Yu. A. Chizmadev, Proc. Acad. Sci. SSSR Phys. Chem. Sect. (Engl.) 157, 778 (1964) (and see review in ref. 3).

5. A.D. Graves and D. Inman in "Electroactive Force Measurements in High-temperature Systems", ed. C.B. Alcock, (IMM, London, UK), 183,(1968).

6. P. Fellner, M. Chrenková-Paučirová, A. Silný and K. Matiašovský, Electrochim. Acta 25, 189 (1980).

7. D. Inman, J.C. Legey and R. Spencer, J. Electroanal. Chem. and Interfac. Electrochem. 61, 289 (1975).

8. D. Inman, T. Vargas, S. Duan and P. Dudley, Proc. 4th Int. Symp. Molten Salts, San Francisco (The Electrochem. Soc., N.J., U.S.A.) 545 (1984).

9. T. Vargas, Thesis (London), (1984).

10. M.P. Hill, D. Inman and T . Vargas, U.K. Patent Appl. 8403184, (1984).

11. D. Inman and S.H. White, J. Appl. Elec., 8, 375 (1978).

12. S. Senderoff, Met. Rev., 11, 97 (1966).

13. D. Inman, R. S. Sethi and R. Spencer, J. Electronal. Chem. and Interfac. Electrochem., 29, 137 (1971).

14. S. Senderoff and G.W. Mellors, J. Electrochem. Soc., 114, 556, (1967).

15. M.H. Miles, G.E. McManis and A.N. Fletcher, Proc. 4th Int. Symp. Molten Salts, San Francisco, (The Electrochem. Soc., N.J., U.S.A.), 662 (1984).

16. G. Baret, D.E.A. Thesis, I.N.P. Grenoble (1985).

17. G.J. Hills and K.E. Johnson, J. Electrochem. Soc.108, 1013, (1961).

18. E. Franks and D. Inman, J. Electroanal. Chem. and Interfac. Electrochem. 26, 13 (1970).

19. E. Franks and A. Mukherjee, J. Electroanal. Chem. and Interfac. Electrochem., 49, 456 (1974).

20. W.J. Mo, D.I.C. Thesis, Imperial College, London (1985).

21. M.D. Ingram, B. Baron and G.J. Janz, Electrochim. Acta 11, 1629 (1966).

22. H.E. Bartlett and K.E. Johnson, J. Electrochem. Soc., 114, 457 (1967).

23. Y.K. Delimarskii, V.I. Shapoval and V.A. Vasilenko, Soviet Electrochemistry, 7, 1255 (1971).

24. G. Mamantov, V.E. Norvell and L. Klatt, J. Electrochem. Soc., 127, 1768 (1980).

25. e.g. I. Markov and M. Ilieva, Thin Solid Films, 74, 109 (1980).

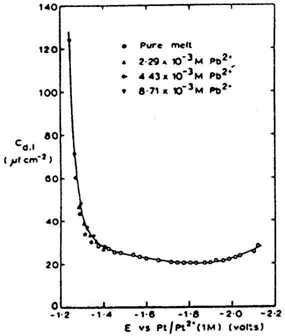

Fig. 1

Fig. 1. Capacitance-potential curve of lead in LiCl-KCl eutectic at 450°C

Fig. 2. Log (capacitance increase)-potential curve of lead in LiCl-KCl eutectic at 450°C (Symbols as in Fig. 1).

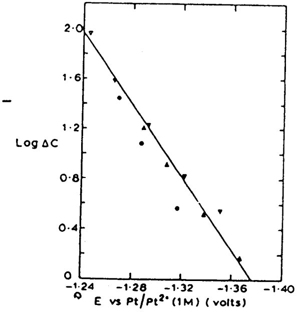

Fig. 2

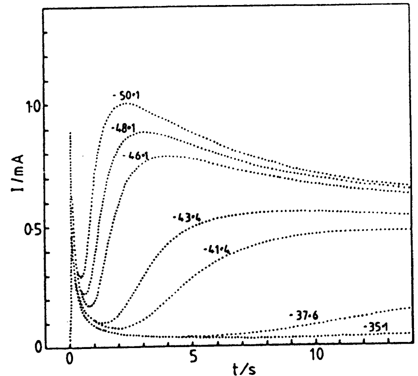

Fig. 3

Fig. 3. Potentiostatic current transients for the electrodeposition of chromium on Nb stabilised 20/25 stainless steel: 0.30 cm^2, c = 0.039 mol dm^{-3} (overpotentials indicated in mV).

Fig. 4. I-$t^{3/2}$ plots for potentiostatic current transients obtained on tungsten: 0.0452 cm^2, c = 0.042 mol dm^{-3} (overpotentials indicated in mV).

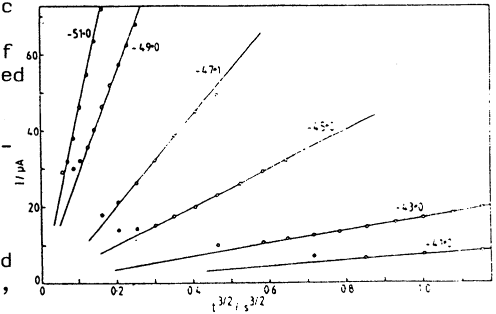

Fig. 4.

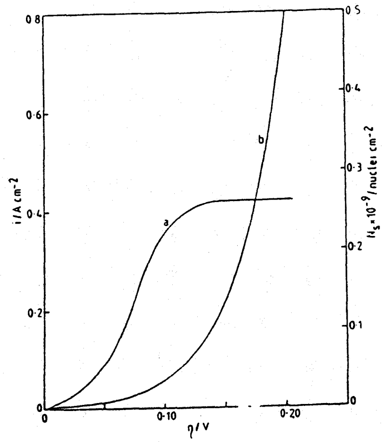

Fig. 5. Example of characteristic curves in the electrocrystallisation of chromium under potentiostatic conditions: tungsten, c = 0.346 mol. dm^{-3}. (a) Sampled current voltammogram (sampling time: 0.1 s), (b) Saturation nucleus density vs overpotential.

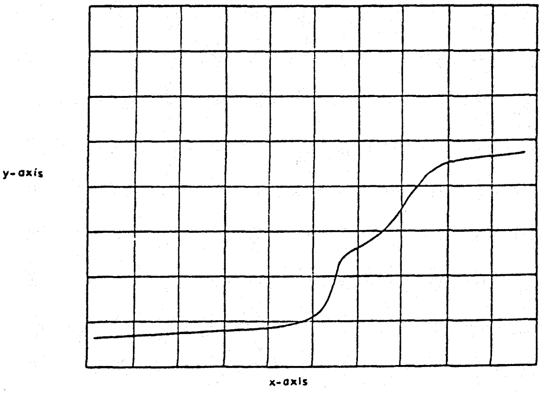

Fig. 6. Molybdenum (III) in NaCl-KCl (20:80 mole %). Double-step chronopotentiogram. Stoichiometric concentration of $MoCl_3$ 7.10^{-1} mol dm^{-3}, y-axis 0.5V cm^{-1}, x-axis 0.15s cm^{-1}.

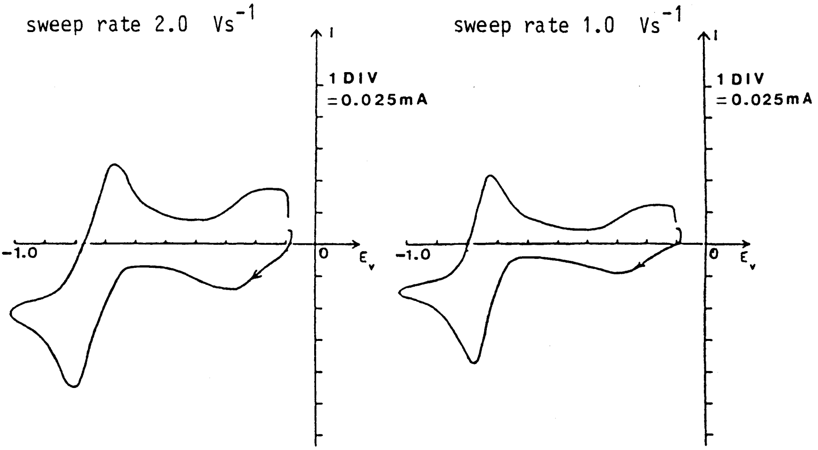
sweep rate 2.0 Vs^{-1}

sweep rate 1.0 Vs^{-1}

Fig. 7

Concentration of $Pb(NO_3)_2$ = 1.07.10^{-3}m. T = 260°C.
$NaNO_3$ / KNO_3 = 1 mole/1 mole
Mercury electrode 6mm^2 Reference potential Ag/Ag^+ 0.1m

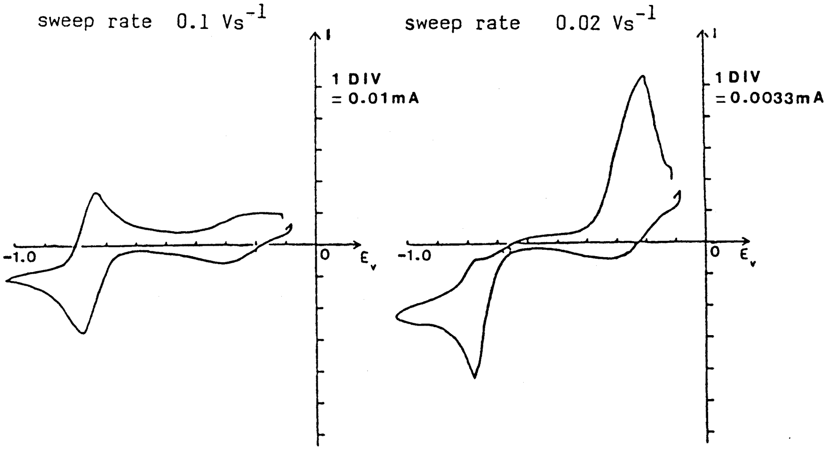
sweep rate 0.1 Vs^{-1}

sweep rate 0.02 Vs^{-1}

Fig. 8

Concentration of $Pb(NO_3)_2$ = 1.07. 10^{-3}m. T = 260°C.
$NaNO_3/KNO_3$ = 1 mole/1 mole
Mercury electrode 6mm^2 Reference potential Ag/Ag^+ 0.1m

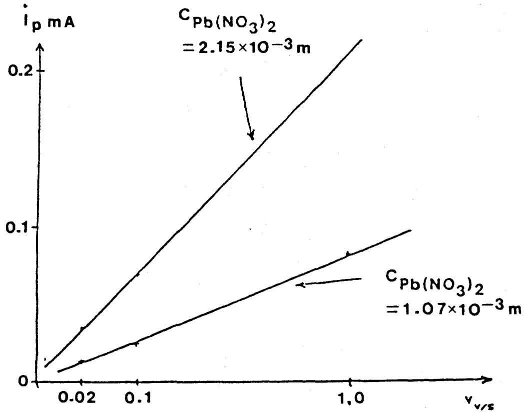

Fig. 9. Randles-Sevcik plot. I_p vs (sweep rate)$^{1/2}$

Fig. 10. Anodic dissolution of lead in mercury
Sweep rate = 2 V/S

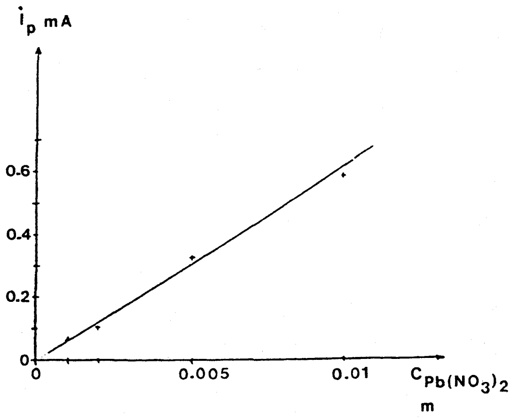

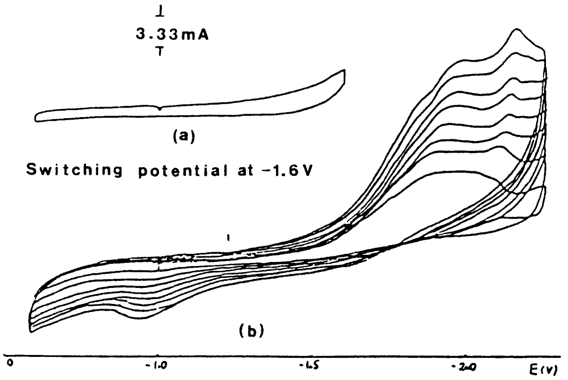

Fig. 11 Typical voltammograms obtained at a stainless steel electrode for the reduction of Na_2CO_3, T - 450°C, electrode area $1.57 \times 10^{-1} cm^2$. $[Na_2CO_3] = 7.87 \times 10^{-2}$ mol/kg.

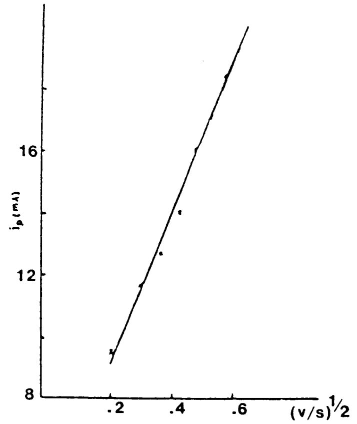

Fig. 12 Relationship between peak current and (sweep rate)$^{\frac{1}{2}}$ for the reduction of Na_2CO_3 at a stainless steel electrode.

DOI: 10.1149/198601.0128PV

AN ELECTROCHEMICAL STUDY OF OXYSPECIES IN CALCIUM CHLORIDE BASED MELTS

H.C. Brookes and D. Inman
Chemistry Department, University of Natal,
Durban, 4001, Republic of South Africa.
Department of Metallurgy and Materials Science,
Imperial College of Science and Technology,
London SW7 2BP, U.K.

ABSTRACT

Oxyspecies in molten $CaCl_2.KCl$ (73:27 mol%) at 700°C were monitored voltammetrically using a Au flag electrode. Hydroxide and moisture were shown to be rapidly converted to oxide in the melt. The nature of the oxyspecies present depends on the purity of the blanketting gas used and an oxide $\leftrightarrows$ peroxide equilibrium pertains with the peroxide ion being stable in the melt.

Gold indicator electrodes proved unsatisfactory for quantitative monitoring of oxide itself, probably because oxidative dissolution of gold occurs at potentials close to the presumed oxide ion oxidation potential. An yttria stabilised zirconia electrode was used to monitor changes in $[O^=]$ potentiometrically. The effects of oxide, peroxide, oxygen, moisture and hydroxide additions were examined. The gold indicating electrode was slowly inhibited by the formation of a surface film in the presence of added oxyspecies. The evidence suggests the following reactions predominate in the melt:

$$Cl^- + H_2O \leftrightarrows HCl + OH^- \quad \text{rapid to the right}$$
$$2OH^- \leftrightarrows O^= + H_2O \quad \text{displaced to the right}$$
$$O_2 + 2O^= \leftrightarrows 2O_2^{2-} \quad \text{displaced to the right}$$

Voltammetric evidence for the following reversible redox processes was obtained:

$$OH^- + e \leftrightarrows O^= + \tfrac{1}{2}H_2(Au)$$
$$O_2^{2-} + 2e \leftrightarrows 2O^{2-}$$
$$O_2 + 2e \leftrightarrows O_2^{2-}$$

INTRODUCTION

Spent nuclear fission material can be reprocessed by converting certain metal oxides to the metal by reduction in molten calcium chloride as redox solvent. Most molten calcium chloride contains oxyspecies which signifantly reduce the efficiency of the redox processes concerned. This investigation involves an electrochemical characterisation of oxyspecies in $CaCl_2$:KCl (73:27 mol%) at 700°C.

Polarographic waves obtained at Pt on CaO addition to $CaCl_2$-NaCl melts were interpreted (1) in terms of the reversible reaction

$$CaO - 2e \rightleftharpoons Ca^{2+} + \tfrac{1}{2}O_2$$

and anodic voltammetry at Pt was proposed as a means of oxide determination in these melts. An unexplained anodic peak was observed which increased in size with the CaO content; it was somehow related to the surface preparation of the Pt electrode, varying from one electrode to another. Addition of water to the melt (2) produced some irreversible electrode process, whereas NaOH addition had no effect. Complex formation between water and $CaCl_2$ melts was proposed.

Additions of H_2O, HCl and $Mg(OH)_2$ to $MgCl_2$-KCl melts (3) gave a voltammetric response at Pt, interpreted as passivation of the Pt due to formation of insoluble MgO on its surface. No such passivation occurred at W electrode.

Reversible two-electron oxidation of $O^{=}$ in LiCl-KCl melt (4), and one electron transfer to H_2O and OH^-, were proposed at Pt at 390°C. However, W electrodes gave irreproducible results. Delarue (5) in contrast found that addition of hydroxide to LiCl-KCl at 400°C produced the same wave at Pt as addition of oxide; this conclusion was confirmed by Polart and Degobert (6). Efforts to develop a reversible oxygen electrode in chloride melts have produced uncertain results with several workers unable to determine if $O^{=}$ or O_2^{2-} were active species in LiCl-KCl (7,8,9). However, Kanzaki et al. state that peroxide is non-existent in LiCl-KCl (10). Using voltammetry at Au, Deanhardt and Stern (11) found peroxide and oxide to be stable in NaCl melts containing 10^{-3} M Na_2O at 830°C. Kazaki and co-workers (12) described a reversible two electron-transfer oxygen electrode at Pt in LiCl-KCl melt, although no such electrode could be constructed at Au where a different electrode reaction appeared to pertain. They also stated (12) that the anodic dissolution of the platinum was prevented by formation of an oxide film in the presence of OH^- or $O^{=}$ ions. However, other workers (7,13) found that a reversible oxygen electrode at Pt could not be constructed in LiCl-KCL, and that anodic films existed on Pt and Au. Takahashi et al (14) found Pt to be passivated by oxide layers present as non-conducting films in LiCl-KCl. More recently Uchida and Laitinen (15) have shown noble metal electrodes to be unsuitable for quantitative monitoring of oxyspecies in chloride melts, with the oxidative dissolution of gold occurring at potentials close to the oxide ion oxidation potential. Metal oxide (RuO_2/SnO_2) indicator electrodes were proposed as alternatives (16).

The preceding discussion highlights the considerable controversy surrounding the study of oxyspecies in chloride melts. Identification of these species and their interactions is probably one of the most complex problems in molten salt chemistry today (18). The above studies show that Pt is probably unsuitable for use as an indicator electrode in such melts. Recent studies, by J. P. Hoare (19) with aqueous sulphuric acid at 25°C, show Pt to be unsuitable as an indicator electrode, Au being preferred due to dissolution of oxygen in Pt but not in Au. Preliminary studies in the $CaCl_2$-KCl melt also showed that Au gave more reproducible results than Pt, and it was therefore used exclusively as indicator electrode in this study.

EXPERIMENTAL

Voltammetry: An Au wire or flag as W.E., Ag/AgCl (0.1 mole fraction in $CaCl_2$-KCl in a mullite tube as R.E. and a 3 mm diam. vitreous carbon (VC) rod as C.E. were used. The counter electrode was suspended on an Inconel 600 rod, with the melt contained in a vitreous carbon crucible inside a quartz tube fitted with a water-cooled brass head.

Chemicals: BDH or Fluka chemicals were used. Chlorides were dried with HCl gas. Other chemicals were dried at 110° in vacuo except for $CaCl_2.2H_2O$ which was used as received. Final drying of chlorides involved vacuum pre-electrolysis at W for 48 hours.

Potentiometry: A Corning 1372 8% yttria-stabilised zirconia (YSZ) tube electrode, 6 mm o.d., 4 mm i.d., 46 cm long was loaded with predried 50-50 mol% Ni-NiO (Alfa) powder mixture. The inner face of the YSZ tube at the bottom was coated with Pt using a technique of overnight firing of successive coatings of Demetron 308D Pt paste at 1000°C,after oven drying at 110°C for an hour. Slow heating and slow (1 day) cooling are essential to avoid cracking. Pt-13% Rh thermocouple wire, suitably spiraled, was pressed to the Pt inner contact before loading with the Ni-NiO mixture. The YSZ tube was sealed containing 1/3 atmosphere argon using a Pyrex cap positioned with epoxy.

RESULTS AND DISCUSSION

Voltammetric Studies:

Effects of hydroxide and moisture:

A reduction peak, E, (Fig. 1) became pronounced on addition of KOH to the $CaCl_2$-KCl (73-27 mol%) melt at 700°C. Cyclic voltammetry showed a related oxidation wave F with E1/2 for the process at -1.05 V vs. Ag/AgCl. Plots of i_p vs. $\nu^{\frac{1}{2}}$ for both peaks were linear through the origin from ν = 100 mV/s to 5 V/s. Addition of moisture as pellets of $CaCl_2.2H_2O$ (up to 9 mmolal KOH or $CaCl_2.2H_2O$) produced similar redox peaks E, F. The process at E, F is a reversible one electron redox process with ΔE_p = 185 mV (compared to the theoretical value of 192 mV for a one electron reversible process at 700°C). It is proposed that the reversible redox process at -1.05 V is

$$OH^- + e \rightleftharpoons O^= + 1/2H_2(Au) \qquad [1]$$

Added moisture will generate OH^- (20) by the rapid reaction

$$Cl^- + H_2O(g) \rightarrow HCl(g) + OH^- \qquad [2]$$

Addition of larger amounts of KOH resulted in progressive changes in the shape and resolution of the OH^- reduction peak, such changes being more pronounced at higher $[OH^-]$ (Fig. 2), with peak E eventually almost disappearing within an hour of adding 39 mmolal KOH (Fig. 3). Peak E remained resolved at low KOH concentrations less than about 10 mmolal) but the peak height slowly decreased with time (Fig. 4). The phenomenon of slow loss of resolution of the reduction peak at -1.10 V at the Au indicator electrode will be referred to as an "inhibition" of the electrodes indicating properties, and is believed to be related to the formation of an inhibiting film on the electrode. A series of experiments with added CaO, KOH, Na_2O_2 or moisture produced a strongly adhering red-brown film on the electrode, but it was not identified. The decrease in reduction peak height at E is believed to be due to:

$$2OH^- \rightleftharpoons H_2O_{(g)} + O^= \qquad [3]$$

Moisture was added directly as $CaCl_2.2H_2O$, or by equilibration of the melt with four moisture vapor pressures obtained by bubbling argon through three bubblers, to ensure saturation, each containing either $(MgCl_2)_{sat}$ of v.p. 7.84 torr, $(Mg(NO_3)_2)_{sat}$ v.p. 12.4 torr, $(LiCl)_{sat}$ 2.61 torr or $(NH_4Cl)_{sat}$ v.p. 18.6 torr. The presence of moisture in $CaCl_2$-KCl resulted, within 30 minutes of reaching equilibrium, only in enhancement of the peaks E, F. No evidence was found for the $CaCl_2$-water complexes proposed by Grachev et al (2), and no water wave appeared. In $CaCl_2$-KCl at 700°C, reaction [2] is rapid and goes essentially to completion. Treatment with moisture eventually resulted, after many hours, in the same "inhibition" at Au as described for KOH additions (Fig. 3). Accompanying the inhibition phenomenon a rapidly rising current, characteristic of solvent reduction or reduction of ions present in large excess, occurs at progressively more anodic potentials; such process could be due to the reaction:

$$OH^- + Ca^{++} + e \rightarrow 1/2H_2 + CaO(Au) \qquad [4]$$

with CaO being formed as the $O^=$ concentration in the melt increases. If the process involves film formation on the Au electrode then the CaO produced is in a relatively insoluble form. Suggestion of formation of MgO film on Pt in $MgCl_2$ melts has been made by Komura et al (3).

Addition of moisture for short periods (less than 2 hours bubbling of wet argon or simple addition of $CaCl_2.2H_2O$) followed by prolonged equilibration with argon above the melt produced six peaks (Fig. 5). Equilibrium with 12.3 torr moisture followed by argon produced Fig. 6 with G, J due to a reversible, diffusion controlled, two-electron process (ΔE_p = 112 mV and n = 2). The same G, J peaks were obtained on bubbling N_2-3% O_2 through the melt, without added moisture, for five minutes. The fact that prolonged moisture treatment produced the rising current, or inhibition effect (peak E undetectable) suggests that a possible alternative to [4] is:

$$H_2O + Ca^{2+} + 2e \rightarrow H_2 + CaO(s)(Au) \qquad [5]$$

with unlimited supply of H_2O and Ca^{2+} being required. Precisely why the reduction occurs at steadily more anodic potentials, and eventually obliterates even peak C (Fig. 5), remains unclear. Hydroxide reduction at E could not be investigated as a function of nominal added hydroxide concentration due to the oxide formation reaction [3] and interference from proposed reactions such as [4]. Figs. 5 and 6 were only obtained on initially cathodic going scans starting in the cathodic potential region.

Peroxide, oxide and superoxide addition:

Addition under argon of <20 mmolal quantities of Na_2O_2 or KO_2 to the melt produced no new peaks, besides those of Fig. 5. However, insignificant peak enhancement occurred, showing that peroxide and superoxide pellets decomposed at 700°C before dissolving as O_2^{2-} or O_2^- in the melt. Presumably they decomposed yielding oxychloride or oxide species under argon. When the experiment was done under argon voltammograms which were started at or near the anodic polarization limit did not show the smaller peaks G, J (Fig. 5).

Substantial addition of Na_2O_2 eventually resulted in the "inhibition" or passivation of the gold flag electrode as was also found on oxide addition to the melt as CaO. The ultimate result is typified in Fig. 8 where inhibition commences at ca. -0.6 V. As with KOH addition, the inhibition effect became more pronounced with time and was more pronounced under N_2-3%O_2 than pure argon for the same elapsed time.

Addition of oxide produced very slight increases in the smaller peaks C, D and in the even smaller peaks G, J. Again, direct proportionality to added salt was not obtained. Anodic going scans, starting from potentials well anodic of peak D resulted in negligible peak G. Only if the potential region of peak D had been traversed would peak G appear. A well resolved peak J was more difficult to obtain. In general, peak J was best obtained when the partial pressure of oxygen above the melt was relatively high, e.g., when the atmosphere above the melt consisted of 3% O_2:97% N_2, or within 2 hours of such treatment, and only if N_2-3% O_2 treatment was not prolonged.

Peaks C, D were diffusion controlled with reversible behavior with i_p vs. $\nu^{1/2}$ plots for both peaks being linear through the origin with $(\Delta E_p)_{C,D}$ = 108 mV which is in reasonable agreement with the theoretical value of 94 mV at 700°C for n = 2 and for the switching potential, $(E\lambda)_C$, 90 mV cathodic of $(E_p)_C$. Similarly processes G, J may be diffusion controlled with i_p versus $\nu^{1/2}$ plots being linear through the origin. However, $(E_p)_G$ varied with ν, moving slightly anodic at higher sweep rates. $(E_p)_J$ did not move significantly with varying scan rate over the range 10 mV/s to 10 V/s, but G moved 180 mV.

The above considerations are consistent with the following proposed net reaction assignments:

$$\begin{array}{ll} C : O_2^{2-} + 2e \rightarrow 2O^= & E : OH^- + e \rightarrow O^= + \tfrac{1}{2}H_2(Au) \\ D : 2O^= - 2e \rightarrow O_2^{2-} & F : \tfrac{1}{2}H_2(Au) + O^= - e \rightarrow OH^- \\ G : O_2^{2-} - 2e \rightarrow O_2(Au) & \\ J : O_2(Au) + 2e \rightarrow O_2^{2-} & \end{array}$$

Oxygen produced at G is rapidly lost from the vicinity of the electrode at 700°C since under inert argon atmosphere process J did not occur. Using very slow scans, bubbles of oxygen were produced, under vacuum straight after N_2-3% O_2 equilibration at the gold electrode (Fig. 11); the added CaO caused an O_2^{2-} formation followed by oxidation G. The expected redox peaks for

$$O^= - 2e \rightleftharpoons \tfrac{1}{2}O_2$$

were not identified. Holding the potential at D for 5 minutes followed by a scan through G resulted in a four-fold increase in G, confirming that it is related to the species produced at D.

Results of potentiometric studies showing a steady decrease in $[O^=]$ concentration in the melt when coupled with results of cyclic voltammetric studies under argon and oxygen can be interpreted as a slow establishment of the following equilibrium

$$O_2 + 2O^= \rightleftharpoons 2O_2^{2-} \qquad [6]$$

A similar equilibrium was indicated by Stern (11) in Na_2O solutions in NaCl melts, the slightest trace (even 1 ppm) of oxygen being sufficient to oxidize $O^=$. Evidence for initial O_2^{2-} in solution prior to generation at D is seen at C in Fig. 5, due to the ongoing slowly established (∿2 hours after any change) overall equilibria described above. Numerous voltage scan regimes involving C, D and G supported the above analysis.

The evidence suggests that the simple net redox processes proposed above for the six peaks should be viewed as a set of complex equilibria perhaps involving oxychloride species rather than simple oxide ions as shown here. The possibility of such complications cannot be discounted, since addition of Na_2O_2 (21 mmolal) to the melt containing only added hydroxide (1.2 mmolal) resulted in a rapid permanent cathodic drift in G by 200 mV. It seems that added peroxide facilitates peroxide oxidation to some extent, and a complex oxidation mechanism of O_2^{2-} at elemental Au is indicated. Since added peroxide produces oxide, and gold oxides have even been found on gold working electrodes in aqueous solutions at 25°C (22), it is possible that homogeneous peroxide oxidation at gold oxide (or "inhibited gold") occurs more easily than at elemental gold. Further peroxide additions beyond 21 mmolal resulted in no further shift in G after 25 minutes. The peak shift was quite reproducible in melts containing no initial added peroxide with a cleaned gold electrode, averaging a shift of ca. 200 mV at ν = 100 mV/s. Peak separations for G and J, $(\Delta E_p)_{G,J}$, were measured at the final stable position of G, -0.12 V, after peroxide addition. $(\Delta E_p)_{G,J}$ before peroxide addition was not consistent with a reversible n = 2 redox process as indicated above, the ΔE_p separation being up to 200 mV too large, suggesting irreversibility. Additions of Na_2O_2 eventually resulted in electrode inhibition or "passivation," as found for substantial KOH or water additions. The typical hydroxide peaks, E, F (Fig. 1) eventually disappeared and the voltammograms were similar to those found after moisture treatment, again suggesting inhibition.

N_2-3% O_2 atmosphere:

Changing the atmosphere above the melt from argon to 3% O_2:97% N_2 produced dramatic changes in the cyclic voltammograms. The rising edge of what was peak E moved steadily anodic eventually (15 minutes after start of oxygen flow) obliterating peak C. Peak G also disappeared under O_2 and the eventual result after 27 minutes O_2 flow is shown in Fig. 7. It is tempting to ascribe this somewhat featureless voltammogram to a continued "inhibition" of the Au flag, i.e., it is no longer useful for detection of the redox processes outlined above. However, after about 30 minutes oxygen flow the cell was evacuated for three minutes and argon flow recommenced. Peaks G and C reappeared, but not E and F as shown in Fig. 9 after 1 hour of argon flow. This dimunition and regain of peaks G and C with oxygen; vacuum; argon could not be reproduced repeatedly. The precise explanation is unclear, although detection of certain redox processes at Au is reactivated on removal of oxygen. The general steady anodic drift of what was peak E suggests that the reduction process at E

$$OH^- + e \rightarrow O^= + 1/2H_2(Au)$$

is depolarised in the presence of added OH^-, $O^=$ (as CaO), water or oxygen. If the surface of the gold electrode changes in the presence of $O^=$, it is feasible that the above reduction could be occurring at less cathodic potentials, as found experimentally, with the inhibition process being reversible to some extent, in that cell evacuation causes peaks G and C to reappear. Addition of oxide as CaO also resulted, after oxygen treatment as above, in the same sort of "inhibition," and after 34 mmolal CaO addition under oxygen the resulting CV is shown in Fig. 8, where all peaks have been substantially diminished. Cyclic voltammograms taken under argon after evacuation immediately after N_2-3% O_2 equilibration produced peak J (Figs. 6, 10). After vacuo and added CaO, a quite pronounced prepeak, H, is obtained with $(\Delta E_p)_{H-J} = 65$ mV. The prepeak is not necessarily indicative of oxygen adsorption, since peak H does not increase in height as ν, but peaks H, J increase linearly in $\nu^{1/2}$ from 100 mV s^{-1} to 500 mV s^{-1}. Prolonged (30 min.) treatment with O_2/N_2 and 59 mmolal CaO resulted in Fig. 12 after subsequent evacuation and one hour of argon. Here peak H is far larger than G perhaps due to a gold oxide formation process, as found in aqueous solutions (19, 22), when under an N_2-O_2 atmosphere.

Peak J was observed (Fig. 6) immediately after water vapor-saturated argon was bubbled, or after $CaCl_2.2H_2O$ additions. In contrast additions of Na_2O_2 or KOH or CaO produced a more rapid onset of "inhibition" rendering the featureless voltammograms previously described in which peak J could not be resolved. Thus water produces the same results as O_2/N_2 (Fig. 6); the peak separation $(\Delta E_p)_{G,J}$ after equilibration is 114 mV, essentially the same as found after O_2/N_2 treatment. The situation with CaO is complicated by the unexplained peak H (Fig. 12) and by the possibility that the anodic region of peak G may not involve merely simple peroxide oxidation but that oxide itself may be reacting with gold in chloride melts. This is remininiscent of aqueous solutions where multiple oxide layers on gold have been reported (22) to form anodically.

Potentiometry.

The difficulties with noble metal electrodes prompted an exploratory potentiometric monitoring study using yttria-stabilized zirconia (YSZ) electrodes.

The yttria stabilized zirconia (YSZ) electrode (17) monitors the activity of oxide ion in the melt. The YSZ monitoring cell consisted of:

$$\mathrm{Ag}|\mathrm{CaCl_2\text{-}KCl + AgCl\ (10\ mol\%)}|\mathrm{mullite}|\mathrm{CaCl_2\text{-}KCl\ (73\text{-}27)}$$

$$\mathrm{+\ solute}\ |\ \mathrm{YSZ\ electrode,\ 33\ kPa\ O_2}\ |\ \mathrm{Pt\ 13\%\ Rh.}$$

If the cell reaction with molten $CaCl_2$ is

$$2Ag(s) + 1/2O_2(g) + CaCl_2(l) \rightarrow 2AgCl + CaO(l)$$

then the cell e.m.f. for YSZ vs. Ag|AgCl reference would be:

$$E_{cell} = E^{o} - \frac{RT}{2F} \ln \left(\frac{a_{AgCl}^{2}\ a_{CaO}}{P_{O_2}^{1/2}\ a_{CaCl_2}} \right) \text{where } P_{O_2} = 33 \text{ kPa.}$$

Since YSZ is solely an oxide ion conductor, the cell responds to changes in $a_{O^=}$ only (17).

For reactions with molten KCl

$$E_{cell} = E^{o} - \frac{RT}{2F} \ln \left(\frac{a_{AgCl}^{2}\ a_{K_2O}}{P_{O_2}^{1/2}\ a_{KCl}^{2}} \right).$$

Potentiometric studies with an oxide ion specific electrode are useful for monitoring changes in oxide content, but cannot be used to determine absolute oxide ion concentrations unless the activity coefficients and the limiting emfs, E^{o} are known. The YSZ electrode was therefore only used to monitor changes in $[O^=]$, since the oxide activity coefficients are not known in the $CaCl_2$-KCl melt. The only oxide activity coefficients, γ, measured in chloride melts are those of Stern (23) and Combes (24) who who found extremely negative deviations from Raoult's law, e.g., γ = ca. 10^{-5} for Na_2O in NaCl (23).

Gas flow rates:

In general the "pure" argon flow rate had a significant effect (up to 10%) on the emfs recorded between the YSZ and reference electrode. Experimentally the emf of the YSZ electrode vs. Ag|AgCl reference electrode fell, e.g., from -193 mV to -210 mV, for a ten-fold increase in blanketting argon gas flow rate, both emfs being constant ($\pm$ 1 mV) at constant gas flow rates (30 cm^3/min to 300 cm^3/min).

Although a faster (x 10) argon flow rate lowered E_{YSZ} in melts with added (3 mmolal) CaO by about 8%, a similar increase in the flow rate of the N_2:3% O_2 gas mixture lowered E_{YSZ} (i.e., showed a raised $[O^=]$) by only ca. 3.5%. At high pure argon flow rates the partial vapor pressure of O_2 above the melt is reduced driving [6] left, whereas similarly high 97% N_2:3% O_2 flow rates should clearly not reduce the partial vapor pressure of O_2 above the melt as much. Henry's law is not perfectly valid for oxygen dissolution in this melt at 700°C, which is perhaps not surprising since it reacts with oxide to form peroxide. If ideality pertained, then reaction [6] would result in decreased oxide relative to the pure argon case, as opposed to the slight increase found with 97% N_2:3% O_2.

It has been reported by Tremillon (26) that the oxide content of HCl-purified LiCl-KCl melts increased on flushing with argon to remove HCl gas. The $[O^=]$ increased to the level existing before HCl purification, but after vacuum drying and heating. It is well-known

(21, 24) that equilibrium [7] in chloride melts is rapidly attained

$$H_2O_{(g)} + 2Cl^- \rightleftharpoons 2HCl_{(g)} + O^= \qquad [7]$$

In LiCl-KCl the equilibrium constant is 10^{10} at 470°C (20).

Possible interpretations of our results and those of Tremillon are that either the argon is moist thereby driving equilibrium [7] towards higher oxide content and/or the chloride melt is imperfectly dried and the indeed pure argon sweeps out dissolved HCl driving equilibrium [2] to the right. An alternative explanation (17) recently proposed is that local variations in oxygen partial pressure at the electrode could generate changes in ΔE_p. These changes appear numerically reasonable for the present experimental setup. However, the "active" part of the YSZ electrode is below the melt surface, and use of argon does not entirely satisfy the conditions proposed in (17), i.e., only oxygen and not inert gas flow rates were studied.

Oxide monitoring by potentiometry:

Fig. 13 shows the rise in emf (fall in oxide) as N_2-3% O_2 was bubbled through the melt at 30 cm^3/min. The oxide decrease is consistent with peroxide formation via reaction [6] and shows that equilibrium is slowly established.

The YSZ electrode was useful as a means of determining when the melt had reached equilibrium after small solute (CaO, KOH, Na_2O_2, $CaCl_2.2H_2O$) additions. For example, Fig. 14 shows the change in E_{YSZ} on addition of 12.5 mmolal KOH to the $CaCl_2$.KCl melt. The characteristic drop in E_{YSZ} accompanies initial local dissolution of KOH followed by complete dissolution and eventual equilibration of solute throughout the melt and a steady emf after ca. 90 minutes. The fact that E_{YSZ} slowly dropped after hydroxide addition suggests that equilibrium (3) is completed within 90 minutes under 12.35 torr water vapor pressure (Fig. 14). Probably diffusion of solute through the ca. 50 ml of solvent, at 700°C, is the rate-determining factor. The above result also supports the equilibria proposed in reactions [3] and [6]. For example, saturation of the melt with moisture at 2.61 mm Hg water vapor pressure using a saturated LiCl bubbler reduced the $O^=$ activity, whereas addition of OH^- raised the $O^=$ activity, confirming that the equilibrium [3] was operative in the $CaCl_2$-KCl melt at 700°C. Equilibrium [6] was also confirmed as operative using N_2:3% O_2, and the equilibrium appears to be rapid in $CaCl_2$-KCl melt. The rise in E_{YSZ} on switching to the oxygen mixture (Fig. 13) confirmed a decreasing oxide content and when coupled with the results of the cyclic voltammetric studies, it suggests that peroxide formation is most probable. Equilibration with the various water vapor pressures as well as salt additions all confirmed the general direction of changes expected from equilibria [3], [6] and [7]. For example, the decrease in $[O^{=}]$ shown in Fig. 13 after N_2-3%O_2 equilibration with the 50 mmolal formal initial CaO concentration was subsequently reversed on Na_2O_2 addition. However, absolute oxide activities and E^o must remain unknown due to variation in E_{YSZ} with argon flow rates, the steady reaction of added oxide with even the slightest trace of oxygen and the presence of the other ongoing reactions described above.

ACKNOWLEDGMENTS

The authors acknowledge a research grant from the M.O.D. (U.K.) and H.C.B. acknowledges financial support from C.S.I.R. (R.S.A.) and U.N.D. (R.S.A.).

REFERENCES

1. K. Ya. Grachev and V.Z. Grebenik, Zh. Analit. Khimii, 23, 186 (1968).
2. K. Ya. Grachev and V.Z. Grebenik, Zh. Prikl. Kh., 39, 522 (1966).
3. A. Komura, H. Imanaga and N. Watanabe, Denki Kagaku, 10, 762 (1972).
4. C.A. Melendres, J.P. Ackerman and R.J. Steunenberg, Proc. Int. Symp. Molten Salts, Ed. J. Braunstein, Electrochem. Soc., 1976, 575.
5. G. Delarue, J. Electroanal. Chem., 1, 13 (1959).
6. J. Polart and P. Degobert, C.R. Acad, Sci., Sec. C255, 2103 (1962).
7. N.S. Wrench and D. Inman, J. Electroanal. Chem., 17, 319 (1968).
8. D. Inman and M.J. Weaver, J. Electroanal. Chem., 51, 45 (1974).
9. E.P. Mignonsin, L. Martinot and G. Duyckaerts, Inorg. Nucl. Chem. Lett., 3, 511 (1967).
10. Y. Kanzaki, K. Kogawa, S. Yano, O. Matsumoto and M. Takahashi, Denki Kagaku, 43, 178 (1975).
11. M.L. Deanhardt and K.H. Stern, J. Electrochem. Soc., 127, 2600 (1980).
12. Y. Kanzaki and M, Takahashi, J. Electroanal. Chem., 58, 339 (1975).
13. P.G. Zambonin and J. Jordan, J. Amer. Chem. Soc., 91, 2225 (1969).
14. M. Takahashi, Y. Katsuyama and Y. Kanzaki, J. Electroanal. Chem., 62, 363 (1975).

15. I. Uchida and H. Laitinen, Paper I-208 read at the 1st. Intl. Symp. on Molten Salt Chem. and Technol., Japan 1983.

16. R. Waggoner, personal communication.

17. A.-M. Anthony, J.F. Baumard and J. Corish, Pure and Appl. Chem., 56, 1069 (1984).

18. A.A. El Hosary, D.H. Kerridge and A.M. Shams El Din, "Ionic Liquids", Ed. D. Inman and D. Lovering, Plenum Press, London, 1981.

19. J.P. Hoare, J. Electrochem. Soc., 131, 1808 (1984).

20. R. Combes, B. Tremillon, F. de Andrade, M. Lopes and H. Ferreira, Analyt. Letters, 15, 1585 (1982).

21. R. Combes, "Ionic Liquids", ed. D. Inman and D. Lovering, Plenum Press, London, 1981.

22. U. Oesch and J. Janata, Electrochim. Acta, 28, 1247 (1983).

23. K.H. Stern, Electrochim. Acta, 24, 509 (1979).

24. R. Combes, J. Vedel and B. Tremillon, Electrochim. Acta, 20, 191 (1975).

25. K.H. Stern, J. Electrochem. Soc., 127, 2375 (1980).

26. B. Tremillon and G. Picard, paper presented at First Intl. Symp. on Molten Salt Chem. and Technol., Japan, 1983.

27. K.H. Stern, Rm. Panayappan and D.R. Flinn, J. Electrochem. Soc., 124, 641 (1977).

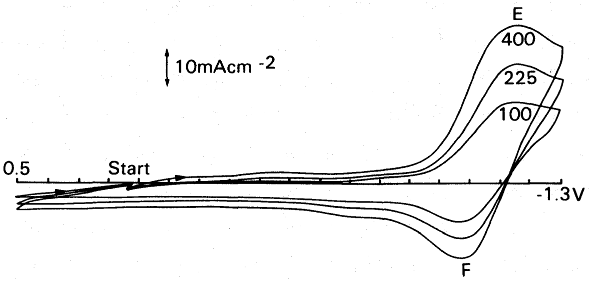

Fig 1 At Au. n = 1 for E, F. γ = 100, 225, 400 mV/S 2 mins after 9 mmolal KOH added.

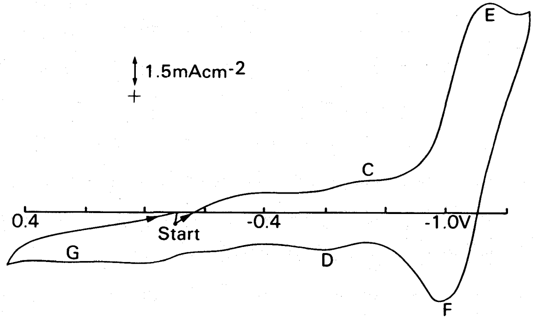

Fig 2 100mV/s 22 mins after KOH added (39 mmolal)

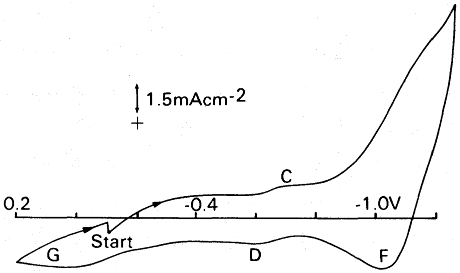

Fig 3 100mV/s 45 mins after 39 mmolal KOH addition

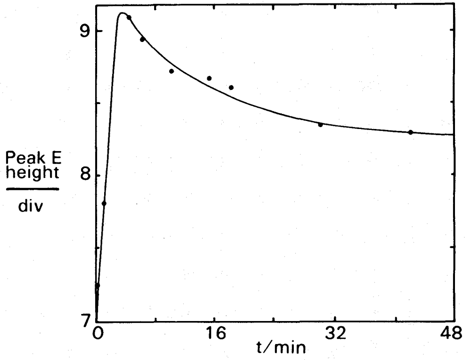

Fig 4 Change in current at Peak E after 6 mmolal KOH addition

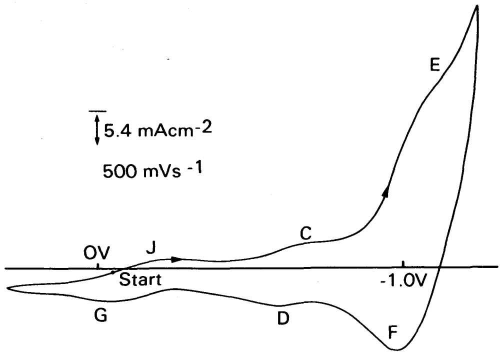

Fig 5 Peaks obtained with 2.61 torr moisture, then 2 hrs under argon.

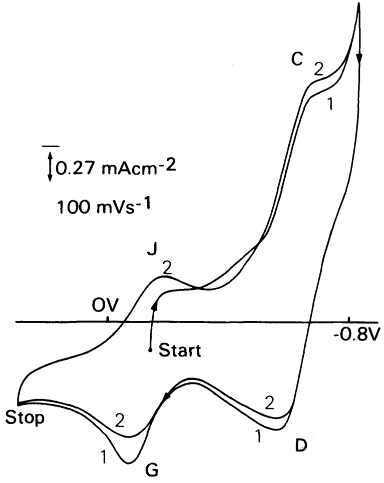

Fig 6 Water produces J, as does N_2-O_2 12.3 torr moisture (or 5 min N_2-O_2) Shows n = 2, ΔEp=112mV for G,J,

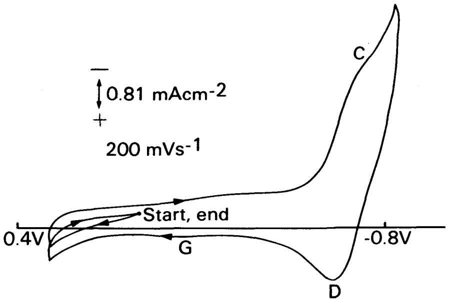

Fig 7 Under N_2/3% O_2 with 28 mmolal Na_2O_2 C changed, G almost gone, D unchanged

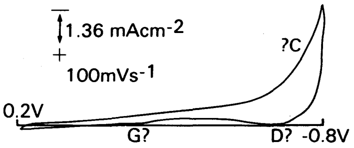

Fig 8 34 mmolal CaO and 90 min N_2/3% O_2 flow

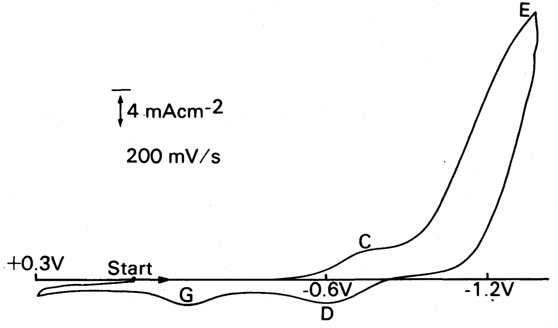

Fig 9 Peaks G, C reappear after evacuation while under argon, 28 mmolal Na_2O_2

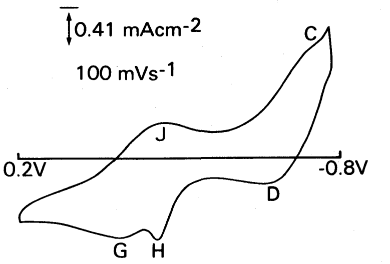

Fig 10 34 mmolal CaO ⟶ N_2 3% O_2 ⟶ vacuum ⟶ argon, peaks reappear

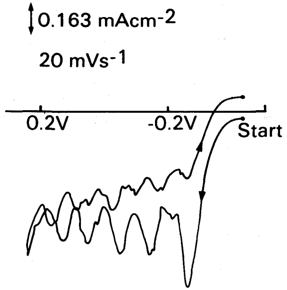

Fig 11 Oxygen evolution under vacuum at Au with 0.1 molal CaO.

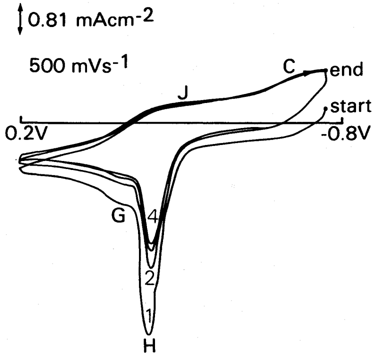

Fig 12 Successive cycles through peak H with 59 mmolal CaO, under argon. Peak H decreases on cycling

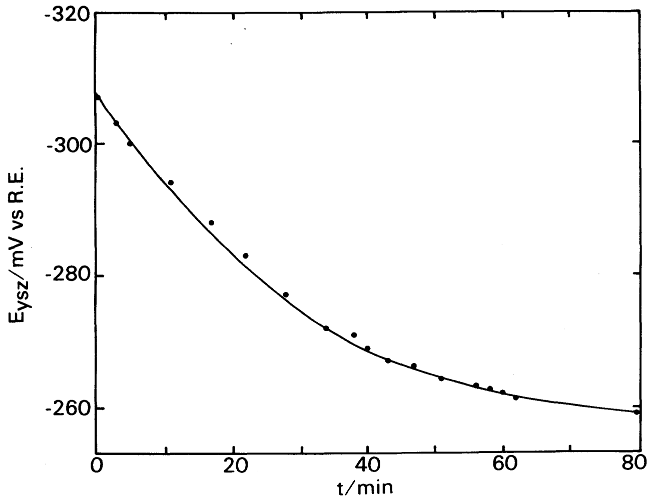

Fig 13 Rise in emf as O_2/N_2 equilibrates in melt. 50 mmolal CaO

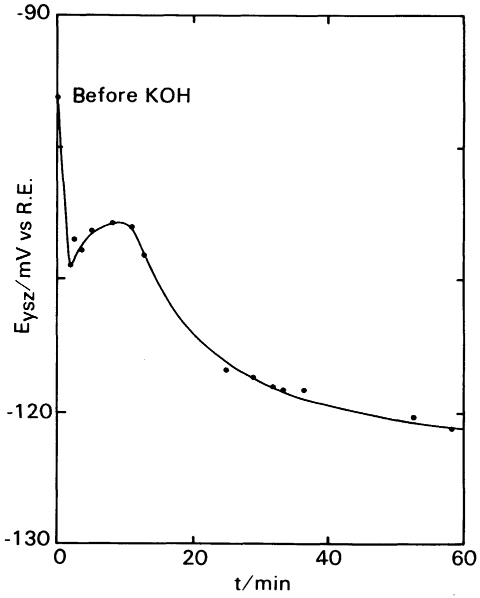

Fig 14 Change in E_{ysz} after KOH (12m molal) addition, under argon.

DOI: 10.1149/198601.0144PV

GaAs FILM FORMATION FROM LOW TEMPERATURE CHLOROALUMINATE MELTS

S.P. Wicelinski and R.J. Gale
Department of Chemistry
Louisiana State University
Baton Rouge, LA 70803

ABSTRACT

Prospects of electrochemically forming layers of the III-V semiconductor gallium arsenide from a room temperature $AlCl_3$: 1-butylpyridinium chloride melt are discussed. Electrochemical behaviours of gallium and arsenic species are investigated by voltammetry and coulometry, and the complexation is discussed in acid-base terms. Potentiostatically controlled reduction of mixtures of Ga(III) and As(III) halides in the melt leads to films containing both gallium and arsenic. Films have been analyzed by X-ray fluorescence spectroscopy, X-ray diffraction, and their compositions verified by inductively coupled plasma (ICP) and electron dispersive scattering analyses.

INTRODUCTION

In 1982, Tremillon and coworkers (1) reported that impure gallium arsenide could be deposited from a potassium tetrachlorogallate melt at 300° C containing arsenic triiodide. Relatively little, however, is known concerning the electrochemical kinetics of gallium and arsenic species reduction in non-aqueous media (2-4), even though the ability to electrowin these materials and/or electrodeposit and electroform semiconducting films of useable quality would be of value. In principle, electrochemical methods have the advantages of precise control of layer thicknesses and economical usage of materials. Since considerable interest has arisen in the past decade in molten salt systems that are liquids at ambient room temperatures, e.g.(5-7), we have embarked on a study of gallium and arsenic electrochemistry in low temperature chloroaluminate melts. The aprotic nature and the freedom of oxygen of these media, as well as the lower temperature which reduces the problems with volatile arsenic species, all suggest the use of these media as candidates for thin film fabrication of compound semiconductors and/or purification of precursor materials important to the semiconductor industry. Gale (8) has reviewed semiconductor electrodeposition and anodization with high temperature molten salts.

EXPERIMENTAL

Procedures used for purification of $AlCl_3$ (Aldrich Chemical Co.), the synthesis and purification of 1-butylpyridinium chloride, and the preparation of the melts were similar to those described by Gale and Osteryoung loc.cit. Arsenic(III) chloride (Aesar, 99.999%)

and gallium(III) chloride (Aesar, 99.999%) were used as received.

All electrochemical experiments were performed in a dry box under a purified nitrogen atmosphere. Trace amounts of oxygen were removed by Cu-0803 T 1/8 copper catalyst (Harshaw). The cell temperature was maintained to within ±1°C with the aid of a solid-state temperature controller (Omega, model 20M). Working electrodes used for voltammetry were Pt button electrodes sealed in glass (area = 0.810 mm^2). Glassy carbon (area = 1.6 cm^2) was employed as the counter electrode and the reference electrode consisted of a high purity, coiled Al wire immersed in a 2:1 $AlCl_3$:1-BPC melt contained within a glass fritted tube. Coulometric and voltammetric investigations were made with a PAR Model 175 Universal Programmer and a PAR Model 173 Potentiostat/Galvanostat containing a Model 179 Digital Coulometer. Voltammograms were recorded with a PAR 9002A X-Y recorder.

X-ray fluorescence spectra were obtained with a Phillips Electronics Instrument, Type 12215, X-ray fluorescence spectrometer. A North American Phillips Co., Type 12045, X-ray diffractometer was used to determine the powder diffraction angles of the deposits, which were removed by mechanical means from their substrates. Also, films were dissolved in conc. HNO_3, followed by dilution, and their compositions were verified using a Perkin Elmer ICP-6500 and a Trecor Northern ARL-EMX-SM with an EDS detector.

Gallium Voltammetry

Gallium chlorocomplexes behave in many respects similar to aluminum complexes (9, 10) and it is reasonable that the major species present in the acidic regime, i.e. 1.1:1 to 2.0:1 molar ratio $AlCl_3$:1-butylpyridinium chloride (1-BPC), respectively, is a mixed Ga $AlCl_7^-$ complex,

$$GaCl_3 + AlCl_4^- \rightleftharpoons GaAlCl_7^- \qquad [1]$$

and, in basic melts (<1.0:1), a tetrachlorogallate species,

$$GaCl_3 + Cl^- \rightleftharpoons GaCl_4^- \qquad [2]$$

Ga(III), added as $GaCl_3$ to acidic melts, shows two poorly defined waves at approximately +0.87V and +0.29V vs. Al(2:1) reference. These are illustrated in figures 1 and 2 for a 1.37:1 $AlCl_3$:1-BPC melt composition. The first reduction peak is usually assigned to the quasi-reversible reduction of Ga(III) to Ga(I), cf.(7). However, in low temperature melts this reaction does not give a well-defined peak on the forward (negative going) sweep and it is feasible (in principle at least) that the reaction is complicated by the involvement of some mixed oxidation state or Ga(II) species. It was noted that at intermediate melt acidities (e.g., 1.1:1 to 1.7:1) the first reduction peak was smaller than that of the second. As the melt acidity was increased by $AlCl_3$ addition to 2:1, the first peak did become more distinct and its currents were larger than those of the second peak (figure 3). This latter behavior is more consistent with the expected two-step mechanism,

$$Ga^{3+} + 2e^- \longrightarrow Ga^+ \quad [3]$$
$$Ga^+ + e^- \longrightarrow Ga(0) \quad [4]$$

The sharp anodic peak at circa +1.1V presumably is the Ga(0) stripping peak and the shoulder at positive potentials may be due to Ga(I) to Ga(III) oxidation. In the presence of an excess of Ga(III), the following equilibrium would cause spontaneous loss of any gallium metal film,

$$Ga^{3+} + 2Ga(0) \rightleftharpoons 3\ Ga^+ \quad [5]$$

It is to be noted that Ga(III) species could not be reduced directly to Ga(0) in a KCl melt at 300°C(9). Our interpretation is largely consistent with the following E° values which have been reported for a ternary $AlCl_3$-NaCl-KCl melt at 135°C; Ga(I)/Ga(0)+0.199V, Ga(III)/Ga(0)+0.577V, and Ga(III)/Ga(I)+0.766V vs. Al reference(7). In basic melts it was not possible to reduce the $GaCl_4^-$ species prior to reduction of the butylpyridinium cation.

Constant potential electrolysis at +0.8V of a melt containing Ga(III) resulted in formation of the Ga(I) species. Figure 4 contains a cyclic voltammogram of a melt after partial reduction of the Ga(III) to Ga(I). The cathodic peak for Ga(I) reduction shows some structure but the stripping currents are now better resolved because of the reduced Ga(III) activity. The Ga(I) oxidation peak resolves as a separate peak at about +1.4V. A 2-electron reduction depletes the melt entirely of Ga(III) species.

Arsenic Voltammetry

Figure 5 contains a cyclic voltammogram at scan rates $20mVs^{-1}$ to $1Vs^{-1}$ for As(III) added to the chloroaluminate melt as $AsCl_3$. A single reduction peak, apparent at low scan rates, becomes a double peak at faster scan rates. Arsenic is deposited as a black film from this melt and presumably is removed in the single stripping peak at circa +1.9V.

In basic melt compositions, the electrochemistry of arsenic is more distinctive (figure 6). The reduction waves shift considerably negative and 3 well-resolved peaks are featured on the reverse scan. Presumably, the chloro complexes of the intermediate valence states of arsenic are stable but we have not investigated the nature of these processes further.

Electrolysis of Ga(III) and As(III) Mixtures

A series of experiments have been conducted to establish the prospects of producing GaAs films by codeposition at room temperature. In view of the slow kinetics for Ga(III) reduction relative to As(III) reduction, a large excess of $GaCl_3$ over $AsCl_3$ was used in most experiments. As the voltage was scanned to increasingly more negative potentials past the first reduction peak of gallium, a single oxidation wave at about +1.6V shifted positive slightly and split into a double wave (figure 7). A smaller anodic peak is present at about +1.3V and can be assigned to Ga(I) oxidation.

To assist in the characterization of these peaks, we attempted anodization of an ion beam sputtered GaAs film (nominal 50Å thickness) which had been coated onto a molybdenum substrate. Upon scanning positive from the rest potential (approx. +0.6V) two waves appeared prior to the melt oxidation at +1.8 and +1.9V. Unfortunately, it is difficult to assign these waves by electrochemical methods alone, so physical and chemical methods of the film analyses have been employed.

Characterization of Electrodeposits

Electrodeposits, performed under potentiostatic conditions in acidic melts with the Ga(III) concentration being greater than the As(III) concentration, were analyzed by various methods. X-ray fluorescence used to determine the presence of the major elemental constituents of the films, showed that gallium and arsenic were present. Peaks, corresponding to fluorescence lines, were observed at the following 2Θ angles (LiF): 30.5° and 34.0°, confirming the presence of arsenic, and 35.0° and 38.9°, confirming the presence of gallium. Inductively coupled plasma analysis of the films dissolved in nitric acid showed that gallium and arsenic were the two major components. In addition, trace amounts of aluminum and iron were detected. Electron dispersive scattering analysis of a film on platinum foil also confirmed the presence of gallium and arsenic, but did not indicate the presence of aluminum or iron. To determine if the films were indeed GaAs, X-ray powder diffraction was performed. Analysis of the powder obtained by mechanical removal of the films produced the following 2Θ diffraction angles: 27.5°, 45.5°, 53.9° and 82°. These results are consistent with the diffraction pattern that is produced by GaAs. Unlike the result obtained by Tremillon and coworkers for galvanostatic deposition, we did not observe any diffraction lines due to arsenic. This may be due to the excess of Ga(III) over As(III) and the effect of reaction (5) in removing excess gallium metal from the deposit.

CONCLUSIONS

Voltammetric studies of Ga(III) and As(III) in a room temperature acidic chloroaluminate melt have revealed that gallium and arsenic can each be electrodeposited. Arsenic species, in several oxidation states, are stabilized in chloride-rich media and this warrants further investigations of the complexation. When both Ga(III) and As(III) are present in acid melts, with Ga(III) in excess, electrodeposits are obtained which consist primarily of crystalline GaAs. As concluded by Tremillon and coworkers, codeposition from the +3 oxidation states is difficult to control due to the slow kinetics behavior of Ga(III). However, the equilibrium between Ga(III), Ga(0) and Ga(I) may help eliminate codeposition of Ga(0), and, significantly, gallium arsenide can be produced electrochemically at room temperature. We are currently investigating low temperature melts based on gallium chloride species and the optimization of film quality.

ACKNOWLEDGEMENTS

We wish to thank Douglas Arent, Princeton University, for the ion beam sputtered coatings of GaAs on Mo substrates. The ICP analyses were made by Dr. Ronald D. Snelling and EDS measurements by Paul K. Carpenter in the Department of Geology at LSU.

REFERENCES

1. I.G. Dioum, J. Vedel, and B. Tremillon, J. Electroanal. Chem. 139 (1982) 329.
2. H.L. Chum and R.A. Osteryoung, "Ionic Liquids", D. Inman and D.G. Lovering (Eds.), Plenum Press, New York (1981), p. 407.
3. R.J. Gale and R.A. Osteryoung, "Molten Salt Techniques", Vol. 1, R.J. Gale and D.G. Lovering (Eds.), Plenum Press, New York (1983), p. 55.
4. C.L. Hussey, "Advances in Molten Salt Chemistry", G. Mamanatov and C.B. Mamantov (Eds.), vol. 5, Elsevier (1983), p. 185.
5. T.I. Popova, I.A. Bagotskaya, and E.D. Moorhead, "Encyclopedia of Electrochemistry of the Elements", A.J. Bard (Ed.), vol. VIII, Marcel Dekker, Inc. (1978), p. 207.
6. A.P. Tomilov and N.E. Chomutov, "Encyclopedia of Electrochemistry of the Elements", A.J. Bard (Ed.), vol. II, Marcel Dekker, Inc. (1974), p. 21.
7. U. Anders and J.A. Plambeck, Can. J. Chem. 47 (1969) 3055.
8. R.J. Gale, "Molten Salt Technology", D.G. Lovering (Ed.), Plenum Press (1982), p. 507.
9. I.G. Dioum, J. Vedel, and B. Tremillon, J. Electroanal. Chem. 137 (1982) 219.
10. J.H. von Barner, Inorg. Chem. 24 (1985) 1686.

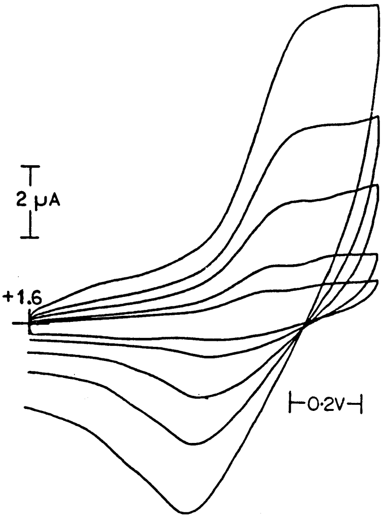

FIGURE 1. CV of approx. 16 mM Ga(III) at 10,20,50, 100 and 200 mV/s, Pt button area 0.810 mm^2, in 1.37:1 $AlCl_3$:1-BPC, 30°C.

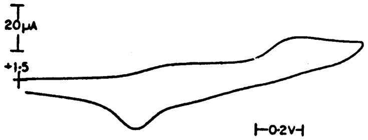

FIGURE 2. CV of approx. 16 mM Ga(III) at 200 mV/s, Pt button area 0.810 mm^2, in 1.37:1 $AlCl_3$:1-BPC,30°C.

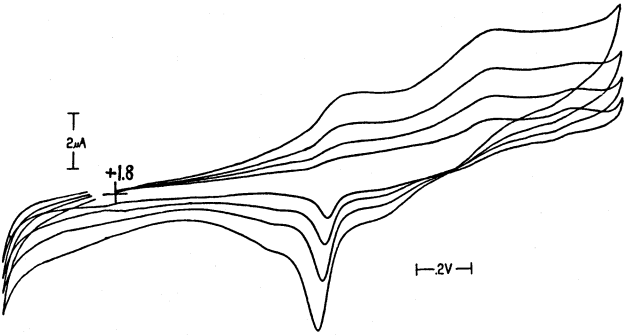

FIGURE 3. CV of 6mM Ga(III) at 2,5,10 and 20 mv/s, Pt button area 0.810 mm^2, in 1.8:1 $AlCl_3$:1-BPC, 40°C.

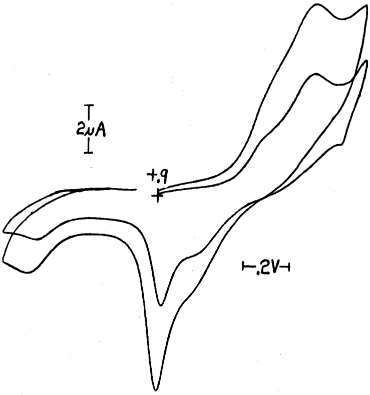

FIGURE 4. CV of 16mM Ga(III) at 20 and 50mV/s after partial electrolysis, Pt button area 0.810mm^2 in 1.37:1 $AlCl_3$:1-BPC, 30°C.

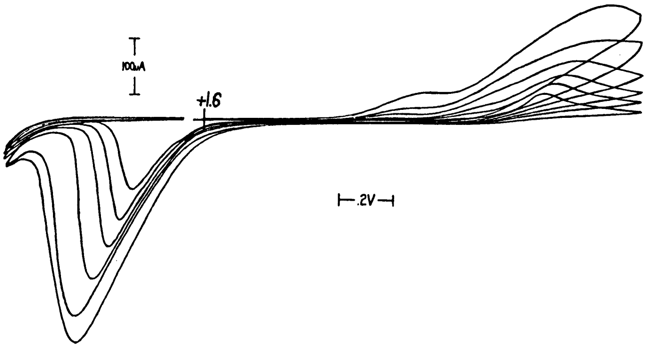

FIGURE 5. CV of 60mM As(III) at 20,50,100,200,500 and 1000mV/s, Pt button area 0.810mm^2, in 1.36:1 AlCl$_3$:1-BPC, 40^{o}C.

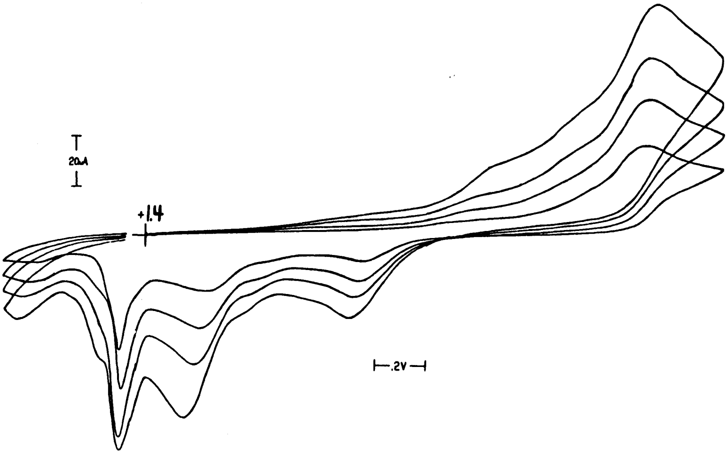

FIGURE 6. CV of 43mM As(III) at 20,50,100 and 200mV/s, Pt button area 0.810mm^2, in 1:1 AlCl$_3$:1-BPC, 40^{o}C.

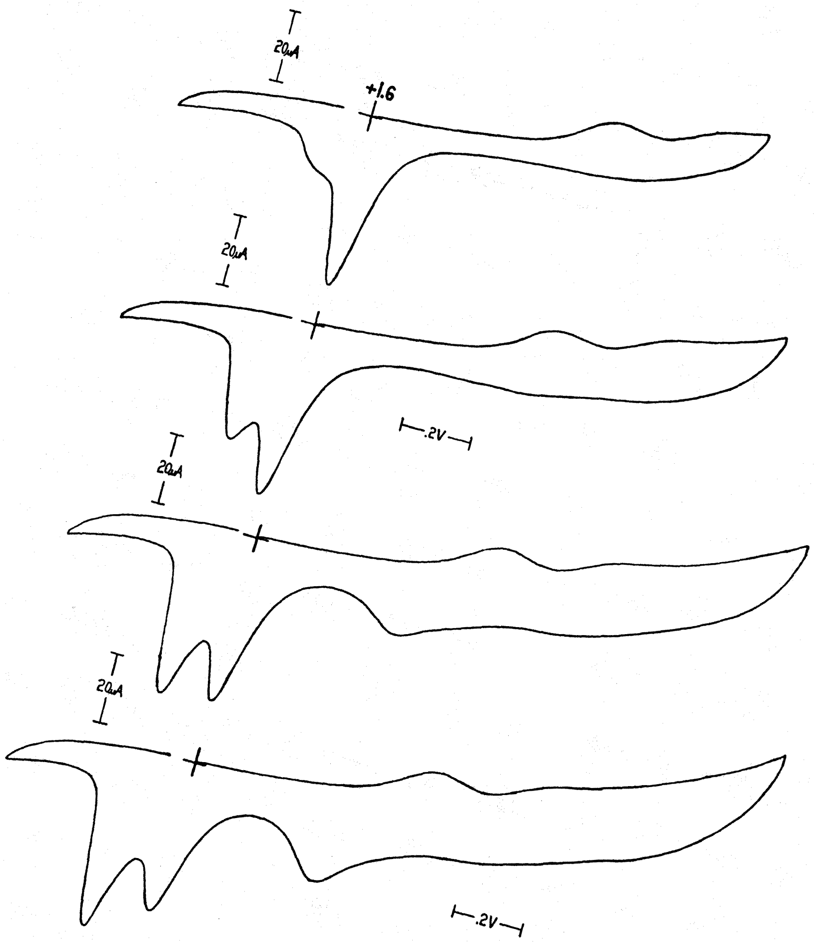

FIGURE 7. CV's of 6mM As(III) with 153mM Ga(III) at 200mV/s scanning progressively more cathodic, Pt button area 0.810mm^2, in 1.82:1 $AlCl_3$:1-BPC, 40°C.

DOI: 10.1149/198601.0153PV

GALVANIC CELLS USING ROOM TEMPERATURE CHLOROALUMINATE MOLTEN SALTS

G. F. Reynolds and C. J. Dymek, Jr.

The Frank J. Seiler Research Laboratory
United States Air Force Academy
Colorado Springs, CO 80840

ABSTRACT

Two galvanic cells were tested using as electrolytes room temperature molten salts formed by mixing $AlCl_3$ with 1-methyl-3-ethylimidazolium chloride (MEICl). Zn and Cd, each with basic melt (containing Cl^- and $AlCl_4^-$) were the anodes. Br_2 dissolved in basic melt with a reticulated vitreous carbon current collector was the cathode in each case. MEI^+-selective NAFION® was used as a separator. The Zn electrode was found to be irreversible, while the Cd/Br_2 cell appears to be reversible with an open circuit voltage of 2.0V, an extended temperature range of operation, and potential for high specific energy.

INTRODUCTION

Chloroaluminate molten salts formed by mixing 1-methyl-3-ethylimidazolium chloride (MEICl) with $AlCl_3$ are liquid at and well below room temperatures (1,2). These melts are formed in the following reactions:

$$MEI^+ + Cl^- + AlCl_3 \leftrightharpoons MEI^+ + AlCl_4^- \qquad K \gg 1 \qquad (1)$$

$$MEI^+ + AlCl_4^- + AlCl_3 \leftrightharpoons MEI^+ + Al_2Cl_7^- \qquad K \gg 1 \qquad (2)$$

Melts with apparent $AlCl_3$ mole fraction, $\underline{N}$, less than 0.5 contain Cl^- and $AlCl_4^-$ and are basic (Cl^- acts as a Lewis base). Acidic melts have $\underline{N} > 0.5$ and contain $AlCl_4^-$ and $Al_2Cl_7^-$ (a Lewis acid). Using equations 1 and 2, we can calculate the anion mole fractions of these melts as a function of $\underline{N}$ as shown in Fig. 1. We report here on our efforts to determine the feasibility of using these melts as electrolytes in reversible batteries.

In previous work (3) we reported results of preliminary studies of room temperature chloroaluminate cells combining Cd and Zn anodes in basic melt with aluminum cathodes in acidic melt. These candidates for reversible batteries have open-circuit potentials of 0.7 to 1 volt. We also investigated an aluminum/bromine cell employing an aluminum anode in basic chloroaluminate melt and a bromine cathode in basic melt giving an open-circuit potential of over 2 volts. However, as has been shown earlier (4), aluminum cannot be reversibly plated from a basic $MEICl/AlCl_3$ melt. Although the Al/$\underline{N}$ = 0.6 melt electrode is highly reversible, the reduction of the MEI^+ ion appears to occur preferentially to deposition of Al from the $AlCl_4^-$ in basic melts.

We thus focused on combining other metal anodes in basic melt with the Br_2 electode in basic melt using an RVC (reticulated vitreous carbon) current collector. The open circuit potentials of the anodes Cd, Zn, Fe, Ni and Cu immersed in $\underline{N}$ = 0.33 basic melt were measured relative to the Al/$\underline{N}$ = 0.60 reference electrode shown in Fig. 2. Only the Cd and Zn electrodes gave stable potentials. The open circuit voltages of the stable electrodes are given below:

Electrode	Measured Potential (V)
Br_2(13% w/w in $\underline{N}$ = 0.42) + $2e^- \rightarrow 2Br^-$	0.82
Al^{3+}($\underline{N}$ = 0.60) + $3e^- \rightarrow Al$	0.00
Cd^{2+}($\underline{N}$ = 0.33) + $2e^- \rightarrow Cd$	-1.18
Zn^{2+}($\underline{N}$ = 0.33) + $2e^- \rightarrow Zn$	-1.35
Al^{3+}($\underline{N}$ = 0.33) + $3e^- \rightarrow Al$	-1.45

An important point to note about these half-cell reactions is that while the cations are shown for simplicity as uncomplexed, these cations in the basic melts are present as the chloro complexes. Also, the bromine is probably present as Br_2Cl^- as will be discussed later.

EXPERIMENTAL

All melts were prepared as reported previously (5). All operations described below were carried out in a He-atmosphere dry box. The galvanic cells were constructed as shown in Fig. 3. The anodes were 0.25 mm thick metal foils of Zn (City Chemical Corp., NY, 99.9%) and Cd (Johnson Matthey Chemicals Ltd, UK, 99.9975%). In some cells, Zn mesh was used as the anode, although no attempt was made to measure mass changes of these anodes. The surfaces of the foils used were abraded with carborundum paper, rinsed with acetonitrile, and blotted dry before they were weighed and then incorporated into the cells. The active area of the anodes varied from 3 to 5 cm^2. The cathode current collector was reticulated vitreous carbon (RVC) from Energy Research & Generation with a porosity grade of 80 (pores per linear inch). It was generally about 1 cm^2 and 0.3 cm thick and connected to the potentiostat using Pt wire.

The separator was clear unsupported NAFION® 117 film which had been soaked for at least 15 hrs in a 15% w/w MEICl/acetonitrile solution which was continuously stirred. This process replaces the H^+ cations in the film with MEI^+ ions as indicated by the mass change in the film, which was generally within 15% of the weight change calculated from the known equivalents of H^+ per unit weight of film. NAFION® treated in this manner has been shown to be selective to MEI^+ transport in the melts (6).

Weights of the anolytes and catholytes in the assembled cells ranged from 1.5 to 2.5 g. The electrolyte composition and masses were selected to insure that in each cell the anode reaction was the limit on the cell capacity. The catholytes were prepared by adding liquid Br_2 (Baker Analyzed Reagent) to the melt of known mass and composition. Since the cells were operated open to the dry box atmosphere, experiments were done to determine the rate of Br_2 loss from these melts as a function of the mole ratio, Br_2/Cl^-. Melts containing Br_2 were placed in open jars and weighed periodically on a Mettler AE163 balance in the dry box at ambient temperatures of about 26°C. The cross-sectional areas of the samples exposed to the dry box atmosphere were all kept at about 7 cm^2.

The cells were operated at constant current using a PAR 173 Potentiostat/Galvanostat with a PAR 179 Coulometer. Voltages were recorded on a chart recorder and monitored with a Hewlett-Packard 3455A Digital Voltmeter, both of which were connected to the PAR summing amplifier output. At various points during discharges, voltage/current behavior was recorded by varying the constant current. In some cells, a reference electrode was used to obtain information on distribution of the cell overpotential or overall "internal resistance" measured from the voltage/current plot slopes. The reference electrode was an $Al/\underline{N} = 0.60$ melt as shown in Fig. 2. Following operation of the cell, it was disassembled, and the anode was rinsed in acetonitrile, blotted dry, and weighed.

The nuclear magnetic resonance chemical shift data were taken with a JEOL FX-90Q NMR spectrometer using 5 mm or 10 mm tunable probes. Sample temperature was controlled to within about ±1° using JEOL NMR variable temperature control. The ^1H and ^{13}C chemical shifts were referenced to an external TMS standard. The external reference for the Cd NMR shifts was a capillary containing a concentrated solution of $CdCl_2$ dissolved in 20% $HClO_4$.

RESULTS AND DISCUSSION

(a) The $Br_2/\underline{N} < 0.5$ electrode

Initial experiments were designed to test the stability and reversibility of the electrode formed by adding bromine to basic chloroaluminate melt. We were interested in determining what weight loss, if any, occurred by allowing basic melts containing bromine to be open to the inert atmosphere in a dry box. We also observed that the appearance of the basic melts containing bromine that were subjected to charge and discharge changed as expected.

Based on observations of similar systems made by Osteryoung and coworkers (7,8), the dissolution of bromine in basic chloroaluminate melt probably results in the formation of a trihalide anion:

$$Br_2 + Cl^- \rightarrow Br_2Cl^- \qquad (3)$$

Additional work in this laboratory by Wilkes et al (9) showed that when chlorine gas is dissolved in these same basic melts to give yellow-green solutions, the main species produced is the trichloride anion:

$$Cl_2 + Cl^- \rightarrow Cl_3^- \qquad (4)$$

Since the species Cl_3^- slowly reacts with MEI^+ in basic chloroaluminate melt forming 4,5-dichloro-1-methyl-3-ethyl-imidazolium chloride and degrading the electrochemical properties of the melt (9), we examined bromine saturated basic melts for evidence of reaction using NMR spectroscopy. Over the period of several days at probe temperature of about 27°C, no change was observed in either the ^1H or ^{13}C NMR resonances of MEI^+, thus indicating a negligible rate of reaction of Br_2Cl^- with the basic melt.

Weight loss measurements were made on solutions of Br_2 in basic melts of composition $\underline{N} = 0.38$ and $\underline{N} = 0.44$ in which the Br_2/Cl^- mole ratio was varied from 0 to 1.1. From the species profile shown in Fig. 1, it is evident that the moles of Cl^- (before the addition of Br_2) can be determined directly from the concentration of the melt and the weight of the melt sample. The results of these weight loss measurements are shown in Fig. 4. It can be seen that the mg/hr weight loss rate for the samples is rather small until the Br_2/Cl^- ratio exceeds 1.0, after which there is a very large increase in the rate of weight loss. This supports the conclusion that Br_2 added to basic melts reacts stoichiometrically with the available Cl^- to form the relatively non-volatile Br_2Cl^- anion as shown in equation (3). After a 1/1 mole ratio is reached, the marked increase in rate of weight loss can be ascribed to the presence of volatile molecular Br_2 dissolved in the melt.

Cyclic voltammetry was employed by L. F. Koons of this laboratory (10) to determine conditions under which the bromine electrode is reversible in basic melt. He added small amounts of bromide ion (in the form of added MEIBr) and/or Br_2 to a neutral $\underline{N} = 0.5$ chloroaluminate melt. The cyclic voltammogram shown in Fig. 5

shows that bromide in the melt is oxidized to bromine in a two-step process.

From previous as yet unpublished work in this Laboratory on a cell using RVC as a current collector in an electrode containing Cl_2 dissolved in a basic chloroaluminate melt, it had been found that the condition of the RVC deteriorated with time. Therefore, the RVC was examined after removal from cells where it had been in contact with Br_2 dissolved in basic melt. In these cases, no evidence could be found of any deterioration of the RVC current collectors.

(b) Nature of the Cd and Zn chlorocomplexes in basic melt

Weight measurements on several Cd and Zn electrodes in basic melt, before and after passage of current with the metals as anodes in electrochemical cells, confirmed that the oxidation of the Cd and Zn occurred with the loss of two electrons. Several methods can be used to show that in basic melt having available Cl^-, the species formed are $CdCl_4^{2-}$ and $ZnCl_4^{2-}$, respectively. One of the most direct methods is an NMR study of basic melts containing dissolved $CdCl_2$ and $ZnCl_2$.

In the case of the $MEICl/AlCl_3$ melts containing dissolved $CdCl_2$, the cadmium, proton and carbon chemical shifts as a function of concentration can be used to obtain information on the nature of the complex formed. Basic $MEICl/AlCl_3$ melts having intial mole fractions of $AlCl_3$ of 0 to 0.43 were used as well as an acidic melt with N=0.60. To these melts were added high purity anhydrous $CdCl_2$ so that the mole ratio of $CdCl_2/MEICl$ was always 0.16. The ^{111}Cd NMR chemical shifts at 30°C increased by only 1% for these neat molten salt samples from very basic to near neutral melt (a large decrease in chemical shift was observed for the sample containing $CdCl_2$ dissolved in the acidic $\underline{N} = 0.60$ melt). These results indicate that a single type of cadmium chloride complex is formed in the basic melts. Melts near equimolar $MEICl/AlCl_3$ would not dissolve observable amounts of $CdCl_2$, thus showing that $CdCl_2$ does not complex with $AlCl_4^-$ as it does with Cl^- and $Al_2Cl_7^-$.

A confirmation that $CdCl_4^{2-}$ was formed in the basic melts was obtained in a second series of experiments in which the $MEICl/AlCl_3$ mole ratio was held constant at 2.0. Various amounts of cadmium chloride were added and the ^1H and ^{13}C NMR chemical shifts of the MEI^+ measured. From previous NMR results on binary $MEICl/AlCl_3$ melts (11,12), it is known that the observed chemical shifts for both ^1H and ^{13}C of the proton and carbon of position 2 on the imidazole ring can be expressed as a function of the Cl^- anion fraction, Y_{Cl^-}:

$$\text{observed shift} = a + bY_{Cl^-} + c(Y_{Cl^-})^2 \qquad (5)$$

In the limit of small additions of added $CdCl_2$, this same equation can be used to calculate the number of chloride ions complexed, M, since the dominate effect on the observed MEI^+ chemical shifts should be the decrease in the chloride ion concentration (13). In the equations below for the given complexing reaction, we show that the value of Y_{Cl^-} in equation (5) is a function only of the initial chloride anion fraction (before $CdCl_2$ addition but after reaction of $AlCl_3$ with Cl^-), $Y°_{Cl^-}$, the measured $CdCl_2$ mole fraction, N_{Cd}, and the constant of interest, M.

$$(M+1)Cl^- + AlCl_3 + CdCl_2 \rightarrow AlCl_4^- + CdCl_{M+2}^{-M} \qquad (6)$$

	$(M+1)Cl^-$	$AlCl_3$	$CdCl_2$	$AlCl_4^-$	$CdCl_{M+2}^{-M}$	
initial moles}	a	x	y	0	0	, $a > (x + My)$
final moles}	a-x-My	0	0	x	y	

$$Y_{Cl^-} = \frac{a-x-My}{a-(M-1)y}$$

$$= \frac{\frac{a-x}{a} - \frac{My}{a}}{\frac{a-(M-1)y}{a}}$$

$$= \frac{Y°_{Cl^-} - \frac{My}{a}}{1 - \frac{(M-1)y}{a}}$$

$$= \frac{\frac{Y°_{Cl^-}(a+x)}{(a+x+y)} - \frac{My(a+x)}{a(a+x+y)}}{\left(\frac{a+x}{a+x+y}\right) - \frac{(M-1)y}{(a+x+y)}\left(\frac{a+x}{a}\right)}$$

$$= \frac{Y°_{Cl^-}\left(1 - \frac{y}{a+x+y}\right) - \frac{My}{a+x+y}\left(2 - \frac{a-x}{a}\right)}{\left(1 - \frac{y}{a+x+y}\right) - \frac{(M-1)y}{a+x+y}\left(2 - \frac{a-x}{a}\right)}$$

$$Y_{Cl^-} = \frac{Y°_{Cl^-}(1 - N_{Cd}) - MN_{Cd}(2 - Y°_{Cl^-})}{(1 - N_{Cd}) - (M-1)N_{Cd}(2 - Y°_{Cl^-})}$$

Assuming 1, 2, or 3 chloride ions (M = 1, 2, or 3), respectively, are involved in forming the chlorocadmium complex in basic melts, a series of theoretical curves was generated using the calculated Y_{Cl^-} values and equation (5) for the ^1H chemical shifts as shown in Fig. 6. The plot of measured ^1H chemical shifts versus N_{Cd} should approach one of the theoretical curves in the limit of small concentrations of added $CdCl_2$. As shown by the experimental data points represented by squares in Fig. 6, the results indicate M=2 and the formation of the complex $CdCl_4^{2-}$.

Results similar to those for the ^1H chemical shifts were also obtained for the ^{13}C chemical shifts of carbon 2 of the imidazole ring, except that the experimental conditions produced somewhat more scatter in the ^{13}C chemical shift data. A more comprehensive treatment to account for all species influencing the NMR chemical shifts is being developed (13).

(c) Galvanic cell performance

The open circuit voltages of the cells were 2.1 V for the Zn/Br_2 system and 2.0 V for the Cd/Br_2 system, with slight dependences on the electrolyte composition ranges shown in Table 1. On the first discharge of either cell (Figs. 7, 8, and 9), several hours were required for the cell to reach maximum voltage under load. This is due to the fact that the NAFION® separator is only slowly wetted by the melt and it thus is the major contributor to the high internal resistance (up to 2000 Ω) initially observed. In subsequent cycles, the observed total "internal resistance" obtained from slopes of the voltage/current plots ranged from 200-300Ω for the Zn/Br_2 cells and from 150-200Ω for the Cd/Br_2 cells.

The net discharge in coulombs, Q discharge - Q charge, for each cell listed in Table 1 was used to calculate the predicted mass loss of the anodes based on the reactions:

$$Cd + 4\,Cl^- \rightarrow CdCl_4^{2-} + 2e^- \qquad (7)$$

$$Zn + 4\,Cl^- \rightarrow ZnCl_4^{2-} + 2e^- \qquad (8)$$

The loss predicted for the non-reversible case, i.e., if oxidation occurred but redeposit of the metal did not, was calculated from ΣQ discharge. When these two calculated losses are compared with the observed mass losses, it is clear that only the Cd anode is reversible. This is also evident in the obvious degradation of the Zn/Br_2 cell performance, Fig. 7, as compared with the relatively reproducible cycles observed in the Cd/Br_2 cell, Figs. 8 and 9.

The higher observed loss in Cd mass over the calculated value is due to corrosion of the Cd. The rate of corrosion was determined by placing strips of Cd with the same area as the active cross-sections of Cd used in the cells in different samples of N = 0.33 melt. The strips were periodically removed and weighed and the corrosion rate was found to be about 0.05 mg cm^{-1} hr^{-1}. The observed loss of Cd in excess of the loss calculated from the net discharge is within about 15% of the corrosion loss calculated from this measured rate. Precise comparisons cannot be made because the active area of the Cd varies during the cycling as does the mole fraction of the anolyte. It was noted that after a number of weeks soaking the strips, their observed mass loss was orders of magnitude less than what would have been projected from the initial corrosion rate. This suggests that a passivating layer may be formed after which the corrosion rate significantly decreases.

In Fig. 8, a plot of the potential difference between the Cd electrode and the Al|N = 0.60 reference electrode -[WE (Cd) - RE] is also shown. The reference electrode (Fig. 3) was placed in the anolyte as close as possible to the Cd anode. It shows that the overpotential at the Cd electrode accounts for less than 20% of the total "internal resistance" of the cell. Placing the RE in the catholyte showed that the Br_2 electrode overpotential was also relatively small, less than 10% of the total "internal resistance," so that the bulk of the internal resistance is in the NAFION® separator. This condition also holds approximately in the Zn/Br_2 cells, except that the Zn anode overpotential was observed to increase after the first cycles. This is probably due to the decreased conductivity of the anolyte near the Zn surface as it becomes contaminated by the product of the reduction of the MEI^+ ion, which apparently occurs preferentially to $ZnCl_4^{2-}$ reduction as indicated by the characteristic orange color noted in the anolyte.

The temperature in the dry box in which the cells were cycled generally ranged from 24 to 27°C. We did some initial probing into the effect of temperature on cell performance and found a significant dependence of the cell "internal resistance" on temperature. Raising the temperature from 24 to 50°C resulted in a ten-fold decrease in the overall cell resistance. By placing the reference electrode on either side of the separator, we found that almost all of this "internal resistance" decrease was in the separator. Further efforts are planned to explore this effect.

The MEI^+-selective separator appears to be effective in preventing migration of Br_2Cl^- or Br_3^- into the anolyte. No corrosion of the Cd beyond that due to the corrosion occurring in basic melt as described above was observed and no Br_2 coloration of the anolyte was observed. However, the cell in which MEI^+ is the conducting ion is definitely limited in specific energy as the MEI^+ is neither a product nor a reactant in either electrode reaction. It is effectively excess baggage increasing the electrolyte mass. A clearly preferable transport mechanism would have the halide ions formed in the catholyte and consumed in the anolyte conducting the charge. At present, a halide ion-selective separator which works in these melts has yet to be demonstrated (6).

The cells were generally run with the anolyte limiting cell capacity. The Cd anode could easily be discharged to 70% of capacity with no apparent effect on rechargeability. In one of the Zn/Br_2 cells, the anolyte was removed near the end of a discharge and replaced with more basic anolyte so that the Br_2 cathode became the limiting reagent for the then recontinued discharge. The cell continued to discharge until over 90% of the Br_2 in the catholyte was consumed.

Examination of the Cd electrode used in the cell cycled as shown in Fig. 9 showed an effect resulting from the fairly large dependence of melt density on mole fraction. The top 2-3 mm of the electrode was stripped almost all the way through its 0.25 mm thickness, while the bottom 2-3 mm of the electrode had a spongy deposit of Cd about 1 mm thicker than the deposit which covered the central portion of the active surface. Since the more basic melt is less dense, it rises to the top of the anolyte and stripping occurs preferentially at the top of the electrode. The more neutral melt sinks to the bottom of the electrolyte, and during the charging cycle, deposition occurs preferentially at the bottom of the active surface. Overcoming this effect of this density induced concentration gradient is therefore an important step in improving the cycle life of this system.

CONCLUSION

The Cd/Br_2 cell using room-temperature molten salt electrolytes formed from MEICl and $AlCl_3$ is a reversible battery with open circuit potential of 2.0 V. The cell electrochemistry is at this time best desribed as:

$$\text{anode:} \quad Cd + 4Cl^- \rightarrow CdCl_4^{2-} + 2e^-$$

$$\text{cathode:} \quad Br_2Cl^- + 2e^- \rightarrow 2Br^- + Cl^-$$

$$\text{cell:} \quad Cd + 3Cl^- + Br_2Cl^- \rightarrow CdCl_4^{2-} + 2Br^-$$

Problems with the change of the Cd electrode shape due to concentration gradients and Cd corrosion have been identified. However, if these problems can be solved and a separator which is selective for Br^- or Cl^- transport can be developed, the cell has promise for a high specific energy reversible battery with an extended operating temperature range.

REFERENCES

1. A. A. Fannin, Jr., L. A. King, J. A. Levisky, and J. S. Wilkes, J. Phys. Chem., 88, 2609 (1984).

2. A. A. Fannin, Jr., D. A. Floreani, L. A. King, J. S. Landers, B. J. Piersma, D. J. Stech, R. L. Vaughn, J. S. Wilkes, and J. L. Williams, J. Phys. Chem., 88, 2614 (1984).

3. G. F. Reynolds and C. J. Dymek, Jr., J. Power Sources, 15, 109 (1985).

4. J. S. Wilkes and J. J. Auborn, "Electrodeposition of Aluminum in a Room Temperature Molten Salt," Bell Laboratories Technical Memorandum 83-11528-16, June 1983.

5. J. S. Wilkes, J. A. Levisky, R. A. Wilson, and C. L. Hussey, Inorg. Chem., 21, 1263 (1982).

6. C. J. Dymek, Jr. and L. A. King, "Transport Numbers of Species in Room Temperature Imidazolium Chloroaluminate Ionic Liquids," Program and Abstracts, Symposium on Electrochemistry, the 27th Rocky Mountain Conference, Denver, CO, July 1985.

7. Z. J. Karpinski and R. A. Osteryoung, Inorg. Chem., 23, 4561 (1984).

8. M. Lipsztajn and R. A. Osteryoung, Inorg. Chem., 23, 1735 (1984).

9. F. M. Donahue, J. A. Levisky, G. F. Reynolds and J. S. Wilkes, "Reaction of Chlorine with Ambient Temperature Chloroaluminate Molten Salts," the Fifth International Symposium on Molten Salts, 168th Meeting of the Electrochemical Society, Las Vegas, NV, Oct. 1985.

10. L. F. Koons, "A Study of the Electrochemical Behavior of the Bromine/Bromide Couple in Melts Composed of Aluminum Chloride and 1-Methyl-3-ethylimidazolium Chloride," 1985 USAF-UES Summer Faculty Research Program Final Report, the F.J. Seiler Research Laboratory, USAF Academy, CO, 80840, 16 Sep. 1985.

11. J. S. Wilkes, J. A. Levisky, J. L. Pflug, C. L. Hussey, and T. B. Scheffler, Anal. Chem., 54, 2378 (1982).

12. J. S. Wilkes, J. S. Frye, and G. F. Reynolds, Inorg. Chem., 22, 3870 (1983).

13. G. F. Reynolds, "Application of Multinuclear NMR Spectroscopy to the Study of Chloroaluminate/Chlorocadmium Molten Salts," Program and Abstracts, the 1984 International Chemical Congress of Pacific Basin Societies, Honolulu, HI, Dec. 1984.

14. T. B. Scheffler, H. E. Klei, G. F. Reynolds and J. S. Wilkes, "Preliminary Studies of New Molten Salt Systems Based on 1-Methyl--3-ethylimidazolium Chloride and Chloride Salts other than Aluminum Chloride," the Fifth International Symposium on Molten Salts, 168th Meeting of the Electrochemical Society, Las Vegas, NV, Oct. 1985.

Table I.

Cell	# Cycles	Calculated Δm anode (net disch)	Calculated Δm anode (disch only)	Observed Δm anode
Zn|N=0.33||N=0.42(13%Br$_2$),RVC	2	0.038 g	0.125 g	0.127 g
Zn|N=0.37||N=0.42(12%Br$_2$),RVC	1	0.030	0.051	0.048
Cd|N=0.35||N=0.42(13%Br$_2$),RVC	2	0.041	0.104	0.043
Cd|N=0.33||N=0.44(11%Br$_2$),RVC	2	0.036	0.124	0.046
Cd|N=0.33||N=0.44(9%Br$_2$),RVC	7	0.029	0.448	0.094

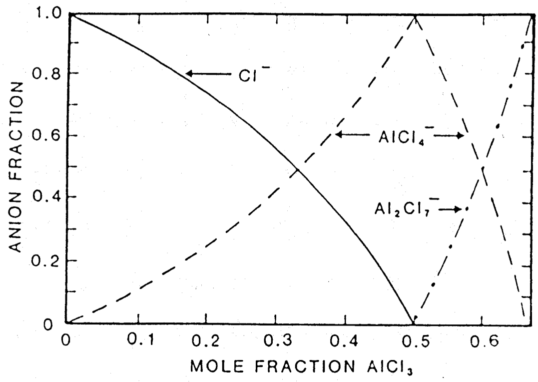

Fig 1. Anion fractions in MEICl-AlCl$_3$ melts as a function of mole fraction of AlCl$_3$.

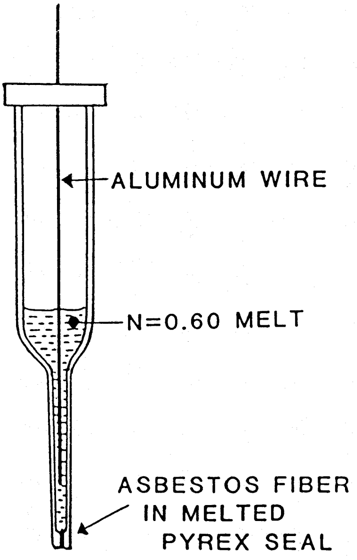

Fig 2. Al|N=0.6 melt reference electrode.

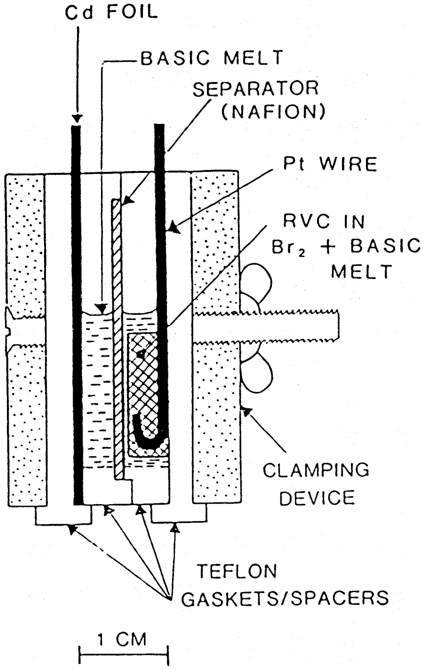

Fig 3. Galvanic cells for testing Zn/Br$_2$ and Cd/Br$_2$ couples.

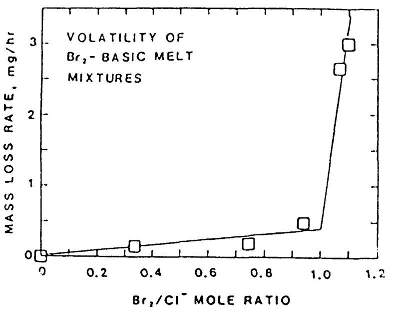

Fig 4. Rate of mass loss from Br_2-basic melt mixtures as a function of Br_2/Cl^- mole ratio.

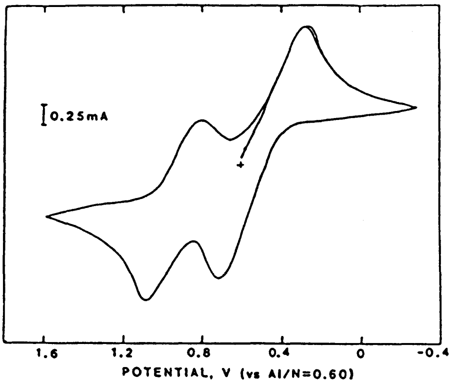

Fig 5. Cyclic voltammogram of near neutral MEICl/$AlCl_3$ melt containing Br_2 and Br^- (from ref (10)).

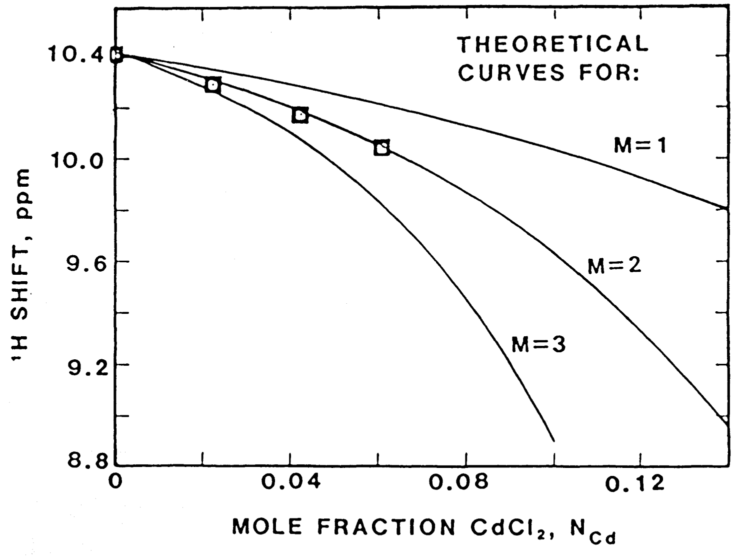

Fig 6. Theoretical and observed ^1H NMR shifts of the position 2 hydrogen on MEI^+ as a function of mole fraction of $CdCl_2$ in N=0.33 MEICl-$AlCl_3$ melts.

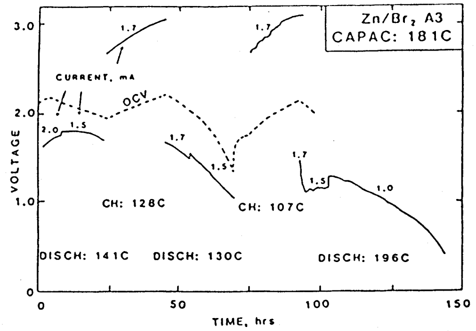

Fig 7. Charge-discharge curves for Zn/Br$_2$ cell. Capacity shown determined by anolyte composition.

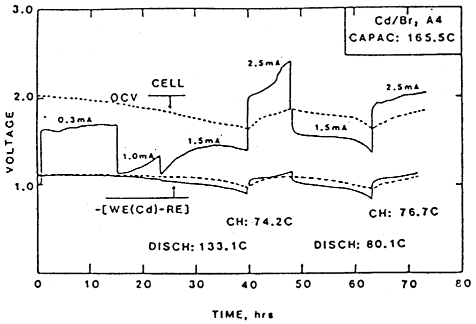

Fig 8. Charge-discharge curves for Cd/Br$_2$ cell with RE in anolyte. Capacity shown determined by anolyte composition.

Fig 9. Charge-discharge curve for reversible Cd/Br$_2$ cell. Capacity shown determined by anolyte composition.

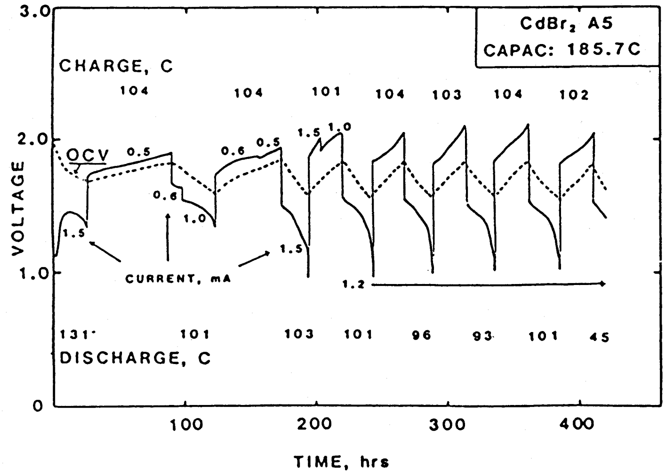

DOI: 10.1149/198601.0167PV

VOLTAMMETRY OF SODIUM POLYSULFIDES AT METAL ELECTRODES[*]

J. C. Dobson,[**] E. J. Cairns and F. R. McLarnon

Applied Science Division
Lawrence Berkeley Laboratory, and
Chemical Engineering Department
University of California
Berkeley, California 94720

ABSTRACT

The interaction of sodium polysulfides and candidate metals for the current collector/cell casing in sodium/sulfur cells at 300 and 350°C is explored using cyclic voltammetry. The metals investigated are chromium and molybdenum, and data for voltammetric sweeps at rates of 10 to 500 mV/sec in Na_2S_4 are reported. The results are compared with those of previous experiments conducted at carbon and platinum electrodes, and mechanisms are proposed to explain the data in terms of specific melt-metal interactions. A model describing the observed cathodic sweep data is presented.

---

[*] This work was supported by the Assistant Secretary for Conservation and Renewable Energy, Office of Energy Systems Research, Energy Storage Division of the U.S. Department of Energy under Contract No. DE-AC03-76SF00098.

[**] Present address: Tegal Corporation, 11 Digital Drive, Novato, California 94948

INTRODUCTION

The sodium/sulfur battery has been under development as a means for efficient storage of electricity for over 20 years. Two major applications being considered for this technology are electric vehicles and load-leveling devices. Corrosion of the cell casing during cycling of the cell has been identified as one of the key areas affecting cell performance and lifetime (1,2). The high operating temperature of the cell (300-350°C) coupled with the sulfur-polysulfide mixture present in the positive electrode causes most metals to lose their effectiveness as current collectors for a number of reasons. Typical problems are the formation of a non-conductive passivating layer (e.g., aluminum) or rapid corrosion which causes an increase in cell resistance or attack of the ceramic electrolyte by dissolved corrosion products in the melt (e.g., many steels). Two metals which have shown promise under normal cycling conditions are chromium, in the form of coatings on steels (1), and molybdenum (3).

Much research, both fundamental and applied, has been conducted to understand the phenomena occurring in the sulfur electrode. Cyclic voltammetry of sodium polysulfides at carbon (graphite or vitreous carbon) electrodes has been conducted by several investigators, and a review of this research is available (4). Carbon was used as an electrode material in these investigations since it is relatively inert to attack by sodium polysulfides; furthermore the bulk of the cell reaction occurs at the carbon felt current collector in the sulfur electrode. Since the wetting properties of metals by sulfur and polysulfide melts are quite different than those of carbon (5), melt-metal interactions could be quite different than those experienced with carbon in the previous earlier studies. More notably, the metal electrode is not inert with respect to these melts, so shifts in potential within the melt could change the stable phase(s) present on the surface of the electrode. Also, the corrosion scale could be reduced to the metal at sufficiently low potentials. This study attempts to identify these interactions and indicate how they may be of significance in sodium/sulfur cell design and operation.

BACKGROUND

During discharge of a Na/S cell, the sulfur reacts with sodium ions to form sodium polysulfides by the generalized reaction:

$$2Na^{+} + S_{x} + 2e^{-} \rightarrow Na_{2}S_{x} \qquad [1]$$

where x varies from 2 to at least 6, depending on the overall composition of the melt. The reaction proceeds until an overall composition equivalent to x=3 is achieved. At this point, Na_2S_2 begins to precipitate at the electrolyte, increasing the cell resistance sufficiently to prevent effective utilization of the remaining active material. This is illustrated by the Na-S phase diagram (Figure 1). Other interesting features of this system (at the operating temperature) are the large two-phase (therefore constant-potential) region and the high potentials associated with the various melt compositions (6). Due to the changes in composition, the current collector not only must withstand corrosion in molten sulfur, but also in sodium polysulfides.

PHYSICAL PROPERTIES OF SODIUM POLYSULFIDES

In order to begin to understand the electrochemistry of sodium polysulfides, a preliminary discussion of the melt properties is necessary. A detailed literature review on this subject has been published (4), so only a brief overview of the more pertinent points is presented here.

First, transference experiments of Cleaver and Davies (7) show that the melt is completely ionized, containing Na^+ and polysulfide ions only. In the temperature range of this work (300 to 350°C), the general conclusion based on a number of studies is that the predominant polysulfide species are $S_2^=$, $S_4^=$ and $S_5^=$, with some $S_6^=$ present near and within the two-phase region (5). It has been concluded that $S_3^=$ is not stable in the liquid (8,9), and since Na_2S is not thermodynamically stable in the presence of the single-phase melt at these temperatures, $S^=$ is not expected in significant concentrations.

The findings of Ludwig and Tischer (5) also indicate that at an overall composition of $Na_2S_{4.0}$, the major polysulfide species is $S_4^=$. At a composition of Na_2S_3, the melt probably consists of a nearly equimolar mixture of $S_4^=$ and $S_2^=$.

The physical properties of sodium polysulfides are strong functions of temperature, which has a considerable effect on the results of these experiments. A summary of some properties of $Na_2S_{4.0}$ is given in Table 1.

Table 1

Properties of $Na_2S_{4.0}$ (10,11)

Property	Units	300°C	350°C
Density	g/cm^3	1.92	1.89
Conductivity	$ohm^{-1}cm^{-1}$	0.284	0.489
Viscosity	cP	38.5	17.8

PREVIOUS ELECTROCHEMICAL STUDIES IN SODIUM POLYSULFIDES

The electrochemistry of sodium polysulfides has been studied by several investigators, beginning with the voltammetry studies of Selis (12) at graphite and platinum electrodes in 1970, followed by similar studies by several other researchers (13-15). As stated above, the bulk of this previous work was performed with carbon electrodes, although one study has been performed using aluminum electrodes (16). Although much remains to be learned about this system, several conclusions can be reached considering the results of this earlier research.

Most of the major features of the voltammetry of sodium polysulfides at carbon electrodes can be summarized making use of Figure 2. This figure is a slightly extended version of a typical voltammogram shown by Ludwig and Tischer (5). The most prominent feature of the diagram is the cathodic peak A. This feature is observed on voltammograms of metal electrodes as well as carbon electrodes. It is generally accepted that the melt, beginning at a composition of $Na_2S_{4.0}$, is reduced to lower polysulfides until a blocking film is formed at peak A. This results in a sudden increase of cell resistance and an accompanying decrease in cathodic current. It has been proposed that the layer consists of solid Na_2S_2 formed by a diffusion-limited electrochemical reaction, since a plot of peak current versus the square root of sweep rate yields a straight line passing through the origin (5). The slight increase in cathodic current at peak B has been ascribed to a rearrangement of the Na_2S_2 layer during the reduction of the Na_2S_2 to Na_2S. The increase in current near -1.85 V is probably caused by the reduction of Na_2S to elemental sodium (9,12,15). In one study, a second current maximum was seen near -1.3 V, particularly at low sweep speeds; this maximum has been attributed to the reduction of Na_2S_2 to Na_2S (12). The return sweep is uneventful, showing only the steady reduction of various polysulfides, until "peak" D is reached. The sudden increase in cathodic current probably reflects the complete dissolution of the blocking layer, which reduces the resistance and allows the further reduction of higher polysulfides. As the potential is swept anodically, oxidation quickly follows. Changes in the dominant reaction are probably responsible for the changes in slope of the voltammetric trace near -0.2 V and 0.25 V (E). The oxidation to sulfur proceeds uninhibited until peak F is reached near +0.4V. This probably represents blocking of the electrode with a nonconductive liquid sulfur layer. The exact sulfur species formed is uncertain and, for discussions of the phenomena observed, unimportant, since molten sulfur exists as a mixture of sulfur chains ranging from 2 to 8 sulfur atoms at 350°C (17). The decrease in current is coupled with a dramatic rise in resistance of the melt. The resistance remains constant for the remainder of the sweep although a final current rise is seen above +1.0V. Since no other explanation seems suitable, this is postulated by Ludwig and Tischer to be further oxidation of sulfur to a positively charged sulfur species (5).

On the return sweep, polysulfides continue to be oxidized until the sulfur layer is dissolved at H. This part of the trace probably represents competing reactions: production of sulfur by electrochemical oxidation and a chemical dissolution of sulfur of the type:

$$S_4 + 4S_4^{=} \rightarrow 4S_5^{=} \qquad [2]$$

This reaction would be expected to be more significant in the presence of higher concentrations of $S_4^{=}$ or lower polysulfides. This is substantiated by the fact that in this potential range currents are much lower in $Na_2S_{5.2}$ and higher in Na_2S_3 than in Na_2S_4 (5).

Earlier researchers (12,14) proposed that the first cathodic peak (A) represented an uncomplicated, first-order, reversible, two-electron reduction, probably:

$$S_4^{=} + 2e^{-} \rightarrow 2S_2^{=} \qquad [3]$$

Analysis using the current function tabulations of Polcyn and Shain (18) by Ludwig and Tischer led them to believe that the peak must result from a two-step reaction with two superimposed reversible peaks (5). However, this analysis assumes that the observed i_p is a true peak current for a diffusion-limited reaction. Due to the sudden blocking of the electrode by a film, it is possible that the peak current for the initial reduction reaction(s) is never reached. Therefore, analysis by this equation is uncertain, since the value of the current function, χ_p, (which depends on the peak current) must be known for quantitative analysis. Also, at 300°C the formation of Na_2S is favored at a potential only 219 mV cathodic of the formation of Na_2S_2, which is near the potential of peak A. If a significant amount of Na_2S is formed then the number of electrons involved in the overall electrode reaction is not certain.

EXPERIMENTAL PROCEDURE

For the reasons mentioned above, the metals studied using cyclic voltammetry were molybdenum and chromium. A detailed description of the preparation of the electrodes has been reported elsewhere (19). The sodium polysulfides used in these experiments were made by melting together the correct amounts of sulfur and sodium monosulfide. The sulfur was purchased from Noah Chemical Company with a reported purity of 99.999% and used without analysis. The sodium sulfide (Na_2S) was also purchased from Noah Chemical with a reported purity of 99.9%. The sulfide content was checked by titrating with silver nitrate using an Orion sulfide electrode to detect the endpoint. A sulfide content consistent with 99.6% purity was obtained by this method. After opening, the Na_2S was stored in a helium atmosphere glove box.

Molybdenum has been observed to corrode very slowly in sodium and lithium polysulfides (2,20), and MoS_2 is the only observed corrosion product. Earlier data suggested that a passivating layer was formed and that corrosion essentially ceased after ~100 hours at 350°C, but recent work shows that corrosion continues slowly for up to 4000 hours (21).

The behavior of chromium in both polysulfides studied is known to be different than that of molybdenum as the result of corrosion studies by several researchers (2,22-25). The fundamental difference in the observed behavior in static-corrosion studies of the two metals is that chromium corrodes steadily, following a parabolic rate law, whereas molybdenum forms what appears to be a passivating layer. Chromium has also been observed to form a ternary compound in these melts ($NaCrS_2$), whereas the only phase reported for molybdenum is MoS_2 (21). The layers formed on chromium therefore become much thicker than on molybdenum, so it is anticipated that any peaks representing reactions involving these films as a result of voltage-sweep experiments would be more prominent. Chromium sulfides are known to be more soluble in sodium polysulfides than those of molybdenum, although this solubility is slight, <50 µg/g in $Na_2S_{4.0}$ at 375°C (26), and should have little or no effect on the data from these experiments.

A schematic representation of the cell used in these experiments is shown in Figure 3. This cell contained a molybdenum "reference electrode" which monitored the potential of the melt in contact with it. The exposed electrode area was 1.770 cm^2. The cell resistance was measured at various temperatures, and the contribution of the melt to this resistance was subtracted, giving a contact resistance of ~0.8 ohms. The data of Cleaver, et al (10) were used to calculate the resistance of the melt.

The potential of the working electrode versus the reference was controlled using a PAR model 173 potentiostat fitted with a model 376 IR compensation unit. Partial IR compensation was accomplished by a voltage-feedback method.

In order to study the entire range of sulfur and polysulfide activities present in the system most easily, an initial composition in the center of the single-phase region was chosen. This initial composition ($Na_2S_{4.0}$) represents a specific potential (~1.95 V vs Na/Na^+ at 350°C) which served as the reference potential for each experiment.

In order to insure repeatable results, the most reliable pretreatment method found was simply to wait between runs to allow the system to equilibrate. This was determined by monitoring the potential between all of the electrodes at open circuit after each experiment. The waiting time necessary for the potentials to reach values less than 20 mV from each other was about 20 minutes at 350°C.

In order to identify the reactions occurring at metal electrodes, experiments similar to those performed by Ludwig and Tischer were conducted at molybdenum and chromium electrodes. Cyclic voltammetry was performed with a polished metal electrode using a variety of sweep rates and voltage ranges. Two temperatures were used for these experiments, Due to the complexity of the melt, coupled with the additional possibility of interaction between the melt and the electrode being studied, an attempt was made to conduct as many variations on sweep rate, initial scan direction, and turnaround voltages as the durability of the experimental apparatus would allow. Failure of the cell prevented the completeness desired in some cases, particularly with molybdenum at 350°C.

To ease analysis of the data, a list of the standard potentials for the reactions expected to occur on or near each electrode is given in Table 2. These were obtained by adding the potential calculated for the overall reaction shown to the reference potential of $Na \rightarrow Na^+ + e^-$.

Table 2

Equilibrium Potentials for Possible Electrode Reactions in Sodium Polysulfides

Reaction	Temp. (°C)	$-\Delta G_{rxn}$ (kcal/mole) (6,27,28)	E° vs Na/Na^+ (V)	E° vs "Na_2S_4"† (V)
$2Na + 5S \rightarrow Na_2S_5$	300 350	96.0 95.7	2.082 2.075	0.115 0.108
$Na_2S_2 + 2Na \rightarrow 2Na_2S$	300	72.3	1.568	-0.399
$2Na_2S_3 + 2Na \rightarrow 3Na_2S_2$	300	82.4	1.787	-0.180
$3Na_2S_4 + 2Na \rightarrow 4Na_2S_3$	300 350	90.4 89.8	1.960 1.947	-0.007 -0.005
$4Na_2S_5 + 2Na \rightarrow 5Na_2S_4$	300 350	95.0 94.6	2.060 2.051	+0.093 +0.100
$Na_2S_4 + 2Na \rightarrow 2Na_2S_2$	300	84.9	1.841	-0.126
$MoS_3 + 2Na \rightarrow MoS_2 + Na_2S$	300 350	89.87 89.57	1.949 1.942	-0.018 -0.010
$Mo_2S_3 + 6Na \rightarrow 2Mo + 3Na_2S$	300 350	151.48 149.72	1.095 1.082	-0.872 -0.870
$MoS_2 + 4\ Na \rightarrow Mo + 2Na_2S$	300 350	100.97 99.38	1.095 1.082	-0.872 -0.870
$Cr_2S_3{}^* + 2\ Na \rightarrow 2CrS + Na_2S$	350	47.6	1.03	-0.922
$Cr_2S_3{}^* + 6Na \rightarrow 2Cr + 3\ Na_2S$	350	126.4	0.913	-1.039
$CrS + 2\ Na \rightarrow Cr + Na_2S$	300 350	41.98 39.41	0.910 0.855	-1.057 -1.097

---

* ΔG_f estimated based on data of (28) and (29).

† Equivalent to 1.967V vs Na/Na^+.

When analyzing the data presented in the current-potential curves, it is important to recall that the data as presented are not completely IR corrected. The uncorrected resistance of the melt was estimated by plotting the current versus the potential at blocking layer formation (peak A in Figure 4) at various sweep rates. The slope of the resulting line gives an effective resistance for the melt, and the intercept is the potential associated with the formation of a blocking layer.

RESULTS

Molybdenum Electrodes in Sodium Polysulfides

In Figure 4, a typical run at 300°C is presented and shall serve as a base case for discussion of the study of this metal. When comparing the sweep in Figure 4 with those conducted at carbon electrodes (Figure 2), the most striking difference is the absence of a major peak on the anodic sweep for molybdenum. Experiments were conducted at many sweep rates up to the 1-amp current limit of the potentiostat (at up to 500 mV/sec), but no blocking of the electrode during anodic sweeps was evident under any condition. The most plausible explanation for this phenomenon lies in the difference in wetting properties between most metals and carbon by sulfur and polysulfides. The preferential wetting of metals by polysulfides has been observed by others during the inspection of sodium/sulfur cells which had been frozen and sectioned at various states of charge. Polysulfides were seen to collect near the β"-alumina electrolyte, and to a lesser but significant extent at the cell container wall (30). Experiments have also shown that stainless-steel electrodes formed sulfur blocking layers much less readily than carbon (5). If the sulfur formed near the molybdenum electrode during the anodic sweep was readily displaced by polysulfides, the oxidation of polysulfides to sulfur could continue uninterrupted to higher potentials than in the case of the carbon electrodes.

In contrast to the differences between molybdenum and carbon encountered on the anodic sweep, the cathodic data are strikingly similar for these two materials. A steady increase in cathodic current, followed by a sharp decrease near -400 mV (A) is seen, indicative of a blocking layer. A notable difference is the 'shoulder' (B). This feature was reproducible under a variety of experimental conditions, and it is discussed in detail below. The cathodic current remains essentially constant from about -600 mV to a potential of about -1.8 V, where it begins to rise due to production of liquid sodium (C). The return sweep is very similar to those for carbon electrodes up to about -225 mV, where a small anodic peak is seen before the dip in the curve (D) corresponding to the dissolution of the Na_2S_x blocking layer. As oxidation continues, a change in slope of the trace is evident near 200 mV (E), which may indicate that the dominant reaction product has shifted from higher polysulfides to molecular sulfur. The change in the sweep at F probably is related to the formation of liquid sulfur, but it does not significantly affect the rate of increase of anodic current.

Figure 5 shows the results of sweeps performed at higher rates. As expected, higher current values are observed at higher sweep rates. Besides the evidence of a small peak (C) between about -1700 mV and the formation of sodium (depending on sweep rate), which was not noticeable at lower sweep rates, a significant feature is the increase in the relative size of the 'shoulder' (B) with sweep rate. This result supports the idea that the 'shoulder' is indicative of continued reduction of polysulfides after the formation of the blocking layer. As the sweep rate is increased, the time that passes before the formation of the blocking layer (t_p) decreases significantly. If the layer-forming reaction is diffusion-limited, as the data of earlier researchers suggests (4), reducible species would be present in higher concentrations near the electrode if the blocking layer were formed more quickly. This would make more reducible species available for the continued formation of Na_2S_2 or Na_2S. The absence of an abrupt drop in current after the peak current raises the possibility that these curves are essentially those expected for diffusion-limited reactions, but distorted by the formation of a blocking layer. This hypothesis, however, defies modeling for even well-characterized systems with known reactants due to the complex interaction of diffusion and resistance control.

Since it is not known if the observed peak current is equal to the peak current of the reaction(s) associated with the first cathodic wave, use of the standard equations for cyclic voltammetry may not be justified. Using the arguments reported previously for voltammetry of lithium polysulfides (31), is reasonable to assume that a specific amount of material (equivalent to electrical charge) must be formed before precipitation of a solid phase can block the electrode. The amount of charge will be referred to as Q_∞. The total amount of charge passed up to $t = t_p$ (Q) should be equivalent to the sum of Q_∞ and any material consumed by a following chemical reaction, for example

$$Na_2S_2 + 2S_5^{=} \rightarrow 2Na^+ + 3S_4^{=} \qquad [4]$$

Such a reaction would also complicate the analysis of a diffusion-limited reaction, as it supplies species for further reduction at the electrode surface. By extrapolating the data to $t_p = 0$ (where a following chemical reaction could have no effect), an estimate of about 2.26 coulombs for Q_∞ for this system is obtained at 300°C. This corresponds to a 3.9-μm thick layer of Na_2S_2, if one assumes a density of 1.8 g/cm^3 and a roughness factor of 2, the latter probably being conservative. This seems rather thick for a blocking layer. The thickness is reduced to about 1.8 μm if the reduction product is assumed to be Na_2S. However, probably only a fraction of this amount represents solid, with the rest of the charge contributing to the formation of $S_2^{=}$ ion, which is very soluble in the melt.

Assuming that the dissolution reaction is first order with respect to the reduction product (Na_2S_x), it is possible to develop an expression for the dependence of the amount of material on the electrode versus time. The final expression is

$$Q_p - Q_\infty = \frac{I_p}{t_p k}\left[\frac{-e^{-kt_p}}{kt_p} + \frac{kt_p}{2} - 1 + \frac{1}{kt_p}\right] \qquad [5]$$

where I_p/t_p is the slope of the curve up to the formation of the blocking layer at a specific sweep rate (coulomb/sec^2), and k is the rate constant of the following chemical reaction (sec^{-1}). Details of the derivation of Equation [5] are reported elsewhere (19). The equation as presented contains terms for both t_p and I_p. In order to plot the results in a useful fashion, one of these must be eliminated. This is accomplished by determining the empirical relationship between I_p and t_p over a range of sweep rates, which was simplified by the fact that a log-log plot of these two variables forms a straight line. For molybdenum electrodes at 300°C, this expression is

$$I_p = 2.83\ t_p^{-.686} \qquad [6]$$

A plot of equation [5] for various values of k along with experimental data is shown in Figure 6, with a qualitative fit obtained for a range of reaction rates and a reasonably quantitative fit for k = 0.075 sec^{-1}. The largest discrepancies between the data and the model occur at long times, i.e. low sweep rates. This is not unexpected, since at long times, diffusion of reactants to the electrode surface could become a limiting step, and the model does not consider diffusion in the electrolyte.

As mentioned, the dissolution reaction supplies reducible species for the electrochemical reaction, and is hence autocatalytic. This case has been solved analytically by Nicholson and Shain (32), and the current function has been tabulated for various values of $kRT/nF\nu$. Assuming n = 2, for the case of molybdenum electrodes at 300°C, this parameter ranges from 0.0037 at ν = 500 mV/sec to 0.185 at ν = 10 mV/sec. The latter case represents about a 19% increase in I_p over that predicted for a simple diffusion-limited, reversible, electrochemical reaction, while at higher sweep rates, this value is essentially unchanged from this base case.

Conducting similar experiments on molybdenum at 350°C yields some interesting differences. Figure 7 shows an experiment using the same conditions as those in Figure 4, with the exception of higher temperature. A small hook in the curve can be seen at A, indicating a change in the rate of electrochemical reaction at the electrode. This probably represents a change in the dominant reaction occurring just before the blocking layer is formed. Also, the 'shoulder' evident at 300°C is replaced by a peak (B). The same explanations offered for the 'shoulder' apply here. Peak B occurs at too high a potential for the reduction of MoS_2, but a ternary sulfide or a molybdenum polysulfide could cause such a peak. The potential for the reduction of MoS_3 is close to the potential of this peak, although its existence in significant quantities would be surprising.

It is clear that the behavior of the melt at molybdenum is different than that observed at carbon, platinum, aluminum, and as will be shown, chromium. If continued reduction of polysulfides was the cause of the second peak (B), one would expect the same result for other materials if all of them were covered with an identical Na_2S_x phase. This indicates an interaction between the molybdenum electrode, which almost certainly is covered with a thin layer of MoS_2 at the beginning of each experiment, and the Na_2S_x layer formed. One possibility is that MoS_2 acts as a catalyst for the further reduction of Na_2S_2 to Na_2S by the overall reaction:

$$Na_2S_2 + 2e^- \rightarrow Na_2S + S^= \qquad [7]$$

Several metal sulfides, including MoS_2, have been shown to reduce the overpotential for the reduction of polysulfides in aqueous solution (33). The $S^=$ formed would have to react with a polysulfide in order to be incorporated into the melt, which could explain the diffusion-controlled shape of the curve.

Also of interest in Figure 7 is the small Peak C near -1450 mV, in a similar position to those occasionally observed on carbon electrodes by South (14). This peak was explained as the reduction of the Na_2S_2 to Na_2S, but it has not been observed by others. Reduction to Na_2S seems unlikely, however, since the potential of this peak is grossly inconsistent with the potential calculated for this reaction from thermodynamic data. The size of this peak relative to the first cathodic peak is much smaller than that observed by South. The reduction of the thin MoS_2 layer on the electrode is a possible explanation, although the potential of the peak is somewhat more cathodic than that predicted by thermodynamic calculations for the reduction of MoS_2 to molybdenum (-1340 mV vs -1080 mV calculated), which could be a result of kinetic limitations. Other than the expected increase in current and shift in peak potential, no significant changes were observed in the data at higher sweep rates. The experiments conducted at 350°C did not produce sufficient data at various sweep rates with other variables held constant to allow useful comparison with the model of Equation 5.

Chromium Electrodes in Sodium Polysulfides

A typical voltammogram for chromium in Na_2S_4 at 300°C is shown in Figure 8. The cathodic sweep shows a striking similarity to the data gathered at carbon electrodes (5,14). At the formation of the blocking layer (A), the current decrease is quite sudden and uncomplicated by other peaks in contrast to molybdenum. Reduction to sodium (C) is evident near -1.85 V, and a peak (D), albeit small, is observed near -250 mV, which is consistent with the dissolution of the blocking layer. The anodic sweep, on the other hand, is very much like those seen with molybdenum electrodes. Again, no blocking layer is evident up to 800 mV. The turnaround voltage of the anodic sweep was extended as far as the one-ampere limitation of the potentiostat would allow, and no peak due to the blocking of the electrode with elemental sulfur was seen. The small deviation from linearity in the curve (E) is present, as it was for molybdenum. As for molybdenum, it is possible that this represents the point at which sulfur is formed, but preferential wetting of the electrodes by the polysulfides allows oxidation to continue practically undisturbed.

Reversing the sweep just after the formation of the blocking layer eliminated the dissolution peak (D, Figure 8). A possible explanation is that the dissolution of Na_2S_2 is slow compared with that of Na_2S. Behavior of the sweeps in this potential range for experiments at 350°C is relatively insensitive to sweep rate, so the smaller turnaround voltage, which prevents further reduction of the blocking layer, seems to be responsible for this change.

Further support of this idea is given by Figure 9, which shows an experiment run at 20 mV/sec and 350°C. The curve does not show a significantly increased cathodic current due to sudden exposure of the electrode to a reducing environment in the expected potential range (D). Extending the cathodic sweep (Figure 10), however, shows a marked change in this section of the curve. Therefore, the nature of reactions occurring in this potential range is affected by the turnaround voltage of the experiment. This suggests that the structure of the blocking layer is not constant up to the formation of sodium, and that the reactions associated with these changes are not completely reversible.

Also in Figure 9, a temperature effect on the anodic sweep is evident. The current becomes unsteady beyond about 350 mV, which is different than the data for 300°C (Figure 8). The trace recalls the unsteady behavior of the current observed in the anodic region of experiments on carbon (Figure 2). Possibly the wetting characteristics of the electrode by sulfur are nearer to those of polysulfides at 350°C, and sulfur is not displaced by polysulfides as readily here as at 300°C or for molybdenum electrodes. Also, the reduction of cathodic current at blocking (A) is not as sudden at 350°C as it was at 300°C, possibly due to an increased reaction rate for the reduction of Na_2S_2 to Na_2S.

Returning to Figure 10, the most remarkable feature of the data gathered on chromium is the peak near -1250 mV (C), which is very large compared to the similar peak observed on molybdenum, and the appearance of a peak on the return sweep near -700 mV (D). This latter peak is unique to the chromium studies. Peaks C and D were observed for all sweep rates at 350°C, regardless of the initial direction of the sweep. These peaks were not evident at 300°C, however, unless the initial sweep direction was anodic, and then, not for all runs. This could possibly be the result of additional scale being formed during an anodic sweep.

The most obvious explanation of these peaks is that the sulfide scale on the electrode is being reduced at C and reformed at D. The broad separation of the two peaks (~320 mV after correcting for the IR drop of the melt) suggests a high degree of irreversibility, however, as a completely reversible reaction would occur at nearly the same potential irrespective of sweep direction (32). Consulting Table 2, a plausible reaction corresponding to the potential of peak D is the oxidation of chromium to Cr_2S_3. Although we are unable to postulate a candidate reaction to explain the location of peak C, it is almost certainly a reduction reaction involving the scale, with metallic Cr as a likely reaction product. Limited thermodynamic data for $NaCrS_2$ indicate that it is probably not stable below the potential corresponding to the formation of Na_2S_2, although this finding is questionable, since $NaCrS_2$ has only been observed for corrosion of chromium in Na_2S_4 and lower polysulfides (15). This fact, coupled with the +3 oxidation state for chromium in this compound, probably means that its reduction potential in sodium polysulfides is near to that of Cr_2S_3. Therefore, a possible explanation for peak C is that the reduction of the sulfide layer is blocked kinetically until some intermediate reaction can take place, possibly in the blocking layer. The separation of the peaks might then be the result of a difference in reaction path for the forward and reverse reaction.

Further evidence for a difference in reaction path was obtained using experiments which allowed more detailed examination of these peaks. The data from the first of these is shown in Figure 11a. Extending the sweep to -1750 mV has a dramatic effect on the size and shape of peak D. The flattened top of the peak suggests two overlapping reactions, possibly representing the sulfidation of chromium to Cr_2S_3 and a reaction within the Na_2S_x layer which is made possible by the former reaction. The dual nature of this peak was confirmed by holding the sweep at a potential slightly anodic of peak C (Figure 11b), which suggests that the two peaks represent competing reactions. The relative importance of the reactions seemed to depend on the phases present in the system during the return sweep.

Analyses of the first cathodic peak using Equation [5] were made to support further the arguments given above concerning the significance of t_p. After determining the dependence of I_p on t_p at various sweep rates, plots like Figure 6 were calculated for chromium electrodes at 300 and 350°C. Two plots were made from data obtained in two different cells at 350°C. The best fit for the data at 300°C yields a k of about 0.1 sec^{-1}, slightly higher than the value obtained with a molybdenum electrode at the same temperature, but within experimental error. This result may indicate that the composition of the layers formed on the two electrodes is fairly similar. The rate constants estimated for the experiments at 350°C are in good agreement, and are, on the average, somewhat higher (about 0.17 sec^{-1}) than those found at 300°C. These values are about one order of magnitude lower than the rate constants observed for the dissolution of Li_2S formed during cathodic cycling of these electrodes in lithium polysulfides at 400°C (31), indicating that the Na_2S_x blocking layer is considerably more stable.

The values obtained for Q_∞ for the different experiments ranged from 1.58 to 3.2 coulombs, probably as a result of changes in roughness of the electrodes, which were expected to change dramatically due to the repeated formation and reduction of metal sulfides on the surface. The variation between experiments was probably most strongly affected by the total number of sweeps performed at the electrode or the total time at temperature or both.

Additional data gathered using both electrode materials are available (19).

CONCLUSIONS

The reactions occurring in sodium polysulfides at chromium and molybdenum electrodes during voltammetry show many similarities, but important differences do exist. While more experiments would be necessary to understand these completely, the conclusions which seem reasonable from the data given above include:

1. The initial cathodic peak for both metals represents a diffusion-limited charge-transfer reaction followed by an autocatalytic chemical dissolution reaction.

2. The peak indicates interruption of the above reaction due to the formation of a solid blocking layer, which causes a considerable increase in the resistance at the electrode surface.

3. The blocking layer probably consists of mostly Na_2S_2 with possibly some Na_2S.

4. Both metals show peaks which represent the reduction of the sulfide layer on them at 350°C at a potential more than 1 volt cathodic of the rest potential. In addition, chromium shows a prominent peak which represents the reestablishment of this layer near 750 mV cathodic of the rest potential.

5. Neither metal shows evidence of a stable blocking layer during sweeps anodic of the rest potential, probably because of the preferential wetting of the electrodes by polysulfides, which could prevent the establishment of an effective blocking layer. This behavior is in marked contrast to that observed on carbon.

REFERENCES

1. Wicker, A., Corrosion of Chromium-Coated Steel in Sodium Polysulfide Environments," EPRI Report #EM-2947 (March 1983).

2. Hartmann, B., J. Power Sources 3, 227 (1978).

3. Levine, C.A., "Sodium-Sulfur Cells with Glass Electrolytes," from The Sulfur Electrode, Tischer, R.P., ed., pp. 327-338, Academic Press (1983).

4. Aikens, D.H., "The Sulfur Electrode in Molten Polysulfide and Thiocyanate Melts", from The Sulfur Electrode, Tischer, R.P., ed., pp. 151-190, Academic Press (1983).

5. Ludwig, F.A. and Tischer, R.P., "The Sulfur Electrode in Non-Aqueous Media", from Advances in Electrochemistry and Electrochemical Engineering, Vol. 10, C.W. Tobias and H. Gerischer, eds., Wiley Interscience (1977).

6. Gupta, N.K. and Tischer, R.P., J. Electrochem. Soc. 119, 1033 (1972).

7. Cleaver, B. and Davies, A.J., Electrochim. Acta 18, 733 (1973).

8. Oei, D.G., Inorg. Chem. 12, 438 (1973).

9. Janz, G.J., et. al., ibid. 15, 1751 (1976).

10. Cleaver, B., Davies, A.J. and Hames, M.D., Electrochim. Acta 18, 719 (1973).

11. Cleaver, B. and Davies, A.J., ibid. 18, 727 (1973).

12. Selis, S.M., ibid. 15, 1285 (1970).

13. "Research on Electrodes and Electrolyte for the Ford Sodium-Sulfur Battery. Annual Report for the Period June 30, 1973 to June 29, 1974," NSF Contract #NSF C-805 (AER-73-07199) (July, 1974).

14. South, K.D., Sudworth, J.L. and Gibson, J.G., J. Electrochem. Soc. 119, 554 (1972).

15. Armstrong, R.D., et. al., Electrochim. Acta 21, 935 (1976).

16. Knoedler, R. and Mennicke, S., ibid. 28, 1033 (1983).

17. MacKnight, W.J. and Tobolsky, A.V., "Properties of Polymeric Sulfur", from Elemental Sulfur, B. Meyer, ed., Interscience (1965).

18. Polcyn, D.S. and Shain, I., Anal. Chem. 38, 370 (1966).

19. Dobson, J.C., McLarnon, F.R. and Cairns, E.J., "Behavior of Metals in Sulfur/Polysulfide Melts," Lawrence Berkeley Laboratory Report No. LBL-19518 (August 1985).

20. Argonne National Laboratory, Chemical Engineering Division, Annual Report - 1970, ANL-7675 (1971).

21. Battles, J.E. and Brown, A.P., Polysulfide Containment Materials, Annual Report, January-December, 1984, Chemical Technology Division, Argonne National Laboratory (1985).

22. Park, D.S. and Chatterji, D., Thin Solid Films 83, 429 (1981).

23. Kinsman, K.R. and Winterbottom, W.L., ibid., 417 (1981).

24. Dubin, R.P., Materials Performance 20, 13 (1981).

25. Kinsman, K.R. and Oei, D-G., Extended Abstracts, Vol. 77-2, Electrochemical Society, Abstract No. 57 (1977).

26. Bailey, R.A. and Skeaff, J.M., J. Chem. Eng. Data 24, 126 (1979).

27. Barin, I. and Knacke, O., Thermochemical Properties of Inorganic Substances, Springer-Verlag (1973).

28. Barin, I. and Knacke, O., Thermochemical Properties of Inorganic Substances: Supplement, Springer-Verlag (1977).

29. Young, D.J., et. al., J. Electrochem. Soc. 120, 1221 (1973).

30. Smaga, J.A., et. al., Extended Abstracts, Electrochemical Society, 166th Meeting, Vol. 84-2, Abstract No. 108 (1984).

31. Dobson, J.C., Cairns, E.J. and McLarnon, F.R., "Voltammetry of Lithium Polysulfides at Metal Electrodes," Lawrence Berkeley Laboratory Report No. LBL-20248. Submitted to J. Electrochem. Soc. (1985).

32. Nicholson, R.S. and Shain, I., Anal. Chem. 36, 706 (1964).

33. Remick, R.J. and Camara, E.H., "Electrochemistry of the Sulfide/Polysulfide Couple", Institute of Gas Technology, Lawrence Berkeley Laboratory Report No. LBL- 16850 (July 1983).

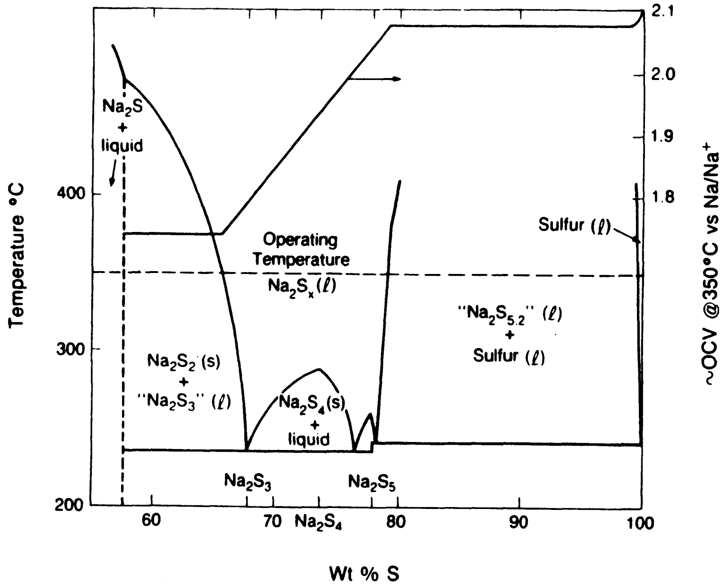

Figure 1. Partial Na-S Phase Diagram (6).

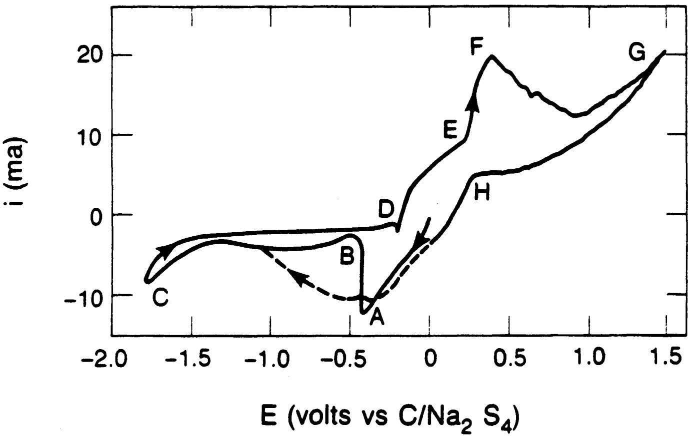

Figure 2. Typical current-potential curve obtained by voltammetry of $Na_2S_{4.0}$ at 340°C at carbon electrodes. (based on 5) Electrode area = 0.00407 cm^2

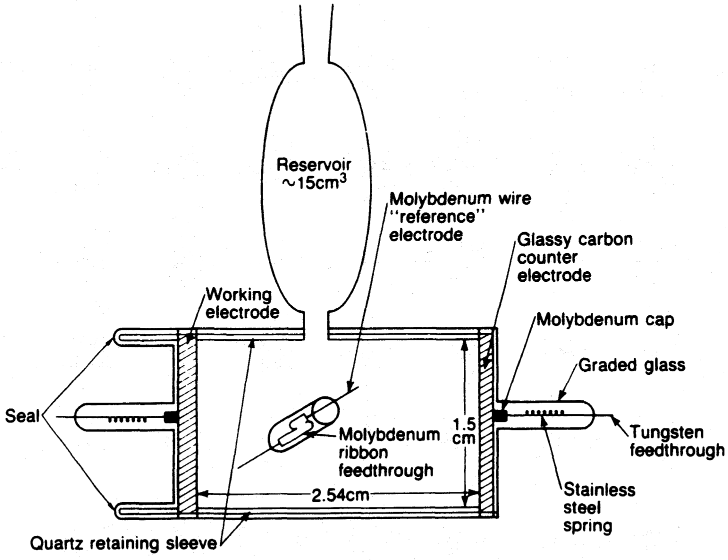

Figure 3. Experimental apparatus for voltammetry experiments.

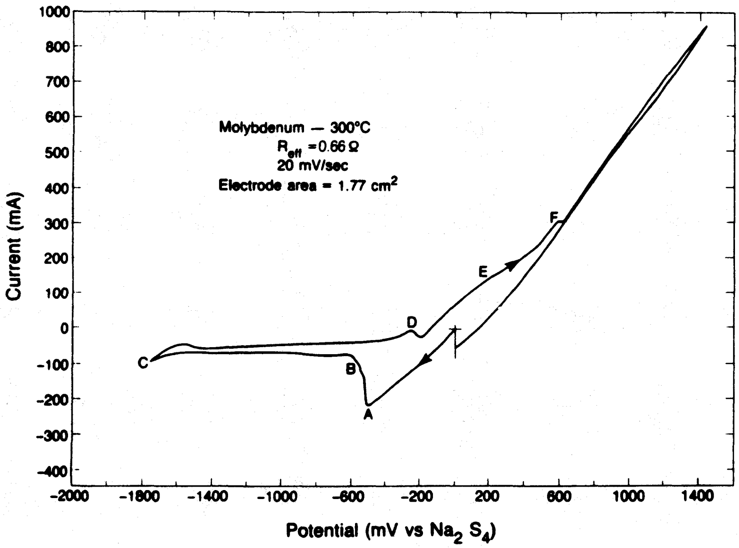

Figure 4. Current-potential data for conditions indicated.

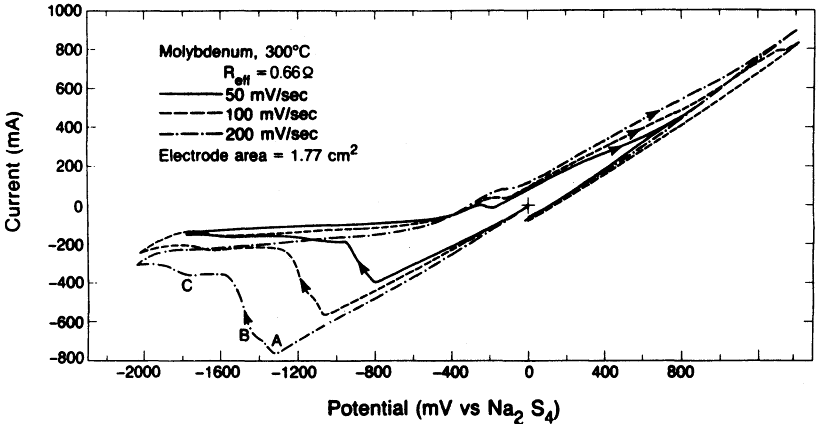

Figure 5. Current-potential data for conditions indicated.

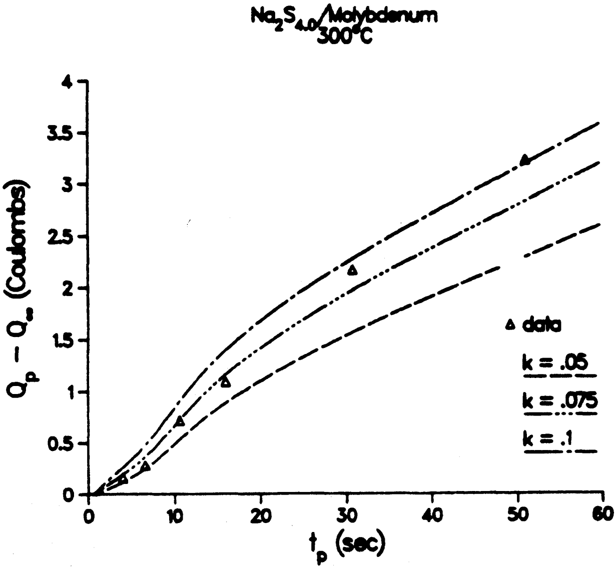

Figure 6. Plot of model for various rate constants for conditions indicated.

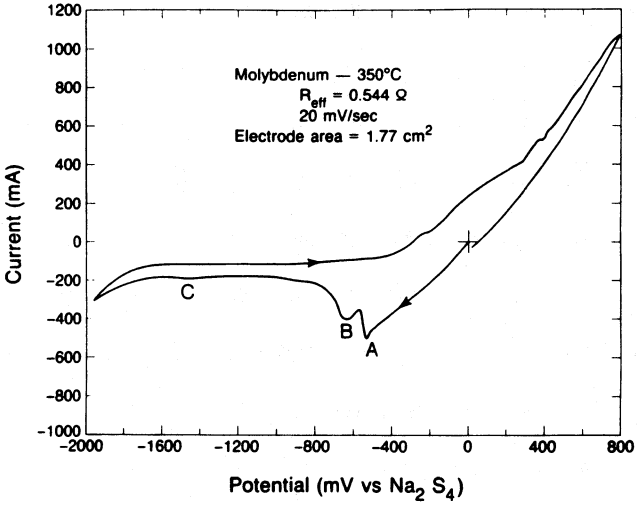

Figure 7. Current-potential data for conditions indicated.

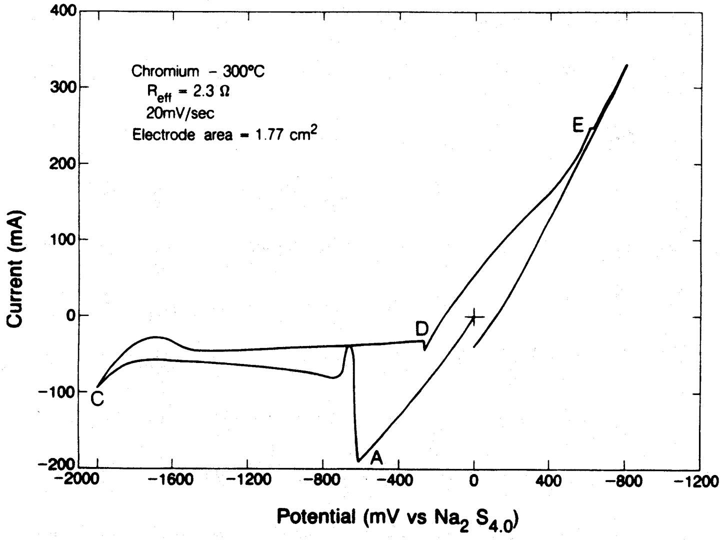

Figure 8. Current-potential data for conditions indicated.

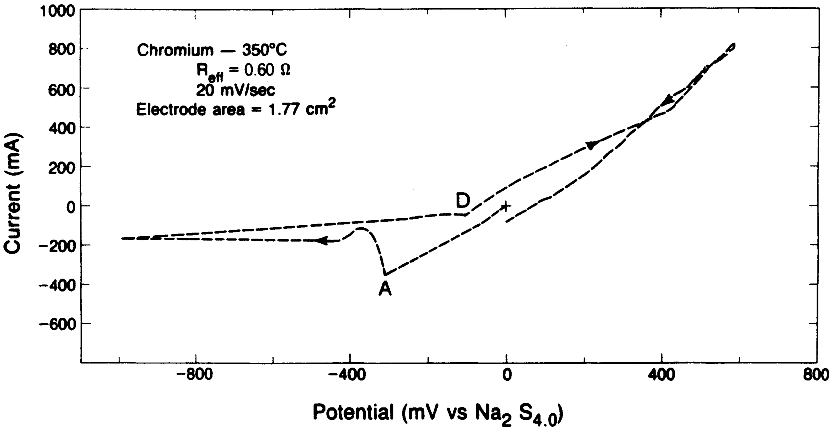

Figure 9. Current-potential data for conditions indicated.

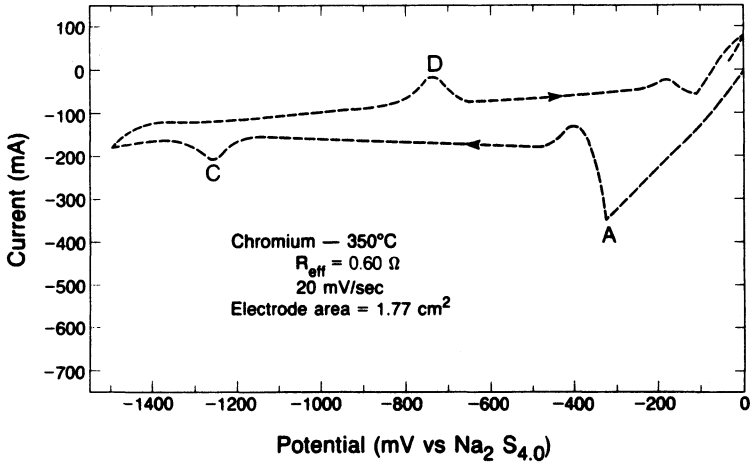

Figure 10. Current-potential data for conditions indicated.

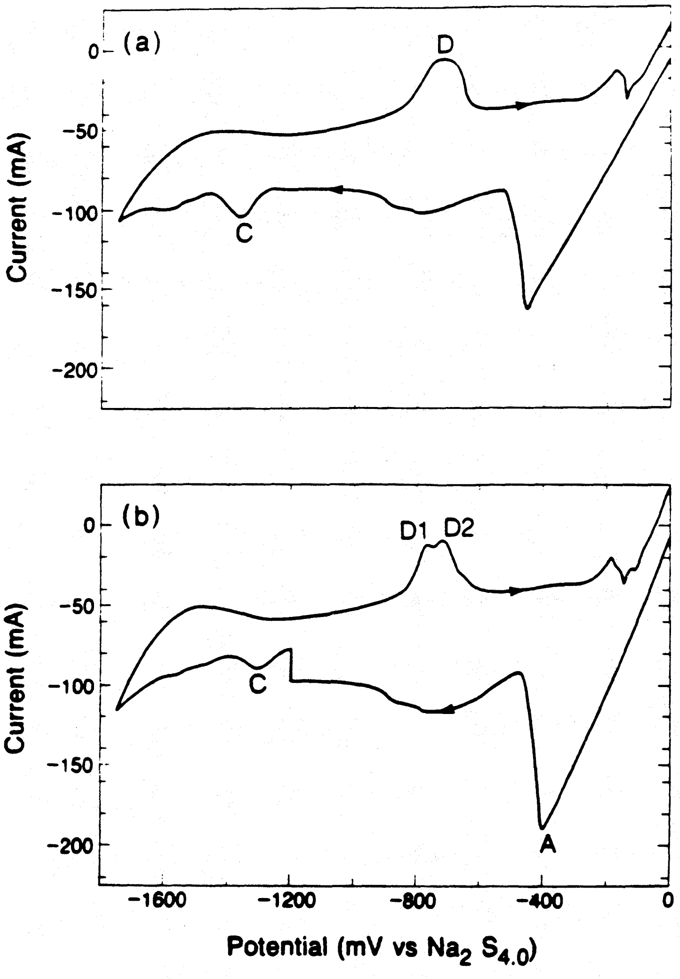

Figure 11. Sweep at chromium electrode at 10 mV/sec at 350°C.
(a) Continuous sweep.
(b) Holding time at -1250 mV was 30 seconds.

DOI: 10.1149/198601.0189PV

ACIDIC AND REDOX PROPERTIES OF SOME LANTHANIDE IONS IN MOLTEN LiCl-KCl EUTECTIC

G.S. Picard, Y.E. Mottot and B.L. Trémillon
Laboratoire d'Electrochimie Analytique et Appliquée
associé au CNRS (UA 216)
Ecole Nationale Supérieure de Chimie de Paris
11 rue P. et M. Curie - 75231 PARIS Cedex 05 - FRANCE

ABSTRACT

We have studied the stability of some lanthanide(III) oxychlorides and oxides, especially those of the ceric group, in molten LiCl-KCl eutectic. Solubility products of oxychlorides and oxides have been deduced from the potentiometric titration curves of lanthanide chlorides by sodium carbonate. These values, combined with standard potentials of the Ln(III)/Ln(s) electrochemical systems determined from potentiometric and voltammetric measurements, have enabled us to establish potential-pO^{2-} diagrams which summarize the properties of the lanthanide oxy-compounds. The possibilities of solubilizing lanthanide(III) oxychlorides and oxides by using gaseous reagents are discussed.

INTRODUCTION

The two main limiting factors for obtaining high efficiency in the electrowinning of metals from their chlorides are the presence of impurities and the metal solubility in the electrolyte.

In this paper, only the first case has been taken into consideration, the second will be the subject of another paper. The major impurities are water, hydroxide and oxide anions, which can lead to the formation of metal oxychlorides and oxides (1). As a result, the physical properties of the electrolytic bath (viscosity, density,.) change and the electrolysis yield often decreases.

So it is of primary importance for the electrowinning of lanthanide metals to study the lanthanide(III) oxychloride and oxide stabilities. The oxoacidic behavior (acceptor power towards O^{2-} ion) of cerium(III) and yttrium(III) ions had been shown respectively in NaCl-KCl at 1000 K (2) and in NaCl at 1100 K (3), but no systematic study had been achieved previously.

We present here a study of the chemical and electrochemical stabilities of some lanthanide chlorides, oxychlorides and oxides, especially those of the ceric group, in molten LiCl-KCl eutectic.

EXPERIMENTAL RESULTS AND INTERPRETATION

- Technical.

The cell, the furnace, the programmable regulation and the preparation of the melt have already been described (4-7).

Potentials were measured by means of a reference electrode (Ag/Ag^+ 0.75 $mol.kg^{-1}$). All the values are given vs. the standard chlorine electrode.

The values of pO^{2-} were deduced from potential measurements with an yttria-stabilized zirconia electrode, which has been shown to behave properly in the melt used. The description and the standardization procedure of this electrode were described earlier (4,8,9).

The voltammetric scans were performed with a Tacussel "PRT 30" fast-rise potentiostat coupled with a GSTP 3 function generator.

The i(E) curves were recorded on a XY Sefram TRP 10-100. The indicator electrode used was made from 0.5 mm diam. tungsten rod supplied by Johnson Matthey.

X-ray diffraction patterns were obtained with a C.G.R. diffractometer employing $CoK\alpha_1$ radiation.

- Potentiometric titrations of Ln(III) by oxide ions.

Potentiometric titrations of Ln^{3+} were performed by addition of sodium carbonate, at 723 K. Fig. 1 gives the experimental curves obtained under low carbon dioxide pressures ($10^{-3} < P(CO_2)/atm < 10^{-2}$). During these titrations, the variations of the oxide ion activity present only one equivalence point for α (mole number of CO_3^{2-} added per mole of total Ln(III)) equal to 1 for ceric lanthanides, and to 1.5 for yttrium. From that observation, we deduce that the titration reaction is the following :

$$Ln^{3+} + CO_3^{2-} + Cl^- \rightarrow LnOCl(s) + CO_2(g)$$

except in the case of yttrium for which insoluble oxide is directly obtained according to the reaction :

$$2\ Ln^{3+} + 3\ CO_3^{2-} \rightarrow Ln_2O_3(s) + 3\ CO_2(g)$$

The precipitates obtained at the end of the titrations are colored as follows: white for lanthanum and cerium oxychlorides, pale-green for praseodymium oxychloride, grey-blue for neodymium oxychloride and white for yttrium oxide.

The conclusion from the titration curves has been confirmed by X-ray diffraction patterns of the recovered precipitates. In particular, no trace of oxide was visible on patterns for the oxychlorides.

- Electrochemical study.

The redox properties of ceric lanthanides were characterized by the joint use of several electrochemical techniques : potentiometry, (cyclic) voltammetry, chronoamperometry and current reversal chronopotentiometry (10). Only a part of this work is presented here.

- La^{3+}, Ce^{3+} and Pr^{3+} reduction :

Fig. 2-a shows the typical voltammograms for the reduction of lanthanum(III), cerium(III) and praseodymium(III), corrected for residual current and obtained from experiments carried out with a tungsten electrode (area A) [potential sweep rate = 0.2 $V.s^{-1}$]. These voltammograms present only one reduction peak, with a sharp variation of the current which can be interpreted as due to the formation of a metal deposit, according to the reaction :

$$Ln^{3+} + 3e^- \rightarrow Ln(s)$$

This is confirmed by the reoxidation peaks observed in cyclic voltammetry experiments (10). The reaction reversibility can be appreciated by semi-integral electroanalysis. Fig. 2-a shows the neopolarograms m(E) (11) which were deduced from the voltammograms by current semi-integration (12-15). The m(E) curves so obtained have been analysed by plotting the cologarithm of (m_∞-m) as a function of potential (m_∞ = maximum or limiting value of m). Fig. 2-b shows linear variations, the slopes of the straight lines being very close to the theoretical value for a reversible process. The numbers of faradays per mole of lanthanide (III) ion deduced from the experimental slopes are : 2,9 for lanthanum and cerium, and 3.0 for praseodymium. The voltammogram corresponding to the latter shows that the metal activity is equal to unity from the very beginning of the deposit. The diffusion coefficient values have been calculated from the limiting values m_∞ of the reduction waves m(E), given by the relation :

$$m_\infty = nFAD^{1/2}|Ln^{3+}|$$

We obtained from the experiments reported in Fig. 2 : $7.2.10^{-6}$, $5.8.10^{-6}$ and $6.8.10^{-6}$ $cm^2.s^{-1}$ respectively for $D(La^{3+})$, $D(Ce^{3+})$ and $D(Pr^{3+})$.

The standard potentials have been determined from the half-wave potentials on the m(E) curves by using the classical relations (16). The values obtained in the case of the experiments reported here are : -3.160 V, -3.155 V and -3.150 V for $E°(La^{3+}/La(s))$, $E°(Ce^{3+}/Ce(s))$ and $E°(Pr^{3+}/Pr(s))$. These values agree very well with those determined by potentiometry and other electrochemical techniques (10), given as a function of temperature in Table 1.

- Nd^{3+} reduction :

Fig. 3-a shows that Nd^{3+} is reduced into metal by a two-step process, differing from the one involved with the other lanthanides(III), and which has been also studied by semi-integral analysis. The neopolarogram of Fig. 3-a exhibits two waves whose relative heights do not vary with the potential sweep rate signifying that the first wave is not due to an adsorption process. So, we have to consider the existence of an intermediate oxidation state which probably corresponds to one of the neodymium sub-chlorides $NdCl_{2.37}$, $NdCl_{2.27}$ or $NdCl_2$ characterized by Druding and Corbett (17).

According to the value of the ratio of the limiting values $m_{1\infty}$ and $m_{2\infty}$, the two steps of Nd(III) reduction would be :

$$Nd^{3+} + e^- \rightarrow Nd^{2+}$$

followed by :

$$Nd^{2+} + 2e^- \rightarrow Nd\,(s)$$

This is confirmed by the logarithmic analysis of the neopolarogram (Fig. 3-b) according to the equation :

$$E_1 = E^1_{1/2} + \frac{RT}{F} \ln \left[(m_{1\infty} - m)/m\right]$$

with :

$$E^1_{1/2} = E^\circ(Nd^{3+}/Nd^{2+}) + \frac{RT}{2F} \ln \frac{D(Nd^{3+})}{D(Nd^{2+})}$$

and :

$$E_2 = E^2_{1/2} + 0.5\ RT.F^{-1} \ln\left[m_{2\infty} - m\right]$$

with :

$$E^2_{1/2} = E^\circ\left(Nd^{2+}/Nd(s)\right) + 0.5\ RT.F^{-1} \ln\left[|Nd^{2+}|/2\right]$$

The experiments relative to the curves of Fig. 3 have led to the diffusion coefficient and the standard potential values :

$D(Nd^{3+}) = 9.7.10^{-6} cm^2.s^{-1}$; $E^\circ(Nd^{3+}/Nd^{2+}) = -3.102$ V

and : $E^\circ(Nd^{2+}/Nd(s)) = -3.123$ V

Besides by using the relation :

$$E^\circ(Nd^{3+}/Nd(s)) = \frac{1}{3}\left[E^\circ(Nd^{3+}/Nd^{2+}) + 2\,E^\circ(Nd^{2+}/Nd(s))\right]$$

We obtained :

$$E^\circ(Nd^{3+}/Nd(s)) = -3.116 \text{ V}$$

By experiments at various temperatures (10) we have determined the temperature-dependence of the standard potentials of the neodymium systems (table 1). The proximity of the values of the standard potentials relative to the two steps of the Nd(III) reduction is responsible for a noticeable solubility of the metal in the neodymium(III) chloride solutions according to the equilibrium :

$$Nd(s) + 2\,Nd^{3+} \rightleftarrows 3\,Nd^{2+}$$

The constant of this equilibrium can be easily deduced from the standard potentials :

$$\log\left[K/mol.kg^{-1}\right] = 2.51 - 1575\ T^{-1}$$

in the temperature range from 650 to 850 K.

EXPLOITATION OF THE RESULTS

- Solubility products of lanthanide(III) oxychlorides and oxides.

• Values deduced from the experimental titration curves. The lanthanide(III) oxychlorides and oxides can be dissolved into the melt according to the following equilibria :

$$LnOCl(s) \rightleftarrows Ln^{3+} + O^{2-} + Cl^-$$

and :

$$Ln_2O_3(s) \rightleftarrows 2\ Ln^{3+} + 3\ O^{2-}$$

The solubility products are given by:

$$Ks(LnOCl) = |Ln^{3+}|\,|O^{2-}|$$

and :

$$Ks(Ln_2O_3) = |Ln^{3+}|^2\,|O^{2-}|^3$$

As in the case of a previous work concerning aluminum (4), we have employed a simulation method for determining the values of the solubility products. The functions $\alpha = f(pO^{2-})$ deduced from the equations of mass balance and mass action law are the following :

$$\alpha = 1 + Co^{-1}\left\{ |O^{2-}|\left[P(CO_2).K_D^{-1} + 1\right] - Ks(LnOCl).\ |O^{2-}|^{-1}\right\} \qquad (1)$$

For yttrium :

$$\alpha = 1.5 + Co^{-1}\left\{ |O^{2-}|\left[P(CO_2).K_D^{-1} + 1\right] - 1.5\ \left[Ks(Y_2O_3)\,|O^{2-}|^{-3}\right]^{1/2}\right\} (2)$$

In these expressions, K_D is the dissociation constant of CO_3^{2-} ($K_D = P(CO_2).|O^{2-}|.|CO_3^{2-}|^{-1} = 10^{-2.15}$atm) previously determined (4).

Titration curves have been simulated from eq(1) and eq(2) by giving arbitrary values to the constants Ks. The simulated curves which best fit the experimental points are represented on Fig.1. The corresponding values for Ks(LnOCl) and $Ks(Y_2O_3)$ and the solubilities S are given in Table 2.

- Values deduced from the experimental standard potentials and from the literature thermochemical data. The equilibrium constants like the solubility products of metallic oxychlorides and oxides can be often calculated from the free energies of reactions between pure compounds, the activity coefficients of the metallic ions and oxide anion, and the activities of the components of the melt. Examples of this method of calculation can be found in the literature (18-21). We have obtained the solubility products by using (i) the activity coefficients of Ln^{3+} (collected in Table 3) derived from the standard potentials of Table 1 and from the formation free energies of pure lanthanide(III)chlorides (calculated from the literature data (22)), (ii) the activity coefficient of oxide ion determined according to the method indicated by Séon (1) and given by the relation :

$$\log \gamma\ (O^{2-}) = 1.27 - 4650\ T^{-1},$$

(iii) the activity of LiCl in the eutectic (23), and at last (iv) the free energies of the reactions of formation of solid oxychlorides(*) and oxides from pure metallic chlorides and lithium oxide (22,24-28). Their values are given as a function of temperature in Table 4.

- Comparison between the values deduced from titration curve analysis (Table 2) and those calculated from thermodynamical data (Table 4) shows slight differences. This fact can be explained

---

(*) The temperature dependence of the heat capacities Cp(CeOCl) and Cp(PrOCl) has been estimated from data concerning the lanthanum and neodymium oxychlorides (22) by noticing that the values obtained with the second method strongly depend on the accuracy of the thermochemical data. Yet, this method of calculation leads to pretty good predicted values: the shifts observed between them and those directly obtained from experiments are of about 5% for LaOCl, 10% for NdOCl and 14 and 20% respectively for CeOCl and PrOCl. The estimated value of $pK_s(Y_2O_3)$ presents a shift of around 15% from the experimental value.

CONCLUSION

The stabilities of the oxychlorides and oxides lead to a modification of the redox properties of lanthanides. This can be summarized under the form of potential-(oxo)acidity diagrams. The diagrams in Fig. 4 show the large stability domain of each oxychloride, so that it is impossible to envisage a selective precipitation or a selective chlorination of the lanthanide(III)oxychlorides.

The possibilities of solubilizing lanthanide(III) oxychlorides and oxides by using gaseous reagents, whose chlorinating powers were previously studied (9,29,30), have been examinated. Only results with the gaseous HCl + H_2O and Cl_2 + O_2 mixtures, of an obvious interest for melt purification and lanthanide metals electrowinning, are given here. Diagrams of Fig. 5 have been established with the aid of the solubility products and in the case of the log P(HCl)-log P(H_2O) diagrams, the constant K_1 of the equilibrium :

$$2\ HCl(g) + O^{2-} \rightleftarrows H_2O(g) + 2\ Cl^-$$

is given as a function of temperature by the expression (9,29,30):

$$\log K_1 = -3.477 + 9.98.10^{-3}\ T^{-1}$$

In the case of the log P(Cl_2) - log P(O_2) diagrams, the constant K_2 of the equilibrium:

$$Cl_2(g) + O^{2-} \rightleftarrows \frac{1}{2} O_2(g) + 2Cl^-$$

has a known value of (9,29,30) :

$$\log K_2 = -0.027 + 6.91_2.10^{-3}\,T^{-1}$$

From Fig. 5 one can note that it is possible to dissolve the oxychlorides with hydrogen chloride containing up to 80% (mol. per cent.) of water. This fact confirms the efficiency of the purification technique used for the solutions of lanthanide(III) chlorides in the melt. Fig. 5 also shows that chlorine can easily chlorinate the oxychlorides because the reaction :

$$Cl_2(g) + LnOCl(s) \rightleftarrows Ln^{3+} + \frac{1}{2} O_2(g) + Cl^-$$

takes place even when Cl_2 + O_2 gaseous mixtures are very rich in oxygen, up to 75 mol.% (value calculated for a total concentration of Ln(III) of approximately 1 mol.kg^{-1}, i.e 20 w%, currently used in classical electrolytic baths).

As final conclusions, we saw that the determination of standard potentials and solubility products has led to interesting forecasts concerning the electrowinning of the lanthanide metals in molten LiCl-KCl eutectic. In particular, because the reduction potentials of the ceric lanthanide(III) chlorides are very close to each other and because alloys form (didymium for example), a selective electrolytic extractive method could not be envisaged. Besides, neodymium appeared to have a singular behavior among the ceric lanthanides because of the existence of the intermediate (+II) oxidation state which is responsible for the solubility of a part of the deposited metal, thus complicating the electrowinning of this metal. At last, the ceric lanthanide(III) oxychlorides have appeared not very stable, hence the evolution of chlorine at the anode, in an electrolytic process in molten chlorides, can certainly lead to a "self-purification" of the melted bath.

ACKNOWLEDGMENTS

This work was supported by the French Ministry of Industry and Research (Contract n° 83.F.1273). The authors thank F. Séon and J. Grosbois (Rhône-Poulenc S.A.) for their advice and their contribution to this work. Y.E. Mottot thanks R.P.S.A. for a doctoral grant.

REFERENCES

1. F. Séon, Thesis (Doctorat d'Etat), Paris, France (1981).
2. R. Combes, M.N. Levelut and B. Trémillon, J. Electroanal. Chem., 91, 125 (1978).
3. M.L. Deanhardt and K.H. Stern, J. Electrochem. Soc., 129, 2228 (1982).
4. G. Picard, F. Séon and B. Trémillon, J. Electroanal. Chem., 102, 65 (1979).
5. G. Picard, F. Séon, B. Trémillon and Y. Bertaud, Electrochim. Acta, 25, 1453 (1980).
6. G. Picard, F. Séon and Y. Bertaud, Electrochim. Acta, 27, 401 (1982).
7. F. Séon, G. Picard and B. Trémillon, J. Electroanal. Chem., 138 315 (1982).
8. B. Trémillon and G. Picard, Proc. 1st Intern. Symp. on Molten Salt Chemistry and Technology, Y. Ito (Ed), Kyoto, april 1983, p. 93.
9. B. Trémillon and G. Picard, Rare Metals, 2, 19 (1985).
10. Y. Mottot, Thesis (Doctorat d'Etat), Paris, France, 1985.
11. M. Goto and K.B. Oldham, Anal. Chem., 45, 2043 (1973) ; 48, 1671 (1976).

12. K.B. Oldham, Anal. Chem. 41, 1904 (1969) ; 44, 196 (1972).

13. C.P. Andrieux, L. Nadjo and J.M. Saveant, J. Electroanal.chem. 26, 147 (1970).

14. J.C. Imbeaux and J.M. Saveant, J. Electroanal. Chem., 44, 169 (1973).

15. F. Séon, G. Picard and B. Trémillon, Electrochim. Acta, 27, 1357 (1982).

16. A.J. Bard and L.R. Faulkner, "Electrochemical methods, Fundamentals and Applications", John Wiley & Sons, N.Y. 1980.

17. L.F. Druding and J.D. Corbett, J. Am. Chem. Soc., 83, 2462(1961).

18. G. Picard and J. Vedel, J. Chim. Phys., 6, 767 (1975).

19. B. Trémillon and G. Picard, Anal. Chim. Acta, 82, 273 (1976).

20. G. Picard, F. Séon and B. Trémillon, J. Electrochem. Soc., 129, 1450 (1982).

21. M.L. Saboungi, J.J. Marr and M. Blander, J. Electrochem. Soc., 125, 1567 (1978) ; Metall. Trans. B., 10B, 477 (1979).

22. I. Barin and O. Knacke, "Thermochemical Properties of Inorganic Substances", Springer Verlag, Berlin, Heidelberg, New-York (1973).

23. J. Lumsden, "Thermodynamics of Molten Salt Mixtures", Academic Press, London and New-York, 1966. Chap. 4.

24. V.P. Gilybin and R.B. Dobrotin, Russ. J. Phys. Chem., 45, 898 (1971).

25. C.W. Koch, A. Broido and B.B. Cunningham, J. Am. Chem. Soc., 74, 2349 (1952).

26. C.W. Koch and B.B. Cunningham, J. Am. Chem. Soc, 76, 1471 (1954).

27. A.K. Baev and G.I. Novikov, Russ. J. Inorg. Chem., 11, 1337 (1965).

28. R.H. Schumm, "Selected values of chemical thermodynamic properties", National Bureau of Standards, Washington DC (1973).

29. G. Picard, F. Séon and B. Trémillon, Proc. 1st Intern. Symp. on Molten Salt Chemistry and Technology, Y. Ito (Ed), Kyoto, april 1983, p. 49.

30. G. Picard, F. Séon and B. Trémillon, Proc. 4th Internat. Symp. on Molten Salts (held in San Francisco, May 8-13, 1983), The Electrochem. Society, Physical Electrochemistry Division, vol. 84-2 (1984), p. 694.

31. L. Yang and R.G. Hudson, Trans. Metal. Soc. of A.I.M.E., 215, 589 (1959).

32. Y. Hoshino and J.A. Plambeck, Can J. Chem., 40, 685 (1970).

Table 1 : Standard potentials E° (V/vs.Cl^-/Cl_2 (1 atm)) of ceric lanthanide electrochemical systems in molten LiCl-KCl eutectic (molality scale, temperature range : 650 < T < 850 K).

Electrochemical systems	E°/V = A + B.10^{-4}T A	 B	E°/V at 723 K
$La^{3+}/La(s)$	-3.483	4.4	-3.165
$Ce^{3+}/Ce(s)$	-3.605	6.3	-3.150
$Pr^{3+}/Pr(s)$	-3.565	5.8	-3.146
$Nd^{3+}/Nd(s)$	-3.772	9.1	-3.114
Nd^{3+}/Nd^{2+}	-3.878	10.8	-3.097
$Nd^{2+}/Nd(s)$	-3.721	8.3	-3.121
$Gd^{3+}/Gd(s)$ (*)	-3.500	5.5	-3.102
$Y^{3+}/Y(s)$ (**)	-3.800	9.1	-3.142

Table 2 : Solubility products K_S and solubilities S of ceric lanthanide oxychlorides and yttrium oxide (see text for definition) in molten LiCl-KCl eutectic at 723 K (molality scale).

	Initial concentration of lanthanide	- log K_S	- log S
LaOCl	0.25	7.60	3.80
"	0.15	7.20	3.60
CeOCl	0.065	8.10	4.05
PrOCl	1.25	8.70	4.35
NdOCl	0.1	8.20	4.10
"	0.5	8.20	4.10
"	0.74	8.40	4.20
Y_2O_3	0.20	22.8	7.6

(*) from the work of Yang and Hudson (31)

(**)from the works of Hoshino and Plambeck (32) and Yang and Hudson(31)

Table 3 : Activity coefficients $\gamma(Ln^{3+})$ of some lanthanide(III) chlorides in molten LiCl-KCl eutectic (molality scale, temperature range : $650 < T < 850$ K)

$LnCl_3$		$\log \gamma = A + 1000\ B/T$		$\log \gamma$ at 723 K
		A	B	
$LaCl_3$		- 5.10	2.75	- 1.30
$CeCl_3$		- 4.10	1.31	- 2.29
$PrCl_3$		- 3.58	0.55	- 2.82
$NdCl_3$		- 1.26	- 1.62	- 3.50
$GdCl_3$	(*)	- 4.00	- 1.06	- 5.47
YCl_3	(**)	2.02	- 7.24	- 7.99

(*) from the work of Yang and Hudson (31)

(**)from the works of Hoshino and Plambeck (32) and Yang and Hudson(31)

Table 4 : Solubility products K_S of lanthanide(III) oxychlorides and oxides (see text for definition) in molten LiCl-KCl eutectic (molality scale, temperature range : $650 < T < 850$ K).

	$-\log K_S = A + 1000\,B/T$		$-\log K_S$	$-\log S$
LnOCl	A	B	at 723 K	at 723 K
LaOCl	- 2,69	7.43	7,59	3.80
CeOCl	- 1.23	5.91	6.94	3.47
PrOCl	- 0,86	5,68	7,00	3.50
NdOCl	1,86	4.12	7,56	3,78
GdOCl	- 0,84	5,07	6.17	3,09

	$-\log K_S = A + 1000\,B/T$		$-\log K_S$	$-\log S$
Ln_2O_3	A	B	at 723 K	at 723 K
La_2O_3	- 1,34	9,05	11.2	3,73
Ce_2O_3	2,07	8,55	13,9	4,63
Pr_2O_3	3.37	7.75	14,1	4.70
Nd_2O_3	7,87	4.10	13.5	4,51
Gd_2O_3	2.03	9,35	15.0	4,99
Y_2O_3	12,65	4.81	19,3	6,43

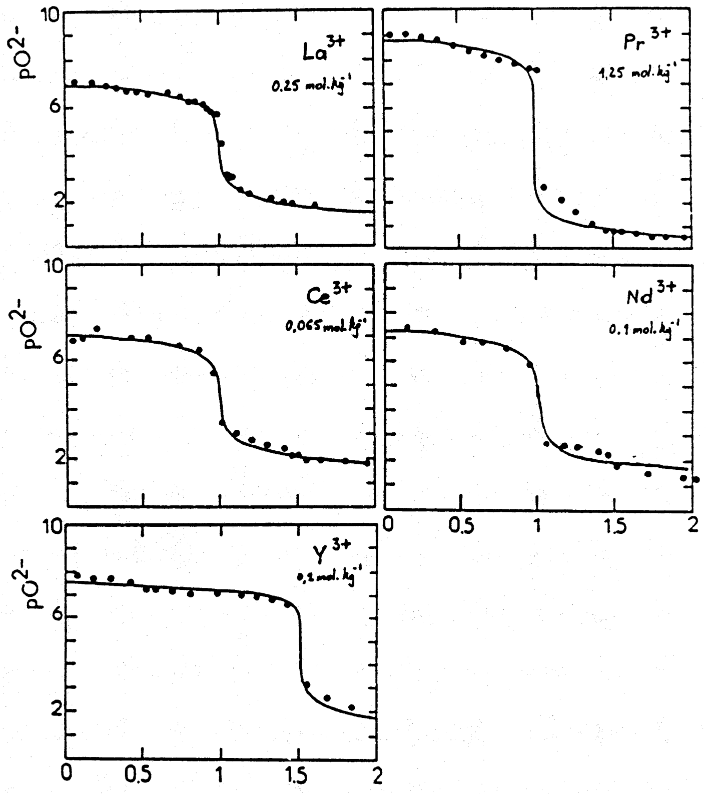

Fig. 1 : Potentiometric titration curves of lanthanide(III) chlorides by sodium carbonate in molten LiCl-KCl eutectic at 723 K.

● : experimental measurements of pO^{2-}

—— : curve calculated assuming only the precipitation of stoichiometric LnOCl (Ln = La, Ce, Nd, Pr) or Y_2O_3.

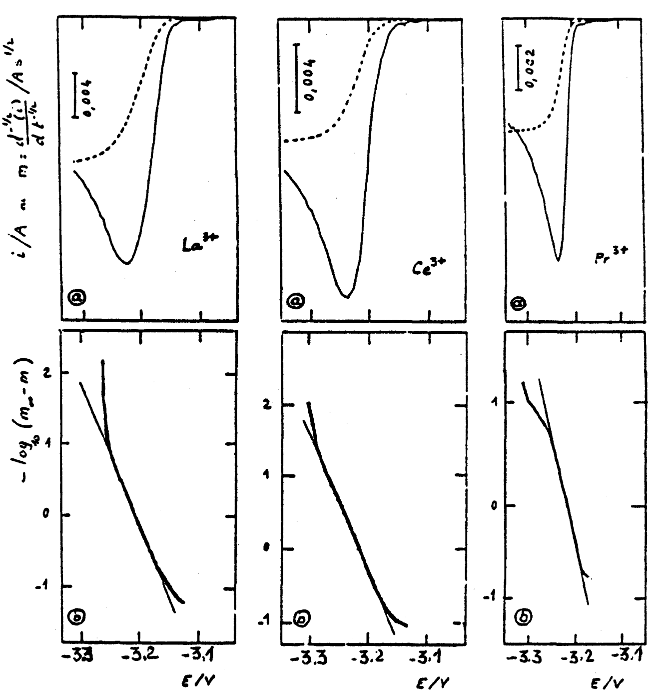

Fig. 2 : Electrochemical study of the reduction of lanthanum(III), cerium(III) and praseodymium(III) in molten LiCl-KCl eutectic at 723 K (tungsten electrode).

a) —— : voltammograms i(E) . ($v = 0.2\ V.s^{-1}$)

--- : corresponding "neopolarograms" m(E).

$|La^{3+}| = 2.0.10^{-1} mol.kg^{-1}$; $A = 5.1.10^{-2} cm^2$

$|Ce^{3+}| = 9.6.10^{-2} mol.kg^{-1}$; $A = 7.0.10^{-2} cm^2$

$|Pr^{3+}| = 6.9.10^{-2} mol.kg^{-1}$; $A = 5.8.10^{-2} cm^2$

b) : logarithmic analysis of m(E) curves.

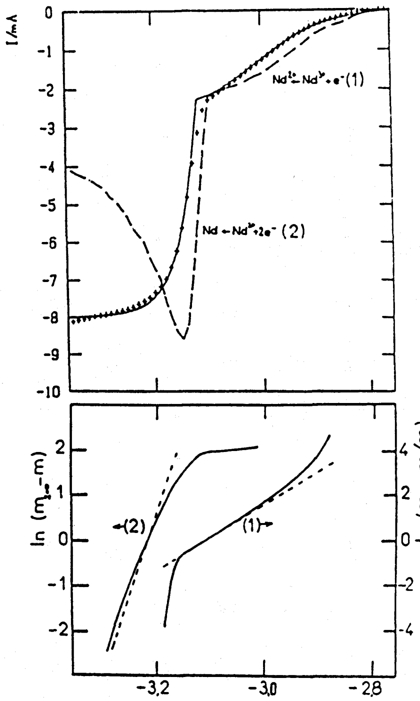

Fig. 3 : Electrochemical study of the reduction of neodymium(III) in molten LiCl-KCl eutectic at 723 K.

a) ----- : voltammogram i(E) . ($v = 0.16\ V.s^{-1}$)

+++++ : corresponding "neopolarogram" m(E)

——— : simulated m(E) curve.

$|Nd^{3+}| = 8.54.10^{-2} mol.kg^{-1}$

b) : logarithmic analysis of m(E) curve.

——— : experimental curves

----- : theoretical slopes.

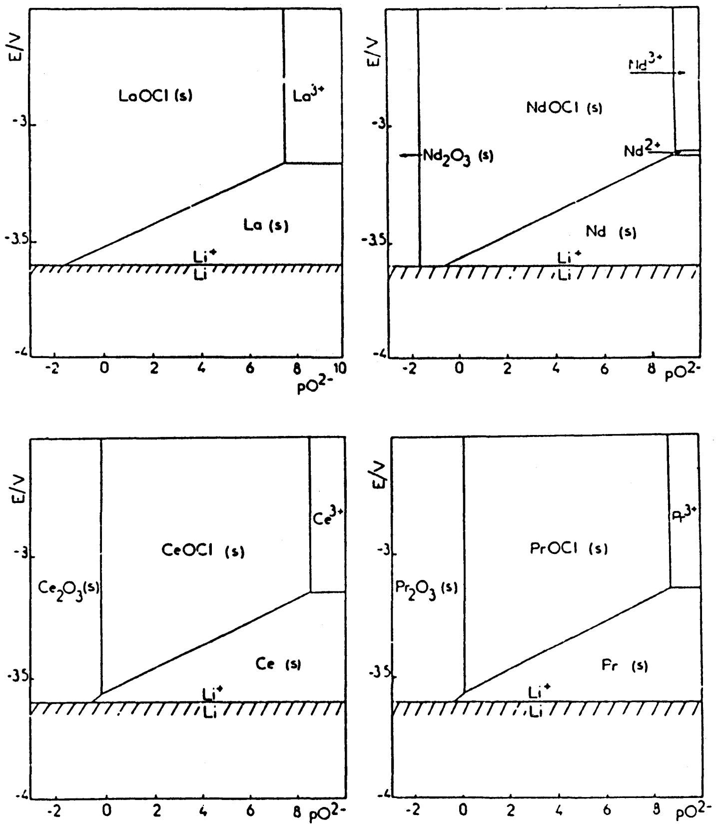

Fig. 4 : Potential-pO^{2-} equilibrium diagrams of ceric lanthanides in molten LiCl-KCl eutectic at 723 K (concentration = 1 mol.kg^{-1})

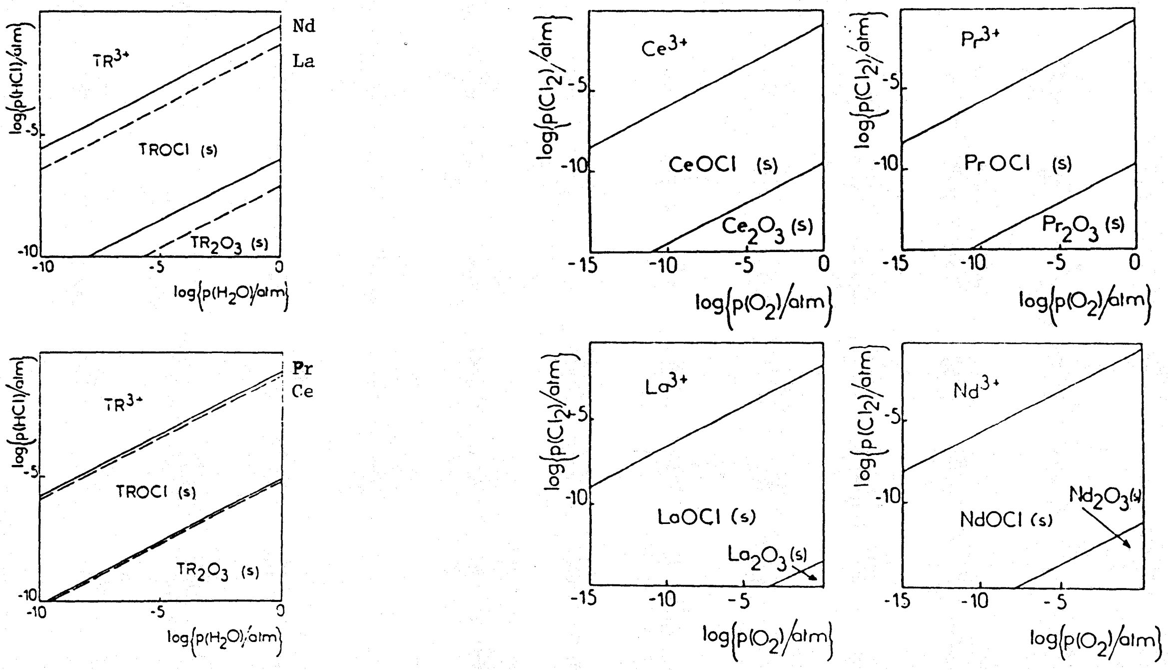

Fig. 5 : Prediction of the solubilization of lanthanide(III) oxychlorides and oxides in molten LiCl-KCl eutectic at 723 K, by using gaseous HCl + H_2O and Cl_2 + O_2 mixtures.

DOI: 10.1149/198601.0205PV

AN ELECTROCHEMICAL STUDY OF INDIUM BEHAVIOUR IN THE FUSED NaCl-KCl MIXTURE

M. J. BARBIER, J. BOUTEILLON, M. TAOUMI

Laboratoire d'Energetique Electrochimique (LA au CNRS n° 265)
ENSEEG, Domaine Universitaire, B.P. 75
38402 SAINT-MARTIN D'HERES, FRANCE

As the photoconductor applications of indium increase, more attention has been devoted to indium recovery. An electrochemical method may be suitable. The electrochemical properties of indium are rather poorly known; however, it seems that indium electrowinning may be done in a fused salt medium such as alkaline chloride mixtures.

We have studied the indium electrochemical properties in a NaCl-KCl mixture. No previous data exist in literature. However, some similarity can be expected with the indium salts electrochemistry in the fused LiCl-KCl equimolar melt, which has been investigated by Laitinen et al. (1) and other research groups (2-4). They obtained some evidence for mono- and trivalent indium ions.

We first tried to characterize the mono- and trivalent indium compounds in the fused equimolar NaCl-KCl mixture, and we measured the In/In(I) equilibrium potential. Afterwards, we studied the kinetics of the electrochemical reactions between indium species.

1. STABLE OXIDATION STATES OF INDIUM

1.1. Theoretical Considerations

Using the free energy of formation (5), we computed the standard potentials e_x°In/In(I) and e_x°In/In(III). These values and some physical properties of indium and its compounds are reported in Table 1.

	$T_{mp.}$(°C)	$T_{b.p.}$(°C)	*ΔG°_f(J.mol.$^{-1}$)	e°_xIn/In(X)/e°_xAg/Ag(I)
In	156	2000		
InCl	225	608	- 140 330	*e°_x In/In(I) = - 0.630 V **e°_xIn(I)/In(III)= -0.390 V
$InCl_3$		586 Sub(300)	** - 335 000	

* values at 700°C ** values estimated from data for gases and solids

Table 1 - Thermodynamic data and standard potentials.

From these data, it can be seen that mono- and trivalent indium salts could be stable in the fused NaCl-KCl equimolar mixture.

1.2. Experimental Results

The experimental apparatus that was used has been described previously (6). The solvent was contained in a quartz vessel and was purified with respect to water and oxygen by heating the melt under vacuum and fusing it under argon. Indium trichloride was added through a lock-chamber. The voltammetric studies were carried out on an anodically polished tungsten working electrode (11).

All potentials were referred to the Ag/AgCl, NaCl-KCl half-cell reference (7).

Figure 1* shows a typical voltammogram. The sweep rate was 0.1 $V.s^{-1}$. The available domain of the melt is 2.4 V. The In(III) ions reduction to metallic indium follows two well-separated electrochemical steps:

- in the potential range +0.4 V to +0.16 V, the A/A' couple corresponds to the In(I)/In(III) exchange;
- in the potential range -0.475 V to -0.275 V, the B/B' couple is related to the In/In(I) exchange.

2. STUDY OF THE In/In(I) EQUILIBRIUM

We have verified that In(III) ions are completely reduced to monovalent indium by metallic indium according to the reaction:

$$\mathrm{In(III)} + 2\ \mathrm{In} \rightarrow 3\ \mathrm{In(I)}$$

The advancement of the reduction process was followed by measuring the indium liquid electrode potential; analyzes for In(I) by spectrophotometry of frozen melt samples were used to control the process.

The values of the electrode equilibrium potentials are reported in Table 2. A plot of potential vs. the logarithm of indium molar fraction yields a curve with a slope that fits a single electron transfer and gives the following for the apparent standard electrode potential:

$$e^\circ_x\mathrm{In/In(I)}\ :\ (-0.36 \pm .02)\ \mathrm{V}\ /\ e^\circ_x\mathrm{Ag/Ag(I)}$$

---

*Editor's note: In the figure captions, E/R is used to designate the reference electrode.

Number of $InCl_3$ moles added	Molar fraction of In(I) (spectrophotometric analysis)	Equilibrium indium electrode potential
$1.963\ 10^{-4}$	$8.60\ 10^{-5}$	- 0.550 V
$2.313\ 10^{-4}$	$9.46\ 10^{-5}$	- 0.538 V
$4.578\ 10^{-4}$	$1.84\ 10^{-4}$	- 0.496 V
$6.040\ 10^{-4}$	$2.52\ 10^{-4}$	- 0.458 V
$9.655\ 10^{-4}$	$3.90\ 10^{-4}$	- 0.428 V

Table 2 - In/In(I) equilibrium potential

3. REDUCTION MECHANISM OF THE TRIVALENT INDIUM IONS

3.1. The In(I)/In(III) Step

The In(I)/In(III) step was studied on a glassy carbon and on a gold electrode in trivalent indium chloride solutions.

Voltammetric experiments

Figure 2 presents two voltammograms related to the A/A' exchange. Curve A was obtained on a gold electrode and curve B on a glassy carbon one. The sweep rate was 4 $V.s^{-1}$. The shape of the curves is characteristic of a soluble-soluble transfer.

Owing to the high current flowing through the electrode, the voltammetric transients were altered by the ohmic drop interferences and were consequently analysed using convolution procedures (8,9).

The reversibility test was performed by comparing the semi-integral curves recorded at different sweep rates. We observed that the curves were very close and were the same during the forward and reverse scan. The semi-integral curve related to the voltammogram curve A of Figure 2 is shown in Figure 3. This behaviour proves that the electron exchange is very fast. The logarithmic transform of the semi-integral curve is shown in Figure 4. It follows that the electrode potential varies linearly versus ln $(m^*-m)/m$, where m is the semi-integral of the current density and m* the cathodic limiting value of these functions obtained at high cathodic overpotentials, according to the Nernst relation:

$$e = e^\circ + RT/2nF \ln D_{ox}/D_{red} + RT/nF \ln (m^*-m/m)$$

The slope of the linear part of curve a in Figure 4 yields the number of the exchanged electrons:

$$n = 2.1 \pm 0.1$$

These results agree with the hypothesis that the A/A' couple is In(I)/In(III) and prove the reversibility of this couple.

Chronopotentiometric experiments

Figure 5 presents some chronopotentiometric transients obtained on a glassy carbon electrode. Only one transition is observed and the shape of the curve is characteristic of a soluble-soluble transfer.

The value $i\tau^{1/2}/c$ remains constant when the current density is varied. Hence, the Sand relation is verified.

The logarithmic analysis of the chronopotentiograms (Figure 6) indicates a reversible soluble-soluble transfer (curve a) and an exchange of two electrons.

To summarize, we showed that the In(I)/In(III) exchange occurs reversibly on glassy carbon and gold electrodes. Finally, the apparent standard potential e_o' In(I)/In(III) was determined from the half peak potential of the convolution curves or from the quarter transition time potential. The trivalent diffusion coefficient of the indium ion was computed. The results are reported in Table 3.

method of analysis	$e_{1/2}$ or $e_{\tau/4}$	$D_{In(III)}$ $(cm^2.s^{-1})$
Convolutional voltammetry	- 0.360 V	$(4.2 \pm .4)\ 10^{-5}$
Chronopotentiometry	- 0.356 V	$(4.5 \pm .6)\ 10^{-5}$

Table 3 - The apparent In(I)/In(III) standard potential, the In(III) diffusion coefficient

3.2 The In/In(I) step

The In/In(I) step was studied on both tungsten and liquid-indium electrodes since glassy carbon and gold electrodes were not suitable.

The tungsten electrode reacts with the trivalent indium solutions but the kinetics is slow, and this electrode can be used for the study of the In/In(I) exchange. Figure 7 presents a voltammogram obtained on a tungsten electrode. The corresponding semi-integral curve is shown in Figure 8; two plateaus can be observed.

To obtain a reproducible behaviour with the liquid-indium electrode, it was necessary to proceed by chronopotentiometry with current reversal from a stationary oxidation state (10). Figure 9 presents a typical chronopotentiogram, corrected for the ohmic drop, obtained in the absence of indium species. The anodic and cathodic current densities were equal to 50 $mA.cm^{-2}$.

The logarithmic analysis of the curve (Figure 10) indicates that the anodic pulse shape is characteristic of the metal oxidation. The following electrochemical step was postulated to explain departure from reversibility:

$$In \rightarrow In(III) + 3e$$

This electrochemical step is coupled to a slow chemical reaction:

$$In(III) + 2\ In \rightarrow 3\ In(I).$$

Finally, the values deduced for the apparent standard In/In(I) potential are the same from voltammetric, chronopotentiometric, and equilibrium measurements (-0.38 V).

REFERENCES

(1) H. A. Laitinen, C. H. Liu, J. Am. Chem. Soc., 80 (1958) 1015.

(2) J. M. Shafir, J. A. Plambeck, Can. J. Chem., 48 (1970) 2131.

(3) H. A. Laitinen, C. H. Liu, W. S. Ferguson, Anal. Chem., 30 (1958) 1266.

(4) J. A. Plambeck, U. A. Anders, Can. J. Chem., 47 (1969) 3055.

(5) A. Glassner, USAEC Argonne Natl. Lab. Rept., 5750 (1957).

(6) J. Bouteillon, A. Marguier, Surf. Techn., 22 (1984) 205.

(7) R. Littlewood, Electrochimica Acta, 3 (1961) 270.

(8) K. B. Oldham, Anal. Chem., 44 (1972) 196.

(9) J. C. Imbeaux, J. M. Saveant, J. Electroanal. Chem., 44 (1973) 169.

(10) A. Kisza, U. Twardoch, Bull. Acad. Polon. Sci., Ser. Sci. Chem., 20 (1972) 1063; 23 (1975) 341.

(11) M. Taoumi, These, Grenoble 1985.

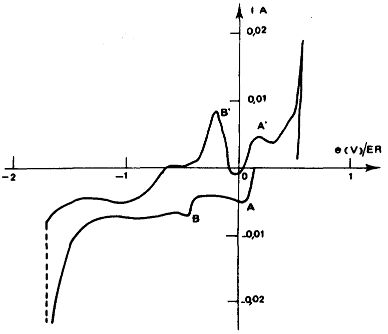

Figure 1 **Voltammetric study of a $InCl_3$ solution**

Temperature : 700C ; electrolyte : 2.33 10^{-2} molar $InCl_3$ solution ;
working electrode : tungsten (area : 0.63 cm^2) ;
v = 0.2 $V.s^{-1}$; cycle : + 0.15 V → - 1.66 V → + 0.56 V/ER.

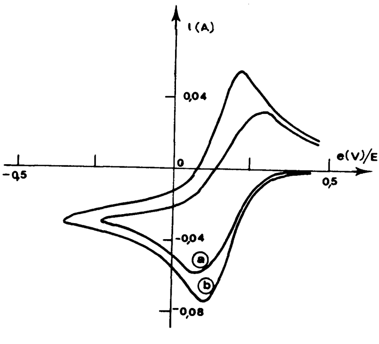

Figure 2 **Voltammetrics study of the In(I)/In(III) couple**

Temperature : 700C
a) working electrode : Gold (area : 1 cm^2)
electrolyte : $1.3.10^{-2}$ molar $InCl_3$ solution ; v = 4 $V.s^{-1}$
cycle : + 0.45 V → + 0.24 V → + 0.48 V/ER

b) working electrode : glassy carbon (area : 0.65 cm^2)
electrolyte : $1.58.10^{-2}$ molar $InCl_3$ solution ; v = 4 $V.s^{-1}$
cycle : + 0.45 V → - 0.24 V → + 0.48 V/ER

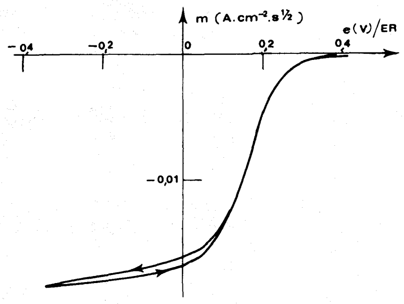

Figure 3 **Convolutional analysis**

Semi integral curve of the voltammogram a, figure 2

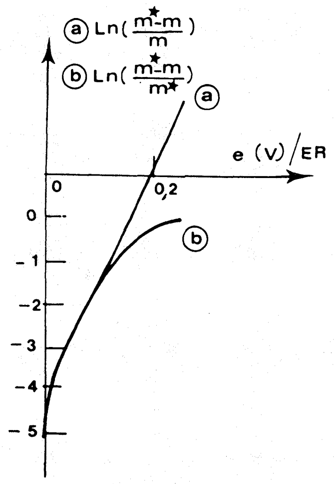

Figure 4 **Logarithmic analysis**

Analysis of the semi integral curve figure 3, according : a) soluble-soluble hypothesis ; b) soluble-insoluble hypothesis

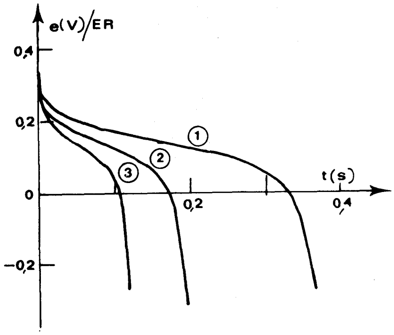

Figure 5 **Chronopotentiometric study of the In(I)/In(III) couple**

Temperature : 700C ; electrolyte : 1.06 10^{-2} molar $InCl_3$; solution :
working electrode : glassy carbon (area : 0.65 cm^2) ;
current density :
$|i_c|$; 1 : 0.023 $A.cm^{-2}$; 2 : 0.031 $A.cm^{-2}$;
3 : 0.038 $A.cm^{-2}$

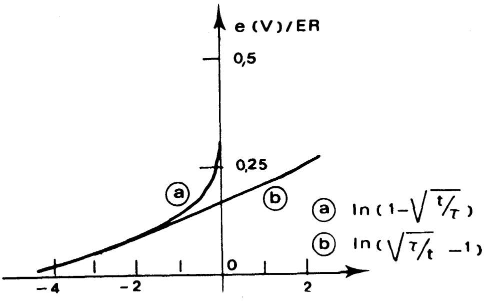

Figure 6 **Logarithmic analysis**

Analysis of a chronopotentiogram (figure 5) according to : a : the soluble-insoluble model : b : the soluble-soluble model

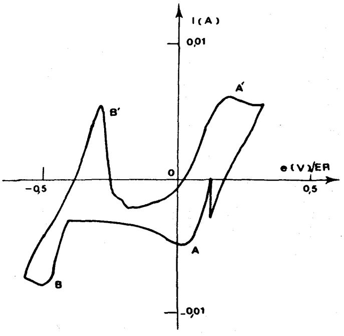

Figure 7 **Voltammetric study of the In/In(I) couple**

Temperature : 700C ; electrolyte : 2.6 10^{-3} molar $InCl_3$ solution ; working electrode : tungsten (area : 0.63 cm^2) ; v = 0.5 V.s^{-1}
cycle : + 0.12 V → - 0.58 V → + 0.32 V → + 0.12 V/ER

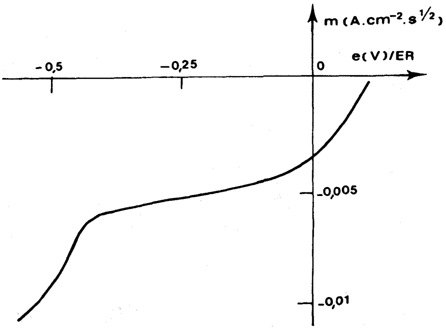

Figure 8 **Convolutional analysis**

Semi integral curve of the voltammogram figure 7

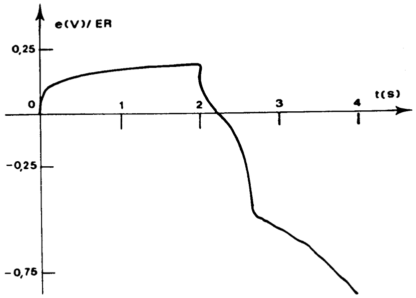

Figure 9 **Current reversal chronopotentiometry from a stationary oxidation state study**

Temperature : 700C ; working electrode : indium (area : 1cm²) ;
t_a : 2 s ; $i_a = | i_c | = 0.05$ A.cm^{-2}
electrolyte : NaCl.KCl equimolar solution, without $InCl_3$

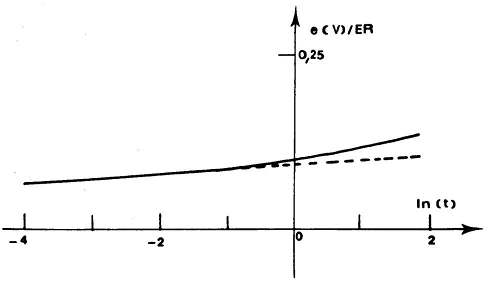

Figure 10 **Logarithmic analysis**

Analysis of the anodic pulse according to the reversible hypothesis

DOI: 10.1149/198601.0216PV

POTENTIOMETRIC INVESTIGATIONS OF Al(III), Nb(V) AND Ta(V) OXOCHLORO COMPLEX FORMATION IN NaCl-AlCl$_3$ MELTS AT 175°C.

J.H. von Barner,* N.J. Bjerrum† and R.W. Berg†

* The Institute of Mineral Industry, The Technical University of Denmark, Building 204, 2800,Lyngby Denmark

† Chemistry Department A, The Technical University of Denmark, Building 207, 2800 Lyngby, Denmark

ABSTRACT

Potentiometric measurements were performed with chlorine/chloride or aluminum concentration cells. The experiments on NaCl-AlCl$_3$-AlOCl melts were explained by the equilibrium: $(AlOCl)_2 \rightleftharpoons (AlO^+)_2 + 2Cl^-$, with a pK-value of 9.88±0.06 (molar units). The aluminum oxochloro species probably exist in solvated forms like $(AlOCl)_2(AlCl_4^-)_2$ and $(AlO^+)_2(AlCl_4^-)_2$, for which possible structures are proposed. For NaCl-AlCl$_3$-MOCl$_3$-melts (M=Nb, Ta), the best model was a two equilibria model: $MOCl_4^- \rightleftharpoons MOCl_3 + Cl^-$ (i) and $MOCl_3 \rightleftharpoons MOCl_2^+ + Cl^-$ (ii) with pK-values of 2.21(i) and 3.95(ii) for M=Nb and 2.74 (i) and 4.52 (ii) for M=Ta, respectively.

INTRODUCTION

The reactions of oxide in chloroaluminate melts are important both from a fundamental and applied point of view, e.g. oxide contaminations cause consumption of graphite electrodes during production of aluminum from such melts. This work deals with the identification and equilibrium chemistry of oxochloro complexes formed in NaCl-AlCl$_3$ melts. These properties have so far only been investigated in rather few cases, most of which are concerned with the oxochloro complex formation of Al (III) in NaCl-AlCl$_3$ melts (1-6).

The acid-base properties of NaCl-AlCl$_3$ melts can be described (7) by a three equilibria model:

$$2AlCl_4^- \rightleftharpoons Al_2Cl_7^- + Cl^- \qquad (1)$$
$$3Al_2Cl_7^- \rightleftharpoons 2Al_3Cl_{10}^- + Cl^- \qquad (2)$$
$$2Al_3Cl_{10}^- \rightleftharpoons 3Al_2Cl_6 + 2Cl^- \qquad (3)$$

for which the pK-values recently have been determined in the temperature range 175-300°C.

Concerning the oxochloro complexes of Al(III) formed in $NaCl-AlCl_3$ melts, the existence of $(AlOCl)_n$ is etablished (1-6) in neutral and moderately acidic melts at 175°C ($1.13<pCl<4.25$). From cryoscopic measurements (6) it has been shown that n is equal to two i.e. $(AlOCl)_2$.
In contrast to the agreement about the $(AlOCl)_n$ species, there has been some dispute on whether $AlOCl_2^-$ (or solvated forms thereof) exists in basic melts. For acidic melts with pCl values greater than 4.25 no data are reported in the literature.

Apart from clarifying the basic chemistry of oxides in $NaCl-AlCl_3$ melts, it is of interest to develop general methods to determine the amounts of oxide contamination in chloroaluminate solvents and to find oxide ion getters that are able to "neutralize" the undesired effects of oxide in applications of these melts.

In this connection the pentachlorides of niobium and tantalum are interesting candidates. Recently, $TaCl_5$ has been successfully applied as a probe solute for voltammetric determination of oxide in NaCl(sat'd)-$AlCl_3$ melts (8); oxochlorides of Nb(V) are formed in $KCl-AlCl_3$ melts as shown in a previous work (9). We therefore decided to investigate the oxochloro chemistry of Nb(V) and Ta(V) in more detail.

EXPERIMENTAL

The preparation of NaCl, AlOCl, $AlCl_3$ and $NbCl_5$ has previously been described (4, 6, 7, 9). $TaCl_5$ (99,5%, from Fluka) was purified by repeated sublimations at 200°C using the same procedure as for $NbCl_5$ (9).

The $NaCl-AlCl_3$ solvent was formed by mixing equal molar amounts of NaCl and $AlCl_3$ for at least 2 days at 175°C.

$$NaCl + AlCl_3 \rightarrow NaAlCl_4 \qquad (4)$$

Concentration cells (consisting of aluminum or chlorine/chloride electrodes with reference to a $NaAlCl_4$ melt saturated with NaCl) were measured for each batch of $NaAlCl_4$. As shown later, this enables us to calculate the oxide content of the solvent melt. Further amounts of oxide were added to the melt as AlOCl or as Na_2O. In the latter case quantitative conversion to AlOCl was assumed according to:

$$Na_2O + AlCl_4^- \rightarrow AlOCl + 2Na^+ + 3Cl^- \qquad (5)$$

$MOCl_3$ (M=Nb,Ta) was prepared directly in the melts by reacting MCl_5 and AlOCl at 175°C:

$$MCl_5 + AlOCl \rightarrow MOCl_3 + AlCl_3 \quad (M=Nb,Ta) \qquad (6)$$

These reactions took place quantitatively within a period of 2 hrs.

The experimental techniques used for potentiometric and spectrophotometric measurements have been described elsewhere (9-12).

RESULTS AND DISCUSSION

NaCl-AlCl$_3$-AlOCl melts.

The results of the potentiometric investigations with chlorine/chloride and aluminum electrode concentration cells (10) can be seen from Figure 1. In this figure the experimental average chloride coordination number $\bar{n}(AlO^+)$ for the AlO$^+$ unit is plotted as a function of the chloride concentration (pCl, molar units). From the measured emf values the chloride concentrations can be calculated (10). By means of mass balances, the charge balance and the mass action expressions of equilibria (1-3), $\bar{n}(AlO^+)$ can be found. (The value of $\bar{n}(AlO^+)$ denotes the average number of chlorides bound to one AlO$^+$ unit at the appropriate pCl).

From Figure 1 it is seen that $\bar{n}(AlO^+)$ remains constant in the pCl range from 1.128 to 4.25. An average value of 1.01±0.05 can be calculated from ten measurements in this range. A value of one is in agreement with previous results by Taulelle et al. (5). In conclusion, this indicates that the aluminum oxochloro species present must be of the type $(AlOCl)_n(AlCl_4^-)_m$, where n and m are integers.

In more acidic melts (i.e. for pCl>4.25), $\bar{n}(AlO^+)$ drops below one (Figure 1), reflecting the formation of new less chloride rich aluminum oxochloro complexes. Based on seven measurements performed in this pCl range, equilibria models of the type shown by equation (7) were tested for n and p values of one or two (q is just an integer to avoid fractions).

$$q(AlOCl)_n = \frac{q \cdot n}{p}(AlO^+)_p + qn\,Cl^- \qquad (7)$$

To perform the test, a computer program, which was able to calculate optimized equilibrium constants and the corresponding minimum variances for each model, had to be developed (13). A statistical F-test in which the minimum variance of each model is compared to the experimental variance, allowed us to discriminate between the models (significance of more or less than e.g. 90%). The test results for the two (non-solvated) models that explained the potentiometric measurements with a significance of more than 90% are shown in Table I (models 1 and 2). Model 2, i.e. the equilibrium:

$$(AlOCl)_2 = (AlO^+)_2 + 2Cl^- \qquad (8)$$

is considered to be the best one. A pK-value of 9.88±0.06 (molar units) could be calculated for this equilibrium at 175°C. Equilibrium 8 is in agreement with cryoscopic measurements performed in near neutral melts (6) as well as with preliminary cryoscopic results from acidic $NaCl$-$AlCl_3$ melts, both indicating the formation of dimeric aluminum oxochloro species.

From a structural point of view, it is, however likely that $(AlOCl)_2$ and $(AlO^+)_2$ exist in solvated forms. Figure 2 shows structures for solvated species: $(AlOCl)_2(AlCl_4)_2$ (a), and $(AlO^+)_2(AlCl_4^-)_2$ (b), which allow Al to adopt tetrahedral coordination and have the di-oxo stoichiometry.

In support of these two species it can be mentioned that two salts containing the ion $[Al_4O_2Cl_{10}]^{2-}$ (i.e. $(AlOCl)_2(AlCl_4^-)_2$) have been characterized by X-ray crystal structure determinations (14, 15). An acidic species with the formula $(AlO^+)_2(AlCl_4^-)_4$ has recently been proposed by Rytter (16).

By means of a computer program (13) we can make calculations on equilibria in which the number of solvent ions bound to aluminum oxochloro species is restricted to the same number on both sides of the equilibrium arrows. The results of the computations for the two solvated models of this type, that gave the lowest variances, are shown as models 3 and 4 in Table I. It can be seen that these models also are able to explain the potentiometric measurements within a significance level of 90%.

<u>Determination of oxide in $NaCl$-$AlCl_3$ melts.</u>

$AlCl_3$ is a highly moisture sensitive substance. The reaction $AlCl_3 + H_2O \rightarrow AlOCl + 2\,HCl(g)$ is probably taking place with water vapor in glove boxes or with water absorbed on glass surfaces. Oxide may also be introduced by attack of $AlCl_3$ vapor on pyrex glass containers used for sublimation of $AlCl_3$ (6). Since $AlOCl$ is inert with respect to chloride ions in the pCl-range 1.128-4.25 at 175°C, $AlOCl$ impurities in $AlCl_3$ will not react with chloride when near-equimolar amounts of $NaCl$ and $AlCl_3$ are mixed, and hence an excess of chloride ions will be detected by potentiometric measurements on such a melt.

For a pure melt of $NaAlCl_4$ it can be seen from eq. (1) that $[Cl^-]=[Al_2Cl_7^-]$. In reality when weighing $NaCl$ and $AlCl_3$ in exactly the ratio of their molar weights, an excess of chloride of typically 0.03M was found. Since the difference $[Cl^-]-[Al_2Cl_7^-]$ corresponds to that fraction of originally weighed $AlCl_3$, which was actually AlOCl, the weight of AlOCl, W(AlOCl), can be calculated from W(AlOCl)= $([Cl^-]-[Al_2Cl_7^-])\cdot V \cdot M(AlCl_3)$, where V is the volume of the melt and $M(AlCl_3)$ is the molar weight of aluminum chloride.

This method of oxide determination in a batch of melt can be used for experiments, in which knowledge of the initial oxide level is important. Of course a continuous determination of the oxide contents would be more desirable.

In this connection, it should be mentioned that Mamantov and co-workers (8) have developed an oxide ion sensitive electrode based on β-alumina that gives a reasonable response in NaCl sat'd. NaCl-$AlCl_3$ melts. It is of interest to investigate whether oxide ion conductors like Y_2O_3stabilized zirconia can be used in this kind of electrode.

NaCl-$AlCl_3$-$MOCl_3$ melts (M=Nb, Ta).

These melts were investigated potentiometrically with chlorine/chloride concentration cells. The results of the potentiometric investigations are shown in Fig. 3, in which the average chloride coordination number for the MO^{3+} unit, $\bar{n}(MO^{3+})$, is shown as a function of pCl. It is seen from this figure that the average coordination numbers for both NbO^{3+} and TaO^{3+} are near four in the most basic melts (low pCl). It seems reasonable to believe that ions of the type $MOCl_4^-$ are formed in the basic melts. When the pCl is raised, the average coordination numbers gradually fall towards two. The $MOCl_4^-$ ions must be in equilibrium with species with lower chloride coordination numbers like $(MOCl_2^+)_m$ and/or $(MOCl_3)_n$. Consequently an equilibrium model of the type:

$$m\ MOCl_4^- \rightleftharpoons (MOCl_2^+)_m + 2m\ Cl^- \tag{9}$$

and two equilibria models such as:

$$\begin{aligned} n\ MOCl_4^- &\rightleftharpoons (MOCl_3)_n + n\ Cl^- \\ p(MOCl_3)_n &\rightleftharpoons q(MOCl_2^+)_m + mq\ Cl^- \end{aligned} \tag{10}$$

were tested.

The computations made so far seem to indicate that only models involving two equilibria are able to explain the potentiometric measurements on a 90% significance level. In Table I, the computed statistics for the best models are given. From this table it can be seen that sets of equilibria of the type:

$$\begin{aligned} MOCl_4^- &\rightleftharpoons MOCl_3 + Cl^- \\ MOCl_3 &\rightleftharpoons MOCl_2^+ + Cl^- \end{aligned} \tag{11}$$

give the lowest variances for both M=Ta and M=Nb.

Acknowledgements. Thanks are due to the Danish Council for Scientific and Industrial Research and to the Ministry of Energy for financial support to this work and to C.A. Jørgensen and K. Zachariassen for assistance with the experiments.

REFERENCES

1. Letisse, G; Tremillon, B.: *J. Electroanal. Chem.* 1968, 17, 387.
2. Tremillon, B.; Bermond, A.; Molina, R.: *J. Electroanal. Chem.* 1976, 74, 53.
3. Gilbert, B.; Osteryoung, R.A.: *J. Am. Chem. Soc.* 1978, 100, 2725.
4. Fehrmann, R.; von Barner, J.H.; Bjerrum, N.J.; Nielsen, O.F.: *Inorg. Chem.* 1981, 20, 1712.
5. Taulelle, F.; Piolet, C.; Tremillon, B.: *J. Electroanal. Chem.* 1982, 134, 131.
6. Berg, R.W.; Hjuler, H.A.; Bjerrum, N.J.: *Inorg. Chem.* 1984, 23,557.
7. Hjuler, H.A.; Mahan, A.; von Barner, J.H.; Bjerrum, N.J.: *Inorg. Chem.*, 1982, 21, 402.
8. Laher, T.M.; McCurry, L.E.; Mamantov, G.: *Anal. Chem.* (In press.)
9. von Barner, J.H.; Bjerrum, N.J.; Smith, G.P.: *Acta Chem. Scand.* 1978, A 32, 837.
10. von Barner, J.H.; Bjerrum, N.J.: *Inorg. Chem.* 1973, 12, 1891.
11. Andreasen, H.A.; Bjerrum, N.J.; Foverskov, C.E.: *Rev. Sci. Instrum.* 1977, 48, 1340.
12. Laursen, M.M.; von Barner, J.H.: *J. Inorg. Nucl. Chem.* 1979, 41, 185.
13. Zachariassen, K.; Berg, R.W.; Bjerrum, N.J.; von Barner, J.H., *Submitted to J. Electrochem. Soc.*
14. Thewalt, U.; Stollmaier, F.: *Angew. Chem. Int. Ed. Engl.* 1982, 21, 133; *Angew. Chem. Suppl.* 1982, 209.
15. Jentsch, D.; Jones, P.G.; Schwarzmann, E.; Sheldrick, G.M.: *Acta Crystallogr.* 1983, C39, 1173.
16. Rytter, E.: *Abstract submitted for the 168th meeting, The Electrochemical Soc., Las Vegas* 1985.

Table I. pK-values and Variances for Different Models for the Oxochloro Complex Formation of Al(III) in Acidic NaCl-$AlCl_3$ Melts (pCl>4.25) and of Nb(V) and Ta(V) in NaCl-$AlCl_3$ Melts (pCl>1.13) at 175°C.[a]

No.	Equilibrium	pK	Variance	F_{model}[b]
1	$2AlOCl \rightleftharpoons (AlO^+)_2 + 2Cl^-$	8.50(7)	0.0032	1.2
2	$(AlOCl)_2 \rightleftharpoons (AlO^+)_2 + 2Cl^-$	9.88(6)	0.0028	1.1
3	$(AlOCl)_2(AlCl_4^-)_2 \rightleftharpoons (AlO^+)_2(AlCl_4^-)_2 + 2Cl^-$	9.69(5)	0.0025	0.95
4	$(AlOCl)_2(AlCl_4^-)_4 \rightleftharpoons (AlO^+)_2(AlCl_4^-)_4 + 2Cl^-$	9.52(5)	0.0033	1.3
5	$NbOCl_4^- \rightleftharpoons NbOCl_3 + Cl^-$	2.21(4)	0.00188	1.16
	$NbOCl_3 \rightleftharpoons NbOCl_2^+ + Cl^-$	3.95(5)		
6	$2NbOCl_4^- \rightleftharpoons (NbOCl_3)_2 + 2Cl^-$	3.31(7)	0.00231	1.43
	$(NbOCl_3)_2 \rightleftharpoons 2NbOCl_2^+ + 2Cl^-$	8.99 (10)		
7	$TaOCl_4^- \rightleftharpoons TaOCl_3 + Cl^-$	2.743(15)	0.00020	1.00
	$TaOCl_3 \rightleftharpoons TaOCl_2^+ + Cl^-$	4.521(13)		
8	$TaOCl_4^- \rightleftharpoons TaOCl_3 + Cl^-$	2.68(4)	0.00125	6.25
	$2TaOCl_3 \rightleftharpoons (TaOCl_2^+)_2 + 2Cl^-$	8.35(5)		

[a] pK = -log K, where K is the molar concentration equilibrium constant, with the standard error on last digit indicated inside parentheses.

[b] F_{model} = variance of model divided by the estimated experimental variance. For Al(III), the experimental variance was $2.59 \cdot 10^{-3}$ and the 90% significance level F-value, $F_{0.10}(6,9)$, was 2.55. For Nb(V) and Ta(V) experimental variances were $1.61 \cdot 10^{-3}$ and $2.0 \cdot 10^{-4}$ respectively. $F_{0.10}(8,8)$ = 2.59.

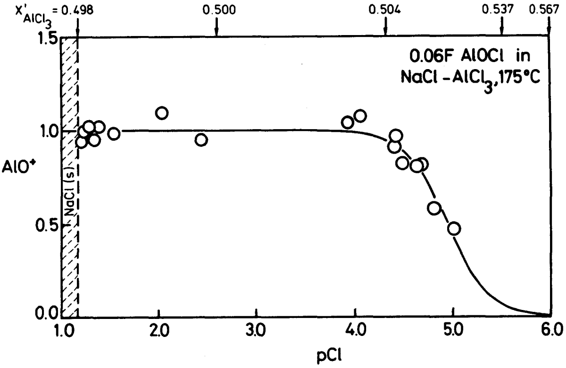

Figure 1. Average experimental coordination number for AlO^+ as a function of the chloro acidity (pCl in molar units) at 175°C. $\bar{n}_{AlO^+}$ is defined as: $(3C'_{AlCl_3} + C'_{AlOCl} + C'_{NaCl} - 4[AlCl_4^-] - 7[Al_2Cl_7^-] - 10[Al_3Cl_{10}^-] - 6[Al_2Cl_6])/C'_{AlOCl}$, where C'_i is the formal concentration of the i'th species (weighed molar amount divided by the volume of the molten mixture in litres). The full line corresponds to equation (8) assuming pK = 9.88.

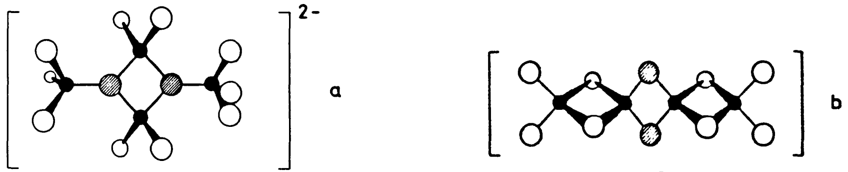

$Al_4O_2Cl_{10}^{2-}$

2-para-$Al_4O_2Cl_8$

Figure 2. Proposed structures for solvated aluminum oxo-chloro complexes in NaCl-$AlCl_3$ melts. (a) $Al_4O_2Cl_{10}^{2-}$ ~ $(AlOCl)_2(AlCl_4^-)_2$, (b) $Al_4O_2Cl_8$ ~ $(AlO^+)_2(AlCl_4^-)_2$. Several other isomeric forms of both species can be imagined. An ion like (a) exists in crystals.

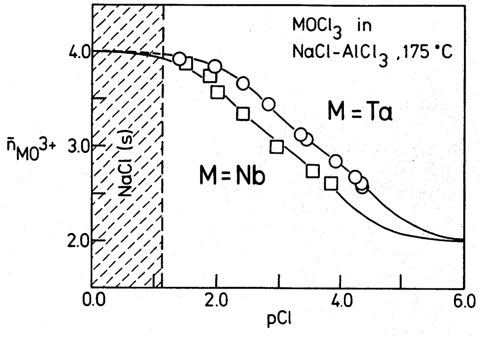

Figure 3. Average experimental coordination number for MO^{3+} (M=Nb,Ta) as a function of pCl at 175°C. The formalities C' of $NbOCl_3$ and $TaOCl_3$ were 0.10 M and 0.28 M, respectively. The full lines correspond to equation (11) with the equilibrium constants given in Table I.

DOI: 10.1149/198601.0225PV

CHEMICAL AND ELECTROCHEMICAL STUDY OF ZN(II) IN THE MOLTEN NAOH-KOH EUTECTIC MIXTURE

G. PEETERS, J. GLIBERT and P. CLAES
Université Catholique de Louvain
Laboratoire d'Electrochimie des Liquides Ioniques
et de Chimie des Radiations
B-1348 Louvain-la-Neuve, Belgique

ABSTRACT

A hydroxyion is formed by dissolution of zinc oxide in acidic NaOH-KOH melt at 210°C. Its formation was determined by a voltammetric measurement of the diminution of the water concentration. The solubility of this ion is low and a solubility product was calculated. The electrochemical behaviour of the $Zn(OH)_n^{(n-2)-}$ species was carried out at a platinum electrode. The behaviour of the H_2O/H_2 couple was analyzed too. A zinc or a glassy carbon working electrode was used to check the interpretation of the successive electrochemical reactions.

INTRODUCTION

Although molten alkali metal hydroxides are frequently used as solvent media for chemical reactions, data on the nature and the solubility of the dissolved species are still very scarce.

During the last few years, a series of studies was carried out in our laboratory in order to determine the chemical and electrochemical properties of the elements of the groups IV, V and VI (1). The reactions were investigated in the NaOH-KOH (49 mole%) eutectic mixture at 210°C.

The specific acid-base behaviour of fused hydroxides has been suggested by B. TREMILLON and coworkers (2). The dissociation equilibrium is expressed by the relationship :

$$2\ OH^- \rightleftarrows H_2O + O^{2-}$$

where the H_2O molecules and the O^{2-} ions are defined as the acidic and basic species, respectively.
According to the pH_2O or pO^{2-} value of the melt, the dissolution of the above-mentioned solutes is described by the general equation :

$$M_xO_y + 2n\ OH^- \rightleftharpoons x\ MO_{(\frac{y+n}{x})}^{(2n/x)-} + n\ H_2O$$

An original linear sweep voltammetric method (3,4) using a cylindrical stationary electrode was adopted to determine the variations of the water or oxide concentrations and to explicit the composition of the formed oxyanions. A few examples of representative stoechiometries out of the studied reactions (1) are as follows :

$$SiO_2 + 4\ OH^- \rightleftharpoons SiO_4^{4-} + 2\ H_2O$$

$$SnO_2 + 2\ OH^- \rightleftharpoons SnO_3^{2-} + H_2O$$

$$PbO + 2\ OH^- \rightleftharpoons PbO_2^{2-} + H_2O$$

$$As_2O_3 + 6\ OH^- \rightleftharpoons 2\ AsO_3^{3-} + 3\ H_2O$$

All these solutes act as Lux-Flood acids and the purpose of the present work is to investigate the mechanism of dissolution of zinc oxide. This compound seems to be particularly interesting because of its basic behaviour. Only acidic melts were considered in this paper.

EXPERIMENTAL

The experiments were carried out in a previously described cell assembly (4,5,6). Reagent grade chemicals were used. The eutectic mixture was fused in a glassy carbon crucible (Le Carbone Lorraine VN 25) and dehydrated by maintaining the temperature at 450°C for several hours in a flowing atmosphere of dry nitrogen. The acidity of the melt was adjusted by addition of weighed pellets of untreated potassium hydroxide (15,1% weight H_2O). A 1 mm diameter platinum wire (Johnson Matthey chemicals) fixed to a micrometric screw was used as working electrode to determine the water concentration. Its immersion depth was increased by reproducible increments and the proportionality constant measured at 210°C (4) by linear sweep voltammetry (40 mV sec^{-1}) between current density and water concentration was given by the following equation :

$$i\ (\mu A\ mm^{-2}) = 4.27\ C_{H_2O}\ (mM)$$

A platinum foil (0.43 cm^2) was used as indicator electrode in the acidic melts containing Zn(II) ions. Some experiments were carried out at a zinc or vitreous carbon working electrode to check the interpretation of the successive electrochemical reactions. In all cases, a platinum helix and a platinum wire served as counter and quasi-reference electrodes, respectively.

The voltammetric scans were performed with a Tacussel PRG.5 polarograph coupled with a Tacussel GSTP.3 function generator. The current-voltage curves were recorded on a Goerz t-Y or X-Y recorder.

RESULTS AND DISCUSSION

Chemical behaviour :

Addition of controlled minute amounts of zinc oxide to acidic melts yields a diminution of the water content of the hydrated hydroxides. A typical evolution of the water concentration as a function of time is shown in Fig. 1. The total dissolution process was achieved after 5 hours. The final ratio of consumed water to added zinc oxide is found to be 0.95. This result suggests an equilibrium described as :

$$\mathrm{ZnO} + \mathrm{H_2O} \overset{\mathrm{OH^-}}{\rightleftarrows} [\mathrm{Zn(OH)_2}]_{\mathrm{solvated}}$$

where $[\mathrm{Zn(OH)_2}]_{\mathrm{solv.}}$ is most probably an hydroxyion such as $\mathrm{Zn(OH)_n^{(n-2)-}}$; however the value of n cannot be approached from the present measurements. The solubility of the Zn(II) ion is low and a solubility product given by :

$$K_S = \frac{[\mathrm{Zn(OH)_2}]_{\mathrm{solv.}}}{[\mathrm{H_2O}]}$$

may be investigated by examining the influence of the $\mathrm{pH_2O}$ value on a ZnO saturated melt. The existence of this solid phase after aging of the solution was confirmed by x-ray diffraction.

As we shall see, the electrochemical Zn(II) reduction wave cannot be used to determine the Zn equilibrium concentrations. This wave is indeed strongly perturbed by the very close water reduction signal. Only voltammetric measurements performed under low water concentrations on zinc or carbon electrodes would allow us to establish a calibration curve. In order to relate the influence of the acidity of the solvent on the solubility of Zn(II), quenched samples of the melt free of solid particles were dissolved in water and analyzed by atomic absorption.

The solubility values of Zn(II) (X_i) were correlated with the corresponding equilibrium water concentration (Y_i-X_i) (Fig. 2). A linear plot was obtained and a K_s value of 0.56 ± 0.05 was calculated from the slope of the line.

Electrochemical behaviour of Zn(II) in acidic melts :

a) Platinum working electrode

Figure 3 shows a current-voltage curve obtained at a platinum electrode by single sweep voltammetry. The potential values are referred to the cathodic limit of the solvent. The profile of the voltammogram reveals the existence of three peaks. The shape of the first one assigned to the water reduction (4) is deformed by a hump at a potential close to that measured by potentiometry for the Zn(II)/Zn(0) couple.

Repeated cathodic sweeps without standing at the starting potential significantly decrease the intensity of the first peak so that a second peak clearly appears. The corresponding peak intensity is dependent on the Zn(II) concentration and the occurrence of a zinc deposit was confirmed by a x-ray diffraction analysis after a controlled potential electrolysis.

The last signal depends on the water concentration and current irregularities are indicative of the evolution of hydrogen bubbles from the electrode surface. This leads to the conclusion that the remaining peaks are due to the discharge of the zinc ions and to the water reduction on a zinc substrate. An overpotential is therefore required for this hydrogen evolution.

A cyclic voltammogram (Fig. 4) shows that the reverse anodic scan is characterized by a sharp current peak. A progressive modification of the reverse potential demonstrates that this reaction is due to the re-oxidation of the zinc deposit. The rapid dissolution of the metal yields a large amount of scarcely soluble Zn(II) ions; a passivation process by precipitation of zinc oxide occurs at the surface electrode.

An additional anodic wave, which is very weakly reproducible, appears at 0.75 V. A probable explanation is that the plating of the platinum substrate is not complete so that the hydrogen oxidation can occur.

Though the electroreductions are very close, an attempt has been made to estimate the number of electrons involved in the electrode processes using I/E displays obtained by differential pulse voltammetry (Fig. 5). The width at the half-peak height ($W_{1/2}$ = 3.53 RT/nF) allows us calculate an n-value of about 1.15 and 2.4 for the peaks I and II, respectively.

From the foregoing data, it is safe to present the following reactions :

$$H_2O + e^- \xrightarrow{Pt} OH^- + \frac{1}{2} H_2 \quad (E_p \cong 0.67 \text{ V vs } Na^+/Na)$$

$$Zn^{2+} + 2\ e^- \longrightarrow Zn \quad (E_p \cong 0.55 \text{ V})$$

$$H_2O + e^- \xrightarrow{Zn} OH^- + \frac{1}{2} H_2 \quad (E_p \cong 0.24 \text{ V})$$

b) Zinc working electrode

The use of a zinc electrode as the working electrode allowed us to confirm the above observations. In order to avoid local modifications of the melt composition owing to corrosion reactions occurring at the surface electrode, the zinc rod must be immersed in the acidic hydroxide a few moments before the voltammetric runs begun.
The area of the immersed part was unknown and quantitative determinations were not possible. Besides, as the Zn(II)/Zn(0) couple is reversible, great care had to be taken in selecting the initial applied potential of the cathodic scans.
As can be seen (Fig. 6) two reduction reactions were observed and the peak currents were dependent on the zinc (II) and water concentrations, respectively. The general features of the current-voltage curves obtained in this way were reproducible but, as for the former experiments, the final parts are altered by the hydrogen evolution.

c) Glassy carbon working electrode

In this case, the electrode was a partially immersed glassy carbon rod.

The reduction reactions (Fig. 7) are identical to those obtained at a zinc electrode.
A direct comparison of the E_p potentials corresponding to the discharge of the Zn (II) and H_2O species with the values measured at platinum and zinc electrodes is nevertheless inadequate because the electrochemical window recorded on carbon electrode is shorter.
A cyclic sweep shows one anodic peak attributed to the zinc oxidation. As on the zinc electrode, the H_2O/H_2 couple presents an irreversible electrochemical behaviour.

ACKNOWLEDGMENTS

One of the authors (J. Glibert) is much indebted to the Fonds National de la Recherche Scientifique de Belgique for financial assistance in this work.

REFERENCES

1. Y. Dewilde, G. Peeters, J. Glibert and P. Claes, to be published.
2. J. Goret and B. Tremillon, Bull. Soc. Chim., 67 (1966).
3. C. Canoo and P. Claes, Electrochimica Acta, <u>19</u>, 37 (1974).
4. P. Tilman, J.P. Wiaux, C. Dauby, J. Glibert and P. Claes, J. Electroanal. Chem., <u>167</u>, 117 (1984).
5. C. Dauby, J. Glibert and P. Claes, Electrochim. Acta, <u>24</u>, 35 (1979).
6. C. Dauby, J. Glibert and P. Claes, Electrochim. Acta, <u>25</u>, 1077 (1980).

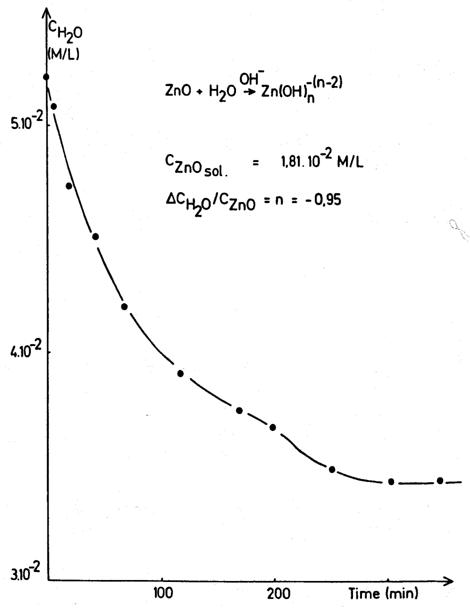

Figure 1 : Evolution of the water concentration after addition of a defined amount of zinc oxide.

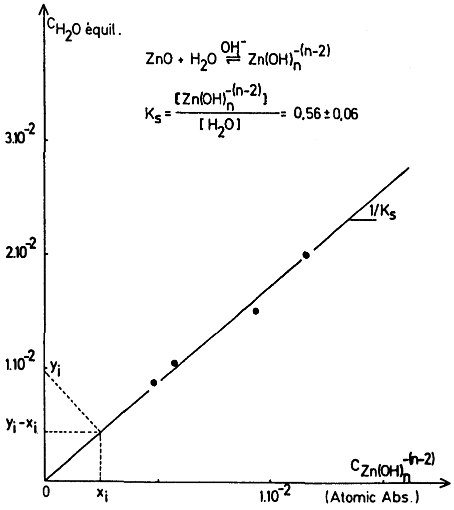

Figure 2 : Relation between the water and Zn(II) equilibrium concentrations of melts characterized by different initial pH_2O values.

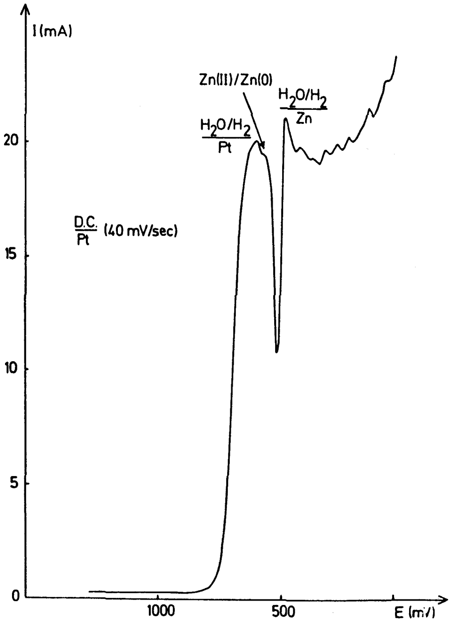

Figure 3 : Single sweep voltammogram at a platinum electrode (sweep rate : 40 mV/sec, area : 0.43 cm^2).

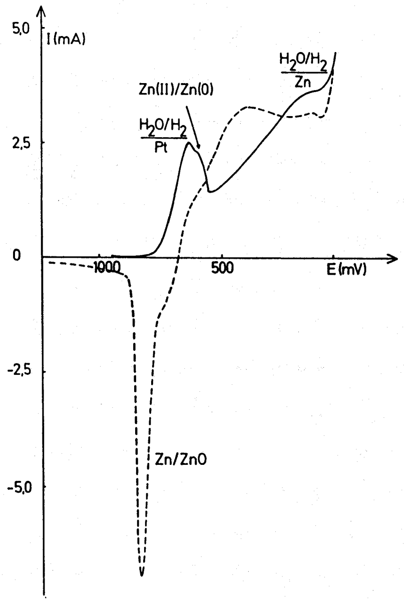

Figure 4 : Cyclic voltammetry at a platinum electrode (sweep rate : 40 mV/sec, area : 0.43 cm^2).

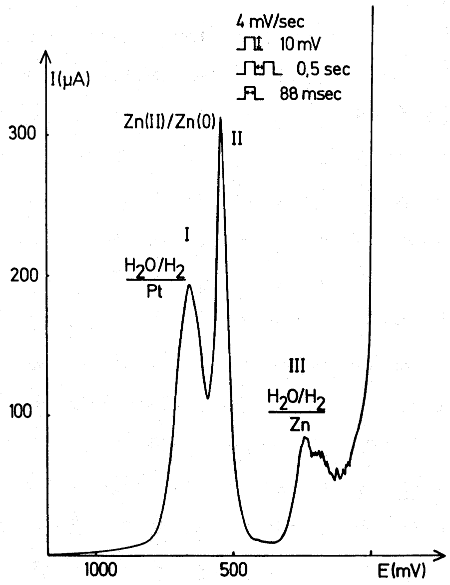

Figure 5 : Differential pulse voltammetry at a platinum electrode (area : 0.43 cm^2).

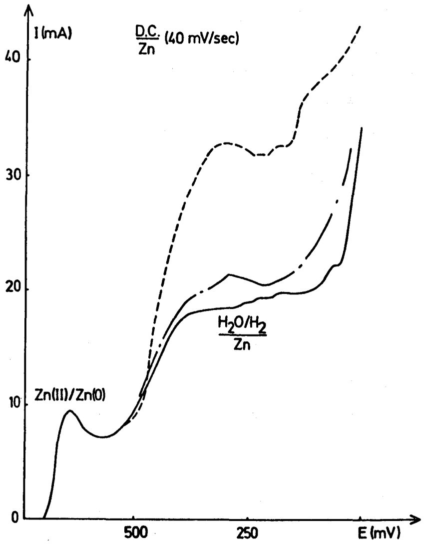

Figure 6 : Single sweep voltammograms obtained at a zinc electrode by varying the water concentration (sweep rate : 40 mV/sec).

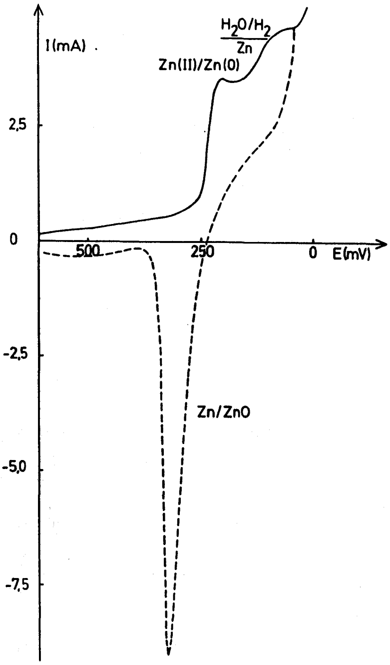

Figure 7 : Cyclic voltammograms at a glassy carbon electrode (sweep rate : 40 mV/sec).

DOI: 10.1149/198601.0234PV

PROBLEMS ASSOCIATED WITH THE ELECTROCHEMICAL REDUCTION OF METAL IONS IN MOLTEN NITRATES

M. H. Miles, G. E. McManis, and A. N. Fletcher
Chemistry Division, Research Department
Naval Weapons Center, China Lake, California 93555

ABSTRACT

Electrochemical studies of Ag^+, Tl^+, Cd^{++}, Pb^{++}, Zn^{++}, and In^{+++} metal ions on platinum electrodes in molten $LiNO_3$-KNO_3 show that only silver ions are readily reduced to the metal within the electrostability region of the melt. The other metal ions form nitrato complexes that are reduced directly to the metal oxide at potentials less negative than solvent reduction. For divalent metal ions, these reactions can be represented by $(MONO_2)^+ + 2e^- \rightarrow MO + NO_2^-$. Electrons, rather than metal ions, transfer the charge across the double layer. Scission of the O-N bond likely occurs in the first electron transfer step. The $(InONO_2)^{++}$ nitrato complex is reduced to InO^+ and NO_2 gas in a single electron transfer reaction. Investigations of Cd and Zn metals and amalgams show that the much faster M^{++}/M electrode reactions occur at considerably more negative potentials. The controversial water wave in nitrate melts can be explained by the analogous reduction of the $HONO_2$ complex to OH^- and NO_2^-.

INTRODUCTION

Studies of silver ions in molten nitrates (1-3) show that silver salts are readily reduced to the free metal in reversible electrode reactions such as

$$AgNO_3 + e^- \rightleftharpoons Ag + NO_3^- \qquad (1)$$

This reaction is the basis for the usefulness of the Ag^+/Ag reference electrode in nitrate melts (4). The deposited silver is reasonably stable in molten nitrates, but there is a small corrosion rate that varies with the composition of the melt (1).

Various eletrochemical investigations using mercury or platinum working electodes have shown that the additions of Tl^+, Cd^{++}, Pb^{++}, Zn^{++}, In^{+++} and other metal ions to molten nitrates produces new cathodic waves (4-17). It is generally assumed that the cathodic reactions, like that of silver ions, involve the reduction of metal ions to the free metal. However, the expected anodic wave due to the oxidation of the deposited netal is not observed when the current flow or potential sweep is reversed. This unusual observation has been attributed to the reaction sequence

$$M^{++} + 2\ e^- \longrightarrow M \qquad (2)$$

$$M + NO_3^- \longrightarrow MO + NO_2^- \qquad (3)$$

where reduction to the metal is followed by the rapid oxidation of the deposited metal phase by the nitrate melt (7, 11-13, 16). Similar reactions can be written for monovalent and trivalent metal ions such as Tl^+ and In^{+++}.

A completely different reaction mechanism yielding the same final products is given by

$$(MONO_2)^+ + 2\ e^- \longrightarrow MO + NO_2^- \qquad (4)$$

where the NO_3^- ion in the $(MONO_2)^+$ nitrato complex is the actual substance reduced in the eletrochemical reaction (18). Reduction to the free metal never occurs for this mechanism since electrons, rather than metal ions, transfer the charge across the double layer. Furthermore, the O-N bond scission occurs directly in the electrochemical step rather than by the chemical reaction of the nitrate ion with the deposited metal. A possible stepwise mechanism for this reaction is given by

$$(MONO_2)^+ + e^- \longrightarrow MO + NO_{2(ads)} \qquad (5)$$

$$NO_{2(ads)} + e^- \longrightarrow NO_2^- \qquad (6)$$

with the first electron transfer being the slow step. The strong electric field of the metal ion aids both the electron transfer and the rupture of the O-N bond in the initial step.

EXPERIMENTAL

The electrochemical cell was constructed from Pyrex glass tubing (3.2 cm diameter and 48 cm length) with a design similar to that described in a previous study (19). The platinum working electrode was in the form of a wire sealed in glass. The geometrical area varied somewhat due to the use of different electrodes as well as periodic flame treatments to ensure a good seal, but the area was usually about 0.1 - 0.2 cm^2 (0.09 cm diameter). For exhaustive electrolysis studies, a large platinum sheet electrode (A = 13 cm^2) was used. Electrodes consisting of Au, Ni, Ag, Mo and Cu were also sealed in glass and trimmed to give areas close to 0.1 cm^2. The mercury and amalgam electrodes were contained in a cup constructed from glass tubing bent into a U-shape at the end (0.5 cm diameter, A = 0.2 cm^2). A platinum wire sealed in the tubing provided electrical contact with the mercury. The counter electrode consised of a platinum wire coil at the bottom of the cell. All potentials were measured against the $AgNO_3$ (0.1 m)/Ag reference electrode as described elsewhere (19) except that the lower melting $LiNO_3$-KNO_3 eutectic was used as the solvent. Electrochemical measurements were made with the cell placed in a fluidized sand bath (Tecam) where the temperature was controlled within ±3°C and monitored with a chromel-alumel thermocouple digital thermometer (Fluke 2165A).

The analytical reagent grade nitrate salts (Mallinckrodt) used in the cell were dried under vacuum at 130°C for several days. In each experiment, 22.0 g KNO_3 and 11.0 g $LiNO_3$ were added to the cell to give the eutectic melt (X_{KNO_3} = 0.58, mp = 124°C). The electrochemical cell was always soaked in concentrated nitric acid, rinsed well with deionized water and acetone (spectrophotometry suitable), baked dry with a heat gun, and then baked again in the sand bath prior to adding the nitrate salts. The bubbling of helium gas through the molten salt in the cell at 330°C for at least 3 hours was used to remove any residual water. This helium (99.995%, oil and water-vapor free) was passed through indicating Drierite and two tubes of P_2O_5 (Aquasorb, Mallinckrodt) and a tube filled with fiberglass before being admitted into the nitrate melt. The helium was then exhausted from the cell through another P_2O_5-filled tube and an oil-bubbler to prevent any backflow of atmospheric water vapor. The helium flow continued throughout the experiments except during measurements requiring mass transport by diffusion such as cyclic voltammetry whereupon both the sand bath and the helium flow were turned off to give a quiescent solution.

The salts used in the study of the effects of added metal ions were $AgNO_3$ (Mallinckrodt, Analytical Reagent), $Pb(NO_3)_2$ (Baker, Analyzed Reagent), $Cd(NO_3)_2 \cdot 4\ H_2O$ (Mallinckrodt, Analytical Reagent), $In(NO_3)_3$ (Alfa, 99.99%), $ZnCl_2$ (Matheson, Coleman, and Bell, Reagent) and TlCl (Fairmount, CP). Both $Pb(NO_3)_2$ and $Cd(NO_3)_2 \cdot 4\ H_2O$ were dried in a vacuum oven for several days at 130°C. The weight loss of $Cd(NO_3)_2 \cdot 4\ H_2O$ corresponded closely to that expected for the loss of all water molecules. All salts were dried in the melt by bubbling helium for 15-20 minutes before making the electrochemical measurements. No evidence for any water wave was ever observed under these conditions.

Experimental measurements invloved the use of a potentiostat/galvanostat (PAR 173) equipped with a digital coulometer plug-in (PAR 179). In potential scan studies, a programmer was also used (PAR

175). Results were monitored with an X-Y recorder (HP-7047A) and occasionally also with a digital oscilloscope (Nicolet Model 4562). The reproducibility of the potential scan experiments was improved by bubbling helium through the melt for several minutes between successive potential sweeps followed by a waiting time of 30 seconds at the initial potential before beginning another sweep. Anodic treatments of the platinum electrode were avoided since they introduced platinum ions into the melt that increased the cathodic background currents. The background currents shown in the figures are those measured just prior to the study of interest. Potential scan rates were generally 50 mV/s.

In the attempted deposition of cadmium into mercury, the working electrode consisted of a pool of mercury at the bottom of the cell (76.27 g Hg, $A = 7\ cm^2$) while a platinum coil near the top of the melt was used as the counter electrode. The atomic absorbance analysis of the mercury cathode was performed by dissolving 0.5 g in nitric acid and diluting to 100 mL with deionized water. A Perkin-Elmer 303 Atomic Absorption Spectrophotometer was used for the analysis of cadmium at 228.80 nm.

RESULTS

Cyclic voltammetric studies of reactions involving cadmium ions in molten $LiNO_3$-KNO_3 are shown in Fig. 1. For the platinum electrode, the addition of 0.02 m $Cd(NO_3)_2$ to the melt at 350°C results in a significant increase in the cathodic current and gives a new peak characterized by Ip = 2.35 mA and Ep = -0.46 V vs. Ag^+ (0.1 m)/Ag. The current remains cathodic over a considerable portion of the reverse sweep in theanodic direction. At potentials positive to the Ag^+/Ag reference, largeanodic peaks appear that are readily explained in terms of Eq. 4 by the oxidation of nitrite ions and cadmium oxide, i.e.,

$$NO_2^- \longrightarrow NO_2\uparrow + e^- \tag{7}$$

$$CdO \longrightarrow Cd^{++} + 1/2\ O_2\uparrow + 2\ e^- \tag{8}$$

The use of a cadmium wire electrode in the same melt containing the added $Cd(NO_3)_2$ yields an open-circuit potential of -0.76 V at 310°C (mp Cd = 321°C) and sharply increasing currents in either the anodic or cathodic direction from this reversible potential (Fig. 1). These observations are consistent with the kinetic and thermodynamic properties expected for the reversible electrode reaction

$$Cd(NO_3)_2 + 2\ e^- \rightleftharpoons Cd + 2\ NO_3^- \tag{9}$$

involving the reduction of cadmium ions to the metal.

Studies of 0.02 m $Cd(NO_3)_2$ in molten $LiNO_3$-KNO_3 at 180°C displayed in Fig. 2 show a double cathodic peak beginning near -0.5 V. Despite the much lower temperature that should greatly decrease the corrosion rate, there is no hint of any reversible anodic peak to suggest the deposition of cadmium metal. Investigations of a Cd(Hg) amalgam electrode (X_{Cd} = 0.01) yielded open-circuit potentials significantly more negative than the cathodic peak. The addition of 1.0 g LiCl (0.7 m) to break down the passivating oxide film that forms on the amalgam surface gave even more negative potentials and steeper $\delta I/\delta E$ slopes that reflect faster kinetics. The Cd(Hg) amalgam electrode was sufficiently stable in the $LiNO_3$-KNO_3 + LiCl melt to maintain an open-circuit potential of -1.033 ± 0.001 V for 5-10 minutes. This is close to the reported standard potential at 450 K (177°C) of E^0 = -0.998 V vs. Ag^+ (1.0 m)/Ag for the Cd^{++}/Cd electrode in $LiNO_3$-KNO_3 (4, 20).

The stability of any cadmium metal deposited from nitrate melts could be greatly enhanced by the use of a mercury cathode. A Cd(Hg) amalgam would be formed as the deposited metal diffused into the mercury. Experimental details and atomic absorbance analysis results are given in Table I for a long-term, constant current electrolysis of $Cd(NO_3)_2$ in molten $LiNO_3$-KNO_3 at 180°C. Theoretically, this study would have given an amalgam containing 4880 ppm Cd if the only reaction at the cathode was metal deposition. Quenching the melt and washing away the salt, followed by atomic absorbance analysis of the mercury cathode showed less then 1 ppm Cd. This was practically the same as the analysis of the stock mercury that was never subjected to electrolysis. The open-circuit voltage measurement of 0.03 V following electrolysis also showed that there was not any cadmium amalgam formation. This experiment provides concrete evidence that the electrode reaction was not the reduction of cadmium ions to cadmium metal. The actual electrode reaction involves the reduction of $(CdONO_2)^+$ nitrato complexes to CdO as represented by Eq. 4. The dark brown precipitate of CdO that formed during the electrolysis was readily visible.

Cyclic voltammetric studies of two concentrations of lead ions in molten $LiNO_3$-KNO_3 at 160°C are shown in Fig. 3. The irreversibility of the new cathodic peaks produced by the additions of $Pb(NO_3)_2$ indicates that the electrode reaction involves the reduction of nitrate ions in $(PbONO_2)^+$ nitrato complexes (Eq. 4). At higher concentrations of $Pb(NO_3)_2$, two distinct cathodic peaks are observed. All anodic peaks can be explained by the oxidation of nitrite ions and lead oxide. Previous studies using very fast scan rates (1000 V/s) gave no indication for the deposition of lead in molten nitrates (18).

For comparisions, Fig. 4 shows a cyclic voltammetric study of 0.02 m $AgNO_3$ in molten $LiNO_3$-KNO_3 at 180°C. Similar to higher temperature investigations of $AgNO_3$ in nitrate melts (1-3, 18), the cathodic and anodic waves begin at about the same potential (near -0.1 V). The sharply increasing currents near the reversible potential are typical for reversible reactions involving metal depositions. The deposition of silver significantly increases the real surface area of the platinum electrode and results in large capacity and solvent reduction currents. More normal currents are observed at positive potentials following the anodic stripping of the silver deposits from the platinum electrode. None of these distinctive features for metal deposition are seen in Figs. 1-3.

Results for 0.02 m and 0.04 m additions of $ZnCl_2$ to $LiNO_3$-KNO_3 at 180°C are given in Fig. 5. The Zn^{++} additions produce a broad cathodic wave that begins near -0.1 V. Two cathodic peaks are visible at the higher concentration. Additions of KCl to $LiNO_3$-KNO_3 at 180°C in a separate experiment shows that the anodic wave near 0.8 V is largely due to the oxidation of chloride ions. The potential scans give no evidence for any deposition of zinc metal, hence the cathodic wave is the reduction of the $(ZnONO_2)^+$ nitrato complex as expressed in Eq. 4. Studies using both a zinc electrode ($A = 0.3$ cm^2) and a Zn(Hg) amalgam electrode ($X_{Zn} = 0.05$) show that the Zn^{++}/Zn electrode reaction occurs at potentials significantly more negative than the cathodic waves produced by the $ZnCl_2$ additions. The open-circuit potential of -1.30 V measured for the Zn^{++}/Zn electrode is close to that reported by other investigators (4, 20).

Investigations of 0.02 m TlCl in $LiNO_3$-KNO_3 at 180°C are shown in Fig. 6. There is no evidence for the deposition of any thallium metal prior to the reduction of the melt near -1.1 V. However, a slight increase in the cathodic current near -1.0 V indicates possible reduction of the neutral $TlONO_2$ nitrato complex to TlO^- and NO_2^-. In aqueous solutions, E^0 for Tl^+/Tl is -1.136 V at 25°C vs. Ag^+/Ag while in molten $LiNO_3$-KNO_3 at 177°C, $E^0 = -1.251$ V (4, 20). Extending the cathodic scan gave evidence for the Tl^+/Tl electrode reaction in $LiNO_3$-KNO_3 near -1.2 V, but this reaction is largely obscured by solvent reduction. The major current increases resulting from the TlCl addition are found at positive potentials (Fig. 6) and may involve both the Cl^-/Cl_2 and the Tl^+/Tl^{+++} electrode reactions in molten nitrates. The cyclic voltammogram suggests that reversible couples are involved. In aqueous solutions, E^0 is 0.46 for Tl^+/Tl^{+++} and 0.5604 V for Cl^-/Cl_2, both given versus the standard potential for Ag^+/Ag.

The cyclic voltammetric study of 0.02 m $In(NO_3)_3$ in LiNO-KNO_3 at 180°C presented in Fig. 7 is very unusual with respect to the complete absence of any change in the anodic current. The addition of In^{+++} produces a broad cathodic wave that begins near 0.0 V, but the anodic scan at positive potentials is nearly identical to the background trace. A possible explanation is the single electron transfer reaction

$$(InONO_2)^{++} + e^- \longrightarrow InO^+ + NO2\uparrow \qquad (10)$$

to directly form InO^+ and NO_2 gas. There would be no NO_2^- ions or insoluble oxide produced to support any new anodic reactions.

Exhaustive electrolysis studies of $In(NO_3)_3$ in molten $LiNO_3$-KNO_3 at 180°C using a large platinum electrode in rapidly stirred solutions support the concept of the transfer of only one electron per indium ion in the cathodic reaction. Results for a constant current study are given in Fig. 8. Five experiments using both constant current and potentiostatic coulometry gave an average electron yield per indium ion of 0.76 ± 0.23. The major experimental errors in these coulometry experiments such as loss of material, decomposition of $In(NO_3)_3$ to the oxide, poor solubility and inadequate mass transport would all lead to smaller electron yields.

The investigation of other electrode materials showed that the cathodic wave produced by the 0.02 m $Pb(NO_3)_2$ addition to molten $LiNO_3$-KNO_3 at 180°C could also be observed at about the same potential on Au, Ag, Cu, and Hg electrodes. However, no reduction wave was seen when Ni or Mo electrodes were used. Both of these metals show significant passivation in molten nitrates. It seems likely that the oxide film on passivated metals may hinder the absorption and reaction of $(PbONO_2)^+$ and other nitrato complexes.

DISCUSSION

The errors in the literature relating to the reduction of metal ions in molten nitrates could have been avoided by careful consideration of the thermodynamics of the reactions. Table II presents both experimental and theoretical standard electrode potentials near 180°C in the $LiNO_3$-KNO_3 melt for the metal ions considered in this study. Experimental values were converted to unit activities by use of the Nernst equation and reported with reference to the standard Ag^+(1.0 m)/Ag electrode (4, 20). Details of the theoretical thermodynamic calculations are given elsewhere (21, 22). The reversible electrode potentials measured for the Cd and Zn electrodes (Figs. 1, 2, and 4) are reasonably consistent with reported E^0 values of other investigators as shown in Table II. It is interesting to note that E^0 valves for metal ion/metal reactions in nitrate melts do not differ widely from those in aqueous solutions (20).

Studies of calcium, magnesium, lithium, zinc, and other metals in molten nitrates have shown that the rate of the anodic reactions are limited mainly by passivating oxide films (19, 21, 23). High current densities are possible when passivating film effects are minimized. Similarly, the electro-deposition of metals from nitrate melts should exhibit fast kinetics controlled mainly by mass transfer in the absence of passivating films. For the Cd electrode results in Fig. 1, $(\delta I/\delta E)_T$ = 120 mA/V near the reversible potential, hence i_o = 15 mA/cm^2. The slowly increasing cathodic current of the new wave that begins near 0.0 V when 0.02 m $Cd(NO_3)_2$ is added to the melt reflects the slow kinetics expected for the reduction of the nitrate ion in the nitrato complex. Similarly, the $Cd^{++}/Cd(Hg)$ and Zn^{++}/Zn reactions displayed in Figs. 2 and 4 show much faster kinetics than the waves resulting from the reduction of the nitrato complexes.

The nitrate group is a versatile ligand and numerous modes of coordination with metal ions have been found for nitrato complexes as shown by the work of C. C. Addison and others (24, 25). Electrostatic effects such as the change-to-size ratios of metal ions can also play a role in the reduction of nitrate melts (18, 26, 27). Another concept is that metal ions act as Lux-Flood acids (oxide ion acceptors) in nitrate melts (28, 29). These concepts are interrelated in that some type of interaction of the metal ion with the nitrate ligand facilitates its reduction to form the metal oxide. In many instances, especially at the higher temperatures, metal ions can react directly with the nitrate melt to form the metal oxide even without the aid of any electrochemical reaction (18, 30).

Multiple cathodic peaks such as those seen in Fig. 2 and 3 are often observed in mixed nitrate melts such as $LiNO_3$-$NaNO_3$-KNO_3 (5) or $Ba(NO_3)_2$-$NaNO_3$ (12) where the cations differ considerably in their charge-to-size ratios. Therefore, nitrato complexes of different energy states may exist depending upon the melt cation that they are associated with. For example in Fig. 2, $(CdONO_2)^+\cdots Li^+$ would be somewhat more easily reduced than $(CdONO_2)^+\cdots K^+$. Only a single cathodic peak is observed for $Pb(NO_3)_2$ or $Cd(NO_3)_2$ additions to either molten $LiNO_3$ or KNO_3 at higher temperatures (18). The existence of two nitrate groups in different energy states has been proposed for $Ba(NO_3)_2$-KNO_3 melts (31).

Numerous electrochemical determinations of diffusion coefficients in nitrate melts have been reported (5, 7-11, 13, 14, 17, 32). The use of this data presents a problem since it is the nitrate ligand and not the metal ion that is reduced. The diffusion coefficient should be assigned to the nitrato complex rather than simply to the metal ion since the size of the diffusing particle is largely determined by the NO_3^- ligand.

Nitrato complexes may also be involved in the electrochemical reactions of water in nitrate melts. The water wave in molten nitrates is unusual since water is not reduced to hydrogen gas. Instead, this reaction involves the reduction of the nitrate ion to form nitrite and hydroxide ions (33, 34), i.e.,

$$H_2O + NO_3^- + 2\ e^- \longrightarrow NO_2^- + 2\ OH^- \qquad (11)$$

The mechanism for this reaction has been a source of considerable controversy (33-36). However, this reaction can be simply explained by the formation of nitrato complexes with protons

$$H_2O + NO_3^- \rightleftharpoons HONO_2 + OH^- \tag{12}$$

$$HONO_2 + 2\ e^- \longrightarrow NO_2^- + OH^- \tag{13}$$

and the scission of the O-N bond in the electron-transfer step. The water molecules do not actually undergo any reduction. This is analogous to the reduction mechanism proposed for nitrato complexes of metal ions except that H^+ acts as the complexing cation. In molten nitrates, the water wave is observable on Pt, Ir, Ag, and Au electrodes but not on Ni electrodes (27). Thus, the effect of the electrode material for the water wave is very similar to that for the reduction of nitrate complexes of metal ions. Protons are similar to metal ions in that they can function as a Lux-Flood acid in molten nitrates.

CONCLUSIONS

The irreversible cathode waves produced by the addition of Cd^{++}, Pb^{++}, Zn^{++}, Tl^+, and In^{+++} to nitrate melts are due to the reduction of nitrato complexes rather than the metal ion. The actual reduction of these metal ions are fast, reversible reactions that occur at more negative potentials consistent with the kinetic and thermodynamic properties expected for such reactions.

REFERENCES

1. M. H. Miles, G. E. McManis, and A. N. Fletcher, J. Electrchem. Soc., 131, 2075 (1984).

2. T. Visan, D. P. Geana, and S. Sternberg, Rev. Roum. Chim., 21, 1153 (1976).

3. G. J. Hills, D. J. Schiffrin, and J. Thompson, Electrochim. Acta, 19, 657 (1974).

4. J. A. Plambeck in "Encyclopedia of Electrochemistry of the Elements," Vol. 10, pp. 165-232, A. J. Bard, Ed., Dekker, Inc., New York (1976).

5. M. Steinberg and N. H. Nachtrieb, J. Amer. Chem. Soc., 72, 3558 (1950).

6. J. E. B. Randles and W. White, Z. Elektrochem. Ber. Bunsenges. Physik. Chem., 59, 666 (1955).

7. D. Inman and J. O'M. Bockris, J. Electroanal. Chem., 3, 126 (1962).

8. Yu. K. Delimarskii and G. V. Shilina, Elektrokhimiya, 1, 532 (1965)

9. D. Inman, D. G. Lovering, and R. Narayan, Trans. Faraday Soc., 63, 3017 (1967).

10. M. Francini and S. Martini, Z. Naturforsch., 23a, 795 (1968).

11. G. Mamantov, J. M. Strong, and F. R. Clayton, Jr., Anal. Chem., 40, 488 (1968).

12. W. K. Behl and H. C. Gaur, J. Electroanal. Chem., 32, 293 (1971).

13. S. Casadio, A. Conte, and F. Salvemini, Electrochem. Acta, 16, 1533 (1971).

14. M. V. Susiê, D. A. Markovic, and N. N. Hercigonja, J. Electronal. Chem., 41, 119 (1973).

15. M. Saito and T. Miura, Bull. Chem. Soc. Japan, 50, 1347 (1977).

16. V. Jiamsakul, Ph.D. Dissertation, University of Southampton (July 1978).

17. D. G. Lovering and R. M. Oblath, J. Electrochem. Soc., 127, 1997 (1980).

18. M. H. Miles, G. E. McManis, and A. N. Fletcher, Proc. Electrochem. Soc., 84-2 (Molten Salts), 662 (1984).

19. M. H. Miles, D. A. Fine, and A. N. Fletcher, J. Electrochem. Soc., 125, 1209 (1978).

20. G. A. Mazzocchin, G. G. Bombi, and M. Fiorani, Ric. Sci., 36, 338 (1966).

21. M. H. Miles, G. E. McManis, and A. N. Flecher, Electrochim. Acta, 30, 889 (1985).

22. A. K. Adya and H. C. Gaur, Indian J. Chem., 12, 748 (1974).

23. M. H. Miles, J. Appl. Electrochem, 11, 325 (1981).

24. C. C. Addison, N. Logan, S. C. Wallwork, and C. D. Garner, Quart. Revs., 25, 289 (1971).

25. N. N. Greenwood and A. Earnshaw, "Chemistry of the Elements," pp. 541-544, Pergamon Press, Oxford (1984).

26. A. N. Fletcher, M. H. Miles and M. L. Chan, J. Electrochem. Soc., 126, 1496 (1979).

27. M. H. Miles and A. N. Fletcher, J. Electrochem. Soc., 127, 1761 (1980).

28. G. G. Bombi and M. Fiorani, Talanta, 12, 1053 (1965).

29. A. Baraka and R. M. S. Baraka, J. Appl. Electrochem., 14, 305 (1984).

30. N. B. Singh and S. P. Pandey. Thermochim. Acta, 67, 147 (1983).

31. D. A. Tkalenko and N. A. Chmilenko, Elektrokhimiya, 18, 192 (1982).

32. G. J. Janz, C. B. Allen, N. P. Bansal, R. M. Murphy, and R. P. T. Tomkins, "Physical Properties Data Compilations Relevant to Energy Storage. II. Molten Salts: Data on Single and Multicomponent Salt Systems," pp. 132-166, NSRDS-NBS 61, Part II, U.S. Government Printing Office, Washington, DC (1979).

33. D. G. Lovering, R. M. Oblath and A. K. Turner, J. Chem. Soc. Chem. Comm., 673 (1976).

34. P. G. Zambonin. E. Desimoni, F. Palmisano, and L. Sabbatini, J. Electroanal. Chem., 161, 31 (1984).

35. P. G. Zambonin, V. L. Cardetta and G. Signonile, J. Electroanal. Chem., 28, 237 (1970).

36. S. H. White and U. M. Twardoch, Proc. Electrochem. Soc., 84-2 (Molten Salts), 392 (1984).

TABLE I. Atomic absorbance analysis results for the mercury cathode used in the constant current reduction of $Cd(NO_3)_2$ in the $LiNO_3$-KNO_3 melt.[a]

Reaction	Theoretical (ppm Cd)	Experimental (ppm Cd)
$Cd^{++} + 2\ e^- \rightarrow Cd(Hg)$	4880	<1
$(CdONO_2)^+ + 2\ e^- \rightarrow CdO + NO_2^-$	0	<1

[a] Experimental conditions: I = 30 mA for 25,600 seconds, T = 180°C, E ≈ −0.5 ± 0.1 V vs. Ag^+/Ag, Hg (76.27 g, A = 7 cm^2), $LiNO_3$ (11 g), KNO_3 (22 g), $Cd(NO_3)_2$ (0.76 g).

TABLE II. Experimental and theoretical standard potentials in molten $LiNO_3$-KNO_3 at 180°C. For comparison, standard potentials in aqueous solutions at 25°C are also listed. All potentials are referred to the standard silver electrode.

Couple	E^0, V (Experimental)	E^0, V (Theoretical)	E^0, V (Aqueous, 25°C)
Li^+/Li	-3.535	-3.544	-3.83
Zn^{++}/Zn	-1.28 -1.32[b]	-1.22[a]	-1.563
Tl^+/Tl	-1.251[b]	-1.236	-1.136
Cd^{++}/Cd	-1.091 -0.998[b]	-1.08[a]	-1.203
Pb^{++}/Pb	-0.93[b]	-1.05[a]	-0.926
In^{+++}/In	...	...	-1.14

[a] Estimate based on ΔH^0 due to lack of thermodynamic data.
[b] See (4, 20).

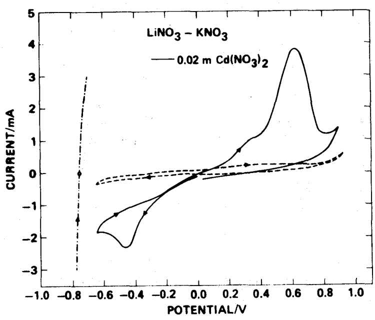

Fig. 1. Cyclic voltammetric studies of 0.02 m $Cd(NO_3)_2$ at 50 mV/s in molten $LiNO_3$-KNO_3 using Pt and Cd wire electrodes (A = 0.2 cm^2) at 350 and 310°C, respectively.

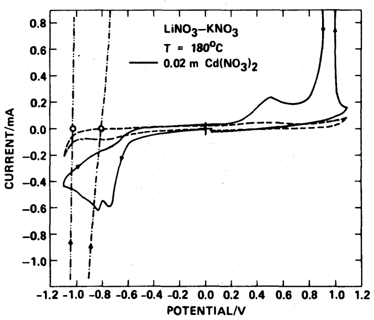

Fig. 2. Cyclic voltammogram at 50 mV/s for 0.02 m $Cd(NO_3)_2$ in molten $LiNO_3$-KNO_3 at 180°C using a Pt electrode (A = 0.15 cm^2). Similar studies using a Cd(Hg) amalgam electrode (A = 0.2 cm^2, X_{Cd} = 0.01) are shown before and after the addition of 1.0 g LiCl.

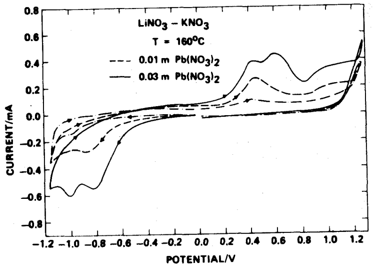

Fig. 3. Cyclic voltammograms at 50 mV/s for $Pb(NO_3)_2$ additions to molten $LiNO_3$-KNO_3 at 160°C using a Pt electrode (A = 0.2 cm^2). Background current is given by the dash-dot line.

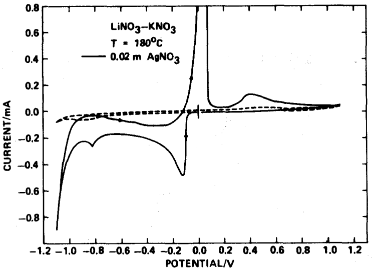

Fig. 4. Cyclic voltammetric study at 50 mV/s for 0.02 m $AgNO_3$ in molten $LiNO_3$-KNO_3 at 180°C using a Pt electrode (A = 0.1 cm^2).

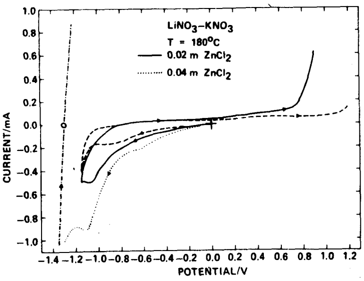

Fig. 5. Cyclic voltammograms at 50 mV/s for $ZnCl_2$ additions to molten $LiNO_3$-KNO_3 at 180°C using a Pt electrode (A = 0.1 cm^2). Results using a zinc electrode (A = 0.3 cm^2) in 0.04 m $ZnCl_2$ at 50 mV/s are shown by the dot-dash line.

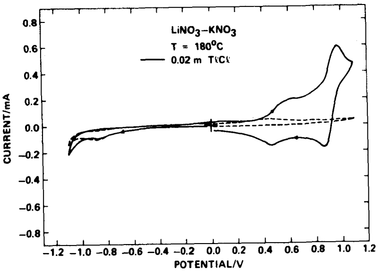

Fig. 6. Cyclic voltammetric study at 50 mV/s for 0.02 m TlCl in molten $LiNO_3$-KNO_3 at 180°C using a Pt electrode (A = 0.1 cm^2).

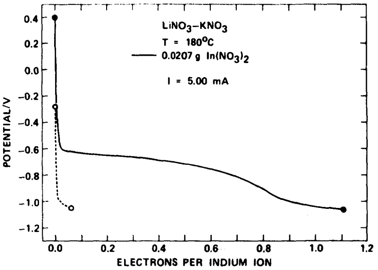

Fig. 8. Constant current exhaustive electrolysis study of $In(NO_3)_3$ in molten $LiNO_3$-KNO_3 at 180°C using a large Pt sheet electrode (A = 13 cm^2). Dashed line shows results for an identical study before $In(NO_3)_3$ was added.

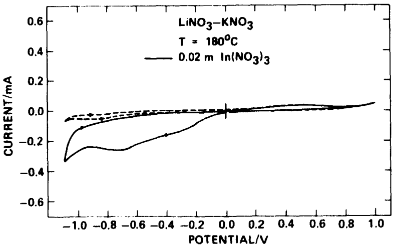

Fig. 7. Cyclic voltammetric study at 50 mV/s for 0.02 m $In(NO_3)_3$ in molten $LiNO_3$-KNO_3 at 180°C using a Pt electrode (A = 0.1 cm^2).

DOI: 10.1149/198601.0248PV

VOLTAMMETRIC STUDIES OF MAGNESIUM IN CHLORIDE MELTS

S. Duan, P.G. Dudley and D. Inman

Dept. of Physical Chemistry, Beijing University of Iron and
Steel Technology, Beijing, China.
Dept. of Metallurgy and Materials Science, Imperial College of
Science and Technology, London SW7 2BP, U.K.

ABSTRACT

The electrochemical reduction of Mg^{2+} ions in NaCl-KCl eutectic melt at temperatures between 700 and 750°C has been investigated using the techniques of cyclic voltammetry and chronoamperometry. The reduction was studied over the concentration range of 0.05 to 0.22 mol $MgCl_2$/kg. Three working electrode substrates were of interest, platinum and tungsten and the more industrially-applicable stainless steel. The reduction was diffusion-controlled. Diffusion coefficients for Mg^{2+} were calculated at $D = 5.2 \times 10^{-5} cm^2/s$.

The reduction of Mg^{2+} ions and the reoxidation of Mg metal were also studied using the $MgCl_2$-KCl-NaCl (50:30:20 m/o) eutectic melt over the temperature range of 480-510°C by the techniques of cyclic voltammetry and chronoamperometry at a platinum electrode as a function of switching potential. The current-time profiles indicate some effects of electro-nucleation and -growth.

INTRODUCTION

The use of molten salt solvents for the large-scale electrowinning of metals has found its most prominent success with the metals aluminium and magnesium.

During the last few years a sharp increase in the use of Mg has occurred. Indeed it has been reported (1) that by 1985 an annual growth rate of about 5% will have been achieved.

The electrolytic manufacture of magnesium is well established and the historical developments have been described by Eger (2), Kirk-Othmer (3) and Emley (4). The two processes now used were developed by the Dow Chemical Company and by I.G. Farbenindustrie. The main difference between them is that the former accepts a $MgCl_2$ feed prepared from sea water and containing 25% H_2O, whereas the latter operates on dehydrated molten carnallite. A detailed description of the two processes has been given by Krenzke (5). In both types of cell graphite anodes dip into the electrolyte from above; the molten magnesium is diverted upwards by the cathodes in the Dow cell which are very close to the anodes and are cone-shaped, whereas in the IGF cell ceramic spacers between the electrodes separate the products. Some of the sea water feed flashes off as it is added to the melt and reacts with the chlorine to form HCl, so that a pronounced graphite consumption and reduced cathodic efficiency are inevitable.

In both types of cell the electrical consumption is about 18,000 KwH/ton Mg. A reduction of this would significantly reduce the production costs. Recent major technical advances have included development of the cell without a diaphragm, increased current capacity and introduction of the multipolar cell (6). H. Ishizuka (7,8) made improvements by designing the bipolar cell using the $MgCl_2$-NaCl-$CaCl_2$ melt as the electrolyte, leading to a current efficiency of approximately 94% and power consumption of about 8920 KwH/ton Mg. The overall operational efficiency of the process is very dependent on impurities.

Research work involving magnesium chloride has centred principally on two systems.

(a) $MgCl_2$-NaCl-KCl (50:30:20 m/o) (m.p. 396°C), and
(b) $MgCl_2$-KCl (32.5:67.5 m/o) which is close to the eutectic composition which melts at about 410°C. The density of the $MgCl_2$-NaCl-KCl melt does not appear to have been measured but it may be estimated at about 2.0 ± 0.2 kg/l on the basis of the measurement of Silcox and Haendler (9). The anodic and cathodic limiting processes in this melt are chlorine evolution and magnesium deposition. These reactions determine the range of potentials accessible in the melt, ~ 2.7V.

Magnesium metal does not react with these melts and it is possible to obtain stable potentials for the couple Mg(II)/Mg(0). Gaur and Behl (10) have extrapolated their direct measurements on the Mg(II)/Mq(0) couple in $MgCl_2$-NaCl-KCl to give an E_0 (unit mole fraction) value of 1.966V.

The present experiment in China is to use a completely dehydrated $MgCl_2$ feed obtained from sea water. The difficulty in removing the last 25% of H_2O has led to the addition of a ferrous chloride catalyst which leads to a high impurity level as the subsequent removal of the iron ions by pre-electrolysis has met with only limited success.

As part of a programme to determine and quantify the role of iron ion impurities on the magnesium reduction process we have recently reported on the electrochemical reduction and oxidation of Fe^{2+} ions in the $MgCl_2$-NaCl-KCl eutectic melt (11, 12). Voltammetric techniques have been used in the present work to characterise the Mg^{2+} reduction process at different electrode substrates in the $MgCl_2$-NaCl-KCl ternary eutectic melt and dilute solutions of $MgCl_2$ in an NaCl-KCl eutectic solvent.

EXPERIMENTAL

Full details of equipment, chemicals, electrodes and the experimental procedures have been published (11).

Melt purification. Molten salts (in particular hygroscopic salts) require rigorous purification in order to remove hydrolysis products and heavy metal and organic impurities. Various procedures have been developed and adopted to remove these hydrolysis products, i.e. OH^-, O^{2-} employing anhydrous hydrogen chloride or chlorine, vacuum pre-electrolysis, or a combination of these techniques. Heavy metal impurities may be removed by electrolysis. All these treatments are usually completed by filtration through a fine sintered glass frit. A critical review by White (13) discusses the effectiveness of these procedures.

$MgCl_2$-KCl-NaCl eutectic. Anhydrous magnesium chloride was first prepared by the method of Behl and Gaur (14). This method involves the preparation of a double salt with ammonium chloride; $MgCl_2.NH_4Cl.6H_2O$ (ammonium carnallite) which may subsequently be dehydrated and finally decomposed.

Dehydration takes place in the following way:

(i) hexahydrate to tetrahydrate (373 K);
(ii) tetrahydrate to dihydrate (413 K);
(iii)dihydrate to anhydrous salt (433 K).

The procedure was as follows. The double salt ($\sim$ 200 g) was kept in an oven at a temperature of 453 K until dehydration was complete ($\sim$ 12 hrs). The resulting anhydrous magnesium ammonium chloride was transferred to a cylindrical glass vessel and heated in a furnace. The temperature was gradually raised to 623 K over a period of six to eight hours; this treatment decomposed the magnesium ammonium chloride. The hot anhydrous $MgCl_2$ was then transferred to the port of the dry box where it was left to cool under vacuum and finally placed in the dry box where it was mixed with the appropriate quantities of NaCl and KCl.

The $MgCl_2$-KCl-NaCl mixtures were purified by slow vacuum drying and melting, followed by HCl bubbling and pre-electrolysis, followed by filtration through a fine sintered glass frit. The purified melt was subsequently transferred to the dry box. Using this procedure approximately 500 g of eutectic was purified.

RESULTS AND DISCUSSION

Melt purity and electrochemical stability. Cyclic voltammetry was used to check the residual currents. The potential "window" available using the various electrodes is given in Table 1.

In the case of an "inert" electrode the potential range available corresponds to the decomposition limits of the solvent melt; these are the anodic evolution of chlorine and the cathodic deposition of magnesium.

TABLE 1

The potential limits available at VC, W and Pt electrodes in the $MgCl_2$-KCl-NaCl eutectic melt.

Electrode	Anodic limit	Cathodic limit
VC	+1.1V	-1.7V
W	+1.1V	-1.7V
Pt	+0.6-0.7V	-1.7V

The tungsten and vitreous carbon electrodes are considered "inert" as shown in figures 1 and 2. The potential "window" is limited for certain metallic electrodes by the electrode dissolution potential which was found to occur at approximately +0.6V with respect to the Ag(I)/Ag reference electrode as shown in figure 3.

Because of the very long time ($\sim$15 days) required to purify the $MgCl_2$-KCl-NaCl eutectic melt, some initial experiments employed a less purified melt. In this case a pre-purified batch of $MgCl_2$ (method unknown) which had been stored in the dry box was mixed with the appropriate amounts of pre-dried Analar NaCl and KCl, vacuum dried and finally vacuum melted. A typical cyclic voltammogram obtained at a platinum electrode in this melt is shown in figure 4. Clearly several major impurities are present: the first at -0.5V corresponds to the reduction of Fe(II) and a further cathodic process occurs at -1.25V.

The melt was subsequently electrolysed potentiostatically at -1.4V (vs. ref.) between two carbon electrodes until the current became very low. Sufficient purity was thus obtained for electrochemical investigations to proceed.

The remaining melt was vacuum electrolysed at 2.2V between a graphite anode and a stainless steel cathode for four days but even so in situ electrolysis was found to be necessary.

Surprisingly, the "normally" purified melt was found to exhibit quite a large residual current, see for example figure 5. However, no definite processes could be identified and so in situ electrolysis with a graphite anode and a cathode potentiostatically controlled at − 1.4V, was usually carried out overnight.

Figures 1, 2, 6 and 7 show typical cyclic voltammograms obtained at various electrodes in this melt, indicating the degree of electrochemical purity normally achieved.

The in situ electrolysis at potentials very close to the Mg reduction potential became a standard practice. This is a particularly useful procedure for studies of redox systems at very cathodic potentials.

The reduction of Mg^{2+} in the NaCl-KCl eutectic. The NaCl-KCl eutectic was used in an attempt to characterise the electrochemical reduction of Mg^{2+} ions (added as anhydrous $MgCl_2$) to yield a liquid magnesium product. The reduction process was studied over the concentration range of 0.05 to 0.22 mol $MgCl_2$/kg and within the temperature range of 700-750°C. Three electrode substrates were of interest, platinum, tungsten and stainless steel.

The natures and shapes of the typical voltammograms obtained for the reduction of Mg^{2+} at the concentration 0.164 mol/kg at 725°C for each of the substrates employed, are shown in figures 8, 9 and 10. The well defined voltammograms obtained show clearly the reduction and reoxidation processes.

On platinum, a substrate which can be expected to alloy more readily with the Mg product than for instance tungsten, the cyclic voltammogram does not exhibit the sharp increase in current for the reduction process which would be consistent with the formation of an insoluble product. The rising portion of the cathodic wave obeys the Heyrovsky-Ilkovic relationship (figure 11) and this indicates that the product is soluble. Another notable feature which is absent is the very large reoxidation wave expected for an insoluble metal deposit; on the other hand the ratio of the peak currents is greater than unity which indicates an insoluble product. At the sweep rate used (0.15 V/s) the peak potential for the reduction process was E_p^c = -1.48V and the $E_{\frac{1}{2}}$ value -1.46V.

The value of the potential difference between the peak potentials for the cathodic and reoxidation processes is greater than would be expected for a simple reversible process. Increasing the sweep rate shifts the cathodic peak potential slightly in the cathodic direction while the E_p^a value remains constant.

The cyclic voltammograms obtained for tungsten and stainless steel indicate that the liquid magnesium product is less soluble in the electrode substrate in these cases, as can be seen from figures 9 and 10. The reduction of Mg^{2+} occurs at $E_{\frac{1}{2}}$ = -1.63V on a stainless steel electrode and at $E_{\frac{1}{2}}$ = -1.59V on a tungsten electrode.

The degree of interaction (alloying) of the product with substrate material increases in the series tungsten, stainless steel and platinum. In a similar manner the reversibility of the reduction/reoxidation process decreases in the same series. This is shown by the increase in the $\Delta E = E_p^a - E_p^c$ value.

Plots of the cathodic peak current (I_p^c) versus (sweep rate) were found to be linear with zero intercepts for all concentrations and electrodes used (figure 12) which indicates that the process is diffusion-controlled. Figure 13 shows the cathodic peak current increasing linearly with increasing concentration with a zero intercept, as is to be expected from the Randles-Sevcik equation. A diffusion coefficient value was determined from the slope of this plot. For the particular case of the platinum electrode the value of $D = 5.2\times10^{-5}$ cm²/s is calculated at a temperature of 1000K on the assumption that a soluble product is formed. This value is comparable with the values obtained by Katelnikova et al (15) using chronopotentiometry, i.e. $D_{Mg^{2+}} = 6.24\times10^{-5}$ cm²/s at 1020K.

The current/time profiles obtained as a result of a potential step perturbation were found to obey the Cottrell equation. The linear I versus $t^{-\frac{1}{2}}$ dependency for several applied potentials is shown in figures 14 and 15, which again confirms the diffusion-controlled behaviour.

The reduction of Mg^{2+} in the $MgCl_2$-KCl-NaCl eutectic. The reduction of Mg^{2+} ions and reoxidation of Mg metal on different electrode substrates (platinum, tungsten and stainless steel) was studied using the $MgCl_2$-KCl-NaCl (50:30:20 m/o) eutectic melt over the temperature range 480-510°C. The temperature range is below that of the melting point of magnesium metal. Because of the very negative working voltages used, the solvent was further purified by in situ vacuum pre-electrolysis and by employing a sacrificial electrode in the potentiostatic mode at a potential very close to the cathodic limit. Each working electrode was held initially at a potential of -1.0V, the potential then being swept cathodically to different negative potentials.

The nature of the reoxidation wave(s) was observed as a function of the cathodic switching potential (E_λ) and sweep rate (5-400mV/s). Figure 16 shows the reduction of Mg^{2+} ions and reoxidation of Mg metal at a platinum flag electrode with increasing E_λ. The Mg^{2+} reduction current starts to increase at cathodic potentials of -1.7V with a single reoxidation wave at -1.5V. As the cathodic limiting potential is gradually made more cathodic, the reoxidation peak current increases and the peak potential shifts anodically. At a cathodic potential of -1.8V a second reoxidation wave occurs at -1.59V and its peak current increases rapidly with increasing E_λ (more cathodic). The two reoxidation waves may be attributed to differing magnesium activity states on the platinum substrate. Figure 17 shows that throughout the range of E_λ used, all the magnesium deposited is reoxidised to Mg^{2+} ions.

At a stainless steel rod electrode a single reoxidation wave is observed down to cathodic potentials of -2.0V (figure 18). The total cathodic charge is available on reoxidation as shown in figure 19. It is also interesting to note the effect of increasing scan rate for a given value of E_λ (figure 20). At low sweep rates, 5-60 mV/s, a single maximum reoxidation wave is seen but, as the scan rate increases within this range, the peak current decreases. At scan rates of 100 mV/s and above, the peak current of the now broader reoxidation wave begins to increase and the corresponding peak potential rapidly shifts towards more anodic potentials.

At the inert tungsten electrode the Mg^{2+} reduction current starts to increase at a potential of -1.8V and a single reoxidation wave is observed at a peak potential of E_p^a = 1.64V (figure 21). A large degree of hysteresis is noted. The current/time profiles (figure 22) manifest minor electro-nucleation and -growth effects.

REFERENCES

1. K.E. Woodward Jnr. and E.J. Rudd, J. Electrochem. Soc. <u>127</u>, 251C (1980).
2. S. Eger, Handbuch der Technischen Electrochemie, Band 111, 2nd Edition, 1961, A. Kad. Verlag, Leipzig.
3. Kirk-Othmer (Ed) "Encyclopaedia of Chemical Technology", Interscience, New York, 2nd Edition, 1964.
4. A.S. Emley, "Principles of Magnesium Technology", Pergamon Press Oxford, 1966.
5. F.J. Krenzke in C.A. Hampel (Ed) "The Encyclopaedia of Electrochemistry", Reinhold, New York (1964).
6. T. Ikeshima, presented at the Fifth Int. Conf. on Titanium, Munich, Fed. Republic of Germany, Sept. 10-14, 1984.
7. H. Ishizuka, European Patent 0054527.
8. H. Ishizuka, European Patent 0027016.
9. N.W. Silcox and H.M. Haendler, J. Phys. Chem. 64, 303 (1960).
10. H.C. Gaur and W.K. Behl in "Proceedings of the First Australian Electrochemistry Conference", Sidney-Hobart, 1963, Pergamon Press, Oxford, 1964, p543.
11. S. Duan, P. Dudley and D. Inman, J. Electroanal. Chem. 142, 215 (1982).
12. S. Duan, P. Dudley and D. Inman, to be published.
13. S.H. White in "Ionic Liquids", D. Inman and D.G. Lovering (Eds) Plenum Press, 1980.
14. W.K. Behl and H.C. Gaur, J. Sci. Ind. Res., 20B, 231 (1961).
15. G.A. Katelnikova and P.V. Polyakov, IZV. Vyssh Uchob, Zaved, Tsvet Metal., 118, 153 (1975).

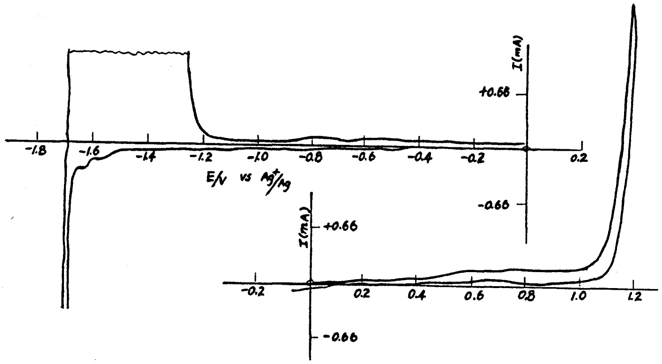

Fig. 1 Typical residual current obtained at W electrode. Melt: fully purified, sweep rate=0.05V/s, A(area)=0.03142 cm^2.

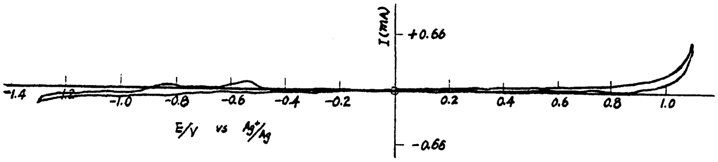

Fig. 2 Typical residual current obtained at a VC electrode. Melt: fully purified, sweep rate=0.05V/s, A=0.049 cm^2.

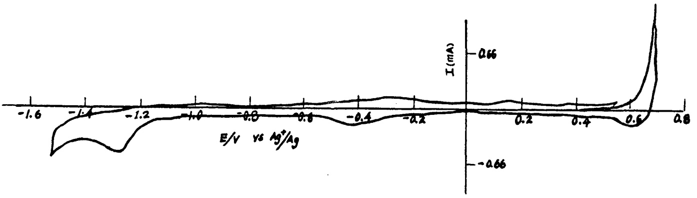

Fig. 3 Typical voltammogram obtained at a Pt electrode illustrating the limiting Pt dissolution potential. Sweep rate=0.05V/s, A=0.4 cm^2.

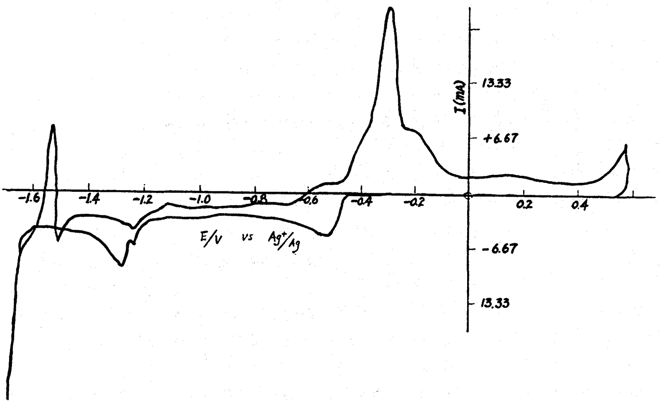

Fig. 4 Residual current obtained at a Pt electrode for a vacuum melted $MgCl_2$-KCl-NaCl mixture, sweep rate=0.05V/s, A=0.4 cm^2.

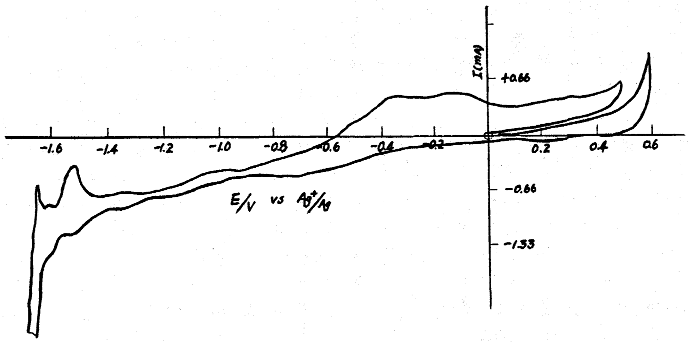

Fig. 5 Residual current for a "normally purified" $MgCl_2$-KCl-NaCl eutectic melt without "in-situ" electrolysis, sweep rate= 0.05V/s, A=0.2 cm^2.

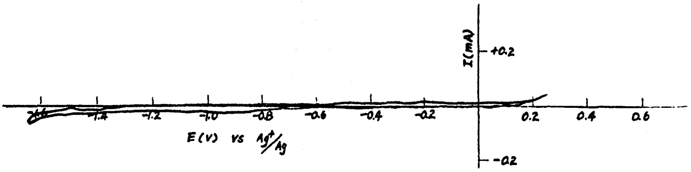

Fig. 6 Residual current obtained at a W electrode. Melt: fully purified plus "in-situ" electrolysis. Sweep rate=0.05V/s, A=0.0314 cm^2.

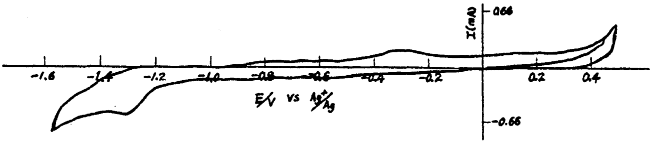

Fig. 7 Residual current obtained at a Pt electrode. Melt: fully purified plus "in-situ" electrolysis. Sweep rate=0.05V/s, A=0.2 cm^2.

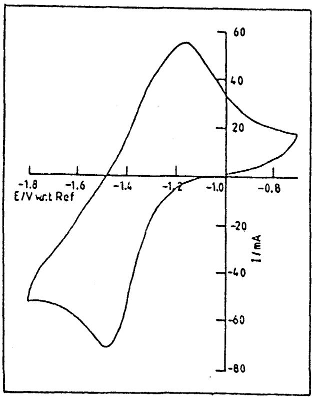

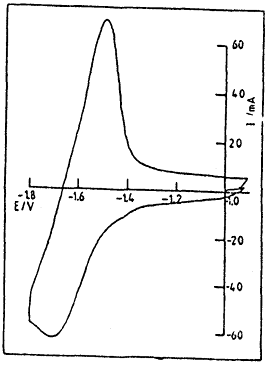

Fig. 8 A typical voltammogram for the reduction of Mg^{2+} at a Pt electrode in a NaCl-KCl melt at 725°C, sweep rate=0.15V/s, A=0.18 cm^2.

Fig. 9 A typical voltammogram for the reduction of Mg^{2+} at a stainless steel electrode in a NaCl-KCl melt at 725°C. Sweep rate=0.15 V/s, A=0.285 cm^2.

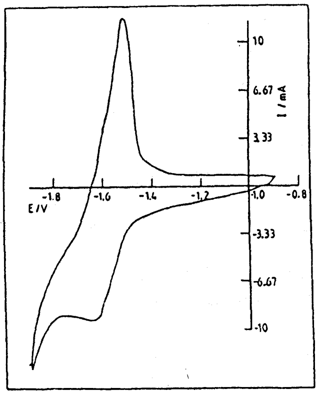

Fig. 10 A typical voltammogram for the reduction of Mg^{2+} at a W electrode in NaCl-KCl melt at 725°C. Sweep rate=0.15V/s, A= 0.0314 cm^2, ($MgCl_2$)=0.164 mol/kg.

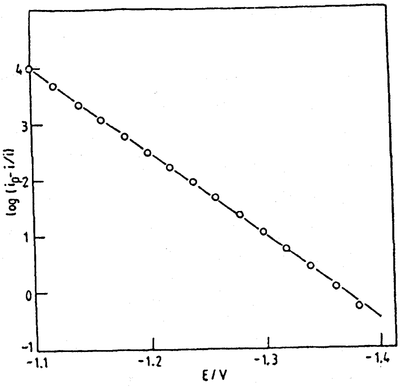

Fig. 11 A plot of log (i_p-i)/i vs E for the reduction of Mg^{2+} at Pt electrode. A=0.18 cm^2, ($MgCl_2$)=0.164 mol/kg.

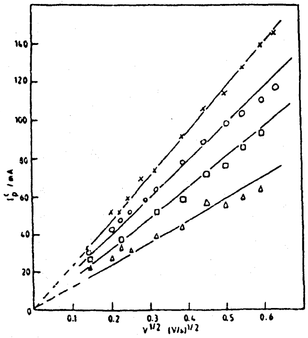

Fig. 12 A plot of the cathodic peak current as a function of (sweep rate)$^{1/2}$ for the reduction of Mg^{2+} at a Pt electrode ($MgCl_2$) =(Δ)0.103; ( )0.164; ( ) 0.187; (x)0.22 mol/kg.

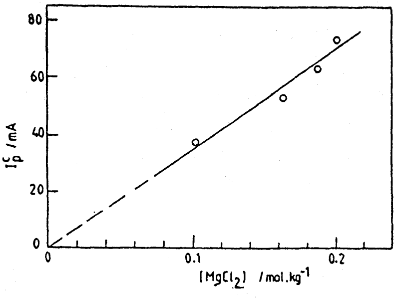

Fig. 13 A plot of the cathodic peak current as a function of ($MgCl_2$) for the reduction of Mg^{2+} at a Pt electrode.

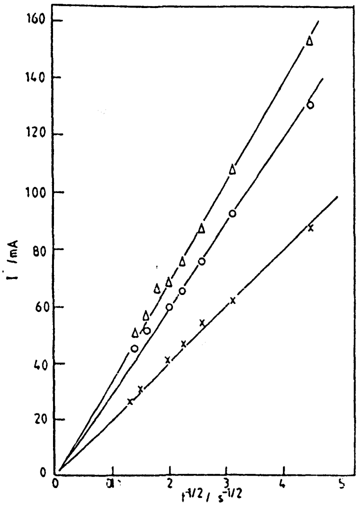

Fig. 14 A plot of I vs $t^{-1/2}$ for the reduction of Mg^{2+} at a Pt electrode for the applied potentials of (x)-1.65V; (0)-1.75V; (Δ)-1.8V; wrt ref. $(MgCl_2)$=0.103 mol/kg.

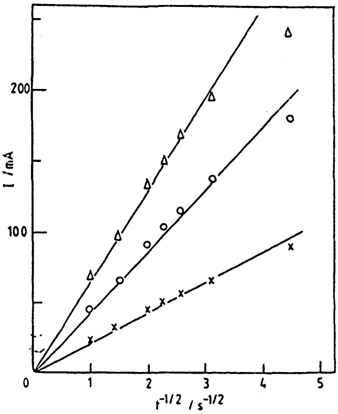

Fig. 15 A plot of I vs $t^{-1/2}$ for the reduction of Mg^{2+} at a stainless steel electrode for the applied potentials of (x)-1.65V; (0)-1.75V; (Δ)-1.80V; $(MgCl_2)$=0.103 mol/kg.

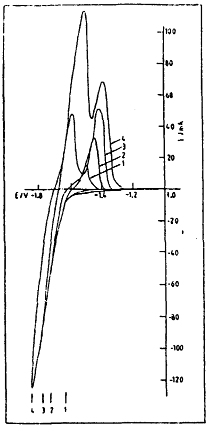

Fig. 16 A typical voltammogram at a Pt electrode as a function of switching potential A=0.2 cm^2.

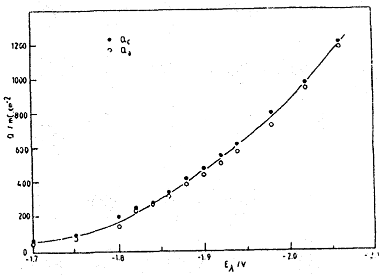

Fig. 17 A plot of the coulombic efficiency as a function of switching potential for the reduction of Mg^{2+} and reoxidation at a Pt electrode, A=0.2 cm^2.

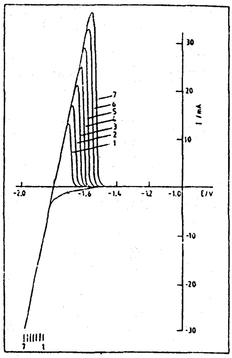

Fig. 18 A typical voltammogram at a stainless steel electrode as a function of switching potential, A=0.4 cm^2.

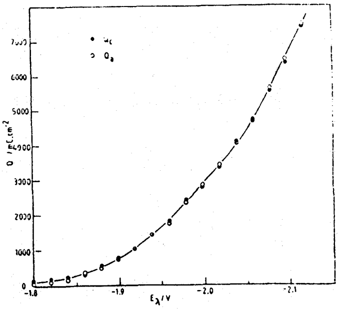

Fig. 19 A plot of the coulombic efficiency as a function of switching potential for the reduction of Mg^{2+} and reoxidation at a stainless steel electrode, A=0.4 cm^2.

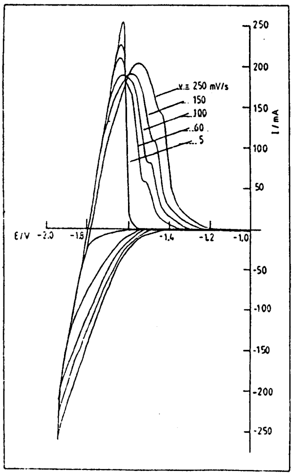

Fig. 20 The effect of sweep rate on the reduction and reoxidation of Mg^{2+} at a stainless steel electrode at E=1.95V; A=0.2 cm^2.

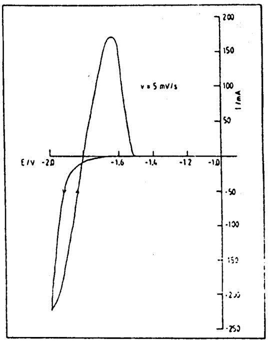

Fig. 21 A typical voltammogram at a W electrode as a function of switching potential, A=0.03 cm^2.

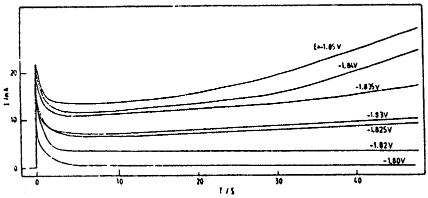

Fig. 22 Typical I-t transients for the reduction of Mg^{2+} in the $MgCl_2$-KCl-NaCl melt at various potentials at a W electrode, A=0.2 cm^2; T=450°C.

DOI: 10.1149/198601.0262PV

MODELS OF HALO-ALUMINATE MELTS

Ernest W. Dewing

Alcan International Limited
P.O. Box 8400
Kingston, Ontario K7L 4Z4 Canada

ABSTRACT

$NaCl-AlCl_3$ melts at ~200°C contain entities such as $AlCl_4^-$ and $Al_2Cl_7^-$, and thermodynamic activities can be accounted for with simple equilibrium models. At much higher temperatures (800-1000°C) $LiF-AlF_3$ mixtures can be represented by

$$2\ LiF + LiAlF_4 \rightleftharpoons Li_3AlF_6,$$

but, contrary to general opinion, the analogous model does not fit the $NaF-AlF_3$ melts. There it is necessary to postulate major amounts of Na_2AlF_5.

In dilute solution in Na_3AlF_6, LiF is present as 'molecules', i.e. long-lived associations of Li^+ and F^- ions.

The implications of dissociation models for diffusion processes are considered. In $LiF-AlF_3$, diffusion coefficients are unusually high, apparently due to the strong gradient of chemical potential associated with the non-ideality. But in $NaCl-AlCl_3$, which is also non-ideal, diffusion coefficients are normal. In that case, the driving force acts only on the $Al_2Cl_7^-$ ions, and not on the $AlCl_4^-$.

INTRODUCTION

It is well known that any experimental data can be represented within their accuracy with a finite number of terms in a series of appropriate form. Energy of mixing data, for example, can be represented by power, or other, series, and such series are very useful for collation and interpolation, but in themselves the values of the coefficients carry no structural implications. A specific structural model can be regarded as significant only when it succeeds in representing the data with fewer parameters than a general series, and if there is some physical evidence (e.g. spectroscopic) to back it up, so much the better.

First, let us look at two models which do work, because we shall need to examine them rather closely to convince ourselves later that certain others do not.

In the case of NaCl-$AlCl_3$, melts the evidence is overwhelming that the equilibrium

$$Cl^- + Al_2Cl_7^- \rightleftharpoons 2AlCl_4^- \qquad (1)$$

exists, and is displaced far to the right. Figure 1 (1) is quite obviously a titration curve with the end-point at $N_{AlCl_3} = 0.5$. What is not so obvious is that Figure 2, for LiF-AlF_3 (2), can be represented as the equilibrium

$$2F^- + AlF_4^- \rightleftharpoons AlF_6^{3-}. \qquad (2)$$

The equilibrium constant is much smaller, and the changes on passing through the stoichiometric composition much less abrupt. At 800°C one parameter represents all the data with a standard deviation of ±9 mV.

Because equilibrium (1) lies so far to the right, the concentration of free Cl^- ions when $N_{AlCl_3} > 0.5$ is negligible, and hence it follows that a_{AlCl_3} (as determined from vapor pressure or electrochemical measurements) should be proportional to $[Al_2Cl_7^-]/[AlCl_4^-]$, or to $(1 - 2N_{NaCl})/(3N_{NaCl} - 1)$ when mole fractions are expressed conventionally in terms of NaCl and $AlCl_3$. Figure 3 (data from (3)) shows that for $N_{AlCl_3} > 0.55$ deviations start to appear (due presumably to neglect of the other species which must appear in very acid melts), but that in the limit of $N_{AlCl_3} \rightarrow 0.5$ the relation is very good. The abrupt step in the titration curve at $N_{AlCl_3} = 0.5$ shows the presence of $AlCl_4^-$; the linearity of the plot in Figure 3 near the origin shows $Al_2Cl_7^-$.

Let us now try similar logic on the data of Figure 2. In this case we are on the basic side of $LiAlF_4$, and close to that composition the excess LiF will be present as Li_3AlF_6, so that

$$a_{LiF} \propto \sqrt{a_{Li_3AlF_6}/a_{LiAlF_4}}$$
$$\propto \sqrt{(\tfrac{1}{2} - N_{AlF_3})/(2N_{AlF_3} - \tfrac{1}{2})} \qquad (3)$$

Figure 4 shows the plot. Again, it is linear and passes through the origin for low deficits of AlF_3. (Note that the AlF_3 liquidus lies at $N_{AlF_3} = 0.425$ at 800°C, so the end of the curve is inaccessible experimentally). Thus we have confirmed that when LiF is added to $LiAlF_4$, Li_3AlF_6 is formed.

We are now in a position to look at sodium cryolite.

THE SYSTEM NaF - AlF_3

Equilibrium (2) has long been used as a model to represent sodium cryolite, but ever since reasonably good activity data became available in 1972 (4) it has been apparent that it simply does not work. At that time a hybrid model involving non-ideal mixing of NaF and $NaAlF_4$ was proposed, but it was not really satisfactory either and it can now be abandoned.

To show that the AlF_6^{3-} model does not work for the sodium system, we have only to plot the equivalent of Figure 4. (The activity data are taken from a revision of the 1972 work, but one would reach the same conclusions with the earlier figures). Figure 5 shows that the line is not straight, even in the limit, which is, in this case, accessible. The curve looks much more like a parabola. Why? Because of the square root in the abcissa. Why is it there? Because we are postulating Na_3AlF_6, which requires the addition of two NaF's to $NaAlF_4$. Suppose instead we postulate Na_2AlF_5. Then

$$a_{NaF} \propto a_{Na_2AlF_5}/a_{NaAlF_4}$$

$$\propto (1 - 2N_{AlF_3})/(3N_{AlF_3} - 1) \qquad (4)$$

Figure 6 shows the resulting plot which is linear. It is offset somewhat from the origin, implying that $NaAlF_4$ itself is dissociated. Obviously some more acid species must exist, since the AlF_3 liquidus occurs at $N_{AlF_3} > 0.5$.

We thus conclude that in the sodium system Na_2AlF_5 must be a major species. To proceed further we use a method introduced by Sterten (5). The activity of a species $mNaF.nAlF_3$ is proportional to

$$\phi = (a_{NaF})^m \cdot (a_{AlF_3})^n, \qquad (5)$$

and we wish to find a set of equilibrium constants, k, such that $\Sigma k_i\phi_i = 1$ at all compositions, i being taken over all the species postulated to exist. We already know that the k value for NaF must be one, or an absurdity is reached in pure NaF, so the condition is $\Sigma k_i\phi_i = 1 - a_{NaF}$, where i is now taken over all species except NaF. Since experimental activities are available, this is a straightforward least-squares regression analysis problem. The results, (Figure 7) are satisfactory; the sum has a standard deviation of $\pm$ 0.02. However, there is one vital condition yet to be fulfilled. The calculation has been done in terms of activities and we have said nothing about compositions; do the postulated species sum to the composition at which they are alleged to occur? They do; the mean difference in N_{AlF_3} is 5×10^{-5} with a standard deviation of ± 0.006.

Figure 7 is quite different from any work which has been presented in the past. Na_2AlF_5 is a major, and indeed dominant, species. The calculations are remarkably clear; but is there any physical evidence to back them up?

The answer is yes and no. Raman spectra (6,7) can be interpreted solely in terms of AlF_4^- and AlF_6^{3-}. But Holm (8) has demonstrated a major anomaly in the heat capacity of liquid NaF-AlF_3 mixtures. Figure 8 is based on a re-calculation of the original data (8-10) and the uncertainties are standard errors. The maximum lies near $N_{AlF_3} = 0.33$ (i.e. Na_2AlF_5). The anomaly is undoubtedly due to the heat absorbed by the dissociation of a compound as the temperature is raised. Presumably the compound is Na_2AlF_5.

In the absence of spectrocopic proof for Na_2AlF_5, the model has the status of 'a mathematical trick which works'. However, it must be very firmly stated that equilibrium (2), as applied to NaF-AlF_3 melts, is a mathematical trick which does <u>not</u> work.

In talking of models which do not work, what happened to the Neumann-Kopp rule that $\Delta\bar{C}_p = 0$? (i.e. that plots such as Figure 8 should be straight.) In this case, at $N_{AlF_3} = 0.5$, $\Delta\bar{C}_{pNaF} \simeq + 60$ cal K^{-1} mol^{-1}, while $\Delta\bar{C}_{pAlF_3} \simeq - 60$ cal K^{-1} mol^{-1}! This, in turn, means that partial molar enthalpies derived from the work of Hong and Kleppa (11) should have very high temperature coefficients.

OTHER CRYOLITE MIXTURES

For other mixtures there is little to say - for lack of data.

$LiF-NaF-AlF_3$ melts have recently yielded some information (12). The most conspicuous feature is that while γ_{AlF_3} in Li_3AlF_6 is $\sim 10^{-1}$, in Na_3AlF_6 it is $\sim 10^{-3}$, reflecting the much stronger complexation. In Na_3AlF_6 the AlF_3 activity is so low that added LiF is not complexed at all, and its activity coefficient is unity. This points to another model which does not work - the primitive Tempkin model where cation activity is identified with cation fraction, so that $a_{M^+} = n_{M^+}/\Sigma n_{M^+}$. Hence $a_{MF} = K \cdot a_{M^+} \cdot a_{F^-}$ and, regardless of the behaviour of a_{F^-},

$$a_{NaF}/a_{LiF} = N_{Na^+}/N_{Li^+} \qquad (6)$$

or

$$\gamma_{NaF} = \gamma_{LiF} \qquad (7)$$

This is not even approximately true, and it is apparent that the environment of Li^+ ions is quite different from that of Na^+ ions.

$NaF-AlF_3-Al_2O_3$ melts were treated by Sterten (5) along the lines already indicated. Unfortunately he assumed that equilibrium (2) applied to the alumina-free melts, and the discrepancies he encountered he then attributed to the oxide. It would be worthwhile redoing the calculation with a better base-model for the binary subsystems.

It is known (13) that MgF_2 in $NaF-AlF_3$ melts acts as a weak acid, and Fellner, Grjotheim and Kvande (14) have suggested the formation of MgF_4^{2-} ions. It sounds plausible.

DIFFUSION

We must now turn from free-energy models to consider some problems which arise in interpreting diffusivities in these melts, and we are going to compare LiF-AlF_3 melts with NaCl-$AlCl_3$ melts. As we have seen, both of these follow simple dissociation models for the free energy of mixing.

In LiF-AlF_3 melts diffusion coefficients (corrected for volume changes during diffusion caused by anomalous densities) are very high (15). At 1000°C and $N_{AlF_3} = 0.42$, D for AlF_3 is $\sim 1.5 \times 10^{-3}$ cm^2 s^{-1}. This value seems to be associated with a high thermodynamic driving force coming from the non-ideality of the melts. The thinking behind Fick's law is that the driving force is given by the gradient of RT ln(c); if in fact it is given by the gradient of RT ln(a), then the numbers derived will be high by the factor $\partial \ln(a)/\partial \ln(c)$ which is in this case, about 60. The diffusivity based on the thermodynamic gradient is $\sim 2.5 \times 10^{-5}$ cm^2 s^{-1}, a value well in the normal range.

In NaCl-$AlCl_3$ melts things are different. Ødegard et al (16) measured $D = 3.5 \times 10^{-5}$ cm^2 s^{-1} at 820°C, and Rolland and Mamantov (17) found $D \simeq 5 \times 10^{-6}$ cm^2 s^{-1} at 175°C. Both these values are quite normal. And yet the melts are extremely non-ideal - at 175°C $\partial \ln(a)/\partial \ln(c)$ is > 1000 close to $N_{AlCl_3} = 0.5$, within the range covered by the chronopotentiometric experiments.

What is happening is that, because equilibrium (1) is so far to the right, the melts can be regarded, both thermodynamically and kinetically, as dilute solutions of $Al_2Cl_7^-$ in $NaAlCl_4$, the latter acting as an inert solvent. As $[Al_2Cl_7^-]$ goes towards zero (at $N_{AlCl_3} = 0.5$), the gradient of RT ln $[Al_2Cl_7^-]$ becomes extremely high, but the resulting force acts only on the $Al_2Cl_7^-$ ions. The flux is dependent on the concentration times the gradient, and $[Al_2Cl_7^-]$ d ln $[Al_2Cl_7^-]$ = d $[Al_2Cl_7^-]$. The logarithmic term disappears, a linear term is left, Fick's law works, and the diffusion coefficients are normal.

There are several implications in this. Either, with the benefit of our detailed model, we regard a [d ln(a)] gradient as acting on a small minority of the Al atoms in the mixture, or, without knowing anything about the thermodynamics at all, we regard a d [ln(c)] gradient (where c is the total concentration of $AlCl_3$) as acting on all the atoms of Al. The results are identical. At a deeper level, because equilibrium (1) lies so far to the right, no change in the complexation occurs during diffusion, and the free energy of the complexation process cannot couple to the diffusion.

In LiF-AlF_3 the situation seems to be different. As AlF_4^- ions diffuse into a region rich in F^-, they are at least partly complexed to AlF_6^{3-}, and the resulting free energy change can couple to the diffusion.

It is apparent that there is nothing fundamental in making the $[\partial \ln(a)/\partial \ln(c)]$ correction to get a "thermodynamic" diffusivity. In some cases it is certainly not appropriate; in others it may or may not be, and to an unknown extent. It is a fundamental assumption of the thermodynamic gradient models that all atoms of a given type are in statistically equivalent environments. It is a fundamental postulate of dissociation models that they are not. The two models (i.e., thermodynamic gradient and dissociation models) are not compatible.

GENERAL

In talking of these dissociation models one point has gone unmentioned: it has all along been assumed that the various species postulated mix ideally. Why should they, when the ions differ radically in size and charge (e.g. F^-, AlF_4^-, AlF_6^{3-})?

To begin the discussion, let us go back to the case of LiF in dilute solution in Na_3AlF_6: its activity coefficient is close to one. I believe this makes sense only if we regard the LiF in this environment as a molecule and not as a pair of independent ions. Before the word "molecule" is misunderstood let me hasten to say that I do not regard the bond as permanent, as it is in an organic molecule; but I believe that there is a high statistical probability that in the close vicinity of an Li^+ ion there is an F^-. After all, when we say that γ_{LiF} is one because the activity of AlF_3 is too low to complex LiF, we imply that the F^- has not been removed from the Li^+. The moment we postulate that it has, and that the Li^+ is independent, we have problems explaining why $\gamma_{LiF} \neq \gamma_{NaF}$.

So let us regard LiF as a molecule; it is neutral, and the point made above about charges becomes, for it, irrelevant. Can we take the same attitude for all the other species postulated? i.e. can we regard Na_3AlF_6 or Na_2AlF_5 as "permanent", neutral, species? For the moment the question must be left open, but, if we can, it is easier to understand (a) why they would mix ideally and (b) why there seem to be different anionic species when the cation is changed.

Regardless of the question of the permanence of the association between anions and cations, the question of the permanence of the anions themselves remains. There is some evidence (18) that, when F^- is depleted electrochemically in NaF - AlF_3 - Al_2O_3 melts at 1020°C, it takes of the order of a millisecond for whatever complex is present to dissociate to replace it. That is a very long time in terms of atomic vibrations, so it is not surprising that the anionic complexes can be regarded as permanent. This general field has been very little investigated - we know much about the equilibria between the complexes and little about the kinetics of their interconversion.

Dare we say that we 'understand' the halo-aluminate melts? Yes and no. We have mathematical tricks that work, and the implied models look plausible. In some cases we have physical evidence which confirms them, in others it is lacking. And we know virtually nothing about dynamic processes. There is ample room for more work.

REFERENCES

1. G. Torsi, and G. Mamantov, Inorg. Chem., 1971, vol. 10, pp. 1900-02.
2. E.W. Dewing, J. Electrochem. Soc., 1976, vol. 123, pp. 1289-94.
3. E.W. Dewing, Met. Trans. B, 1981, vol. 12B, pp. 705-19
4. E.W. Dewing, Met. Trans., 1972, vol. 3, pp. 495-501.
5. Å. Sterten, Electrochimica Acta, 1980, vol. 25, pp. 1673-77.
6. B. Gilbert, G. Mamantov, and G.M. Begun, J. Chem. Phys., 1975, vol. 62, pp. 950-55.
7. E. Rytter, and S.K. Ratkje, Acta Chem. Scand., 1975, vol. A29, pp. 565-66.
8. J.L. Holm, High Temp. Science, 1974, vol. 6, pp. 16-36.
9. B.J. Holm, and F. Grønvold, Acta Chem. Scand., 1973, vol. 27, pp. 2043-50.
10. J.L. Holm, Thermochim. Acta., 1973, vol. 7, p. 293-96.
11. K.C. Hong, and O.J. Kleppa, J. Phys. Chem., 1978, vol. 82, pp. 176-82.
12. E.W. Dewing, Light Metals 1985, Edited H.O. Bohner, Metallurgical Society of AIME, pp. 737-49.
13. E.W. Dewing, and E. Th. van der Kouwe, Papers presented at 2nd Czech. Aluminium Symposium, Banská Bystrica, 1972, p. 52.

14. P. Fellner, K. Grjotheim, and H. Kvande, Acta Chem. Scand., 1984, vol. A38, pp. 699-702.

15. E.W. Dewing, J. Electrochem. Soc., 1984, vol. 131, pp 1073-78.

16. R. Ødegård, A. Bjϕrgum, Å. Sterten, J. Thonstad, and R. Thunold, Electrochimica Acta, 1982, vol. 27, pp. 1595-98.

17. P. Rolland, and G. Mamantov, J. Electrochem. Soc., 1976, vol. 123, pp. 1299-1300.

18. E.W. Dewing, and E. Th. van der Kouwe, J. Electrochem. Soc., 1977, vol. 24 pp. 58-64.

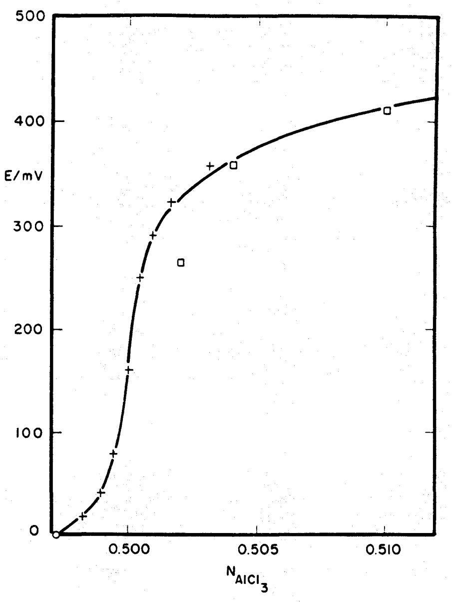

FIGURE 1

Emf of the cell

$$\mathrm{Al}\left|\begin{matrix}\mathrm{NaCl(sat)}\\ \mathrm{AlCl_3}\end{matrix}\right\|\begin{matrix}\mathrm{NaCl}\\ \mathrm{AlCl_3}\end{matrix}\left|\mathrm{Al}\right.$$

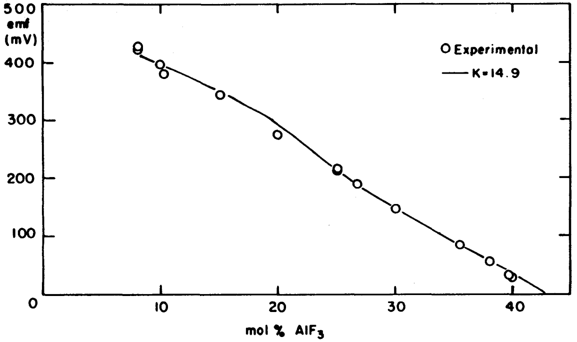

FIGURE 2 Emf of the cell $\mathrm{Al}\left|\begin{matrix}\mathrm{AlF_3(sat)}\\ \mathrm{LiF}\end{matrix}\right|\left|\begin{matrix}\mathrm{AlF_3}\\ \mathrm{LiF}\end{matrix}\right|\mathrm{Al}$

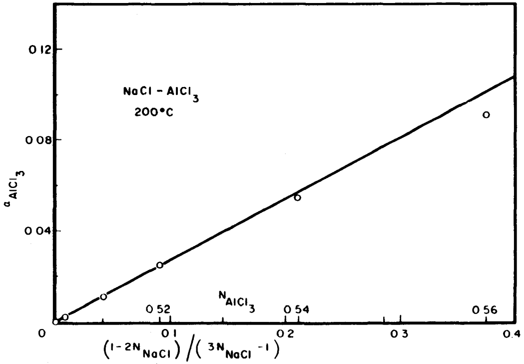

FIGURE 3 Plot to show existence of $NaAl_2Cl_7$

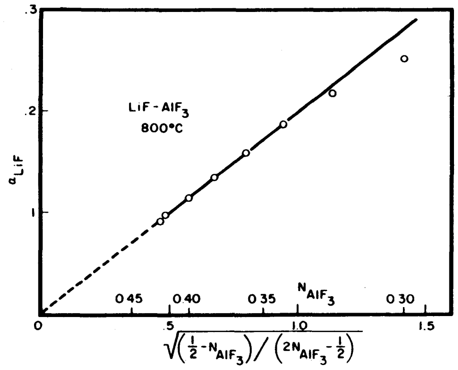

FIGURE 4 Plot to show existence of Li_3AlF_6

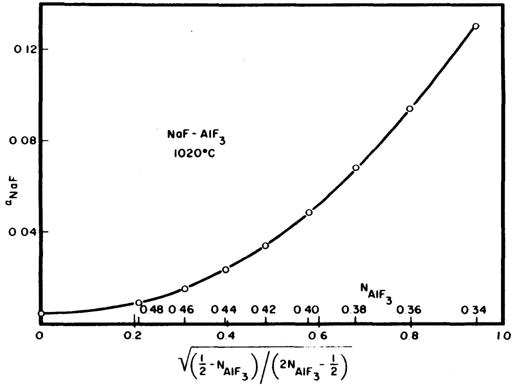

FIGURE 5 Plot to test for existence of Na_3AlF_6

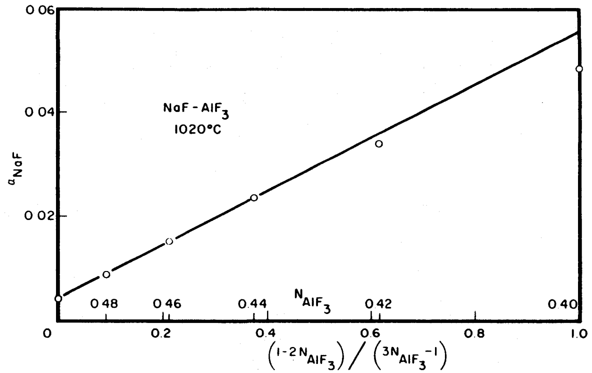

FIGURE 6 Plot to show existence of Na_2AlF_5

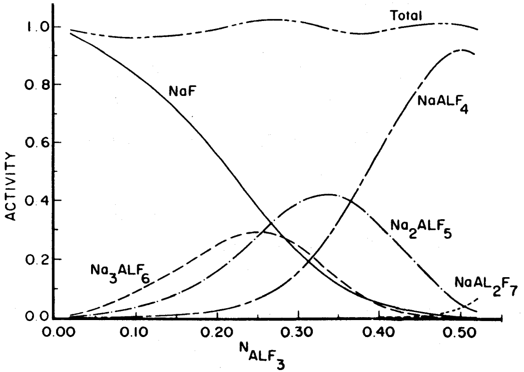

FIGURE 7 Species present in NaF-AlF$_3$ melts at 1020°C

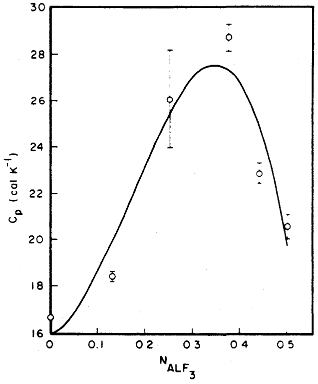

FIGURE 8 Heat capacities of NaF-AlF$_3$ mixtures.

DOI: 10.1149/198601.0275PV

INFORMATION ON STRUCTURE AND BONDING OF MOLTEN CHLOROALUMINATES FROM INFRARED SPECTROSCOPY

Erling Rytter
Institute of Inorganic Chemistry, The Norwegian
Institute of Technology, University of Trondheim,
N-7034 Trondheim-NTH, Norway.

ABSTRACT

The theoretial and experimental basis for obtaining infrared emission and specular reflection spectra of molten salts in general, and particularly of chloroaluminates, has been described. New quantities, ε* and r*, which use a thick (opaque) melt as the reference, give excellent representations of the absorption bands. This method eliminates band splitting due to variations in surface reflectivity or as a result of a cold surface layer of the sample. From the recorded spectra it has been concluded that $AlCl_4^-$ acts as a tridentate ligand towards Mg^{2+}, but as a bidentate ligand towards Zn^{2+}. From the direct observation of anion-cation vibrations it has been shown that the interaction increases in the series $Cs^+ < Rb^+ < K^+ < Na^+ < Li^+ < Mg^{2+} < Zn^{2+}$. Of the alkali ions, only lithium is able to stabilize a bent bridge for $Al_2Cl_7^-$. Another effect of a highly polarizing counterion is a reduction in Cl-Al-Cl bending frequencies as a consequence of more ionic Al-Cl bonds.

INTRODUCTION

In order to obtain infrared (IR) spectra of molten salts, a number of techniques have been described in the literature. The methods include transmission, emission, attenuated total reflection and specular surface reflection.[1] Nevertheless, practical problems due to the corrosive nature, vapour pressures and high melting points of many of the systems have made the construction of a standard experimental set-up difficult. Today, IR spectroscopy of melts has not yet reached the popularity of the much simpler Raman method. Some of the problems can be circumvented in emission or reflection spectroscopy as at least one of the IR windows can be avoided. In the pioneering work of Wilmshurst,[2] however, it was found that band splitting occurred for intense bands presumably due to a too thick sample. We have seen the same effect both in emission and specular reflection. Fortunately, the distortions of the band profiles can be eliminated by using a thick, i.e., IR opaque, melt as the reference.[3-5]

The emission/reflection technique has in this laboratory so far been applied to neutral and acidic mixtures of $AlCl_3$ with LiCl,[6] NaCl,[6] KCl,[6] RbCl,[6] CsCl,[6] $MgCl_2$,[7] $MnCl_2$,[8] $FeCl_2$,[8] $CoCl_2$,[8]

$ZnCl_2$,[4,8] and $NaAl_2OCl_5$-$NaAlCl_4$,[8] $GaCl_3$ with KCl and CsCl,[6] $InCl_3$ with KCl[6] and $GaBr_3$ with RbBr.[9] Addition of Cs_2O to acidic and basic melts close to the $CsAlCl_4$ composition[10] and pure $AlCl_3NH_3$[11] also have been studied. It is the intention here to give a short summary of the experimental and theoretical basis for emission and specular reflection spectroscopy of thin films and to demonstrate the types of information that can be deduced from infrared spectroscopy of molten salts. Although the examples are from chloroaluminates , the principles are general.

PRINCIPLE

Specular Reflection Spectroscopy. The experimental set-up used in the present work consists schematically of a molten sample contained between a window and a reflecting backplate (Fig. 1). The sample property of interest is the internal transmittance (or permeability)

$$p_2 = \exp(-K_2 d_2) \qquad (1)$$

where K_2 is the absorption coefficient and d_2 the thickness.

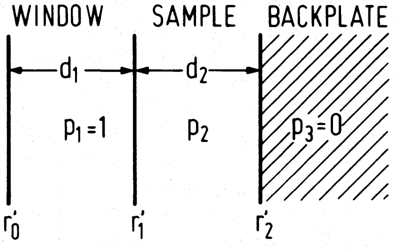

Fig. 1. Sample between a non-absorbing window and a reflecting backplate ($r_2' \approx 1$).

In reflection spectroscopy, the beam from the source passes the window and the sample before it is reflected at the backplate. The beam thus is transmitted through the sample twice before it reaches the detector. Therefore, the spectrum will be close to the standard transmittance spectrum of a slab with thickness $2d_2$. The spectral intensity of the sample (I_S) is measured with an unperturbed beam as reference. In practice, the reference spectrum (I_o) is measured using a cell without window and melt, but with a highly reflecting backplate. It turns out, however, that the reflectance obtained,

$$r = I_S/I_o, \qquad (2)$$

may give a poor representation of p_2 for strong bands. The resulting band distortions are a consequence of the experimental difficulties involved in obtaining a thin enough melt.

The origin of the problem can be understood by studying a thick melt, e.g., with a thickness of a few mm. Then the sample becomes opaque in the IR, and the beam is reflected from the window/sample interphase (giving the I_{OS} spectrum) without ever reaching the backplate. The reflectance approaches the reflectivity ($\mathbf{r}'$) of the system and, taking multiple reflections in the window into account,

$$\mathbf{r}' = I_{OS}/I_O =$$

$$r_o' + (1-r_o')^2 r_1' p_1^2 + (1-r_o)^2 r_1' p_1^2 (r_o' r_1' p_1^2) + (1-r_o)^2 r_1' p_1^2 (r_o' r_1' p_1^2)^2 + .. \quad (3)$$

See Fig. 1 for notations. By recognizing the geometric series and assuming that the window is non-absorbing ($p_1 = 1$), the reflectivity becomes

$$\mathbf{r}' = (r_o' + r_1' - 2r_o' r_1')/(1 - r_o' r_1'). \qquad (4)$$

Note that if the window also is non-reflecting ($r_o' = 0$), then naturally $\mathbf{r}' = r_1'$, the reflectivity of the sample. It was this last quantity that was measured in the work by Wilmshurst.[2]

For strong bands, the reflectivity of the sample varies considerably in the frequency range corresponding to a vibrational transition. In intermediate cases where the sample is not completely opaque, the bands with the highest absorption coefficients reach the $\mathbf{r}'$ limit. Thus, distortions and false splittings will occur in the spectra.

For a non-absorbing window, it is seen from eq. (4) that $\mathbf{r}'$ is equal for both front and back reflection. Similar to eqs. (3) and (4), the reflectance $\mathbf{r}$ for the complete system in Fig. 1 thus may be expressed by

$$\mathbf{r} = (\mathbf{r}' + r_2' p_2^2 - 2\mathbf{r}' r_2' p_2^2)/(1 - \mathbf{r}' r_2' p_2^2), \qquad (5)$$

which rearranged yields

$$r_2' p_2^2 = (\mathbf{r} - \mathbf{r}')/(1 - 2\mathbf{r}' + \mathbf{r}\mathbf{r}'). \qquad (6)$$

Usually, r_2' is close to unity for a polished metal backplate and therefore may be neglected. The last equation shows that the undistorted internal transmittance p_2 can be calculated by measuring the **absolute** spectra of a reasonably thin and an opaque melt relative to I_o. Fortunately, however, a simpler procedure that does not require absolute measurements may be employed in practice.

It has been shown experimentally that the new quantity

$$\boxed{\mathbf{r}^* = 1 - \mathbf{r}'/\mathbf{r} = 1 - I_{OS}/I_S} \qquad (7)$$

is a good approximation of the internal transmittance (eq. 6).[4,8] A theoretical justification is provided elsewhere.[5] Eq. (7) implies that the reference I_o of eq. (2) is replaced by I_{OS} of a thick melt. Note that only the **relative** intensities of two single beam spectra determine the band shapes in **r***. The 1- term is included to obtain bands pointing downwards as in transmission spectroscopy.

For very thin melts, and generally for weak bands, **r** and **r*** work equally well. That the unmodified reflectance spectrum is suitable for weak bands is demonstrated by assuming $\mathbf{r}' \ll \mathbf{r}$ in eq. (6), giving $r_2' p_2^2 \approx r$.

Emission Spectroscopy. Infrared emission spectroscopy of thin melts is closely related to the reflection method. According to conservation of energy, a light flux which falls upon a body is divided into three fractions: reflectance, absorptance, and transmittance. Since the spectral energy absorbed is equal to the energy emitted, ε, one has

$$\mathbf{r} + \varepsilon + \mathbf{t} = 1. \qquad (8)$$

No energy is transmitted through the system in the present set-up, and hence

$$\varepsilon = 1 - \mathbf{r} = (I_S - I_{BG})/(I_{BB} - I_{BG}) \qquad (9)$$

and

$$\varepsilon' = 1 - \mathbf{r}' = (I_{OS} - I_{BG})/(I_{BB} - I_{BG}). \qquad (10)$$

A blackbody at the same temperature as the melt provides the reference spectrum, I_{BB}. In addition, it is usually necessary to correct for background radiation, I_{BG}.

Spectral distortions are readily avoided if

$$\boxed{\varepsilon^* = \varepsilon/\varepsilon' = (I_S - I_{BG})/(I_{OS} - I_{BG})} \qquad (11)$$

is used instead of ε.[3] An additional advantage of ε^* is that the blackbody reference is cancelled out and need not be measured.

Introduction of eqs. (9) and (10) into (6) yields an accurate expression for the internal transmittance:

$$r'_2 p_2^2 = (\varepsilon' - \varepsilon)/(\varepsilon' - \varepsilon + \varepsilon\varepsilon'), \qquad (12)$$

now requiring the blackbody spectrum. It is seen that $(1 - r'_2 p_2^2) \approx \varepsilon$ for weak bands, $\varepsilon' >> \varepsilon$. Therefore, the standard emittance spectrum gives sufficient spectral information in this case. Further details have been reported previously.[3]

The origin of the splitting of intense emission bands has variably been referred to as dispersion of the sample surface reflectivity, as discussed above, or as self-absorption of emitted radiation by cooler outer layers.[12] We have found that, at least for our emission cell, mainly the former effect is operating. Fortunately, however, theoretical calculations of band shapes based on a damped harmonic oscillator model show that both types of distortions are eliminated by employing ε*.[3,5]

EXPERIMENTAL

The cell designed for chloroaluminate melts is shown in Figure 2. It consists of a steel cylinder (I) containing a gold plated support (J), a steel piston (B) and a sample container of nickel (D). The melt (M) is compressed against an 8 mm Ø, 1 mm thick diamond (type II a) window (G) by a movable piston of nickel (E). Sealing of the system is assured by using steel bolts (A) and a gold gasket (F) between the nickel container and the window. The materials are matched to give a slightly increased sealing pressure at higher temperatures. In recent experiments, the metal parts which come into contact with the melt have been gold plated. The cell design provides a good alignment of the sample container and a resulting

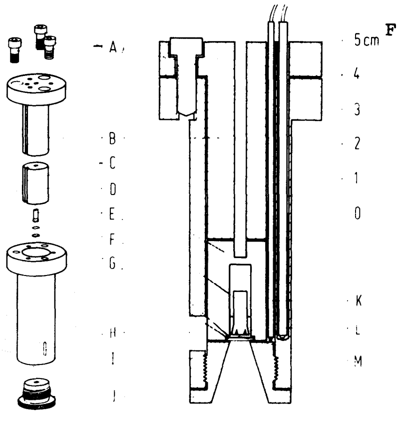

Fig. 2. Infrared emission/reflection cell for chloroaluminate melts:

(A) steel bolts, (B) stainless steel piston, (C) thermocouple slit, (D) sample container of nickel, (E) nickel piston, (F) gold gasket, (G) diamond window, (H) viewing slit, (I) stainless steel cylinder, (J) gold-plated support, (K) measuring thermocouple, (L) controlling thermocouple, and (M) sample.

even pressure on the window, reducing the risk of breaking it. Further details, particularly regarding filling and measuring procedures, have been reported by Hvistendahl et al.[6,12]

The following features of the cell are important for obtaining high-quality spectra of chloroaluminate melts:

a) A closed sample compartment which allows vapor pressures of several atmospheres and assures equilibrium conditions.
b) An available spectral region of 0 - 1800 cm^{-1} (and 2100 cm^{-1} →).
c) A limiting temperature as high as 600°C. At approximately this temperature the diamond turns opaque for infrared radiation.
d) High thermal conductivity of the window resulting in a uniform melt temperature.
e) The formation of thin melt films.
f) Inert conditions for most samples.
g) No spectral influence of the vapor phase.
h) Low background emittance.

The experiments have been performed with evacuable Bruker 114c and 113v Fourier transform spectrometers. In the emission experiments, the furnace was mounted on the standard optical bench of the source compartment.[12] Only a flat mirror had to be added. Reflection required a special reflection unit constructed by Bruker (Fig. 3). The unit provides a focus above the sample compartment, suitable for a horizontal melt layer.

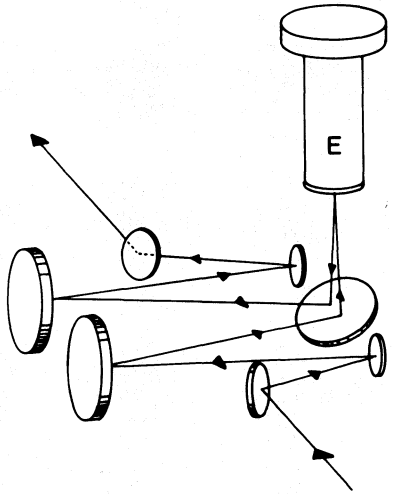

Fig. 3. Optical path in the FTIR sample chamber with the emission cell (E) employed for specular reflection spectroscopy of melts.

Choice of method depends on several factors. Apart from the need for a special optical unit in reflection spectroscopy, the reflecting backplate of the cell becomes an integral part of the optical path. Therefore, the cell position must be adjusted accurately, but it turns out that this adjustment is easy to perform. On the other hand, reflection has two major advantages compared to emission spectroscopy. First, the standard alignment of the instrument need not to be altered. The reflection unit is simply placed in the sample compartment. This system also reduces any damage to the instrument in case of leaks in the cell, because the sample will be well removed from the interferometer. Second, the energy of a high temperature source is employed instead of the sample itself, which is at a considerably lower temperature. The energy thus gained may be of particular importance in the lowest frequency range. Up to 80 % of the full energy, i.e., without the reflection attachment, has been obtained in reflection experiments.

APPLICATIONS AND DISCUSSION

This section is focused on the special features of IR-spectroscopy and the different types of information that can be deduced, rather than giving a full description of the individual systems that have been investigated. Comparison is specifically made with the Raman technique.

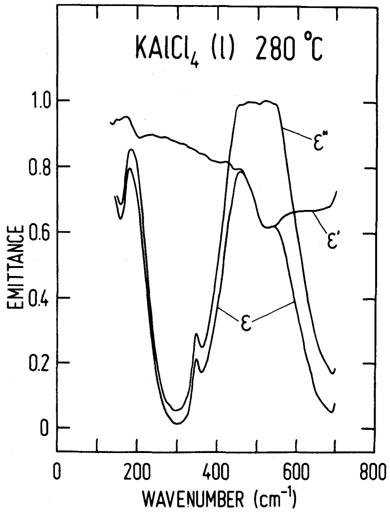

Fig. 4. Emission spectra of molten $KAlCl_4$. ε: emittance; ε′: emissivity (opaque sample); $\varepsilon^* = \varepsilon/\varepsilon'$.

Removal of Band Distortions. Fig. 4 shows emission spectra of molten $KAlCl_4$ at 280 °C. The spectrum depicts a clear asymmetric splitting around 500 cm^{-1} due to a too thick sample. The asymmetry in the distortion implies that reflectivity variations prevail over selfabsorption by cooler outer layers. It is evident from the figure that the emittance reaches the maximum level in the region 460 to 550 cm^{-1} where it follows the emissivity (ε') of an opaque sample. With the latter sample as the reference, the ε^* spectrum is obtained and the high-frequency shoulder disappears. Thus, it is essential to use ε^* (or r^*) to check shoulders and split bands. The resulting spectra may of course become flat at the top of the most intense peaks. This feature corresponds to the flat bottom of the transmission spectrum of a thick sample.

IR vs. Raman. During the 70's Raman spectroscopy became a standard method for structural investigations of molten salts, particularly for the identification of complex ions and other structural entities. In alkali chloride - aluminium chloride mixtures, the $Al_2Cl_7^-$ ion and higher polymers have been recognized and approximate equilibrium calculations have been performed for the reaction

$$2\ Al_2Cl_7^- = 2\ AlCl_4^- + Al_2Cl_6. \qquad (13)$$

Cation-anion interactions have been inferred from the relative abundance of the chloroaluminate species Al_2Cl_6, $Al_2Cl_{10}^-$, $Al_2Cl_7^-$ and $AlCl_4^-$.

In order to obtain a more complete comprehension of the melt structure, it is important that the complementary IR technique is used in addition to Raman. Apart from giving a more detailed vibrational picture of the melt together with the Raman spectra, IR has several particular advantages:

a) Only small sample amounts are needed and ultra-purity is not required (in Raman problems with fluorescence frequently occur). Attention, however, must be given to the homogeneity of the sample and possible composition changes due to vaporization.
b) Coloured melts do not cause problems, cf. the investigation of $MnCl_2$, $CoCl_2$ and $FeCl_2$ mixtures with $AlCl_3$.
c) Perturbation of high symmetry species may be detected by the activation of the totally symmetric stretching mode. This feature is demonstrated in Fig. 4 with the appearance of the ν_1 totally symmetric stretching mode of $AlCl_4^-$ at 350 cm^{-1}. For a perfect tetrahedron, this mode is inactive in the IR. Similar arguments are valid for most highly symmetric entities, e.g., MX_2 (linear $D_{\infty h}$), MX_3 (planar D_{3h}), MX_4 (tetrahedral T_d, or planar D_{4h}), MX_5 (trigonal bipyramidal D_{3h}), MX_6 (octahedral O_h, tetragonally distorted octahedron D_{4h}, or planar D_{6h}) and M_2X_7 (linear bridge D_3, D_{3h} or D_{3d}). The detection of ν_1, however, does not tell anything about the nature or magnitude of the perturbation.
d) Degenerate stretching modes of symmetric species give rise to intense bands in the infrared, as shown by the ν_3 band of $AlCl_4^-$

at ca. 490 cm^{-1} (Fig. 4). It follows that strong anion-cation interactions should be detected as descent in symmetry and band splitting.

e) Chemical bonds with a high degree of ionisity give bands in the infrared spectra with reasonable intensities. An example is Al-O (and Al-N) bonds which clearly are seen in the infrared, but are not detected in Raman because the polarizability fluctuations involved are extremely small. Thus, apart from obtaining important structural information on oxide systems, a test of the preparational procedures automatically is performed. Strong oxide bands found at 680 and 800 cm^{-1} in pure $NaAlOCl_5$ and its mixtures with $AlCl_3$ or $NaAlCl_4$ have been attributed to a vibrating unit of the following type:

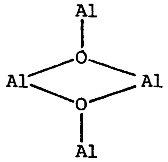

The $AlCl_4^-$ Unit. From Raman spectroscopy and other methods it is well known that aluminum is coordinated to four chlorine atoms in chloroaoluminate melts. An $AlCl_4$ unit with tetrahedral symmetry has four fundamental vibrations, observed in Raman at 350 (ν_1, A_1), 122 (ν_2,E), 487 (ν_3,F_2) and 182 cm^{-1} (ν_4,F_2) for $KAlCl_4$. As demonstrated by the correlation diagram in Table 1, only ν_3 and ν_4 are IR-active, although it has been mentioned that ν_1 is activated by perturbations.

Table 1. Perturbational splitting of the fundamental vibrations of $AlCl_4^-$. In F_2 only the splitting of ν_3 (487 cm^{-1}) is given.

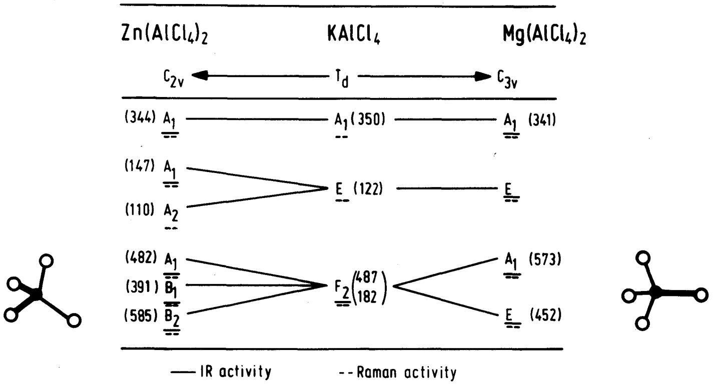

The perturbations may be due to fluctuations in the melt structure in general or to more localized cation-anion interactions. In Table 1 it is shown that the triply degenerate ν_3 vibration of $AlCl_4^-$ (T_d) is split into three components when it is a bidentate ligand (C_{2v}) and into two components when it is a tridentate ligand (C_{3v}). These two cases are found for $Zn(AlCl_4)_2$ and $Mg(AlCl_4)_2$ melts, respectively. In Fig. 5 the vibrational spectra of $ZnAl_2Cl_8$ are compared. The three components of $\nu_3(F_2)$ are very distinct in the IR-spectrum, whereas the Raman spectrum shows a strong resemblance with a nonreacting mixture of $ZnCl_2$ and Al_2Cl_6. This artifact comes from the vibrational similarity of Al_2Cl_6 with the more likely structure

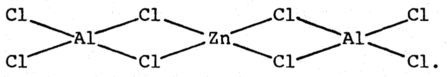

Thus, it clearly is demonstrated that infrared spectroscopy in addition to Raman is necessary in order to deduce the correct melt structure.

Fig. 6 shows the resemblance between molten and solid $MgAl_2Cl_8$, both having tridentate $AlCl_4^-$ towards Mg^{2+}. The weak band at ca. 680 cm^{-1} indicates trace amounts of oxide impurities.

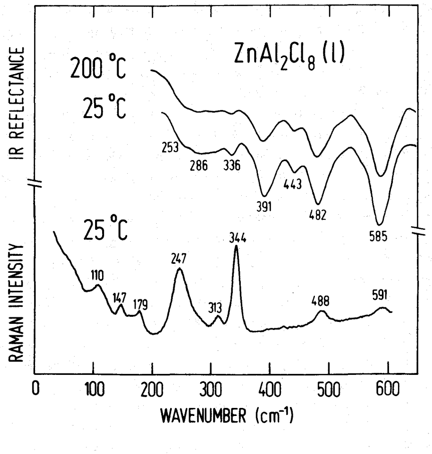

Fig. 5. Vibrational spectra of liquid $ZnAl_2Cl_8$.

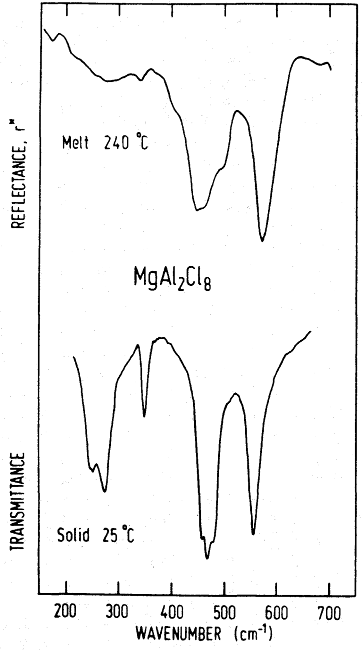

Fig. 6. IR spectra of molten and solid $MgAl_2Cl_8$.

The $Al_2Cl_7^-$ Unit. Raman spectroscopy has verified the existence of $Al_2Cl_7^-$ in chloroaluminate melts as a chlorine bridged ion. There are, however, discussions as to the structure, particularly regarding a linear or bent Al-Cl-Al bridge. With basis in the available melt data for KAl_2Cl_7, it has been possible to perform an assignment of the fundamental modes in terms of a staggered linear configuration (Table 2). The low number of observed bands points to a high symmetry. However, Fig. 7 shows that as the polarizing power of the cation increases, ν_{11} (E_u) is split into two components. Since Li is not able to induce a similar band separation in $LiAlCl_4$,[6] we conclude that the splitting is due to the formation of a stable bent bridge only for $LiAl_2Cl_7$ and $Mg(Al_2Cl_7)_2$. (The splitting for $Mg(Al_2Cl_7)_2$ in the figure is somewhat fortuitous as the melt contains a considerable amount of $AlCl_4^-$ due to evaporation of Al_2Cl_6 in the sample container).

Table 2. Vibrational fundamentals of KAl_2Cl_7 in terms of D_{3d} structure.

A_{1g}	ν_1	432	$AlCl_3$	stretch	E_g	ν_8	-	$AlCl_3$ stretch
	ν_2	311	AlClAl	stretch		ν_9	97	$AlCl_3$ def.
	ν_3	161	$AlCl_3$	def.		ν_{10}	-	skel.bend
A_{1u}	ν_4	i.a.	torsion		E_u	ν_{11}	525	$AlCl_3$ stretch
A_{2u}	ν_5	381	$AlCl_3$	stretch		ν_{12}	158	$AlCl_3$ def.
	ν_6	331	AlClAl	stretch		ν_{13}	-	skel bend
	ν_7	179	$AlCl_3$	def.		ν_{14}	-	AlClAl bend

Al_2Cl_6. The infrared emission spectra of Al_2Cl_6 and other dimeric aluminium halides are very similar in the liquid and gas phase. Neighbour interactions show up in a slight reduction in stretching frequencies, typically 12-14 cm^{-1} for terminal Al-Cl stretch.[13]

It is worthwhile to compare the calculated stretching and bending force constants for the chloride, bromide and iodide.[14] In Fig. 8 the ratio between a bending constant and the average of the stretching constants of the bonds forming the angle, is plotted as a function of difference in Pauling's electronegativities. As might be expected, a more ionic bond gives a reduction in relative resistance against angle bending. A similar situation is found for $LiAlCl_4$. Higher ionisity of the Al-Cl bond compared to the melts with larger alkali counterions, results in a reduction in the ν_4 bending mode from ca. 180 cm^{-1} to 170 cm^{-1} for Li.

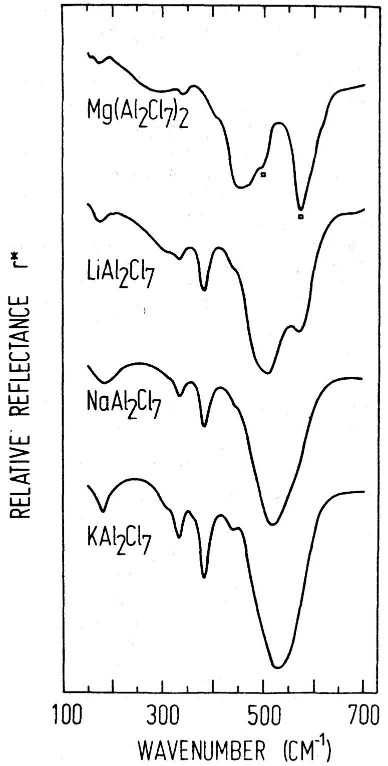

Fig. 7. IR spectra of molten $M(Al_2Cl_7)_n$.

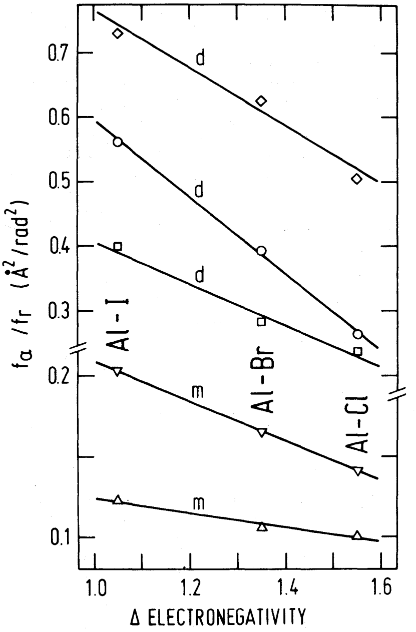

Fig. 8. Ratio between bending and stretching force constants for dimeric (d) and monomeric (m; gas) $AlCl_3$, $AlBr_3$ and AlI_3.

Cation Coordination. Apart from giving rise to perturbations of the anion, cation-anion interactions in melts containing $AlCl_4^-$ can be observed directly as a broad band below 300 cm^{-1}, see Figs. 4,5 and 6. The comparison with the solid state in Fig. 6 verifies that the 288 cm^{-1} band of the melt indeed is an Mg-Cl vibration. This mode cannot be observed in Raman due to the high ionisity and consequently low polarizability variation during the vibration.

The results for different counterions are compared in Table 3. Calculations of the force constants are for an antisymmetric stretching mode employing the formula (high and low frequency separation)

$$2\,\Pi^2 c^2 \nu^2 \approx f(2\mu_{\text{cation}}\sin^2(\alpha/2) + \mu_{\text{ligand}}) \qquad (14)$$

where α is the ligand-cation-ligand angle between opposite cation-ligand bonds. Tetrahedral geometry and an effective ligand mass of Cl + Al were used for all melts. Introducing different coordination numbers for the cations enhance the trend in the force constant. It can be concluded that the M-$AlCl_4$ frequency shift is not only a mass effect, but is a genuine consequence of the variations in polarizing power.

As the alkali melts may be regarded as ionic Alk^+-$AlCl_4^-$ systems, the energy well that determines the force constant may be approximated by a Born type lattice energy expression:

$$(\delta^2 U/\delta r^2) = 4.04\ (n' - 1)/r^3_{\text{cation-anion}} \qquad (15)$$

$$f_{\text{Alk-Cl}} = (\delta^2 U/\delta r^2)/n \quad (\text{mdyn/Å}) \qquad (16)$$

when an average Madelung constant of 1.75 is introduced, n′ is the exponent in the repulsion term (taken from the pure alkali chlorides) and n is the number of Alk-Cl bonds (taken as 4). The derived anion-cation distances are included in Table 3. Subtracting the cation radii from crystal structure determinations of $AlkAlCl_4$ yields remarkably constant and reasonable values for the $AlCl_4^-$ dimension.

Table 3. Cation-anion frequencies, force constants and distances for $MAlCl_4$ melts.

Melt	Frequency (cm^{-1})	f (mdyn/Å)	$r_{M\text{-}AlCl_4}$ (Å)	$r_{AlCl_4^-}$ (Å)
$Zn(AlCl_4)_2$	286	1.324		
$Mg(AlCl_4)_2$	288	0.690		
$LiAlCl_4$	300	0.253	2.92	2.21
$NaAlCl_4$	140	0.156	3.63	2.59
$KAlCl_4$	108	0.137	3.82	2.37
$RbAlCl_4$	86	0.138	3.97	2.34
$CsAlCl_4$	64	0.093	4.71	2.87

REFERENCES

1. R.E. Hester, In **Advances in Molten Salt Chemistry**, Vol. I, J. Braunstein, G. Mamantov and G.P. Smith, (Eds.). Plenum, New York (1971).
2. J.K.Wilmshurst, **J. Chem. Phys.** 39, 2545 (1963)
3. J. Hvistendahl, E. Rytter and H.A. Øye, **Appl. Spectrosc.** 37, 182 (1983).

4. E. Rytter and M.A. Einarsrud, In **Abstracts of Papers**, EUCHEM Conference on Molten Salts, Denmark, 1984.
5. E. Rytter, **Spectrochim. Acta**, submitted.
6. J. Hvistendahl,P. Klæboe, E. Rytter and H.A. Øye, **Inorg. Chem.** 23, 706(1984).
7. M.A. Einarsrud, H. Justnes, E. Rytter and H.A. Øye, **Polyhedron**, submitted.
8. M.A. Einarsrud and E. Rytter, unpublished results.
9. A. Manteghetti and E. Rytter, unpublished results.
10. R. Berg and T. Østvold, unpublished results.
11. T. Østvold, E. Rytter and G.N. Papatheodorou, **Polyhedron**, in print.
12. E. Rytter, J. Hvistendahl and T. Tomita, **J. Molec. Struct.** 79, 323 (1982).
13. T. Tomita, C.E. Sjøgren, P. Klæboe, G.N. Papatheodorou and E. Rytter, **J. Raman Spectrosc.** 14, 415 (1983).
14. C.E. Sjøgren, P. Klæboe and E. Rytter, **Spectrochim. Acta** 40, 457 (1984).

DOI: 10.1149/198601.0289PV

AB INITIO MOLECULAR ORBITAL CALCULATION OF THE VIBRATIONAL FREQUENCIES OF XY_4^{-n} ANIONS

Larry A. Curtiss and Robert Nichols†
Chemical Technology Division/Materials Science and Technology Program
Argonne National Laboratory
Argonne, Illinois 60439

ABSTRACT

The vibrational frequencies of a series of XY_4^{-n} anions (BeF_4^{-2}, BF_4^-, AlF_4^-, $MgCl_4^{-2}$, and $AlCl_4^-$) have been calculated by *ab initio* molecular orbital theory using the 3-21G and 6-31G* basis sets. The predicted harmonic frequencies are for the most part in good agreement with the observed frequencies of these anions in molten alkali halide mixtures. At the 3-21G basis set level the average difference between the observed and predicted frequencies is 12% while at the 6-31G* basis set level the average difference is 6% . Calculations of this type may be helpful in predicting the vibrational frequencies of other anions in molten salts.

I. INTRODUCTION

In this paper we investigate the use of *ab initio* molecular orbital theory for predicting the vibrational frequencies of anions which are present in molten salts. *Ab initio* molecular orbital calculations at the Hartree-Fock (HF) level predict harmonic vibrational frequencies of neutral molecules which are, in general, 10 - 15% higher than the observed anharmonic vibrational frequencies.[1-2] This degree of accuracy is often very useful in helping to assign vibrational frequencies in the observed infrared and Raman spectra of gas phase molecules and in calculations of thermodynamic properties.

More recently *ab initio* molecular orbital theory has been helpful in the determination of the vibrational frequencies of cationic species.[3] Well known problems exist in the applications of these methods to anions since they are often unbound with respect to dissociation to a neutral and a free electron. However, Radom[4] has pointed out that at the HF level certain properties such as structures and frequencies can probably be fairly well determined. Lee and Schaeffer[5] studied a

---

†Undergraduate Research Participant from Davidson College, North Carolina.

series of small anions and concluded that at the HF level vibrational frequencies can be obtained reliably if a large enough basis set is used.

Since the vibrational frequencies of XY_4^{-n} anions in molten alkali halide mixtures do not appear to be greatly perturbed by the alkali cation,[6-7] one would expect the frequencies of such anions to be similar to those of the gas phase anions which can be calculated by *ab initio* molecular orbital methods. To test the ability of *ab initio* molecular orbital methods in predicting the vibrational frequencies of anions in melts we have calculated the frequencies of a series of XY_4^{-n} anions (BeF_4^{-2}, BF_4^-, AlF_4^-, $MgCl_4^{-2}$, and $AlCl_4^-$) and compared the results to the observed frequencies for these anions in molten alkali halide mixtures. Previous work has found that *ab initio* molecular orbital calculations of the energies of gas phase reactions are very similar to the energies of related reactions in molten salt systems.[8]

II. THEORETICAL METHODS

All of the calculations in this study were done at the Hartree-Fock level of calculation. Two basis sets were used. They are the split valence 3-21G basis,[9] and the polarized split valence 6-31G*[10] basis. The latter basis has d-functions on all heavy atoms (*i.e.*, atoms of larger atomic number than H). For neutral molecules containing first row atoms (Li-F) both basis sets do about equally well in the calculation of vibrational frequencies.[1] However, for molecules containing second row atoms (Na-Cl), the 3-21G basis set is less reliable.[9]

Harmonic vibrational frequencies were obtained using the Wilson FG matrix method,[11] which is based on solution of the set of equations given by

$$(GF - E\lambda_k)L_k = O \tag{1}$$

where G is the inverse kinetic energy matrix, F is the force constant matrix, λ_k are the eigenvalues and L_k are the eigenvectors. The eigenvalues are related to the vibrational frequencies ν_k by

$$\lambda_k = 4\pi^2\nu_k^2. \tag{2}$$

Coordinates based on tetrahedral symmetry were used. These had the usual form:

$$S_r(A_1) = (\Delta r_1 + \Delta r_2 + \Delta r_3 + \Delta r_4)/2 \tag{3}$$

$$S_\alpha(E) = (2\Delta\alpha_{12} - \Delta\alpha_{13} - \Delta\alpha_{14} - \Delta\alpha_{23} - \Delta\alpha_{24} + 2\Delta\alpha_{34})\sqrt{12} \tag{4}$$

$$S_r(T_2) = (\Delta r_1 + \Delta r_2 - \Delta r_3 - \Delta r_4)/\sqrt{2} \tag{5}$$

$$S_\alpha(T_2) = (\Delta\alpha_{12} - \Delta\alpha_{34})/\sqrt{2} \qquad (6)$$

The geometries of the XY_4^{-n} anions were optimized with tetrahedral symmetry. Quadratic force constants corresponding to the symmetry coordinates were calculated by fitting points on the potential energy surface about the equilibrium geometry.[2,12] Both diagonal and off-diagonal symmetry force constants were determined.

III. RESULTS AND DISCUSSION

The optimized bondlengths and total energies of the XY_4^{-n} anions at both basis set levels are given in Table I. The two basis sets give similar bondlengths for all anions except $AlCl_4^-$, where the 3-21G basis is deficient and gives too large a value. The theoretical bondlengths of BeF_4^{-2}, BF_4^-, AlF_4^-, and $AlCl_4^-$ are close to bondlengths for these species estimated from experimental data (see Table I). The agreement between the calculated and estimated geometries indicates that the level of theory being used is capable of describing the structure of these anions reasonably well.

The calculated harmonic vibrational frequencies of the XY_4^{-n} anions are given in Table II. When compared with the observed fundamentals[6,7,13–16] (which include anharmonic effects), the average absolute deviation is 12% at the 3-21G level and 6% at the 6-31G* level. The improvement at the 6-31G* level indicates the importance of d-functions in the calculation of potential energy surfaces of these anions. The agreement is actually better than that found between experiment and theory for neutral molecules (10–15%) at the 6-31G* level.

Only two of the 6-31G* frequencies differ more than expected (>15%) from the experimental values: $\nu_2(E)$ for $MgCl_4^{-2}$ is 17% lower than the observed value of 100 cm^{-1} and $\nu_3(T_2)$ for AlF_4^- is higher by 29% than the observed value of 760 cm^{-1}. The discrepancy for $MgCl_4^{-2}$ is not of great concern since it is only 17 cm^{-1}. However, the discrepancy for $\nu_3(T_2)$ of AlF_4^- (187 cm^{-1}) is appreciable for this level of calculation. The asymmetric stretching modes of the other anions are all within 12% of the observed values. In addition, for AlF_3 and $AlCl_3$, calculated asymmetric stretching frequencies are within 12% of the observed values.[17] We also note that the band in the AlF_4^- spectra that is assigned to the asymmetric stretch (ν_3) is a weak one.[16] Hence, the assignment of this band might need reexamination.

IV. CONCLUSIONS

Good agreement has been found between the vibrational frequencies of anions predicted by *ab initio* molecular orbital theory and their observed frequencies in melts. For the five anions considered here, the agreement is as good as that found between theory and experiment for gas phase neutral molecules. The fact that the frequencies of the gas phase anions are similar to the frequencies of the anionic species in melts is consistent with the idea that these anions are not greatly perturbed by the cations in the melts. This study also suggests that theoretical calculations could be of use in assigning the bands of related anions such as S_3^-, AlF_3O^{-2}, $AlCl_3O^{-2}$, and $Al_2Cl_7^-$ where the assignments of the bands are more in doubt. Theoretical calculations on such anions could also provide a reasonable estimate of their thermodynamic properties.

ACKNOWLEDGMENTS

We thank M. Blander and V. A. Maroni for helpful discussions. This work was performed under the auspices of the Division of Materials Science, Office of Basic Energy Sciences of the United States Department of Energy.

REFERENCES

1. J. A. Pople, H. B. Schlegel, R. Krishnan, D. J. Defrees, J. S. Binkley, M. J. Frisch, R. A. Whitesides, R. F. Hout, and W. J. Hehre, Int. J. Quant. Chem., S15, 269(1981).
2. R. F. Hout, B. A. Levi, and W. J. Hehre, J. Comp. Chem. 3, 234(1982).
3. M. E. Colvin, G. P. Raine, and H. F. Schaefer, J. Chem. Phys. 79, 1551(1983).
4. L. Radom, in Modern Theoretical Chemistry, edited by H. F. Schaefer (Plenum, New York, 1977), Vol 4, pp. 333–352.
5. T. J. Lee and H. F. Schaefer, J. Chem. Phys. 83 1784(1985).
6. M. H. Brooker and G. N. Papatheodorou, in Advances in Molten Salt in Chemistry, edited by G. Mamantov, (Elsivier, Amsterday, 1983), Vol. 5 pp. 27–165.
7. J. Hvistendahl, P. Klaeboe, E. Rytter, and H. Øye, Inorg. Chem., 23, 706(1984).
8. L. A. Curtiss and M. Blander, J. Electrochem. Soc., 131, 2271(1984).
9. J. S. Binkley, J. A. Pople, and W. J. Hehre, J. Am. Chem. Soc. 102, 939(1980); M. S. Gordon, J. S. Binkley, J. A. Pople, W. J. Pietro, and W. J. Hehre, J. Am. Chem. Soc. 104, 2797(1982).
10. P. C. Hariharan and J. A. Pople, Theoret. Chimi. Acta. 28, 213(1973).
11. E. B. Wilson, J. C. Decius, and P. C. Cross, Molecular Vibrations, (McGraw-Hill Book Company, New York, 1955).

12. L. A. Curtiss and J. A. Pople, J. Mol. Spectros., **48**, 413(1973).
13. A. S. Quist, J. B. Bates, and G. E. Boyd, J. Phys. Chem. **76** 78(1972).
14. A. S. Quist, J. B. Bates, and G. E. Boyd, J. Chem. Phys. **54** 4896(1971).
15. V. A. Maroni, J. Chem. Phys. **55**, 4789(1971).
16. B. Gilbert, G. Mamantov, and G. M. Begun, J. Chem. Phys. **62**, 950(1975).
17. L. A. Curtiss and R. Nichols, to be published.
18. V. P. Spiridonov and E. V. Erokhin, Zh. Neorg. Khim. **14**, 636(1969).
19. N. C. Baenziger, Acta Crystallogr. **4** 216(1951); K. N. Semenenko, V. N. Surov, and N. S. Kedrova, Russ. J. Inorg. Chem. **14** 481(1969).

Table I. 3-21G and 6-31G* Optimized Geometries and Energies of XY_4^- Anions[a]

Species	Symmetry	Method/Basis	R[b]	Energy
$[BeF_4]^{-2}$	T_d	HF/3-21G	1.539	−410.31086
		HF/6-31G*	1.576(1.56)[c]	−412.49980
$[BF_4]^-$	T_d	HF/3-21G	1.402	−420.49247
		HF/6-31G*	1.394(1.39)[d]	−422.72515
$[AlF_4]^-$	T_d	HF/3-21G	1.667	−636.59204
		HF/6-31G*	1.677(1.69)[e]	−640.03990
$[MgCl_4]^{-2}$	T_d	HF/3-21G	2.441	−2028.05333
		HF/6-31G*	2.431	−2037.84440
$[AlCl_4]^-$	T_d	HF/3-21G	2.235	−2070.20141
		HF/6-31G*	2.170(2.11-2.16)[f]	−2080.23047

[a] Bondlengths in Å, Energies in a.u.

[b] Bondlengths in parentheses are values estimated from experimental data.

[c] Ref. 13.

[d] Ref. 14.

[e] Ref. 18.

[f] Ref. 19.

Table II. Calculated and Experimental Vibrational Frequencies[a] of XY_4^- Anions

Species	Symmetry	3-21G	6-31G*	Expt.	Ref.[b]
$[BeF_4]^{-2}$	A_1	598	533	547	13
	E	247	250	255	
	T_2	417	384	385	
	T_2	1038	873	800	
$[BF_4]^-$	A_1	855	812	777	14
	E	375	372	360	
	T_2	561	561	533	
	T_2	1358	1203	1070	
$[AlF_4]^-$	A_1	706	669	622	16
	E	231	219	210	
	T_2	343	339	322	
	T_2	944	947	760	
$[MgCl_4]^{-2}$	A_1	236	224	252	15
	E	87	83	100	
	T_2	139	138	142	
	T_2	361	328	330	
$[AlCl_4]^-$	A_1	297	353	351	7
	E	110	121	121	
	T_2	162	192	186	
	T_2	431	510	490	

[a] The theoretical frequencies are harmonic values; whereas the experimental frequencies are anharmonic values.

[b] Reference for the experimental frequencies.

DOI: 10.1149/198601.0296PV

X-RAY DIFFRACTION ANALYSIS OF SOME MOLTEN SALTS WITH LOW MELTING POINT

Hideo OHNO,Kazuo IGARASHI*,Yasuhiko IWADATE*,
Mitsuhisa MUROFUSHI*,Junichi MOCHINAGA*
and Kazuo FURUKAWA**

Function Materials Laboratory,Department of Fuels
and Materials Research,Japan Atomic Energy Research
Institute,Tokai-mura,Ibaraki 319-11,JAPAN

* Department of Synthetic Chemistry,Faculty of
Engineering,Chiba University,Yayoi-cho,Chiba-shi
260,JAPAN

** Institute of Research and Development,
Tokai University,Hiratsuka,Kanagawa 259-12,JAPAN

ABSTRACT

X-ray diffraction experiments of molten NaSCN, KSCN and CsSCN were performed; average nearest-neighbour distances and coordination numbers were obtained. The linear SCN^- ion is stable in these melts and C-N and C-S distances are 1.15 and 1.65Å ,respectively. The three dimensional arrangement in the near-neighbour cation-SCN^- pair has also been demonstrated by the correlation method.

INTRODUCTION

In recent years ionic liquids with low melting points such as alkali thiocyanates or $AlCl_3$-NaCl-KCl system have been proposed for use as reductant in some chemical reactions or as electrolyte in molten salt batteries and photoelectrochemical cells[1,2,3].

The existence of SCN^- ion in alkali thiocyanates has been reported using the analysis of thermodynamic properties and Raman spectroscopy studies. However, the structure of the complex ions has not yet been determined.

We report here X-ray diffraction analysis of molten NaSCN,KSCN and CsSCN and the structure factors of complex ion such as atomic distances and coordination numbers are determined. The three dimensional arrangement in the near-neighbours has also been demonstrated by the correlation method.

EXPERIMENTAL

The scattering intensity was measured by an X-ray diffractometer having parafocusing reflecting geometry of the θ-θ type, with a curved graphite monochromator mounted in the diffracted beam. Measurements were made using the step-scanning technique for a fixed time at every 0.25 change in the range($3 \leqslant \theta \leqslant 45$) (from 0.93 to 12.5Å^{-1} in $Q=4\pi \sin\theta / \lambda$) for MoK$_\alpha$ radiation. The temperature was controlled with maximum error of 5°C.

The experimental intensity data were corrected for background, polarization, absorption and compton radiation by the usual methods and were scaled to the independent scattering factor for the stoichiometric unit using the Krogh-Moe-Norman method.

The radial distribution function(r.d.f.),D(r),of electron density around the atom is given per molecule by the following equations:

$$D(r) = 4\pi r^2 \sum_m \bar{K}_m g_m(r)$$

$$= 4\pi r g_0 \sum_m \bar{K}_m + \sum_m (\bar{K}_m)^2 2r \Big/ \pi \int_0^{Q_{max}} Q \cdot i(Q) \sin(rQ)\, dQ \qquad (1)$$

$$i(Q) = I_{eu}^{coh}(Q) \Big/ \sum_m f_m^2(Q) - 1 \qquad (2)$$

where $\bar{K}_m$ is the effective number of electrons in the atom m, $g_m(r)$ the effective electron density at distance r, g_0 is the average electron density, $f_m(Q)$ is the independent atomic scattering intensity. $I_{eu}^{coh}(Q)$ is the total coherent intensity function and Q_{max} is the maximum value of Q reached in the experiments. Summation is over the stoichiometric unit for m.

The average correlation function G(r) is obtained using the equation

$$G(r) = 1 + \sum_m (\bar{K}_m)^2 \Big/ (\sum \bar{K}_m \pi r^2 g_0 r) \int_0^{Q_{max}} Q \cdot i(Q) \sin(rQ)\, dQ. \qquad (3)$$

RESULTS

(a)NaSCN

Fig.1 shows the observed Qi(Q) curve for molten NaSCN at 320°C. Fig.2 shows D(r),function D(r)/r and G(r) curves.

G(r) has peaks at r=1.15,1.65,2.30,2.80 and 4.15Å. The first and second peaks correspond to C-N and C-S distances and the observed coordination number of N or S around a carbon is one. The results show that SCN^- ion is stable in the melt.

The peak between 2.3 and 3.0Å corresponds to the interaction between Na^+ and SCN^- ions. The peak at 2.35Å corresponds to Na-N and/or Na-C distance. The peak at 2.80Å corresponds to Na-S distance. S-N distance in SCN^- ion also contributes to this peak. The peak at about 4.1Å is the interaction between the nearest neighbour Na^+-Na^+ and SCN^--SCN^- pairs

(b)KSCN

Figs.3 and 4 show Qi(Q),D(r) and G(r) curves for molten KSCN at 200°C. G(r) has peaks at r=1.15,1.65 and 3.25Å. The peaks at 1.15 and 1.65Å correspond to C-N and C-S distances and the observed coordination numbers of both nitrogen and sulphur around a carbon is one. This means that SCN^- is also stable in molten KSCN. The strong peak at around 3.25Å corresponds to the nearest-neighbour interaction between K^+ and SCN^- ions.

(c)CsSCN

Figs.5 and 6 show Qi(Q),D(r) and G(r) curves for molten CsSCN at 230°C. G(r) has peaks at r=1.15,1.65,3.65 and 5.4Å. The first and second peaks correspond to C-N and C-S distances in SCN^- ion. The small shoulder at 2.8Å corresponds to S-N distance in SCN^- ion. The strong peak at around 3.65Å corresponds to the interaction between Cs^+ and SCN^- ion. The peak at around 5.4Å is the interaction between the nearest-neighbour Cs^+-Cs^+ and SCN^--SCN^- pairs.

DISCUSSION

X-ray diffraction analysis of molten NaSCN,KSCN and CsSCN shows that SCN^- ion is stable in these melts and the atomic distances of C-N and C-S are 1.15 and 1.65Å. For the analysis of the structure of SCN^- ion in detail, pulsed neutron diffraction was applied to molten KSCN.

Coherent scattering cross-section of thermal neutron $(d\sigma/d\Omega)_{coh}$ is given by equation(4).

$$(d\sigma/d\Omega)_{coh} = (\sum_i x_i b_i)^2 \, I_N(Q), \qquad (4)$$

where x_i and b_i are the atomic fractions and scattering amplitudes of i-th atom. The structure factor $I_N(Q)$ is mainly contributed from SCN^- ion at high Q values and is expressed by equation(5).

$$I_N(Q)=b_C^2+b_N^2+b_S^2+2[b_Cb_N\sin(Qr_{CN})/Qr_{CN}$$
$$+b_Nb_S\sin(Qr_{NS})/Qr_{NS}+b_Cb_S\sin(Qr_{CS})/Qr_{CS}]$$
$$/(b_K+b_C+b_N+b_S)^2. \quad (5)$$

Fig. 7 shows the observed $I_N(Q)$. Dotted line shows the calculated curve using equation (5) with parameters listed in Table 1. The N-S distance is summation of C-N and C-S distances and the result indicates the linear SCN^- ion.

Most probable arrangement of cation around SCN^- ion was analyzed using the following procedure by the correlation method. We assumed that the scattering intensity was divided into two contributions from short-range and long-range arrangements of a stoichiometric unit, and these contributions were incoherent with each other. In molten alkali thiocyanates, the short-range and long-range arrangements were indicative of arrangements of the cations around a SCN^- ion within one stoichometric unit and among different stoichiometric units, respectively.

The intensity function in equation (2) is defined by equation (6) as the sum of three terms,namely;

$$I_{eu}^{coh}(Q) = I_\alpha(Q) + I_\beta(Q) + I_\gamma(Q). \quad (6)$$

The first and second terms in equation (6) describe the scattering intensities of the short-range arrangement and third term describes the scattering intensity of the long-range arrangement. $I_\alpha(Q)$, $I_\beta(Q)$, and $I_\gamma(Q)$ are given by the following equations;

$$I_\alpha(Q)= \sum_m f_m^2 , \quad (7)$$
$$I_\beta(Q)=\sum\sum_{i\neq j} f_if_j[\sin(Qr_{ij})/(Qr_{ij})] \exp(-b_{ij}Q^2), \quad (8)$$
$$I_\gamma(Q)=\sum\sum_{i\neq j} F_iF_j[\sin(Qr_{ij})/(Qr_{ij})] \exp(-b_{ij}Q^2). \quad (9)$$

where f_m, f_i and f_j are the atomic scattering factors of m, i and j atoms,respectively. F_i and F_j are the unit scattering factors of i and j units. r_{ij} is the inter-atomic distance between the i-th and j-th atoms or the inter-unit distance between the i-th and j-th units. b_{ij} is the temperature factor that is the half the mean square variation in r_{ij}.

The function $I_\gamma(Q)$ decays to zero much faster than the function $I_\alpha(Q)$ and $I_\beta(Q)$, so that equation (6) can be written approximately, as follows at large values of Q;

$$I'(Q)= I_\alpha(Q) + I_\beta(Q). \qquad (10)$$

Namely, the scattering intensity contains a contribution from only the short-range arrangement at large values of Q.

By the analysis of third peak in D(r), three cations are expected to be in near SCN^- ion in molten NaSCN,KSCN and CsSCN. Fig.8 shows three typical arrangements of cations around a SCN^- ion. The short-range arrangement of these molten salts based on three models was analyzed by applying Debye's equation to the observed scattering intensity. The parameters are listed in Table 2. The calculated Qi(Q) of molten NaSCN,KSCN and CsSCN based on three models,(a), (b), and (c), are shown in Figs.1,3 and 5 with the measurements, respectively.

In molten CsSCN, the calculated Qi(Q) based on model (a) is in relatively good agreement with the observed one. On the other hand, all three models will be acceptable in molten NaSCN. The result indicates that large cations will occupy the position near to the central atom of SCN^- ions and small cations will occupy all the positions around SCN^- ions.

CONCLUSION

(1) The SCN^- ion is stable in molten NaSCN,KSCN and CsSCN and the atomic distances of C-N and C-S are 1.15 and 1.65Å. The linear SCN^- ion in molten KSCN is verified by the analysis of pulsed neutron diffraction.

(2) Most probable arrangement of cation around a SCN^- ion is examined by the correlation method. The large cation has high probability to occupy the position near to the central atom of SCN^- ion and the small cation will occupy all the positions around SCN^- ion.

REFERENCES

[1] D.H.Kerridge:Advance in Molten Salt Chemistry, Ed. by J.Braunstein et al.,Vol.3,249(1975).

[2] R.A.Carpio,L.A.King,R.E.Lindstrom,J.C.Nardi and C.L.Hussey: J.Electrochem.Soc.,126,1644(1979).

[3] R.Thapar and K.Rajeshwar: ibid,129,560(1982).

Table 1 Distances of atomic pairs in SCN^- ion.

i	j	$r_{ij}/Å$
C	N	1.15_0
C	S	1.65_0
N	S	2.80_0

Table 2 Number of interactions, N_{ij}, atomic distances, r_{ij}, and associated root mean square displacements $\langle \Delta r_{ij}^2 \rangle^{1/2}$

Molten NaSCN(320°C)						
	i	j	N_{ij}	$r_{ij}/Å$	b_{ij}	$\langle \Delta r_{ij}^2 \rangle^{1/2}/Å$
SCN^-	S	C	2.0	1.65	0.0022	0.066
	C	N	2.0	1.15	0.0019	0.062
	S	N	2.0	2.80	0.021	0.065
Model(a)	M	S	2.0	2.88	0.0285	0.239
	M	C	2.0	2.35	0.0475	0.308
	M	N	2.0	2.50	0.0485	0.311
Model(b)	M	S	1.0	2.88	0.0285	0.239
	M	C	1.0	2.35	0.0475	0.308
	M	N	1.0	2.50	0.0485	0.311
	M	S	0.5	2.80	0.028	0.237
	M	C	0.5	3.67	0.054	0.329
	M	N	0.5	5.11	0.068	0.369
	M	S	0.5	4.41	0.056	0.335
	M	C	0.5	3.44	0.048	0.310
	M	N	0.5	2.35	0.035	0.265
Model(c)	M	S	1.0	2.80	0.028	0.237
	M	C	1.0	3.67	0.054	0.329
	M	N	1.0	5.11	0.068	0.369
	M	S	1.0	4.41	0.056	0.335
	M	C	1.0	3.44	0.048	0.310
	M	N	1.0	2.35	0.035	0.265

Table 2 Continued

			Molten KSCN(200°C)				Molten CsSCN(230°C)		
	i	j	N_{ij}	$r_{ij}/\text{Å}$	b_{ij}	$\langle \Delta r_{ij}^2 \rangle^{1/2}/\text{Å}$	$r_{ij}/\text{Å}$	b_{ij}	$\langle \Delta r_{ij}^2 \rangle^{1/2}/\text{Å}$
SCN^-	S	C	2.0	1.65	0.0072	0.120	1.65	0.0018	0.060
	C	N	2.0	1.15	0.0081	0.127	1.15	0.0018	0.060
	S	N	2.0	2.80	0.0077	0.124	2.80	0.0018	0.060
Model(a)	M	S	2.0	3.28	0.0157	0.177	3.62	0.0239	0.219
	M	C	2.0	2.80	0.0255	0.226	3.20	0.0468	0.306
	M	N	2.0	3.02	0.0338	0.260	3.40	0.0355	0.266
Model(b)	M	S	1.0	3.28	0.0157	0.177	3.62	0.0239	0.219
	M	C	1.0	2.80	0.0255	0.226	3.20	0.0468	0.306
	M	N	1.0	3.02	0.0338	0.260	3.40	0.0355	0.266
	M	S	0.5	3.23	0.0152	0.174	3.54	0.0235	0.217
	M	C	0.5	4.12	0.043	0.293	4.81	0.0568	0.337
	M	N	0.5	5.57	0.062	0.352	5.81	0.0710	0.377
	M	S	0.5	4.93	0.045	0.300	5.21	0.0578	0.340
	M	C	0.5	3.95	0.033	0.257	4.25	0.0480	0.310
	M	N	0.5	2.78	0.028	0.237	3.09	0.0345	0.263
Model(c)	M	S	1.0	3.23	0.0152	0.174	3.54	0.0235	0.217
	M	C	1.0	4.12	0.043	0.293	4.81	0.0568	0.337
	M	N	1.0	5.57	0.062	0.352	5.81	0.0710	0.377
	M	S	1.0	4.93	0.045	0.300	5.21	0.0578	0.340
	M	C	1.0	3.95	0.033	0.257	4.25	0.0480	0.310
	M	N	1.0	2.78	0.028	0.237	3.09	0.0345	0.263

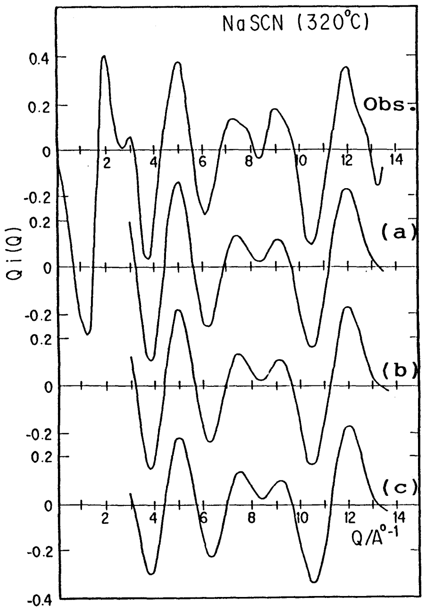

Fig.1 Observed and calculated Qi(Q) of molten NaSCN at 320°C

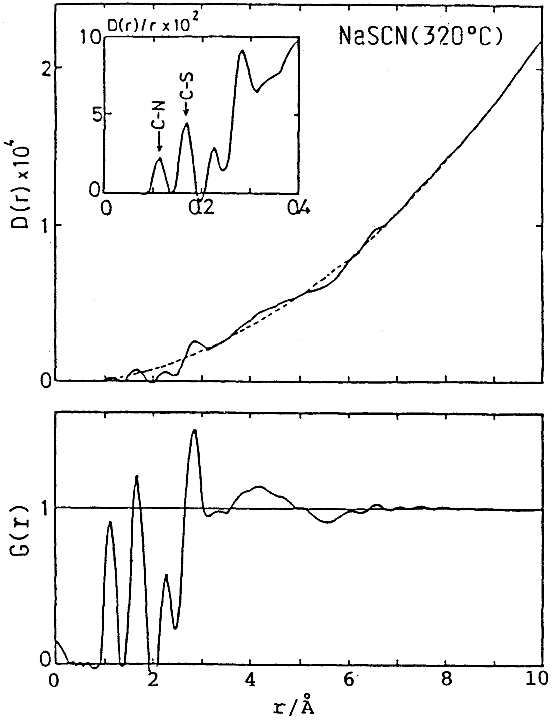

Fig.2 D(r),D(r)/r and G(r) of molten NaSCN at 320°C.

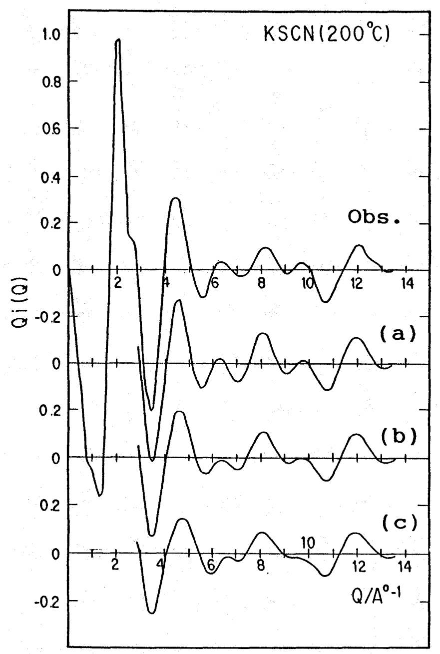

Fig.3 Observed and calculated Qi(Q) of molten KSCN at 200°C.

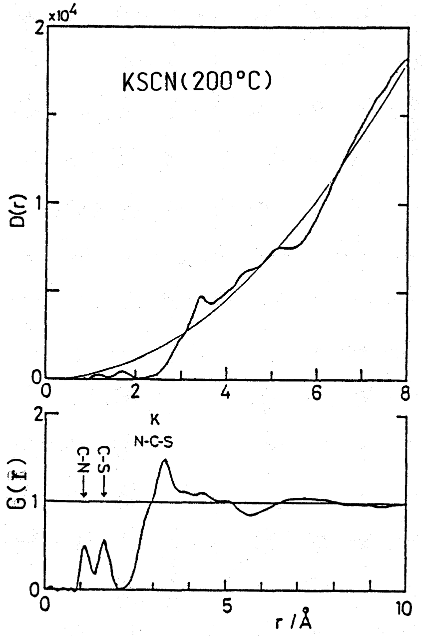

Fig.4 D(r) and G(r) of molten KSCN at 200°C.

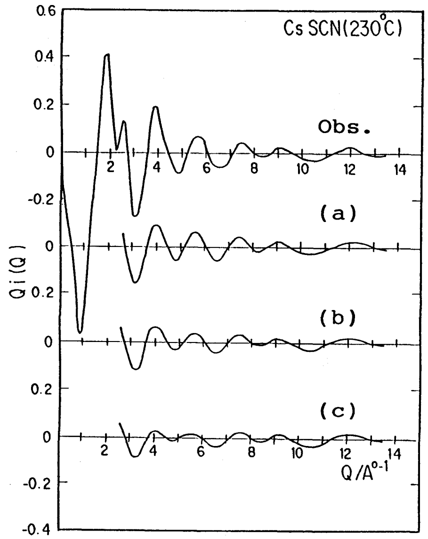

Fig.5 Observed and calculated Qi(Q) of molten CsSCN at 230°C.

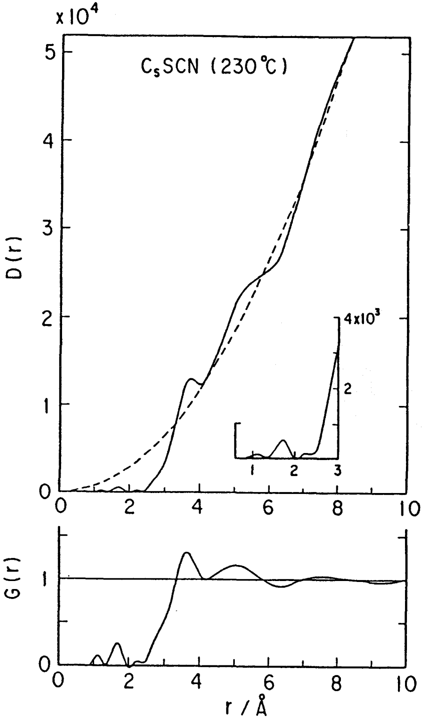

Fig.6 D(r) and G(r) of molten CsSCN at 230°C.

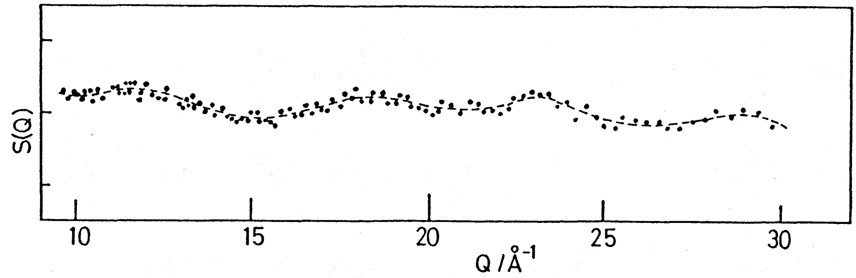

Fig.7 S(Q) obtained by pulsed neutron diffraction. Dotted line shows the calculated curve using the Debye equation with parameters listed in Table 1.

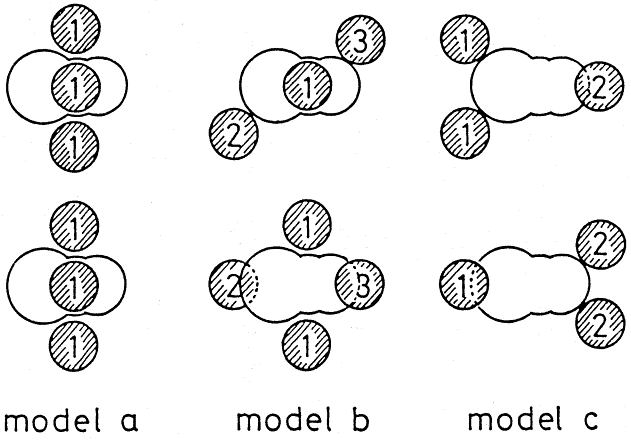

Fig.8 Three typical arrangements of cations around a SCN$^-$ ion.

DOI: 10.1149/198601.0307PV

"ALUMINIUM BROMIDE-1-METHYL-3-ETHYLIMIDAZOLIUM BROMIDE IONIC LIQUIDS. DENSITIES, VISCOSITIES, ELECTRICAL CONDUCTIVITIES, AND PHASE TRANSITIONS"

John R. Sanders, Edmund H. Ward, and Charles L. Hussey*
Department of Chemistry
University of Mississippi
University, MS 38677

ABSTRACT

The solid-liquid phase diagram, experimental glass transition points, densities, viscosities, and electrical conductivities are reported for the aluminium bromide-1-methyl-3-ethylimidazolium bromide ionic liquid. Certain compositions of this two component molten salt are liquid at room temperature. Density, viscosity, and conductivity data were collected over the range of aluminium bromide mole fractions from ca. 0.35 to 0.75 and over the range of temperatures from ca. 25 to 100 °C. Equations are presented which describe both the composition and temperature dependence of the densities and transport properties. Both the viscosities and the conductivities displayed the non-Arrhenius temperature dependence typically associated with glass forming ionic liquids. Temperature dependent activation energies were derived for these transport processes by using the Vogel-Tammann-Fulcher equation.

INTRODUCTION

Certain mixtures of aluminium bromide ($AlBr_3$) and 1-methyl-3-ethylimidazolium bromide (MeEtimBr) are liquid at room temperature and display physical and chemical characteristics similar to binary aluminium chloride-organic chloride molten salt systems like aluminum chloride-1-butylpyridinium chloride ($AlCl_3$-BupyCl) and aluminium chloride-1-methyl-3-ethylimidazolium chloride ($AlCl_3$-MeEtimCl). In fact, the $AlBr_3$-MeEtimBr system is the bromide analog of the latter melt. All of these molten salts fall into the same general class of solvents that are known as room temperature haloaluminate ionic liquids. Several reviews which discuss these systems have been published (1-3).

$AlBr_3$-MeEtimBr molten salts may be useful solvents for electrochemical and spectroscopic investigations that are concerned with the chemistry of bromo complexes and related species since they are expected to display adjustable Lewis acid-base characteristics similar to those exhibited by the related chloroaluminate systems. However, the utilization of these melts as solvents presupposes knowledge of their physical properties and liquid range. The study reported herein was undertaken in an effort to obtain information about the densities, transport properties, and phase transitions of this new ionic solvent system. It is the first reported comprehensive investigation of the preparation and physical properties of a room temperature bromoaluminate melt.

EXPERIMENTAL

Melt preparation.-The preparation of melt samples and the loading of these samples into the apparatus described below were conducted in the nitrogen-filled drybox system described previously (4). Anhydrous aluminium bromide (Fluka, 98 %) was sublimed under vacuum in this drybox a minimum of three times beforeuse. 1-Methyl-3-ethylimidazolium bromide was prepared by combining stoichiometric quantities of ethyl bromide (Baker, reagent grade) and freshly distilled 1-methylimidazole (Aldrich, 99%). The ethyl bromide was added drop wise to the chilled 1-methylimidazole in a flask fitted with a reflux condenser. (**Caution**: a rapid exothermic reaction takes place between these components.) The flask was cooled and the resulting white solid was recrystallized twice from anhydrous acetonitrile in Kontes Airless-ware. Great care was taken to avoid exposure of the salt to atmospheric moisture. The melting point of the purified product was 77 °C. The aluminum bromide-1-methyl-3-ethylimidazolium bromide melts were prepared by combining precisely weighed quantities of the purified components inside the drybox. These melts appeared somewhat photosensitive and developed a yellow coloration due to the formation of free bromine after exposure to ordinary room lighting for several days. Appropriate precautions were taken to avoid unnecessary exposure of the $AlBr_3$-MeEtimBr melt to light, and no measurements were performed with highly discolored samples.

Phase transition measurements.-Melting and glass transition points were determined in sealed quartz EPR tubes with the temperature controlled apparatus described in a recent publication (5). The experimental methodology used during these experiments was similar to that described previously. In addition, some melting points were measured in melting point capillaries with a MEL-TEMP apparatus (Laboratory Devices, Cambridge, Mass.).

Density measurements.-Densities were determined in a Pyrex dilatometer that was constructed from the bulb of a 10 mL pipet and a length of graduated capillary tubing. The diameter of the capillary tube bore was 1.74 mm, and etched graduations were provided every 1.00 mm on the capillary tube. One end of the capillary tube was attached to the pipet bulb while a ROTAFLO TF6/13 Teflon vacuum stopcock was affixed to the other end. A similar stopcock was also attached to the remaining end of the pipet bulb. The dilatometer was weighed, filled and sealed in the drybox, and then weighed again before being placed in an external water bath. The temperature of the water bath was controlled to ± 0.1°C by means of either a Precision Scientific No. 66530 constant temperature bath controller or a B. Braun Model 1420 Thermomix immersion controller. The temperature of the bath was monitored with calibrated Brooklyn thermometers. The upper stopcock protruded above the surface of the water bath and was vented to the atmosphere through a drying tube and then sealed each time the water bath temperature was changed. The dilatometer was calibrated over its entire working volume with distilled water. No corrections for thermal expansion of the apparatus were found necessary over the range of temperatures that was investigated. It was estimated that the density measurements could be reproduced with a precision of ± 0.11 %.

Viscosity measurements.-Viscosity measurements were made with a modified Cannon-Fenske No. 200 viscometer (Fisher Scientific). The viscometer was made airtight by cutting-off both upright tubes horizontally just above the upper reference mark and then attaching the open ends of a U-shaped piece of large bore Pyrex tubing to the ends of the severed tubes of the viscometer. A ROTOFLO TF6/18 vacuum stopcock was also attached to the viscometer. With these modifications the viscometer could be filled and sealed in the drybox and then removed and evacuated prior to immersion in the water bath described above. The viscometer was mounted in the water bath on a vertical plate which could be manually rotated in order to recharge the viscometer. The bearings which supported this plate were fitted with a mechanism which stopped the rotation of the plate in a reproducible manner when the viscometer was exactly horizontal. The viscometer was calibrated with freshly distilled ethylene glycol over the appropriate range of temperatures. The viscometer was typically charged with 10.0 mL of sample. The efflux time of the sample in the viscometer was measured with a stopwatch to ± 0.1 s. The estimated reproducibility of a given measurement was ± 2 %.

Conductivity measurements.-Conductivity measurements were made with a Yellow Springs Instrument Co. No. 3403 dip type conductivity electrode equipped with platinized platinum-iridium electrodes. When in use, the electrode was sealed airtight with a Teflon bushing and Teflon encased o-ring into a cell constructed by closing the end of a #15 Ace-Thred adapter tube. This cell could be filled and sealed in the drybox before immersion in the water bath (*vide supra*). Resistance measurements were made at 1 kHz with a General Radio Type 1650-A impedance bridge. Resistance measurements taken at 5 kHz with this bridge and an auxiliary oscillator were identical to those made at 1 kHz. The conductivity cell was calibrated at 25 °C with 0.001, 0.01, 0.1, and 1.0 M solutions of KCl in freshly boiled, distilled, deionized water. The data given by Janz and Tompkins (6) were used to calculate the cell constant which was *ca.* 1.0. No corrections for changes in the cell constant with temperature were found necessary over the range of temperatures examined in this study. It was determined that the resistance of a given solution at a fixed temperature could be reproduced to within + 0.31 %.

RESULTS AND DISCUSSION

Phase transitions.-A phase diagram for the $AlBr_3$-MeEtimBr melt system is shown in Fig. 1. Both melting points and glass transition points were obtained for some of the $AlBr_3$-MeEtimBr mixtures. In a few cases it was not possible to induce the crystallization of certain melts even at the temperature of liquid nitrogen, and therefore, only experimental glass transition points are reported for these liquids.

The phase diagram for the $AlBr_3$-MeEtimBr system is similar in general appearance to that for its chloroaluminate analog (5). However, there are some important temperature differences between the phase diagrams for the bromoaluminate and chloroaluminate systems that should be noted. The solid-liquid phase transitions for the latter system are considerably lower than those for the former melts for mixtures in the range $0 < \underline{X} < 0.60$ while the melting points for $AlBr_3$-MeEtimBr mixtures with $\underline{X} > $ ca. 0.75 are lower than those for the corresponding $AlCl_3$-MeEtimCl mixtures. The lower melting points found in very acidic $AlBr_3$-MeEtimBr melts versus those for the $AlCl_3$-MeEtimCl system probably reflect the lower melting point of $AlBr_3(Al_2Br_6)$ relative to that of $AlCl_3(Al_2Cl_6)$.

Densities.-Experimental density data for all of the melt compositions examined in this study are shown in Fig. 2. Experimental densities, ρ, were found to vary linearly with temperature. Data for each composition were fitted to equations of the form

$$\rho = \underline{a} + \underline{b}T \qquad [1]$$

The solid lines that appear in Fig. 2 were calculated for each composition from the values of a and b obtained from these fits. It was found that the variation of the parameters a and b with X could be represented by polynomials of the type

$$\underline{a} = \underline{a}_0 + \underline{a}_1\underline{X} + \underline{a}_2\underline{X}^2 + \underline{a}_3\underline{X}^3 + \dots \qquad [2]$$

$$\underline{b} = \underline{b}_0 + \underline{b}_1\underline{X} + \underline{b}_2\underline{X}^2 + \underline{b}_3\underline{X}^3 + \dots \qquad [3]$$

A third order polynomial was needed in order to adequately represent the the variation of a and b with X in melts with compositions in the range $0.50 < \underline{X} \leq 0.75$ (acidic melts) while a second order polynomial was found to be sufficient for melts in the range $0.30 \leq \underline{X} \leq 0.50$ (neutral and basic melts). The parameters obtained from non-linear least squares fits of a and b as a function of X are collected in Table I. The parameters collected in this table reproduced the experimental density data in acidic melts with a standard deviation, s, of 1.69×10^{-3} and in neutral and basic melts with $\underline{s} = 1.81 \times 10^{-3}$. The standard deviations reported here and elsewhere (vide infra) were corrected for the total number of model parameters used to reproduce the experimental data. Figure 3 shows a three dimensional plot, produced from the constants in Table I with Eq. [1] to [3], which gives an overall perspective of the variation of density with composition and temperature and, in addition, delineates the range in which densities were determined.

Viscosity.-The experimental kinematic viscosities for $AlBr_3$-MeEtimBr mixtures were converted to absolute viscosities with the density data presented above. Arrhenius plots for the absolute viscosities, η, are shown in Fig. 4, and it can be seen that $\ln\eta$ does not vary linearly with 1/T. Similar behavior was noted for the viscosities of the $AlCl_3$-MeEtimCl and related 1,3-dialkylimidazolium chloride-based chloroaluminate molten salts (5). This non-Arrhenius behavior is a characteristic of glass forming melts (7). Therefore, the logarithmic form of the three parameter Vogel-Tammann-Fulcher (VTF) equation (7) was used to represent the variation of the absolute viscosities as a function of the absolute temperature:

$$\ln\eta = \underline{k}_\eta/(\underline{T}-\underline{T}_o) + 1/2\ln\underline{T} + \ln\underline{A}_\eta \qquad [4]$$

$\underline{k}_\eta$, $\underline{T}_o$, and $\ln\underline{A}_\eta$ are empirical parameters in this equation. However, $\underline{k}_\eta\underline{R}$, where $\underline{R}$ is the universal gas constant, is frequently identified with the Arrhenius activation energy, and $\underline{T}_o$, often designated as the "ideal" glass transition temperature, has been given quasi-thermodynamic significance through the free volume theory of Cohen and Turnbull (8) and the configurational entropy approach of Adams and Gibbs (9). However, a detailed study of these parameters was not the goal of this study.

It was determined that each of the three parameters in Eq. [4] could be fitted as a function of $\underline{X}$ to cubic polynomial equations of the form

$$f(\underline{X}) = \underline{c}_o + \underline{c}_1\underline{X} + \underline{c}_2\underline{X}^2 + \underline{c}_3\underline{X}^3 \qquad [5]$$

in neutral and basic melts and to to quadratic equations of the form

$$f(\underline{X}) = \underline{c}_o + \underline{c}_1/\underline{X} + \underline{c}_2/\underline{X}^2 \qquad [6]$$

in acidic melts. Values obtained for the constants in these equations are collected in Tables II and III. Eq. [4] and [5], with the appropriate parameters from Table II, reproduced the experimental viscosity data in neutral and basic melts with $\underline{s} = 2.71 \times 10^{-2}$ while a value of $\underline{s} = 4.63 \times 10^{-2}$ was obtained in acidic melts by using Eq. [4] and [6] and the parameters in Table III.

A three dimensional plot of viscosity as a function of temperature and composition, constructed by using Eq. [4] - [6] and the parameters collected in Tables II and III, is depicted in Fig. 5. Qualitatively, the viscosities of the melt rise from a poorly defined minimum at $\underline{X}$ = 0.50 as $\underline{X}$ is increased or decreased from this value. The irregular increase in the viscosity in acidic melt as $\underline{X}$ is increased was experimentally reproducible and did not appear to be the result of an artifact in the experimental method or the procedure used to fit the data. These results are somewhat different than those obtained for the chloroaluminate analog (5) where the viscosity was found to decrease continuously with $\underline{X}$.

Conductivity.-Experimental specific conductivity values, κ, were converted to equivalent conductivities by using the equation

$$\Lambda = \kappa \underline{M}_E/\rho \qquad [7]$$

where $\underline{M}_E$ is the equivalent weight of the molten mixture and is given by the equation

$$\underline{M}_E = 191.07 + x/(1-\underline{X})266.71 \qquad [8]$$

This method for representing the molecular weight of a haloaluminate melt is advantageous because it takes into consideration the number of ions in the mixture (5,10).

Arrhenius plots for the equivalent conductance of the $AlBr_3$-MeEtimBr melt are shown in Fig. 6. Like viscosity (vide supra), the equivalent conductance exhibits non-Arrhenius behavior. Therefore, the equivalent conductivities were fitted to the logarithmic form of the VTF equation for equivalent conductance (7):

$$\ln\Lambda = -\underline{k}_\Lambda/(\underline{T}-\underline{T}_o) - (1/2)\ln\underline{T} + \ln\underline{A}_\Lambda \qquad [9]$$

As for viscosity, the parameters $\underline{k}_\Lambda$, $\underline{T}_o$, and $\ln\underline{A}_\Lambda$ were fitted to Eq. [5] in basic and neutral melt and to Eq. [6] in acidic melt. The values of the constants that resulted are collected in Tables II and III. These equations and the associated model parameters reproduced the experimental data in acidic melts with $\underline{s} = 4.58 \times 10^{-2}$ and in basic melt and neutral melts with $\underline{s} = 5.13 \times 10^{-2}$.

A three dimensional plot which delineates the range of composition and temperature over which conductance was studied is shown in Fig. 7. The maximum conductivity of the $AlBr_3$-MeEtimBr system occurs at exactly $\underline{X} = 0.50$, and the conductivity decreases noticeably as $\underline{X}$ is increased or decreased from this composition. The organic cation has been determined to transport over 70 % of the charge in the $AlBr_3$-MeEtimBr (11) and the $AlCl_3$-MeEtimCl systems (4,12,13). In addition, the formation of ion pairs and larger aggregates between the organic cation and the anions in basic melt, especially bromide ion, have been shown to be important (14). Therefore, the decrease in equivalent conductance shown in Fig. 7 as $\underline{X}$ is decreased from 0.50 probably results from a decrease in the mobility of the organic cation as the relatively weak aggregates that involve $MeEtim^+ \ldots AlBr_4^-$ ion pairs are substituted for those containing the stronger $MeEtim^+ \ldots Br^-$ ion-pair interactions. The replacement of relatively weak aggregates by those with stronger anion-cation interactions may also account for the concomitant increase in viscosity that is found when $\underline{X}$ is decreased in basic melt. The decrease in the equivalent conductance and the increase in viscosity with increasing $\underline{X}$ noted in acidic melts can not be explained in this fashion since ion-ion interactions are believed to become less important as $\underline{X}$ is increased in this composition region (14).

ACKNOWLEDGEMENT

The authors wish to express their gratitude to Drs. J. S. Wilkes and A. A. Fannin,Jr. of the F. J. Seiler Research Laboratory for helpful discussions about this work and for use of their facilities to obtain the phase transition data. We are indebted to Mr. K. G. Ray for verifying the experimental glass transition points. This work was supported by the National Science Foundation through Grant No. CHE 8412730.

REFERENCES

1. H. L. Chum and R. A. Osteryoung in "Ionic Liquids", D. Inman and D. G. Lovering, Eds., Plenum Press, New York, N.Y., 1981, pp. 407-423.
2. C. L. Hussey, Adv. Molten Salt Chem., 5, 185 (1983).
3. R. J. Gale and R. A. Osteryoung in "Molten Salt Techniques", Vol. 1, D. G. Lovering and R. J. Gale, Eds., Plenum Press, New York, N.Y., 1983, pp. 55-78.
4. C. L. Hussey and H. A. Øye, This Journal, 131, 1621 (1984).
5. A. A. Fannin,Jr., D. A. Floreani, L. A. King, J. S. Landers, B. J. Piersma, D. J. Stech, R. L. Vaughn, J. S. Wilkes, and J. L. Williams, J. Phys. Chem., 88, 2614 (1984).
6. G. J. Janz and R. P. T. Tompkins, This Journal, 124, 55c (1977).
7. C. A. Angell and C. T. Moynihan in "Molten Salts Characterization and Analysis", G. Mamantov, Ed., Marcel-Dekker, New York, N.Y., 1969, pp. 315-375.
8. M. H. Cohen and D. Turnbull, J. Chem. Phys., 31, 1164 (1959).
9. G. Adam and J. H. Gibbs, ibid., 43, 139 (1965).
10. R. A. Carpio, L. A. King, R. E. Lindstrom, J. C. Nardi, C. L. Hussey, This Journal, 126, 1644 (1979).
11. J. R. Sanders and C. L. Hussey, unpublished data.
12. C. L. Hussey, J. R. Sanders, and H. A. Øye, This Journal, in press.
13. C. J. Dymek, Jr. and L. A. King, This Journal, 132, 1375 (1985).
14. J. S. Wilkes, C. L. Hussey, and J. R. Sanders, Polyhedron, in press.

Table I. Parameters for density, Eq. [1]-[3].

Range	a_o	a_1	a_2	a_3
$0.30 \le X \le 0.50$	1.0588	3.8594	-2.8945	0.00
$0.50 < X \le 0.75$	-5.8410	$3.7009\text{x}10^{1}$	$-5.6829\text{x}10^{1}$	$3.0474\text{x}10^{1}$
Range	b_o	b_1	b_2	b_3
$0.35 \le X \le 0.50$	$1.2907\text{x}10^{-3}$	$-1.0448\text{x}10^{-2}$	$1.1519\text{x}10^{-2}$	0.0
$0.50 < X \le 0.75$	$1.7946\text{x}10^{-2}$	$-9.0089\text{x}10^{-2}$	$1.4121\text{x}10^{-1}$	$-7.4099\text{x}10^{-2}$

Table II. Parameters for conductivity and viscosity in basic melt, $0.35 \le X \le 0.50$, Eq. [4],[5] and [9].

		c_o	c_1	c_2	c_3
conductivity	T_o	$-4.0191\text{x}10^{1}$	$1.9867\text{x}10^{3}$	$-4.5874\text{x}10^{3}$	$2.4562\text{x}10^{3}$
	k_Λ	$3.3582\text{x}10^{3}$	$-2.0888\text{x}10^{4}$	$4.8630\text{x}10^{4}$	$-3.3051\text{x}10^{4}$
	$\ln A_\Lambda$	$-2.8631\text{x}10^{1}$	$1.8526\text{x}10^{2}$	$-4.4919\text{x}10^{2}$	$3.4788\text{x}10^{2}$
viscosity	T_o	$2.1405\text{x}10^{3}$	$-1.5128\text{x}10^{4}$	$3.9396\text{x}10^{4}$	$-3.4596\text{x}10^{4}$
	k_η	$-1.4147\text{x}10^{4}$	$1.1709\text{x}10^{5}$	$-3.0743\text{x}10^{5}$	$2.6769\text{x}10^{5}$
	$\ln A_\eta$	$-1.3581\text{x}10^{1}$	$1.8522\text{x}10^{2}$	$-5.1772\text{x}10^{2}$	$4.7652\text{x}10^{2}$

Table III. Parameters for conductivity and viscosity in acidic melt, $0.50 < X \le 0.75$, Eq. [4],[6], and [9].

		c_o	c_1	c_2
conductivity	T_o	$-8.8020\text{x}10^{2}$	$1.3485\text{x}10^{3}$	$-4.2335\text{x}10^{2}$
	k_Λ	$9.3588\text{x}10^{3}$	$-1.1072\text{x}10^{4}$	$3.4117\text{x}10^{3}$
	$\ln A_\Lambda$	$-3.2068\text{x}10^{2}$	$3.5633\text{x}10^{1}$	$-1.0983\text{x}10^{1}$
viscosity	T_o	$-3.8691\text{x}10^{2}$	$7.6383\text{x}10^{2}$	$-2.6176\text{x}10^{2}$
	k_η	$6.6201\text{x}10^{3}$	$-7.8145\text{x}10^{3}$	$-2.5214\text{x}10^{3}$
	$\ln A_\eta$	$2.5515\text{x}10^{1}$	$-2.2656\text{x}10^{1}$	7.3019

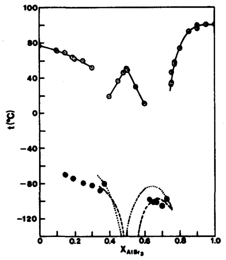

Figure 1. Phase diagram for the $AlBr_3$-MeEtimBr molten salt system; (○) melting points; (●) experimental glass transition points.

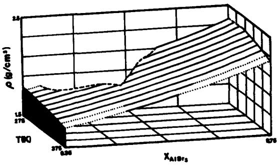

Figure 3. Dependence of the fitted densities on composition and temperature; (- -) limit defined by phase transitions; (····) projected data.

Figure 4. Absolute viscosity data as a function of temperature for melts with the following mole fractions of $AlBr_3$:(a.);
(▼) 0.3496, (■) 0.3750,
(●) 0.4000, (▽) 0.4450,
(□) 0.4752, (○) 0.4998,
(b.); (○) 0.4998,
(□) 0.5251, (▽) 0.5490,
(●) 0.5750, (■) 0.6003,
(▼) 0.6671, (⊖) 0.7498.

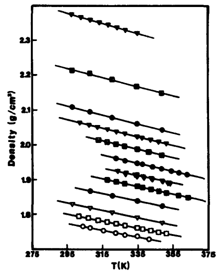

Figure 2. Density data as a function of temperature for melts with the following mole fractions of $AlBr_3$:
(○) 0.3496; (□) 0.3750;
(▽) 0.4000; (●) 0.4444;
(■) 0.4752; (▼) 0.4996;
(⊖) 0.5251; (⬓) 0.5490;
(⧨) 0.5750; (◐) 0.6003;
(◧) 0.6671; (▼) 0.7500.

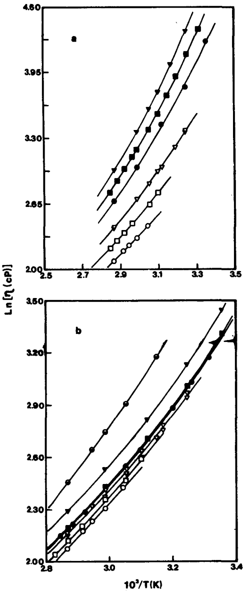

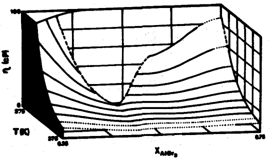

Figure 5. Dependence of the fitted values of the absolute viscosities on composition and temperature; (- -) limit defined by phase transitions; (····) projected data.

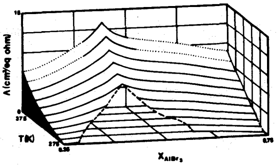

Figure 7. Dependence of the fitted values of the equivalent conductivity on composition and temperature; (- -) limit defined by phase transitions; (····) projected data.

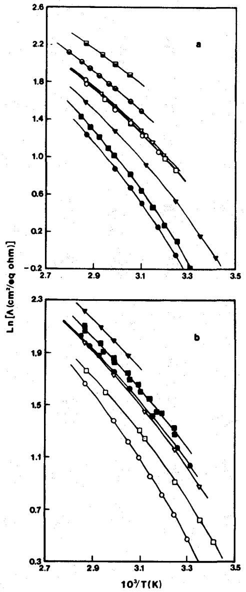

Figure 6. Equivalent conductivity data as a function of temperature for melts with the following mole fractions of $AlBr_3$:
(a); (●) 0.3493, (■) 0.3750,
(▼) 0.4000, (○) 0.4444,
(▽) 0.4450, (□) 0.4454,
(⊖) 0.4752, (⊟) 0.4999,
(b.); (▼) 0.4999, (■) 0.5490,
(●) 0.5750, (▽) 0.6003,
(□) 0.6671, (○) 0.7500.

DOI: 10.1149/198601.0317PV

POTENTIOMETRIC AND VAPOR PRESSURE MEASUREMENTS OF ACIDIC $LiCl-AlCl_3$ MELTS

Ronald A. Carpio, Armand A. Fannin, Jr.,
Roger Bunting, and Lowell A. King

The Frank J. Seiler Research Laboratory (Air Force Systems Command)
United States Air Force Academy, Colorado 80840

ABSTRACT

Vapor pressures of $LiCl-AlCl_3$ melts were measured in the temperature range 170-270°C and the $AlCl_3$ mole fraction range 0.525-0.65. Potentiometric measurements of the concentration cell

$$Al \mid LiCl(sat'd),AlCl_3 \parallel LiCl,AlCl_3(N) \mid Al$$

were made at 175°C, where the mole fraction, N, varied from approximately 0.49 to 0.65. Values of 3×10^{-5} for the dissociation constant of the reaction

$$2\ AlCl_4^- = Al_2Cl_7^- + Cl^-$$

and the composition of LiCl-saturated melt, $N_0 = 0.490$ were obtained from the precise coulometric measurements made at 175°C in the region, N = 0.49 to 0.52. The $LiCl-AlCl_3$ system is compared with the closely related $NaCl-AlCl_3$ system.

Introduction

Quantitative information on the equilibria between the various species present is essential for the utilization of binary and ternary alkali halide - aluminum chloride molten salts as battery electrolytes. For example, in our recent study (1) of acidic LiCl -

$NaCl - AlCl_3$ melts, the behavior of the transport properties was interpreted on the basis of the equilibrium

$$2Al_2Cl_7^- \quad = \quad 2AlCl_4^- + Al_2Cl_6 \qquad [1]$$

We and others have characterized the equilibrium properties of the $NaCl - AlCl_3$ melts (2-5). In addition, the equilibria in the $KCl - AlCl_3$ system have been studied (6). The $LiCl - AlCl_3$ binary was studied in the near-equimolar composition range by Torsi and Mamantov (7). Recently, room temperature $AlCl_3$ melts consisting of an N-alkylpyridinium chloride or a dialkylimidazolium chloride have been investigated (8-10). Emphasis has been placed on chloroaluminate equilibria, since varying the $MCl/AlCl_3$ ratio changes the Lewis acidity and thereby the redox and coordination chemistry of solutes in these melts.

A convenient method of studying acid-base reactions near the equimolar composition is by means of concentration cells of the type

$$Al \mid MCl(sat'd),AlCl_3 \parallel MCl,AlCl_3(N) \mid Al$$

where N is the mole fraction of $AlCl_3$. It is common to fix the concentration of the electrolyte on one side of the barrier (usually a frit) and vary the concentration of the melt in the other portion of the cell by controlled-current anodization of an aluminum electrode. At compositions away from the equimolar region the concentration cell potential changes very little with composition. Therefore, we employed vapor pressure measurements, since the vapor pressure is more sensitive to composition in this region. Moreover, the vapor pressure measurements are important in their own right, since these data are required for our own work and for models such as used in the Alcoa electrowinning process for aluminum (11).

Experimental

Sample preparation and potentiometric measurements were performed in an argon-filled glovebox equipped with a Model MO-40 DRI-TRAIN (Vacuum Atmospheres Co.). The sum of the moisture and oxygen concentrations was maintained below 10 ppm.

Details of the electrolyte preparation are given elsewhere (12). Lithium chloride-saturated melts were prepared by mixing excess LiCl with $AlCl_3$. The melts were purified by electrolysis, using aluminum (Alfa/Ventron, m5n) electrodes. Aluminum chloride-rich melts were prepared by mixing powdered LiCl(sat'd)-$AlCl_3$ with Fluka $AlCl_3$ which previously had been purified by a sublimation procedure (13). Mole fractions were known to ± 0.001.

The LiCl-saturated melt was titrated by coulometric anodization of aluminum to an $AlCl_3$ mole fraction of approximately 0.52. A Princeton Applied Research Model 173 potentiostat/galvanostat, equipped with a Model 179 plug-in coulometer, was used. The cell and procedure were essentially the same as those described by Boxall et al. (5), except we employed a LiCl-saturated melt with an excess of LiCl as the reference. For the compositions above 0.52, the melts were prepared individually by weighing the components. We made the customary assumption that the alkali ion carries all the charge (14). The cell may be represented as

$$\mathrm{Al} \mid \mathrm{LiCl(sat'd)},\mathrm{AlCl_3} \mid \mathrm{Frit} \mid \mathrm{LiCl},\mathrm{AlCl_3}(N) \mid \mathrm{Al}$$

Frit = "fine" porosity fritted Pyrex disk

Boxall et al. (5) reported problems with NaCl(sat'd)-$AlCl_3$ reference melts. Like Dewing (15) we attempted to avoid these problems by saturating the melt at the highest temperature used, since saturation is more quickly attained upon cooling than upon heating (see Results and Discussion section). The reverse coulometric titration as done by Boxall et al. was not attempted because of complications of Li-Al formation in these melts (16).

The vapor pressure measurements were made by a differential pressure method in the apparatus shown in Fig. 1. The two sample chambers were connected by a mercury manometer. The LiCl - $AlCl_3$ sample was placed in one compartment and a NaCl - $AlCl_3$ mixture in the other. The NaCl - $AlCl_3$ composition was chosen such that its vapor pressure would approximate the expected vapor pressure of the LiCl - $AlCl_3$ melt. The cell was repeatedly degassed by melting, freezing, and then evacuating the vapor space. Solidification was needed to avoid loss of $AlCl_3$ during evacuation. This process was repeated at least five times for each sample. The apparatus then was sealed below the ground glass joints.

The apparatus was immersed in a molten $NaNO_2$-$NaNO_3$-KNO_3 eutectic bath. The temperature of the bath was controlled to ± 0.05°C by a Bayley Model 124 proportional temperature controller. Temperature measurements were made to 0.01°C with a calibrated four wire platinum resistance thermometer. The samples were agitated at temperature, for at least one-half hour to insure equilibration, then the pressure difference was determined by measuring the mercury column heights to 0.02 mm with a cathetometer. The vapor pressures of the melts were calculated from the following relationship:

$$P = (H_c - H_s)D_T/13.596 + P_c \pm P_r(T/300)$$

where P = vapor pressure (torr)

H_c = height of mercury in the counterbalance arm (mm)

H_s = height of mercury in the sample arm (mm)

D_T = density of mercury at the temperature of the measurement (g/cm^3)

P_c = vapor pressure in counterbalance arm (torr)

P_r = residual pressure at room temperature (torr)

T = absolute temperature (K)

The first term of this equation gives the pressure difference in the two arms of the manometer, corrected to the density of mercury at 0°C; the second term is calculated from published data on the NaCl/$AlCl_3$ system (17), and the third term corrects for residual gas pressure in the system, and is added if $H_c < H_s$ and subtracted if $H_c > H_s$ when measured at room temperature. The vapor pressure data computed in this manner is given in Table II.

Two approximations have been made in the method. The pressure due to residual gas was assumed to obey the ideal gas law. No correction was made for $AlCl_3$ volatilization in either melt since the estimated difference between the mole fraction changes in the two compartments would never exceed 0.2% of the smaller $AlCl_3$ mole fraction. Maximum pressure differences were approximately 100 torr, and the volumes of the cell compartments above the samples were 14.5 ± 1.5 ml.

Results and Discussion

The potentiometric data at 175°C are given in Table I and shown in Fig. 2. The emf data for the LiCl - $AlCl_3$ system were fitted to Eq. [12] of Ref. (2), originally derived for the corresponding NaCl - $AlCl_3$ system,

$$E = \frac{-4RT}{3F} \ln \left\{ \frac{(1-2N)}{(1-N)} + \left[\left(\frac{[1-2N]}{[1-N]} \right)^2 + \frac{4K_2}{K_1} \right]^{1/2} \right\} + D \qquad [2]$$

where E, R, and F have their usual electrochemical significance, D is a constant which fixes E = 0 at $N = N_0$, the reference composition.

The constants K_1 and K_2 are as defined by the equilibrium model

$$2AlCl_3 = Al_2Cl_6 \qquad K_0 \qquad [3]$$

$$Cl^- + AlCl_3 = AlCl_4^- \qquad K_1 \qquad [4]$$

$$AlCl_4^- + AlCl_3 = Al_2Cl_7^- \qquad K_2 \qquad [5]$$

The fit yielded $K_2/K_1 = (3 \pm 1) \times 10^{-5}$ and $N_0 = 0.490 \pm 0.003$. The solid curves in Fig. 2 are the loci of Eq. [2]. The value of K_2/K_1 is actually the equilibrium constant for the dissociation reaction

$$2AlCl_4^- = Al_2Cl_7^- + Cl^- \qquad [6]$$

Our values of K_2/K_1 may be compared to 5.0×10^{-5} obtained for Eq. [6] by Torsi and Mamantov (7).

This uncertainty is larger than we obtained for the corresponding NaCl-$AlCl_3$ system. The fitted value of the ratio is sensitive to the degree of saturation of LiCl in the melt. The electrolysis used to purify the melts appeared to deplete Li from the melt, probably by the half reactions

$$4\ e^- + LiAlCl_4 = LiAl(s) + 4\ Cl^-$$

$$Al = Al^{3+} + 3\ e^-$$

Replacement of the Li^+ in the melt was from excess solid LiCl present. The kinetics of LiCl dissolution are extremely slow; even with care, we could not be certain that the initial and reference melts remained saturated.

An independent value of K_2 may be derived from vapor pressure data. These vapor pressure data were fitted to a function of temperature and composition of the following form:

$$\text{Log } P = -A/T + B$$

where

$$A = a_0 + a_1N + a_2N^2$$

and

$$B = b_0 + b_1N + b_2N^2$$

The values of the parameters a_i and b_i and the standard deviation of the fit are given in Table III. Fig. 3 shows a comparison of the vapor pressure as a function of composition for the $LiCl-AlCl_3$ and the corresponding $NaCl-AlCl_3$ systems at 175°C.

It was shown (18) for near equimolar $NaCl-AlCl_3$ melts that K_2 could be obtained from the expression

$$\frac{1}{K_2} = X_{AlCl_3}\left[\frac{1}{\dfrac{2N-1}{1-N} - \dfrac{2\,(X_{AlCl_3} + 2\,X_{Al_2Cl_6})}{1 - X_{AlCl_3} - X_{Al_2Cl_6}}} - 1\right]$$

Under analogous conditions, namely $K_1 >> 1$ and assuming the solution to be ideal, the same equation may be used for the $LiCl-AlCl_3$ system . This procedure yields a value of K_2 of 1.2×10^4 at 175°C. The value of $\underline{K}_1$ from the experimentally derived ratio is then 4.0×10^8. The equilibrium constant for Eq. [1], given by $K_0/(K_2^2)$, is 0.20. These values are compared to the corresponding values for the $NaCl-AlCl_3$ system in Table IV. As inferred in earlier physicochemical measurements (1), the equilibrium constant of Eq. [1] for the $LiCl-AlCl_3$ system is greater than for the $NaCl-AlCl_3$ system.

It is informative to compare the values of the equilibrium constant for Eq. [6], i.e., K_2/K_1, which have been determined to date for the various chloroaluminates, even though comparison at the same temperature is not always possible. This comparison is shown in Table V. These data can be rationalized on the basis of the differences in polarizing character of the cations. In the $LiCl-AlCl_3$ melts, Li^+ cations effectively compete with $AlCl_3$ for the Cl^- anions, thus lowering the activity and hence the stability of the $AlCl_4^-$ species. In fact, it appears that the $AlCl_4^-$ is least stable in the $LiCl-AlCl_3$ melts. The differences in the stability of the $AlCl_4^-$ species accounts for the approximate 2.2 V electrochemical window in the $LiCl-AlCl_3$ melt near the equimolar composition which is bounded by Li-Al deposition at the cathodic limit, while the 1:1 butylpyridinium chloride-$AlCl_3$ and 1:1 imidazolium chloride-$AlCl_3$ melts have electrochemical windows of 3.6 and 4.4 V, respectively which are attributable to a cathodic limit established by the reduction of the organic cation rather than reduction of the $AlCl_4^-$ species (19). The smaller change in emf that occurs in the titration curve of the LiCl-$AlCl_3$ system, which is shown Fig. 2, is also a consequence of the reduced Cl^- ion activity in these melts. This is in accord with the relative stabilities of the metal tetrachloroaluminates reported by Juvet et al. (20) using a gas chromatographic technique. It is perhaps more obvious if it is recalled that the potential of the concentration cell in the vicinity of the 1:1 composition is given by the equation:

$$\Delta E = -RT/F \left\{\ln [Cl^-]_{II}/[Cl^-]_I\right\}$$

where $[Cl^-]_{II}$ and $[Cl^-]_I$ are the chloride concentrations in the working and reference compartments, respectively.

REFERENCES

1. R. A. Carpio, F. C. Kibler, Jr., L. A. King, W. Brockner, K. Tørklep, and H. A. Øye, Ber. Bunsenges. Phys. Chem., 85, 31 (1981).

2. A. A. Fannin, Jr., L. A. King, and D. W. Seegmiller, J. Electrochem Soc., 119, 801 (1972).

3. B. Tremillon and G. Letisse, J. Electroanal. Chem., 17, 371 (1968).

4. G. Torsi and G. Mamantov, Inorg. Chem., 10, 1900 (1971).

5. L. G. Boxall, H. L. Jones, and R. A. Osteryoung, J. Electrochem. Soc., 120, 223 (1973).

6. B. B. Brekke, J. H. von Barner, and N. J. Bjerrum, Inorg. Chem., 18, 1372 (1979).

7. G. Torsi and G. Mamantov, Inorg Chem., 11, 1439 (1972).

8. J. Gale and R. A. Osteryoung, Inorg. Chem., 18, 1603 (1979).

9. J. P. Schoebrechts and B. P. Gilbert, J. Electrochem. Soc., 128, 2679 (1981).

10. J. S. Wilkes, J. A. Levisky, R. A. Wilson, and C. L. Hussey, Inorg. Chem., 21, 1263 (1982).

11. H. A. Øye, Abstract No. 742, "Thermodynamic Properties of $AlCl_3$ -Containing Melts," Extended Abstracts 163rd Meeting of the Electrochemical Society May 8-13, 1983.

12. R. A. Carpio, L. A. King, F. C. Kibler, Jr., and A. A. Fannin, Jr., J. Electrochem. Soc., 126, 1650(1979).

13. R. A. Carpio, L. A. King, and A. A. Fannin, Jr., J. Chem. Eng. Data, 24, 22 (1979).

14. H. A. Øye and L. A. King, Inorg. Nucl. Chem. Letters, 16, 547 (1980).

15. E. W. Dewing, Met. Trans. 12B, 705 (1981).

16. R. A. Carpio and L. A. King, J. Electrochem. Soc.,128, 1510 (1981).

17. J. T. Viola, L. A. King, A. A. Fannin, Jr., and D. W. Seegmiller, J. Chem. Eng. Data, 23, 122 (1978).

18. A. A. Fannin, Jr., L. A. King, and D. W. Seegmiller, F. J. Seiler Laboratory Technical Report SRL-TR-71-0018, October, 1971.

19. M. Lipsztajn and R. A. Osteryoung, J. Electrochem. Soc., 130, 1968 (1983).

20. R. S. Juvet, Jr., V. R. Shaw, and M. A. Khan, J. Am. Chem. Soc., 91, 3788 (1969).

21. K. Schulze, D. Steinle, and H. Hoff, Z. Naturforsch., A, 28, 1847 (1973).

22. C. L. Hussey, T. B. Scheffler, J. S. Wilkes, and A. A. Fannin, Jr., Frank J. Seiler Research Laboratory Technical Report SRL-TR-83-0007, June 1984.

23. T. Matsumoto and K. Ichikawa, J. Am. Chem. Soc., 106, 4316 (1984).

Table I
Potentiometric Data for the LiCl/AlCl$_3$ System

Composition N, (AlCl$_3$)	EMF V	Composition N, (AlCl$_3$)	EMF V
0.492306	0.001	0.502446	0.147
0.492608	0.001	0.503396	0.158
0.492954	0.003	0.504392	0.178
0.493324	0.005	0.595317	0.187
0.493731	0.009	0.506282	0.195
0.494129	0.012	0.507233	0.201
0.494534	0.015	0.508191	0.207
0.495383	0.023	0.509169	0.213
0.4958	0.028	0.510154	0.218
0.496407	0.035	0.511151	0.223
0.497014	0.043	0.512142	0.227
0.497619	0.052	0.513141	0.232
0.49822	0.063	0.49227	0.001
0.49878	0.078	0.49257	0.001
0.499379	0.087	0.49292	0.003
0.500006	0.103	0.49329	0.005
0.500648	0.118	0.4937	0.009
0.501253	0.131	0.4941	0.012
0.501859	0.148	0.4945	0.015
0.502465	0.153	0.49535	0.023
0.50312	0.162	0.49577	0.028
0.503744	0.17	0.49638	0.035
0.505335	0.186	0.49698	0.043
0.490144	0.002	0.49758	0.052
0.49098	0.0045	0.49819	0.063
0.492332	0.0115	0.49875	0.078
0.493738	0.021	0.49935	0.087
0.495281	0.034	0.49997	0.103
0.496455	0.047	0.50062	0.118
0.497325	0.059	0.50122	0.131
0.498213	0.079	0.50183	0.148
0.499177	0.097	0.50243	0.153
0.499597	0.106	0.50309	0.162
0.500496	0.124	0.50371	0.17
0.50146	0.133	0.5053	0.186

Table II
Vapor Pressure Data for the LiCl/AlCl$_3$ System

Composition N, (AlCl$_3$)	Pressure Torr	Temperature °C
0.525	4.75	169.47
0.525	5.66	179.56
0.525	7.15	189.33
0.525	8.76	199.12
0.525	8.81	199.59
0.525	10.92	209.50
0.525	13.28	219.17
0.525	13.28	219.19
0.525	16.50	229.18
0.525	19.94	239.03
0.525	24.20	249.06
0.525	29.20	258.95
0.525	34.89	268.95
0.55	9.96	169.43
0.55	13.61	179.63
0.55	15.91	184.79
0.55	23.80	199.12
0.55	33.11	211.87
0.55	44.56	223.45
0.55	64.22	239.26
0.55	79.69	249.29
0.55	98.02	259.44
0.55	118.25	269.42
0.60	67.94	169.72
0.60	90.74	179.66
0.60	119.10	189.68
0.60	153.24	199.44
0.60	197.65	209.73
0.60	244.46	219.09
0.65	311.20	168.95
0.65	401.07	179.14
0.65	497.38	188.11
0.65	633.67	198.90
0.65	780.47	208.60
0.65	960.98	218.74
0.65	1169.72	228.76
0.65	1392.99	238.19

Table III
Parameters for the Vapor Pressure Equation
Log P(Torr) = -A/T + B

$$A = a_0 + a_1N + a_2N^2$$

$$B = b_0 + b_1N + b_2N^2$$

a_0=42815	a_1=-155453	a_2=132865
b_0=-107.836	b_1=379.507	b_2=-311.493

σ=0.014

Table IV

Comparison of Equilibrium Constants for the $LiCl-AlCl_3$ and the $NaCl-AlCl_3$ Systems at 175°C

Equilibrium Constant	Equilibrium Equation	$LiCl-AlCl_3$ System	$NaCl-AlCl_3$ System
K_1	[4]	4.0×10^8	3.2×10^{11}
K_2	[5]	1.2×10^4	2.5×10^4
$K_0/(K_2^2)$	[1]	2.0×10^{-1}	4.6×10^{-2}

Table V
Comparison of K_2/K_1 for Various Cations

Cation	Value of K_2/K_1	Temperature(°C)	Reference
Li^+	3×10^{-5}	175	This work
Li^+	1.6×10^{-4}	400	(7)
Na^+	7.77×10^{-8}	175	(2)
Na^+	8.00×10^{-8}	175	(4)
Na^+	1.06×10^{-7}	175	(5)
Na^+	1.33×10^{-7}	175	(3)
Na^+	1.0×10^{-5}	400	(7)
Na^+	5.78×10^{-7}	450	(21)
K^+	3×10^{-4}	289	(20)
K^+	1.6×10^{-6}	400	(7)
Rb^+	2.87×10^{-7}	450	(21)
Cs^+	4.0×10^{-8}	400	(7)
Cs^+	7.58×10^{-7}	450	(21)
Tl^+	6.5×10^{-3}	315	(20)
$N\text{-}n\text{-}BuPy^+$	4×10^{-14}	30-75	(23)
$N\text{-}n\text{-}BuPy^+$	1.5×10^{-12}	60	(9)
$N\text{-}n\text{-}BuPy^+$	$<5.7 \times 10^{-12}$	60	(8)
$N\text{-}n\text{-}BuPy^+$	1.7×10^{-8}	175	(9)
$N\text{-}n\text{-}BuPy^+$	$<1.2 \times 10^{-8}$	175	(8)
$1\text{-}Me\text{-}2\text{-}EtIm^+$	4×10^{-16}	60	(22)

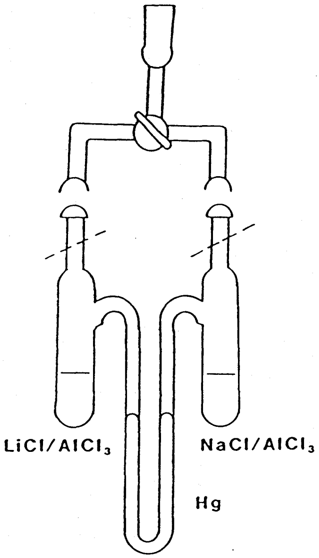

Fig 1. Cell used for differential vapor pressure measurements.

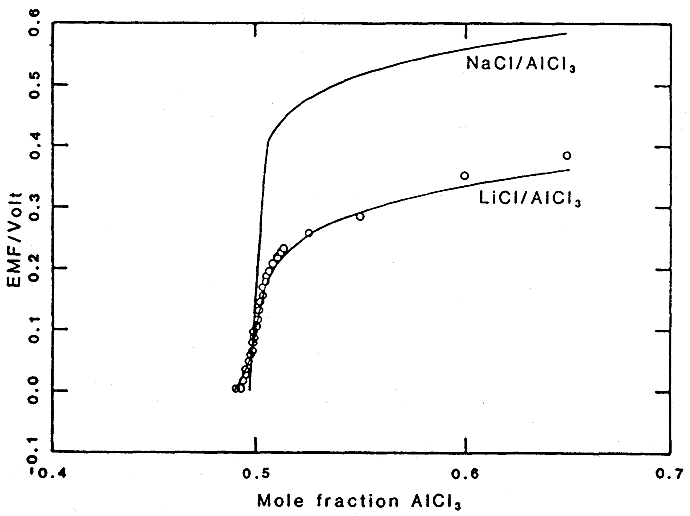

Fig 2. EMF vs composition for the LiCl- and NaCl-$AlCl_3$ systems (saturated alkali metal salt reference).

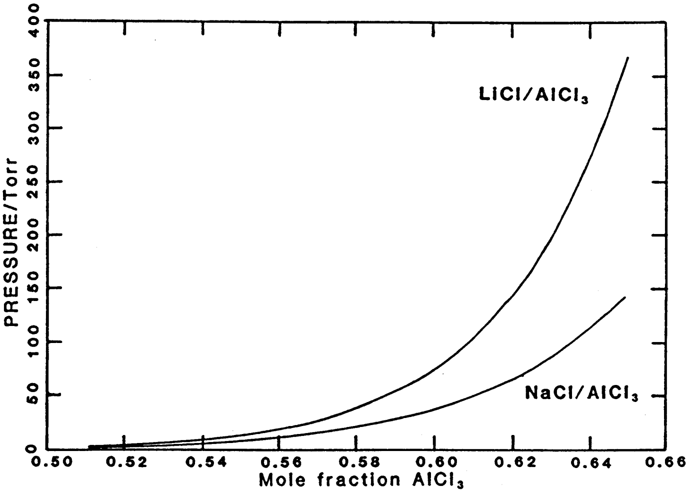

Fig 3. Vapor Pressure vs composition for LiCl- and NaCl-$AlCl_3$ systems.

DOI: 10.1149/198601.0332PV

REACTION OF CHLORINE WITH AMBIENT TEMPERATURE CHLOROALUMINATE MOLTEN SALTS

Francis M. Donahue†, Joseph A. Levisky,
G. Fredric Reynolds, and John S. Wilkes

The Frank J. Seiler Research Laboratory
United States Air Force Academy
Colorado Springs, CO 80840

ABSTRACT

Chlorine is a potentially useful cathode in electrochemical cells using low melting chloroaluminate molten salts as the electrolyte. Chlorine generated electrochemically in 1-methyl-3-ethylimidazolium chloride - aluminum chloride melts or bubbled in the melt reacts with the imidazolium cation. The melt may be converted quantitatively to one where the cation is 4,5-dichloro-1-methyl-3-ethylimidazolium. Both basic and acidic melts are chlorinated, but the basic melts react at a much slower rate. Once the cation has been fully chlorinated, the melts appear to be resistant to further attack by chlorine. The chlorinated melts have higher melting points, higher viscosities and lower electric conductivities than the unchlorinated melts.

INTRODUCTION

The behavior of chlorine has been studied in chloroaluminate molten salts composed of alkali chloride - aluminum chloride mixtures (1,2), but little is known about the reactions of chlorine in the related organic chloride - aluminum chloride melts. Mixtures of 1-methyl-3-ethylimidazolium chloride (MeEtImCl) and aluminum chloride are salts that are liquid at room temperature and below (3). The anodic limit of this and other chloroaluminate melts is the oxidation of chloride. A chlorine electrode would have the greatest possible potential as a cathode in a battery utilizing the chloroaluminate melts. The cell where chlorine is the cathode and aluminum is the anode (i.e. an $AlCl_3$ formation cell) would have a cell voltage of 2.2 V and a theoretical energy density of 1315 Wh/kg (based on

---

† present address: Department of Chemical Engineering, University of Michigan, Ann Arbor, MI 48109.

electrode weights alone).

If chlorine is to be a useful electrode in the low temperature chloroaluminate molten salts, its physical and chemical behavior in the melts must be studied. We report here some details about the reactivity of chlorine in the MeEtIm chloroaluminate melts and some physical properties of melts that have reacted with chlorine.

In basic melts, the anodic oxidation of chloride produces trichloride (Cl_3^-) ion (4). Chloride oxidation at the anodic limit of acidic MeEtIm and the similar 1-(1-butyl)pyridinium chloroaluminate melts produces dissolved Cl_2 (5). The apparent lack of any interfering processes suggested to the authors that the the equilibrium chloride electrode potentials could be used in potentiometric experiments to determine accurately the equilibrium constant for the tetrachloroaluminate dissociation. Lipsztajn and Osteryoung did note that approximately 3 hours after anodic oxidation of Cl^- in basic melt, the chlorine reduction wave disappeared and the expected increase in the chloride oxidation wave was not observed. There may, in fact, be a chemical interference with the Cl^-/Cl_2 couple in both acidic and basic MeEtIm chloroaluminate melts.

EXPERIMENTAL

The preparation of the melts was as reported earlier (1). The melting points, electric conductivities and viscosities were measured as reported for the unchlorinated melts (5). NMR spectra were recorded on a JEOL FX90Q spectrometer.

Completely chlorinated melt could be prepared by slowly bubbling chlorine gas through a stirred sample of the melt at approximately 90°C. The time necessary to completely convert the imidazolium cation depended on the melt composition. The progress of the reaction could be monitored using NMR spectroscopy by observing the disappearance of the protons at the 4 and 5 positions of the imidazolium ring.

RESULTS AND DISCUSSION

When 1 atmosphere of chlorine was introduced over a sample of basic MeEtImCl-$AlCl_3$ melt, the melt rapidly took up the chlorine and became yellow-green in color. This is consistent with the dissolution of Cl_2 followed by the rapid reaction with free Cl^- to form Cl_3^-. Surprisingly, after several hours the melt returned to colorless, indicating some chemical reaction of Cl_3^- with the melt. The process of chlorine introduction followed by slow reaction could be repeated many times with the same melt. A similar experiment done on an acidic melt gave similar results with two notable exceptions. The color produced when chlorine was dissolved was light yellow, indicating that Cl_3^- was not formed, and the disappearance of the color from the dissolved chlorine was much more rapid. The weight gain of a sample that was exhaustively treated with chlorine, then degassed in vacuo corresponded to one mole of chlorine (Cl_2) gained per mole of melt.

The consumption of very large amounts of chlorine implies that the reaction is not solely with impurities in the melt, but with a component of the melt itself. Figures 1 and 2 show ^1H and ^{13}C NMR spectra taken regularly over several hours while chlorine was bubbled into an acidic MeEtIm melt. The resonances for the 4 and 5 protons at 7.9 ppm decrease in intensity and eventually disappear. The ^{13}C NMR spectra show that at the end of the reaction there are still five carbons in the organic cation, but during the chlorination process two intermediates are present. The spectra clearly show that chlorine reacts with the MeEtIm cation, and that the cation is quantitatively converted to the 4,5-dichloro-1-methyl-3-ethylimidazolium ion, as shown in equation 1.

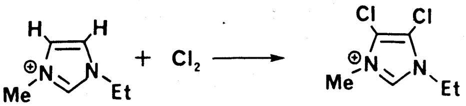

(1)

The same conversion occurs in basic melts, but at a much slower rate.

Once all of the MeEtIm had reacted, the melts were apparently resistant to further reaction with chlorine. An acidic melt completely reacted with chlorine retained the yellow color of dissolved chlorine indefinitely, unless a vacuum was applied to it. This suggests that while the MeEtIm chloroaluminate melts are not suitable for use with chlorine electrodes, the dichloro-MeEtIm chloroaluminate melts might be. The dichloro-MeEtIm melts are new materials and are likely to have physical properties different from the parent melts. We measured the electrical conductivities and viscosities of the dichloro-MeEtIm melts as a function of melt composition. We also determined a rough phase diagram for the new melts.

Figure 3 shows that the phase diagram for the dichloro-MeEtIm melts is qualitatively similar to the MeEtIm melts (6), but the melting points are about 50° higher than the parent melts. Interestingly, the dichloro-MeEtIm melts have normal melting points in the regions of the phase diagram where the MeEtIm melts only undergo glass transitions.

The electrical conductivities of the dichloro-MeEtIm melts are significantly lower than for the parent melts, as seen in Figure 4.

They also do not show the strong composition dependence that the parent melts have.

Reduced electrical conductivities are often caused by elevated viscosities, and this is born out by the comparison shown in Figure 4. Only a few compositions were measured, but the trend toward higher viscosities in basic compositions is present in the chlorinated samples as in the unchlorinated ones.

The reduced electrical conductivities of the chlorinated melts and the higher melting points make them less attractive as electrolytes. A cation that is resistant to attack by chlorine would be welcome, but not at the expense of the desirable thermal properties of the MeEtIm chloroaluminate melts or if there is a substantial conductivity penalty. The electrochemical properties of the 4,5-dichloroimidazolium melts were not examined in detail, but the electrochemical window is probably shorter on the cathodic end. Work on low temperature chloroaluminate melts having cations resistant to attack by chlorine is in progress.

REFERENCES

1. O. Waernes and T. Østvold, Acta. Chem Scand. A., 37, 293 (1983).
2. R. A. Carpio, L. A. King, A. P. Ratvik, T. Østvold and H. Øye, Light Met., 325 (1981).
3. J. S. Wilkes, J. A. Levisky, R. A. Wilson, and C. L. Hussey, Inorg. Chem., 21, 1263 (1982).
4. M. Lipsztajn and R. A. Osteryoung, Inorg. Chem., 23, 1735 (1984).
5. Z. J. Karpinski and R. A. Osteryoung, Inorg. Chem., 23, 1491 (1984).
6. A. A. Fannin, Jr., D. A. Floreani, L. A. King, J. S. Landers, B. J. Piersma, D. J. Stech, R. L. Vaughn, J. S. Wilkes and, J. L. Williams, J. Phys. Chem., 88, 2614 (1984).

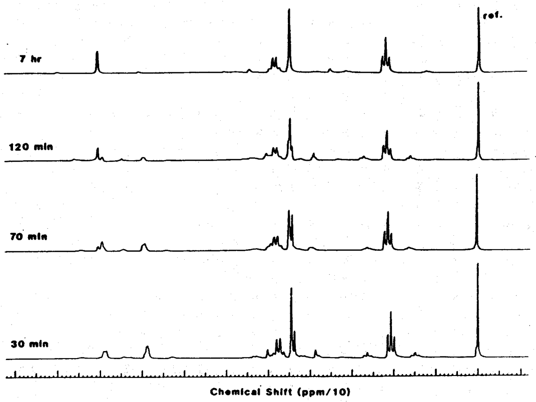

Fig. 1. ^{1}H NMR spectrum of 0.60 $AlCl_3$ mole fraction MeEtImCl-$AlCl_3$ melt at 90°C. External reference is hexamethyldisiloxane.

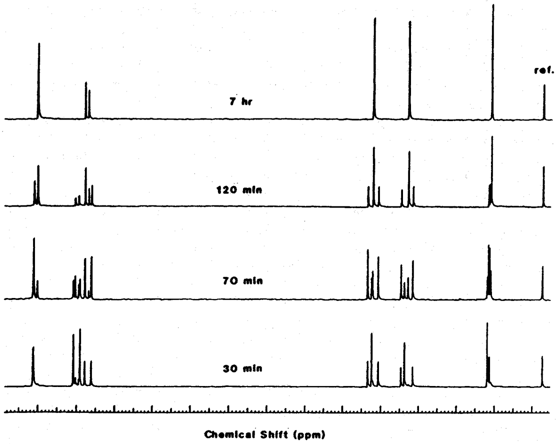

Fig. 2. ^{13}C NMR spectrum of 0.60 $AlCl_3$ mole fraction MeEtImCl-$AlCl_3$ melt at 90°C. External reference is hexamethyldisiloxane.

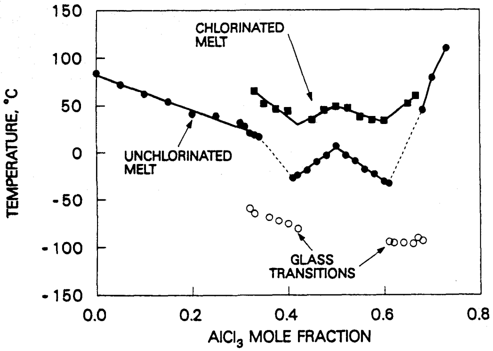

Fig. 3. Phase diagram.

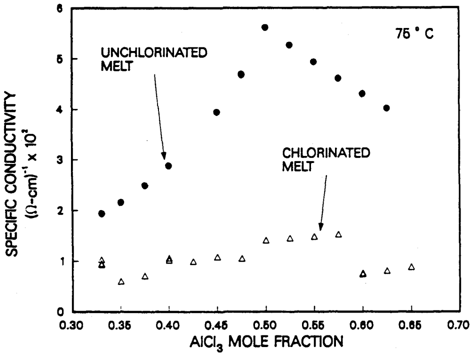

Fig. 4. Specific conductivities as function of melt composition.

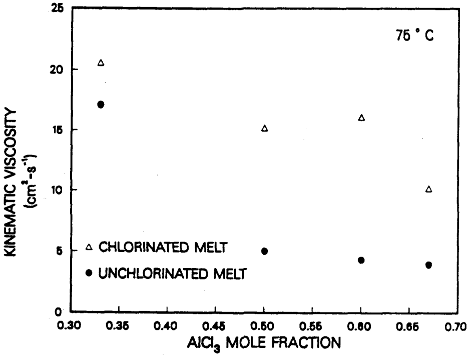

Fig. 5. Kinematic viscosities as function of melt composition.

DOI: 10.1149/198601.0338PV

A REVIEW OF THE PHASE EQUILIBRIUM RELATIONSHIPS, MELTING TEMPERATURES, AND Al_2O_3 SOLUBILITIES OF HALL CELL ELECTROLYTE COMPOSITIONS

Jesse J. Brown, Jr.
Department of Materials Engineering
College of Engineering
Virginia Polytechnic Institute and State University
Blacksburg, Virginia 24061

ABSTRACT

The electrolyte used in the Hall process for producing aluminum metal consists basically of a fused mixture of alumina (Al_2O_3) and cryolite (Na_3AlF_6). Other ingredients including AlF_3, LiF, and CaF_2 are added to modify properties such as bath density, electrical conductivity, and freezing temperature. Historically, a variety of experimental techniques has been employed to determine the phase diagrams of systems important to the Hall process. Many of the early experiments were conducted using open containers. This practice resulted in the publication of some inaccurate phase diagrams because of the decomposition of many of the fluoride compounds at high temperatures. In more recent years, it has become standard procedure to encapsulate all samples in sealed platinum containers. Quenching and differential thermal analysis (DTA) experiments using samples sealed in the platinum containers have been used to revise some of the early phase diagrams and to investiage new systems. In this paper, the phase diagrams that are known in the Na_3AlF_6-CaF_2-AlF_3-Al_2O_3 system are reviewed in a systematic manner, with special emphasis on the Hall cell electrolyte composition region.

Aluminum is the most abundant metallic element in the earth´s crust and ranks after oxygen and silicon as the third most abundant of all elements. Because of its strong affinity for oxygen, it is not found in nature in the elemental state, but in combined forms such as oxides, silicates, etc. In 1886, Charles Martin Hall and Paul L. T. Heroult discovered almost simultaneously the process in which alumina is dissolved in molten cryolite (Na_3AlF_6) and decomposed electrolytically. This reduction process is known as the Hall-Heroult process.

The electrolyte consists basically of a fused mixture of cryolite, aluminum fluoride, calcium fluoride, lithium fluoride, and alumina. Aluminum fluoride is added to the bath to alter the cryolite ratio ($3NaF/AlF_3$) from the stoichiometric value of 1.5 to some lower value. Calcium fluoride is added in amounts between 5 and 6 wt % to permit lower operating temperatures, with additions of approximately 0.1 wt % LiF used to increase electrical conductivity.

While the basic process for the production of aluminum has not changed significantly since its discovery 90 years ago, the phase equilibrium diagrams involving the components of the electrolyte are in many cases contradictory and in some cases unknown. To some extent this is due to the experimental difficulties encountered in working in these systems (e.g., cryolite decomposes on melting, AlF_3 is volatile, supercooling is often present, and the primary crystallization of Al_2O_3 is difficult to detect by conventional techniques). The inter-relationships between the various fluorides in the bath and their influence on the melting temperature and alumina solubility of the electrolyte can best be understood when reliable phase diagrams for the electrolyte exist.

One Component Systems

Cryolite

Cryolite has been the subject of numerous investigations because of its importance in the industrial production of aluminum. The compound exists in both a low temperature (α) and high temperature (β) polymorphic form. The naturally occurring low temperature polymorph is monoclinic, space group $P2_1/n$, with cell parameters a_o = 5.40 Å, b_o = 5.60 Å, c_o = 7.78 Å and = 90°11′ (1). Between 560 and 572°C, cryolite undergoes a rapid reversible transition to the high temperature cubic form, a_o = 7.962 Å, with a heat of transition of 2238 cal/mole (2-6). Landon and Ubbelohde (3), on the basis of electrical conductance and thermal arrest data, reported the existence of a third polymorphic variety which they designated γ-cryolite. The β-γ inversion reportedly took place at 881°C with an estimated heat of transition of 200 cal/mole. Attempts by Foster (7) to confirm this transition by electrical conductivity and high temperature X-ray diffraction (XRD) methods were unsuccessful. More recent investigations have also failed to confirm the existence of a gamma form.

The melting point of natural cryolite has received a great deal of attention because of its importance in cryoscopic calculations. Melting points ranging from 977 to 1027°C have been reported (3-6,8-13), with the majority of the more recent investigations yielding values close to 1009°C. Foster (14), working with samples contained in sealed platinum tubes under carefully controlled conditions, used quenching methods to determine a melting temperature of 1009.2°C for natural Greenland cryolite. On the basis of a plot of the liquid fraction as a function of the temperature from which the samples were quenched, the melting point of pure cryolite was determined as 1012 ± 2°C.

The determination of the melting point of cryolite is complicated by the partial dissociation of the compound into several ionic subspecies on melting. Frank and Foster (15) employed calculations based on experimental densities to compare several possible reaction mechanisms. It was concluded that cryolite dissociated into $NaAlF_4$ and NaF on melting according to the reaction:

$$Na_3AlF_6 = 2NaF + NaAlF_4$$

Foster and Frank (16) recognized that the calorimetric determination of the heat of fusion of cryolite (27.8 kcal/mole) included a heat effect because of partial dissociation. The true cryoscopic heat of fusion was determined to be 19.9 kcal/mole. The refractive indices of the room temperature alpha form of cryolite are $\alpha = 1.3376$, $\beta = 1.3377$, and $\gamma = 1.3387$ (17).

Aluminum Fluoride

Aluminum fluoride is rhombohedral, space group $R\overline{3}$, with cell parameters $a_{rh} = 5.016$ Å and $\alpha = 58^\circ 32'$ (18). The compound is uniaxial positive with indices of refraction of 1.3765 and 1.3767 (19).

During an investigation of the heat contents of Na_3AlF_6, AlF_3, and NaF, O'Brien and Kelley noted the existence of a new polymorph of AlF_3. The transition to the high temperature form took place at 454°C and was accompanied by a weak heat effect of approximately 150 cal/mole. Holm and Holm (20) used differential thermal analysis (DTA) to confirm the existence of the polymorph, which they designated β-AlF_3, and set the transition temperature at 453°C. The new polymorph, also noted by Schultz et al. (21), could not be quenched to room temperature and no optical or XRD data were reported. Shinn, Crocket, and Haendler (22) reported the existence of a third (gamma) polymorph of AlF_3, which could be obtained either by heating ammonium hexafluoroaluminate to 400°C or decomposing ammonium tetrafluoroaluminate. The transition to the new tetragonal form ($a_o = 3.54$ Å and $c_o = 6.00$ Å) takes place at 300°C. No confirmation of the existence of this polymorph is found in the literature.

Mesrobian, Rolin, and Pham (23) studied mixtures of NaF and AlF_3 under pressure using thermal arrest methods. A peak at 1300°C for samples containing more than 50 wt % AlF_3 was interpreted as resulting from a previously unknown inversion of AlF_3. In addition, the triple point of pure AlF_3 was placed above 200 bars pressure and 1700°C. Aluminum fluoride is normally reported to sublime at 1291°C at one atmosphere pressure.

Calcium Fluoride

Calcium fluoride (fluorite) exists in only one form which has a face centered cubic structure, space group Fm3m, and a cell parameter a_o = 5.4626Å (24). Kojima et al. (25) suggested that the variations in the melting point found in the literature (26) are caused by slight hydrolysis during heating ($CaF_2 + H_2O = CaO + 2HF$). Using anhydrous HF as a deoxidyzing and purifying agent, the melting point of high purity CaF_2 was determined as 1423°C. The refractive index of the compound is 1.434 (27).

Aluminum Oxide

Aluminum oxide exists in at least seven crystalline modifications which are arbitrarily designated as alpha, gamma, delta, eta, theta, kappa, and chi. The most common form, α-Al_2O_3 or corundum, belongs structurally to space group $R\bar{3}c$ with cell parameters a_{hex} = 4.758 Å and c_{hex} = 12.991 Å (28). Corundum is a uniaxial positive mineral with indices of refraction 1.768 and 1.760 (27).

Eta-aluminum oxide, like corundum, has been reported as the crystalline modification of Al_2O_3 present in certain areas of phase diagrams dealing with the electrolyte used in the smelting of aluminum (29). The eta form is cubic with a spinel type structure and cell parameter a_o = 7.94 Å (30). The index of refraction is 1.670.

A metastable alumina phase designated as m-alumina by Foster (31) and later as tau-alumina by Wefers and Bell (32) has also been reported. Tau-alumina converts first to eta- and finally to alpha-alumina on heating. The XRD pattern is similar to that of mullite.

Two Component Systems

System CaF_2-AlF_3

The earliest investigation of the system was conducted by Fedotieff and Iljinsky (8). On the basis of DTA data collected from samples heated in air, a eutectic system was identified. The invariant point was placed at 37.5 mole % AlF_3 and 820°C. Ravez and Hagenmuller (33) and Ravez et al. (34) reinvestigated the system using powder XRD. Samples were encapsulated in copper and reacted at 600, 700, 800, and 840°C. One compound, $CaAlF_5$, was identified and found to exist in both a low (alpha) and high (beta) temperature polymorph. Debye Sherrer patterns of α-$CaAlF_5$ were used to index the compound in the orthorhombic system with cell parameters $a_o = 11.81 \pm 0.03$ Å, $b_o = 9.16 \pm 0.02$ Å, and $c_o = 6.35 \pm 0.01$ Å. The high temperature polymorph was found to be isotypic with $CaFeF_5$ and was also indexed in the orthorhombic system ($a_o = 20.04 \pm 0.03$ Å, $b_o = 9.81 \pm 0.01$ Å, and $c_o = 7.31 \pm 0.01$ Å).

DTA results established the transition and melting temperatures of the compound at 820°C and 850°C, respectively.

Pycnometric methods were used to determine the densities of α- and β-$CaAlF_5$ as 3.09 and 2.96 g/cm^3, respectively.

Holm (35) confirmed the existence of the 1:1 compound and, on the basis of DTA data, showed the α-β transition to take place at 740°C. The compound formed highly twinned crystals with a mean refractive index of 1.375 and a density of 2.947 g/cm^3. Incongruent melting to AlF_3 and a liquid containing 44 mole % took place at 881°C. The eutectic for the system was located at 37 mole % AlF_3 and 828°C. Pronounced supercooling was noted in the area of the diagram containing 60% or more CaF_2 and DTA heating curves were therefore used to gather data in this region. No liquidus data were presented for the portion of the system richer in AlF_3 than the peritectic composition. Malinovsky, Vrbenska, and Cakajdova (36) and Millet, Pham, and Rolin (37) reinvestigated the system using thermal arrest methods and presented diagrams very similar to those of Holm. Both studies confirmed the existence of $CaAlF_5$ in both a low and high temperature polymorphic form. Malinovsky et al. located the invariant points at 37.5 mole % AlF_3 and 829°C and 47.5 mole % AlF_3 and 893°C. Millet et al. reported slightly different compositions and temperatures (36 mole % AlF_3 and 820°C and 44 mole % AlF_3 and 880°C). The latter authors also noted that the extrapolation of the liquidus curve in the high AlF_3 end of the diagram locates the triple point of AlF_3 in the neighborhood of 2250°C.

Using a combination of optical microscopy, powder XRD, quench techniques, and DTA, Craig and Brown (38) also reexamined the CaF_2-AlF_3 system. To prevent volatilization of AlF_3, all heat treatments and DTA experiments were performed on samples encapsulated in sealed platinum tubes. Because pronounced supercooling existed in the system, DTA heating curves at 3°C/min (as opposed to cooling curves) were used to obtain reaction temperatures. Quenching experiments were then performed to verify that these temperatures represented equilibrium data.

Two compounds were found to exist in the system. The 1:1 compound, noted by previous authors, melted incongruently at 873 ± 3°C to AlF_3 and a liquid containing 44 mole % AlF_3. The α-β inversion remained constant at 743 ± 3°C. A previously unreported 2:1 compound, Ca_2AlF_7, was found to melt incongruently at 845 ± 3°C to CaF_2 and a liquid containing 35 mole % AlF_3. The eutectic for the system was placed at 37.5 mole % AlF_3 and 836 ± 3°C.

The authors noted that while Ca_2AlF_7 had not been previously reported, a hydrated form $Ca_2AlF_7 . 2H_2O$ and a hydrated hydroxide $Ca_4Al_2(OH)_{14} . 5H_2O$ (39) are known to exist. The anhydrous compound was successfully formed using either AlF_3, $AlF_3 . 3H_2O$, or $CaAlF_5$ as a starting material. The absence of any previous reports on the existence of the compound was attributed to its sluggish formation and to non-equilibrium cooling. Only the peritectic reaction was consistently observed during DTA heating experiments; but on cooling, three peaks were observed. The lowest corresponded to the α-β $CaAlF_5$ inversion. Powder XRD data of samples after DTA experiments showed a mixture of α-$CaAlF_5$ and AlF_5 which converted back to Ca_2AlF_7 on reheating.

The 2:1 compound was tentatively indexed on the basis of powder XRD data (1/4° 2θ/min-CuK_α) as orthorhombic with lattice parameters a_o = 18.22 Å, b_o = 9.06 Å, and c_o = 7.11 Å. A least squares cell refinement program developed by Evans, Appleman, and Handwerker (40) was used to obtain the final cell parameters.

The structural relationships between β-$CaAlF_5$ and $SrAlF_5$ noted by Ravez et al. (34) were also found to exist between Ca_2AlF_7 and Sr_2AlF_7. These suggest that the a and b parameters of the orthorhombic cell of Ca_2AlF_7 roughly coincide with the face diagonal and 1/2 the face diagonal of the (001) plane of the tetragonal cell of Sr_2AlF_7, with c being common to both cells.

System Na_3AlF_6-CaF_2

The first study of the Na_3AlF_6-CaF_2 binary system was conducted by Pascal (13) in 1913. He was primarily concerned with the liquidus curves, reporting a eutectic at 47.8 mole % CaF_2 and 905°C. Minor modifications of the temperature and composition of the eutectic were made by Fedotieff and Iljinsky (8) (48.1 mole % CaF_2 and 930°C), Matiasovsky and Malinovsky (41) (50.5 mole % CaF_2 and 940°C), and Fenerty and Hollingshead (42) (48.6 mole % CaF_2 and 946°C).

In 1961, Rolin (43) reported solidus data for the system. Using thermal arrest cooling curves of closely spaced compositions containing up to 53.5 mole % CaF_2, the eutectic was placed at 47.3 mole % CaF_2 and 946°C. Samples higher in Na_3AlF_6 than the eutectic composition showed a marked decrease in the eutectic temperature with increasing cryolite content. Rolin concluded that a large solid solution of CaF_2 in cryolite must exist, extending almost to the eutectic composition at 946°C. Following Rolin's suggestion that the system should be re-examined by other methods before the phase relations could be definitely established, Holm (44) studied the system using a combination of thermal analysis, DTA, XRD, quenching techniques, optical microscopy, and density determinations. Again, the eutectic halt on the high cryolite side of the diagram was not observed during DTA; however, a small exothermic peak at 785°C was noted. Because this temperature is close to the reported eutectic temperature for the system NaF-Na_3AlF_6-CaF_2 (8), Holm postulated that the depression of the eutectic temperature seen by Rolin could be caused by volatilization of small amounts of AlF_3 or $NaAlF_4$ rather than by solid solution. As further proof that solid solution of CaF_2 in Na_3AlF_6 does not exist, Holm noted that samples containing 5 to 90 mole % CaF_2 quenched from 950°C showed Na_3AlF_6 or CaF_2 in equilibrium with liquid. In addition, the densities of samples containing up to 60 mole % CaF_2 quenched from 970°C compared closely with calculated densities of mechanical mixtures of CaF_2 and Na_3AlF_6. Holm's simple eutectic system showed no solid solution and a eutectic at 50 mole % CaF_2 and 945.5°C.

Verdan and Monnier (45), using DTA experiments on samples contained in sealed crucibles, studied the system to resolve the controversy between Holm and Rolin over the existence of solid solution. They noted that the presence of a Na_3AlF_6 solid solution would explain the difficulty in purifying cryolite when CaF_2 is present. Liquidus and solidus data were obtained which indicated a solid solution of CaF_2 in Na_3AlF_6 approaching a maximum of 20 mole % CaF_2 at the eutectic temperature. A decrease in the $\alpha-\beta$ Na_3AlF_6 transition from 563°C for pure cryolite to 530°C for a sample containing between 5 and 6 mole % CaF_2 was also noted. A eutectoid reaction was therefore located at 5.5 mole % CaF_2 and 530°C.

Craig and Brown (46) studied samples containing 0 to 30 mole % CaF_2 using DTA of samples encapsulated in sealed platinum tubes. The $\alpha-\beta$ Na_3AlF_6 inversion remained constant at 567°C. Peaks corresponding to a solidus line were not observed and all data agreed well with the simple eutectic diagram of the system presented by Holm.

System Na_3AlF_6-AlF_3

The system Na_3AlF_6-AlF_3 has been investigated periodically since the first published version by Fedotieff and Iljinsky (8) in 1923. Foster (47) gives an excellent review of the more recent publications. The majority of the diagrams agree well with respect to the liquidus curve up to 30 wt % AlF_3; however, disagreement exists above this value as to the location and composition of the invariant point(s), shape of the chiolite ($Na_5Al_3F_{14}$) liquidus curve, and identity of the primary phase in equilibrium with liquid in the high AlF_3 end of the diagram.

A major point of contention is whether $NaAlF_4$ exists as a stable phase. Grjotheim (5) reported $NaAlF_4$ to melt congruently at 731°C. Ginsberg and Wefers (48) agreed with Grjotheim that $NaAlF_4$ is a stable phase in the system, but found it to melt incongruently at 710°C. In addition, a eutectoid reaction was found at 680°C with $Na_5Al_3F_{14}$ and AlF_3 forming at the expense of $NaAlF_4$.

Several other authors (10,42,49,50) have disagreed with the equilibrium existence of $NaAlF_4$ and presented diagrams showing AlF_3 as opposed to $NaAlF_4$ as an equilibrium solid at the eutectic. Holm (50) suggested that $NaAlF_4$ was not a stable phase because solid $NaAlF_4$ collected from the vapor above a melt of the same composition decomposed during DTA at 500°C to $Na_5Al_3F_{14}$ and AlF_3.

Foster (47) working with samples in sealed platinum tubes, used a combination of optical microscopy, DTA, XRD, and quench techniques to establish the diagram. It was concluded that $NaAlF_4$ is not a stable phase because (1) it was only found when liquid was present before quenching; (2) samples quenched from the region reported to contain $NaAlF_4$ and chiolite in equilibrium showed only chiolite and AlF_3; (3) samples quenched from the region of the diagram reported to have $NaAlF_4$ and liquid in equilibrium showed AlF_3 to be the primary crystalline phase; and (4) DTA (in sealed tubes) of melts that precipitated $Na_5Al_3F_{14}$ as the primary phase did not show any peaks that would indicate a phase field containing solid $NaAlF_4$.

Mesrobian et al. (23) studied mixtures of AlF_3 and NaF and, in addition to locating the triple point of AlF_3 above 200 bars pressure and 1700°C, reported two new invariant lines in the system. The first was located by constant temperature peaks of thermal arrest cooling curves for compositions ranging from 45 to 95 wt % AlF_3 at approximately 1300°C. It was postulated that the peaks were caused by an allotropic transformation of AlF_3. A second set of peaks, measurable from 45 to 68 wt % AlF_3 at 1250°C, was considered to represent a peritectic line extending from an incongruently melting compound of possible composition $NaAl_2F_7$. It was felt that, like $NaAlF_4$, this new compound was unstable and decomposed on cooling and, therefore, is not seen in the subsolidus region.

System Na_3AlF_6-Al_2O_3

A number of phase diagrams exist in the literature for the system Na_3AlF_6-Al_2O_3. Roush and Miyake (51) reviewed the diagrams published up to 1925; Phillips, Singleton, and Hollingshead (10) summarized the more recent works. There were significant differences between the various diagrams with the eutectic for the system ranging from 10 to 18.5 wt % Al_2O_3 and 930 to 962°C. Several diagrams showed appreciable solid solubility. The possibility of solid solubility of Al_2O_3 in cryolite creates particular interest in the system because of its significance in the interpretation of the solution mechanism of Al_2O_3 in the Hall electrolyte and in the determination by cryoscopic methods of the number and structure of entities present in the molten binary mixtures.

Foster (7,31) studied the cryolite-alumina binary using a combination of quench methods, optical microscopy, and XRD. The simple eutectic system shows no solid solution and an invariant point at 10.5 wt % Al_2O_3 and 961°C. The primary phase on the low alumina side of the eutectic was identified by XRD and refractive index measurements as cryolite. On the high alumina side of the eutectic, the primary phase was found to be corundum. While the cryolite examined in the low-alumina end of the diagram was α-Na_3AlF_6, the existence of a solid solution in the high temperature form was ruled out because the alpha form did not contain polycrystalline fractures with alumina segregating at the boundaries. It was also noted that extremely rapid quenching from the liquid resulted in a new alumina phase (m- or tau-alumina) with a diffraction pattern similar to mullite. On heating, this phase transformed first to eta-alumina and then to corundum.

Rolin (52) reinvestigated the system using thermal arrest methods. He arrived at the conclusion that if solid solution could not be totally disproved, this new alumina phase was less than 1 wt % Al_2O_3. He presented a simple eutectic diagram with the invariant point at 11.5 wt % Al_2O_3 and 960°C. However, the reported eutectic arrest for a sample containing 1 wt % Al_2O_3 occurred 18°C below the established eutectic temperature. The decrease was attributed to the inability to obtain thermal equilibrium because of a large mass of solid pre-existing at the moment of eutectic crystallization. Duruz and Monnier (53) attempted to verify this assumption by investigating the system using DTA techniques. To avoid the problem of volatility, samples were sealed in a nickel container. Compositions containing amounts as small as 0.5 wt % Al_2O_3 showed a eutectic peak at the same temperature as samples containing 10 wt % or more Al_2O_3. Below 0.5 wt % Al_2O_3, the sensitivity of the equipment was not sufficient to pick up the small thermal effect. A plot of the surface area of the eutectic peak versus the concentration of Al_2O_3 extrapolated through the origin indicated that no solid solution existed between 0 and 0.5 wt % Al_2O_3.

A substantial amount of literature is also available on the reaction mechanism for the solution of alumina in cryolite-alumina melts. Foster and Frank (16) reviewed the proposed reaction mechanisms and used Temkin's ionic model to calculate activities. A graph of $-\log a_c$ versus $1/T$ was then constructed to demonstrate that the most probable scheme was $3F^- + Al_2O_3 = 3/2\ AlO_2^- + 1/2\ AlF_6^{3-}$. However, considerable controversy still exists over the true reaction mechanism (54).

System CaF_2-Al_2O_3

The binary system CaF_2-Al_2O_3 was first studied in 1913 by Pascal (13). Extensive solid solution at both ends of the system was noted. At the eutectic temperature, 20 wt % Al_2O_3 was soluble in CaF_2 and 71.5 wt % CaF_2 was soluble in Al_2O_3. The eutectic was placed at 26.5 wt % Al_3O_3 and 1270°C.

Gunther et al. (55), during a study of the luminescence of phosphors of the aluminum oxide-calcium fluoride type, reported the existence of a 1:5 compound $CaAl_{10}O_{15}F_2$. The compound was obtained by heat treating CaF_2 and $NH_4(SO_4)_2 \cdot 12H_2O$ with small amounts of $MnSO_4 \cdot 4H_2O$ (added as an activator) in air at 1200 to 1450°C.

Using quench methods, Kuo and Yen (56) reported a simple eutectic diagram for the system with the invariant point at 7 mole % Al_2O_3 and 1290°C. Neither the extensive solid solution nor the compound formation reported earlier could be verified. The authors noted that while in a closed system, CaF_2 and Al_2O_3 were the stable coexisting phases; in open air under ordinary atmospheric conditions, $CaAl_4O_7$ formed as the unique product according to one of the two reaction schemes shown below.

1. $CaF_2 + 2\ Al_2O_3 + H_2O = CaAl_4O_7 + 2\ HF$

2. (a) $3\ CaF_2 + 7\ Al_2O_3 = 3\ CaAl_4O_7 + 2\ AlF$

   (b) $2\ AlF_3 + 3\ H_2O = Al_2O_4 + 6\ HF$

Chatterjee and Zhmoidin (57) reinvestigated the system by sintering samples in hermetically sealed capsules. Quenching, DTA, and optical microscopy were used to obtain data which suggested a eutectic system. The invariant point was placed at approximately 2 wt % Al_2O_3 and 1395°C. The liquidus curve had a pronounced "S" shape suggestive of metastable liquid phase separation.

System AlF_3-Al_2O_3

While numerous authors (29,58-61) have reported results in ternary and quaternary systems involving the binary system AlF_3-Al_2O_3, their investigations have been confined to portions of the diagrams far removed from the binary system. At the present time no phase equilibrium data are available on the system.

Three Component Systems

System CaF_2-AlF_3-Na_3AlF_6

Fedotieff and Illjinsky (8) presented a liquidus surface diagram of the CaF_2-AlF_3-NaF ternary system based on the results of DTA experiments performed in air on over 100 compositions. At the time of the work, no ternary compounds were known to exist and only chiolite and cryolite were identified in any of the binary systems. Two ternary eutectics were reported. The first was located at 50.2 mole % NaF, 5.0 % CaF_2, and 44.8% AlF_3 and 675°C with AlF_3 in equilibrium with Na_3AlF_6 and CaF_2. The second eutectic was placed at approximately 73 mole % NaF, 20% CaF_2, and 7% AlF_3 and 780°C with NaF in equilibrium with Na_3AlF_6 and CaF_2. A ternary peritectic was found at approximately 49 mole % NaF, 10% CaF_2, and 41% AlF_3 and 705°C with chiolite, cryolite, and CaF_2 in equilibrium.

Rolin (62), using thermal arrest methods, investigated the portion of the CaF_2-AlF_3-Na_3AlF_6 system containing 24 and 62.5 mole % or less CaF_2 and AlF_3, respectively. Phases precipitating from the melt were identified by the shape and sharpness of the thermal arrest peaks. A ternary eutectic was located at 35.9 mole % cryolite, 56.7% AlF_3, and 7.4% CaF_2 and 682°C, with chiolite in equilibrium with CaF_2 and AlF_3. Two points on the chiolite-CaF_2 boundary curve were also located: the first at 32.7 mole % cryolite, 50.5% AlF_3, and 16.8% CaF_2 and 689°C and the second at 34.3 mole % Na_3AlF_6, 52.7% AlF_3, and 13.0% CaF_2 and 688°C. A point on the CaF_2-AlF_3 boundary was located at 28.7 mole % Na_3AlF_6, 55.3% AlF_3, and 16.0% CaF_2 and 708°C. On the basis of these points, a partial ternary diagram was presented. Supercooling in the region of the diagram containing CaF_2 as the primary phase was noted. At the time of the work, no compounds were known to exist in either the CaF_2-AlF_3 binary or the ternary system.

Pfundt and Zimmermann (63) investigated both the ternary system and the quasi-binary system NaF-$CaAlF_5$ using DTA of samples contained in pressure-tight nickel crucibles. They agreed with the earlier investigations that the ternary system could be divided into two subsystems, NaF-Na_3AlF_6-CaF_2 and CaF_2-AlF_3-Na_3AlF_6. The invariant temperature for the NaF containing system was placed at 780°C.

The diagram of the quasi-binary system contains one compound, $NaCaAlF_6$, which was found to melt incongruently at 740°C. The compound existed in both a low temperature (beta) and high temperature (alpha) form with the transition taking place at 653°C on heating. The beta form exhibited tetragonal symmetry with lattice parameters a_o = 7.32 Å and c_o = 10.18 Å. The existence of the high temperature polymorph at room temperature was noted in both air cooled and water quenched samples, but diffraction data were not reported.

Working with samples encapsulated in sealed platinum tubes and using DTA heating curves taken at 3°C/min, supplemented by optical microscopy, powder XRD, and quench experiments, Craig and Brown (56) investigated the CaF_2-AlF_3-Na_3AlF_6 ternary system. The compound $NaCaAlF_6$, first noted by Pfundt and Zimmermann (63), was found to exist in a previously unreported γ form in addition to the α and β polymorphs. DTA showed the inversion to the new form, characterized by a sharp but small exothermic peak, to take place at 720°C. Gamma-$NaCaAlF_6$ was not quenchable and no diffraction data were reported. The compound melted incongruently at 737°C to CaF_2 and a liquid. In addition to $NaCaAlF_6$, a previously unreported compound $NaCaAl_2F_9$ was identified. Based on powder XRD data taken at scanning speeds of 1/4° 2 θ/min using CuK_α radiation, the compound was indexed as body centered cubic (h + k + l = 2n) with a_o = 10.76 Å. The compound melted incongruently to AlF_3 and a liquid at 715°C; however, metastable congruent melting at 723°C was often observed.

On the basis of samples reacted for 394 h in the solid state, the subsolidus compatibility relationships were established. In the compatibility triangles containing cryolite, a decrease in the α-β inversion temperature was noted. Investigation of the

$NaCaAlF_6$-Na_3AlF_6 ternary join revealed that this decrease from 567 to 525°C was caused by a solubility of approximately 7 mole % $NaCaAlF_6$ in α-Na_3AlF_6.

The authors noted, in support of Holm's (44) simple eutectic diagram for the CaF_2-Na_3AlF_6 system, that slight compositional errors introducing excess AlF_3 to the binary system would result in the solid solution diagrams for the system reported by Rolin (43) and Verdan and Monnier (45). Craig and Brown (46) cited as additional evidence the work of Dewing (64) who postulated that a 50-fold increase in the conductivity of a sample in the CaF_2-AlF_3-Na_3AlF_6 system (as compared to pure Na_3AlF_6) could be explained by a solid solution of CaF_2 in Na_3AlF_6, and that such a solid solution was only reasonable when AlF_3 was present. It was noted that while Dewing was unaware of the existence of $NaCaAlF_6$, the sample studied actually lay on the $NaCaAlF_6$-Na_3AlF_6 ternary join. The conductivity increase, therefore, should be attributed to a solid solution of $NaCaAlF_6$ in Na_3AlF_6 and not to CaF_2 in cryolite. While firm evidence of the solubility of $NaCaAlF_6$ in the low temperature form of cryolite exists, the use of DTA to investigate solubility in the high form of cryolite was complicated by the dissociation of Na_3AlF_6 near its melting point. While a peak corresponding to a solidus line was often observed on cooling, the dissociation of cryolite masked its existence (if indeed it was present) on heating. The solubility of $NaCaAlF_6$ is, therefore, difficult to conclusively confirm.

The full phase diagram for the CaF_2-AlF_3-Na_3AlF_6 presented by Craig and Brown is shown in Figure 1 and the compositions, temperatures, and phase assemblages of the invariant points are given in Table I.

Lee, et al. (67) more recently reexamined the liquidus surface in a portion of this system. Twenty compositions were selected systematically throughout the electrolyte composition range. The liquidus temperatures for these compositions were measured to $\pm$ 2°C. The liquidus surface over the Hall cell electrolyte composition range is not smooth, but instead contains a deep inflection or swale (Figure 2). The liquidus temperatures over this range (CaF_2 from 3.8 to 11.3 wt % and AlF_3 from 5 to 20 wt %) can be calculated using the empirical expression $T_{liquidus}$ (°C) = 1009.4 + 4.059 (CaF_2) - 1.167 $(CaF_2)^2$ + 0.968 (CaF_2) (AlF_3) - 0.105 (CaF_2) $(AlF_3)^2$ + 0.073 $(CaF_2)^2(AlF_3)$ + 0.002 $(CaF_2)^2(AlF_3)^2$ - 4.165 (AlF_3) - 0.054 $(AlF_3)^2$ - 5.33 (Al_2O_3).

System Na_3AlF_6-AlF_3-Al_2O_3

Fenerty and Hollingshead (42) investigated the liquidus curves in the cryolite-rich portion of the system using cooling curve methods supplemented by visual observation of crystallization. The Na_3AlF_6-Al_2O_3 phase boundary showed a gradual decrease in Al_2O_3 up to 25 wt % AlF_3. Above this value the boundary curved sharply with a rapid decrease in Al_2O_3 content. The ternary peritectic and eutectic were both located at alumina contents less than 1 wt %. Rolin's (58) investigation of the system agreed well with the previous authors up to 25 wt % AlF_3. Above this value, however, the boundary curve continued a smooth approach to the ternary peritectic located at 5 wt % Al_2O_3, 28.5% AlF_3, and 66.5% Na_3AlF_6 and 710°C. A ternary eutectic was located at 60 wt % Na_3AlF_6, 37% AlF_3, and 3% Al_2O_3 and 670°C. Possible sources of error which could account for the previous results were noted, such as the slow dissolution of Al_2O_3, the lack of a thermal arrest corresponding to the primary crystallization of Al_2O_3, and the purity of starting materials.

Using samples sealed in platinum tubes, Foster (65) employed quench methods, optical microscopy, and XRD to reinvestigate the cryolite-rich portion of the diagram. In support of Rolin's diagram, the Na_3AlF_6-Al_2O_3 boundary fell regularly to the peritectic composition at 28.3 wt % AlF_3, 4.4% Al_2O_3, and 67.3% Na_3AlF_6 and 723°C. The ternary eutectic was located at 37.3 wt % AlF_3, 3.2% Al_2O_3, and 59.5% Na_3AlF_6 and 684°C. Compositions containing 20 wt % or less AlF_3 precipitated α-Al_2O_3 in the primary phase field of Al_2O_3, while those containing 25 wt % or more precipitated η-Al_2O_3.

System Na_3AlF_6-CaF_2-Al_2O_3

Fenerty and Hollingshead (42) investigated the Na_3AlF_6-CaF_2-Al_2O_3 ternary diagram by the same procedure used in their investigation of the Na_3AlF_6-CaF_2 and Na_3AlF_6-AlF_3-Al_2O_3 systems. On the basis of results obtained for cuts taken at 5, 10, 15, 20, 22, 24, 25, and 26 wt % CaF_2, a simple eutectic diagram with the ternary invariant point at 76.1 wt % cryolite, 21% CaF_2, and 2.9% Al_2O_3 and 933°C was presented. A later investigation by Rolin (43), using the method of thermal arrest, placed the eutectic at 78 wt % Na_3AlF_6, 17% CaF_2, and 5% Al_2O_3 and 927°C. The major difference between the results of the two investigations was in the Al_2O_3 content of the cryolite-alumina phase boundary. Rolin's diagram shows the boundary curve to be higher in Al_2O_3 than that of Fenerty and Hollingshead.

System CaF_2-AlF_3-Al_2O_3

In the CaF_2-AlF_3-Al_2O_3 ternary system, only the CaF_2-AlF_3 and CaF_2-Al_2O_3 binary systems are known. Several authors have investigated quaternary systems involving the ternary (42,60,61,66); however, their work has been confined to areas far removed from the ternary. At the present time, no phase equilibrium data are available on the system.

Four Component Systems

System Na_3AlF_6-AlF_3-CaF_2-Al_2O_3

The quaternary system Na_3AlF_6-AlF_3-CaF_2-Al_2O_3 has been investigated several times. The studies were performed prior to the reported existence of any ternary compounds and were concerned only with very limited portions of the liquidus surface of the system.

Abramov et al. (60) studied the $Na_5Al_3F_{14}$-CaF_2-Al_2O_3 cross section of the quaternary system. The liquidus surface of the section contained phase fields for cryolite, Al_2O_3, and CaF_2. A quaternary peritectic at 34.5 mole % Na_3AlF_6, 45.9% AlF_3, 13.9% CaF_2, and 5.7% Al_2O_3 and 685°C in addition to a quaternary eutectic temperature of 665°C were reported.

Fenerty and Hollingshead (42) studied the system by noting the change in the Na_3AlF_6-Al_2O_3 and Na_3AlF_6-CaF_2 boundary curves as mixed additions of up to 15 wt % AlF_3 and 20 wt % CaF_2 were added to the system Na_3AlF_6-Al_2O_3. An addition of 10 wt % AlF_3 moved the ternary eutectic for the system Na_3AlF_6-CaF_2-Al_2O_3 from 21 wt % CaF_2 and 933°C to 13 wt % CaF_2 and 927°C.

Rolin (61) investigated the portion of the system bounded by 10 wt % CaF_2 and 20% AlF_3. On the basis of thermal arrest data, a partial diagram of the cryolite-rich end of the quaternary system showing the boundary surface between cryolite and Al_2O_3 was proposed. Foster (66) also presented a few selected liquidus curves in the NaF-AlF_3-CaF_2-Al_2O_3 system for compositions with constant NaF/AlF_3 ratios.

Craig and Brown (46), working with samples encapsulated in sealed platinum tubes (reacted in the solid state and in the presence of liquid), established the eight compatibility tetrahedra for the system CaF_2-AlF_3-Na_3AlF_6-Al_2O_3 shown in Figure 3. No quaternary compounds were found to exist, and in all cases where Al_2O_3 was present it was identified by XRD as α-Al_2O_3.

Lee et al. (67) determined the Al_2O_3 solubility in 20 compositions covering typical Hall cell electrolyte compositions. The liquidus temperatures for these compositions containing up to 8 wt % Al_2O_3 were measured to ± 2°C. In all cases the double solubility limit of Al_2O_3 was found to exist below the 8 wt % Al_2O_3 level, and was found to vary from 2.0 to 6.5 wt % Al_2O_3 over a temperature range of 860 to 960°C.

REFERENCES

1. Powder Diffraction File, 12-257, Joint Committee on Powder Diffraction Standards, Philadelphia, PA.

2. A. J. Majumdar and R. Roy, "Test of the Applicability of the Clapeyron Relationship to a Few Cases of Solid-Solid Transitions," J. Inorg. Nucl. Chem. 27 1961-73 (1965).

3. G. J. Landon and A. R. Ubbelohde, "Melting and Crystal Structure of Cryolite (3NaF, AlF_3)," Proc. Roy. Soc. (London) A240 160-72 (1957).

4. C. J. O'Brien and K. K. Kelley, "High Temperature Heat Contents of Cryolite, Anhydrous Aluminum Fluoride and Sodium Fluoride," J. Am. Chem. Soc. 79 5616-18 (1957).

5. K. Grjotheim, "Theory of Aluminum Electrolysis," Kgl. Nor. Vidensk. Selsk. Skr. 2 (5) 1-90 (1957).

6. W. B. Frank, "Thermodynamic Considerations in the Aluminum-Producing Electrolyte," J. Phys. Chem. 65 (11) 2081-87 (1961).

7. P. A. Foster, Jr., "Determination of the Cryolite-Alumina Phase Diagram by Quenching Methods," J. Am. Cer. Soc. 43 (2) 66-68 (1960).

8. P. P. Fedotieff and W. P. Iljinsky, "Uber die Schmelzbarkeit des Ternaren Systems: Natriumfluorid, Calciumfluorid, Aluminumfluorid," Z. Anorg. Chem. 129, 93-107 (1923).

9. M. G. Petit, "Etude Cryoscopique de Solutions de Certains Oxydes Metalliques dans l'Eutectique Cryolithe-Fluorure de Sodium," Compt. Rend. 234, 1281-83 (1952).

10. N. W. F. Phillips, R. H. Singleton and E. A. Hollingshead, "Liquidus Curves for Aluminum Cell Electrolyte," J. Electrochem. Soc. 102 (11) 648-49 (1955).

11. J. L. Holm, "Structural Interpretation of the System Cryolite + Sodium Aluminate," Trans. Faraday Soc. 58 (11) 1104-7 (1962).

12. P. A. Foster, Jr., "A Cryolite Melting Point Through Quenching Methods," J. Phys. Chem. 61 (7) 1005-6 (1957).

13. P. Pascal, "Die Elektrometallurgie des Aluminums. I. Das Ternare System Tonerde-Fluorit-Kryolith.," Z. Electrochem. 19, 610-13 (1913).

14. P. A. Foster, Jr., "Melting Point of Cryolite," J. Am. Cer. Soc. 51 (2) 107-9 (1968).

15. W. B. Frank and L. M. Foster, "The Constitution of Cryolite and NaF-AlF_3 Melts," J. Phys. Chem. 64 (1) 95-8 (1960).

16. P. A. Foster and W. B. Frank, "The Structure of Cryolite-Alumina Melts," J. Electrochem. Soc. 107 (12) 997-1001 (1960).

17. C. Palache, H. Berman and C. Frondel, eds., Dana's System of Minerology, John Wiley and Sons, Inc., New York, 1951.

18. F. Hanic, K. Matiasovsky, D. Stempelova and M. Malinovsky, "Uber die Kristallstruktur Von AlF_3," Acta Chim. Hung. Tomus 32 309-13 (1962).

19. E. Staritzky and L. B. Asprey, "Aluminum Trifluoride, AlF_3," Anal. Chem. 29 984 (1957).

20. J. L. Holm and J. B. Holm, "Phase Relations and Thermodynamic Properties in the Ternary Reciprocal System LiF-NaF-Na_3AlF_6-Li_3AlF_6," Thermochimica Acta. 6 (4) 375-98 (1973).

21. A. H. Schultz, B. Bieker and J. Krogh-Moe, "Phase Equilibrium in the System BaF_2-AlF_3," Acta Chem. Scand. 26 (7) 2623-30 (1972).

22. D. B. Shinn, D. S. Crocket and H. M. Haendler, "The Thermal Decomposition of Ammonium Hexafluoroferrate (III) and Ammonium Hexafluoroaluminate. A New Crystalline Form of Aluminum Fluoride," Inorg. Chem. 5 (11) 1927-33 (1966).

23. G. Mesrobian, M. Rolin and H. Pham, "Etude Sous Pression des Melanges Fluorure de Sodium-Fluorure d`Aluminum Riches en Fluorure d'Aluminum," Rev. Int. Hautes Temp. Refract. 9 (1) 139-46 (1972).

24. Swanson and Tatge, "Calcium Fluoride, CaF_2," Nat. Bur. Std. Circ. 539, Vol. 1, 69-70 (1953).

25. H. Kojima, S. G. Whiteway and C. R. Masson, "Melting Points of Inorganic Fluorides," Can. J. Chem. 46 (18) 2968-71 (1968).

26. E. M. Levin, C. R. Robbins and H. F. McMurdie, eds., Phase Diagrams for Ceramists, American Ceramic Society, Inc., Columbus, Ohio (1964).

27. F. D. Bloss, An Introduction to the Methods of Optical Crystallography, Holt, Rinehart and Winston, New York (1961).

28. Nat. Bur. Stand. U. S. Circ. 539 (9) 3 (1959).

29. P. A. Foster, Jr., "The System Sodium Fluoride-Alumina Investigated by Quenching Methods," J. Am. Cer. Soc. 45 (4) 145-48 (1962).

30. H. C. Stumpf, A. S. Russell, J. W. Newsome and C. M. Tucker, "Thermal Transformations of Aluminas and Alumina Hydrates," Ind. Eng. Chem. 42 (7) 1398-1403 (1950).

31. P. A. Foster, Jr., "The Nature of Alumina in Quenched Crolite-Alumina Melts," J. Electrochem. Soc. 106 (11) 971-75 (1959).

32. K. Wefers and G. M. Bell, "Oxides and Hydroxides of Aluminum," Tech. Paper No. 19 Aluminum Co. of America, Pittsburgh, PA, p. 37, 1972.

33. J. Ravez and P. Hagenmuller, "Les Systemes CaF_2-AlF_3 et SrF_2-AlF_3," Bull. Soc. Chim. 7 2545-48 (1967).

34. J. Ravez, J. Viollet, R. DePape and P. Hagenmuller, "Les Systems MF_2-FeF_3 (M = Ba,Sr,Ca). Les Fluoferrites Alcalino-Terreux," Bull. Soc. Chim. 4, 1325-31 (1967).

35. J. L. Holm, "Phase Equilibria in the System CaF_2-AlF_3," Acta Chem. Scand. 19 (6) 1512-14 (1965).

36. M. Malinovsky, J. Vrbenska and I. Cakajdova, "Phasediagramm dis Systems CaF_2-AlF_3," Chem. Zvesti. 21 (1967).

37. J. Millet, H. Pham and M. Rolin, "Les Diagrammes de Phase des Systemes Binaires NaCl-AlF_3 et CaF_2-AlF_3: Extrapolation du Point Triple du Fluorure d'Aluminium"Rev. Int. Hautes Temp. Refract. (11) 4, 277-83 (1974).

38. D. Craig and J. Brown, Jr., "Phase Equilibria in the System CaF_2-AlF_3," J. Am. Cer. Soc., 60 (9-10) 396-98 (1977).

39. H. Grunhager and J. Mergoil, "Decouverte d'Hydrocalamite et Afwillite Associees a l'Ettringite dans les Porcelonites de Boissejour pres Ceyrat (Puy-de-Dome)," Bull. Soc. Franc. 86 149-57 (1963).

40. H. Evans, D. Appleman and D. Handwerken, Amer. Crystallographic Assoc. Annual Program Meeting, 42-43 (1963).

41. K. Matiasovsky and M. Malinovsky, "Physiochemical Study of Some Species Important in the Production of Aluminum, II. The Phase Diagram of the System Na_3AlF_6-CaF_2-NaCl," Chem. Zvesti. 14, 353-64 (1960) Chem. Abst. 54 (20-21) 22100g (1960).

42. A. Fenerty and E. A. Hollingshead, "Liquidus Curves for Aluminum Cell Electrolyte III. Systems Cryolite and Cryolite-Alumina with Aluminum Fluoride and Calcium Fluoride," J. Electrochem. Soc. 107 (12) 993-97 (1960).

43. M. Rolin, "Le Diagramme Binaire Cryolithe-Fluorure de Calcium. Le Diagramme Ternaire Cryolithe-Fluorure de Calcium-Alumine," Bull. Soc. Chim. 1120-25 (1961).

44. J. L. Holm, "The Phase Diagram of the System Na_3AlF_6-CaF_2, and the Constitution of the Melt in the System," Acta Chem. Scand., 22 (3) 1004-12 (1968).

45. M. Verdan and R. Monnier, "Etude du Systeme Na_3AlF_6-CaF_2 au Moyen de l´Analyse Thermique Differentielle en Creuset Scelle," Rev. Int. Hautes Temp. Refract. 9 (2) 205-8 (1972).

46. D. Craig and J. Brown, Jr., unpublished results.

47. P. A. Foster, Jr., "Phase Equilibria in the System Na_3AlF_6-AlF_3," J. Am. Cer. Soc. 53 (11) 598-600 (1970).

48. H. Ginsberg and K. Wefers, "Thermochemische Unter Suchungen am System NaF-AlF_3," Erzmetall 20 (4) 156-61 (1967).

49. M. Rolin, "Sur la Structure Ionique de la Cryolithe pure Fondue II - Determination Experimentale du Diagramme Binaire Cryolithe. AlF_3," Bull. Soc. Chim. (4) 671-77 (1960).

50. J. L. Holm, Investigation of Structure and Phase Ratio of Some Systems in Connection with Aluminum Electrolytes, Norweigan Technical Institute, Trondheim, Norway 7-13 (1963).

51. G. A. Roush and M. Miyake, "Equilibrium of the Series Cryolite-Alumina," Trans. Am. Electrochem. Soc. 48 153-57 (1925). Chem. Abst. 19 (8-16) 2455 (1925).

52. M. Rolin, "Le Diagramme Binaire Cryolithe-Alumine. I. Partie Experimentale," Bull. Soc. Chim. (6) 1201-3 (1960).

53. J. J. Duruz and R. Monnier, "Une Methode d´Analyse Thermique Differentielle pour les Substances Volatiles a Point de Fusion Eleve: Application au Systeme Cryolithe-Alumine," Chimia 21 (12) 572-5 (1967).

54. E. W. Dewing, "The Structure of Cryolite-Alumina Melts," J. Electrochem. Soc. 108 (6) 611-12 (1961).

55. G. Gunther, G. Anderson and H. Perlitz, "On the Luminescence of Phosphors of the Aluminum Oxide-Calcium Fluoride Type Activated with Manganese," Arkiv Kemi 1, 565-72 (1950).

56. C. Kuo and T. Yen, "Phase Equilibria and Chemical Reactions in the System CaF_2-Al_2O_3," Hua Hsueh Hsueh Pao 30 (4) 381-7 (1964). Chem. Abst. 61 (12-13) 15401h (1964).

57. A. K. Chatterjee and G. I. Zhmoidin, "The Phase Equilibrium Diagram of the System CaO-Al_2O_3-CaF_2," J. Mater. Sci. 7 (1) 93-7 (1972).

58. M. Rolin, "Le Diagramme Ternaire Cryolithe-Fluorure d'Aluminium-Alumine." Bull. Soc. Chim. 1112-1120 (1961).

59. M. Rolin and R. Muhlethaler, "Etude du Systeme Cryolithe de Sodium-Cryolithe de Lithium en tant que Solvant de l'Alumine," Bull. Soc. Chim. 2593-99 (1964).

60. G. A. Abramov, A. A. Kestyukov and L. B. Kulakov, "The Structural Diagram of the Quaternary System Cryolite-Aluminum Fluoride-Calcium Fluoride-Alumina," Electromet. Tsvetnykh Metal. No. 188 45-57 (1957). Chem Abst. 53 (13-16) 11975g (1959).

61. M. Rolin, "Le Diagramme Quaternaire Cryolithe-Fluorure d'Aluminium-Fluorure de Calcium-Alumine," Bull. Soc. Chim. 1404-7 (1961).

62. M. Rolin, "Le Diagramme Ternaire Cryolithe-Fluorure d'Aluminium-Fluorure de Calcium," Bull. Soc. Chim. 1351-54 (1961).

63. H. Pfundt and H. Zimmermann, "The Quasi Binary System NaF-$CaAlF_5$, An Investigation from the Ternary System NaF-AlF_3CaF_5," Ertzmetall 25 (11) 564-72 (1972).

64. E. W. Dewing, "Solid Solubility of CaF_2 in Cryolite," Trans. of The Metal. Soc. of AIME 245 (8) (1969).

65. P. A. Foster, Jr., "Phase Diagram of a Portion of the System Na_3AlF_6-AlF_3-Al_2O_3," J. Am. Cer. Soc., 58 (7-8) 288-91 (1975).

66. P. A. Foster, Jr., "Liquidus Curves in the Quaternary System NaF-AlF_3-CaF_2-Al_2O_3," J. Am. Cer. Soc., 43 (8) 437-38 (1960).

67. S. S. Lee, K. S. Lei, P. Xu, and J. J. Brown, Jr., "Determination of Melting Temperatures and Al_2O_3 Solubilities for Hall Cell Electrolyte Compositions," Light Metals 1984, Metallurgical Society AIME, 841-55 (1984).

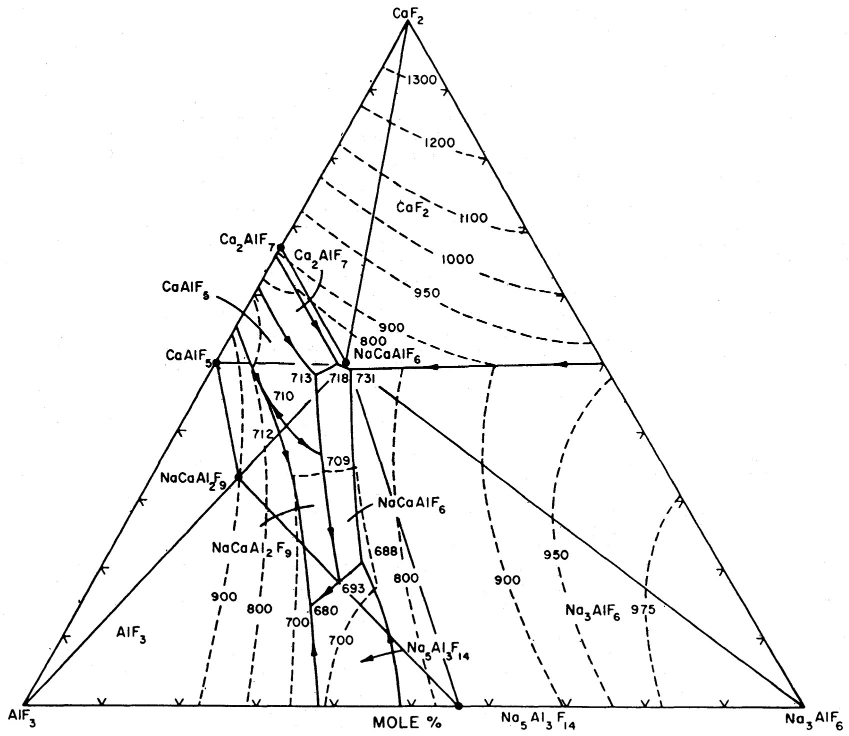

Figure 1. System CaF_2-AlF_3-Na_3AlF_6.[46]

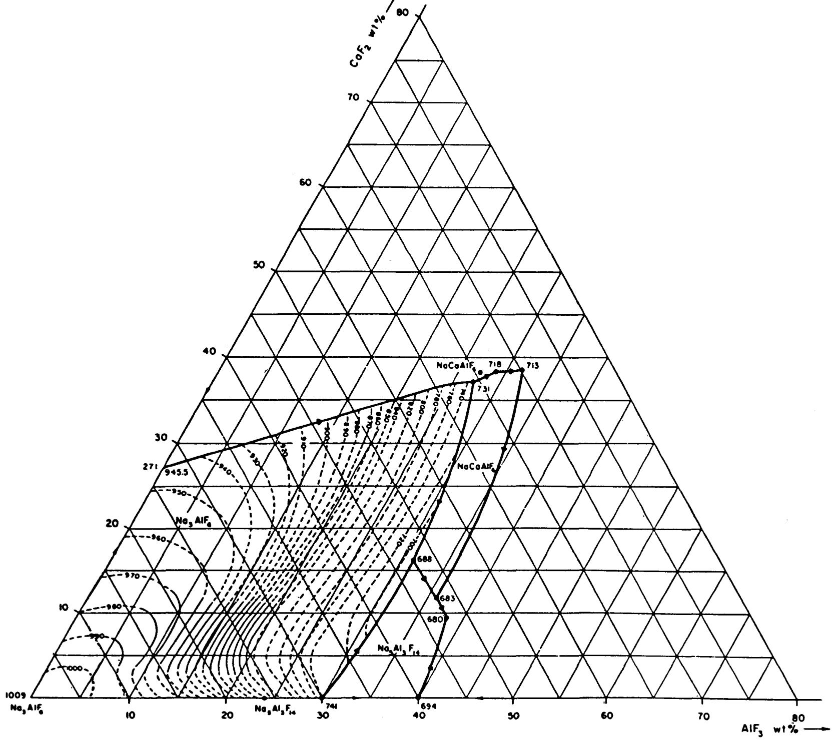

Figure 2. Isotherms for cryolite-rich portion of the ternary system Na_3AlF_6-CaF_2-AlF_3.[67]

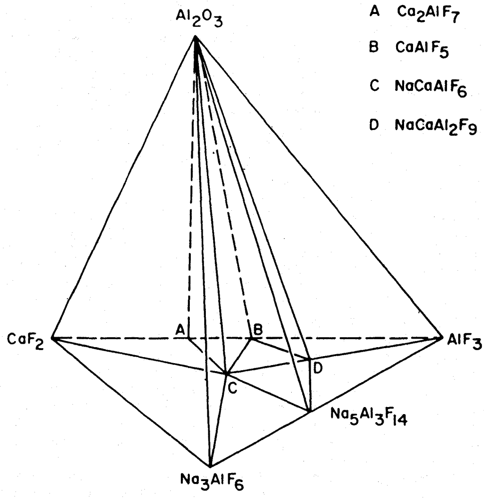

Figure 3. Subsolidus compatibility relationships in the system Na_3AlF_6-AlF_3-CaF_2-Al_2O_3.[46]

Table I. Compositions and Locations of Peritectics, Eutectics, and Saddle Points in the System CaF_2-AlF_3-Na_3AlF_6

Composition (mol%)			Type	T (°C)	Equilibrium phase assemblage
CaF_2	AlF_3	Na_3AlF_6			
49.0	33.5	17.5	Peritectic	731	CaF_2 $NaCaAlF_6$ Na_3AlF_6
49.5	35.0	15.5	Peritectic	718	CaF_2 Ca_2AlF_7 $NaCaAlF_6$
48.5	37.5	14.0	Peritectic	713	Ca_2AlF_7 $CaAlF_5$ $NaCaAlF_6$
43.0	46.0	11.0	Peritectic	710	$CaAlF_5$ $NaCaAl_2F_9$ AlF_3
38.0	44.0	18.0	Peritectic	709	$CaAlF_5$ $NaCaAl_2F_9$ $NaCaAlF_6$
25.0	45.0	30.0	Peritectic	688	Na_3AlF_6 $Na_5Al_3F_{14}$ $NaCaAlF_6$
18.0	52.0	30.0	Peritectic	683	$NaCaAl_2F_9$ $Na_5Al_3F_{14}$ $NaCaAlF_6$
15.0	55.0	30.0	Eutectic	680	AlF_3 $Na_5Al_3F_{14}$ $NaCaAl_2F_9$
49.0	34.0	17.0	Saddle point	735	CaF_2 $NaCaAlF_6$
39.5	47.5	13.0	Saddle point	712	$NaCaAl_2F_9$ AlF_3

DOI: 10.1149/198601.0361PV

ON THE SOLUBILITY OF ALUMINIUM CARBIDE AND ELECTRODEPOSITION OF CARBON IN CRYOLITIC MELTS.

R. Ødegård, A. Sterten and J. Thonstad.

Laboratories of Industrial Electrochemistry
and SINTEF, The Foundation for Scientific
and Industrial Research at
The Norwegian Institute of Technology
N-7034 Trondheim-NTH, Norway.

ABSTRACT

The solubility of aluminium carbide in cryolitic melts was determined as a function of the following parameters, (1): NaF/AlF_3 molar ratio (CR) in NaF-AlF_3 melts at 1020°C, (2): temperature in NaF-AlF_3 melts at CR=1.80, (3): alumina concentration at CR=1.80 and 1020°C, (4): CaF_2 concentration in NaF-AlF_3-CaF_2 melts at CR=1.80 and 1020°C. At 1020°C a maximum concentration of 2.1 wt% aluminium carbide was found at CR=1.80. The following model for the aluminium carbide dissolution reaction based on activity data for NaF and AlF_3, was found to fit the experimental solubility data;

$$Al_4C_3(s) + 5AlF_3(diss) + 9NaF(\ell) = 3Al_3CF_8^{3-} + 9Na^+$$

Carbon could be electrodeposited from NaF-AlF_3 melts saturated with aluminium carbide by electrochemical oxidation of the dissolved carbide species. Voluminous deposits of amorphous carbon were obtained on several different electrode substrates (graphite, vitreouscarbon, iron, tungsten and platinum).

INTRODUCTION

Solubility of ionic carbides in molten salts has been demonstrated both for acetylides (1,2) and methanides (3).

Dewing (3) fitted experimental solubility data for aluminium carbide in NaF-AlF_3 melts to the empirical equation;

$$\log(\text{wt\% } Al_4C_3) = 1.298 - 0.587\cdot(\text{molar ratio NaF}/AlF_3) \quad /1/$$

The aluminium carbide solubility showed no temperature dependence in the temperature range 985-1080°C. Additions of up to 10 wt% of Al_2O_3, NaCl, CaF_2 or LiF had no influence on the measured solubilities, provided that LiF and CaF_2 were replaced by equivalent amounts of NaF when calculating the NaF/AlF_3 molar ratio (CR) used in eq. /1/.

For $2<CR<4.5$ Dewing obtained a good fit between the measured solubilities and the following dissolution reaction,

$$Al_4C_3 + 2AlF_3 = 3Al_2CF_2 \quad /2/$$

Electrodeposition of amorphous carbon has been reported both for cathodic polarization of the working electrode in molten carbonates (4,5,6) and by anodic polarization in melts containing dissolved CaC_2 (7,8). In the latter case the overall anodic reaction was proposed to be (7);

$$C_2^{2-} = 2C(s) + 2e \quad /3/$$

The current for deposition of carbon from dissolved CaC_2 at 850°C was almost independent of stirring in the lower voltage range, while it increased at more positive potentials (7). At higher temperatures (≈1000°C) the current increased with stirring also in the lower potential range (9). These results indicate a shift from reaction control to diffusion control with increasing potential and temperature.

EXPERIMENTAL

A vertical tube furnace with argon atmosphere was used for the aluminium carbide solubility measurements as well as the carbon deposition experiments. The temperature was measured with a standardized Pt·Pt10%Rh thermocouple and it

was kept constant within ± $1^{o}C$.
The molten salt (≈140g, made up of high purity pre-dried components) and aluminium (≈25g, +99.999% Al) were contained in graphite crucibles (44 mm i.d., CS, Union Carbide Norden AB). In the solubility experiments crucibles with close-fitting lids of the same material were used. The crucibles were placed in the isothermal zone of the tube furnace. The melt was kept at temperature for a period of ≈5 hours to ensure saturation with dissolved aluminium carbide formed by the reaction between aluminium and the graphite crucible.

In the solubility experiments the crucible lid was removed by means of a molybdenum wire attached to the lid. A melt sample (≈5g) was then taken, using a thickwalled steel ladle with a steel lid that was kept in the cold part of the furnace. The ladle was quickly lowered into the melt and then withdrawn to the cold zone. This was done without admitting air to the furnace tube. The quenched melt sample was kept in the cold part of the furnace for about five minutes and then quickly transferred to a glove-box with argon atmosphere (< 5ppm H_2O) where the sample was ground to -80 mesh. The sample was treated with a 10% HCl solution and the total volume of gas evolved due to the reactions between the solution and aluminium carbide (CH_4) and aluminium (H_2) was determined volumetrically. The analysis apparatus was similar to that described by Rogers et al. (10). When the gas evolution was completed, the evolved gas was analysed for methane and hydrogen by a gas chromatograph (Varion Aerograph, 90-P). In the calculation of the amount of dissolved aluminium carbide based on the volume of methane, corrections were made for temperature, atmospheric pressure, the partial pressure of water at the temperature of analysis, and the amount of dissolved metal in the melt sample.

In the carbon deposition experiments the graphite crucible was used as counter electrode (cathode) and a variety of electrode materials was applied as working electrode (anode). The aluminium pool (Area ≈ 25 cm^2) with a tungsten rod (2 mm diam.) for electrical contact served as reference electrode.

In constant current experiments a DC power supply (Hewlett Packard 6274B) was used. The cell voltage and current were recorded on a two channel strip chart x-t recorder (W+W, 312). In potentiostatic experiments a high power potentiostat (Wenking HP72) with a potential scan generator (Wenking VSG72) was used. The current was recorded versus the working electrode potential on an x-y recorder (Watanabe WX4301). The IR-drop between the working and the reference electrodes was determined by means of a Solatron 1250 frequency response analyser.

After the deposition experiments, samples for x-ray diffraction analysis (Philips PW 1730/10) were ground to -80 mesh and leached in a 30% $AlCl_3$ solution at 50°C for 24 hours to remove adhering salt. The samples were then washed in distilled water and dried at 150°C for 24 hrs. The same leaching and washing procedure was used for relatively large pieces of deposit (≈5 mm long) which were analysed on a scanning electron microprobe (ARL-SEM Q) and scanning electron microscope (JEOL, JSM-840).

RESULTS AND DISCUSSION

A. Solubility of aluminium carbide.

The concentration of dissolved aluminium carbide as a function of the NaF/AlF_3 molar ratio at 1020 ± 2°C is shown in Fig. 1. A representative selection of Dewing's (3) solubility data is also given in the figure. The broken line in the figure is a representation of Dewing's data in accordance with the present work showing a concentration peak of dissolved aluminium carbide with a maximum of 2.1 wt% Al_4C_3 at CR = 1.80. Because Dewing's measurements were not extended to low CR's the concentration peak shown in Fig. 1 was not detected in that work. For CR's between 1.8 and 4 the two curves show the same trend.

In the present work no variation was found in the amount of dissolved Al_4C_3 as a function of saturation time (4-6 hrs). Also for the shortest holding time (4 hrs) intensely yellow coloured solid Al_4C_3 was found on almost the entire inner surface of the graphite crucibles after experiments. Since Dewing used a 4 hrs holding time the discrepancy in the solubility data between the present work and that of Dewing (3) is therefore probably not due to differences in the degree of saturation. It can rather be due to different sampling procedures. In the work by Dewing the whole crucible containing the melt (≈ 150 g) and aluminium (≈ 20 g) was quenched in tap water. Due to the fairly large mass to be quenched, this procedure probably gave a relatively low cooling rate with a possible loss of dissolved aluminium carbide due to coupled reactions like;

$$Na(diss) = Na(g) \qquad /4/$$

and

$Al_4C_3(diss) + 12NaF(\ell)=3C(s)+12Na(diss) + 4AlF_3(diss)$ /5/
The assumption that reaction /5/ can take place was supported by the observation of small amounts of carbon dust on top of the melt at the end of the experiments. In a run were no lid was used on top of the crucible, a fairly large amount of dust was found in the crucible after the experiment.

The equilibrium vapour pressure of sodium increases with increasing CR (Kvande, 1979, Sterten et al., 1982). During a slow quenching the loss of dissolved aluminium carbide according to eqs. /4/ and /5/ will probably increase with increasing CR. In the present work the temperature of the ≈5g sample was recorded to be lower than 750°C within 3s after sampling. The loss of aluminium carbide during sampling is therefore believed to be small in the present work.

A great number of dissolution models were tested (11) and the best fit to the experimental data was found for the reaction;

$$Al_4C_3(s) + 5AlF_3(diss) + 9NaF(\ell) = 3Al_3CF_8^{3-} + 9Na^+ \quad /6/$$

This model is represented by the full line in Fig.1. Activity data for NaF and AlF_3 given by Sterten and Mæland (12) were used in the calculation which was based on the assumption of constant activity coefficient for $Al_3CF_8^{3-}$. Dewing's solubility model (Al_2CF_2) eq. /2/, does not fit the data of the present work at low NaF/AlF_3 molar ratios. As mentioned a large number of other models have also been tested, but none have been found that give nearly as good prediction of the concentration of dissolved aluminium carbide in $NaF-AlF_3$ melts as the model represented by eq. /6/ does. This model is therefore adopted for the aluminium carbide dissolution reaction in $NaF-AlF_3$ melts. However the presence of minor amounts of $Al_4CF_{12}^{4-}$ can not be excluded at low CR (< 1.50). It should be emphasized that there is no spectroscopic evidence for the $Al_3CF_8^{3-}$ species.

Fig. 2 shows the concentration of dissolved aluminium carbide as a function of temperature in $NaF-AlF_3$ melts with CR = 1.80. The concentration was found to decrease with increasing temperature from 2.96 wt% at 901°C to 1.77 wt% at 1062°C. Dewing (3) did not observe any significant temperature dependence of the concentration, and this could as mentioned above,be due to the difference in quenching procedure.

With the assumptions of ideal solution, no solid solution of aluminium carbide, and no difference in heat capacity between solid and liquid aluminium carbide the apparent heat of solution of aluminium carbide (ΔH) in NaF-AlF$_3$ melts at CR = 1.80 can be calculated from the equation (13);

$$\ln\left[\frac{x}{x''}\right] = \frac{\Delta H\cdot(T-T'')}{R\cdot T\cdot T''} \qquad /7/$$

where x is the mole fraction of Al$_4$C$_3$ at saturation, T is the temperature (K), and R is the gas constant. The calculation yields ΔH= - 41 kJ/mol. In the calculation the concentration in wt% was taken to be proportional to the mole fractions. This melt does not behave ideally (12), and the calculated heat of dissolution should only be regarded as an approximative value for the heat involved in the aluminium carbide solution reaction.

Fig. 3 shows the analysed concentration of dissolved aluminium carbide as a function of the alumina concentration in NaF-AlF$_3$-Al$_2$O$_3$ melts at CR = 1.80 and 1020 ± 2^{o}C. In the calculation of the data in Fig. 3 the methane evolved during hydrolysis was formally treated as being caused only by dissolved Al$_4$C$_3$ (no oxy-carbides).

Contrary to the data of Dewing (3) which indicated no significant variation in the concentration of dissolved aluminium carbide with the alumina concentration, the present work shows a pronounced decrease in the aluminium carbide concentration with increasing concentration of alumina.

Sterten and coworkers have given activity data for NaF and AlF$_3$ in alumina-saturated (14) and alumina-free (12) NaF-AlF$_3$ melts. The activities of NaF and AlF$_3$ were estimated as a function of the alumina concentration at CR = 1.80 and 1020^{o}C. In the estimation the shape of the activity versus alumina concentration curves were assumed to be the same at CR = 1.80 as given by Sterten and Mæland (12) for CR = 3.00. The full line in Fig. 3 represents a model fitting based on dissolution of Al$_4$C$_3$ according to eq. /6/ and the estimated activity data for NaF and AlF$_3$ as a function of alumina concentration. In the model calculation the equilibrium constant used for eq. /6/ was the same as that found to give the best fit in the pure NaF-AlF$_3$ system (K_6 = $6.44\cdot10^{+6}$ at 1020^{o}C).

The occurrence of the $Al_2OC(s)$ compound reported by Grjotheim et al. (15) in experiments with cryolitic melts in presence of aluminium, carbon and alumina, is somewhat controversial since it is not stable in the pure Al_4C_3-Al_2O_3 system (16). Grjotheim et al. claimed $Al_2OC(s)$ to be stable in cryolitic solutions in the intermediate alumina concentration range since high alumina activity is expected to give $Al_4O_4C(s)$ and low alumina activity $Al_4C_3(s)$. The shape of the aluminium carbide solubility curve in Fig. 3 does not give any indication of a new species occurring at medium alumina concentrations. If $Al_2OC(s)$ were formed in the present experiments, the results strongly indicate that its occurrence does not affect the amount of dissolved carbide species.

Fig. 4 gives the concentration of dissolved aluminium carbide as a function of the CaF_2 concentration in NaF-AlF_3-CaF_2 melts at CR = 1.80 and 1020 ± 1°C. Dewing (3) found that CaF_2 addition did not affect the aluminium carbide solubility provided that this addition formally was treated as an equivalent amount of NaF. The same model was tested in the present work and it is given as a broken line in Fig. 4. In the calculation of equivalent NaF/AlF_3 molar ratio with CaF_2 addition, one mole of CaF_2 was treated as being equivalent to two moles of NaF. The corresponding aluminium carbide solubility with addition of CaF_2 was then taken from Fig. 1. As can be seen from Fig. 4 the decrease in aluminium carbide solubility with addition of CaF_2 was considerably larger than caused by an equivalent NaF addition in the present work.

B. Carbon deposition.

In electrolysis experiments with melts containing dissolved aluminium carbide, voluminous black deposits were obtained on the anode for all anode materials tested, i.e. graphite, vitreous carbon, iron, tungsten and platinum. In Fig. 5 is shown photographs of deposits on tungsten, vitreous carbon and iron electrodes. Scanning electron microprobe analysis showed the deposit to be almost pure carbon (≈97 mole % C). The small fraction of non carbon materials was probably due to inclusions of salt although the analysis were a little low in fluoride compared to the equivalent salt composition. Salt inclusions were also reported for deposition of carbon from dissolved CaC_2 in chloride melts (7).

Although deposition of carbon from the NaF-AlF_3-Al_4C_3

system has not been reported before to the authors' knowledge, there are some indications of such a phenomenon in the literature. Sleppy and Cochran (17) observed "swelling" of the anodes during aluminium electrolysis in acidic $NaF-AlF_3-Al_2O_3$ melts at 740°C (CR ≈ 1.3). The relatively large increase in the diameter of the anodes could be interpreted as being due to carbon deposition. In the book; "Metallurgy of aluminium", Beljajew et al. (18) mentioned a tendency of "mushroom formation" ("spikes") on the anode(s) in aluminium cells with high contents of aluminium carbide.

Fig. 6 shows a typical x-ray diffraction response of the deposit. In spite of the fluoride extraction procedure described above, there are several peaks which originate from inclusions of melt remaining in the pores of the deposit. These peaks are marked by "M" in Fig. 6. The shape of the x-ray diffraction response indicates that the deposited carbon is amorphous.

From the weight loss when burning off electrodeposited carbon from a platinum electrode in air the number of electrons involved in the deposition reaction was calculated to be 4.31 and 4.44 in two experiments. The deviation from the expected number of four could be caused by a certain loss of carbon when taking the electrodes out of the furnace, and because a fraction of the current in the experiments will be used for oxidation of dissolved aluminium. Based on these experiments and on the model fitting for the aluminium carbide dissolution reaction (eq. /6/) the overall anodic reaction for aluminium carbide oxidation can be written;

$$Al_3CF_8^{3-} + F^- = C(s) + 3AlF_3(diss) + 4e \qquad /8/$$

Fig. 7 shows a typical potential decay curve recorded in carbon deposition experiments. A constant current of 5 A (≈ 0.5 A/cm^2) was applied for five minutes and then disconnected at time zero. The potential of the vitreous carbon electrode with carbon deposit on it was recorded versus an aluminium electrode. The potential plateau which is clearly visible in Fig. 7, corresponds to an aluminium carbide formation cell with the reaction;

$$4Al(\ell) + 3C(s) = 4Al_4C_3(s) \qquad /9/$$

The semi-stable potential of the carbon electrode was +142.76 mV versus the aluminium electrode when correcting for the thermoelectric effect measured in blank experiments at the temperature of the experiment (1013.0°C). The Gibbs energy of formation of aluminium carbide can be calculated from the equation

$$\Delta G = -nFE^{rev} \qquad /10/$$

$$E^{rev} = E^{o} - \frac{RT}{nF} \ln \frac{a_{Al_4C_3}}{a_{Al}^{4} \cdot a_{C}^{3}} \qquad /11/$$

where $a_{Al} = a_{C} = 1$ (pure liquid aluminium and solid deposited carbon). Solid Al_4C_3 was found in the graphite crucibles after deposition experiments. It is unlikely that the concentration gradients caused by the electrolysis (5A for 5 minutes) persisted for the duration of the semi-stable potential period (≈ 4 mins). Therefore, the shape of the potential curve in Fig. 7 strongly indicates that equilibrium was established between dissolved and solid aluminium carbide during the constant potential period. The activity of aluminium carbide is taken to be unity in that period. Hence E^{rev} in eq. /11/ is equal to the standard potential (E^{o}) and $\Delta G^{o}_{f,Al_4C_3}$ can be calculated from eq. /10/. The value at 1013.0°C is $\Delta G^{o}_{f,Al_4C_3} = -165.294$ kJ/mol. The corresponding thermodynamic data taken from the JANAF tables (19) is $\Delta G^{o}_{f,Al_4C_3} = -142.809 \pm 6.694$ kJ/mol. This value is also in agreement with extrapolated data from Sandberg (20), $\Delta G^{o}_{f,Al_4C_3} = -148.55 \pm 7.95$ kJ/mol. The reason for the deviation from these values in the present work will be further investigated.

Rey (21) suggested to use the aluminium carbide formation cell as a reference cell in NaF-AlF_3 melts. However, the Al/Al_4C_3/C formation cell potential does not appear to be stable. In the present work the potential plateau corresponding to this formation cell was only of short duration. The reason for the lack of stability is probably a slow pick-up of dissolved aluminium or sodium by carbon (22). The carbon potential will therefore gradually decrease relative to the aluminium reference electrode.

Similar to the observations of Morris and Harry (7) for anodic carbon deposition from dissolved CaC_2, the morphology of the carbon deposit in the present work was found to change with the current density. Low current densities gave a dense deposit while a more "spongy" type of carbon was formed at high current densities. This is illustrated in Figs. 8 and 9 which show scanning electron micrographs (SEM) of electrodeposited carbon. The total electrolysis currents were equal to 10.0 A and 1.0 A respectively. The other deposition conditions were identical for the two samples.

Fig. 10 shows a typical current versus potential diagram for a slow potential sweep measurement (sweep rate 2.5 mV/s) in NaF-AlF_3 melts saturated with dissolved aluminium carbide. The curve is corrected for the potential drop between the aluminium reference electrode and the vitreous carbon working electrode.

Due to the carbon deposition which made the area of the carbon electrode increase continuously during the potential sweep measurement, the current on the return scan (decreasing E) is much higher than on the forward scan in the positive potential direction. Due to this growth it is not possible to derive an exact current density versus potential curve from the data in Fig.10. Only very limited kinetic information on the carbon deposition reaction can therefore be gained from steady or semi-steady state electrochemical measurements. However, the steady state measurements seem to indicate that in the investigated potential range ($E_{max} \approx +900$ mV) carbon deposition is reaction controlled, probably by nucleation control.

REFERENCES

1. Mitchell, A., Trans.Met.Soc. AIME <u>242</u>, 2507 (1968).

2. Maillot, J.F. and Morris, D.R., Can.J.Chem. <u>50</u>, 839 (1972).

3. Dewing, E.D., Trans.Met.Soc. AIME <u>245</u>, 2181 (1969).

4. Haber, F. and Tolloczko, St., Z.Anorg.Chem. <u>41</u>, 412 (1904).

5. Dubois, J., Ann.Chim. <u>L.10</u>, 145 (1965).

6. Ingram, M.D., Baron, B. and Janz, G.J., Electrochim. Acta <u>11</u>, 1629 (1966).

7. Morris, D.R. and Harry, J.R., Proceedings of the International Conference on Industrial Carbon and Graphite (Society of Chemical Industry), London,

8. White, S.H. and Morris, D.R., Proceedings of the Richardson Conference, London, 1974, p. 195.

9. Morris, D.R., "Ionic Carbides", in "Molten Salt Technology", ed.: Lovering, D.G., Plenum Press, New York, 1982, p.153.

10. Rogers, P.S., Bevan, D.J.M. and Tomlinson, J.W, Microchim. Acta 12, 1839 (1956).

11. Ødegård, R., "On the Solubility and Electrochemical Behaviour of Aluminium and Aluminium Carbide in Cryolitic Melts", Dr.ing. thesis, The University of Trondheim, NTH, Norway, 1985.

12. Sterten, A. and Mæland, I., Acta Chem. Scand. A39, 241 (1985).

13. Lewis, G. N. and Randall, M., "Thermodynamics", Revised by Pitzer, K.S. and Brewer, L., McGraw-Hill, New York, 1961.

14. Sterten, A., Hamberg, K. and Mæland, I., Acta Chem. Scand. A36, 329 (1982)

15. Grjotheim, K., Herstad, O., Næumann, R. and Øye, H.A., Light Metals 1978, 107th Annual Meeting of AIME, Denver, Colorado, 1978, Vol.1., p. 107.

16. Motzfeldt, K. and Sandberg, B., Light Metals 1979, 108th Annual Meeting of AIME, New Orleans, 1979, p.411.

17. Sleppy, W.C. and Cochran, C.N., Light Metals 1979, 108th Annual Meeting of AIME, New Orleans, 1979, p. 385.

18. Beljajew, A.I., Rapoport, M.B. and Firsanowa, L.A., "Metallurgie des Aluminiums", (German translation), Vol. 1., VEB Verlag Technik, Berlin, 1956.

19. JANAF Thermochemical Tables, 2.ed., Dow Chemical Co., Midland, Michigan, 1971.

20. Sandberg, B., "Karbotermisk reduksjon av aluminiumoksyd", Dr.ing. thesis, The University of Trondheim, NTH, Norway, 1981, (in Norwegian).

21. Rey, M., Electrochim.Acta 14, 991 (1969).

22. Grjotheim, K., Krohn, C., Malinovsky, M., Matiasovsky, K. and Thonstad, J., "Aluminium Electrolysis", 2.ed., Aluminium-Verlag, GMBH, Düsseldorf, 1982.

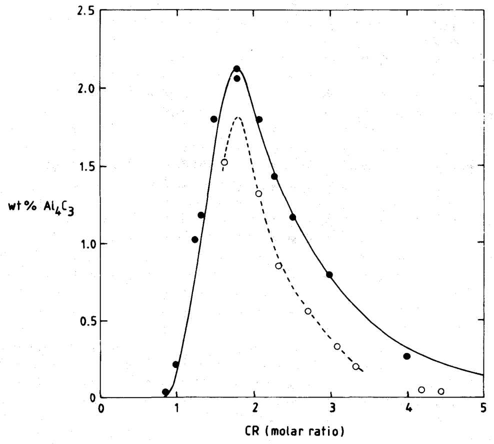

Fig. 1. Concentration of dissolved aluminium carbide in $NaF-AlF_3$ melts as a function of the NaF/AlF_3 molar ratio at 1020 ± 2°C.
●: present work, o: Dewing (3).
Full line based on a dissolution reaction according to eq. /6/ (see text).

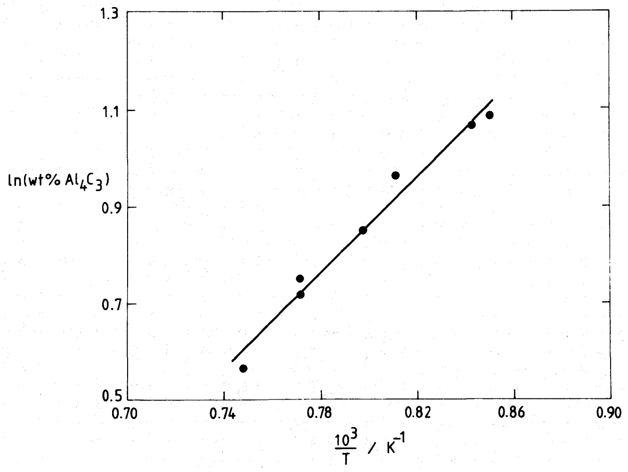

Fig. 2. The natural logarithm of the concentration of dissolved aluminium carbide as a function of reciprocal temperature in $NaF-AlF_3$ melts at CR = 1.80.

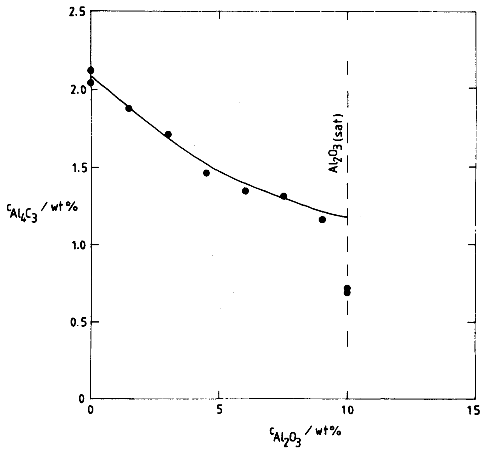

Fig. 3. Concentration of dissolved aluminium carbide as a function of the concentration of alumina in NaF-AlF_3-Al_2O_3 melts at CR = 1.80 and 1020 ± 2^oC.
(●): experimental data
full line: Calculated solubilities according to eq. /6/.

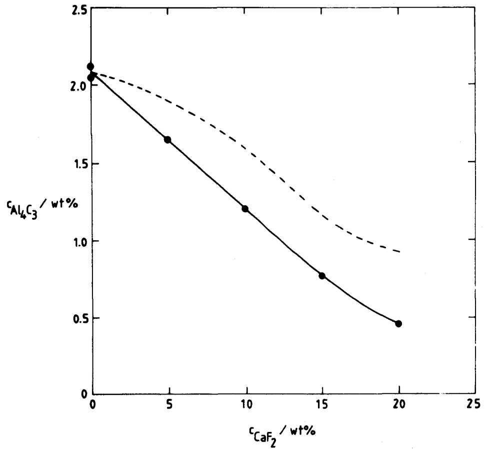

Fig. 4. Concentration of dissolved aluminium carbide as a function of the calcium fluoride concentration in NaF-AlF_3-CaF_2 melts at CR = 1.80 and 1020^oC ± 1^oC.
(●): experimental data.
---: CaF_2 treated as an equivalent NaF addition.

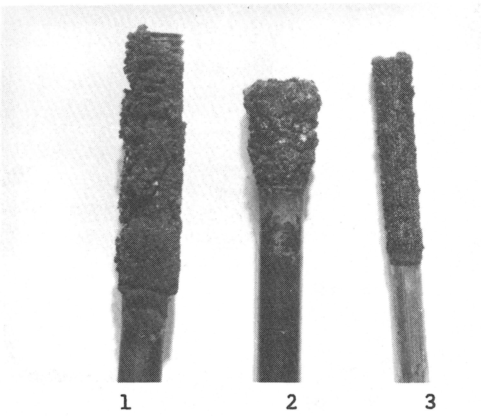

Fig. 5. Carbon deposits on electrodes made of; 1: iron (3 mm diam.), 2: vitreous carbon (3 mm diam.) 3: tungsten (2 mm diam.). Deposition conditions: CR = 1.50, temperature = 1000°C, total current 1-5 A.

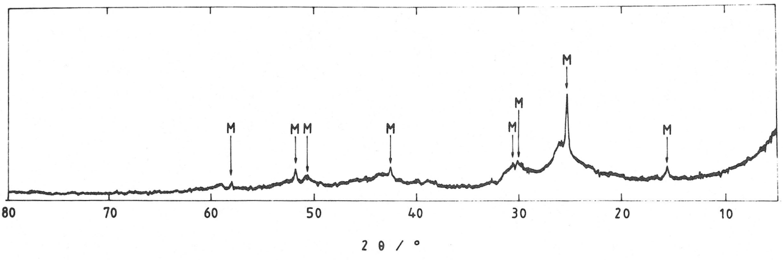

Fig. 6. x-ray diffractogram of electrodeposited carbon. Peaks marked "M" were identified to be due to melt compounds ($NaAlF_4$, $Na_5Al_3F_{14}$). Deposition conditions: CR = 1.50, t = 1000°C, I = 2A. Diffraction angle scan 5-80°.

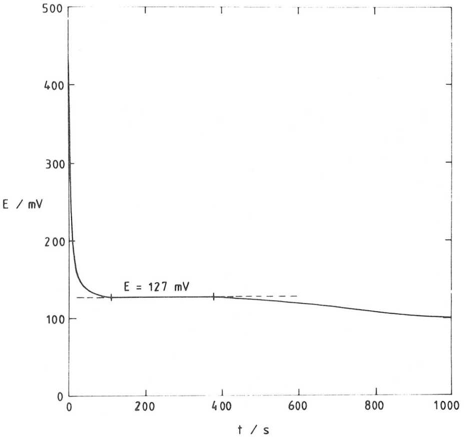

Fig. 7. Potential decay curve recorded in a carbon deposition experiment. The potential of a vitreous carbon electrode with carbon deposit on it was measured versus an aluminium electrode. At $t<0$, $I = 5$ A (≈ 0.5 A/cm^2), Temperature = 1013.0°C, CR = 1.50.

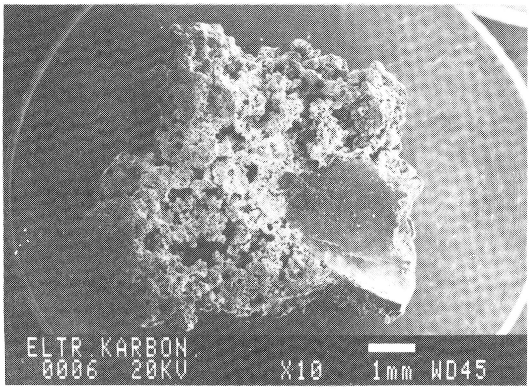

Fig. 8. SEM micrograph of electrodeposited carbon. Deposition conditions: $I = 10.0$ A, $t = 1020^{\circ}$C, CR = 1.50. The smooth area visible on the picture is the contact area to the vitreous carbon electrode (3 mm diam.).

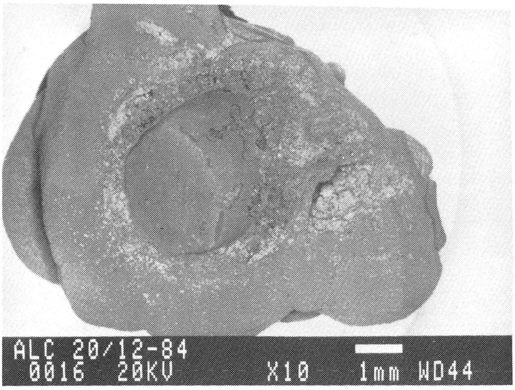

Fig. 9. SEM micrograph of electrodeposited carbon. Deposition conditions: I = 1.0 A, t = 1020°C, CR = 1.50.
The smooth area in the center of the sample is the contact area to the end of the vitreous carbon electrode (3 mm diam.).

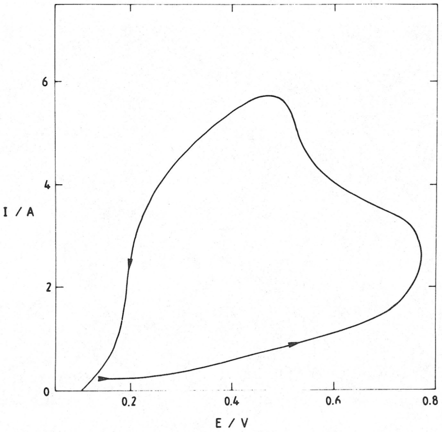

Fig. 10. Current versus potential diagram for a slow potential sweep measurement with vitreous carbon electrode. Sweep rate 2.5 mV/s, CR = 1.50, t = 1020°C. Initial area of the working electrode; $A_i = 1.5\ cm^2$.

DOI: 10.1149/198601.0377PV

ELECTROCHEMICAL INTERCALATION OF LITHIUM IN GRAPHITE USING A MOLTEN-SALT CELL

Rajeeva R. Agarwal
and
J. Robert Selman

Department of Chemical Engineering
Illinois Institute of Technology
Chicago, IL 60616

ABSTRACT

The lithium intercalation compounds $C_{64}Li$, $C_{32}Li$, $C_{18}Li$, $C_{12}Li$ and C_6Li have been generated successively, for the first time, by electrochemical pulse titration. The compounds have been identified coulometrically and in part by NMR spectra. Intercalation of lithium in graphite appears to be sensitive to structural changes in the host graphite and is characterized by overlap of stoichiometric regions, resulting in narrow potential plateaus for the higher intercalation stages. This appears to be related to the extremely rapid diffusion of lithium (diffusivity values of 10^{-5} to 10^{-7} cm^2/s at 400-600°C), in the host graphite.

Studies involving intercalation compounds cover a great diversity of research areas. Investigations range from new intercalation compound synthesis and unraveling of the intercalation mechanism to possible applications exploiting the rapid directional transport characteristics, extremely high anisotropy and reversible nature of intercalation. It is remarkable that among the graphite intercalation compounds the lithium intercalation compounds, which are historically the oldest known, are investigated the least in spite of their significance, in particular for high energy battery electrodes. This appears to be due in large part to the poor resolving power of conventional techniques of intercalation applied to lithium in graphite.

Most of the information about lithium intercalation available in the literature has been obtained by nonelectrochemical methods; a summary is given in Table 1. From these investigations one may conclude that the lowest stoichiometry compounds are C_6Li, $C_{12}Li$ and $C_{18}Li$. For the higher stages varying compositions are reported.

Electrochemical intercalation should yield similar compositions; for example, potential scans should produce current peaks at stoichiometric compositions, and steady-state current passage should yield potential plateaus at such compositions. Early workers[1], found that during electrolysis of LiCl-KCl eutectic at 400°C, using a graphite cathode, the graphite disintegrated at high current densities; at low current densities (0.05 A/cm^2) the intercalation was very slow. The risk of disintegration is probably the reason why later investigators used cyclic voltammetry to explore intercalation electrochemically. James[10], using various types of graphite, showed that lithium is absorbed rapidly into graphite, but he could not observe any current peaks. In more recent work, Pfluger, et al.[11] noted color changes from black to deep blue, light green and golden-yellow in highly-oriented pyrolytic graphite (HOPG). They performed their experiments in water-free aprotic solvents (such as dimethylsulfoxide); the color changes, which are composition-dependent, were controlled by the applied potential (approximately 3 to 5 volts). A golden-yellow coloration observed by these authors was ascribed to the compound C_6Li.

The work reviewed above leaves doubt that well-defined higher-stage lithium-graphite intercalation compounds can be produced individually by electrochemical methods and does not clarify why this should be so. In this work we report results obtained by using the Galvanostatic Intermittent Titration Technique (GITT)[12]; this pulse method allowed us to generate successively, for the first time, the electrochemical potential plateaus for the various intercalation stages, up to a composition of $C_{7.28}Li$. The potential inflections indicate that the stoichiometries of the intercalation compounds obtained are $C_{64}Li$, $C_{32}Li$, $C_{18}Li$ and $C_{12}Li$, with appreciable deviations from stoichiometry.

The experiments were carried out using a cell containing LiCl-KCl eutectic (42 mol% LiCl, m.p. 352°C) or LiF-LiCl-LiBr electrolyte (22 mol%LiF, 31 mol% LiCl, 47 mol% LiBr, m.p. 430°C) as the electrolyte, between 400-600°C, under a rigorously purified argon atmosphere. Figure 1 shows the experimental cell. The graphite working electrode (diameter = 3mm, purity = 99.9995%, density = 1.966 g/cc, Ultra F/U-7 grade obtained from Ultracarbon Corp., MI) was intercalated by step-wise coulometric titration up to the desired composition, at fixed temperature. A few experiments were carried out using rectangular cuts of HOPG (Highly Oriented Pyrolytic Graphite, Union Carbide Corp., Parma, OH) of intercalation width 0.45 to 0.60 cm, height 3.1 to 4.7 cm, and c-axis thickness 0.055-0.160 cm.

The steady potentials obtained from a GITT experiment (Figure 2) exhibit plateaus and slopes typical for, respectively, two-phase and single-phase regions in the case of a binary alloy. In an intercalation process plateaus and slopes indicate, respectively, regular filling of the next intercalation stage, and filling with overlap of more than two stages. Typical for the latter occurrence is that compositional variations for the same stage of intercalation were also observed in repeat experiments. Table 2 indicates the variations observed in various experiments.

Table 2. Stoichiometry of Intercalation Stages LiC_n from Titration Curves

Stage	n	Number of Experiments	Temperature Range (°C)
5	68.4 ± 4.4	6	476-582
4	33.1 ± 2.4	8	465-582
3	17.9 ± 2.1	7	465-582
2	13.1 ± 0.5	4	478-582

The coexistence of stoichiometric compounds (at least in the sloping regions of Figure 2) is also evident from:

(1) NMR characterization of final samples, which showed good agreement with the spectra obtained by Lauginie <u>et al</u> [13] for C_6Li and $C_{12}Li$ (Fig.3)

(2) The bluish color of higher-stage compounds obtained at the higher temperatures (for example at 534°C), while an orange color (expected only for C_6Li) was observed already when the titration had reached $C_{7.2}Li$ (at 465°C in LiCl-LiBr-LiF eutectic); the coloration was uniform over the sample cross-sections.

Temperature variation between 673 and 873K (400-600°C) was found to affect the intercalation significantly. For example, at 690K (413°C) graphite disintegrated soon after the $C_{64}Li$ composition was reached; however, at higher temperature this did not occur at all, within the limits tested (down to $C_{7.2}Li$). Similarly, all plateaus except that of $C_{64}Li$ were found to be broader at 855K (582°C) than at lower temperature.

These aspects of the intercalation process, as well as the diffusivities determined from the nonstationary-potential response to each pulse, will be discussed in a following publication[14].

It appears that lithium intercalation in graphite is not only structurally different from that of the heavier alkali metals (K, Rb, Cs)[15] but that its kinetics are also unique. Lithium intercalation is characterized by very high values of lithium diffusivity (10^{-5} to 10^{-7} cm^2/s at 400-600°C in spectroscopic grade graphite). The diffusivity appears to be related to structural changes and stage formation in the intercalation process. This is concluded from the temperature variations, types of graphite used, and stage formation [14]. It is probably this kinetic characteristic of lithium intercalation in graphite that is responsible for the absence of current peaks in the potential scans as noted above [10].

In summary, the potential plateaus characterizing the lithium intercalation compounds $C_{64}Li$, $C_{32}Li$, $C_{18}Li$, $C_{12}Li$ and C_6Li have been generated successively, for the first time, by electrochemical pulse titration. The potentials have been identified coulometrically and, in the case of $C_{12}Li$ and C_6Li, by NMR Spectra. Intercalation of lithium in graphite appears to occur with overlap of stoichiometric regions, which narrows the potential plateaus, especially in the higher intercalation stages and at low temperatures (400-450°C). This appears to be related to the very rapid diffusion of lithium in the host graphite.

Acknowledgment

This work was supported by the Division of Materials Sciences, Office of Basic Energy Sciences, U.S. Department of Energy. The assistance of Professor K. D. Kopple (Dept. of Chemistry, IIT) and Mr. Robert Short in the NMR analysis and interpretation of samples is gratefully acknowledged.

Bibliography

1. Herold, A., 1955, "Recherches sur les Composes d'Insertion du Graphite", Bull. Soc. Chim. France,

No.187:999-1012.

2. Juza, R. and Wehle, V., 1965, "Lithium-Graphit-Einlagerungsverbindungen", Die Naturwissenschaften, 52:560.

3. Bagouin, M., Guerard, D. and Herold, A., 1966, "Action de la Vapeur de Lithium sur le Graphite", C.R. Acad. Sc. Paris, Ser. C 262: 557-559.

4. Secrist, D.R., 1967, "Compound Formation in the Systems Lithium-Carbon and Lithium-Boron", J. American Ceramic Soc., 50(10): 520-523.

5. Salzano, F.J., Aronson, S., Ingraham, A., 1968, "Comment on Compound Formation in the Lithium-Carbon System", J. American Ceramic Soc., 51 (8): 465.

6. Guerard, D. and Herold, A., 1972, "Nouvelle Methode de Preparation des Composes D'Insertion du Lithium dans le Graphite", C.R. Acad. Sci. Paris, Ser, C 275:571-572.

7. Guerard, D. and Herold, A., 1975, "Intercalation of Lithium into Graphite and Other Carbons", Carbon, 13: 337-345.

8. Herold, A., Billaud, D., Guerard, D. and Lagrange, P., 1977, Mater. Sci. Eng., 31: 25.

9. Basu, S., Zeller, C., Flanders, P.J., Fuerst, C.D., Johnson, W.D. and Fisher, J.E., 1979, "Synthesis and Properties of Lithium Intercalation Compounds", Mater. Sci. Eng., 38:275-283.

10. James, S.D., 1975, "Undervoltage Deposition of Alkali Metal at Carbon Electrodes in the LiCl-KCl Eutectic Melt", J. Electrochem. Soc., 122(7): 921-927.

11. Pfluger, P., Kunzi, H.V. and Guntherodt, H.J., 1979 "Discovery of a New Reversible Electrochromic Effect", Appl. Phys. Lett., 35(10): 771-772.

12. Weppner, W., Huggins, R.A., Wen, J.C., Baukamp, B.A., 1979, "Thermodynamic and Mass Transport Properties of LiAl", J. Electrochem. Soc., 126(12): 2258-2266.

13. Lauginie, P., Letellier, M. , Estrade, H. , Conrad, J. and Guerard, D., 1978, "Studies of Graphite Lithium Interstial Compounds by ^{7}Li N.M.R. and E.P.R.", Proc. 5th Int. Carbon Graphite Conf. Vol. II: 645-653.

14. R.R. Agarwal and J.R. Selman, "Stagewise Electrochemical Intercalation of Lithium in Graphite", submitted to J. Electrochemical Soc. (1985).

15. M.S. Dresselhaus and G. Dresselhaus, in Intercalated Layered Materials (F. Levy, Ed.), Reidel, Dordrecht (1979), p. 423.

Table I. Lithium Intercalation Compounds with Graphite

Authors (Year)	Lithium Intercalation Compounds with Graphite					Method/Remarks
	Proposed Stoichiometry	Stage	Color	a-axis A	c-axis A	
Herold[1] (1955)	C_4Li		yellow-gold			Natural graphite used. 1) electrolysis at 400°C in LiCl-KCl unsuccessful. 2) lithium vapor at 500°C gave C_4Li as an intermediate product, C_2Li_2 final product. 3) at 1000°C, yields C_2H_2.
Juza and Wehle[2] (1965)	C_6Li		bright-yellow	4.290	3.737	Reaction with lithium vapor.
	$C_{12}Li$		dark copper	4.290	7.029	
	$C_{18}Li$		steel-blue	4.280	10.440	
Bagouin, Guerard and Herold[3] (1966)	C_6Li	1	yellow	4.290	3.70	Purified Ceylon graphite with lithium vapor.
	$C_{18}Li$	2	purple	4.290	7.029	Formation of $C_{28}Li$ mentioned in summary only
	$C_{36}Li$	4	blue-black			
	$C_{72}Li$	8	black			

Table I. (Cont'd)

Authors (Year)	Lithium Intercalation Compounds with Graphite					Method/Remarks
	Proposed Stoichiometry	Stage	Color	a-axis X	c-axis A	
Secrist[4] (1967)						Spectroscopic graphite with lithium (2 to 50% at) at 700°C and 50 psig, in sealed iron capsules, gave Li_2C_2 and C or Li.
Salzano, Aronson and Ingraham[5] (1968)	C_6Li		bright-yellow	3.70		Pyrolytic graphite immersed in liquid lithium at 400°C for 2 hours.
Guerard and Herold[6] (1972)	C_6Li	1				Ceylon graphite and solid lithium compressed at 250°C and 200°C. Free Li and C_2Li not found.
	$C_{12}Li$	(1+)2				
	$C_{18}Li$	2(+3)				
	$C_{27}Li$	3(+4)				
Guerard and Herold[7] (1975)	C_6Li	1	brass-yellow	4.305± 0.001	3.706± 0.01	Natural graphite used 1) solid-liquid interaction at 400°C. 2) solid-solid compressed at 25°C. Compounds of n>1 show large variations of stoichiometry.
	$C_{12}Li$	2	steel-blue	4.288± 0.002	7.065± 0.02	
		3	dark-blue			
		4	black			

Table I. (Cont'd)

Authors (Year)	Lithium Intercalation Compounds with Graphite					Method/Remarks
	Proposed Stoichiometry	Stage	Color	a-axis A	c-axis A	
Herold, Billaud, Guerard and Lagrange[8] (1977)	C_6Li					Reaction of liquid or vapor phase sodium-lithium alloys on graphite.
Basu, Zeller, Flanders and Co-workers[9] (1979)	C_6Li-C_8K mixture					Reaction of liquid or vapor phase lithium-potassium mixture on graphite, or compression with mixture at 25°C.

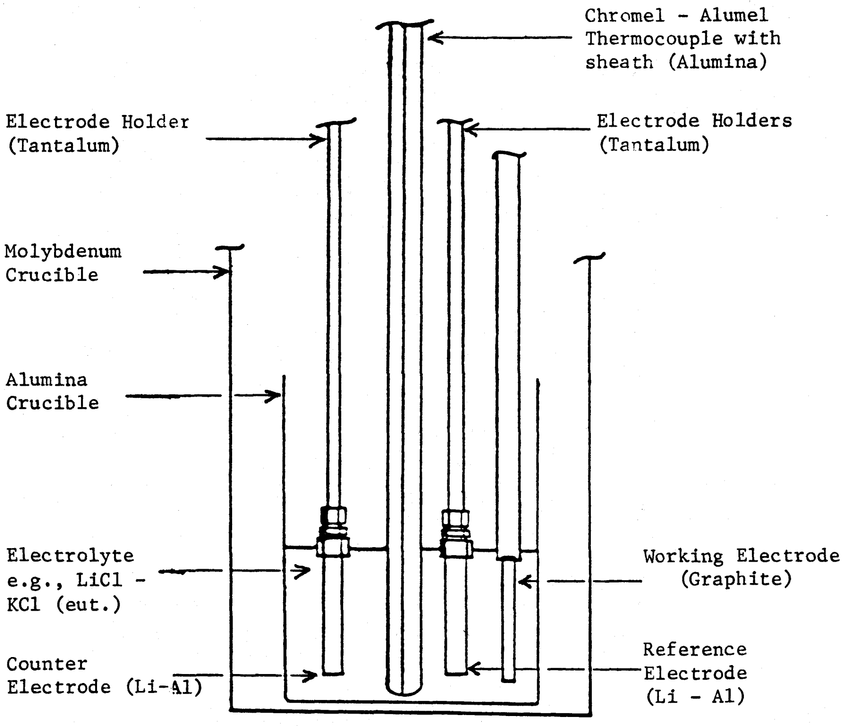

Fig. 1 Cell configuration for intercalation measurements.

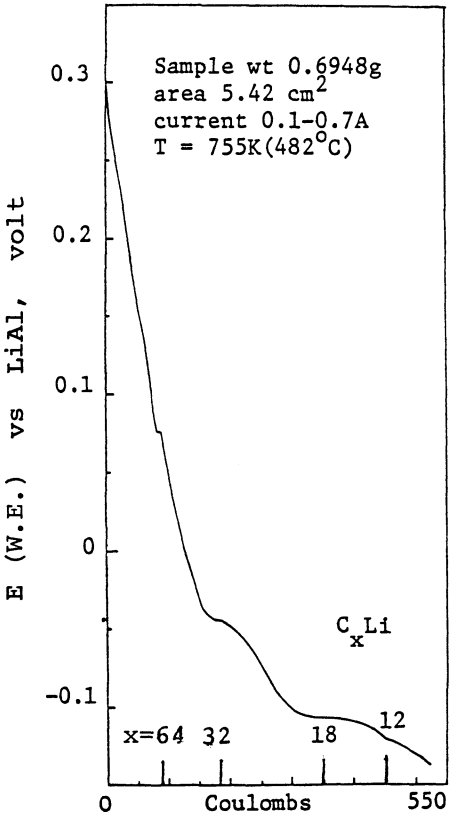

Fig. 2 Sample potentiogram of lithium intercalation in graphite at 482°C.

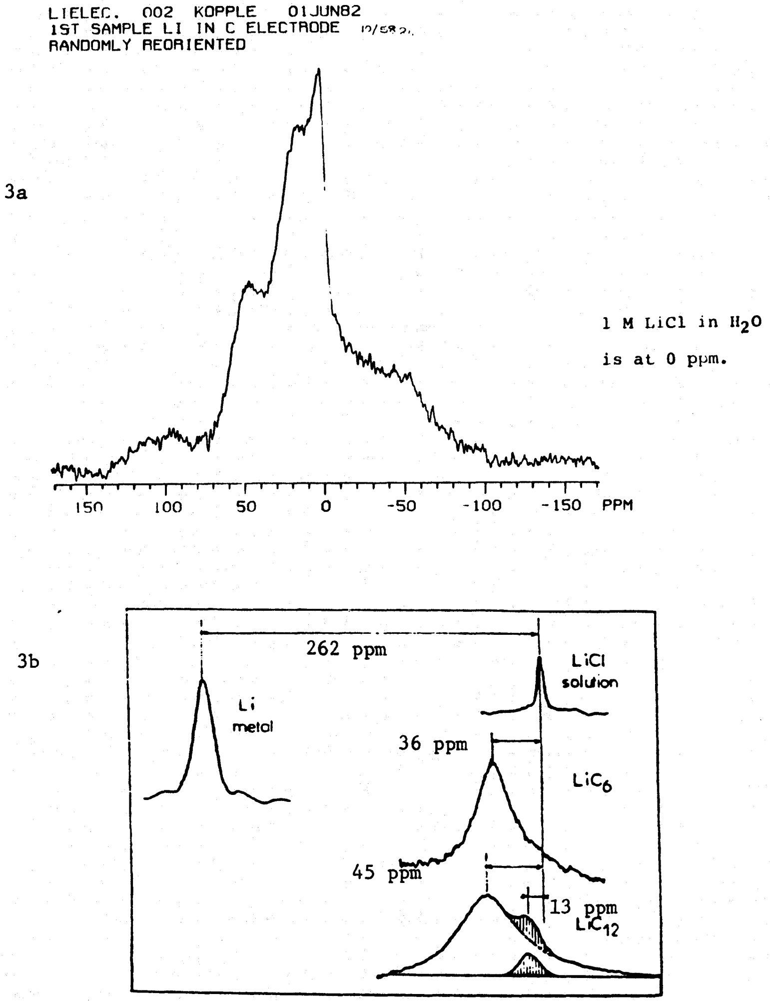

1 M LiCl in H_2O is at 0 ppm.

Fig. 3a NMR spectrum of a highly intercalated sample ($C_{7.28}$ Li)
3b Spectra reported by Lauginie, *et al* [13].

DOI: 10.1149/198601.0389PV

VAPORIZATION THERMODYNAMICS OF MIXED MELTS CONTAINING $AlCl_3$ TOGETHER WITH FERRI- AND FERROCHLORIDE

Thomas Vollheim and Hartmut Wendt
Institut für Chemische Technologie
T. H. Darmstadt, Petersenstr. 20, D 6100 Darmstadt Germany

ABSTRACT

Vapor pressures and vapor composition about $FeCl_3/AlCl_3$ and $FeCl_2/AlCl_3$ mixed melts were determined by Knudsen effusion mass spectrometry at low temperatures and low pressures and by classical vaporization-condensation at high temperatures (up to 480 °C) and high pressures (4 and 5 bars). Above $FeCl_2/AlCl_3$ melts, the species $AlCl_3$ and (mainly) Al_2Cl_6 coexist with $FeAlCl_5$. The presence of this complex enhances the effective volatility of $FeCl_2$ by several orders of magnitude (10^8). Likewise, above $FeCl_3/AlCl_3$ melts, the species $AlCl_3$, Al_2Cl_6, $FeCl_3$, Fe_2Cl_6 and the mixed complex $FeAlCl_6$ are found. Enhancement of effective $FeCl_3$ volatility by formation of the mixed complex $FeAlCl_6$ in the gas phase is only moderate. The so-called equilibrium curve for the system $AlCl_3/FeCl_3$ reveals only moderate deviation from ideal vaporization behavior for the mixtures of $AlCl_3$ with $FeCl_3$.

INTRODUCTION

In relation to aluminum production by electrolysis of $AlCl_3$ containing melts, the question of $AlCl_3$ purification and $FeCl_3$ separation from $AlCl_3$, in particular is of high importance. Hitherto this problem was solved by applying the relatively expensive hydrometallurgical Bayer-process (Fig. 1) for bauxite. Chlorination of the ore followed by distillative purification of the chloride would be a much more effective process.

EXPERIMENTAL

Knudsen effusion mass spectrometry and Knudsen effusion vapor deposition equipment as described elsewhere (1) were used for low temperature/low pressure experiments. The circulation apparatus depicted in Fig. 2 was used for determining boiling-point diagrams. Analysis of condensed vapors and of melts was performed with atomic-absorption spectrometry which is a highly sensitive technique for the determination of low iron content in purified aluminum chloride.

RESULTS

In vapors emanating from mixed melts and crystals of $AlCl_3/FeCl_2$ and $AlCl_3/FeCl_3$, mass spectrometry spectra show ion signals which are indicative of mixed complexes. Thus, in vapors above $FeCl_2/AlCl_3$ mixed crystals, i.e. $FeAlCl_4$ and $FeAlCl_5$, are likely to be generated from the mother molecule $FeAlCl_5$. The mass spectrogram of vapors of $FeCl_3/AlCl_3$ shows (i) $Al_2Cl_4^+$, $AlCl_5^+$, and $Al_2Cl_6^+$ and $Fe_2Cl_4^+$, $Fe_2Cl_5^+$, and $Fe_2Cl_6^+$ which stem from Al_2Cl_6, and Fe_2Cl_6, respectively, and (ii) the "mixed" ions $FeAlCl_3^+$, $FeAlCl_4^+$, $FeAlCl_5^+$, and $FeAlCl_6^+$ generated from $FeAlCl_6$ (Figs. 3a, 3b). (The signal $Al_3OCl_6^+$ is very likely due to the trimeric complex Al_3OCl_7 which increases the volatility of Al_2O_3 when dissolved in $AlCl_3$). A very rough estimation shows that formation of the mixed complex $FeAlCl_5$ strongly increases the effective volatility of $FeCl_2$ (which is slightly volatile) by a factor of about 10^8. However, the effective volatility of $FeCl_3$ is moderately affected by complex-formation with $AlCl_3$ ($FeAlCl_6$) in the gas phase. This indeed is confirmed by the boiling point diagrams obtained with the circulation apparatus. Figs. 4a and 4b respectively show the boiling-point diagram and the so-called equilibrium diagram for the system $AlCl_3/FeCl_3$ measured at 4 bars (0.4 MPa). The measured data are compared with data calculated for ideal mixtures (broken line). The deviation of the liquidus and solidus lines from the ideal curves are moderate across the whole composition range $0<x(AlCl_3)<1$ and azeotropes are not observed. Fig. 4c depicts the enthalpy diagram which enables one to determine mean molar and partial molar vaporization enthalpies across the composition range. The diagram shown in Fig. 5 extends close to $x(AlCl_3)=1$ in order to illustrate that the volatility of $AlCl_3$ is somewhat smaller than predicted from ideal behavior and to demonstrate that enhancing the pressure moderately reduces the separation factor. The diagrams depicted in Figs. 6a and 6b for $AlCl_3/FeCl_2$ can only be extended to $x(AlCl_3)=0.7$ because of the limited solubility of $FeCl_2$ in $AlCl_3$. The composition of the vapors of such melts allows one to clearly identify a pronounced deviation from predicted ideal behavior which is to be expected from the mass spectrometric data.

CONCLUSION

The data clearly demonstrate the existence of mixed complexes $FeAlCl_5$ and $FeAlCl_6$ in $FeCl_2/AlCl_3$, and $FeCl_3/AlCl_3$ melts and their vapors. Complex formation greatly affects the partial vaporization enthalpies of $FeCl_2$ in $AlCl_3/FeCl_2$ vapors while it influences only moderately the vaporization enthalpy of $FeCl_3$ in mixed $AlCl_3/FeCl_3$ melts.

REFERENCES

1. (1.) U. Gesenhues, H. Wendt, Z. Physik. Chem. 139 133/47 (1984)

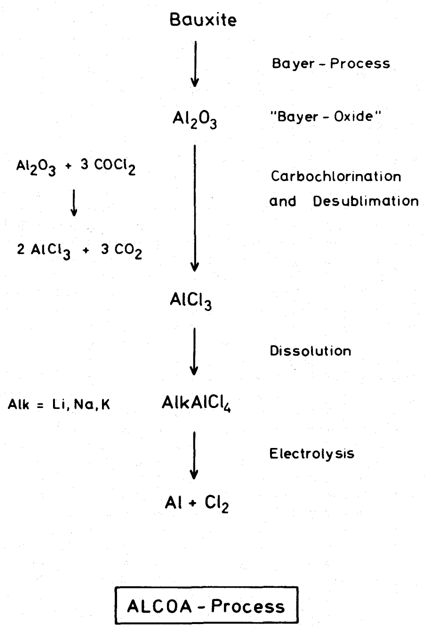

Fig. 1 Flow-sheet of the ALCOA-process

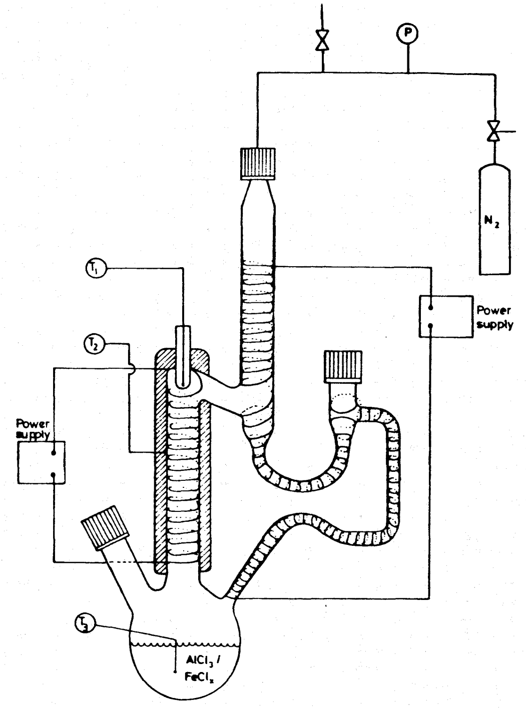

Fig. 2 Recirculation vaporizer for the determination of liquid-gas equilibria

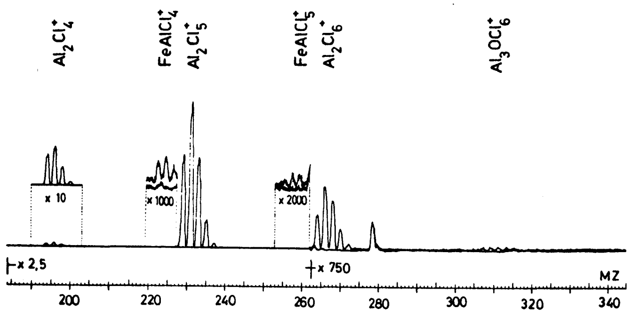

Fig. 3a Mass-spectrogram of vapours emanating from $FeCl_2/AlCl_3$ mixed crystals (T=110°C, x($FeCl_2$)= 0,8)

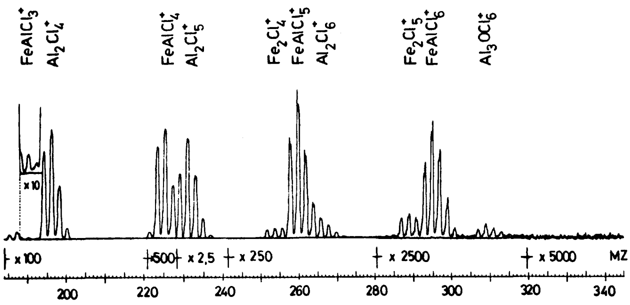

Fig. 3b Mass-spectrogram of vapours emanating from $FeCl_3/AlCl_3$ mixed crystals (T= 94°C, x($FeCl_3$)= 0,8)

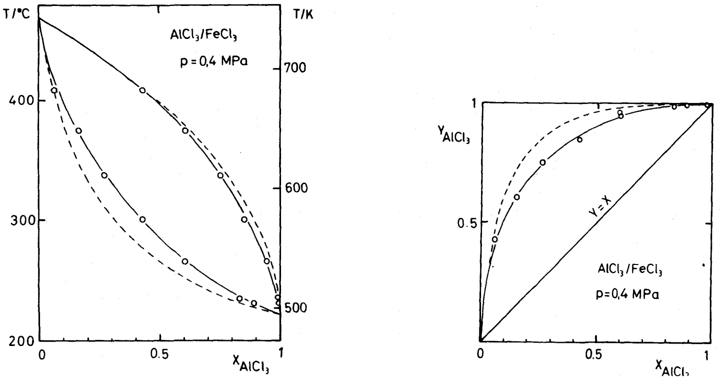

4 a

4 b

Boiling point diagram (Fig. 4a) and equilibrium diagram (Fig 4b) for the system $AlCl_3/FeCl_3$ (p= 4 bar)

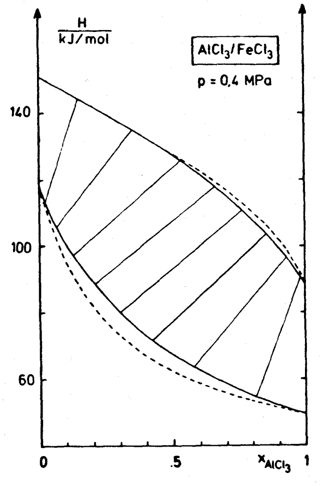

Fig. 4c

Enthalpy /Molar fraction-diagram for the system $AlCl_3/FeCl_3$ (p = 4 bar)

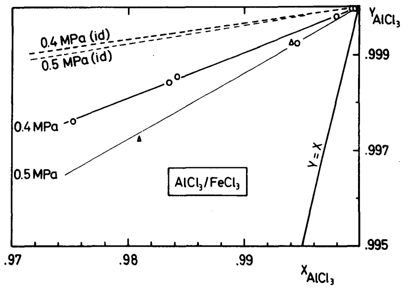

<u>Fig. 5</u> Equilibrium diagram of the system $AlCl_3/FeCl_3$ close to $x(AlCl_3) = 1$; (p = 4 bar)

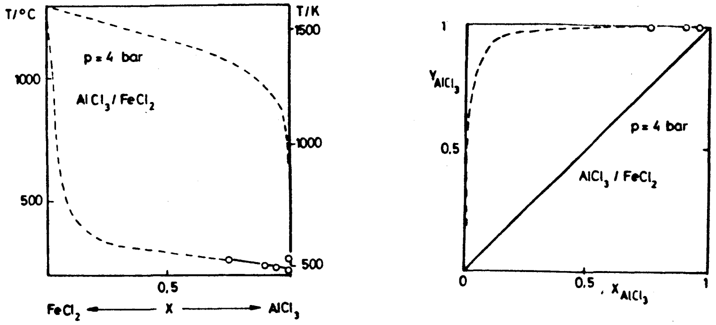

<u>6 a</u>

<u>6 b</u>

Boiling point diagram (Fig. 6a) and equilibrium diagram (Fig. 6b) for the system $FeCl_2/AlCl_3$ (p = 4 bar)

DOI: 10.1149/198601.0396PV

STUDIES OF COMPOSITE ANODES FOR THE PRODUCTION OF MAGNESIUM AND ALUMINUM

A. P. Ratvik, T. M. Laher, G. Mamantov*
Department of Chemistry, University of
Tennessee, Knoxville, TN 37996

and

S. S. Roberts, J. Y. Josefowicz, ARCO
Science and Technology Laboratory,
Chatsworth, CA 91311

ABSTRACT

The production of magnesium and aluminum in LiCl melts with 10-20 mol% NaF using MgO-C and Al_2O_3-C composite anodes has been studied. Magnesium and aluminum were obtained as spherical particles after composite anode electrolysis using nominal current densities in the range 0.2-0.7 A/cm^2. The anodic products were found to be CO_2 and CO; no halogens, HF or HCl were produced.

INTRODUCTION

Electrochemical reduction in molten salts is the method of choice for the production of light metals such as magnesium (1) and aluminum (2,3). Raw material sources for light metals are usually the metal oxides or minerals easily convertible to the oxides. However, with the exception of the cryolite based melts used in the aluminum production, molten salt systems applicable to light metal production do not dissolve oxides to a significant extent. The need to convert the oxides to suitable solutes, usually chlorides, adds to the cost of the cell feed and creates engineering problems. Handling chlorine and metal chloride vapors at high temperatures can create severe problems due to the corrosive nature of these materials.

An alternative method for introducing metal oxides into molten salts is to use composite anodes, that is, calcined blocks made from coal tar pitch mixed with metal oxide powder (4-8). With this approach, oxide solubility in the electrolyte bath is apparently not required. In the present study, the use of MgO or Al_2O_3 containing composite anodes in a LiCl bath with 10-20 mol % NaF was examined. No prior addition of the respective metal ions to be reduced was performed. The advantages of this melt mixture involved factors such as the liquidus temperature below that of Mg and Al, low density, and good conductivity (6,9). Prior studies (6) indicated that the metals are produced as small spheres. The theoretical decomposition voltages of 1.54V and 1.34V for MgO-C and Al_2O_3-C composite anodes at 700°C (10) are also well within the decomposition voltage of the melt.

EXPERIMENTAL

Apparatus for Electrochemical Measurements Electrochemical experiments were conducted in a nickel cell (Fig. 1). About 100g of the purified LiCl-NaF melt (purification procedure described below) was contained within a glassy carbon (Tokai GC-30) or graphite (high-density ATJ) crucible with a diameter of about 6.5 cm. The crucible, to which contact was made by a nickel rod, also served as the cathode and the counter electrode. Ports for electrodes and the gas inlet and outlet were located at the top of the cell body. A slight overpressure was maintained in the cell by a slow argon flow. The temperature of the melt was controlled by means of a Lindberg Crucible Furnace equipped with a PID (proportional-integral-derivative) controller. A NiCr/NiAl type K thermocouple with an ice water cold junction was used to determine the operating temperature inside the cell. Most electrolysis experiments were done at 700°C.

The electrochemical characterization of the melt and the solutes was conducted using gold, tungsten or graphite electrodes. Prior to use the tungsten electrodes were cleaned in a nearly saturated NaOH solution containing a small amount of $NaNO_2$ by inducing bubble formation when passing an AC current. In most experiments, a platinum wire served as a quasi-reference electrode. For some experiments, however, a Ni(II)/Ni reference electrode (11) in a boron nitride compartment containing 0.3 mol % NiF_2 in a 80-20 mol % LiCl-NaF melt in contact with a Ni wire was used. Unfortunately, the BN compartment could not be reused due to the flaking of BN after removal from the melt. Solute additions were made through an addition port which was purged with argon to maintain an inert atmosphere within the cell. Current-voltage curves were recorded using a Princeton Applied Research (PAR) Model 173 Potentiostat/Galvanostat coupled with a PAR 175 Universal Programmer. Controlled current electrolysis was performed with a PAR 371 Potentiostat/Galvanostat at currents above 1 A.

Composite Anodes To make the composite anodes, roughly equal amounts of coal tar pitch binder and the metal oxide were mixed and calcined at 600 to 800°C to drive off the volatiles that potentially could crack the anodes during sintering. About 70 wt% of the binder was lost in this step. After the calcined mixture was ground, about 10-20 wt% of uncalcined binder was added to improve the stickiness before the whole mass was pressed into the desired anode form at 200°C under a pressure of $1.74 \cdot 10^7$ Pa. The anode blocks were slowly heated to 1000°C and sintered for 4 to 6 hours. The final anode composition was about 80 to 85 wt% metal oxide compared to 87 wt% MgO and 86 wt% Al_2O_3 for the stoichiometric compositions necessary for forming the metal and CO_2. Electrolysis experiments were performed using current densities up to 0.7 A/cm^2 based on the geometric area. The anode-cathode distance was usually 1-2 cm.

Electrolysis Product Analysis Several techniques were employed to analyze the products and the melts after the completion of electrolysis. Samples of the melts were examined by X-ray powder diffraction. A Cu K_α radiation source filtered with a Ni filter was used together with a Phillips Debye-Scherrer Powder Camera. Electron Spectroscopy for Chemical Analysis (ESCA) measurements of solidified melt samples were performed with a Perkin-Elmer Phi 5100 ESCA System equipped with a Mg 300 W X-ray source. The off-gases during electrolysis were collected in a glass container by trapping the gases in a liquid nitrogen cooled trap. Prior to gas sampling, the Ni cell was evacuated to reduce the argon content. The gases were analyzed with an HP 5980A Mass Spectrometer.

Salt Purification The salts used for the electrolyte bath were purified prior to use. Anhydrous LiCl (Aesar 99.6%) was heated slowly under vacuum to about 400°C. After a day at 400°C, the salt was purged with HCl gas and melted. The HCl purge was maintained at least 24 hours before high purity N_2 was passed through the melt for about 1 h. The melt was then slowly recrystallized after filtration through a quartz frit. To purify reagent grade NaF (Aldrich, 99%), the salt was first heated to 500°C in a nickel crucible under vacuum. While purging with argon, the salt was melted and recrystallized. Only clear crystals were used in the melt mixtures. Anhydrous $MgCl_2$ (Apache, 98%) was purified in a similar manner as LiCl while anhydrous AlF_3 (ROC/RIC, 98.5%) was used without further purification. The purified salts were handled in a dry box with a moisture content less than 10 ppm.

RESULTS AND DISCUSSION

Electrochemical Measurements To obtain information on the electrochemical processes taking place in the LiCl-NaF melts, cyclic voltammograms were recorded before and at intermittent periods during electrolysis using composite anodes. The potential span using a gold wire electrode was found to be about 2.8 V at 700°C (Fig. 2). Cyclic voltammograms of the melts after electrolysis with MgO-C and Al_2O_3-C composite anodes are shown in Figs. 3 and 4, respectively. The new features observed on the cathodic side of the voltammograms are due to the introduction of Mg(II) and Al(III) species from the consumption of the anodes. This was confirmed using additions of $MgCl_2$ and AlF_3 to the melts. The cyclic voltammograms of Mg(II) on gold indicate alloy formation or a more complex reduction scheme than is the case with Al(III). However, in both cases, the nature of the reoxidation peaks points to a stripping mechanism.

Although oxides are likely to be introduced into the melts during electrolysis of composite anodes, no indication of an electrochemically active oxide species could be detected by cyclic voltammetry. The low oxide solubility was also verified by making MgO and Al_2O_3 pellet and powder additions to the melts; there were no changes in the cyclic voltammograms. Composite anodes immersed in the melts at 700°C for as long as two weeks did not alter the electrochemical behavior of the melts. Visual inspection showed no signs of attack of the composite anodes.

A tungsten wire electrode was found to be better suited than gold for the study of Mg(II) and Al(III) reduction. As seen in Figs. 5 and 6, a small cathodic peak about 1 V positive of the metal reduction was present in all experiments with tungsten electrodes. In anodic scans, the tungsten electrodes usually behaved in an irreproducible manner, possibly due to the chemical dissolution of tungsten. With melts containing Mg(II), a single stripping peak resulted upon potential reversal, while oxidation of reduced Al resulted in several peaks similar to what was observed for magnesium stripping from gold (Fig. 3).

An indication of the number of electrons involved in the reduction steps of Mg(II) and Al(III) was obtained from cyclic voltammograms by plotting log (i_p-i) vs. E. For insoluble products the linear portion of the plots should give a slope equal to 2.2 nF/RT (12). An n-value of 3 was obtained for Al(III) using gold, tungsten and graphite electrodes. However, in the case of Mg(II), an n-value of approximately 1 was obtained using a tungsten electrode. A well defined reduction peak of Mg(II) on graphite could not be obtained as the reduction peak shifted towards the melt limit, possibly due to some overpotential. A possible explanation of the unexpectedly low n-value for the reduction of Mg(II) in this medium is the formation of the Mg_2^{2+} ion, previously reported by Van Norman and Egan (13) and Krumpelt *et al.* (14) from solubility measurements of magnesium in its molten chloride. The Mg_2^{2+} ion is probably not very stable in LiCl-NaF melts and disproportionates to form Mg metal.

Composite Anode Electrolyses Electrolyses of composite anodes in melts were performed both above and below the melting points of the metals. At 700°C, typically a charge equivalent to 40-80% consumption of the anode was needed to produce metal spheres (up to 3 mm in diameter) collectable from the bottom of the frozen melts. Anodic current densities, based on the geometric areas, were usually around 0.3 A/cm^2 resulting in cell voltages of 3-4 V. Current densities up to 0.8 A/cm^2 could be used without any signs of anode effects. However, the evaporation of the melt, condensed at the top of the Ni container, indicated a dependence on the current density, i.e., increased salt entrainment with the off gases at higher current densities. As the composite anodes were found to be penetrated by the melts after electrolysis, the geometric areas may not compare well with the true areas of the composite anode-melt interfaces. Due to this penetration, anodic current efficiencies could not be obtained from weight loss measurements. Based on weight measurements of the produced metals, cathodic current efficiencies of up to 80% have been obtained. The metals, analyzed by atomic absorption spectroscopy, showed purities better than 99%.

Electrolysis of composite anodes below the melting points of the metals, using both nickel and tungsten cathodes, and current densities in the range 0.1 to 0.3 A/cm^2, did not result in uniform metal deposits, although the composite anodes were uniformly consumed and the metal ions were found to be present in the melts. Melts containing up to 5 wt% $MgCl_2$ or AlF_3 gave the same result, i.e., no deposit could be obtained. By using a small cylindrical nickel cathode in a boron nitride crucible totally immersed in the melt, we were able to collect some of the reduced products. Immersing the crucible containing the cathode and reduction products, into water, or in some cases, just exposing it to air, resulted in sparks typical of sodium. A flame test of the resulting basic solution produced an intense orange flame characteristic of sodium. It is apparent that sodium metal is part of the cathodic products at low Mg(II) or Al(III) concentrations in the melts.

<u>Product Analysis</u> To obtain information about the effect on the melts from composite anode electrolysis, melts used in experiments in which a charge equivalent to ~6% anode consumption as well as more than 40% anode consumption had been passed, were analyzed. X-ray powder diffraction results showed that MgO or Al_2O_3 as well as LiCl could be generally detected. The oxide content was more pronounced after electrolysis with MgO-C composite anodes. The presence of oxides was also indicated by ESCA measurements. The metal oxides may have been introduced to the melts through anode disintegration or through back reaction. The reason(s) for the larger oxide concentration seen in magnesium electrolysis compared to aluminum electrolysis, is at present not fully understood. Possibly, sodium production might play a major part in our observations, especially since melts after magnesium electrolysis gave more basic solutions when dissolved in water compared to melts after aluminum electrolysis. As sodium metal is more likely to float on top of the melt, it is also more likely to react with the CO_2 produced at the anode. Although not observed after composite anode electrolysis, addition of Na_2O to a pure melt gave some new anodic features (Fig. 7). However, in the presence of Mg(II) or Al(III) ions, the anodic features disappeared. Clearly, any Na_2O introduced to the melts would react with Mg(II) or Al(III) forming the metal oxides.

The gases produced during the electrolysis were collected for mass spectrometric analysis. CO and CO_2 were the dominant products of the anodic reaction with some traces of N_2, O_2 and H_2O believed to be introduced in the sampling procedure or at the mass spectrometer interface. No Cl_2 or F_2 could be detected in the gas samples, in contrast to the work by Egami and Akashi (4) on conventional $MgCl_2$ electrolyte bath where Cl_2 could be detected in the off gases. Typically, the CO_2/CO ratio decreased during electrolysis; its decrease is believed to be caused by the reaction with excess carbon in the composite anodes. Melts used in experiments where charge passed was equivalent to ~100% anode consumption also tended to be uniformly gray after cooling. Excess carbon seems to exist as a suspension in the melts.

<u>Electrochemical Reactions</u> Based on the present knowledge of the composite anode electrolysis in the LiCl-rich LiCl-NaF melts, it appears that the composite anodes are consumed through the direct reaction between carbon and the metal oxide forming CO_2 and the metal ion. Although CO is possibly formed in the anode reaction, the initial gaseous product in the Hall-Heroult electrolysis is found to be CO_2 (2,3). The main CO sources arise from the reaction of CO_2 with the anode and with the carbon dust floating on the melt. At the cathode, Na(I) is believed to be reduced initially until the concentration of the metal ions migrating from the anode is large enough to participate in the cathodic reduction. The sodium activity is believed to be reduced with time because of evaporation losses and intercalation with the cathode. However, the observation of the initial reduction of Na(I) from the melt, as well as its possible effect on the back reaction, strongly suggests that an initial amount of the metal ion to be reduced should be present in the electrolyte bath initially. The processes believed to take place can be summarized as:

Anodic reactions:

$$Al_2O_3 + 3/2\ C \longrightarrow 2\ Al^{3+} + 3/2\ CO_2 + 6e^-$$

or

$$MgO + 1/2\ C \longrightarrow Mg^{2+} + 1/2\ CO_2 + 2e^-$$

Cathodic processes:

$$Na^+ + e^- \rightarrow Na$$

$$M^{n+} + ne^- \rightarrow M \quad , \quad M = Mg \text{ or } Al$$

Recombination reaction:

$$nNa + M^{n+} = nNa^{+} + M$$

As indicated by the cyclic voltammograms, the reduction of Mg^{2+} might not be a straightforward 2 electron reaction but involve some intermediate steps.

Conclusions It has been shown that both magnesium and aluminum can be produced from the electrolysis of composite anodes in mainly chloride melts without prior additions of the metal ion although such additions should improve the process. The composite anode approach has some advantages with respect to the present methods of magnesium and aluminum electrolysis. Among the attractive aspects are lower operating temperature, good conductivity, elimination of the hygroscopic cell feed, and gas products that are easy to handle.

Problems to be solved before undertaking a realistic comparison between the existing electrolytic processes and the composite anode approach include that of sludge. The formation of sludge should be quantified or ideally eliminated. The sludge in the present magnesium electrolysis, containing 15-20% metal (15), is collected from the bottom of the bath while the metal is extracted at the top. Hence, the nature of the sludge problem is different for the electrolysis of composite anodes where the metal and the sludge have to be collected at the bottom of the cell. The low solubility of the metal oxide in the metal phase (1,2) should be favorable for an effective separation.

The cost of LiCl, in addition to its hygroscopicity, can present some operational problems. The electrolysis apparently requires more inert atmosphere conditions than the present Hall-Heroult electrolysis. The cost of producing larger anode quantities and probably more frequent anode changes should also be considered.

It should be noted that the electrolysis of the composite anodes is not restricted to magnesium or aluminum production; the process might be more favorable for other metals produced in smaller quantities.

ACKNOWLEDGEMENTS

The support of this work by the Atlantic Richfield Company is gratefully acknowledged. A. P. Ratvik is grateful for financial assistance from Norges Teknisk-Naturvitenskapelige Forskningsrad. We also wish to thank Robert Walton for assistance with the X-ray diffraction measurements, and Warren Haupin for making us aware of References 7 and 8.

REFERENCES

1. E. F. Emley, "Principles of Magnesium Technology," Chapters 1-3, Pergamon Press Ltd., Oxford (1966).
2. K. Grjotheim, C. Krohn, M. Malinovsky, K. Matiasovsky, and J. Thonstad, "Aluminium Electrolysis - The Chemistry of the Hall-Heroult Process," Aluminium-Verlag GmbH, Düsseldorf (1977).
3. K. Grjotheim and B. J. Welch, "Aluminium Smelter Technology," Aluminium-Verlag GmbH, Düsseldorf (1980).
4. I. Egami and K. Akashi, Rep. Inst. Ind. Sci., Univ. Tokyo, 19, 255 (1970).
5. J. C. Withers and V. Upperman, U.S. Patent 4,338,177 (1982).
6. J. Y. Josefowicz, S. S. Roberts, and L. Hayashi, unpublished work.
7. H. S.-C. Deville, "Aluminum", Sherwood Press, Cleveland, OH (1933).
8. S. Wilkening, German Patent 2,805,374 (1979).
9. A. G. Bergman, E. L. Kozachenko, and S. I. Berezina, Russ. J. Inorg. Chem., 9, 663 (1964).
10. "JANAF Thermochemical Tables," 2nd ed., NSRDS-NBS 37, U.S. Dept. of Commerce, Wash., D.C. (1971).
11. H. W. Jenkins, G. Mamantov, and D. L. Manning, J. Electrochem. Soc., 117, 183 (1970).
12. G. Mamantov, D. L. Manning, and J. M. Dale, J. Electroanal. Chem., 9, 253 (1965).
13. J. D. Van Norman and J. J. Egan, J. Phys. Chem., 67, 2460 (1963).
14. M. Krumpelt, J. Fischer, and I. Johnson, J. Phys. Chem., 72, 506 (1968).
15. B. K. Parekh and W. M. Goldberger, "A Novel Dry Process for Recovery of Magnesium Metal from Cell Sludge," p. 1507, Light Metals, TMS-AIME (1975).

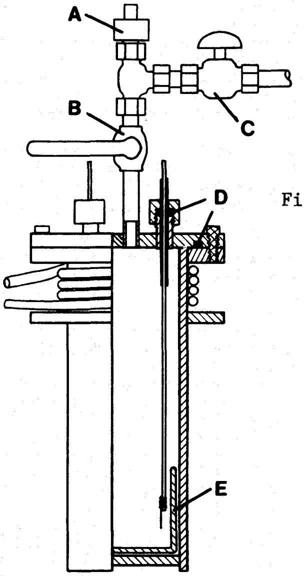

Fig. 1 - Nickel cell for electrochemical studies (not to scale). A-addition port; B-ball valve; C-needle valve; D-Viton O-ring; E-crucible.

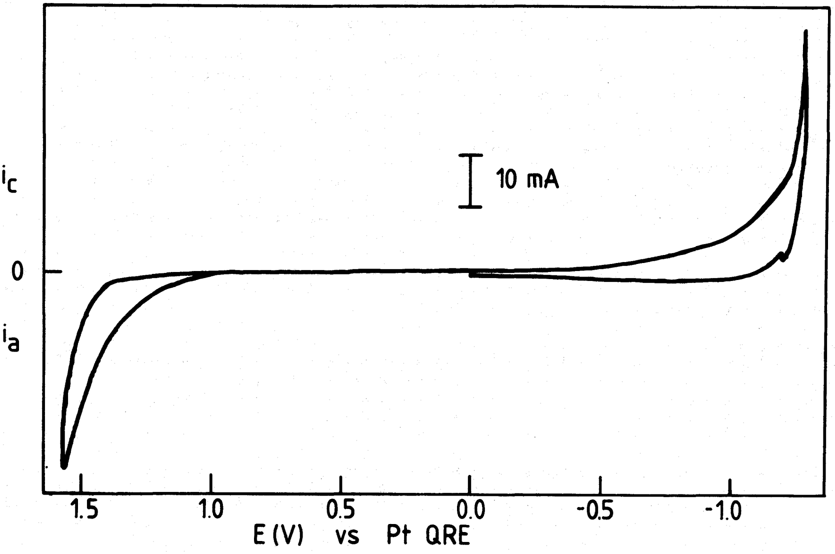

Fig. 2 - LiCl-NaF (80-20 mol%) melt background at 700°C at Au working electrode (0.06 cm^2). Scan rate 100 mV/s.

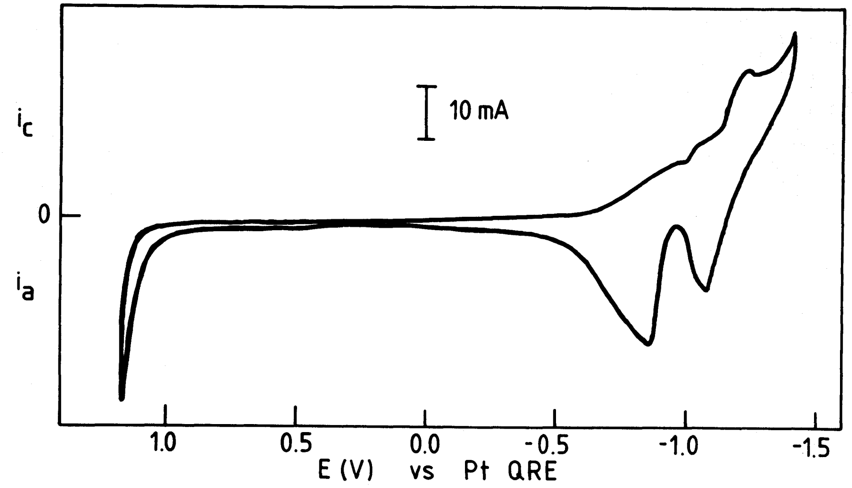

Fig. 3 - Mg(II) reduction in the LiCl-NaF melt at Au working electrode (0.09 cm^2) at 700°C. Scan rate 100 mV/s. After passage of 8000 C through MgO-C composite anode.

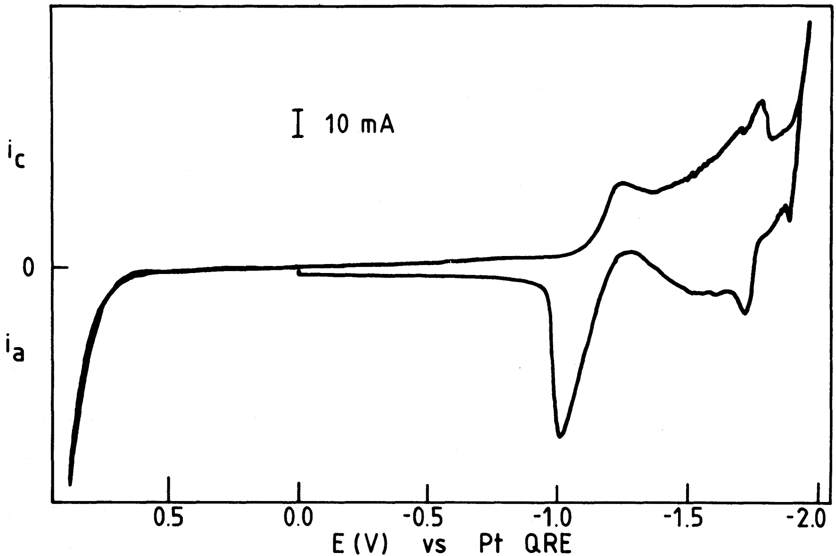

Fig. 4 - Al(III) reduction at Au working electrode (0.09 cm^2) at 700°C. Scan rate 100 mV/s. After passage of 28,000 C through Al_2O_3-C composite anode.

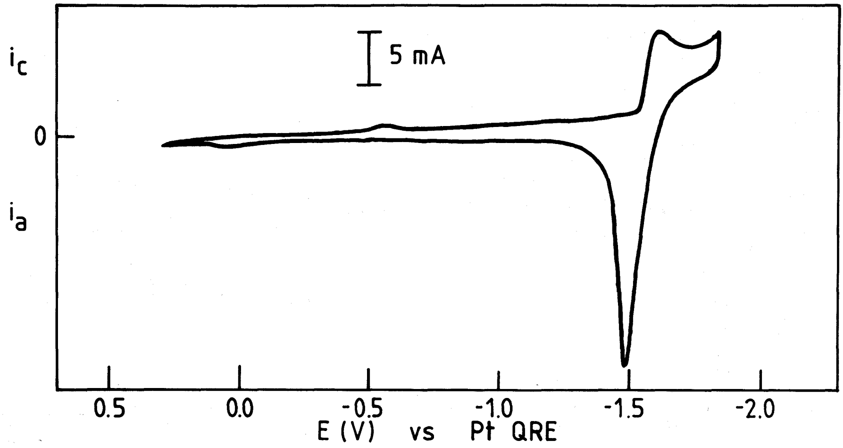

Fig. 5 - Mg(II) reduction at W working electrode (0.09 cm^2) at 700°C. Scan rate 200 mV/s. After passage of 8000 C through MgO–C composite anode.

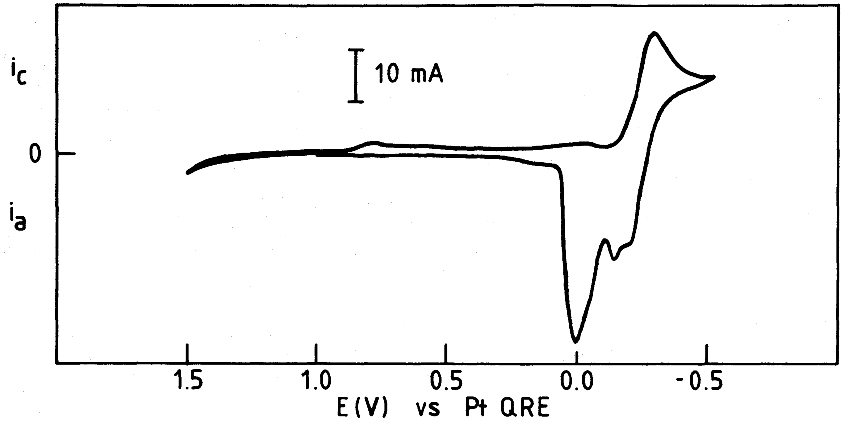

Fig. 6 - Al(III) reduction at W working electrode (0.11 cm^2) at 700°C. Scan rate 100 mV/s. After passage of 28,000 C through Al_2O_3–C composite anode.

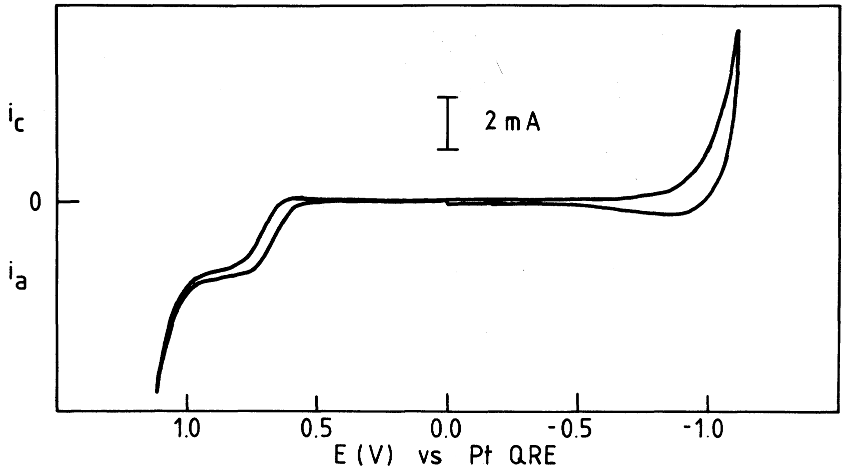

Fig. 7 - Cyclic voltammogram after additions of Na_2O (~0.5 g) to LiCl-NaF (80-20 mol %) melt at 700°C. Au working electrode (0.16 cm^2). Scan rate 50 mV/s.

DOI: 10.1149/198601.0408PV

KINETICS OF THE DEPOSITION OF ALUMINIUM FROM CHLORIDE MELTS.

Reidar Tunold, Yong Jian Zhang*
and Rolf Ødegård.

Laboratories of Industrial Electrochemistry
Norwegian Institute of Technology (NTH),
University of Trondheim, Norway
and
*Central-South Institute of Mining and
Metallurgy, Changsha,
China

ABSTRACT

The cathodic deposition of aluminium from chloride melts has been studied at 975K (702^{o}C) on tungsten and glassy carbon electrodes. The melts studied were dilute solutions of $AlCl_3$ ($5x10^{-5}$-$3.5x10^{-4}$ mol cm^{-3}) in binary equimolar mixtures of LiCl-NaCl, NaCl-KCl and NaCl-CsCl. Measurements were performed using electrochemical relaxation methods.

In the LiCl-NaCl and the NaCl-KCl systems, the reduction reaction seems to be rather fast and contributions from diffusion are mainly observed. On tungsten electrodes the response exhibits effects of alloying. The diffusion coefficient for the diffusing species calculated from results on glassy carbon electrodes, was about $4.5x10^{-5}$ cm^2s^{-1} in the LiCl-NaCl system and about $2.6x10^{-5}$ cm^2s^{-1} in the NaCl-KCl system.

In the NaCl-CsCl system a slow nucleation process is observed. The differences in the rate of phase formation in the three systems are discussed based on variations in the interfacial tension of the melt electrode interface.

INTRODUCTION

Several studies of aluminium deposition on different substrates in chloride melts have been reported. Schulze and Hoff /1/ and Rolland and Mamantov /2/ studied the deposition of aluminium from acidic chloro-aluminate melts at low temperatures. Sal'nikov et al. /3/ and Gol'dshtein et al./4/ studied the deposition of aluminium from NaCl-KCl-$AlCl_3$ melts on tantalum electrodes and liquid aluminium electrodes at 700-800°C. Ødegård et al. /5/ studied the same system also including tungsten electrodes and the binary NaCl-$AlCl_3$ melt. Gabco et al. /6/ used glassy carbon and tungsten electrodes in binaries of $AlCl_3$ with NaCl, KCl and CsCl. Some differences in the interpretation of the results from measurements in basic melts are found. The main dispute concerns whether the reaction is purely diffusion controlled or whether a mixed control involving a charge transfer reaction /5/ or a preceding dissociation of a complex is present /6/. In acidic melts, Takahashi and Komura /7/ found intermediates in the reduction of complex Al(III) species in the melt and interpreted this as a monovalent ionic aluminium species.

EXPERIMENTAL

Experiments were carried out in a gold film furnace (Trans Temp Inc.,USA). The experimental cell was a transparent quartz tube. As working electrodes (WE) glassy carbon (GC) rods, 3mm Φ, type GC-30 from Tokai Carbon Co., Ltd., Japan and tungsten (W) rods, 2 or 4 mm Φ (99.9% purity) from the Tungsten Manufacturing Co.Ltd., England, were employed. After being mirror polished, both types of electrodes were encapsulated in boron nitride with the lower circular cross section exposed to the melt. The apparent area was 0.071 cm^2 for the glassy carbon electrodes and 0.035 cm^2 or 0.125 cm^2 for the tungsten electrodes. Super-purity aluminium (99.999%) contained in a corundum tube in contact with the bulk melt served as reference electrode (RE).

In all cases the base electrolyte was an equimolar binary mixture of alkali chlorides. Aluminium chloride (Fluka, iron-free) was purified by distillation in vacuum. Sodium chloride and potassium chloride (Merck, extra pure) were purified by heating under vacuum, melting and recrystallization in argon atmosphere. Lithium chloride and caesium chloride were heated in

HCl atmosphere, at 400°C and then filtrated in vacuum.

The aluminium chloride content was determined by atomic absorption spectrophotometry from melt samples. The temperature was kept constant at 975 ∓ 1K for all runs. Argon gas flowing through the cell was purified by magnesium perchlorate to remove moisture and by titanium sponge at 600°C to remove oxygen. The cathodic reaction was studied by use of linear sweep voltammetry, chronoamperometry and chronopotentiometry. Measurements were carried out with a PAR Model 173 potentiostat/galvanostat with an IR compensation unit and a PAR model 175 Universal programmer. Slow responses were measured by an X-Y recorder whereas fast responses were recorded and stored on a Nicolet Explorer III A oscilloscope.

RESULTS AND DISCUSSION

The glassy carbon electrode

The LiCl-NaCl-$AlCl_3$ and NaCl-KCl-$AlCl_3$ systems

Cyclic voltammograms for the deposition of aluminium from NaCl-KCl-$AlCl_3$ melts on glassy carbon electrodes are shown in Fig. 1. On the glassy carbon electrode the reduction starts immediately when the potential reaches the reversible value for the aluminium electrode. A sharp cathodic peak corresponding to a very narrow anodic peak and with I_p^a much higher then I_p^c, indicate the deposition and stripping of an insoluble product. The amount of charge during the cathodic half cycle equals that during the anodic half cycle. At low sweep rates (up to 200 mV s^{-1}) the I_p^c vs. $v^{1/2}$ plots (Fig. 2) exhibits straight lines which, within the experimental error, pass through the origin. Additionally, the peak potential remains constant at -25 mV, which is almost exactly the same as the theoretical value of -24mV for a diffusion controlled deposition of an insoluble product with the discharge of three elementary charges. Both features show the diffusion controlled nature of aluminium deposition at low cds. Similar results were also obtained from voltammetric measurements in the LiCl-NaCl-$AlCl_3$ melt.

Results from chronoamperometric measurements in the NaCl-KCl-$AlCl_3$ system are shown in Fig. 3 as limiting current values from potentiostatic transient plotted vs. $t^{-1/2}$. The results show excellent agreement with the Cottrell equation confirming the diffusion controlled nature of the reaction.

In Fig. 4 galvanostatically obtained transition times are plotted as $\tau^{0.5}$ vs i^{-1} from measurements in the LiCl-NaCl-$AlCl_3$ system (curve 1 and 3 for the GC electrode). No sign of a preceeding dissociation reaction is observed.

The NaCl-CsCl-$AlCl_3$ system

Voltammograms obtained in the NaCl-CsCl-$AlCl_3$ melt on GC electrodes seem not to be very different from the corresponding diagrams in the two other melts. When plotting the results in a I_p vs $v^{1/2}$ diagram, the difference is obvious as shown in Fig. 5. The curves do not pass through the origin, a feature which points to nucleation control. Current time transients for this system from potentiostatic measurements on a GC electrode are shown in Fig. 6. For comparison one transient from the LiCl-NaCl system is also plotted in the figure. The transients exhibit features of a nucleation process but are not typical either of instantaneous or progressive nucleation The multiple maxima at higher potentials and times show similarities to transients corresponding to repeated nucleation of several mono-layers of metal /8/.

One singular current-time transient on a GC electrode is shown in Fig.7 as a plot of I_d vs $t^{-0.5}$. The reaction is obviously not controlled purely by diffusion. The same is shown in Fig. 8 which exhibits results from chronopotentiometic measurements also on GC electrodes. The two transients in Fig.8 show both an overshoot of the initial deposition potential of 60-70 mV. The straight lines in the $\tau^{0.5}/i^{-1}$ plot in Fig. 9 do not intersect the origin. All these facts are pointing to a nucleation process that plays a part in the overall control of the reaction. Also in the two systems with LiCl-NaCl and NaCl-KCl melts initial potential overshoots in the voltammetric and the chronopotentiometric measurements were observed, but only in a few cases, and always on fresh electrode surfaces (during the first deposit). These overshoots were insignificant, however, only about 5 mV in magnitude.

The tungsten electrode

Voltammograms for the tungsten electrode are shown in Figs. 10 and 11. A common feature for all the melt systems using this electrode is the cathodic depolarization due to alloy formation between aluminium and tungsten. Aluminium starts to deposit at potentials positive to the reversible potential. This leads to a broadening of the wave and a reduction of the peak cd. The anodic wave is rather different in the three systems. In the NaCl-KCl system, a single anodic wave is observed, a wave which is broadened compared with the anodic wave on GC electrodes. This broadening increases with sweep rate. In the LiCl-NaCl (Figs. 10 and 11) and the NaCl-CsCl systems two more or less distinct anodic waves, denoted by symbols b and e in Fig. 10, are observed. In the LiCl-NaCl system, wave e appears before wave b when the cathodic potential limit is moved to more negative values during cyclic sweeping. In Fig. 11, it is observed that I_p^b/I_p^e decreases with the number of sweeps during repeated cyclic sweeping before reaching a stable value. It seems that wave b in such cases is reduced from a distinct peak to a shoulder. In all the systems the anodic charge is less than the cathodic charge. All these facts show that aluminium is alloyed with tungsten. From the phase diagram of the Al-W system /9/ it is known that a liquid alloy containing 1-2 wt% W is found at 700°C on the aluminium rich side. This phase is in equilibrium with a solid peritectic δ phase and further a high melting peritectic ϵ phase with somewhat higher tungsten content. Peak b then probably corresponds to the oxidation of aluminium from the liquid alloy whereas peak e corresponds to the oxidation of aluminium in the peritectic compound. That this is a compound is likely from the very steep descent of the anodic branch, showing that the aluminium activity is rather constant during the oxidation. That the I_p^b/I_p^e ratio decreases during repeated scans can be explained as a result of an accumulation of aluminium in the tungsten lattice forming more of the above mentioned compound and that the rate of diffusion of aluminium in the lattice increases with repeated cycling. It is known that the concentration of vacancies increases in the surface layer during the socalled development of an alloy electrode /10/.

The prepeak

On the tungsten electrode, a cathodic prepeak at about +0.35 V was found, corresponding to a nearly symmetrical reversed peak only slightly moved in the anodic direction. Signs of these peaks are observed in all the systems, but are especially clear in the LiCl-NaCl system as shown in Fig. 10 and expanded in Fig.12, with the corresponding peaks denoted by d for the cathodic and c for the anodic peak. The peak potential is nearly independent of sweep rate, at sweep rates up to 500 Vs^{-1}. The ratio of the cathodic peak current to the peak current of the main peak (peak a) increases with sweep rate and is larger than unity at a sweep rate of 500 V s^{-1}. At high sweep rates the peak current seems to be directly proportional to the sweep rate. It was also observed that the anodic charge is slightly greater than the cathodic charge which means that aluminium is still retained in the tungsten after the main anodic peaks b and e.

The nature of the prewave is not clear. It has the features of an adsorption wave because of its reversibility and the linearity of the peak current with sweep rate. On the other hand however, the coulombic charge involved corresponds to about 100 monolayers of aluminium. It seems that some sort of a surface compound is formed, a compound which is retained through the main deposition-stripping cycle. One possibility is the formation of a monovalent Al species at the surface by a partial charge transfer. Such a species would probably be more stable in the LiCl-NaCl system where the activity of $AlCl_3$ is much higher than in the two other systems.

The diffusion coefficient

The diffusion coefficient has been calculated from the results of all three methods for both electrodes in all the three melt systems. The results are shown in Table 1. In case the deposition reaction is not purely diffusion controlled, the diffusion coefficient is an apparent one.

For the GC electrode in the LiCl-NaCl-$AlCl_3$ and the NaCl-KCl-$AlCl_3$ systems the results are very consistent, with values of about 4.5x10^{-5} cm^{2}s^{-1} in the former system and about 2.6x10^{-5} cm^{2}s^{-1} in the latter system.

For the tungsten electrode in the same systems, the values differ considerably. The values determined by the chronopotentiometric and the chronoamperometic methods are of the same level as for the GC electrode. The voltammetric values, however, are considerably lower. This is easily explained by the alloying of the deposit with the substrate which leads to a broadening of the cathodic wave and therefore to a reduction of the peak current. The diffusion coefficient is calculated by use of the equation for an insoluble deposit, an equation which is not strictly correct for this type of behaviour. The equation for an ideally soluble product (a redox system) should not be correct either.

Table 1 Diffusion coefficients determined by different methods in three melts on tungsten and glassy carbon electrodes.

$D \times 10^5/cm^2s^{-1}$

Method	Li-Na-Al	K-Na-Al	Cs-Na-Al
I GC	4.6∓0.4	2.5∓0.4	1,8∓0.5
W	3.0∓0.5	1.5∓0.6	1.2∓0.3
II GC	4.6∓0.4	2.5∓0.2	4.2∓0.8
W	4.4∓0.4		3.2∓0.5
III GC	4.4∓0.3	2.7∓0.3	0.4
W	4.6∓0.2	2.8∓0.2	

I - Voltammetry
II - Chronopotentiometry
III - Chronoamperometry

For the NaCl-CsCl-$AlCl_3$ system, the results differ extensively between the three measuring methods. The results from the chronopotentiometric method compare well with the two other systems whereas the potential controlled methods and especially the potentiostatic (chronoamperometric) method results in much lower values. This confirms the nucleation control in this system which leads to a low value of the current in the current-time transient before nucleation is taking part. The apparent diffusion coefficient is then too low. In the galvanostatic method, however, a constant rate is imposed on the interface setting up a corresponding diffusion gradient which leads to a more "correct" value of the transition time and the calculated diffusion coefficient.

The rate of the charge transfer reaction

The rate constant for the rate controlling step of the heterogeneous charge transfer reaction was determined by potential sweep voltammetry at high sweep rates in the LiCl-NaCl and the NaCl-KCl systems. The E_p vs log v diagram for one series in the NaCl-KCl system is shown in Fig.13. The peak voltage is constant up to about 0.1 Vs^{-1} and increases then with log v at higher rates. The relation becomes rather linear at rates higher than about 100 Vs^{-1}. The linearity in this plot indicates that the IR-compensation has been rather effective. From such plots a rate constant of about 0.2 cm s^{-1} was found in both melts.

THE MECHANISM OF THE REACTION

At the low concentrations used in these investigations the aluminium deposition reaction is mainly diffusion controlled in the stationary case. In the LiCl-NaCl and the NaCl-KCl systems the phase formation seems to be rather fast whereas clear evidence of a nucleation control was found in the NaCl-CsCl system, on glassy carbon electrodes but also on tungsten electrodes even if in this case there is an alloy formation. The reason for this is not obvious but has to be connected with the interfacial properties of the system. The most likely explanation is based on differences in interfacial energy. The lighter alkali chlorides, LiCl and NaCl have very high surface tensions 116.2 dyn cm^{-1} for LiCl and 116.1 dyn cm^{-1} for NaCl at 900°C /11/. The surface tension of KCl is 97.0 dyn cm^{-1} and for CsCl as low as 79.5 dyn cm^{-1} at 800°C. This means that the NaCl-CsCl melt wets the electrode surface far better than especially the LiCl-NaCl melt. In the LiCl-NaCl melt, the new molten Al phase is then easily formed and spreads on the electrode interface, perhaps as an extremely thin metal film due to the inferior wetting of the melt. In the CsCl-NaCl system, small nuclea are probably formed in the shape of miniature droplets with a contact angle depending on the surface forces. The apparent repeating feature of the process is difficult to explain. The maximum point does probably not correspond to the formation of a completely covered surface.

No signs of a preceeding chemical reaction, which most likely would be the dissociation of a complex, were found even in the CsCl containing system. An increase in the product $i\tau^{1/2}$ from galvanostatic measurements at low cds is probably due to the role of convection in the mass transfer at times longer than a few seconds. By moving the electrode at these conditions, an immediate effect of convection on the current was observed. This probably means that the deposition takes place directly from the prevailing $AlCl_4^-$ complex ion in these melts or that the complex dissociates quickly before the charge transfer.

The slowest step in the electrodic reaction in the LiCl-NaCl and the NaCl-KCl melt could either be the charge transfer reaction itself or the phase formation. The $(\partial E_p/\partial \log v)$ value of 160-200 mV corresponds to a theoretical value of about $RT/1F$. This points to a rate controlling step comprising two elementary charges which could not be the phase formation step. In the CsCl-NaCl system, however, phase formation is the rate controlling electrodic step.

REFERENCES

1. K. Schulze and H.Hoff, Electrochim. Acta 17, (1972) 119.

2. P. Rolland and G. Mamantov, J. Electrochem. Soc. 123, (1976) 1299,

3. V.I. Sal'nikov, V.P. Butorov, B.V. Mel'nikov, V.A. Lebedev and I.F. Nichkov, Soviet Electrochem. 10, (1974) 1142.

4. S.L. Gol'dshtein, Z.P. Raspopin and V.A. Fedorov, Soviet Electrochem. 13, (1977) 1545.

5. R.Ødegård, A.Bjørgum, A.Sterten, J.Thonstad and R.Tunold, Electrochim.Acta 21, (1982) 1595.

6. M.Gabco, P.Fellner and Z.Lubyova, Electrochim. Acta 29, (1984) 397.

7. S.Takahashi and N.Koura, Denki Kagaku 50, (1982).

8. J.A. Harrison and H.R. Thirsk in Electroanalytical Chemistry ed. A.J.Bard, Vol5 (1971) 67.

9. M.Hansen, Constitution of binary alloys, McGraw-Hill Book Company, New York (1958),

10. Z. Astakhov, Yu. Filinovsky and G.Teplitskaya, Electrokhimiya 13, (1977) 566.

11. B. Berge and J.L. Holm, Rapport til NTH's Fond 14.11.1970 Institute of Inorganic Chemistry, The Technical University of Norway, Trondheim.

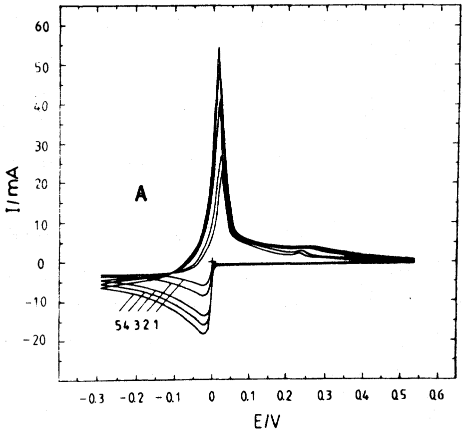

Fig.1. Cyclic voltammograms.
Sweep rate (mV s^{-1}): 1:10; 2:20; 3:50; 4:75; 5:100.
Glassy carbon WE; c_{AlCl_3}=4.72x10^{-4} mol cm^{-3},

Electrode area: 0.071 cm^2, NaCl-KCl equimolar melt.

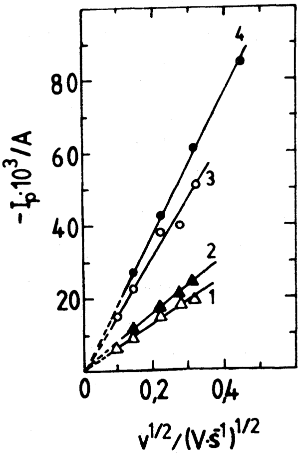

Fig.2.

The cathodic peak current vs. square root of sweep rate in NaCl-KCl equimolar melt. 1:tungsten WE; c_{AlCl_3}=4.20x10^{-4} mol cm^{-3}

2:tungsten WE; c_{AlCl_3}=4.95x10^{-4} mol cm^{-3}

3:glassy carbon WE; c_{AlCl_3}=4.07x10^{-4} mol cm^{-3}

4:glassy carbon WE; c_{AlCl_3}=4.68x10^{-4} mol cm^{-3}

electrode areas; tungsten: 0.035 cm^2, glassy carbon: 0.071 cm^2.

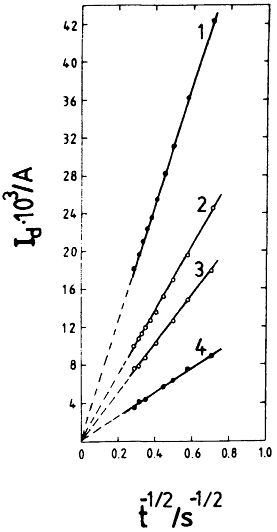

Fig. 3.

Diffusion limiting current vs. $t^{-1/2}$ from potential step measurements in NaCl-KCl equimolar melt.

1 :glassy carbon WE; $c_{AlCl_3}=5.47\times10^{-4}$ mol cm^{-3}

2 :tungsten WE; $c_{AlCl_3}=5.47\times10^{-4}$ mol cm^{-3}

3:glassy carbon WE; $c_{AlCl_3}=3.59\times10^{-4}$ mol cm^{-3}

electrode area GC: 0.071 cm^2

4:tungsten WE; $c_{AlCl_3}=4.39\times10^{-4}$ mol cm^{-3}

electrode area W: 0.035 cm^2.

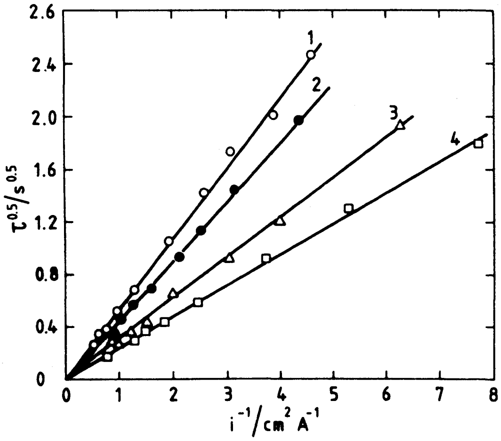

Fig. 4. Variations of $\tau^{1/2}$ with i^{-1} from chronopotentiometric measurements in NaCl-KCl equimolar melt. Glassy carbon WE; $c_{AlCl_3}=3.53\times10^{-4}$ mol cm^{-3}.

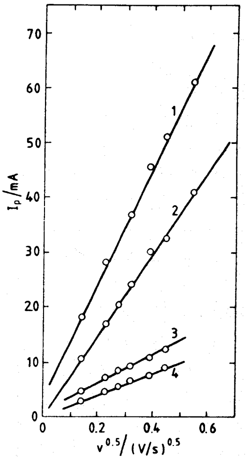

Fig.5.

The cathodic peak current vs. square root of sweep rate in NaCl-CsCl equimolar melts.

1: $c_{AlCl_3}=3.21x10^{-4}$ mol/cm^3

2: $c_{AlCl_3}=2.01x10^{-4}$ mol/cm^3

3: $c_{AlCl_3}=0.91x10^{-4}$ mol/cm^3

4: $c_{AlCl_3}=0.52x10^{-4}$ mol/cm^3

GC working electrode.

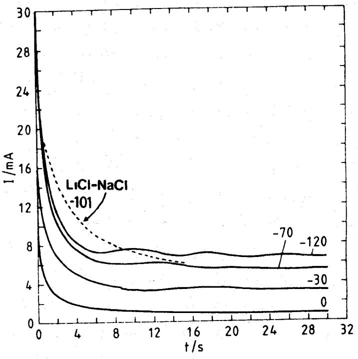

Fig.6. Current versus time from potential step measurements in NaCl-CsCl equimolar melt. $c_{AlCl_3}=2.13x10^{-4}$ mol/cm^3

The dotted line is taken from a similar experiment in LiCl-NaCl equimolar melt. The curve is corrected for a small difference in the concentration of $AlCl_3$. Glassy Carbon working electrode.

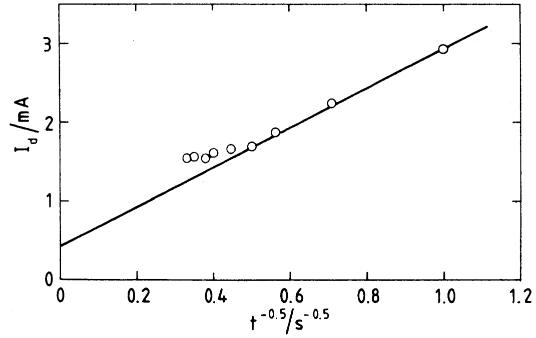

Fig.7. Diffusion limiting current vs $t^{-1/2}$ from potential step measurements in NaCl-CsCl equimolar melts.
Glassy carbon working electrode.
$c_{AlCl_3}=6.14\times10^{-5}$ mol/cm^3.

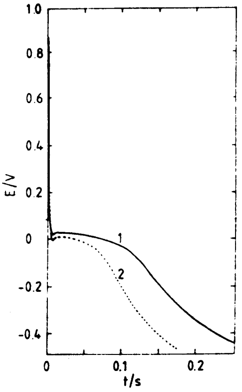

Fig.8.

Chronopotentiometric measurements in NaCl-CsCl equimolar melt.
Glassy carbon working electrode
c_{AlCl_3} = 8.67×10^{-5} mol/cm^3

i_1 = 0.4 Acm^{-2}; i_2 = 0.5 Acm^{-2}

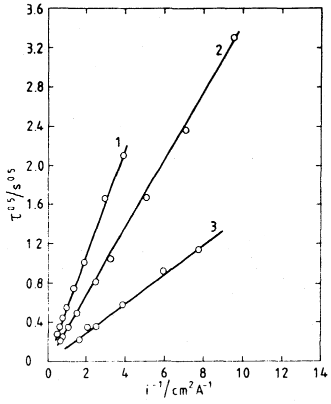

Fig.9. Variations of $i\tau^{1/2}$ with i^{-1} from chronopotentiometic measurements in NaCl-CsCl equimolar melts. Glassy carbon working electrode.
1: $c_{AlCl_3} = 1.25\text{x}10^{-4}$ mol/cm^3

2: $c_{AlCl_3} = 2.20\text{x}10^{-4}$ mol/cm^2

3: $c_{AlCl_3} = 0.87\text{x}10^{-4}$ mol/cm^3.

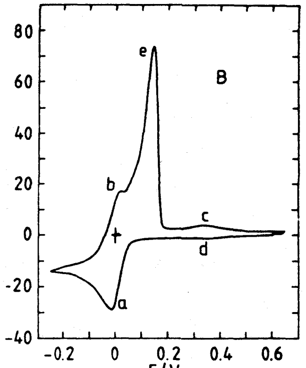

Fig.10. Cyclic voltammogram in LiCl-NaCl equimolar melt.
W Electrode, v= 20 mVs^{-1},
c_{AlCl_3}= 2.08x10^{-4} mol cm^{-3}

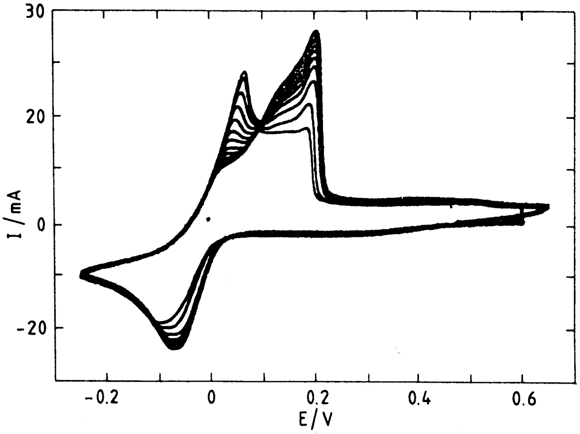

Fig. 11. Repetitive cyclic voltammograms at a tungsten electrode in LiCl-NaCl equimolar melt. v = 50 mVs^{-1}, c_{AlCl_3}=1.09x10^{-4} mol cm^{-3}.

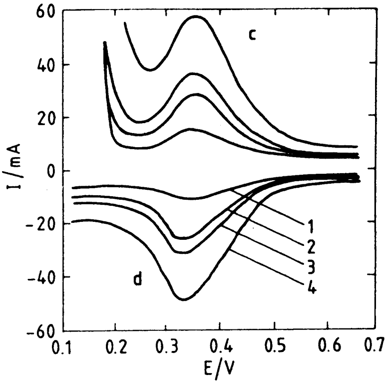

Fig. 12. Cyclic voltammograms of prewaves d and c in equimolar LiCl-NaCl melt at different sweep rates (mVs^{-1});1:200; 2:300; 3:500; 4:1000. c_{AlCl_3}=1.97x10^{-4} mol cm^{-3}.

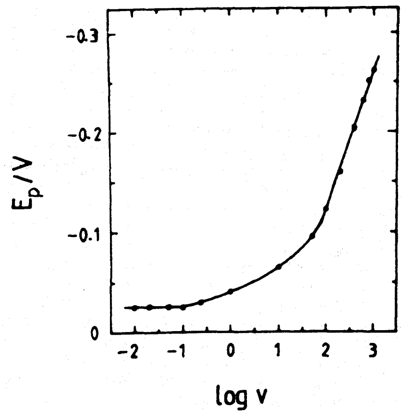

Fig. 13. Cathodic peak potential vs.log v, from voltammetric measurements in NaCl-KCl equimolar melt.
Glassy carbon WE, c_{AlCl_3}= 5.84x10^{-5} mol cm^{-3}.

DOI: 10.1149/198601.0425PV

PROCESS TECHNIQUES FOR $AlCl_3$–PRODUCTION FROM BAUXITE

Thomas Vollheim and Hartmut Wendt
Institut für Chem. Technologie, TH Darmstadt
Petersenstr. 20, D 6100 Darmstadt Germany

ABSTRACT

Direct-carbochlorination of bauxites yields product gas-containing 10 to 40 mol % $FeCl_3$ the rest being mainly $AlCl_3$ with some admixture of $TiCl_4$, $SiCl_4$ and traces of alkali chloride and alkaline earth chloride/aluminum chloride complexes. Distillative separation of this gaseous mixture under moderate pressures (3 to 5 bars) can be performed in distillation columns with only a few theoretical stages. Chlorine bound in sump-product ($FeCl_3$) is recovered by oxidation of $FeCl_3$ with oxygen in a gas-phase incinerator. Purified (99.9%) $AlCl_3$ may either be fed into chloride melt electrolysis cells or converted into Al_2O_3 to be fed into the Hall-Heroult electrolysis potline.

INTRODUCTION

The well known AlCOA-process (Fig. 1), which put for the first time Bunsen's approach of aluminum-electrowinning from chloride melts into technical practice, makes use of the hydrometallurgical Bayer process (dissolution of Al_2O_3 by caustic soda and precipitation of the Al-oxide-hydrate, "Bayerite") in order to purify aluminum oxide to a very high degree. Sublimation/desublimation as a final purification procedure precedes dissolution in the electrolyte melt.

The cost burden of the Bayer process, which causes 40% of total costs for the Hall-Heroult process, is too high for the more complex AlCOA process. Therefore, it is highly desirable to find other process-techniques for recovery of purified aluminum chlorides from bauxite and in particular, to substitute the Bayer process by cheaper process steps.

PROCESS DESCRIPTION

Bauxites contain as main "impurity," iron oxides and oxide-hydrates. It is possible in a carbochlorination step to gasify iron together with aluminum (Eqs.

1 and 2) after a thorough drying and activation procedure.

$$Fe_2O_3 + 3COCl_2 \rightarrow 2FeCl_3 + 3CO_2 \tag{1}$$

$$Al_2O_3 + 3COCl_2 \rightarrow 2AlCl_3 + 3CO_2 \tag{2}$$

Since Al_2O_3-carbochlorination is a well established industrial process (BASF), there is little doubt that carbochlorination of bauxites can be performed likewise on a technical scale.

Processing the gaseous mixtures of $AlCl_3$ and $FeCl_3$ which contain 20 to (maximally) 40 mol % of $FeCl_3$ – for instance by a sublimation/desublimation step – is relatively expensive and ineffective. Separation of $FeCl_3$ from $AlCl_3$ by distillation would be much more attractive, provided the separation factors $(AlCl_3/FeCl_3)_{vapour}/(AlCl_3/FeCl_3)_{liq}$. are high enough and the binary system $AlCl_3/FeCl_3$ does not form any azeotropes.

Because $AlCl_3$ and $FeCl_3$ both sublime and do not boil under ambient pressure, the distillation-step has to be performed under enhanced pressure, though only moderate pressures are sufficient. The final process-steps would then be electrolytic $AlCl_3$-decomposition and homogeneous gas-phase combustion of $FeCl_3$ with pure oxygen (Eq. 3) the latter step allowing total recovery of all chlorine which is bound in the sump-product.

$$2FeCl_3 + 3/2O_2 \rightarrow Fe_2O_3 + 3Cl_2 \tag{3}$$

$FeCl_3$ combustion is, too, an industrially practiced process. Therefore, the feasibility of the distillative separation of $FeCl_3$ and $AlCl_3$ is crucial for this proposed process.

Fig. 2 depicts the enthalpy-composition diagram for $FeCl_3/AlCl_3$ mixtures for a total pressure of 0.4 MPa. No azeotropes can be found on either side of the composition range of the binary mixtures so that a good separation is, in principle, possible. The separation of a $FeCl_3/AlCl_3$ mixture containing 20 mol % $FeCl_3$ into $AlCl_3$ of 99.97% purity and $FeCl_3$ of 97% purity would demand a column with 16 to 18 plates by application of a reflux ratio of 1.

CONCLUSION

Distillative $FeCl_3/AlCl_3$ separation seems to be feasible. Detailed investigations concerning material problems and total cost still have to be performed in order to find out whether this process is economically reasonable.

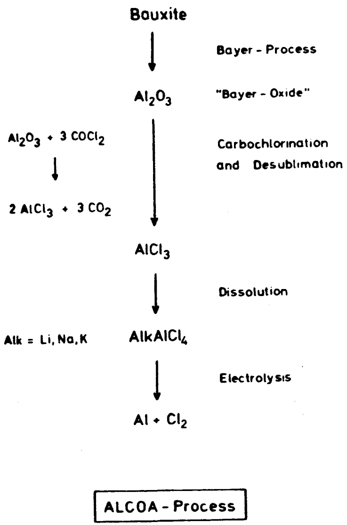

Fig. 1 Flow-sheet of the ALCOA-process.

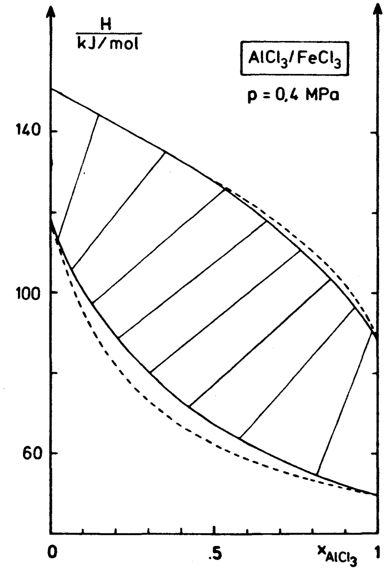

Fig. 2 Enthalpy/Molar Fraction diagram for the system $AlCl_3/FeCl_3$ (p = 4 bar)

DOI: 10.1149/198601.0428PV

THERMODYNAMIC STUDY OF IRON CORROSION IN $NaNO_3$-$NaNO_2$ MIXTURES

G.S. Picard, H.M. Lefebvre and B.L. Trémillon
Laboratoire d'Electrochimie Analytique et Appliquée, associé au CNRS
(UA 216) - Ecole Nationale Supérieure de Chimie de Paris,
11, rue P. et M. Curie - F. 75231 - Paris Cedex 05 - France.

ABSTRACT

The influence of oxoacidity on the corrosion of iron in molten sodium nitrate-nitrite mixtures has been demonstrated by means of potential-pO^{2-} diagrams.

Oxoacidobasic titrations of iron(III) have been done by means of potentiometric measurements with an yttria-stabilized zirconia membrane electrode which measures pO^{2-}. We observe the formation of three different compounds and have determined oxoacidity constants in the temperature range from 693 to 773 K. These results and the thermochemical data have been used to establish the potential-pO^{2-} diagram relative to iron. This diagram leads to the prediction that three different compounds may be formed, according to the pO^{2-}, when iron is in contact with the salt : $Fe_2O_5^{4-}$ or $Na_4Fe_2O_5$(s) in strongly basic media, FeO_2^- or $NaFeO_2$(s) in moderately basic media, Fe_2O_3(s) in acidic media. A good correlation exists between our predictions and the corrosion tests reported in the literature.

INTRODUCTION

Molten alkali nitrate-nitrite mixtures, known for their high heat capacities and their low melting points, have been used as heat transfer fluids for thermal energy storage, for temperatures ranging from 550 to 850 K. The strong oxidizing ability of the nitrate-nitrite mixtures has been one of the major concerns and many corrosion tests of iron and iron alloys have been undertaken showing the formation of oxide films (1-6). The effects of base or acid additions on corrosion have been studied, but the results are contradictory : Notoya and Midorikawa indicated that this has minimal effect on the behavior of iron (7), and El Hosary et al have observed a decrease in the corrosion rate in basic media (2).

Iron oxides and iron nitrides stabilities.

We have undertaken a primary thermodynamic study of iron corrosion using thermochemical data from the literature (8). This study has shown that two processes may be involved (i) the formation of iron oxides, which is the main subject of our study, and, in general, is the only considered one in the literature and (ii) the formation of iron nitrides, due to the presence of nitrogen monoxide which may be formed during the oxidation process.

Equilibria between iron oxides and iron nitrides have been collected in Table 1. The results have been represented by a log $P(O_2)$ - log P(NO) diagram. The stability area of the sodium nitrate-nitrite mixtures has been calculated according to the two decomposition reactions whose constants are given in Table 2,

$$NO_3^- = NO_2^- + \frac{1}{2} O_2$$

$$3NO_2^- = 2NO + NO_3^- + O^{2-}$$

for mixtures with a $N(NO_3^-)/N(NO_2^-)$ ratio varying between 10^{-2} to 10^2 and for positive pO^{2-} (= $-\log m(O^{2-})$) values. The log $P(O_2)$ - log P(NO) diagram (Fig. 1) shows the thermodynamic instability of iron nitrides in the melt. The two essential conditions of nitriding are a sufficiently low oxygen pressure which may be reached in the oxide layers, and a diffusion of nitrogen monoxide through these layers. It shows that oxidation is the first and the major process in corrosion, the nitriding process appearing only as a consequence of the oxidation one. Therefore, we have chosen to report the major portion of our study on the formation of oxides in nitrate-nitrite mixtures.

Presentation of the study.

In order to study the influence of oxoacidity on the corrosive properties of these mixtures towards iron, potential-pO^{2-} diagrams have been established. This sort of presentation has already been used to study the thermodynamic properties of several metals in molten nitrate and molten nitrite salts (11-13). In particular, the diagram relative to iron in molten sodium nitrate has been established by Arvia et al, showing the formation of the oxide Fe_2O_3 (11). But this diagram appears to be incomplete in basic media, because it does not take into account the possible formation of highly basic species of iron(III).

The acidobasic behavior of iron(III), the stable oxidation state in these salts, has therefore been studied in molten sodium nitrate-nitrite mixtures. The experimental results and the thermochemical data for the solid compounds have been used to establish the potential-pO^{2-} diagram and have allowed us to forecast the reaction that will occur according to the pO^{2-} and the oxidizing power of the medium.

TECHNICAL AND PROCEDURE

Preparation of melts and apparatus have been described in detail previously (10). For each experiment, 100 g of the sodium nitrate-nitrite mixture was introduced into a platinum crucible, in order to avoid the effect of silica as an acid. All the products used were supplied by Merck except sodium hydroxide (Prolabo). The concentration m of the dissolved species are given in the molality scale (mol kg^{-1}). The partial pressure of gases are in atmospheres.

In order to determine the different species of iron (III) that are formed in molten sodium nitrate-nitrite mixtures, we have performed oxoacidobasic titrations of sodium hydroxide by ferric nitrate in the temperature range from 693 K to 773 K. An yttria-stabilized zirconia membrane electrode (YZME) has been employed for the measurements of the pO^{2-}. The good response of YZME has been confirmed in molten alkali nitrates (14) and their mixtures with nitrites (10). A description of the constitution of the YZME has been given by Trémillon and Picard (15). The potentiometric cell set up to perform the measurements has been described elsewhere (10).

The calibration of the YZME has been done by the same techniques described by Picard et al (10), using the buffer couple $OH^-/H_2O(g)$:

$$2OH^- = H_2O\ (g) + O^{2-} \qquad K_d = \frac{P(H_2O).m\ (O^{2-})}{m(OH^-)^2}$$

$$pK_d = -4.80 + 5.48.10^3\ T^{-1} \qquad (1)$$

Under nitrogen atmosphere, the dissociation of OH^- can be considered as practically total, and the pO^{2-} is given by :

$$pO^{2-} = \log 2 - \log m(OH^-) \qquad (2)$$

and under a partial pressure of water vapor imposed above the melt, the pO^{2-} is given by :

$$pO^{2-} = pK_d + \log P(H_2O) - 2 \log m(OH^-) \qquad (3)$$

Because of the variation of pK_d with the temperature, the pO^{2-} is dependent on the temperature. So, we have preferred to use the acidity function $\log \left[P(H_2O)/m(OH^-)^2\right]$ which corresponds to the experimentally fixed quantities (water pressure and hydroxide concentration) at a temperature T. The value of pO^{2-} (at T) is related to the acidity function by relation (3).

EXPERIMENTAL RESULTS

Acidic character of iron(III) nitrate :

Kerridge and Khudhari have reported the Lux-Flood acidic behavior of ferric chloride in molten (Li-K) NO_3 eutectic (16); addition of Fe^{3+} leads to the precipitation of ferric oxide Fe_2O_3. The same result has been observed by Tridot et al in $(Na\text{-}K)NO_3$ at 513 K (17). By adding iron(III) nitrate to the melt, we have visually observed evolution of nitrogen dioxide, as well as the formation of a red precipitate. The solid was isolated and then analyzed with X-Rays. The X-Ray diffraction patterns obtained correspond to that of hematite αFe_2O_3 indicating that ferric oxide Fe_2O_3 is the stable species of iron(III) in molten sodium nitrate-nitrite mixtures with the highest acidities.

Titration curves of sodium hydroxide by iron(III) nitrate

Examples of titration curves are given in fig. 2, for various initial concentrations in sodium hydroxide and under different partial pressures of water vapor (Fig. 2-a), and for different temperatures (Fig. 2-b). In this case, the experiments being made under nitrogen atmosphere, the value of pO^{2-} are directly comparable. The residual partial pressure of water vapor being not known we cannot, in this case use the acidity-function. These curves show two equivalence points, $\alpha_1 = 0.2$ and $\alpha_2 = 0.25$, $(\alpha = m(Fe^{3+})_{ad}/m(OH^-))$ corresponding to two successive chemical reactions. Visual observation during these titrations, as well as the shape of the curves, indicates the formation of precipitates of insoluble species. X-Ray diffraction analysis at the end of the titration indicate the presence of sodium ferrate $\beta NaFeO_2$ and hematite αFe_2O_3.

INTERPRETATION OF THE TITRATION CURVES

Qualitative interpretation.

The visual observation of nitrogen dioxide evolution during each iron(III) nitrate addition suggests that the neutralisation of OH^- corresponds to a two step mechanism : (i) first, the decomposition of iron(III) nitrate into ferric oxide, as the following reaction:

$$2Fe(NO_3)_3 \rightarrow Fe_2O_3 + 6NO_2 + \frac{3}{2} O_2$$

$$NO + \frac{1}{2} O_2 \rightarrow NO_2$$

and then (ii) reaction between ferric oxide and sodium hydroxide.

The titration has to be interpreted, according to the equivalence point $\alpha_1 = 0.2$ and $\alpha_2 = 0.25$, as follow :

$$10\ OH^- + 2\ Fe^{3+} \rightarrow Fe_2O_5^{4-} + 5H_2O(g)$$

$$2\ Fe_2O_5^{4-} + Fe^{3+} \rightarrow 5\ FeO_2^-$$

The presence of $NaFeO_2$ at the end of the titration indicates that the reaction between sodium ferrate FeO_2^- and iron(III) nitrate does not take place. This confirms the decomposition of iron(III) nitrate into ferric oxide in the first step of neutralisation.

Determination of equilibrium constants :

By considering quantitative reactions, it is possible to calculate the concentration of each compound as a function of α and of the initial concentration of sodium hydroxide C_o. The balance of the concentrations is collected in table 6. The partial pressure of water vapor remains constant, being fixed above the melt. During the titration, the pO^{2-} is imposed successively by the three buffer couples $OH^-/H_2O(g)$, $Fe_2O_5^{4-}/FeO_2^-$ and $FeO_2^-/Fe_2O_3(s)$. The equilibrium constant of iron(III) species are defined from the following equilibria :

$$Fe_2O_5^{4-} = 2\ FeO_2^- + O^{2-} \qquad K_1 = \frac{m(O^{2-}).\,m(FeO_2^-)^2}{m(Fe_2O_5^{4-})}$$

$$2\ FeO_2^- = Fe_2O_3(s) + O^{2-} \qquad K_2 = \frac{m(O^{2-})}{m(FeO_2^-)^2}$$

From the balance of the concentrations, the pO^{2-} is given in the first part of the titration curve ($\alpha < 0.2$) by the following relations :

$$pO^{2-} = \log 2 - \log C_\circ\ (1 - 5\ \alpha) \text{ under nitrogen} \qquad (4)$$

$$pO^{2-} = pK_d + \log P(H_2O) - 2 \log C_\circ\ (1 - 5\ \alpha) \text{ under a partial pressure of water vapor} \qquad (5).$$

The variations of pO^{2-} versus $\log C_\circ\ (1 - 5\ \alpha)$ are presented in fig. 3. Under a nitrogen atmosphere, the partial pressure of water vapor is sufficiently low to have a total dissociation of hydroxide into O^{2-} and the variations of the pO^{2-} obey relation (5), while under a partial pressure of water vapor imposed above the melt, the theoretical slope of -2 of relation (4) is verified. Fig. 4 shows the dependence of the pO^{2-} on the partial pressure of water vapor imposed above the melt as expected by relation 4. This diagram has permitted the calculation of the maximum pressure of water vapor at which a total dissociation of sodium hydroxide leads to a given concentration into O^{2-}. The relation between this maximum pressure and the concentration of sodium hydroxide can be obtained from equating relations (4) and (5) ; we get:

$$\log P^M_{(H_2O)} = \log 2 + \log K_D + \log m(OH^-)$$

This dependence is verified on fig. 4. This diagram does not allow us to determine a residual pressure of water vapor when the melt is under dry nitrogen ; we can only say that the residual pressure is less than $10^{-3.5}$ atm.

In the second part of the curve ($0.2 < \alpha < 0.25$), the pO^{2-} is imposed by the buffer couple $FeO_2^-/Fe_2O_5^{4-}$. Visual observation as well as the shape of the curve, indicates the formation of species of low solubility. So we have considered four cases in our analysis, depending on the formation of soluble species or not. The four cases are collected in table 3. For each case, the pO^{2-} is given by :

$$pO^{2-} = k - pX \qquad pX = -\log X$$

in which k has a constant value.

The fourth case (d) can be directly studied on the titration curves because the pO^{2-} must have a constant value whatever the value of α between 0.20 and 0.25. No constant value of pO^{2-} is observed, in a sufficiently large domain to be exploited, so we have preferred to determine the values relative to the different equilibria (a), (b), (c) and (d) with the analysis of the pO^{2-} as a function of pX (Fig. 5).

The theoretical slope must have a value of -1, and this is verified for each case, in well defined domains of pO^{2-} and pX. Thus, at the beginning of the second titration reaction (high value of pX, $pO^{2-} < 4$), $Na_4Fe_2O_5$ forms a precipitate, FeO_2^- is soluble, and at the end of this second reaction (low value of pX, $pO^{2-} > 4.6$), $NaFeO_2$ forms a precipitate while $Fe_2O_5^{4-}$ is soluble. For middle values, the concentrations of the sodium ferrates, are such that they are soluble. For each case, the value of k has been determined for different temperatures (693, 743, 773 K) and this has permitted to determine the value of pK_1 and the sodium ferrate solubilities $S(NaFeO_2)$ and $S(Na_4Fe_2O_5)$. The results are given in table 4 as a function of temperature. In the range of temperature that we have studied, the solubilities of the two sodium ferrates do not vary.

$$\log\left[S(Na_4Fe_2O_5)/\text{mol kg}^{-1}\right] = 1.7 \pm 0.1$$

$$\log\left[S(NaFeO_2)/\text{mol kg}^{-1}\right] = 1.5 \pm 0.1$$

In the third part of the titration curve ($\alpha > 0.25$), the pO^{2-} is imposed by the buffer couple $FeO_2^-/Fe_2O_3(s)$ and is given by:

$$pO^{2-} = pK_2 - 2 \log m(FeO_2^-)$$

Two cases may be considered : (i) FeO_2^- soluble ($pO^{2-} = pK_2 - 2 \log \frac{C_\circ}{4}$) or (ii) precipitation of $NaFeO_2$ ($pO^{2-} = pK_2 - 2 \log S(NaFeO_2)$).

As for $\alpha > 0.25$, pO^{2-} is not dependent on $C_\circ$, the first case has to be eliminated. Using an earlier determination of the sodium ferrate solubility $S(NaFeO_2)$, a value of pK_2 is calculated. The result is given as a function of temperature in table 4.

DISCUSSION

Potential-pO^{2-} and solubility diagrams.

The potential-pO^{2-} diagram has been established on the one hand with thermochemical data from the literature (7) for electrochemical systems where only solid species (Fe, FeO, Fe_3O_4, Fe_2O_3) are involved, which has permitted the determination of $E_1^\circ - E_2^\circ$ and E_3° (see table 5), and on the other hand with our experimental results for electrochemical systems where soluble species are involved.

The different redox equilibria and their corresponding Nernst relations are given in Table 5. Standard potential values are given as a function of temperature and versus the Ag/Ag^+ ($m(Ag^+) = 0.057\ \text{mol.kg}^{-1}$ in $(Na\text{-}K)NO_3$) reference system. The superposition of the potential-pO^{2-} diagram relative to iron with the one of equimolar sodium nitrate-nitrite mixture previously determined(10) is shown in

Fig. 6. It allows us to forecast that three different compounds may be formed, according to the oxoacidity level, when iron is in contact with the melt :

- $Fe_2O_5^{4-}$ or $Na_4Fe_2O_5(s)$ in strongly basic media
- FeO_2^- or $NaFeO_2(s)$ in moderatly basic media
- $Fe_2O_3(s)$ in acidic media.

The influence of the temperature has been studied by means of potential-log $[P(H_2O).m(OH^-)^{-2}]$ diagram. As it is shown in fig. 6, the shape of the diagram is not modified in the temperature range from 693 K to 793 K so the temperature influence on corrosion is on the kinetics.

The solubility diagram of iron(III) in sodium nitrate-nitrite mixtures is presented in fig. 7. Note that the temperature has little effect on the distribution of the different species and their solubilities. The maximum of solubility (log S = -1.5) can be reached in moderatly basic media, which corresponds to a log $[P(H_2O).\ m(OH^-)^{-2}]$ value of 1.5.

Literature corrosion tests.

The formation of $\alpha Fe_2O_3(s)$ has been observed in $(Na\text{-}K)NO_3$ and in $(Na\text{-}K)NO_2$ (3,4,18,19) and corrosion tests of stainless steel and Incoloy in $(Na\text{-}K)NO_3$ without contaminants have led to the formation of sodium ferrate $NaFeO_2$ at 873 K (5).
El Hosary et al, in the study of base additions on the corrosion of mild steel in $(Na\text{-}K)\ NO_3$ between 523 and 723 K (2), have observed a decrease of the corrosion rate as the oxide iron content of the melt increased. Furthermore , the variations of the steel electrode potential with the cologarithm of hydroxide concentration have a slope with a mean value of 1.24 λ ($\lambda = \frac{2.3RT}{F}$). As the experiments were not carried out under a controlled atmosphere, the pO^{2-} is given by relation (3) and the slope of the variations of the steel electrode potential with the pO^{2-} becomes 0·62λ. If we assume that the metal functions as a metal/metal oxide electrode, then we can attribute the variations of the potential with pO^{2-} in basic media to one of the following equilibria :

$$Fe_2O_5^{4-} + 6e^- = 2\ Fe + 5\ O^{2-} \qquad (8)$$

$$FeO_2^- + 3e^- = Fe + 2\ O^{2-} \qquad (9)$$

with a slope of 0.83 λ and 0.66 λ, respectively. The value obtained by Ed Hosary et al. is around that of equilibrium (9); we can attribute the decrease of the corrosion rate to the passivating nature of the sodium ferrates.

CONCLUSION

A good correlation between our experimental potential-pO^{2-} diagram and the results on corrosion tests reported in the literature has been observed. This thermodynamic study allows a better understanding of corrosion and of the nature of the oxide layers that are formed in the nitrate-nitrite mixtures. As oxidation of iron leads to different compounds, its corrosion will be dependent on the value of the pO^{2-} which influences the kinetics of reactions involved and the passivating nature of the oxide layers.

At the present time, our research is being completed by a kinetic study, and our first results have confirmed the dependence of corrosion on the oxoacidity level.

ACKNOWLEDGMENTS

We are grateful to Electricité de France Company for its financial support of this study. We express thanks especially to P. SPITERI and J.M. GRAS, of this Company, for their interest in this work.

REFERENCES

1. A. Baraka, A.I. Abdel Rohman and A.A. El Hosary, Br. Corros. J., 11, 44 (1976).
2. A.A. El Hosary, A. Baraka and A.I. Abdel Rohman, Br. Corros. J., 11, 163 (1976).
3. "Corrosion of Fe alloys in HITEC at 823 K" SANDIA report 78-8256 (Feb. 1979).
4. "Molten nitrate salt technology", SANDIA report 80-8052 (Mar.1981).
5. "Thermal convection loop corrosion tests of 316SS and IN 800 in molten nitrate salts" SANDIA report 81-8210 (Feb. 1982).
6. H.V. Venkatasetty and D.J. Saathoff, Proc. of the Intern. Symp. on Molten Salts, the Electrochem. Soc., 1976, p. 329.
7. T. Notoya and R. Midorikawa , Denki Kagaku, 39, 930 (1971).
8. I. Barin, O. Knacke, and O. Kubaschewski, "Thermochemical Properties of Inorganic Substances", Springer Verlag, Berlin-Heildelberg - New-York (1973).
9. G. Sirotkin, Russ. J. Inorg. Chem. 4, 1180 (1959).
10. G. Picard, T. Flament and B. Trémillon, Proc. of the 1st Internat. Symp. on Molten Salt Chemistry and Technology, Y. Ito (ed), Kyoto, April 1983, p. 85 ; Proc. of the 4th Internat. Symposium on Molten Salts (Held in San Francisco, May 9-13, 1983), The Electrochemical Society, Physical Electrochemistry Division, vol. 84-2 (1984), p. 649 ; J. Electrochem. Soc., 132, 863 (1985).
11. S.L. Marchiano and A.J. Arvia, Electrochim. Acta, 17, 861 (1972); ibid, 17, 25 (1972) ; J. Appl. Electrochem., 4, 191 (1974).
12. A. Conte and S. Casadio, Ric. Sci., 36, 488 (1966).

13. A. Conte and M.D. Ingram, Electrochim. Acta., 13, 1551 (1968).

14. R.B. Flinn and K.H. Stern, J. Electroanal. Chem., 63, 191 (1975).

15. B. Trémillon and G. Picard, Proc. of the 1st Internat. Symp. on Molten Salt Chemistry and Technology, Y. Ito (Ed.), Kyoto, April 1983, p. 93

16. D.H. Kerridge and A.Y. Khudhani, J. Inorg. Nucl. Chem., 37, 1893 (1975).

17. G. Tridot, G. Nowogroki, J. Nicole, M. Wozniok and J. Canone, Compt. Rend. 270C, 204 (1970).

18. A.J. Arvia, J.J. Podesta and R.C.V. Piatti, Electrochim. Acta, 16, 1797 (1971) ; 17, 33 (1972).

19. A.Conte and S. Casadio, Ric. Sci., 36, 433 (1966).

TABLE 1 : Equilibria between iron oxides and iron nitrides and their corresponding log $P(O_2)$-log $P(NO)$ relation.

	$\log P(O_2) = A + B.\ 1000\ T^{-1} + C \log P(NO)$		
	A	B	C
$2Fe + O_2 = 2FeO$	6,44	-28.07	0
$6FeO + O_2 = 2Fe_3O_4$	13.19	-30.71	0
$4Fe_3O_4 + O_2 = 6Fe_2O_3$	14.48	-25.48	0
$4Fe + NO = Fe_4N + \frac{1}{2} O_2$	-6.44	+10.61	2
$4FeO + NO = Fe_4N + \frac{5}{2} O_2$	3.84	-20.32	2/5
$2FeO + NO = Fe_2N + \frac{3}{2} O_2$	2.20	-15.45	2/3
$Fe_3O_4 + \frac{3}{2} NO = \frac{3}{2} Fe_2N + \frac{11}{4} O_2$	4.15	-18.20	6/11
$Fe_2O_3 + NO = Fe_2N + 2O_2$	5.03	-18.81	1/2
$Fe_4N + NO = 2Fe_2N + \frac{1}{2} O_2$	-6.32	9.11	2

TABLE 2

Chemical equilibria

Equilibrium	Relation giving the limits of stability	$pK = A + B\ 1000\ T^{-1}$	
		A	B
$NO_3^- = NO_2^- + \frac{1}{2} O_2$	$\log P(O_2) = -2\ pK + 2 \log \frac{N(NO_3^-)}{N(NO_2^-)}$	-5.47	5.48
$3NO_2^- = 2NO + NO_3^- + O^{2-}$	$\log P(NO) = \frac{1}{2}(pO^{2-} - pK) + \frac{1}{2} \log \frac{N(NO_2^-)^3}{N(NO_3^-)}$	-15.8	15.75

TABLE 3 : Interpretation of the titration curves for $0.2 < \alpha < 0.25$ and criteria corresponding to each case.

Interpretation	Criteria : $pO^{2-} = k - pX$	
	k	X
(a) $2Fe_2O_5^{4-} + Fe^{3+} \rightarrow 5FeO_2^-$	pK_1	$\frac{2C_o(5\alpha - 1)^2}{(1 - 4\alpha)}$
(b) $2Fe_2O_3^{4-} + Fe^{3+} + 5Na^+ \rightarrow 5NaFeO_2(s)$	$pK_1 + 2 \log S(NaFeO_2)$	$\frac{2}{C_o(1 - 4\alpha)}$
(c) $2Na_4Fe_2O_5(s) + Fe^{3+} \rightarrow 5FeO_2^- + 8Na^+$	$pK_1 - \log S\ (Na_4Fe_2O_5)$	$Co^2(5\alpha - 1)^2$
(d) $2Na_4Fe_2O_5(s) + Fe^{3+} \rightarrow 5NaFeO_2(s) + 3Na^+$	$pK_1 + 2 \log S(NaFeO_2) - \log S(Na_4Fe_2O_5)$	1

TABLE 4 : Constant K_i of chemical equilibria.

Equilibrium	Mass action law expressions	$pK_i = A + B. 1000\ T^{-1}$	
		A	B
(1) $Fe_2O_5^{4-} = 2FeO_2^- + O^{2-}$	$K_1 = m(O^{2-}) . m(FeO_2^-)^2 . m(Fe_2O_5^{4-})^{-1}$	-3.78	+6.644
(2) $2FeO_2^- = Fe_2O_3(s) + O^{2-}$	$K_2 = m(O^{2-}) . m(FeO_2^-)^{-2}$	-8.83	+7.685

TABLE 5 : Redox equilibria and standard potentials E_i° ($\lambda = 2.3\ RT/F$)

Electrochemical system	Equilibrium potentials	$E_i^\circ = A + B . 1000\ T^{-1}$	
		A	B
$FeO + 2e^- = Fe + O^{2-}$	$E = E_1^\circ + \frac{\lambda}{2} pO^{2-}$	-2.152	0.323
$Fe_3O_4 + 2e^- = 3FeO + O^{2-}$	$E = E_2^\circ + \frac{\lambda}{2} pO^{2-}$	-2.312	0.687
$3Fe_2O_3 + 2e^- = 2Fe_3O_4 + O^{2-}$	$E = E_3^\circ + \frac{\lambda}{2} pO^{2-}$	-2.012	0.699
$Fe_2O_5^{4-} + 6e^- = 2Fe + 5O^{2-}$	$E = \frac{2E_1^\circ}{3} + \frac{2E_2^\circ}{9} + \frac{E_3^\circ}{9} - \frac{\lambda}{6} \lvert pK_1 + pK_2 \rvert + \frac{\lambda}{6} \log m(Fe_2O_5^{4-}) + \frac{5\lambda}{6} pO^{2-}$	-2.639	0.850
$Fe_2O_5^{4-} + 2e^- = 2FeO + 3O^{2-}$	$E = \frac{2E_2^\circ}{3} + \frac{E_3^\circ}{3} - \frac{\lambda}{2} \lvert pK_1 + pK_2 \rvert + \frac{\lambda}{2} \log m(Fe_2O_5^{4-}) + \frac{3\lambda}{2} pO^{2-}$	-3.583	1.880
$FeO_2^- + 3e^- = Fe + 2O^{2-}$	$E = \frac{2E_1^\circ}{3} + \frac{2E_2^\circ}{9} + \frac{E_3^\circ}{9} - \frac{\lambda}{6} pK_2 + \frac{\lambda}{3} \log m(FeO_2^-) + \frac{2\lambda}{3} pO^{2-}$	-2.427	0.735
$FeO_2^- + e^- = FeO + O^{2-}$	$E = \frac{2E_1^\circ}{3} + \frac{E_3^\circ}{3} - \frac{\lambda}{2} pK_2 + \lambda \log m(FeO_2^-) + \lambda\ pO^{2-}$	-2.967	1.560
$6FeO_2^- + 2e^- = 2Fe_3O_4 + 4O^{2-}$	$E = E_3^\circ - \frac{3\lambda}{2} pK_2 + 3\lambda \log m(FeO_2^-) + 2\lambda\ pO^{2-}$	-4.278	3.300

TABLE 6 : Balance of the concentrations during the titration of sodium hydroxide (initial concentration C_o) by ferric nitrate.

α	$m(OH^-)$	$m(Fe_2O_5^{4-})$	$m(FeO_2^-)$	$m(Fe_2O_3)$
$\alpha < 0.2$	$C_o(1 - 5\alpha)$	$\frac{1}{2} C_o\alpha$		
$0.2 < \alpha < 0.25$		$\frac{1}{2} C_o(1-4\alpha)$	$C_o(5\alpha-1)$	
$\alpha > 0.25$			$C_o/4$	$\frac{1}{8} C_o(4\alpha - 1)$

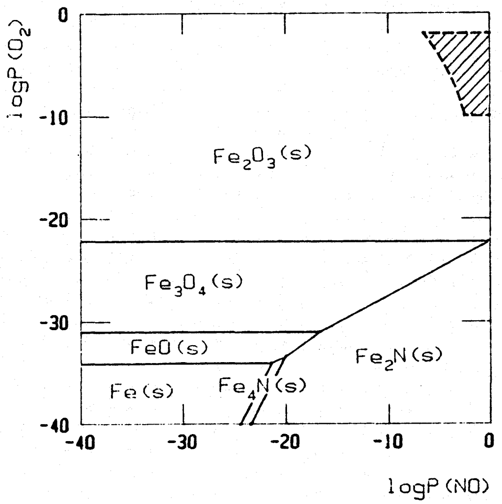

Fig. 1: log $P(O_2)$ - log P (NO) diagram for iron oxides and iron nitrides. T = 693 K.

▨ Stability area of the sodium nitrate-nitrite mixtures.

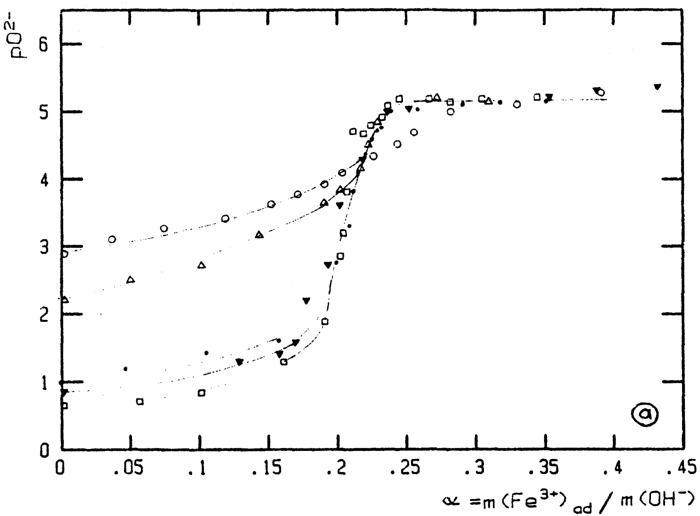

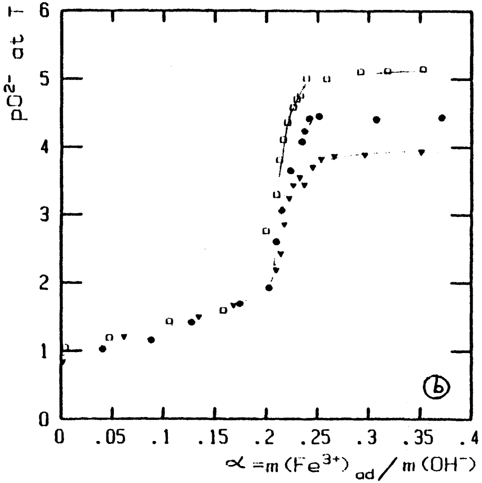

Fig. 2-a : titration of sodium hydroxide (initial concentration C_o) by iron(III) nitrate. T = 693 K.

□ NO_3^- (99) - NO_2^- (1) . C_o = 0,519 mol kg^{-1} - under N_2 atmosphere
▼ NO_3^- (99) - NO_2^- (1) . C_o = 0,266 mol kg^{-1} - under N_2 atmosphere
• NO_3^- (99) - NO_2^- (1) . C_o = 0,209 mol kg^{-1} - under N_2 atmosphere
△ NO_3^- (50) - NO_2^- (50). C_o = 0,219 mol kg^{-1} - $P(H_2O) = 10^{-2,13}$ atm
○ NO_3^- (99) - NO_2^- (1) . C_o = 0,223 mol kg^{-1} - $P(H_2O) = 10^{-1,53}$ atm.

Fig. 2-b : Titration of sodium hydroxide (initial concentration C_o) by iron(III) nitrate.

NO_3^- (99) - NO_2^- (1) . under N_2 atmosphere. ▼ T = 773K. ● T = 743K. □ T = 693K.

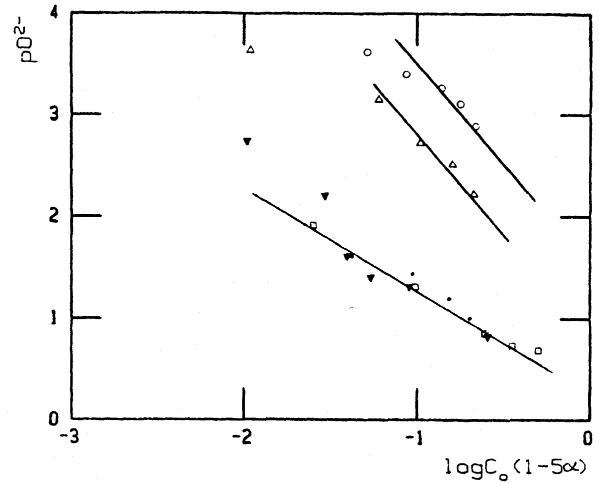

Fig. 3 : Variation of the pO^{2-} in the first part of the titration curve : $pO^{2-} = f(\log|OH^-|)$.
Same legend as fig. 2-a.

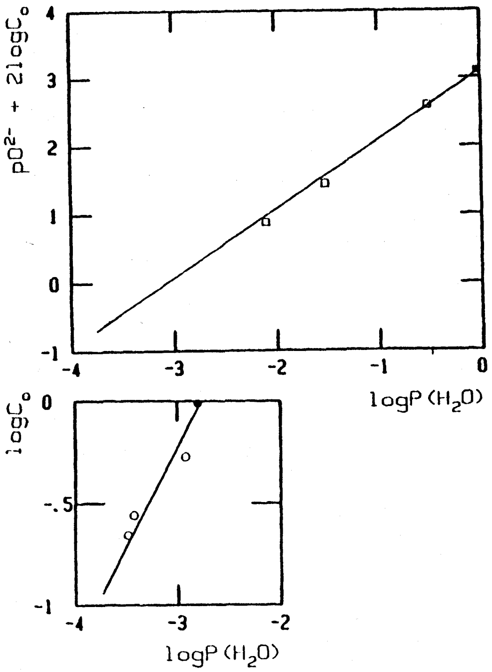

Fig. 4 : Variation of the pO^{2-} with the logarithm of the partial pressure of water vapor and determination of $P^M_{H_2O}$ as a function of $m|OH^-|$. T = 693K.

□ and o : experimental values. ■ and ● : calculated values from $p^K_d(H_2O/OH^-)$.

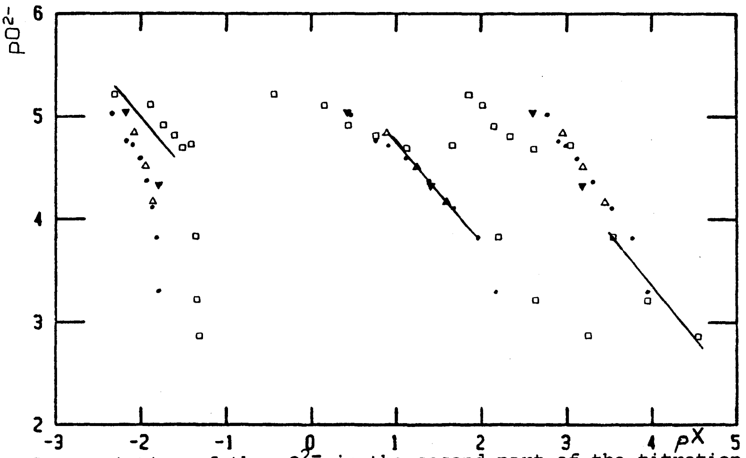

Fig. 5 : Variation of the pO^{2-} in the second part of the titration curve (0,2 < α < 0,25). $pO^{2-} = f(pX)$ (see table 3). T = 693K. Same legend as Fig. 2-a.

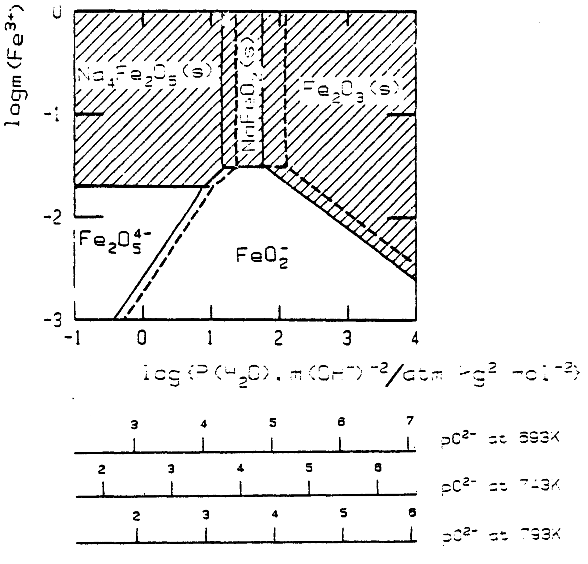

Fig. 7 : Solubility diagram of iron(III) in sodium nitrate-nitrite mixtures and corresponding pO^{2-} at T. —— T = 693K ; --- T = 793K.

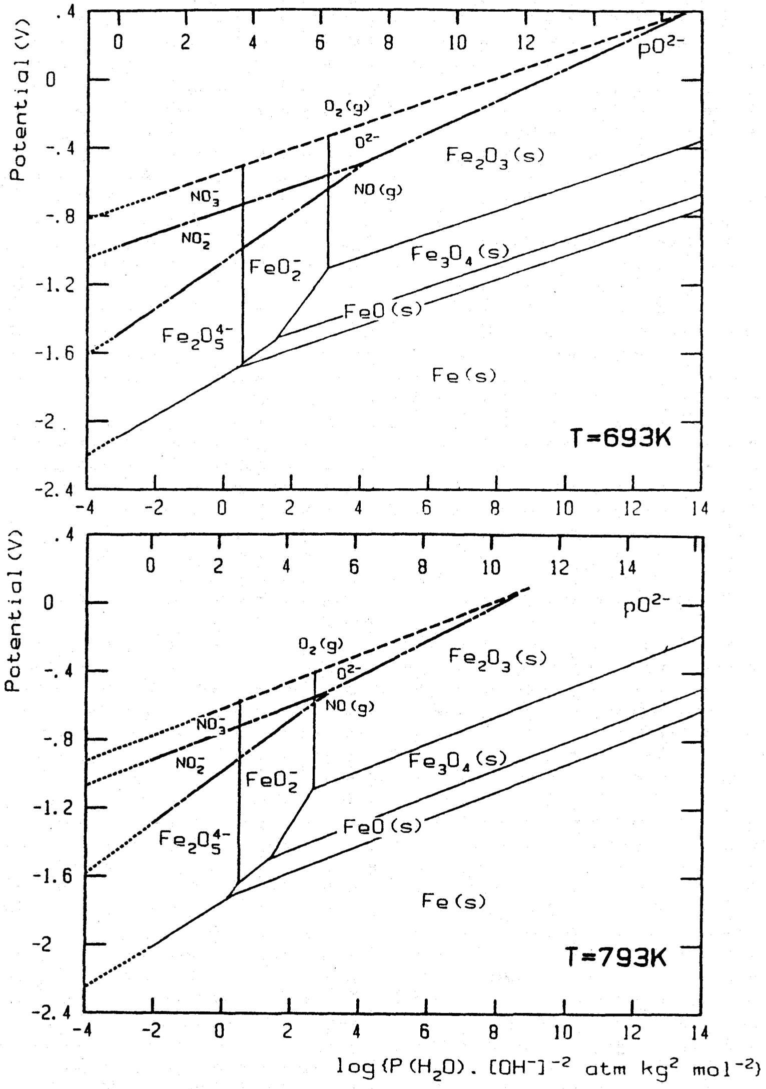

Fig. 6 : Potential-pO^{2-} and potential-log $\left[P(H_2O).m(OH^-)^{-2} \right]$ diagram :

—— iron system (m(Fe(III)) = 10^{-2} mol kg^{-1})

-- — $NaNO_3$-$NaNO_2$-NO system

----- O_2/O^{2-} system

DOI: 10.1149/198601.0445PV

STABILIZED ZIRCONIA AS AN OXIDE ION INDICATOR

Yasuhiko Ito
Department of Nuclear Engineering
Faculty of Engineering
Kyoto University
Sakyo-ku, Kyoto 606, Japan

ABSTRACT

The suitability of stabilized zirconia-air electrode as an oxide-ion concentration indicator for molten Li_2CO_3-Na_2CO_3-K_2CO_3, NaOH and LiF-KF systems has been confirmed. With this indicator, dissociation constants of the reaction : $CO_3^{2-} = CO_2(g) + O^{2-}$ in Li_2CO_3-Na_2CO_3-K_2CO_3 eutectic melts and the reaction : $2OH^- = H_2O(g) + O^{2-}$ in molten NaOH have been determined to be 4.0×10^{-8} [atm] at 873 K and 1.0×10^{-10} [atm] at 623 K, respectively. Solubility products of NiO and ThO_2 in LiF-KF eutectic melt have also been determined.

In order to explain the characteristic potential response of the stabilized zirconia-air electrode to the oxide-ion concentration, a theoretical equation has been derived taking into account the equilibria in the solid electrolyte between oxygen and three charge carriers : electron, hole and oxide-ion vacancy.

1. INTRODUCTION

Recently, it has been shown that a stabilized zirconia solid electrolyte can be used as an oxide-ion concentration indicator in molten chloride systems and with the use of this indicator, the solubility product of metal oxide[1], [2],[3], and the chemical equilibrium associated with the oxide-ion[4] have been investigated. The author and his coworkers have extended these studies to the molten Li_2CO_3-Na_2CO_3-K_2CO_3[5], NaOH[6] and LiF-KF[7] systems and found that the stabilized zirconia-air electrode is suitable for all of these three systems.

This paper describes our recent work with these electrolytes.

2. MOLTEN CARBONATE SYSTEM

Li_2CO_3-Na_2CO_3-K_2CO_3 eutectic melt has been selected as an example of a molten carbonate, and the suitability of a stabilized zirconia-air electrode for an oxide-ion indicator has been confirmed. The dissociation constant of the melt has been determined by the use of this oxide-ion indicator[5].

Experimental cells are shown in Figs 1 and 2. For an oxide-ion concentration indicating electrode, yttria or magnesia stabilized zirconia tube (Nippon Kagaku Togyo Co., Ltd.) was used. The inside of the tube was coated with a platinum powder layer which acted as an air electrode. This electrode is called the stabilized zirconia-air electrode and abbreviated as SZAE. The emf measured with this electrode was converted to the potential of the oxygen (1 atm)(Pt) / stabilized zirconia electrode, taking into account the partial pressure of oxygen in air.

Using the cell shown in Fig.1, preliminary experiments were conducted at 780 K to confirm that the zirconia electrode effectively acts as an oxide-ion indicator. Several kinds of metal electrode, for example Ni and Cu, were used as working electrodes and each electrode was polarized anodically using liquid tin as a counter electrode. The anodic polarization under constant current was measured against the SZAE. After reaching the potential (E_+) of the anodic polarization plateau, each working electrode was then cathodically polarized (again under constant current) and the potential (E_-) of the corresponding plateau was recorded. The plateau potentials thus obtained should correspond to the formation and the reduction of the metal oxides, respectively. In order to confirm this, the measured potentials were compared with the calculated values. In the case of tin oxide, liquid tin contained in the bottom of the cell was used as a working electrode, and nickel plate served as a counter electrode. In the case of Ni, for example, the anodic and cathodic potential plateau values, E_+ and E−, are both in reasonable agreement with the value (−0.88 V) calculated using the thermochemical data [8],[9] for the reaction :

$$NiO(s) = Ni(s) + \frac{1}{2}O_2 \ (1\ atm) \qquad (1)$$

As the plateau potential corresponds to the single electrode reaction :

$$NiO(s) + 2e^- = Ni(s) + O^{2-} \qquad (2)$$

, the above result suggests that the SZAE acts effectively as an oxide-ion indicator in a molten carbonate system, with the single electrode reaction :

$$\frac{1}{2}O_2 + 2e^- = O^{2-} \qquad (3)$$

Fig.3 shows a summary of the relationship between the measured plateau potentials of several metal electrodes and the corresponding potentials calculated from thermochemical data [8],[9] on the assumption that the anodic and cathodic plateau potentials (E_+, E_-) correspond to metal oxide formation and reduction, respectively.

The linear relationship with unit slope in Fig.3 provides strong evidence for the applicability of SZAE as an oxide-ion concentration indicator in a molten carbonate melt. When the partial pressure of CO_2 over the melt is varied, the potential of the SZAE should change according to the Nernst relation. This was tested by carrying out experiments in the cell shown in Fig.2. Fig.4 shows the potential of SZAE at various CO_2 partial pressures over a melt at 873 K. The measured potential is refered to the potential of the same electrode with $P_{CO_2} = 1$ atm. A linear relationship with a slope of $\frac{2.3RT}{2F}$ is observed. Since the dissociation reaction of the molten carbonate is:

$$CO_3^- (l) = CO_2 (g) + O^{2-} (l) \qquad (4)$$

the potential of the SZAE should obey the following Nernst equation (5) when it responds to the oxide-ion concentration :

$$E = E° - \frac{RT}{2F} \ln [O^{2-}] \qquad (5)$$

where E° is the standard potential, and $[O^{2-}]$ is the mole fraction of oxide. Eqn.(5) can be written as :

$$E = E°' + \frac{RT}{2F} \ln P_{CO_2} \qquad (6)$$

where

$$E°' = E° - \frac{RT}{2F} \ln K_d \qquad (7)$$

and K_d is the dissociation constant of reaction (4), and can be expressed as :

$$K_d = P_{CO_2} \cdot [O^{2-}] \qquad (8)$$

A clear Nernst relationship (eqn.(6)) can be observed in Fig.4 and thus verifies the applicability of the SZAE as an oxide ion indicator. If the concentration of the oxide-ion is known at each CO_2 partial pressure over the melt, then the dissociation constant K_d in eqn.(8) can be calculated from each experimental point in Fig.4. However it is very difficult to determine the oxide-ion concentration in equilibrium with CO_2 of a definite partial pressure. Thus, a separate experiment was conducted in order to determine the K_d value. The cell shown in Fig.2 was used. After reducing the CO_2 partial pressure inside the cell to less than 10^{-5} atm by dilution with argon gas, a measured amount of Na_2O was added to the melt. Fig.5 shows the relation between the potential of stabilized zirconia-air electrode(SZAE) and an added amount of $[O^{2-}]$(as Na_2O) at 873 K. As the initial oxide-ion concentration is negligibly small, this added amount of Na_2O can be regarded as the oxide-ion concentration in the melt. The slope of the line in Fig.5 is almost equal to the theoretical value up to an oxide-ion mole fraction of about $10^{-2.5}$. A possible cause of the deviation from the straight line at higher concentrations may be the semiconducting nature of the stabilized zirconia itself, that will be explained in detail in section 5. As the linear part of Fig. 5 corresponds to the extrapolated portion of the line in Fig.4, the relation between the potential of the SZAE and the oxide-ion concentration, or CO_2 partial pressure, can be obtained as shown in Fig.6. From these data, the relation

$$\log[O^{2-}] + \log P_{CO_2} = -7.4$$

can be deduced. That is, the dissociation constant of reaction (4) has been determined to be $10^{-7.4}$ (4.0×10^{-8}) [atm] at 873 K. This value is an order of magnitude higher than the value $10^{-8.75}$ reported by Andersen [10]. The reason for this discrepancy is not yet understood and will be investigated further.

3. MOLTEN SODIUM HYDROXIDE SYSTEM

In the molten hydroxide system, the equilibrium constant K_1 of the reaction :

$$2OH^- = H_2O(g) + O^{2-} \qquad (9)$$

is one of the basic data for the E-pO^{2-} diagram. In order to obtain the dissociation constant K_1, the following electrochemical cell :

Na / β-alumina / NaOH(Na_2O) / ZrO_2-Y_2O_3 / O_2(Air) (Pt) using the SZAE described in the preceding section was constructed and by the use of this cell, the standard chemical potential of Na_2O dissolved in molten sodium hydroxide and the equilibrium constant of the reaction $2OH^- = H_2O(g) + O^{2-}$ could be determined rigorously [6].

The experimental apparatus is shown in Fig.7. Even reagent grade NaOH contains H_2O as impurity, so the apparatus was held at 623 K for several days before the experiments in order to eliminate impurities in the gas refining systems. After preparation, known amounts of reagent grade Na_2O were added and the emf between the β-alumina/sodium electrode and the SZAE was recorded using a digital voltmeter or pen recorder with voltage follower, both of which have high input impedance. After addition of Na_2O, the emf changed slowly and reached a constant value after about 5 min. When necessary, the atmosphere in the nickel container was adjusted by flowing oxygen-free argon which was presaturated by passing through distilled water at constant temperature.

Fig.8 shows emf response to O_2 partial pressure inside the zirconia. Circles represent measured values. All points fit a Nernst slope of $\frac{2.3RT}{4F}$, which indicate the possibility of using stabilized zirconia as an oxide-ion indicating electrode at this temperature (623 K). Fig.9 shows emf response to added Na_2O. The inside of the zirconia tube is filled with air. Circles represent experimental values. The solid line indicates a theoretical Nernst slope $\frac{2.3RT}{2F}$. Experimental values at higher oxide-ion concentration deviate slightly from the theoretical line. One of the reasons for the deviation may be due to the deviation of the activity coefficient of sodium oxide from unity. Other possible reason for the deviation will be discussed later in section 5.

From the extrapolation of the solid line in Fig.9, to the point where the mole fraction of Na_2O is unity, E° is determined as 1.71 V, from which it was found that

$\mu^\circ(Na_2O)$ is -4.71×10^5 J mol^{-1} .

Fig.10 shows the emf response to H_2O partial pressure over the melt. Circles represent experimental values. The solid line has a theoretical Nernst slope of $\frac{2.3RT}{2F}$. Taking into account that the acid-base behaviour of molten hydroxide can be described by the equation :

$$2MOH = H_2O + M_2O \qquad (10)$$

, emf of the cell :

$$E = E^\circ - \left(\frac{RT}{2F}\right)\ln a(Na_2O) + \left(\frac{RT}{4F}\right)\ln P(O_2) \qquad (11)$$

can be replaced by equation (12).

$$E = E^\circ + \frac{RT}{2F}\ln P_{H_2O} + \frac{RT}{4F}\ln P_{O_2} + \text{const.} \qquad (12)$$

(concentration of OH^- is extremely large and can be regarded as constant.)

Experimental data are consistent with equation (12). The extrapolated value of emf to P_{H_2O} = 1 atm and P_{O_2} = 1 atm is 2.23 V. This value agrees well with the emf's of the corresponding cell reaction :

$$Na(l) + \frac{1}{4}O_2(g) + \frac{1}{2}H_2O(g) = NaOH(l) \qquad (13)$$

calculated by thermochemical data (8) and measured by the experiment (11).

From this agreement, it was found that the equilibrium described by eqn. (9) really exists in this system. Then, K_1 of this reaction calculated from the above experimental data is 1.0×10^{-10} atm.

4. MOLTEN FLUORIDE SYSTEM

LiF-KF eutectic melt has been selected as an example of a fluoride melt, and after the suitability of stabilized zirconia-air electrode (SZAE) for an oxide ion indicator has been confirmed, the solubility products of several kinds of oxides in this melt were determined [7],[12]. The experimental cell is shown in Fig. 11.

For an oxide ion concentration indicating electrode, yttria, calcia or magnesia stabilized zirconia tubes were used. The measured emf was converted to the potential of the oxygen(Pt) / stabilized zirconia electrode versus the Li-K/Li^+, K^+ electrode potential. The oxide-ion concentration in the melt was controlled by adding the appropriate amount of dry Na_2O (Aldrich Co. Ltd.). For the solubility product measurements of several kinds of oxides, commercial oxides (Wako Chemicals Co. Ltd.) were added into the melt, and the potential of the SZAE was measured at several values of the amount of added oxides. The other method of determining solubility products is to titrate a dissolved finite amount of metallic ion by oxide-ion, using SZAE as an oxide-ion indicator. The results obtained by both methods are in good agreement as shown later. Fig.12 shows the relation between emf of the cell :

Li-K / LiF-KF-O^{2-} / stabilized ZrO_2 / O_2 (Pt) and oxide ion concentration. Clear Nernst relation can be observed between potential and oxide ion concentration, though a deviation from the Nernst line is observed in the higher concentration range. The other point to be noted is that the potential value depends on the kind of stabilized zirconia used. This behaviour can be explained by the theoretical equation which will be described in the following section.

Fig.13 shows the relation between Pt(O_2) / stabilized zirconia / LiF-KF-O^{2-} electrode potential and the added amount of NiO. When the amount of NiO in the melt is increased gradually, the potential shift is not so clear in an early stage, due to the contaminating oxide-ion, but when the added amount of NiO exceeds the contamination level, the potential shifts towards the negative side obeying the Nernst equation. And when NiO is saturated in the melt, the potential remains constant at any amount of added NiO even in the region where the Nernst relation would otherwise hold. From the figure of the potential shift obtained by the addition of NiO, K_{sp} values can be calculated, though by a calculation, initial oxide-ion concentration due to the contamination should be carefully taken into account. K_{sp} values thus obtained is 1.3×10^{-6} at 823 K.

Fig.14 shows the relation between Pt(O_2)/stabilized zirconia/LiF-KF-O^{2-} electrode potential and the added amount of ThO_2. From the figure of the potential shift obtained by the addition of ThO_2, K_{sp} can be estimated as 1.3×10^{-9} at 823 K.

Fig.15 shows the relation between Pt(O_2)/stabilized zirconia/LiF-KF-O^{2-} electrode potential and the added amount of Na_2O when ThF_4 is dissolved in the melt at a finite concentration. From this titration curve, the K_{sp} value can be estimated by curve fitting, to be $K_{sp} = 1.1 \times 10^{-9}$ at 823 K. The two values are in fairly good agreement and hence the results are concluded to be reliable.

5. THEORETICAL RELATION BETWEEN POTENTIAL OF SZAE AND OXIDE ION CONCENTRATION

As stated above, a clear Nernst relation can be observed in all molten salt systems so far examined. However, in every case, a deviation from the Nernst line is observed in the higher concentration range. The other point to be noted is that the potential value depends on the kind of the stabilized zirconia used.

In order to explain such characteristics, a theoretical relation between the potential of SZAE and oxide ion concentration was deduced as in the following [13] : In the stabilized zirconia, there are three equilibria among oxygen and three charge carriers : electron, hole and oxide ion vacancy. Thus,

$$O_O = O^{2-} + V_O^{2\bullet} \qquad (14)$$

$$O_O = \frac{1}{2}O_2 + V_O^{2\bullet} + 2e' \qquad (15)$$

$$\frac{1}{2}O_2 + V_O^{2\bullet} = O_O + 2e^{\bullet} \qquad (16)$$

Taking into consideration the above three equilibria, a relation between potential and oxide-ion concentration can be derived as follows : Potential difference between the position (i) and (j) can be expressed as :

$$E_{ij} = \phi(i) - \phi(j) = \frac{RT}{F} \sum_{\ell} \int_{a\ell(i)}^{a\ell(j)} \frac{t_\ell}{Z_\ell} \, d\ln a_\ell \qquad (17)$$

, where

$$t_\ell = \frac{k_\ell a_\ell}{k_{V_O^{2\bullet}} \, a_{V_O^{2\bullet}} + k_{e'} a_{e'} + k_{e^\bullet} a_{e^\bullet}} \qquad (18)$$

and

$$k_\ell = Z_\ell U_\ell / \gamma\ell \qquad (19)$$

Integrating equation (17) with appropriate boundary conditions based on the calculation model shown in Fig.16, equation (20) can be derived. Details will appear in the separate paper (13).

$$E = E^\circ - \frac{RT}{2F}\ln[O^{2-}] + \frac{RT}{2F}\ln(1 + K[O^{2-}]) \qquad (20)$$

(K : constant, but depends on the characteristics of stabilized zirconia)

According to eqn.(20), the Nernst equation holds when $[O^{2-}]$ is much smaller than $\frac{1}{K}$, and when $[O^{2-}]$ is increased, positive deviation from the Nernst line will be observed. Hence, this eqn.(20) explains well the behaviour of SZAE described above.

6. CONCLUSION

The suitability of the stabilized zirconia-air electrode (SZAE) for the oxide-ion concentration indicator in molten Li_2CO_3-Na_2CO_3-K_2CO_3, NaOH and LiF-KF systems have been confirmed. And as examples of the application of this indicator, dissociation constants of the reaction :

$$CO_3^{2-}(\ell) = CO_2(g) + O^{2-}(\ell)$$

and

$$2OH^- = H_2O(g) + O^{2}(\ell)$$

have been determined to be 4.0×10^{-8} [atm] at 873 K and 1.0×10^{-10} [atm] at 623 K, respectively.

Solubility products of NiO and ThO_2 in LiF-KF eutectic melt have also been determined.

Finally, in order to explain the characteristic potential response of the stabilized zirconia-air electrode to the oxide-ion concentration, a theoretical relation between potential of stabilized zirconia-air electrode and oxide-ion concentration has been derived taking into account the equilibria among oxygen and three charge carries : electron, hole, and oxide ion vacancy.

ACKNOWLEDGEMENT

The author would like to express his gratitude to the Ministry of Education, Science and Culture for the Grant-in-Aid for Scientific Research, and also would like to thank Nippon Kagaku Togyo Co. Ltd.(C.C) for their courtesy in supplying stabilized zirconia tubes.

REFERENCES

[1] R. Combes, M.N.Levelut, B. Tremillon, Electrochim. Acta, 23, 1291 (1978).
[2] R. Combes, F.de Andrade, A.de Barros, H. Ferreira, ibid, 25, 371 (1980).
[3] K.H. Stern, J. Electrochem. Soc., 127, 2375 (1980).
[4] M.L. Deanhardt, K.H. Stern, ibid, 128, 2577 (1981).
[5] Y. Ito, K. Tsuru, J. Oishi, Y. Miyazaki, T. Kodama, J. Powersources, in press.
[6] H. Hayashi, S. Yoshizawa, Y. Ito, J. Electroanal. Chem. 124, 229 (1981).
[7] Y. Ito, H. Hayashi, Y. Itoh, S. Yoshizawa, Bull. Chem. Soc. Japan, in press.
[8] I. Barin and O. Knacke ed., "Thermochemical Properties of Inorganic Substances", Springer Verlag, Berlin (1973).
[9] I. Barin, O. Knacke and O. Kubaschewski ed., "Thermochemical Properties of Inorganic Substances, Supplement', Springer Verlag (1977).
[10] B.K. Andersen, "Thermodynamic Properties of Molten Alkali Carbonates", Doctoral thesis, Tech. Univ. of Denmark, Lyngby Denmark (1975).
[11] Y. Ito, H. Kaiya, S. Yoshizawa, Proc. Third World Hydrogen Energy Conf., p.221 (1980).
[12] K. Ema, Y. Ito, T. Nakai, H. Yabe, J. Oishi, to be published.
[13] Y. Ito, H. Yabe, K. Ema, T. Nakai, J. Oishi, to be published.

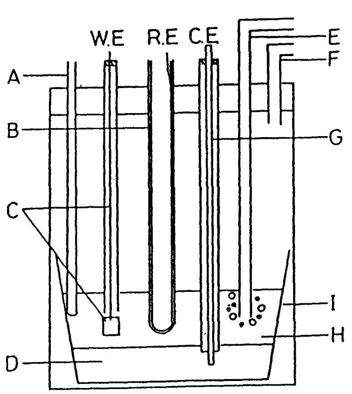

Fig.1 Experimental cell

A : Chromel-Alumel thermocouple
B : Stabilized zirconia
C : Nickel
D : Tin
E : Gas inlet
F : Gas outlet
G : Molybdenum
H : Molten carbonate
I : Alumina crucible

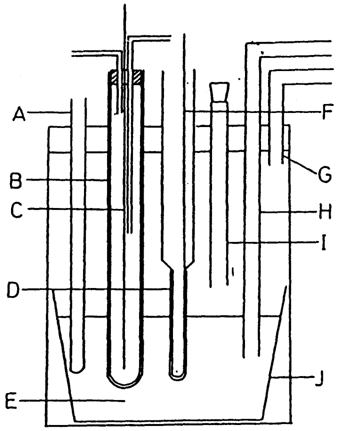

Fig.2 Experimental cell

A : Chromel-Alumel thermocouple
B : Mullite tube
C : Au wire
D : Stabilized zirconia
E : Molten carbonate
F : Pt wire
G : Gas outlet
H : Gas inlet
I : Sodium oxide inlet
J : Alumina crucible

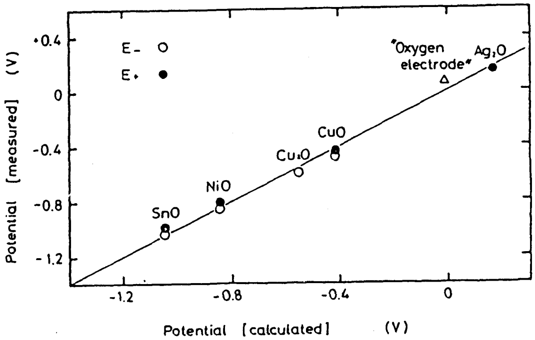

Fig.3 Relation between measured and calculated potentials of stabilized zirconia-air electrode (at 780 K)

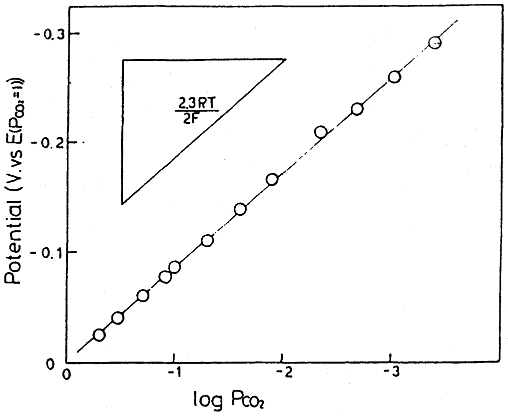

Fig.4 Potential of stabilized zirconia-air electrode at various CO_2 partial pressures over the melt (at 873 K)

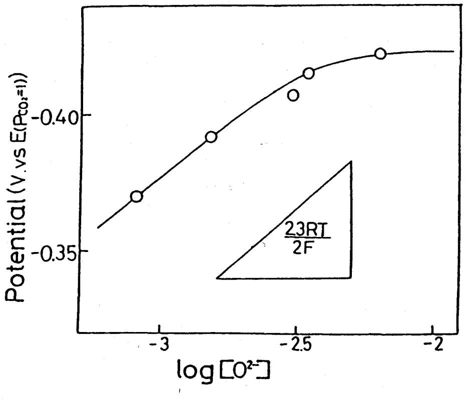

Fig.5 Relation between potential of stabilized zirconia-air electrode and the added amount of Na_2O ($[O^{2-}]$)(at 873 K)

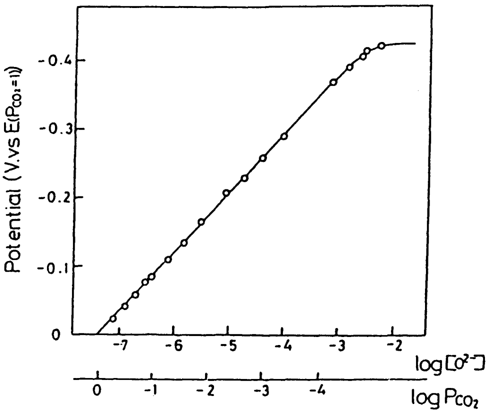

Fig.6 Relation between potential of stabilized zirconia-air electrode and the oxide concentrations and/or CO_2 partial pressure over the carbonate melt (at 873 K)

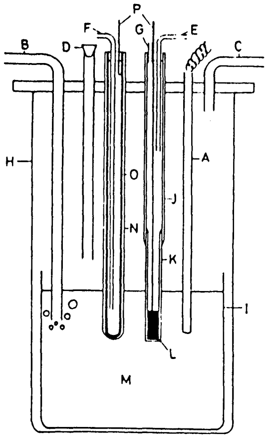

A : Thermocouple
B : Gas bubbler (H_2O, Ar)
C : Gas outlet
D : Na_2O inlet
E : Ar gas inlet
F : O_2 or air inlet (outlet)
G : Ar gas outlet
H : Nickel container
I : Alumina crucible
J : Alumina tube
K : β-alumina
L : Molten sodium
M : Molten NaOH
N : Zirconia tube
O : Pt powder
P : Lead wire
(stainless steel or molybdenum)

Fig.7 Experimental cell

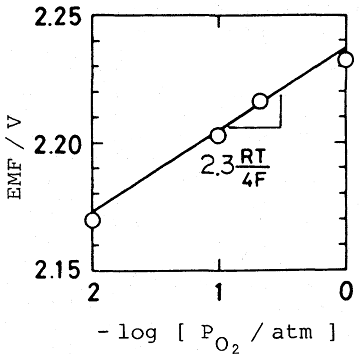

Fig.8 Emf response to O_2 partial pressure inside the zirconia (at 623 K)

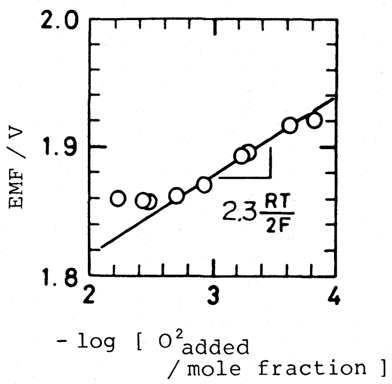

Fig.9 Emf response to added Na_2O (at 623 K)

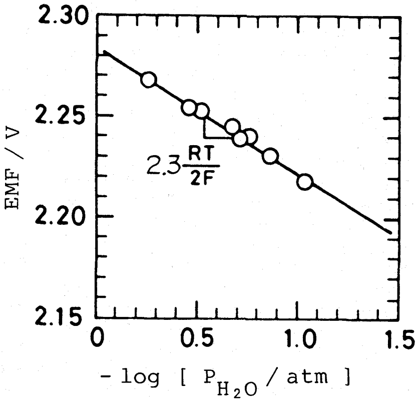

Fig.10 Emf response to H_2O partial pressure over the melt

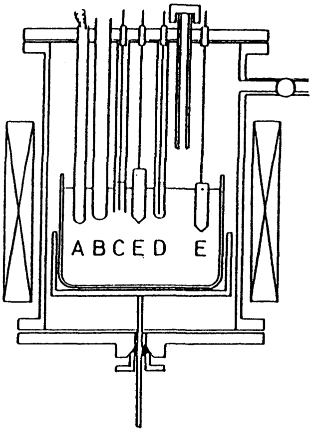

A : Thermocouple
B : Zirconia electrode
C : M/M^+ electrode
(M : Alkali metal)
D : Reference electrode
E : Glassy carbon

Fig.11 Experimental cell

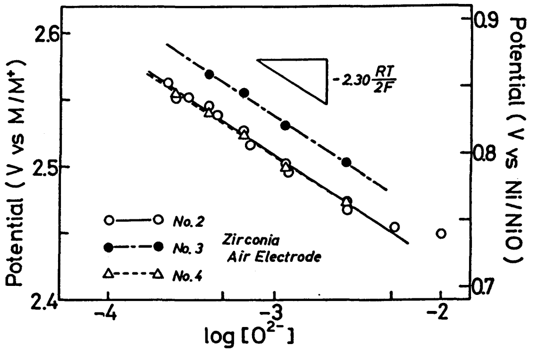

Fig.12 Potential - $\log[O^{2-}]$
$LiF\text{-}KF_{eutectic}$ at 823 K

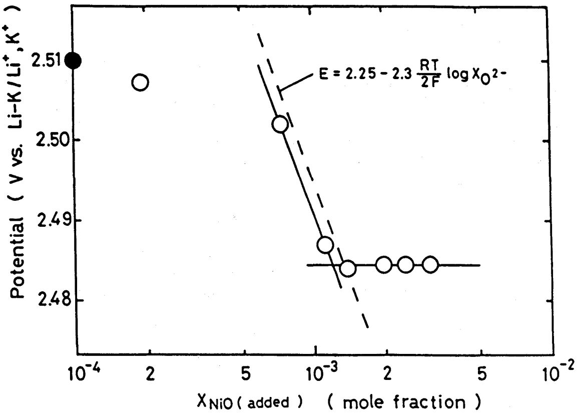

Fig.13 Relation between Pt(O_2) / stabilized zirconia / LiF-KF-O^{2-} electrode potential and the added amount of NiO (mole fraction)

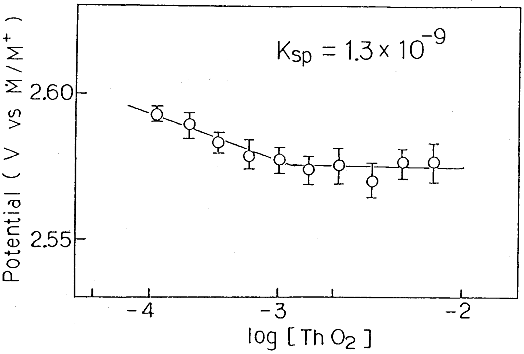

Fig.14 Potential - log[ThO_2] $\text{LiF-KF}_{\text{eutectic}}$ at 823 K

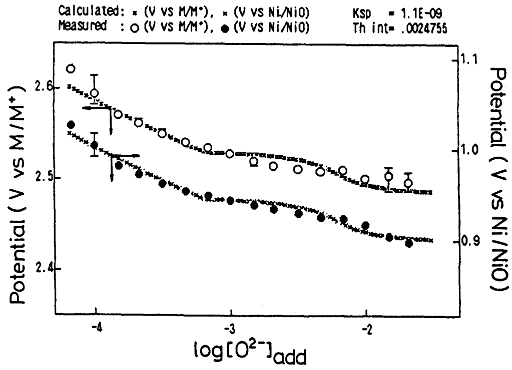

Fig.15 Potential - log$[O^{2-}]_{add}$ LiF-$KF_{eutectic}$ at 823 K

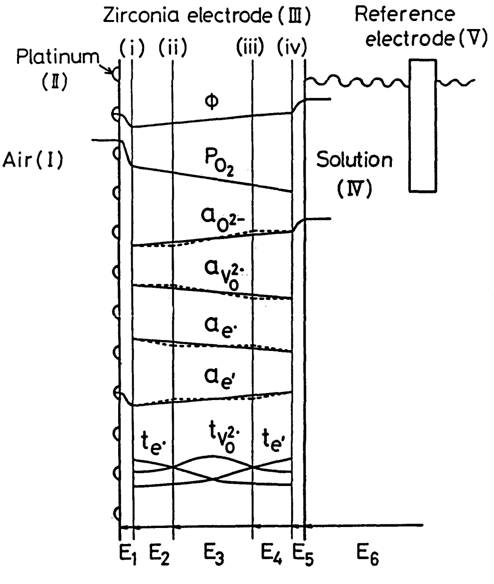

Fig.16 Calculation model

DOI: 10.1149/198601.0460PV

MOLTEN-SALT ELECTROLYSIS OF LEAD CHLORIDE IN A 3,000-AMPERE CELL WITH AN IMPROVED ELECTRODE DESIGN

J. E. Murphy, M. F. Chambers, and J. A. Eisele

Reno Research Center
Bureau of Mines, U.S. Department of the Interior
Reno, NV 89512

ABSTRACT

The Bureau of Mines developed a ferric chloride leaching, molten-salt electrolysis process for producing lead metal from galena concentrates. Previously, the process was demonstrated on a semicontinuous basis in a process development unit (PDU) designed to produce 500 lb of lead metal per day. Electrowinning of lead was accomplished in a 3,000-A cell with horizontal flat-plate electrodes which operated at 450° C using a LiCl-KCl-$PbCl_2$ electrolyte. Current efficiency averaged 93 pct and the energy required was 0.6 kW•h/lb of lead produced. Since electrolysis was energy-intensive, the present investigation was undertaken to determine if improvements in cell design would significantly decrease energy requirements.

Several bench-scale electrode assemblies were tested to determine electrode efficiency. The design that was chosen for scale-up featured a horizontal sawtooth assembly and was operated at 3,000 and 4,000 A in the PDU cell. The electrode assembly increased electrode surface areas, improved chlorine gas removal, and facilitated electrolyte circulation. With the new electrode system operating under identical conditions as the PDU cell, current efficiency was 99 pct and the energy required at 3,000 A was 0.3 kW•h/lb of lead produced.

INTRODUCTION

Chloride leaching of lead concentrates as an alternative to smelting has been the subject of much interest in recent years because of potential health hazards in the smelter from lead-bearing dusts and vapors. An excellent review of the chloride leaching processes has been presented by Dutrizac (3). The Bureau of Mines investigated ferric chloride leaching of galena followed by molten-salt electrowinning of lead from $PbCl_2$-LiCl-KCl electrolyte (4-6,8,14-15). The process involved leaching galena with ferric chloride-sodium chloride solution at 95° C,

$$PbS + 2FeCl_3 \xrightarrow{NaCl} PbCl_2 + 2FeCl_2 + S° \qquad (1)$$

After liquid-solid separation of the slurry, the solution was cooled to crystallize $PbCl_2$ which was dried and fed to a molten-salt electrolytic cell. The cell was operated at 450° C with a $LiCl$-KCl-$PbCl_2$ electrolyte. The cell products were lead metal and chlorine gas,

$$PbCl_2 \xrightarrow{\text{Electrolysis}} Pb + Cl_{2(g)} \qquad (2)$$

The chlorine was used to regenerate the leaching solution,

$$2FeCl_2 + Cl_2 \rightarrow 2FeCl_3 \qquad (3)$$

The process was demonstrated in a 500-lb-of-lead-per-day process development unit (PDU) which consisted of a semi-continuous integrated leaching-electrolysis operation (15). ASARCO, AMAX, Cominco, and St. Joe lead companies cooperated with the Bureau in the effort on a cost-sharing basis.

The PDU successfully demonstrated that the process produced high-purity lead metal with minimum health hazards due to the low temperatures of operation and with little environmental pollution because essentially all of the sulfur in the galena can be recovered as elemental sulfur. The leaching operation was subsequently demonstrated on a continuous basis (9).

A cost evaluation by Phillips (10) showed that electrolysis was the most expensive step in the process. The PDU cell operated intermittently for 2 years. The operating data are shown in table 1. The

TABLE 1. Average operating data for a 3,000-A cell with flat plate electrodes

Current........................A..	3,000
Voltage........................V..	4.7
Electrolyte temperature.......°C..	450
Electrode current density..A/in^2..	4.5
Electrode spacing.............in..	0.75
Current efficiency...........pct..	93
Ampere-hours consumed.............	3,005,064
Lead produced.................lb..	23,655
Energy requirement.......kW·h/lb..	0.60

energy requirement given in table 1 is essentially twice that obtained in previous bench-scale work (5). The main reason was that the cell voltage was higher than in bench-scale cells that operated at comparable current densities and electrode spacing. Secondly, a small decrease in current efficiency was experienced in the 3,000-A cell. Using an energy requirement of 0.6 kW•h/lb as found in the 3,000-A PDU electrolytic cell and an electrical energy cost of $0.05/kW•h, the electrolysis cost was $0.03/lb of lead produced. Despite the advantages of the process, the high electrolysis cost coupled with persistently low lead prices make industrial adoption of the process unlikely.

The present investigation was undertaken to determine if the electrolysis cost could be substantially decreased. The objective was to design and operate a 3,000-A cell which would require less energy for electrolysis. Alternative bench-scale electrode assemblies were designed that would promote chlorine removal, maximize the effective electrode area, and allow the interelectrode spacing to be decreased as much as possible.

MATERIALS AND APPARATUS

All reagents used in the bench-scale experiments were reagent grade. Technical grade $PbCl_2$ was used in the 3,000-A cell; other salts used in this cell were reagent grade. The electrolyte composition for all experiments was 6.5 wt pct LiCl, 16.5 wt pct KCl, and 77 wt pct $PbCl_2$, the same as had been used in previous electrolysis work.

In all experiments, the ampere-hour data were obtained by averaging the output from two Curtis 1002 integrating meters. Voltages were measured with a Fluke Model 8026B multimeter calibrated against a potentiometer. Current was measured with a potentiometer and a calibrated shunt.

3,000-A Cell

The 3,000-A cell that was operated in the PDU is shown in figure 1. The overall cell dimensions were 53-in long, 44-in wide, and 30-in high. The enclosure was made of 3/8-in mild steel plate. The cell cavity was 34-in long, 25-in wide, and 18-in deep. The interior walls were constructed of silica brick surrounded by castable refractory and insulating brick. The mild-steel lid had a 3-in layer of lightweight castable insulation. The cell had two graphite plate anodes, 24-in long, 14-in wide, and 3-in thick. A 6-in-diam graphite rod was screwed into each anode and connected to an anode busbar on the other end. The graphite rods were protected from air oxidation by mullite sleeves. The cathode, also of graphite, was 29-in long, 24-in wide, and 2-in thick. The cathode was supported 3 in above the cell bottom by four 3-in-diam graphite rods. The molten lead metal collected beneath the cathode and contacted a 6-in wide by 2-in thick steel plate that projected through the sides of the cell. The steel plate served as the cathode bus. The anode and cathode plates were grooved with six 1/4-in-wide channels which served to direct chlorine to one side of the cell and lead metal to the other side. Two auxiliary 3-in-diam graphite electrodes projected through the top of the cell and into the electrolyte to a depth of 2 in. These electrodes were connected to an ac power supply which kept the electrolyte molten when the cell was not in use. During electrolysis no supplemental heat was required.

Bench-Scale Cells

A bench-scale cell was designed in which the space between the cell wall and electrodes was minimized so that the effective bath area was essentially the same as the electrode surface area as was the case in the PDU cell. The cell is shown in figure 2. The electrode assembly consisted of two 1/2-in-thick disks of graphite with a diameter of 3-1/8 in. One-half-inch-diameter rods of graphite were screwed into the graphite disks which were held at the desired spacing with 1/8-in-diam alumina rods. The electrode assembly was placed in a 1-L tallform Pyrex glass beaker which had a 3-1/4-in inside diameter. The distance from the sides of the electrode plates to the container walls was 1/16 in. Hence, the effective bath area was very close to the electrode area.

The cell assembly was placed in a stainless steel container and heated to the operating temperature in a temperature-controlled pot furnace. The cell was operated at 450° C with an electrode spacing of 0.75 in to obtain data to compare with the 3,000-A PDU cell.

Three other electrode designs were selected for testing on a bench scale. The results were compared with the horizontal flat plate assembly. An electrode spacing of 0.5 in was selected for all the experiments because Welch and Iwanec (11-12) suggested that 1 cm (0.4 in) was the minimum electrode spacing for lead chloride electrolysis and earlier work by the Bureau of Mines showed that decreasing the electrode spacing from 1 to 0.5 in decreased the energy requirement for lead electrowinning.

The electrode designs are shown in figures 3-5. The electrode assemblies are referred to as vertical flat plate (fig. 3), square wave (fig. 4), and sawtooth (fig. 5). The angles of the triangular cuts in the sawtooth electrodes were 60° which gave the maximum effective electrode area at 1/2-in electrode spacing. Current density-voltage curves were obtained for all electrode designs by increasing the current density incrementally. Electrolysis was continued for 1 min at each selected current density.

EXPERIMENTAL RESULTS AND DISCUSSION

The cell voltage is plotted as a function of the current density in figure 6 for the bench-scale, horizontal flat-plate electrode cell. Also shown in figure 6 are data obtained previously with the 3,000-A PDU cell.

The decomposition voltage was 1.30 V in the PDU cell and 1.33 V in the bench-scale cell. Calculating the decomposition voltage from the free energy of formation of $PbCl_2$ as given by Wicks and Block (13) at 450° C yields a decomposition potential of 1.31 V, which is in good agreement. As the current density increases, the voltage of the 3,000-A cell becomes progressively higher than the bench-scale cell. At 3,000 A, which corresponded to a current density of 4.5 A/in^2, the voltage was 4.0 V. At the comparable current density in the bench-scale cell, the voltage was 3.4 V.

The voltage difference between the cells can be explained by the position of the voltage measuring probes. In the 3,000-A cell, voltages were measured outside the cell, from the graphite rod connected to the anode plate to the steel bar that served as the cathode bus. In the small cell, glass-encased tungsten probes were used to measure the voltage directly between the electrodes. The voltage drop between the points of measurements and the electrodes was not measured in the PDU cell during operation at 3,000 A. Subsequently, the voltage losses in the electrode leads were carefully determined in a cell of similar size and design. Subtracting the lead voltage losses from the PDU voltages makes the PDU current density-voltage curve virtually identical to the curve for the bench-scale cell in figure 6.

The cell voltage is the sum of several voltages and is given by:

$$V_{cell} = V_d + N_a + N_c + R_eI + R_mI \qquad (4)$$

where V_d is the decomposition potential of lead chloride, N_a is the anode overvoltage, N_c is the cathode overvoltage, R_eI is the voltage drop in the electrode leads and the electrodes, and R_mI is the voltage drop in the electrolyte (I is cell current). The cathode overpotential should be very small and will be assumed to be negligible in the analysis of cell potentials. The anode overpotential is probably small but significant (0.1 to 0.2 V).

In the bench-scale experiments, the R_eI term was zero. As stated before, at a current density of 4.5 A/in^2, the cell voltage was 3.4 V. Assuming a decomposition voltage of 1.3 V and an anode overvoltage of 0.2 V, the R_mI term can be estimated from equation 4 to be 1.9 V. At 4.5 A/in^2 current density in the PDU cell, assuming the R_eI term is 0.6 V, R_mI is also 1.9 V. The R_mI voltage is related to the effective electrolyte conductivity, K^*, by (1)

$$R_m I = \frac{LI}{K^*A} \qquad (5)$$

where L is the electrode spacing and I/A is the electrode current density. At a current density of 4.5 A/in^2 K^* is:

$$K^* = \frac{4.5\ \text{A/in}^2 \times 0.75\ \text{in}}{1.9\ \text{V}} = 1.78\ \Omega^{-1}\ \text{in}^{-1} = 0.70\ \Omega^{-1}\ \text{cm}^{-1} \qquad (6)$$

K^*, the effective electrolyte conductivity, differs from K, the absolute electrolyte conductivity, because of gas buildup in the electrolyte, chlorine in the present case. According to DeLaRue and Tobias (2), K^* is related to K by

$$K^* = K(1-E)^{1.5} \qquad (7)$$

where E is the gas fraction in the electrolyte. Using a K value of 1.165 Ω^{-1} cm^{-1} based on the work of Mikhail et al. (7), the gas fraction entrained in the electrolyte is calculated to be 29 pct.

The 4.0 V recorded in the 3,000-A PDU cell and used in the foregoing calculation was obtained during momentary operation of the cell. Under the continuous operating conditions shown in table 1, when the cell current is normalized to 3,000 A, the cell averaged 4.7 V. If the 0.7 V difference is accounted for by a buildup of chlorine gas on the anode, the chlorine gas fraction from equation 7 then becomes 42 pct. These calculations show the need for an improved electrode assembly design that would increase the rate of chlorine removal from between the electrodes.

Bench-Scale Experiments With Other Electrode Designs

Current density-voltage curves were developed for the other bench-scale electrode assemblies. The results are plotted in figure 7. Also shown in figure 7 is the theoretical current density-voltage relationship based on electrolyte conductivity data and assuming a decomposition voltage of 1.3 V and overvoltages of zero.

The lowest voltages were recorded with the vertical flat-plate electrodes. The voltages were nearly the same as would be expected from the electrolyte conductivity assuming zero electrode overvoltages and no chlorine gas fraction. However, the horizontal surfaces on the top and bottom of the vertical electrodes were neglected in calculating the electrode surface area.

The sawtooth assembly yielded the next lowest voltages followed by the square-wave and horizontal flat-plate assemblies. The relatively poor performance of the square-wave assembly was somewhat surprising because the square wave is really a combination of vertical and horizontal flat plates. A portion of the electrode surface area is relatively dead to electrolysis with both the square-wave and sawtooth electrodes which helps to explain the poor performance of the square-wave electrodes.

3,000-A Cell Operation With Sawtooth Electrodes

The sawtooth electrode design was chosen for scale-up rather than the vertical-plate design even though the vertical plate design had performed better in the bench-scale tests. One important factor was that the electrode assembly should occupy the same volume in the cell cavity and that the cell would use the same shell as the PDU cell. Thus, it was considerably easier to incorporate the sawtooth electrode design. Equally important, the sawtooth electrodes could be easily fabricated from a rectangular block of graphite and placed in the cell housing with little modification. A photograph of the electrode assembly is shown in figure 8. The two anodes were cut from 24-in by 14-in by 4-in thick graphite plates. As in the bench-scale cell, the angle of the triangles was 60°. The anodes had 1/2-in-diam holes cut in the top of the trough and spaced 3 in apart to permit chlorine escape. The cathodes were similar to the anodes without the holes. The molten lead collected beneath it and made contact with the steel plate, as in the PDU cell. Two auxiliary electrodes were used to provide ac heating.

The sawtooth cell was operated continuously at 3,000 A for 6 days. The results are shown in table 2. The current efficiency of 98.7 pct is similar to the current efficiencies obtained in previous bench-scale tests (5,8). The energy requirement of 0.3 kW•h/lb of lead metal produced is a significant improvement over the 0.6 kW•h/lb obtained in the PDU cell. The voltage of 2.5 V given in table 2 was measured, as in the PDU cell, from the anode connecting rod to the cathode steel busbar. Measuring the voltage between electrodes with glass-encased tungsten rods gave an average voltage of 1.9 V. Thus, the voltage drop in the electrode leads at 3,000-A cell current was 0.6 V. The R_mI voltage drop at 3,000 A for the sawtooth electrodes with a decomposition potential of 1.3 V and an anode over-potential of 0.2 V is 0.4 V.

TABLE 2. Data for cell operation in a 3,000- and 4,000-A cell with sawtooth electrodes

Current........................A..	3,000	4,000
Voltage........................V..	2.5	3.0
Electrolyte temperature.......°C..	450	450
Electrode current density..A/in^2..	2.3	3.1
Electrode spacing.............in..	0.50	0.50
Current efficiency...........pct..	98.7	99.5
Ampere-hours consumed............	426,527	230,640
Lead produced.................lb..	3,592	1,952
Energy requirement.......kW•h/lb..	0.30	0.35

This R_mI value agrees closely with a value of 0.39 V calculated by using equation 5. Thus, at 3,000 A in the sawtooth cell, chlorine gas did not influence the electrolyte conductivity very much, while it had played a major role in the PDU cell with horizontal flat-plate electrodes at 3,000 A.

Much less heat was generated by the electrolysis because the potential drop through the electrolyte was dramatically decreased by the sawtooth electrodes. As a result, 6 kVA had to be furnished by the ac power supply during electrolysis to keep the electrolyte at 450° C.

Following cell operation at 3,000 A, the cell was operated at 4,000 A for 58 h. The operational data at 4,000 A is also given in table 2. Current efficiency was excellent at 99.5 pct. The cell voltage increased to 3.0 V which resulted in an energy requirement of 0.35 kW•h/lb. The voltage losses in the leads at 4,000 A increased to 0.9 V. Cell potential from anode to cathode was 2.1 V, which again shows little influence of chlorine gas on the electrolyte conductivity. At 4,000 A, the ac power requirement to keep the electrolyte at 450° C was decreased to 4 kVA.

SUMMARY AND CONCLUSIONS

Lead metal was electrowon from a $LiCl-KCl-PbCl_2$ electrolyte at 450° C at 3,000 and 4,000 A with a sawtooth electrode assembly. At 3,000 A, the energy required was 0.3 kW•h/lb of lead metal produced which is a large improvement compared to the 0.6 kW•h/lb required previously in the PDU cell with horizontal flat-plate electrodes. The decrease in the energy resulted from decreasing the electrode spacing from 0.75 in to 0.5 in, greatly facilitating the removal of chlorine gas from the anode and doubling the electrode surface area. Chlorine gas did not noticeably increase the electrolyte resistance with the sawtooth electrodes at either 3,000 or 4,000 A cell current while chlorine doubled the electrolyte resistance with the flat-plate electrodes.

REFERENCES

1. Bockris, J. O'M., and A. K. N. Reddy, Modern Electrochemistry, Plenum Press, v. 1, 1970, pp. 354-357.

2. DeLaRue, R. E., and C. W. Tobias, On The Conductivity of Dispersions, J. Electrochem. Soc., v. 106, 1959, pp. 827-833.

3. Dutrizac, J. E., The Chloride Processing of Lead Concentrates, CANMET Division Report MRP/MSL 84-41, April 1984, 44 pp.

4. Elges, C. H., M. M. Wong, and R. G. Sandberg, Producing Lead Metal From Lead Chloride in a 3,000-Ampere Cell, Chloride Electrometallurgy, ed. P. D. Parker, Metallurgical Society of AIME, Warrendale, PA, 1982, pp. 89-110.

5. Haver, F. P., C. H. Elges, D. L. Bixby, and M. M. Wong, Recovery of Lead From Lead Chloride by Fused-Salt Electrolysis, U.S. Bur. Mines Rep. Invest. 8166, 1976, 18 pp.

6. Haver, F. P., and M. M. Wong, Ferric Chloride-Brine Leaching of Galena Concentrate, U.S. Bur. Mines Rep. Invest. 8105, 1976, 17 pp.

7. Mikhail, S. A., L. R. K. MacLean, and A. H. Webster, Electrical Conductivity in the Fused Salt System $PbCl_2$-LiCl-KCl, CANMET Division Report MRP/MSL 84-42, Mar. 1984, 11 pp.

8. Murphy, J. E., F. P. Haver, and M. M. Wong, Recovery of Lead From Galena by a Leach-Electrolysis Procedure, U.S. Bur. Mines Rep. Invest. 7913, 1974, 8 pp.

9. Murphy, J. E., B. R. Eichbaum, and J. A. Eisele, Continuous Ferric Chloride Leaching of Galena, Minerals and Metallurgical Processing, Feb. 1985, pp. 38-42.

10. Phillips, T. A, Economic Evaluation of a Leach-Electrolysis Process for Recovering Lead From Galena, U.S. Bur. Mines Inf. Circ. 8773, 1978, 23 pp.

11. Welch, B. J., and J. Iwanec, Electrolysis of Lead and Zinc Chlorides, Unisearch House, Kensington, N.S.W., Australia, 1969, 49 pp.

12. Welch, B. J., and J. Iwanec, 100 Ampere Scale Up Electrolysis of Lead and Zinc Chlorides, Unisearch House, Kensington, N.S.W., Australia, 1970, 101 pp.

13. Wicks, C. E., and F. E. Block, Thermodynamic Properties of 65 Elements--Their Oxides, Halides, Carbides, and Nitrides, U.S. Bur. Mines Bull. 605, 1963, 146 PP.

14. Wong, M. M., F. P. Haver, and R. G. Sandberg, Ferric Chloride Leach-Electrolysis Process for Production of Lead, Lead-Zinc, Tin '80, ed. J. M. Cigan, T. S. Makey, and T. J. O'Keefe, Metallurgical Society of AIME, Warrendale, PA, pp. 445-454.

15. Wong, M. M., R. G. Sandberg, C. H. Elges, and D. C. Fleck, Integrated Operation of Ferric Chloride Leaching, Molten-Salt Electrolysis Process for Production of Lead, U.S. Bur. Mines Rep. Invest. 8770, 1983, 21 pp.

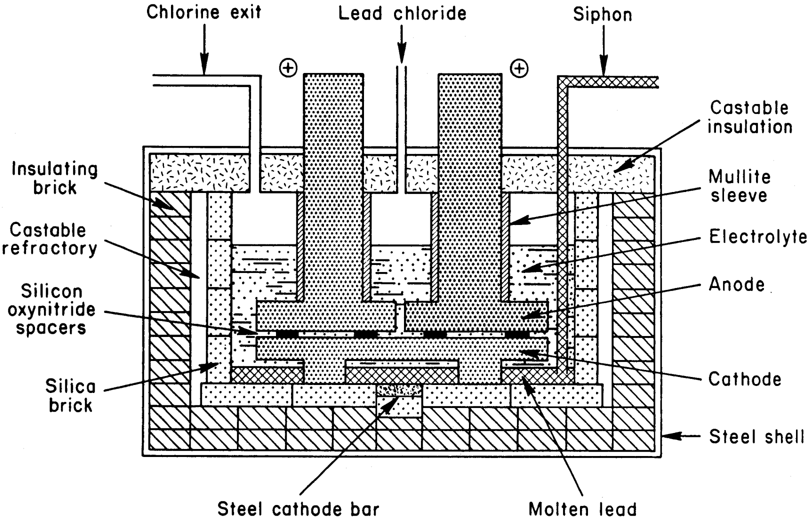

FIGURE 1. 3,000-A PDU cell.

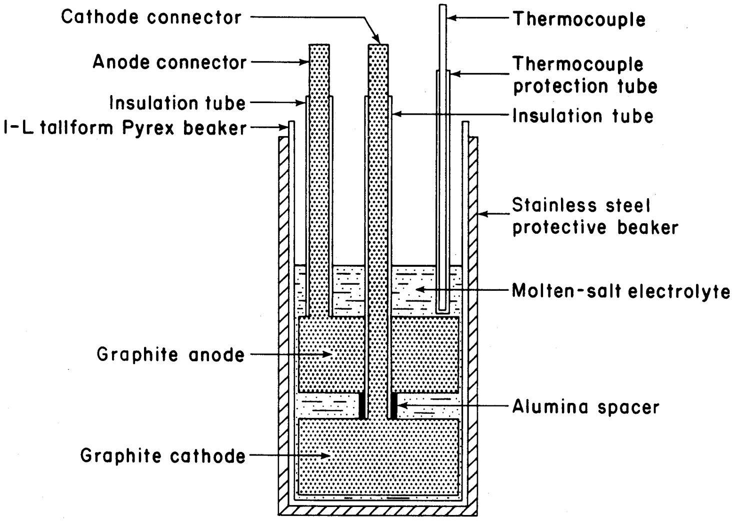

FIGURE 2. Bench-scale cell with horizontal flat plate electrodes.

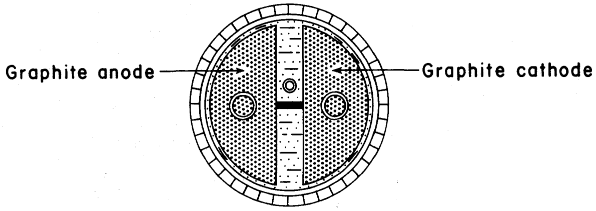

TOP VIEW

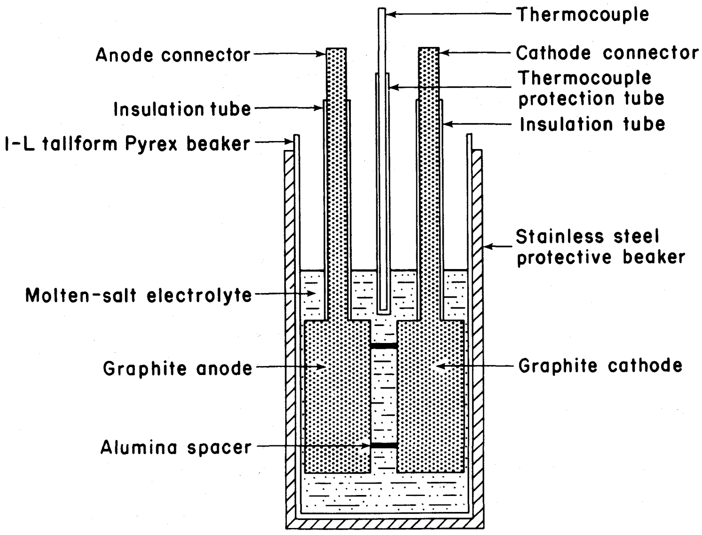

SIDE VIEW

FIGURE 3. Vertical flat plate electrodes.

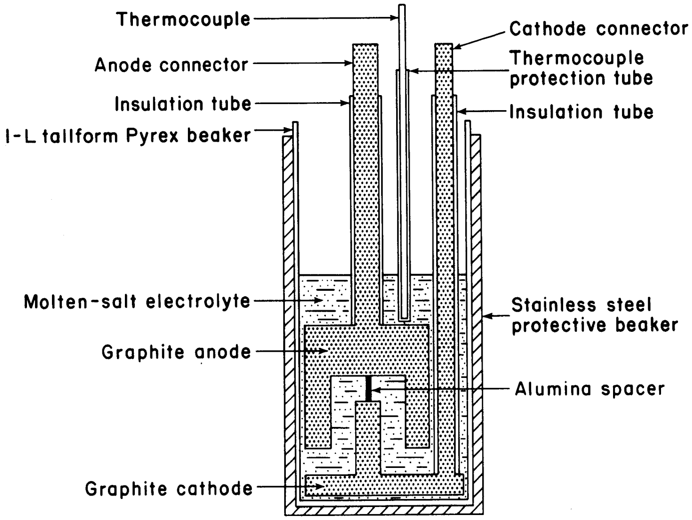

FIGURE 4. Square wave electrodes.

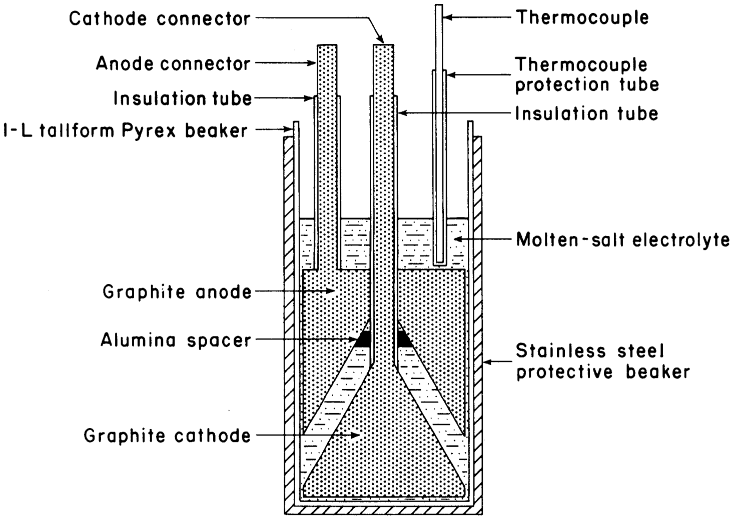

FIGURE 5. Sawtooth electrodes.

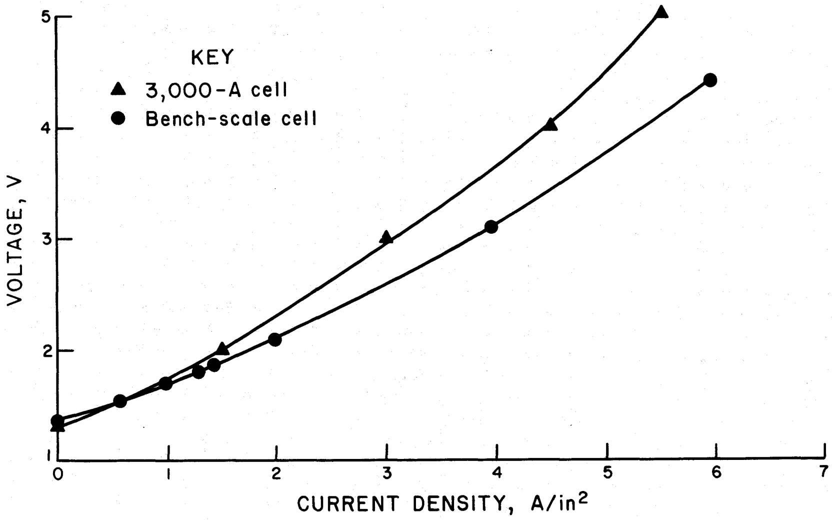

FIGURE 6. Current density versus voltage curves for flat plate electrodes at 0.75 in spacing.

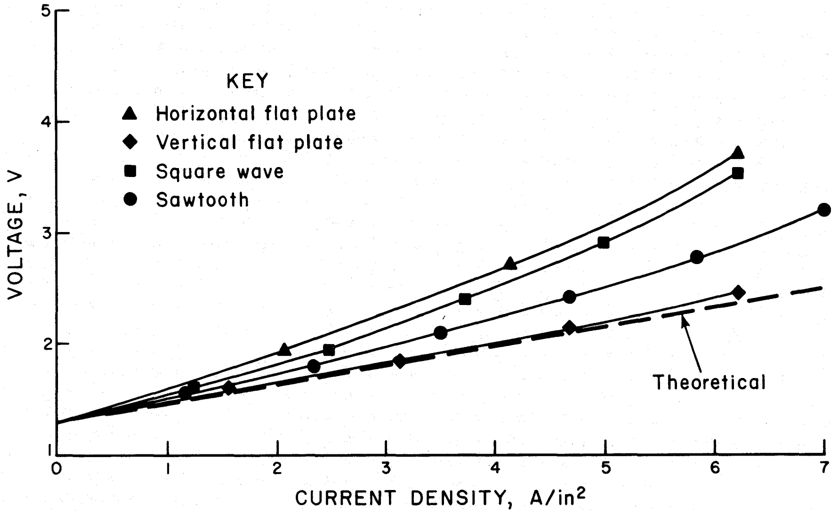

FIGURE 7. Current density versus voltage curves for electrode assemblies at 0.5 in spacing.

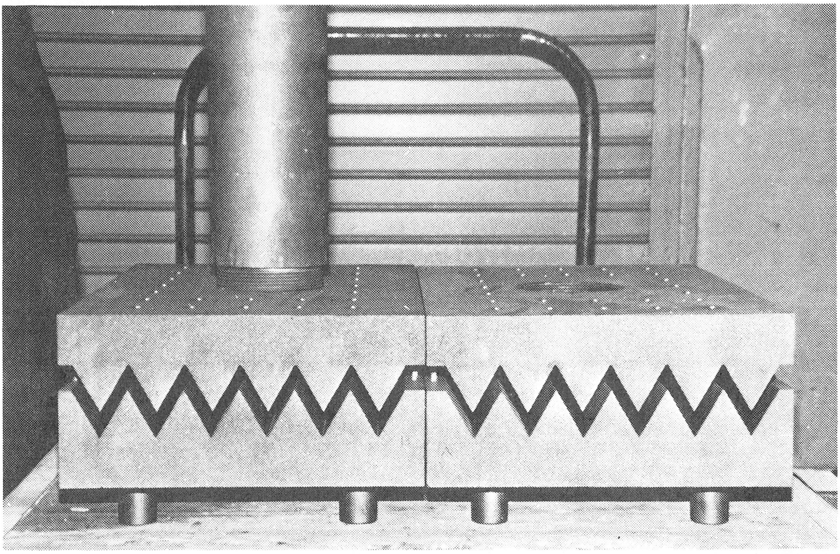

FIGURE 8. Sawtooth electrode assembly for 3,000-A cell.

DOI: 10.1149/198601.0474PV

RECOVERY OF PLUTONIUM BY PYROREDOX PROCESSING*

James A. McNeese, David F. Bowersox and
Dana C. Christensen

Plutonium Metal Technology Group
Division of Materials Science and Technology
Los Alamos National Laboratory
Los Alamos, New Mexico 87545

ABSTRACT

Using pyrochemical oxidation and reduction, we have developed a process to recover the plutonium in impure scrap with less than 95% plutonium. This plutonium metal was further purified by pyrochemical electrorefining. During development of the procedures, depleted electrorefining anodes were processed, and over 80% of the plutonium was recovered as high-purity metal in one electrorefining cycle. Over 40 kg of plutonium has been recovered from 55 kg of impure anodes with our procedures.

Introduction

The purpose of our pyrochemical research and development programs is to examine new techniques for producing high-purity plutonium metal from impure oxides, metals, and scrap. Los Alamos has demonstrated pyrochemical processes by taking plutonium scrap, converting it to oxide, and then, through a series of operations, producing high-purity plutonium metal.(1) The last purification step, electrorefining, is most effective when the metal feed exceeds 95% plutonium. We developed the pyroredox process to upgrade the scrap of low plutonium content to meet the feed requirements for effective electrorefining.

The two basic steps for the pyroredox process are oxidation,

$$2Pu\ (\text{impure}) + 3ZnCl_2 \xrightarrow[750°C]{ZnCl_2\text{-}KCl} 3Zn + 2PuCl_3 \qquad (1)$$

and reduction,

---

*Work done at the Material Science and Technology Division Los Alamos National Laboratory under the Auspices of the Department of Energy.

$$2PuCl_3 + 3Ca \xrightarrow[850°C]{CaCl_2} 2Pu + 3CaCl_2 \qquad (2)$$

The plutonium product can be separated mechanically from the salt and cycled into our primary pyroprocessing facility. This oxidation-reduction scheme was initially proposed and studied by J. G. Reavis* for reprocessing plutonium reactor fuels. In his research, zinc chloride in molten sodium chloride oxidized plutonium metal to the trichloride salt, and, in a second step, calcium was added to reduce the plutonium to metal. J. B. Knighton and coworkers at Rocky Flats Plant (3) have also studied these reactions.

The pyroredox process upgrades lower-purity plutonium metal scrap into a form suitable for electrorefining. Our principal application has been for spent anodes containing plutonium, gallium, and other less electropositive elements. The major impurity is usually gallium, which is added in casting to ensure a critically safe anode during electrorefining.(4,5) As electrorefining takes place, plutonium is oxidized from the anode pool into the molten eutectic salt and migrates to the cathode. There it is reduced to high-purity metal and drips into the annular chamber of the cell. Under the conditions of the process, elements less electropositive than plutonium remain in the anode pool. The run is automatically terminated when this pool solidifies about 90% plutonium depletion. Although the plutonium remaining in these anodes can be recovered by aqueous reprocessing,(6) we believe that pyroredox is far more compact, rapid, and efficient. Most of the experiments described in this report were conducted with spent anodes. Additional work with plutonium and simulated scrap, however, indicates that our conclusions are valid for other low-grade mixtures of plutonium.

Experimental Program

A. Equipment

The description of equipment used in this program has been published previously.(1) A typical experiment set up is shown in Fig. 1. Reactions take place in an inner crucible, usually constructed of tantalum or magnesia to minimize reagent attack. The crucible is centered in the heat zone of a 15-cm-diameter clam-shell furnace. Safety containers of stainless steel or tantalum are placed around the reaction crucible to catch any leakage. In addition, the stainless steel furnace tube is extended below the furnace to provide a cool area in which to collect and freeze any molten products in case of a catastrophic leak at higher temperatures. Type K thermocouples, enclosed in a double-walled tantalum-nickel thermocouple well, measure temperature in the melt. Small microprocessor units program and monitor temperature profiles.

---

*See Ref. 2 and J. G. Reavis, "Fused Salt Oxidation-Reduction Process for Plutonium Recycle Fuel," AIME, Detroit, Michigan, October 1961.

B. Reagents

In the oxidation process, dried Baker's analytical reagent grade zinc chloride and potassium chloride are mixed at a 31-mol% zinc chloride ratio, placed in a large pyrex reaction tube, and melted. The melt is sparged with anhydrous hydrogen chloride for 1 h, flushed with dry argon, and, finally, filtered, (in an argon atmosphere) through a coarse pyrex frit and a heated quartz transfer tube into a pyrex crucible. The white eutectic is sealed in a plastic bag in an argon atmosphere and stored in argon until needed. This salt, which melts at 462°C, met purity requirements and was sufficiently moisture-free to prevent foaming during oxidation reactions.

For the reduction process, Malinckrodt food grade calcium chloride was vacuum dried at 225°C for a minimum of 5 days and placed in a platinum crucible for purification. The salt and crucible were placed in a stainless steel furnace tube; the equipment was assembled and the system heated to 800°C. Anhydrous hydrogen chloride was passed through the melt for 2 h. An argon purge followed. The melt was then transferred through a heated tantalum tube into an erbia-coated, split mold of stainless steel. The resulting salt cast was sealed into a plastic bag and stored in argon until needed.

Pfitzer triple-distilled calcium was presssed into an ingot of ∿80% theoretical density to reduce the surface area and, consequently, the rate of reaction in the reduction sequence.

C. Procedures

For the oxidation step, depleted anodes were placed in a tantalum crucible, and 10% excess zinc chloride (calculated) was added as a 32-mol% $ZnCl_2$-KCl eutectic. The system was assembled, evacuated, backfilled with argon, and heated to 470°C, which is above the melting point for the eutectic. The melt was then stirred while being heated to 750°C to ensure complete reaction. After 1 h at temperature, the mixture was heated and kept at 850°C for 1 h to promote phase separation. The stirrer and thermocouple well were then raised from the melt. After another 4 h at temperature, the system was cooled at a 200°C/h rate to ambient temperature. The two-phase product was removed, and the lighter salt phase was mechanically separated from the zinc button.

For the reduction step, the salt from the oxidation reaction was crushed and mixed with 1 kg of dried calcium chloride. The calculated amount of calcium was added as a pressed ingot; the mixture was placed in a magnesia crucible and the vessel assembled. The vessel was evacuated, backfilled with argon, and heated to salt melt at about 700°C. The thermocouple well and the stirrer were then lowered into the liquid, and the mixture was stirred. During the reaction, the temperature rose gradually to 850°C; after 20 min, the stirrer and thermocouple well were raised above the melt. The system was maintained at 850°C for 15 min, then cooled without power to ambient temperature. The product was broken out of the crucible for liquation or mechanical separation of the phases.

Results and Conclusions

A. Oxidation

As shown in Eq. (1), the main reactions in oxidation are forming plutonium trichloride in the salt phase while reducing zinc chloride to zinc metal. The free energies of formation of selected chloride are listed in Table I. All chlorides with energies higher than zinc should be oxidized with the plutonium into the salt phase. Those impurities with lower energies concentrate in the zinc phase. If equilibrium conditions are met, aluminum, americium, uranium, and the rare earths

TABLE I. BEHAVIOR OF IMPURITY ELEMENTS

Element	$-\Delta F°$ Atom Cl (kcal/g)
Ir	2
W	5
Ni	18
Cu	21
Ta	27
Pb	27
Fe	27
Si	28
Cd	30
Cr	32
Ga	32
Zn	34
Mn	41
Ti	43
Al	46
U	54
Np	55
Zr	56
Mg	58
Th	59
Pu	59
Ce	66
Am	67
Na	76
Ca	77
Li	78
K	92

would transfer into the salt phase with plutonium. Iron, tantalum, and gallium would concentrate in the zinc-rich metal phase.

In our experiments, the oxidation was exothermic. The reaction rate and temperature were controlled by slowing the stirrer rates. This eliminated foaming and overflow from the crucible. After the post reaction heat cycle (5 h at 850°C), good phase separation occurred. The relatively slow cooling rate promoted shrinkage of the product from the crucible walls so that the tantalum crucible could be reused. With simulated anodes containing more than 95% plutonium as feed, a green salt, most likely K_3PuCl_6 in a potassium chloride matrix, and a bottom metal phase of zinc formed. After these phases were mechanically separated, the zinc phase could be discarded. The green salt was then reduced to plutonium metal.

B. Reduction

The main reactions in reduction of the green salt are the reduction of tripositive plutonium to the metal and oxidation of calcium to calcium chloride (Eq. 2). However, the excess zinc chloride added for the oxidation step is also reduced.

$$ZnCl_2 + Ca \rightarrow CaCl_2 + Zn \quad . \qquad (3)$$

The reduction is slowed by adding 1000 g of dried calcium chloride to the green salt prior to heating, using pressed calcium, and stirring slowly at a rate lower than 200 rpm. The calcium chloride addition adsorbs calcium oxide formed in reactions and also minimizes formation of black salts. Yields are usually greater than 98% and, under optimum conditions, have reached calculated values of 99.5%. Results showing the purification attained by the two-step process are given in Table II. The high zinc and aluminum concentrations do not interfere with further purification by electrorefining.

In most cases, the reduction product was a salt phase above a two-phase button. The salt phase was mechanically separated and discarded. The bottom, denser phase was plutonium and contained small amounts of calcium and zinc. The upper metal phase was typically 50-60% plutonium, 20-25% zinc, and 4% calcium. Several buttons were collected and coalesced to consolidate phase separation. This step, liquation, is discussed below under the heading additional processing steps.

C. Additional Processing Steps

To recover spent anodes containing gallium and the impurities that collect in the anode during electrorefining, additional processing steps were necessary. We do not know whether these would be necessary with other scrap.

TABLE II. PURIFICATION OF PLUTONIUM ANODES BY PYROREDOX PROCESSING[a,b]

Element	Feed	Product
Pu	79%	85%
Ga	5.5%	---
Zn	---	790
Ca	7.5%	1.35%
Al	1%	300
Ta	0.1%	100
Na	5%	5
Si	280	25
K	0.5%	40
W	500	10
B	200	3
Mg	1	3000
Ni	230	5
Fe	3000	1000
Am	2100	30

[a] Run D01 results, which are typical of the series.

[b] Feed and product are in ppm unless otherwise indicated.

1. Polishing

When we processed spent anodes rather than plutonium-gallium mixtures, three phases formed during oxidation. The upper phase (a green salt) and the bottom phase (metallic zinc) were similar to phases obtained with the simulated anodes. The third (intermediate) phase was a grey salt that we attributed to impurities in the anode. It consisted mainly of a fog of uncoalesced zinc in the salt matrix with some evidence of plutonium oxychloride formation. This third phase was minimized by a polishing step prior to the oxidation of the anode. The spent anode, 300 g of calcium, and 3000 g of calcium chloride were placed in a magnesia reaction crucible. The reaction system was assembled, evacuated, and backfilled with argon. The system was heated to 800°C, and stirring was begun and increased from 200 to 600 rpm as the temperature rose to 850°C.

The product was homogeneous and plutonium loses during polishing were quite low (less than 5 g). The metal button could be mechannically separated from the salt and transferred for the oxidation step. Polishing markedly reduced grey salt formation, probably by reducing any partially oxidized species in the spent anode. Additional zinc chloride was now needed, however, to oxidize both the plutonium and the excess calcium contained in the button. Yields in the oxidation step increased to greater than 80% after polishing.

2. Liquation

Liquation removes zinc and calcium from the reduction product while preparing most of the plutonium for further purification. The liquation step is a gravity separation of the two-phase button formed in the reduction. Several of these buttons, totaling 4.5 kg, were placed in a long, narrow magnesia crucible. The reaction system was assembled, evacuated, and backfilled with argon. The vessel was heated and maintained at 850°C for 6 h. The resulting ingot consisted of a lighter upper phase and a more dense plutonium-rich lower phase. Results of several liquations are summarized in Table III. The bottom phase containing most of the plutonium could be electrorerefined without further treatment. The upper phase was recycled to the oxidation step for removal of calcium and zinc.

TABLE III. COMPOSITION OF LIQUATION PHASE

	Plutonium		Calcium		Zinc		Density (g/cm^3)	
Experiment No.	Top (%)	Bottom (%)	Top (%)	Bottom (%)	Top (%)	Bottom (%)	Top (%)	Bottom (%)
1	42	89	5	130 ppm	8	600 ppm	5.7	15.6
2	0.7	93	20	700 ppm	30	0.4	2.5	15.0
3	55	95	51	--	12.5	--	--	--
4	47	90	24	1.8%	25.5	3.5	--	--

D. The Electerorefined Product

Even though electrorefining is a mature process, we demonstrated the liquated buttons could be further processed to high-purity metal. Table IV summarizes data from experiments in which the denser phase from the liquation step was electrorefined. Yields were satisfactory; purity of the product ring was excellent (see Table V).

TABLE IV. RESULTS OF LIQUATION EXPERIMENTS

		Phase	
	Ingot	Top	Bottom
Pu, g	4340	1220	3120
Total Pu, %	99.3	28.1	71.9
Density, g/cm^3	--	7.5	25

TABLE V. PRODUCT OF ELECTROREFINING PYRODOX METAL

Component	Plutonium Content (g)	Plutonium Content (%)
Product Ring	4081	78.4
Shot	26	0.5
Cathode	9	0.2
Crucible	83	1.6
Salt	671	12.9
Anode	334	6.4
Yield[a]	--	80.1

[a] Yield -- 100X (Pu ring + shot)/Pu Feed.

IV. SUMMARY

We have developed a method for removing impurities from plutonium scrap that contains less than 95% plutonium so that it meets the 95%-purity criterion for effective electrorefining. The process consists of oxidation of plutonium to the trichloride followed by reduction to metal. The flow diagram (Fig 2) shows the process, as modified for recovering plutonium from spent anodes in our production demonstration facility. The liquated product has been purified by electrorefining. Yields from pyroredox processing in our demonstration facility are greater than 80%. We believe that the process is ready for transfer to production facilities.

The 31 mol% $ZnCl_2$-KCl eutectic was successfully prepared in 5-kg batches by drying, heating to a melt, filtering through a coarse pyrex frit, and transferring the melt into a warm quartz crucible. The moisture-free salt did not froth or overflow during the oxidation step.

Prepolishing and liquation were effective steps for treating the impure spent anodes to adapt the general, generic process to our specific requirements.

We are studying methods for minimizing or eliminating the grey salt phase that forms during oxidation. We recycle this phase when necessary.

REFERENCES

1. D. C. Christensen and L. J. Mullins, "Plutonium Metal Production and Purification at Los Alamos," in Plutonium Chemistry, W. T. Cornall and G. R. Chopkin, Eds. (ACS Symposium Series, American Chemical Society, New York, 1983), pp. 409-432.

2. J. G. Reavis and J. A. Leary, "Nonaqueous Dissolution of Massive Plutonium," US Patent No. 2,886,410, May 12, 1959.

3. J. B. Knighton, R. G. Auge, and J. C. Brown, "Purification of Plutonium by Oxidation-Reduction Process," RFP-1691-A, in "Research and Development Annual Progress Report, November 1, 1980 to September 30, 1981," Frend John Miner, Ed., Rockwell International, Rocky Flats Plant, Golden, Colorado (August 11, 1982).

4. L. J. Mullins and J. A. Leary, "Fused Electrorefining of Molten Plutonium and Its Alloys," Los Alamos Scientific Laboratory report LA-3118 (November 1964).

5. L. J. Mullins, J. A. Leary, A. N. Morgan, and W. J. Maraman, "Plutonium Electrorefining," Ind. Eng. Chem. Process Des. Develop. 2, 20, (1963).

6. C. E. Baldwin and J. D. Navratil, "Plutonium Process Chemistry and Rocky Flats," in Plutonium Chemistry, W. T. Cornall and G. R. Chopkin, Eds. (ACS Symposium Series, American Chemical Society, New York, 1983), pp. 369-380.

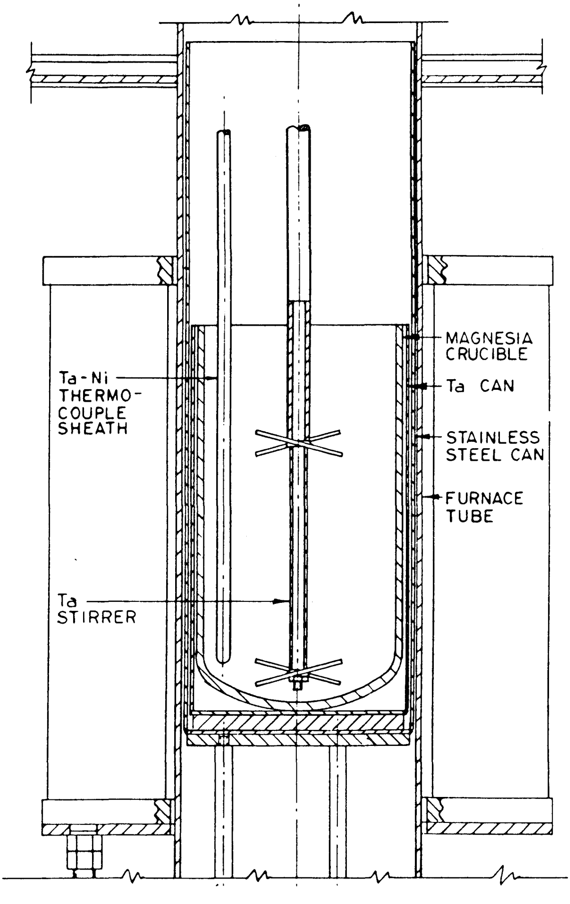

Fig. 1. Experimental apparatus.

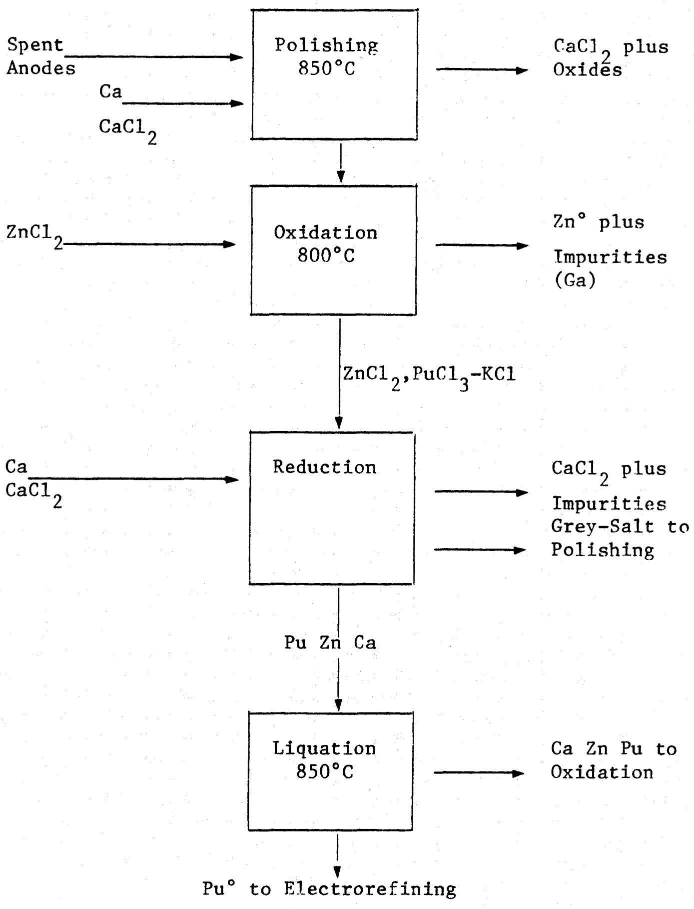

Fig. 2. Recovery of plutonium by pyroredox processing

DOI: 10.1149/198601.0485PV

STUDY ON ELECTROWINNING OF INTERMETALLIC COMPOUNDS TANTALUM-NICKEL AND NIOBIUM-NICKEL IN MOLTEN LiF-NaF

Pierre TAXIL, Zhi Yu QIAO*

Laboratoire de Chimie Physique et d'Electrochimie
associé au CNRS (UA 192)
Université Paul-Sabatier, 118 Route de Narbonne
31062 TOULOUSE Cédex (France)

ABSTRACT

A study of the mechanism of the electrochemical reduction of K2 TaF7 or K2 NbF7 on a nickel electrode in molten LiF-NaF allows the range of potentials to be defined where Nb-Ni or Ta-Ni alloys are formed. Further static potential measurements in a galvanostatic intermittent electrolysis allow the intermetallic compounds to be identified in each case and the Gibbs energy of the Ta-Ni compounds. Then surface alloys are prepared by electrolysis at a controlled positive potential ; only NbNi3 and TaNi3 stable phases are detected in the bulk of the layer. A parabolic law of growth is stated, involving the intermetallic diffusion coefficient $\tilde{D}$ and a parameter α depending on solid composition at the boundaries of the layer ; values of both α and $\tilde{D}$ were estimated after combination of electrochemical measurements and diffusion equation.

INTRODUCTION

Nickel is known to give very corrosion-resistant alloys with refractory metals such as tantalum and niobium. So, these materials can be used as insoluble anodes in chlorine or oxygen gas production [1,2] ; if we consider the high melting point of Ta and Nb (respectively 3,000 °C and 2,500 °C), the metalliding process is an advantageous mean of obtaining these compounds since the temperature range involved here is moderate (800 - 1 100 °C). This technique was firstly developed by COOK [3] : in this particular case, it consists of the electrochemical reduction of tantalum or niobium ions combined with the diffusion of the deposited elements in the nickel substrate [4,5].

*Beijing University of Iron and Steel Technology
Department of Physics and Chemistry of Metals
BEIJING (China)

In addition of the pratical aim of the work, we intend to obtain fundamental data concerning the solid compounds which are formed and the intermetallic diffusion in each system ; today, only few investigations over this subject, based on conventional techniques of the solid state science have been carried out. Electrochemistry in molten salts have been shown to be a powerful technique in this field since the measured current and potentials during the electrodeposition process are very sensitive to the diffusion of the anodic metal element [6,9].

In this work, the use of electrochemical techniques leads to the estimation of thermodynamic values concerning the formation of tantalum-nickel compounds and of kinetic parameters concerning the intermetallic diffusion into both systems.

EXPERIMENTAL PART

Technical

The cell consists of a refractory steel lid placed in a regulated furnace and provided with a vacuum supply and an argon gas circuit. The device was described elsewhere (fig. 1).

The melt is previously dehydrated by a slow fusion under vacuum followed by argon gas bubbling during 16 hours. Then all the experiments are performed under argon atmosphere.

For the electrochemical part, a multipurpose installation was used, based on a TACUSSEL PRT 20-10X potentiostat monitored by a periodical triangular signal generator TACUSSEL Model GSTP : voltammograms, chronoamperograms and chronopotentiograms were recorded with a X-Y recorder, and a TACUSSEL recorder type EPLI. The micrographic analysis was performed by means of an electronic microscope and Xray microprobe.

Salts

The electrolytic bath consists of a solution of $K_2 TaF_7$ or $K_2 NbF_7$ in the eutectic melt LiF-NaF (freezing point 650° C).

As a single valence (V) is noted for tantalum ions in the fluoride melt, two valences are to be considered in the case of niobium solutions, according to the following equilibrated reaction :

$$Nb + 4Nb^{V} \rightleftharpoons 5\ Nb^{IV} \qquad (1)$$

In order to get good cathodic efficiencies in the electrodeposition process, a valence of niobium ions close to 4 is required ; a further addition of metallic niobium of the bath displaces the equilibrium (1) in the right hand and leads to an average valence approximatelv equal to 4.2.

Electrodes

Tantalum and niobium foils [3 X 1,5 X 0,05 cm] are used as counter electrode and reference electrode. The working electrode is either a nickel and molybdenum wire (diameter 0,1 cm) or nickel sheets (3 X 0,5 X 1 cm) All these metals were provided from ALPHA INORGANICS (purity 99.9 %).

PRELIMINARY THERMODYNAMIC MEASUREMENTS

Electrochemical techniques allow one to identify the formation of the tantalum-nickel compounds.

Voltammetric curves

The reduction of the Ta $F7^{=}$ions at 1 050 °C was carried out by cyclic voltammetry alternatively with molybdenum and nickel as working electrode. A typical voltammogram is shown on fig. 2 ; since only the second metal gives alloys with tantalum at this temperature [10] it is concluded that :

1 - the nucleation step, observed in both cases, is located at negative potentials with respect to the Ta reference electrode.

2 - the peaks and plateaus at positive potentials observed in the case of a nickel cathode are characteristics of the intermetallic compounds formation.

Potentials of formation of the tantalum-nickel compounds

The accurate determination of these potentials is available by means of an intermittent galvanostatic electrodeposition of tantalum on a nickel cathode. During the off-times, the diffusion of electrodeposited Ta occurs and promotes a change in the composition of the external layer. On fig. 3, the evolution of the static potential of the nickel electrode (potential during the off-time) exhibits several definite plateaus ; each plateau is characteristic of a biphased equilibrium which takes place at the surface of the electrode [11] :

$$Ta_x\,Ni + y\,Ta \rightleftharpoons Ta_{x+y}Ni \qquad (2)$$

The phases diagram of the tantalum-nickel system includes the following compounds : Ta_2Ni, $TaNi$, $TaNi_2$ and $TaNi_3$ [12]. According to fig. 3, they are supposed to be formed at respectively 20,45,200 and 245 mV versus the Ta reference. The reaction (2) is associated to a cell, the e.m.f. of which would be expressed as :

$$\mathcal{E} = -\frac{RT}{5yF}\ \ln \frac{aTa\ [Ta\ (x+y)\ Ni]}{aTa\ \ [Ta\ (x)\ Ni]} \qquad (3)$$

5 is the number of electrons exchanged in the discharge of tantalum ions, and
aTa is the activity of the refractory metal in the intermetallic phase.
The values of the GIBBS free energy of each plateau, deduced from the potentials of the plateaus are given in Table I. The values for $TaNi_3$ and $TaNi_2$ agree with those calculated from the emf measurements of NESTERENKO [13] and LYAKISHEV [14] using solid galvanic cells. No other measurements are reported for $TaNi$ and Ta_2Ni.

ELECTROWINNING AND ANALYSIS OF TANTALUM-NICKEL AND NIOBIUM-NICKEL ALLOYS

According to fig. 2, the alloys can be readily obtained on a nickel cathode in potentiostatic condition at a slightly positive potential (a few millivolt) versus the Ta or Nb reference electrode ; since the refractory metals are more reactive than nickel, the alloy formation is available by means of a galvanic cell involving the nickel as cathode and tantalum or niobium as anode. In both cases the variation of the metalliding current shows an hyperbolic decrease which is characteristic of a diffusion-controlled process (fig. 4); furthermore, an other technique consists of a mixed electrodeposition-diffusion process : in a first time, the refractory metal is electrodeposited by means of a galvanostatic electrolysis, in a second time the electrical circuit is open and the metal diffuses in the nickel substrate. Complete diffusion is achieved when the potential of the cathode is 200 mV versus the Ta reference or 30 mV versus the Nb reference.

The weight of the diffused refractory metal per surface unity $\frac{\Delta m}{s}$ is shown to be proportional to the square root of the metalliding treatment on fig. 5.
According to an X-ray analysis, performed with the microprobe on several samples, the composition of the layer is uniform and corresponds to $TaNi_3$ and $NbNi_3$ compounds. Since, the other compounds of each system are metastable

(see table I for tantalum and [15] for niobium), this evolution is normal.

It is to be noted that the other compounds are quantitatively formed in the case of techniques such as diffusion welding involving an overpressure exerted on the couples of metals [16,17]. In our experiments, the metastable compounds Ta2 Ni, Ta Ni, Ta2 Ni, on one hand [5] and NbNi on the other hand [4] appear only during transient phenomena.

The preceding results allow us to determine the thickness of the layer, by means of the following equation:

$$X = \frac{\Delta m}{S} \cdot \frac{1}{W \rho} \qquad (4)$$

where X is the thickness of the layer, W the massic fraction of the refractory metal in the alloy and ρ the density of the alloy.
The growth of the layer obeys a parabolic relationship :

$$X^2 = K\ t \qquad (5)$$

The values for KTa and KNb are given in the first line of tables II and III, respectively.

DETERMINATION OF THE INTERMETALLIC DIFFUSION COEFFICIENT

The theoretical treatment of metalliding is to be included into the general problem of an unsteady state diffusion with moving boundary [18] : the motion of the nickel interface is only due to the intermetallic diffusion and the rate of the process is controlled by the flux of the diffusing species, termed by J, at this boundary :

$$J = - \tilde{D}\left(\frac{\partial C}{\partial x}\right)_{x = X} \qquad (6)$$

$\tilde{D}$ is the intermetallic diffusion coefficient, c the composition of the alloy layer, x the abscissa in the layer (x = 0 at the liquid interface). The process is described by the FICK's second equation.

$$\frac{\partial c}{\partial t} = \tilde{D}\ \frac{\partial^2 C}{\partial x^2} \qquad (7)$$

The appropriate boundary conditions are the following :

$$t = 0 \qquad c = 0 \qquad x \geqslant 0 \qquad (8)$$
$$t > 0 \qquad c = C_0 \qquad x = 0 \qquad (9)$$
$$t > 0 \qquad c = 0^0 \qquad x = \infty \qquad (10)$$

The solution of equation (7) leads to the following expression of C and J :

$$C = C_0 \ \operatorname{erfc} \frac{x}{2\ (\tilde{D}t)\ 1/2} \qquad (11)$$

$$J = \frac{Co\ \tilde{D}^{\frac{1}{2}}}{(\pi t)^{\frac{1}{2}}} \exp \left[- \frac{x}{2(\tilde{D}t)^{\frac{1}{2}}} \right] \qquad (12)$$

So, the theoretical expression of the metalliding current density, taking account of equation (5) is :

$$i = \frac{n\ F\ \tilde{D}^{1/2}\ Co}{(\pi t)^{1/2}} \ .\ \exp(-\alpha^2) \qquad (13)$$

[n is the number of electrons exchanged (5 for Ta and 4 for Nb]

$$\text{with} \quad \alpha = \frac{1}{2} \left(\frac{K}{\tilde{D}} \right)^{\frac{1}{2}} \qquad (14)$$

α is a dimensionless parameter depending on Co, Cx and Cm which are respectively the composition of the layer at x=0, x = X and the average composition [19].
The evolution of the metalliding current, observed on fig. 4 follows the theoretical expression, as it is shown on figs. 6 and 7 : on fig. 6, equation [13] is verified, in the case of niobium, at various temperatures. In each run, the potential of the cathode is close to zero. So, the composition of the external layer is supposed to be saturated in niobium ($Co = Co^s$). It is stated elsewhere that Co^s corresponds to the NbNi compound ($Co^s \simeq 0{,}051$ at. g./cm3 [4].

Fig. 7 shows in the case of tantalum the dependence of the slope of the straight lines, $i = f\ (t\ {-1/2})$, on the potential of the cathode i.e. on Co.

An increase of the slope is observed when the potential is decreased, meaning that the external composition in tantalum is increased. A maximum is reached when the potential is about 10 mV : thus for this potential, Co is close to the saturated value, Co^s, corresponding to the Ta2 Ni compound ($Co \simeq 0{,}068$ at. g./cm3) [5].

The slopes of the straight lines, for $Co = Co^s$, termed by p^sNb and p^sTa are given in the second line of tables II and III.

The combination of equations (13) and (14) gives:

$$\frac{\exp\ (\ -\alpha^2)}{\alpha} = \frac{2\ \pi^{\frac{1}{2}}\ \ p^s}{n\ F\ Co\ K^{\frac{1}{2}}} \qquad (15)$$

From equation (15), the parameters for Ta and Nb are available. These values, which are given in the third line of tables II and III confirm that this parameter does not depend on temperature. The intermetallic diffusion coefficient, determined from equation (14) obeys ARRHENIUS law (values on the fourth lines of tables II and III) :

$$\tilde{D}Nb = 1.3.10^{-4} \quad \exp \left[- \frac{16\ 700}{T} \right] \mathrm{cm}^2 .\ \mathrm{sec}^{-1} \qquad (16)$$

$$\tilde{D}Ta = 1.1.10^{-6} \quad \exp \left[- \frac{10\ 400}{T} \right] \mathrm{cm}^2 .\ \mathrm{sec}^{-1} \qquad (17)$$

CONCLUDING REMARKS

- The experimental values of α can be compared with other more theoretical ones which are available as follows. According to DANCKWERTS [16], the expression of the moving rate of the nickel interface is the following :

$$\frac{dX}{dt} = B \left[- D \left(\frac{c}{x} \right)_{x = X} + Cx \frac{dx}{dt} \right] \qquad (18)$$

B is a proportionality constant between the thickness of the layer and the mass of diffusion species crossing the interface. It is clear that $B = 1/w\rho$ [equation (4)] and that $1/w\rho = Cm$. Then, after combination of equations (5), (19) and (18), we obtain :

$$\frac{Co - Cx}{Cm - Cx} = \pi^{1/2} . \mathrm{erf}\, \alpha . \alpha . \exp(\alpha^2) \qquad (19)$$

and

$$\frac{Co}{Cm} = \frac{1}{\frac{\pi^{-\frac{1}{2}} \exp(-\alpha 2)}{\alpha} + \mathrm{erfc}} \qquad (20)$$

Eq. (19) shows the dependence of α on Co, Cx and Cm. Eq. (20) allows to determine α . αNb and α Ta are found to be respectively 0.85 and 0.92. As the order of magnitude is similar, the agreement with the experimental values can be considered satisfactory.

- Nevertheless the mathematical treatment which is used in this work fails on one point : the composition of the layer, given by equation (11) involves an uniform variation of the composition of the layer which is not confirmed by the Xray analysis. On the other hand, the expression of the metalliding current, related to the flux, which is given by equation 13, leads to coherent results. Thus, the structural arrangement leading to the compounds Ta Ni3 and Nb Ni3 is supposed to have no effect on the rate of the process.

LITERATURE CITED

[1] : T.FUJII, H. BABA Boshoku Gijutsu 29, 457 (1980)

[2] : G.N. TRUSOV, E.P. GOCHALIEVA, B.A. GONCHARENRO, V.S. MIKHEEV Elektrokhimiya 13, 1 056 (1977)

[3] : N. C. COOK Sci. American 221, 38 (1964)

[4] : P. TAXIL, QIAO ZHI YU, J. Appl. Electrochem. to be published in 1985

[5] : P. TAXIL J.less comm. Metals to be published in 1985

[6] : W. WEPPNER, R.A. HUGGINS J. Electrochem. Soc, 124, 1 569 (1977)

[7] : W. WEPPNER, R.A. HUGGINS J. Electrochem. Soc 125, 7 (1976)

[8] : F. LANTELME, S. BELAIDOUNI Electrochemica Acta 26, 1 225 (1981)

[9] : G.S. PICARD, Y.E. MOTTOT, B.L. TREMILLON Proc. of the 4th Intern. Symp. on Molten Salts San Francisco (1983)

[10]: M. HANSEN, K. ANDERKO Constitution of binary alloys Mc Graw Hill New York (1958)

[11]: A. BRENNER Electrodeposition of alloys vol I p 39, Acad. Press New York (1963)

[12]: F.B. SHENK Structure of binary alloys, Metallurgica, Moscou (1973)

[13]: S.N. NESTERENKO, L.L. MESHKOV, C. M. SOKOLOVSKAYA Vest. Mosk. Univ; Ser 2. Khim. 22, 305 (1981)

[14]: N.P. LYAKISHEV, Yu P. SNITKO, V.I. ALEKSEIEV Dokl. Akad. Nauk. SSSR 258, 1 404 (1981)

[15]: V.I. ALEKSEIEV, G.B. PETROV, G.V. SHERBETINSKII Iszv. Akd. Nauk SSSR Met 6, 59 (1958)

[16]: Y. MURAMATSU Trans. Nat. Res. Inst. Met. 17, 21 (1975)

[17]: V.N. PIMENOV, YU E. UGASTE, K.A. AKKUSHKAROVA Iszv. Akad. Nauk. SSSR Mer. 1, 184 (1977)

[18]: P.V. DANCKWERTS Trans-Faraday Soc. 46, 701 (1950)

[19]: W. JOST Diffusion in solids, liquids, gases p. 72 Academic Press New York (1960)

Compound	ζ (mV) at 950° C	ΔG (kcal/mole) this work	ΔG (kcal/mole) Ref. 13	ΔG (kcal/mole) Ref. 14
Ta Ni_3	$\simeq$ 245	- 28.2	- 26 $\pm$6.8	- 31.7
Ta Ni_2	200	- 25.7	- 22.9 $\pm$ 6.4	- 28.9
Ta Ni	45	- 15.4	-	-
Ta_2 Ni	20	- 8.8	-	-

Table I : GIBBS free energy of Tantalum Nickel compounds

t °C	850	900	940	1 000	1 050
$K_{Nb} \cdot 10^{10}$ ($cm^2 . sec^{-1}$)	0.58	1.12	1.93	3;46	6.91
p^s Nb (A. $sec^{1/2}$)	0.061	0.068	0.098	0.115	0.164
α Nb	0.54	0.62	0.58	0.65	0.65
$\tilde{D}$ Nb.10^{10} cm2. sec^{-1}	0.50	0.73	1.43	2.04	4.09

Table II : Determination of kinetic parameters of the intermetallic diffusion Niobium-Nickel

t °C	850	950	1 050
K Ta.10^{10} (cm 1.sec^{-1})	1.3	2.6	5.9
p^s Ta (A.$sec^{1/2}$)	0.094	0.150	0.23
α Ta	0.70	0.68	0.68
$\tilde{D}_{Ta}$ 10^{10} (cm2.sec^{-1})	0.65	1.42	2.98

Table III : Determination of kinetic parameters of the intermetallic difusion Tantalum-Nickel

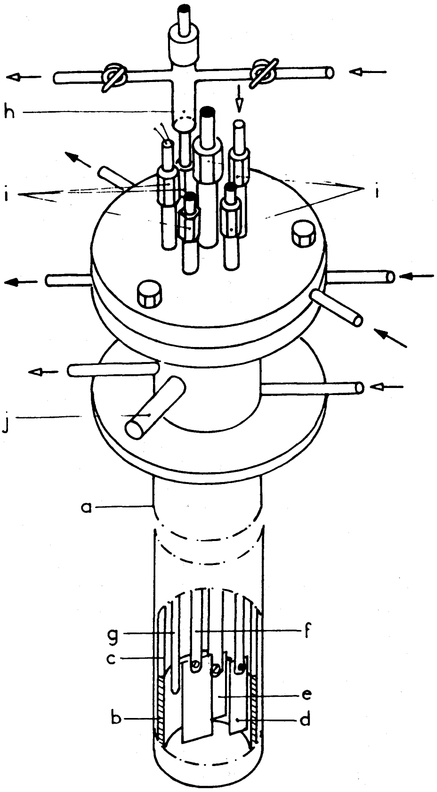

Fig 1 : The experimental cell :
a : Refractory steel lid ; b = nickel crucible ; c = nickel liner ; d : counter electrode ; e = working electrode ; f = reference electrode ; g = thermocouple ; h = addition of solute set up ; i = electrode fittings ; J = vacuum connection ; —▷ Argon : ➞ water cooling circuit

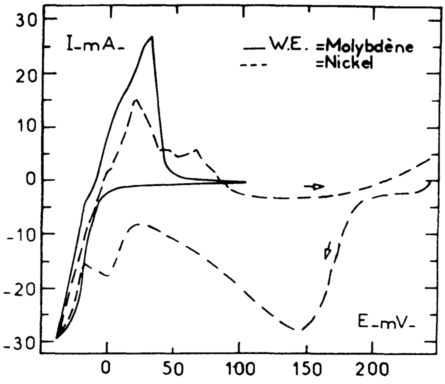

Fig 2 : Voltammogram of the LiF-NaF. K2 Ta F7 at 1 050° C on different cathode materials (Reference : tantalum foil ; potential sweep : 2 mV per sec.)

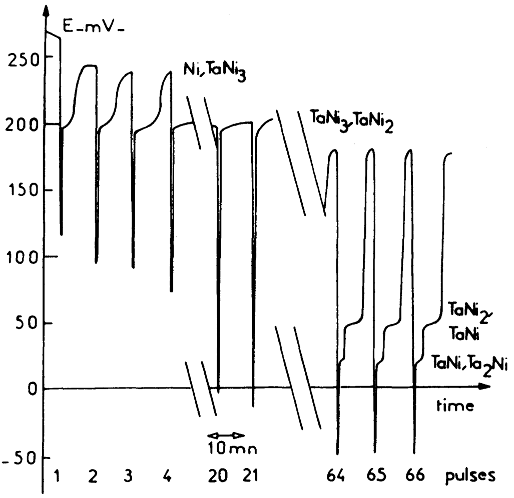

Fig 3 : Determination of the potentials of biphased equilibria of the tantalum nickel system by a galvanostatic intermittent electrolysis (t = 1 050° C ; i = 16 mA. cm^{-2} , duration of each pulse : 10 sec.)

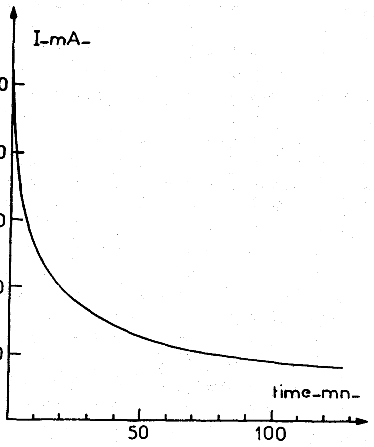

Fig 4 : Typical current-time observed during the metalliding of nickel with niobium (t = 1 050° C ; s = 3. 6 cm2)

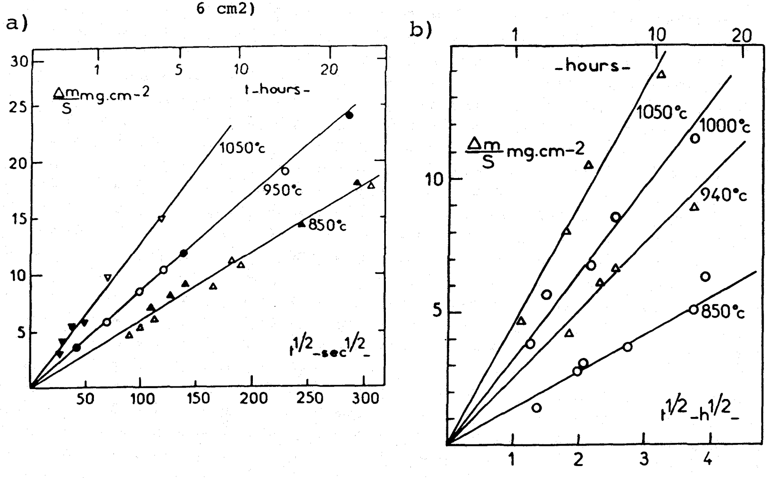

Fig 5 : Linear relationship between $\frac{\Delta m}{s}$ and the square root of time for metalliding of nickel with refractory metals at several temperatures
a) with tantalum
▼●▲ Electrodeposition-diffusion technique
▽○△ potentiostatic or galvanic technique
b) with niobium

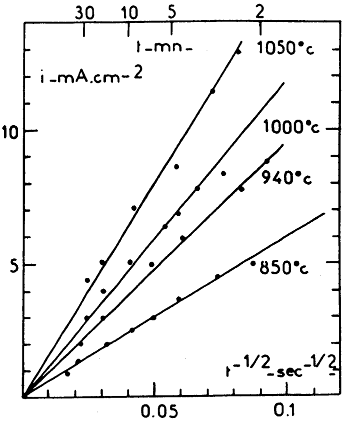

Fig 6 : Typical linear relationship between the metalliding current density and the reciprocal square root of time in the case of niobium-nickel alloy formation at various temperatures

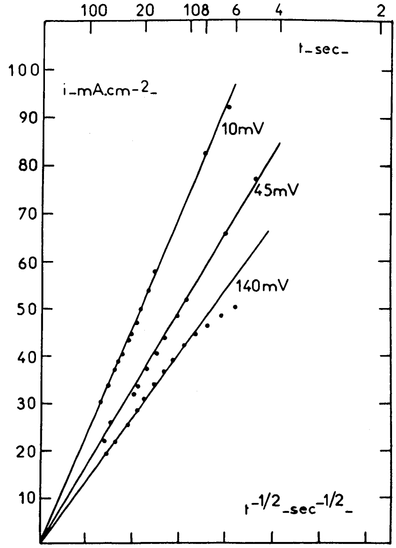

Fig 7 : Typical linear relationship between the metalliding current density and the reciprocal square root of time in the case of tantalum-nickel alloys formation at various potentials (temperature 950° C)

DOI: 10.1149/198601.0498PV

EFFECT OF MELT COMPOSITION ON THE REACTIONS OF THE ANTHRACENE RADICAL CATION IN $SbCl_3$-RICH MELTS: CHLORINATION VERSUS ARYL-ARYL COUPLING

D. M. Chapman,* G. P. Smith,** A. C. Buchanan, III,** and G. Mamantov*

*Department of Chemistry, The University of Tennessee
Knoxville, Tennessee 37996

**Chemistry Division, Oak Ridge National Laboratory
Oak Ridge, Tennessee 37831

ABSTRACT

In $SbCl_3$-$AlCl_3$-BPCl melts (BPCl = N-(1-butyl)pyridinium chloride) reactions of anthracene (AN) oxidized either coulometrically or with Sb(V) were highly selective in a way that depended on melt composition. In basic 60-19-21 m/o melts the only significant products were 9-chloroanthracene (CA) and 9,10-dichloroanthracene (DCA) with CA constituting >99% of the yield for partial oxidations up to 80%, while in acidic 60-21-19 m/o melts the only products found in significant amounts were condensed AN's, principally 2,9′-bianthracene. In $SbCl_3$-10 m/o BPCl oxidative chlorination occurred without condensation, while in $SbCl_3$-6 m/o KCl both chlorination and condensation took place. These results are discussed in terms of the effect of the acid/base properties of $SbCl_3$-rich melts on the manifold of reaction pathways available to AN radical cations. It is proposed that the half-regeneration pathway (an ECE process) is the primary chlorination route with a $Cl^-/SbCl_3$ complex we denote Cl^-(cpx) serving as the nucleophile. In basic melts the concentration of Cl^-(cpx) is substantial and chlorination reactions are dominant over condensation reactions while in acidic melts the concentration of Cl^-(cpx) is enormously suppressed so that chlorination reactions become much slower and condensation predominates.

INTRODUCTION

Solutions of aromatic compounds in anhydrous $SbCl_3$-rich melts undergo a variety of reactions, some of which are quite unusual and most of which are strongly influenced by the presence of relatively small amounts of added chloride ion acceptors (Lewis acids, such as $AlCl_3$) or chloride ion donors (Lewis bases, such as KCl) (1-3). In the present study we examined the effect that such donors and acceptors have on the reactions of anthracene (AN) radical cations in molten $SbCl_3$ modified by the presence of ~2 M N-(1-butyl)pyridinium tetrachloroaluminate ($BP[AlCl_4]$). We found the effect to be very large and in melts with excess BPCl to lead to an unusually selective chlorination reaction. (Structural formulae of AN and other relevant molecules are shown in Fig. 1).

The melts used in this study were prepared by mixing $SbCl_3$, $AlCl_3$ and BPCl in the following proportions: 60-19-21 m/o (mol %), respectively, and 60-21-19 m/o, respectively. These mixtures are liquid at 25°C and some of their physical and electrochemical properties have been reported (4). Since $AlCl_3$ and BPCl react virtually stoichiometrically, a 60-19-21 melt consists of $SbCl_3$, $BP(AlCl_4)$ and a small excess of BPCl (5). The Cl^- ions from the latter are complexed by $SbCl_3$ to give an entity we denote Cl^-(cpx). Likewise, a 60-21-19 melt consists of $SbCl_3$, $BP(AlCl_4)$ and a small excess of $AlCl_3$. The latter reacts with $SbCl_3$ to form $AlCl_4^-$ and a chloride-deficient species we denote $SbCl_2^+$(cpx). (For a discussion of the structures of these complexes see Ref. (6).) The 60-19-21 and 60-21-19 melts are, respectively, basic and acidic in the Lewis sense. AN has been shown to be stable over extended periods in basic $SbCl_3$-$AlCl_3$-BPCl melts, and to undergo a very slow melt-catalyzed decomposition in acidic compositions of this system (5).

EXPERIMENTAL

Materials. — The synthesis and purification of BPCl, and the purification of $SbCl_3$ and $AlCl_3$ have been described (5). $SbCl_5$ (Alfa, Ultrapure), AN (Reilly Tar and Chemical Corp., Scintillation Grade), 9-chloroanthracene (CA) (Pfaltz and Bauer, Inc.) and 9,10-dichloroanthracene, (DCA) (Pfaltz and Bauer, Inc.) were used without purification. The preparation of solvents and solutions has been described (5) and all handling of materials, including weighings, was performed in an argon-atmosphere glove-box in which H_2O and O_2 were kept below 2 ppm.

Procedures for experiments not involving product separation. — Cyclic voltammetry (CV) and spectroelectrochemistry (SE) were performed as described elsewhere (4). The reference electrode for all potentials reported here was $SbCl_3$-BPCl(liquid), $SbCl_3$(solid)/Sb. Optical spectra of a solution in the SE cell were measured before and after electrolysis with a Cary 14 spectrometer. The technique used to rapidly measure optical spectra during the chemical oxidation of AN was based on the use of an OMA-2 optical multichannel analyzer (EG&G model 1215), a linear diode array detector (EG&G model 1412), interfaced to a large-aperture flat-field spectrograph (Instruments SA model HR 320S). In particular, 31 spectra (visible region) were measured during a 180-s period immediately following the mixing of 0.54 mg of AN in 1.0 ml of a 60-19-21 melt with ~5 mg of $SbCl_5$ in 1.0

ml of a 60-19-21 melt at 40°C. The measurement of each spectrum required ~0.2 s.

Procedures for experiments involving product separation. — All macroscale reactions were performed in a glove box at 26 ± 2°C unless otherwise noted. Electrochemical oxidations of AN were done in a glassy carbon crucible that also served as the working electrode. The counter electrode was a large-area Pt foil contained in a compartment separated from the analyte by a medium porosity Pyrex frit. Oxidations of solutions of AN in 60-19-21 melts were carried out at a controlled potential of +0.625 V with currents in the range of 5-25 mA while stirring the melt. These solutions initially contained 50-80 mg of AN in 4 ml of 60-19-21.

The solution for the coulometric oxidation of anthracene in a 60-21-19 melt was prepared by mixing just prior to electrolysis 67 mg of AN dissolved in 4 ml of a basic 60-19-21 melt with 4 ml of an acidic 60-23-17 melt and then electrolyzing at +0.90 V. The duration of the electrolysis (1 h) was short enough so that no significant decomposition of unoxidized AN took place (5).

Chemical oxidations of AN by Sb(V) were performed in the following three ways: (A) $SbCl_5$ (~10 μl) was added by syringe directly to a reaction mixture containing anthracene. (B) $SbCl_5$ (~100 μl) was added to 2 ml of a 60-19-21 melt. Aliquots of this solution were then added by pipette to AN solutions. (C) Sb(V) was generated coulometrically by oxidation of an appropriate composition of basic solvent (slightly rich in $SbCl_3$) at +0.9 V such that the composition after electrolysis was ~60-19-21. Aliquots of this solution were then added to solutions of AN.

Separation and identification of products. — Reaction mixtures were removed from the glove box, hydrolyzed with 3 M HCl, and the organics were extracted into CH_2Cl_2. The CH_2Cl_2 layer was dried over $MgSO_4$, filtered and concentrated to 10 ml by rotary evaporation. Gas chromatography (GC), high-performance liquid chromatography (HPLC) and GC-mass spectrometry (GC-MS) were used to separate and identify reaction products. Authentic samples were used to calibrate GC retention times. HPLC fractions were quantitatively analyzed by UV-VIS spectroscopy. For chlorination reactions the mass balance between the total products collected after evaporation of CH_2Cl_2 (microbalance weighing) and the sum of the amounts of separated products (listed in Table I) agreed to within ±1%.

RESULTS AND DISCUSSION

Electrochemical and spectroscopic considerations. — The cyclic voltammetric (CV) and spectroelectrochemical (SE) behavior of molecular AN in 60-19-21 melts have been briefly reported (4). The onset of

Table I. Recovery of compounds after oxidation of anthracene in $SbCl_3$-$AlCl_3$-BPCl (60-19-21 m/o)

Method	Temp. (°C)	Recovery, m/o of initial AN AN	 CA	 DCA	 Total	n_{ox}/n_{Cl}[a]
Anodic	26	63	26	0	89	2.2
Sb(V), A[b]	26	65	31	0	96	1.7
Sb(V), B[b]	26	22	75	0.2	97	2.5
	100	19	80	0.9	100	—[c]
Sb(V), C[b]	26	75	21	0	96	2.2
	26	33	66	0.3	99	1.8
	26	23	77	0.6	101	1.8
	26	20	79	0.6	100	2.0
	26	2	93	3.5	99	2.2

[a] n_{ox} = equivalents of Sb(V) or faradays of current, n_{Cl} = moles of Cl substituted.

[b] Methods A, B and C for adding Sb(V) are described in the text.

[c] Not measured.

irreversible oxidation of a solution of AN in a 60-19-21 melt occurred at ~+0.6 V vs the $SbCl_3$-BPCl (liquid), $SbCl_3$ (solid)/Sb electrode for a scan rate of 0.2 Vs^{-1}, while the onset of solvent oxidation occurred at ~+0.8 V and corresponded to the conversion of Sb(III) to Sb(V). At a sweep rate of 0.2 Vs^{-1}, no well-defined reduction of oxidized substrate or reaction products was observed.

Previous SE studies (4) of the oxidation of AN in molten $SbCl_3$-10 m/o KCl at 75°C showed that, although the anthracene radical cation ($AN^{+\bullet}$) is very reactive in this melt, it is present at a sufficient concentration to be detected as a weak spectrum during the early stages of oxidation. In similar studies using 60-19-21 melts at 26°C (electrolysis at +0.825 V) the $AN^{+\bullet}$ spectrum was too weak to be observed against the background of AN and product spectra. From the present investigation (see below) we know that 9-CA is the stable reaction product when AN is oxidized in a 60-19-21 melt. We measured the spectrum of an authentic sample of this compound in a 60-19-21 melt (λ_{max} = 358, 378 and 396 nm) and found it to match the product spectrum in the previous SE study.

We also used fast optical spectroscopy to search for reactive intermediates when AN was oxidized by Sb(V) in a 60-19-21 melt. However, just as in the case of the SE measurements, the only absorptions found were those of AN and 9-CA.

Macroscale reactions. – A series of reactions was run in which AN in basic 60-19-21 m/o melts was partially oxidized either coulometrically or by Sb(V). The degree of oxidation was controlled by controlling the quantity of current passed or the amount of Sb(V) added. The results, summarized in Table I, are grouped by oxidation method. Oxidation by Sb(V), method B, was carried out at 26 and 100°C, as indicated. All other oxidations were at 26°C. Oxidations by Sb(V), method C, are listed in the order of increasing degree of oxidation, as indicated by the amount of unreacted AN recovered. The recovery of organics in these reactions was >95% in all but one case and the only substances found by HPLC were CA, DCA and unreacted AN. CA was by far the dominant product. DCA was produced in amounts of less than 1% for conversions up to 80%, and only 3.5% was produced for a conversion near 100%. In these reactions the number of electrons transferred per chlorine atom in the products (n_{ox}/n_{Cl}) was 2. As shown in Table I, four different methods of oxidation involving different sources of error all gave consistent results. The oxidation of CA by Sb(V) in a 60-19-21 melt at 26°C was also investigated. The sole product found was DCA and the n_{ox}/n_{Cl} ratio was 2. These results for both AN and CA are consistent with the stoichiometry in equation [1]

$$\mathrm{ArH} + \mathrm{Cl}^- \longrightarrow \mathrm{ArCl} + \mathrm{H}^+ + 2e^- \qquad [1]$$

where ArH is an aromatic molecule. The source of Cl^- and the fate of H^+ will be discussed later.

Such highly selective oxidative chlorination reactions are quite unusual. More commonly, when aromatic hydrocarbons are oxidized in the presence of halide ions, a variety of halogenated products result together with products of aryl-aryl coupling reactions (7-14). Of the latter we found none in 60-19-21 melts.

The oxidation of AN in an acidic 60-21-19 melt at 26°C pursued an entirely different course from that in a 60-19-21 melt, described above. Following a partial (50%) coulometric oxidation of AN in a 60-21-19 melt at +0.90V, 60 w/o (wt %) of the starting AN was recovered as AN and 17 w/o was recovered as 2,9′-BA. A substantial amount of more highly condensed material was also found but no chlorinated and only a very little hydrogenated (<1%) material could be detected. Hydroaromatics are among the decomposition products of AN in 60-21-19 melts and their very low yield in the present experiment provides verification that the decomposition of AN was insignificant during the relatively brief period required for the oxidation reaction. This result is not unexpected because the rate of decomposition is known to be very slow (5).

These experiments display the striking consequence of going from slightly on the basic side of the neutral (60-20-20) composition to slightly on the acidic side. Although the change in formal composition was small, the change in products was very large.

A few additional experiments were done in basic $SbCl_3$-rich melts with substantial Cl^-(cpx) concentrations but without a $AlCl_4^-$-containing electrolyte. For a $SbCl_3$-10 m/o BCPl melt at 100°C the products recovered following partial oxidation by Sb(V) were unreacted AN (26%), CA (50%) and DCA (11%), while a similar oxidation in $SbCl_3$-6 m/o KCl at 80°C yielded AN (53%), CA (13%), 2,9´-BA (10%), 1,1´-BA (10%), and small amounts of chlorinated bianthracenes.

Mechanistic considerations. — Mechanisms of the reactions of radical cations of aromatic substances have been intensively investigated in recent years with AN and substituted ANs frequently serving as model compounds, and nucleophilic substitution reactions receiving special emphasis. Key aspects of this chemistry are summarized in references (15-17). These studies have demonstrated that radical cations follow a multiplicity of reaction pathways. Two of these have been demonstrated for nucleophilic substitution, namely, half-regeneration and disproportionation. Both are plausible routes for chlorination in $SbCl_3$-rich melts although, for reasons given later, the disproportionation pathway may be inactive in the case of anthracene. There are also two proposed pathways for aryl-aryl coupling reactions, namely, radical-radical dimerization and radical-neutral dimerization, and both are plausible in $SbCl_3$-rich melts.

The half-regeneration pathway is summarized in Fig. 2. $AN^{+\bullet}$, generated in reaction [2], undergoes nucleophilic attack by a Cl^- donor to give the radical $I^\bullet$ in reaction [3]. This radical is oxidized further to I^+ in reaction [4] with the regeneration of half of the total AN. Finally, I^+ is deprotonated in reaction [5]. In the disproportionation pathway (Fig. 3), $AN^{+\bullet}$ disproportionates in reaction [6] to form the anthracene dication (AN^{++}) which undergoes nucleophilic attack in reaction [7] to form I^+. The latter deprotonates in reaction [5].

It is doubtful that AN^{++} in a 60-19-21 melt is stable with respect to oxidation of solvent Sb(III). For that reason the disproportionation pathway appears to be an improbable route for the oxidative chlorination of AN in this melt. The potential difference between the onset of oxidation of AN and the onset of oxidation of the 60-19-21 melt is only 0.2 V. This value is much smaller than the ~0.6-V difference between the peak potential for the irreversible oxidation of $An^{+\bullet}$ to An^{++} and that for the partially reversible oxidation of AN to $AN^{+\bullet}$ reported (18) in a CV study of the oxidation of AN in a molten $AlCl_3$-BPCl mixture with the mole ratio 1.2:1, respectively. Although this potential difference may be smaller in a 60-19-21 melt, it is unlikely to be smaller by a factor as great as three as would be required for AN^{++} to be stable with respect to solvent oxidation. For example, the range of values for the difference between the formal potentials for the oxidation of diphenylanthracene (DPA) to $DPA^{+\bullet}$ and that for $DPA^{+\bullet}$ to DPA^{++} in various aprotic solvents is 0.34 to 0.48 V (19).

Let us consider the role of the melt in the chlorination reaction. The Cl^-(cpx) complex is the strongest Cl^- donor in a $SbCl_3$-rich melt while $SbCl_2^+$(cpx) is the strongest acceptor. The concentrations of these species are related through equation [8]

$$SbCl_3 \rightleftarrows SbCl_2^+(cpx) + Cl^-(cpx) \qquad [8]$$

The ion product constant (K_i) for this reaction is not accurately known but is unquestionably very small. Conductivity data for molten $SbCl_3$ indicate that $K_i \leq 3 \times 10^{-11}$ M^2 at 99°C (20). Assuming that K_i is this small or smaller for $SbCl_3$-$AlCl_3$-BPCl melts at 26°C, it can be shown that

$$\frac{\text{Conc. of } Cl^-(cpx) \text{ in 60-19-21}}{\text{Conc. of } Cl^-(cpx) \text{ in 60-21-19}} \geq 10^9 \qquad [9]$$

Therefore, in a basic 60-19-21 melt the probable Cl^- donor is Cl^-(cpx) and equation [3] becomes equation [10].

$$AN^{+\bullet} + Cl^-(cpx) \rightleftarrows I^\bullet \qquad [10]$$

Given the facts that $SbCl_3$ is the solvent with a virtually constant activity, that $AN^{+\bullet}$ and Cl^- are dilute, and that the ionic strength is fixed by the concentrated spectator electrolyte, $BPAlCl_4$; it can be shown from equation [10] that the $I^\bullet/AN^{+\bullet}$ ratio is approximately proportional to the Cl^-(cpx) concentration. In an acidic melt the Cl^-(cpx) concentration is so small compared with that of $SbCl_3$, that if chlorination occurred, $SbCl_3$ would be the more probable donor and equation [3] would take the form of equation [11]

$$AN^{+\bullet} + SbCl_3 \rightleftarrows I^\bullet + SbCl_2^+(cpx) \qquad [11]$$

However, [10] and [11] are thermodynamically related through [8] in such a way that the $I^\bullet/An^{+\bullet}$ concentration ratio is proportional to the Cl^-(cpx) concentration irrespective of what the actual donor may be. (Physically, this is a consequence of the presence in acidic melts of $SbCl_2^+$(cpx) with which any other Cl^- acceptor must compete.) Thus, equation [9] implies equation [12]

$$\frac{\text{I}^{\bullet}/\text{AN}^{+\bullet} \text{ in 60-19-21}}{\text{I}^{\bullet}/\text{AN}^{+\bullet} \text{ in 60-21-19}} > 10^9 \qquad [12]$$

It follows that chlorination reactions which proceed readily in basic melts will be very much slower in acidic melts.

A consideration of the deprotonation reaction [5] does not alter the above conclusion. In a basic melt Cl^-(cpx) is the most plausible proton acceptor, yielding HCl as the end product. In acidic melts, as discussed below, experiments show that unreacted AN is the proton acceptor with the 9H-anthracenium ion being the final product. Combining these considerations with equation [1] we obtain equations [13] and [14] (Fig. 4) as the net oxidative chlorination reactions for AN and CA, respectively, in basic melts.

The experiments show that when AN is oxidized by Sb(V) in a 60-19-21 melt the almost exclusive product is CA until most of the AN is consumed even though Sb(V) readily oxidizes CA to DCA in the absence of AN. Almost certainly CA oxidizes at a higher potential than AN so that reaction [15] may provide an effective means of reducing $CA^{+\bullet}$ in the presence of AN and thereby blocking DCA formation. Another possibility is that CA oxidizes more slowly than AN.

$$CA^{+\bullet} + AN \longrightarrow CA + AN^{+\bullet} \qquad [15]$$

The pathways leading to condensed products are illustrated in Fig. 5 (radical-radical dimerization) and Fig. 6 (cation-neutral dimerization). Both pathways involve the formation of very strong protic acids, II in reaction [16], V in [19], and VII in [20]. The manner in which such acids deprotonate during the oxidative condensation of AN in acidic $SbCl_3$-rich melts was demonstrated in a study in which $SbCl_3$-10 m/o $AlCl_3$ served as the medium (21). It was shown by means of in situ ^{1}H-NMR that unreacted AN quantitatively captures these protons to form the 9H-anthracenium ion (IV) as shown in equation [18]. Although AN is a very weak protic base, it is apparently the strongest available and in $SbCl_3$-10 m/o $AlCl_3$ it proved to be quite stable at elevated temperatures. It has also been shown (5) that IV is stable in a 60-22-18 melt. When such melts are quenched with aqueous HCl, hydrolysis of IV regenerates AN (21). We anticipate a similar behavior in a 60-21-19 melt so that prior to quenching, IV was a stable product and the AN recovered after quenching included the hydrolysis product in addition to unreacted AN.

The above considerations suggest that in acidic $SbCl_3$-rich melts the rate of anthracene chlorination is greatly suppressed by the virtual absence of an effective Cl^- donor and that aryl-aryl coupling reactions take over. A prior study of the ESR spectra of $AN^{+\bullet}$ in $SbCl_3$-8 m/o $AlCl_3$ melts indicated that these coupling reactions are quite sluggish (22). The oxidation of 1-10 mM solutions of AN in this melt gave strong, well-resolved spectra of $AN^{+\bullet}$ that were very persistent at temperatures as high as 125°C. In basic melts with their substantial Cl^-(cpx) concentrations chlorination becomes very much faster. In $SbCl_3$-10 m/o BPCl at 100°C, and 60-19-21 at both 26 and 100°C this effect was so strong that only chlorinated products were found. On the other hand in $SbCl_3$-6 m/o KCl at 75°C chlorination and condensation proceeded at similar rates and it is interesting to note that previous SE studies (4), described above, indicate that $AN^{+\bullet}$ reacts more slowly in $SbCl_3$-10 m/o KCl at 75°C than in a 60-19-21 melt at 26°C. There is also a known case in which a condensation reaction is the dominant mode in $SbCl_3$-10 m/o KCl (3). In this case the substrate was 1,2-di-9-anthrylethane and the coupling was intramolecular.

Concluding remarks. — This study demonstrates a close coupling between the acid/base properties of $SbCl_3$-rich melts and the reaction pathways followed by solute AN radical cations. This coupling is rationalized in terms of the wide swing in Cl^- donor strength that occurs about the neutral point of these melts and the effect that this has on the rates of chlorination reactions in competition with condensation reactions. This study also demonstrates that in basic melts other compositional factors including the presence or absence of $BP(AlCl_4)$ and K^+ exert a strong control over the selectivity of chlorination reactions to such a degree that a single isomer can be produced in substantial yields, virtually free of other products. In most other media radical cation halogenations are rarely this selective. Such selectivity suggests potential uses for $SbCl_3$-rich melts in organic synthesis.

Acknowledgment

The authors are grateful to M. V. Buchanan for GC-MS measurements. This research was carried out at the Oak Ridge National Laboratory and was sponsored by the Division of Chemical Sciences, Office of Basic Energy Sciences, U.S. Department of Energy under contract DE-AC05-84OR21400 with Martin Marietta Energy Systems, Inc. DMC was a recipient of an Atlantic-Richfield Foundation supplemental fellowship.

REFERENCES

1. G. P. Smith, A. C. Buchanan, III, A. S. Dworkin, M. Sørlie, and M. V. Buchanan, in "Proceedings of the Third International Symposium on Molten Salts," G. Mamantov, M. Blander, and G. P. Smith, Editors, p. 393, The Electrochemical Society Softbound Proceedings Series, Pennington, NJ (1981).

2. A. C. Buchanan, III, A. S. Dworkin, and G. P. Smith, in "Proceedings of the Fourth International Symposium on Molten Salts," M. Blander, D. S. Newman, M.-L. Saboungi, G. Mamantov, and K. Johnson, Editors, p. 234, The Electrochemical Society Softbound Proceedings Series, Pennington, NJ (1984).

3. A. C. Buchanan, D. M. Chapman, and G. P. Smith, *J. Org. Chem.*, **50**, 1702 (1985).

4. D. M. Chapman, G. P. Smith, M. Sørlie, C. Petrovic, and G. Mamantov, *J. Electrochem. Soc.*, **131**, 1609 (1984).

5. S. P. Zingg, A. S. Dworkin, M. Sørlie, D. M. Chapman, A. C. Buchanan, III, and G. P. Smith, *J. Electrochem. Soc.*, **131**, 1602 (1984).

6. G. P. Smith, A. C. Buchanan, III, M. Sørlie, and G. Mamantov, in "Proceedings of the Fourth International Symposium on Molten Salts," M. Blander, D. S. Newman, M.-L. Saboungi, G. Mamantov, and K. Johnson, Editors, p. 109, The Electrochemical Society Softbound Proceedings Series, Pennington, NJ (1984).

7. P. Kovacic, in "Friedel-Crafts and Related Reactions," G. Olah, Editor, Vol. 4, p. 111, Interscience Publishers, New York, NY (1965).

8. L. Eberson and K. Nyberg, *Acta Chem. Scand.*, **B32**, 235 (1978).

9. I. Tanimoto, K. Kushioka, T. Kitagawa, and K. Maruyama, *Bull. Chem. Soc. Jpn.*, **52**, 3586 (1979).

10. A. Ledwith and P. J. Russell, *J. Chem. Soc., Perkin 2*, 1503 (1975).

11. J. Burdon and I. W. Parsons, *Tetrahedron*, **36**, 1423 (1980).

12. T. Sugiyama, *Bull. Chem. Soc. Jpn.*, **55**, 1504 (1982).

13. J. F. Carpenter, L. H. Ekes, P. F. King, H. A. Mariani, M. M. Zadeh, R. F. O'Malley, and V. J. Roman, *J. Electrochem. Soc.*, **130**, 2170 (1983).

14. S. R. Ellis, D. Pletcher, W. N. Brooks, and K. P. Healy, *J. Appl. Electrochem.*, **13**, 735 (1983).

15. H. N. Blount and J. F. Evans, in "Characterization of Solutes in Nonaqueous Solvents," G. Mamantov, Editor, p. 105, Plenum Press, New York, NY (1978).

16. O. Hammerich and V. D. Parker, Acta Chem. Scand., **B36**, 519 (1982).

17. V. D. Parker, Acc. Chem. Res., **17**, 243 (1984).

18. J. Robinson and R. A. Osteryoung, J. Amer. Chem. Soc., **101**, 323 (1979).

19. J. O Howell and R. M. Wightman, J. Phys. Chem., **88**, 3915 (1984).

20. E. C. Baughan, in "The Chemistry of Nonaqueous Solvents," J. J. Lagowski, Editor, Vol. IV, p. 145, Academic Press, New York, NY (1976).

21. A. C. Buchanan, III, A. S. Dworkin, and G. P. Smith, J. Am. Chem. Soc., **102**, 5262 (1980).

22. A. C. Buchanan, III, R. Livingston, A. S. Dworkin, and G. P. Smith, J. Phys. Chem., **84**, 423 (1980).

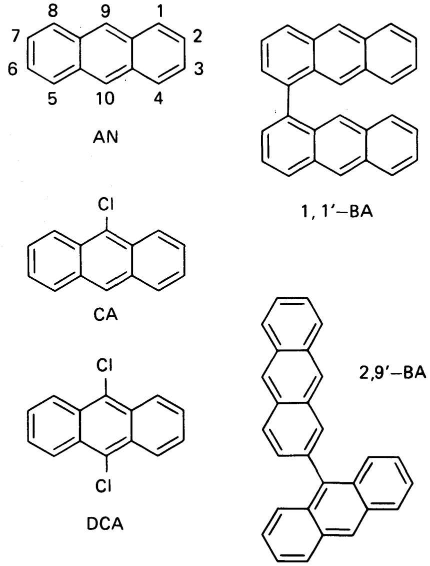

Figure 1.
Structures and notations for anthracene (AN) and the principle reaction products, 9-chloroanthracene (CA), 9,10-dichloroanthracene (DCA), 1,1´-bianthracene (1,1´-BA) and 2,9´-bianthracene (2,9´-BA).

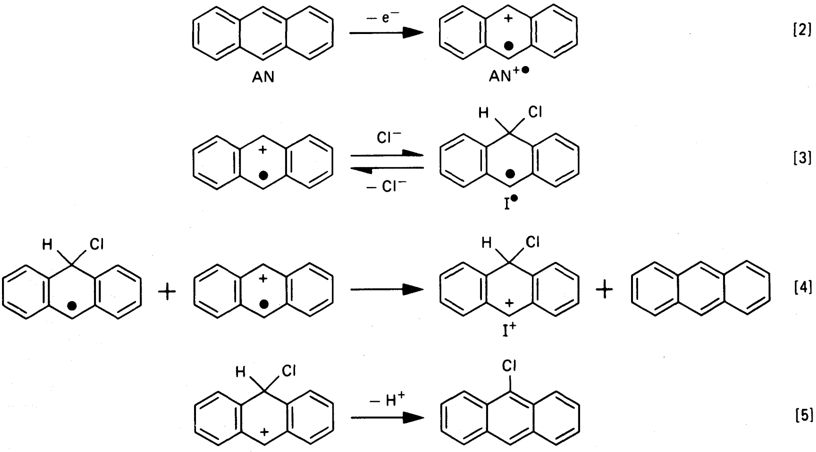

Figure 2. The half-regeneration pathway for oxidative chlorination.

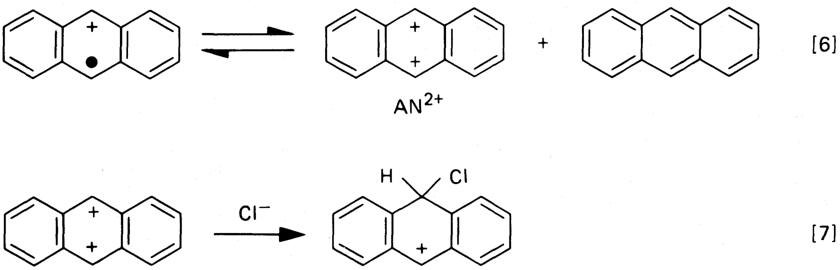

Figure 3. These reactions, preceded by [2] and followed by [5] (Fig. 2) form the disproportionation pathway for oxidative chlorination.

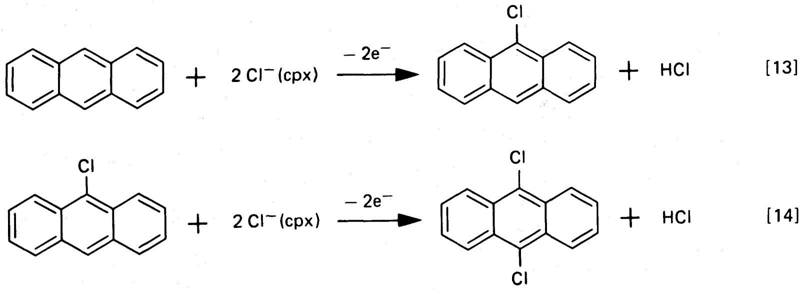

Figure 4. Reaction stoichiometries for the two observed oxidative chlorination reactions in basic melts.

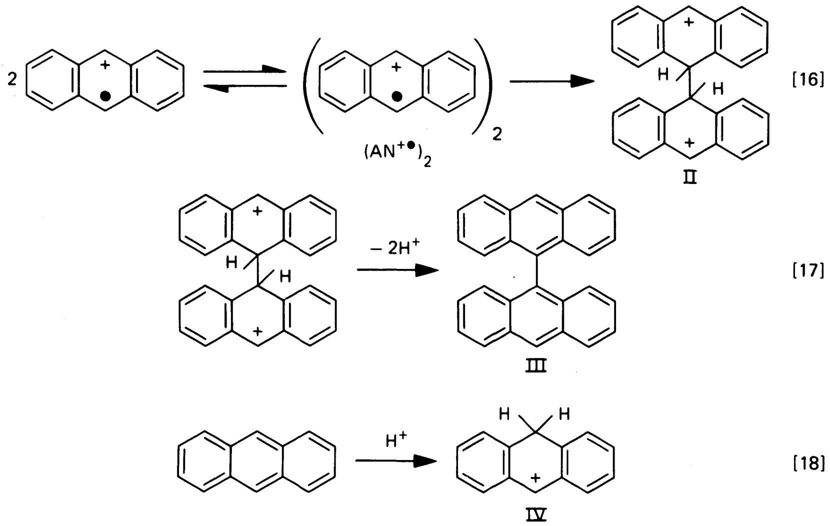

Figure 5. The radical-radical dimerization pathway to bianthracene.

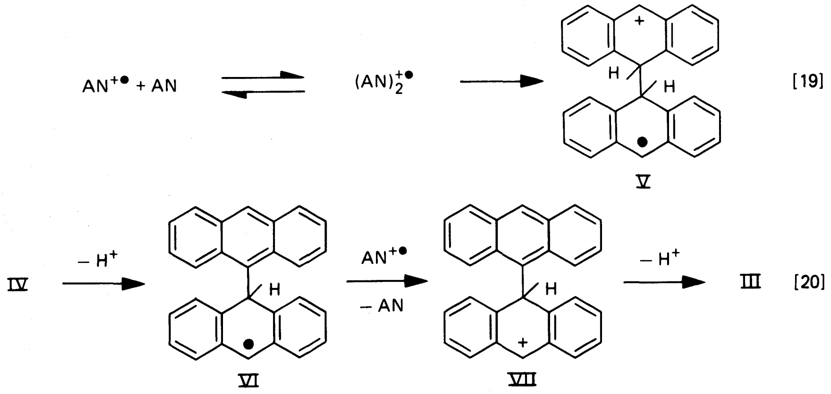

Figure 6. The cation-neutral dimerization pathway to bianthracene.

DOI: 10.1149/198601.0512PV

COMPARISON OF PHOSGENE, CHLORINE, AND HYDROGEN CHLORIDE AS REAGENTS FOR CONVERTING MOLTEN $CaO \cdot CaCl_2$ TO $CaCl_2$

Keith W. Fife
David F. Bowersox
Egan D. McCormick

Plutonium Metal Technology Group
Division of Materials Science and Technology
Los Alamos National Laboratory
Los Alamos, New Mexico 87545

ABSTRACT

One method used at Los Alamos for preparing impure plutonium metal from the impure oxide is batch reduction with calcium metal at 850°C in a $CaCl_2$ solvent. The solvent salt from this reduction is currently discarded as low-level radioactive waste only because it is saturated with the CaO by-product. We have demonstrated a pyrochemical technique for converting the CaO to $CaCl_2$, thereby incorporating solvent recycle into the batch reduction process. We discuss the effectiveness of HCl, Cl_2, and $COCl_2$ as chlorinating agents and present initial data on regenerating and recycling actual, spent solvent salts.

Introduction

Impure plutonium metal is produced by the pyrochemical reduction of impure plutonium dioxide using molten calcium metal in a liquid calcium chloride solvent (1).

$$PuO_2 + 2Ca° \xrightarrow[850°]{11CaCl_2} Pu° + 2CaO\ 11CaCl_2 \qquad (1)$$

This direct oxide reduction (DOR) process is a batch operation in which the solvent salt performs a variety of functions during the reaction: it acts as a heat sink during the exothermic reduction of PuO_2, it provides a medium to control the reaction, and it dissolves the CaO by-product to 18 mol% (10 wt%), which permits good plutonium-metal coalescence after the reduction is complete.

Because of the limited solubility of CaO in $CaCl_2$, the solvent salts are discarded as low-level radioactive waste after each reduction. Developing a procedure to regenerate the spent salts offers numerous advantages (2); briefly they include

- reduction of process waste from DOR,
- improvement in overall process yields,
- potential for producing a pure solvent salt,
- potential for producing a pure plutonium product from pure reagents,
- potential for optimizing the DOR process, and
- potential for oxidizing excess calcium metal to meet WIPP disposal criteria.

We have initiated a program to define a process that addresses each of these advantages and also determines the feasibility of DOR salt regeneration and recycle. This paper summarizes our experience in salt recycle, in both radioactively hot and cold settings.

In theory, the regeneration of spent DOR salts could be accomplished through any of three approaches: the electrolytic reduction of CaO and subsequent recovery of the calcium metal (3), precipitation of CaO, or the chemical conversion of CaO to $CaCl_2$ using an appropriate chlorinating agent. Preliminary work at Argonne National Laboratory on the electrolytic reduction of CaO was promising, but it was felt too much time was required for proper cell design and development. Precipitation studies were unsuccessful because of poor phase separation and incomplete CaO solute removal from the $CaCl_2$ solvent. The final approach, CaO conversion to $CaCl_2$ by chlorination, appeared promising from initial small-scale experiments.

This initial success encouraged us to scale the system to nearly full scale (3-5 kg spent salt) and to begin a program investigating the parameters necessary for spent-salt recycle.

Because of our long-range goal to convert the DOR process from a purely batch to a semicontinuous operation by regenerating and recycling spent salts, we felt it necessary to accomplish regeneration of 5 kg salt in approximately 2 h. This regeneration would provide the basis for further process development.

The success of this recycle program depends on maintaining or improving salt quality during regeneration. Plutonium is an active metal solvent and tends to strip metal impurities from salt (Table I). This reaction is the principal reason the DOR process has not been able to produce a "pure" metal (>99.9%) from "pure" reagents. If we can regenerate a salt while maintaining or improving its quality, then pure-metal production from this process is more feasible. We have selected three major analytical determinations to help evaluate the final salt: it will be necessary to maximize CaO rechlorination, to minimize residual oxides present in the salt (oxygen is a calcium consumer in DOR), and to minimize or eliminate the introduction of metallic impurities into the salt.

TABLE I. ESTIMATES OF ELEMENT SOLUBILITIES IN PLUTONIUM AT 800°C (4)

Element	Atom %	Wt%	Element	Atom %	Wt%
Silver	6.5	2.6	Niobium	1.5	0.6
Aluminum	10.0	1.2	Nickel	45.0	16.7
Gold	7.0	5.8	Lead	14.0	12.4
Beryllium	7.0	0.3	Platinum	9.0	4.2
Carbon	2.3	0.1	Rhodium	19.0	9.2
Cadmium	1.0	0.5	Silicon	7.5	0.9
Cobalt	38.0	13.1	Tin	0.9	0.4
Copper	52.0	22.4	Titanium	22.5	5.5
Iron	27.0	8.0	Thulium	4.1	2.9
Gallium	23.0	8.0	Vanadium	1.5	0.3
Hafnium	11	8.4	Tungsten	0.01	0.01
Magnesium	22.5	2.9	Yttrium	16.0	6.6
Manganese	30.8	9.3	Zinc	30.0	10.5
Molybdenum	2.8	1.1	Zirconium	5.4	2.1

Regeneration Procedure

All research and process development was conducted in radioactively cold settings using synthetic, spent, DOR salt ($CaCl_2$ 10 wt% CaO 1 wt% Ca°). We did not make any attempt to simulate the trace plutonium metal that would be present in the actual salts.

The method used in all experiments was to place 3.0 kg salt in a 15-cm-o.d. by 38-cm-tall vitrified magnesia crucible that was nested in a stainless steel containment can inside a stainless steel furnace tube (Fig. 1). After placing an argon atmosphere above the salt, the apparatus was resistance heated to 850°C using a Lindberg Model 6015S furnace. The melt was sparged with a chlorinating agent (HCl, Cl_2, or $COCl_2$) for a fixed time at a fixed flow rate. Samples were withdrawn from the melt initially and at selected intervals during the regeneration cycle to determine CaO conversion profiles and residual oxygen profiles as functions of gas contact time. After chlorination, the system was purged with argon and the salt cooled. All off-gas from the system was directed through a caustic scrubber system before venting to the atmosphere.

Results

It is possible to write several thermodynamically stable chemical reactions describing the stoichiometry of CaO and calcium metal conversion to $CaCl_2$ using HCl, Cl_2, and $COCl_2$ (5,6). The kinetics of these reactions, however, are not understood nor do we anticipate any future investigations into this area. For the three regenerant gases, general relationships can be written to help describe the reactions:

$$\mathrm{Ca + CaO + 4HCl \rightarrow 2CaCl_2 + H_2O + H_2} \qquad -136\ \text{kcal/molCaO} \qquad (2)$$
$$\mathrm{Ca + 2CaO + 3Cl_2 \rightarrow 3CaCl_2 + O_2} \qquad -\ 71\ \text{kcal/molCaO} \qquad (3)$$
$$\mathrm{Ca + CaO + 3Cl_2 \rightarrow 2CaCl_2 + Cl_2O} \qquad -154\ \text{kcal/molCaO} \qquad (4)$$
$$\mathrm{Ca + 4CaO + 6Cl_2 \rightarrow 5CaCl_2 + 2ClO_2} \qquad -\ 47\ \text{kcal/molCaO} \qquad (5)$$
$$\mathrm{Ca + CaO + 2COCl_2 \rightarrow 2CaCl_2 + CO_2 + CO} \qquad -249\ \text{kcal/molCaO} \qquad (6)$$
$$\mathrm{Ca + 2CaO + 2COCl_2 \rightarrow 2CaCl_2 + CaCO_3 + CO} \qquad -211\ \text{kcal/molCaO} \qquad (7)$$

Additional phosgene reactions that incorporate the oxychlorine and oxygen products from the chlorine reactions can also be written.

Regeneration experiments with phosgene, chlorine, and anhydrous hydrogen chloride indicate that CaO alkalinity can be effectively reduced by any of the three reagents (Fig. 2). But since residual oxygen in final salt will react with calcium metal in the recycle step to form CaO, the residual oxygen profiles shown in Fig. 3 are better indicators of regeneration efficiency. These profiles illustrate the difficulty in removing residual oxygen from the system. Regeneration with chlorine results in the best performance, followed by HCl and then $COCl_2$. Possible explanations for these results may be the oxygenated by-products from the potential reactions. In most cases, these by-products have low boiling points (<100°C) so that their vapor pressures at 850°C are large. Their solubilities in molten $CaCl_2$, however, are unknown. This solubility or the possibility of secondary reaction may contribute to the slower oxygen removal rates exhibited by the HCl or $COCl_2$.

When considering $COCl_2$ as the regenerant, CO_2 and $CaCO_3$ are proposed by-products in the conversion reactions. Originally, we felt the carbonate reaction was predominant because of the slow oxygen removal rate and also because of the carbonate profiles shown in Fig. 4. This figure shows the dependence of carbonate concentration (as determined by carbonate specific-ion electrode) on the regenerant gas flowrate. We felt the carbonate concentations peaked during regeneration as a result of $CaCO_3$ formation and then decomposed (calcite decomposes $\sim$900°C). Only after x-ray diffraction analysis on the salt indicated the absence of $CaCO_3$ did we consider dissolved CO_2 as both the carbon and oxygen source illustrated in Figs. 3 and 4. Additional tests are being conducted to help verify this new assumption.

In either case, the presence of carbon in reagents is detrimental to the success of pyrochemical operations because of the carbon's ability to form plutonium carbide, a high-melting alloy at relatively low carbon concentrations. This compound is extremely difficult to separate pyrochemically. The resulting stability of carbon and oxygen in phosgene-regenerated salts and also the extreme toxicity and corrosiveness of the reagent have encouraged us to eliminate phosgene as a candidate for DOR salt-regeneration experiments. Hydrogen chloride and chlorine, however, were evaluated further and are currently undergoing comparison in regenerating the actual, spent, DOR salts.

Because of our desire to rapidly regenerate the salt (∿5 kg in ∿2 h), we initiated an optimization program for HCl and Cl_2 to maximize regeneration and minimize residual oxygen. Because we felt constrained to use existing equipment (our reaction vessel configuration was fixed), we concentrated on optimizing our gas/solution contact mechanism. Operating at high gas flow rates while minimizing solution splashing would give us efficient regeneration in the minimum time and with minimum salt loss. We are currently using an open-end ceramic tube for gas introduction and have been able to effectively regenerate 5+ kg in 2 h using chlorine at flow rates between 3 and 5 ℓ/min. Before deciding on open-end tubing, we made several attempts at constructing suitable gas dispersion devices. Our high-porosity metal frits and perforated metal and ceramic tubes all suffered from mechanical failure or severe corrosion.

Figures 5 and 6 illustrate the effect of HCl flow rate on CaO conversion and residual oxygen during the course of typical regenerations. The trend of these curves is not surprising because an increase in flow rate results in quicker regeneration. Profiles using chlorine are similar, though its performance is much improved over HCl as was shown previously in Fig. 2.

Semiqualitative metal analyses were performed on all of our regenerated salts to determine the extent of dissolution of wetted parts and other internal portions of the apparatus shown in Fig. 1. In all cases there was evidence of salt contamination by constituents of the apparatus. Figures 7 and 8 show the corrosive effects of HCl, Cl_2, and $COCl_2$ on the wetted ceramic parts. For the gas introductory tube we used alumina or vitrified magnesia, and the reaction vessel was always vitrified magnesia. Also in many cases we have seen high levels (500-1000 ppm) of stainless steel components present in the salt (Fe, Cr, Ni, Cu, Mn). We feel this is due, in part, to the circulation of corrosive off-gas in the vapor space above the salt before it actually vents from the system.

We have been successful, however, in minimizing contamination from stainless steel by gold-plating the top furnace flange, by raising the magnesia reaction vessel as high in the furnace tube as possible, and by introducing an argon flush line to the system to sweep the vapor space and force the off-gas out of the system as quickly as possible. The alumina contamination can be eliminated by changing to a magnesia sparge tube. The magnesia contamination, however, is inevitable but does not pose a major problem at this time. It reduces to magnesium during the recycle step by reacting with the calcium, volatilizes, and collects in the cooler vapor space of the furnace tube.

Results of Actual DOR Salt Regeneration and Recycle

As a result of experiments using synthetic spent salts, we have adapted gloveboxes in our plutonium facility and are currently demonstrating DOR salt recycle on a full-scale batch basis. We regenerate 5.0 to 5.5 kg salt in ∿2 h with chlorine or HCl at flow rates between 3 and 5 ℓ/min. At these flow rates, both reagents effectively regenerate the salt. Chlorine, however, produces the better-quality salt as indicated by its regeneration performance and subsequent recycle performance.

The presence of trace plutonium in the salts does not appear to effect regeneration in any way. The excess free calcium metal, however, does not behave as we expected. We felt the free calcium would react quickly with the regenerant gas and be converted to $CaCl_2$ early in the process. Our experience is that the buoyant calcium is effectively pushed to the wall of the reaction vessel by the gas bubbling through the salt. As this occurs, its ability to contact the chlorinating agent is severely reduced and it goes through the regeneration procedure partially intact. The absence of total reaction is not a major problem; it only reduces the possibility of relying on this technique to fix or oxidize the calcium to meet WIPP criteria for ultimate disposal.

Plutonium metal produced from the recycle step has proven to be of larger quantity and better quality than we originally expected. Metal yields from our recycle step have averaged slightly better than in production DOR (96% vs 94%). This higher yield is due in part to our using a consistent, high-quality PuO_2 as opposed to production DOR using the lesser-quality foundry grade PuO_2 in the process.

We are using the high-quality feed to minimize variables in the process and allow us to better evaluate regeneration and recycle and also to evaluate the potential for pure-metal production from pure reagents. Several DOR runs using this feed material have produced metal products whose plutonium content exceeds 99%. Metal impurities are essentially the ones we previously discussed -- stainless steel components and ceramic components. This product from DOR does not meet plutonium product specifications and will need further treatment. We are currently generating several kilograms of this metal to evaluate in subsequent processing steps.

Conclusions

- Regeneration of actual, spent, DOR salt can be effectively accomplished with either HCl or chlorine.
- Based on regeneration experiments using synthetic spent salts, phosgene was eliminated from further consideration as a regenerant gas because of carbon and oxygen stability in the product salt.
- We have demonstrated the ability to effectively regenerate 5+ kg

of spent DOR salt in ∿2 h using chlorine at flow rates between 3 and 5 ℓ/m.

- Calcium metal appears to be incompletely converted to $CaCl_2$ during regeneration.
- Plutonium metal yields and metal quality using recycled salt are comparable to results from the production DOR process.

Future Topics

For the short term (calendar 1985), we are planning our first series of tests in converting the DOR process from a purely batch system to a semicontinuous system. We will also continue with our materials compatibility studies and our modest equipment-development program.

For the longer term, our goal is to develop a semicontinuous DOR process. In order to accomplish this we must first answer questions concerning materials compatibility, equipment design and development, and off-gas handling.

Acknowledgment

Without the help of dedicated technicians who routinely performed and commented on these experiments, the development of this program would have suffered. For these reasons and more, we would like to thank A. E. Buchholz, W. J. Chavez, W. K. Drennon, D. W. Anderson, and J. Y. Coulter for their contributions in regenerating the synthetic spent salts; and also J. J. Simpson and C. C. Davis for their contributions in regenerating and recycling the actual spent salts.

REFERENCES

1. L. J. Mullins, D. C. Christensen, and B. R. Babcock, "Fused Salt Processing of Impure Plutonium Dioxide to High-Purity Plutonium Metal," Los Alamos National Laboratory report LA-9154-MS (January 1982).

2. M. S. Coops and D. F. Bowersox, "Nonaqueous Processing Methods," Los Alamos National Laboratory report LA-10169-MS (September 1984).

3. R. E. Barletta et al., "Molten Salt Recycle, Electrolysis of CaO in Molten Salt," Argonne National Laboratory report ANL-79-99 (April 1979).

4. F. H. Ellinger, W. H. Minor, D. R. O'Boyle, and F. W. Schonfeld, "Constitution of Plutonium Alloys," Los Alamos Scientific Laboratory report LA-3870 (December 1968).

5. R. C. Weast, Ed. CRC Handbook of Chemistry and Physics (CRC Press, Boca Raton, Florida, 1985, 65th Ed.), pp. D52-D93.

6. K. K. Kelley, "Contributions to the Data on Theoretical Metallurgy, XIII; High Temperature Heat Content, Heat Capacity, and Entropy Data for the Elements and Inorganic Compounds," USBM Bulletin 584 (1960).

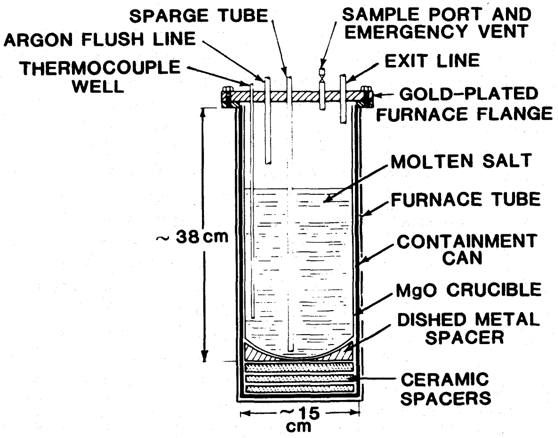

Fig. 1. Apparatus for spent-salt regeneration.

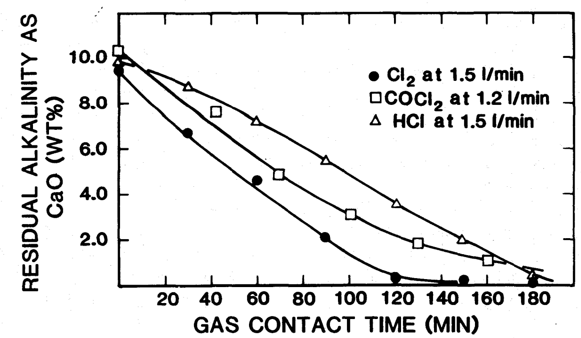

Fig. 2. Residual calcium oxide in regenerated salts.

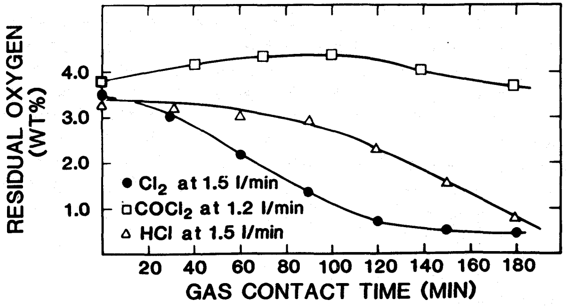

Fig. 3. Residual oxygen in regenerated salts.

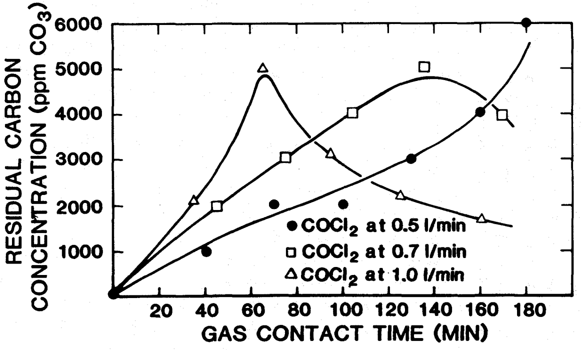

Fig. 4. Residual carbon (as CO_3) in regenerated salts as a function of phosgene flow rate.

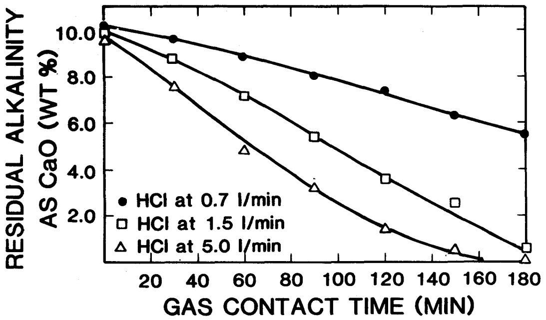

Fig. 5. Residual calcium oxide in regenerated salts as a function of HCl flow rate.

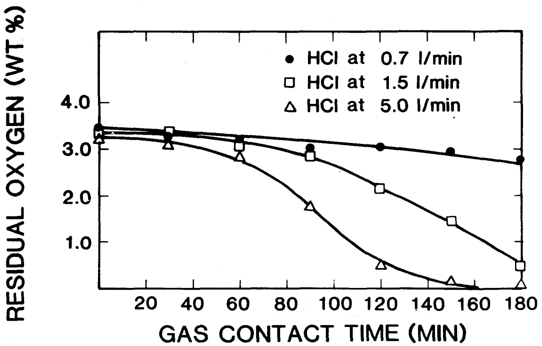

Fig. 6. Residual oxygen in regenerated salts as a function of HCl flow rate.

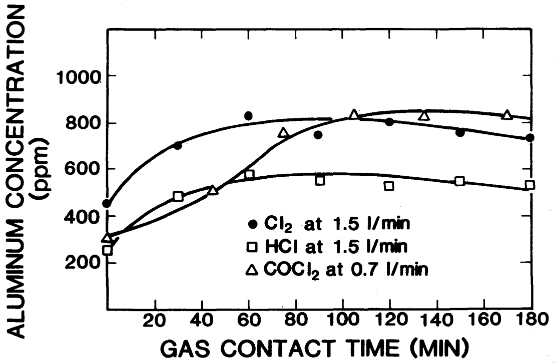

Fig. 7. Aluminum build-up in regenerated salts from dissolution of alumina hardware.

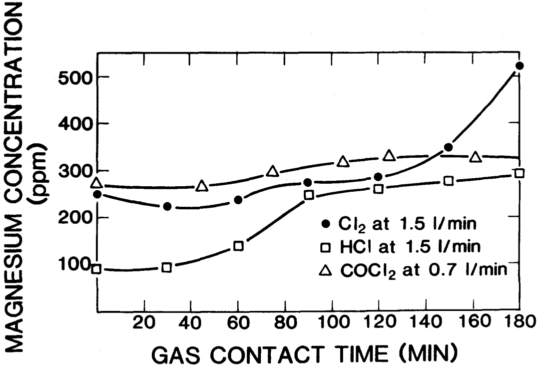

Fig. 8. Magnesium concentration in regenerated salts from dissolution of magnesia hardware.

DOI: 10.1149/198601.0522PV

CORRELATIONS BETWEEN STRUCTURE AND TRANSPORT PROPERTIES OF MOLTEN PYRIDINIUM HALIDE BINARY MIXTURES

David S. Newman, Leuh Fang, Randall Davy, Paul Endres,
Alfred R. Ebert, Steven L. Gatton

Department of Chemistry
Bowling Green State University
Bowling Green, Ohio 43403

INTRODUCTION:

Hypotheses about the nature of ion transport mechanisms, ionic interactions, and complex species in molten salts have often been tested by examining the macroscopic properties of binary mixtures of inorganic salts with a common cation or common anion. The common ion serves as a reference in much the same way that water serves as a reference in aqueous electrolyte solutions. A fixed reference is necessary for microscopic measurements to be useful, but it masks molecular contributions to the observed phenomenon. It is therefore desirable to have a microscopic measurement accompany the thermodynamic or transport measurement to unmask the microscopic details. The most powerful microscopic technique is, in principle, neutron diffraction, but adequate neutron sources are not generally available and neutron diffraction patterns are very difficult to interpret. The high temperatures necessary for most inorganic molten salt studies make optical spectroscopic measurements difficult to make and NMR measurements impossible. Moreover, optical spectra do not give information about radial distribution functions as do diffraction patterns, so their applicability to the microscopic interpretation of transport properties is limited. This limitation is further exacerbated because no one has defined a complex to everyone's satisfaction. As a result, there are no specific criteria for differentiating between "quasi-lattice vibrations" and "species vibrations" (1) so that even when optical spectra are available, their interpretations are often ambiguous.

By investigating binary mixtures of pyridinium salts with a common ion, much of the same sort of information can be obtained as can be obtained with inorganic salts, but many more subtle questions can be answered because of the great structural variability of these systems, and many of the experimental difficulties of high temperature chemistry are avoided. Since these mixtures are liquid at low enough temperatures for their HNMR spectra to be obtained, one additional microscopic measurement is available that is unavailable for most inorganic mixtures. Since the pyridinium mixtures are also potentially useful as solvents and as electrolytes for batteries, the properties of these melts can be of practical importance as well.

In previous studies we have observed correlations between transport properties, structure, and HNMR spectra of molten 4-methyl pyridinium iodide (4-mepyrI) and molten 4-methyl pyridinium chloride (4-mepyrCl) (2,3). These two salts have similar melting points and liquid ranges, and consequently make a particularly suitable system upon which to test a variety of ideas about binary mixtures with a common ion. In this case the anion is mixed and the cation is common to both salts.

The primary purpose for our investigation is to demonstrate the usefulness of pyridinium binaries as sources of general information about molten salts. This we do by answering a fundamental question as to whether or not there is a "mixed univalent anion effect" in these organic melts that is similar to the mixed univalent cation effect described by Moynihan for inorganic salts (4). A mixed univalent ion effect is the deviation from additivity of a physical property as a function of composition, as one ion is isothermally substituted for the other. The second question we will attempt to answer is whether or not there are correlations between HNMR spectra and transport properties. The third question is what is the role of hydrogen bonding in a binary mixture when one of the components hydrogen bonds and the other does not. In order to answer these questions, the conductivity, viscosity, density and HNMR spectra were measured as a function of composition and as a function of temperature. From the isothermal measurements of density vs. composition, the excess partial molar volumes were calculated.

EXPERIMENTAL PROCEDURE

The methyl pyridinium salts were synthesized and analyzed by methods already described in the literature (5,6). The 4-mepyrI melted at 171°C and turned yellow upon melting. The yellow color disappeared upon freezing. The 4-mepyrCl melted at 167°C and remained water clear. Analysis of the single salt before and after an experiment showed that there was no discernable decomposition of the chloride and about 2% decomposition of the iodide over the course of about ten hours at temperatures approaching 200°C. This was considered negligible. All transfer operations and preparation of salt mixtures were done in a Kewaunee dry box under nitrogen atmosphere.

Density measurements were made with a modified Lipkin bicapillary arm pycnometer (7). The precision of these measurements was ± 0.1%. Conductivity measurements were made with a Jones bridge at a frequency of 1000 Hz using a capillary cell with cylindrical platinum electrodes. The cell constant was 199.53 cm^{-1}, a Cannon - Fenske viscometer was used to measure the melt's viscosity. The HNMR spectra were obtained using the variable temperature probe of a Varian CFT 20 NMR machine and an external standard of DMSO.

RESULTS

The measured density, ρ, in g/cm^3, is given by an equation of the form

$$\rho = A - B \times 10^{-4} \; T\,(K) \qquad (1)$$

The values of A, B, and the temperature range for each of the pure melts and the mixtures are given in Table I.

TABLE I - Density

Salt	A	B	Temperature Range (K)	Correlation Coefficient
4-mepyrCl	1.3655	6.590	443-468	0.998
4-mepyrI	1.9513	7.420	442-468	0.999
74.63% 4-mepyrCl/ 25.37% 4-mepyrl	1.5368	6.743	438-463	0.9953
51.19m% 4-mepyrl/ 48.81m% 4-mepyrCl	1.6994	7.571	423-463	0.9997
71.53m% 4-mepyrCl/ 28.47m% 4-mepyrl	1.5202	6.134	432-452	0.9973
56.49m% 4-mepyrCl/ 43.51m% 4-mepyrl	1.6506	6.985	429-460	0.9994
25.53m% 4-mepyrCl/ 74.47m% 4-mepyrl	1.8065	6.817	423-458	0.9994

The specific conductances of the melts followed Arrhenius behavior over the temperature range studied and are given by an equation of the form

$$\ln \kappa\,(\Omega\ \mathrm{cm})^{-1} = P - Q/T(K) \qquad (2)$$

The values of P and Q for the melts are listed in Table II.

TABLE II Specific conductances of binary mixtures

Salt	P	Q	Correlation coeff.
4-mepyrI(18.32m%)/ 4-mepyrCl(81.79m%)	3.341	2564	0.999
4-mepyrI (34.58m%)/ 4-mepyrCl(65.42m%)	3.285	2557	0.999
4-mepyrI(49.16m%)/ 4-mepyrCl(50.84m%)	3.161	2507	0.999
4-mepyrI(76.08m%)/ 4-mepyrCl23.92m%)	2.978	2451	0.999

The equivalent conductance, Λ , was calculated from the density and specific conductance using the equation

$$\Lambda = \kappa M/\rho \qquad (3)$$

where M is the equivalent weight of the salt mixture and is calculated from the equation:

$$M = x(\mathrm{Mw4\text{-}mepyrCl}) + (1-x)(\mathrm{Mw4\text{-}mepyrI})$$

and ρ is the density of the corresponding mixture. Figure 1 shows plots of Λ vs. x for the binary mixture at several different temperatures. It is clear that there is a negative deviation from additivity and that this negative deviation becomes less pronounced as temperature increases.

Viscosity also followed Arrhenius behavior over the temperature range studied and can be described by an equation of the form:

$$\ln \eta = -Y + Z/T \qquad (4)$$

where η is given in centipoise. The values of Y and Z are listed in Table III for the pure melts and several binary mixtures. Fig. 2 shows several viscosity vs composition isotherms and again there is a negative deviation from additivity which diminishes with increasing temperature.

TABLE III VISCOSITY

Salt	Y	Z	Correlation Coeff.
4-mepyrI	11.46	3493	0.997
4-mepyrCl	11.58	3464	0.999
67.8%4-mepyrI/ 32.2%4-mepyrCl	11.29	3382	0.999
49.2%4-mepyrI/ 50.8%4-mepyrI	11.36	3396	0.999
29.74-mepyrI/ 70.34-mepyrCl	11.52	3453	0.999

Figure III shows the HNMR spectrum of a binary mixture at 175°C. The essential features of the spectrum were the same at each composition and were relatively insensitive to temperature. Figure IV is a graph of the $>$N-H chemical shift vs composition at 175°C.

DISCUSSION

The molar volume of mixing, $\Delta_{mix} V_m$, is given by the equation

$$\Delta_{mix} V_m = [(1-x)M_{Cl} + xM_I 1/\rho_m - (1-x)M_{Cl}/\rho^*_{Cl} - xM_I/\rho^*_I \qquad (5)$$

where the ρ_i are the densities and the M_i are the molecular weights.

The excess molar volume, V_m^E is defined by the equation:

$$V_m^E = \Delta_{mix} V_m - \Delta_{mix} V_m^{ideal} \qquad (6)$$

Since $\Delta_{mix} V_m^{ideal}$ is 0, $V_m^E = \Delta_{mix} V_m$. Figure 5 shows a graph of V_m^E vs. composition for two selected temperatures and, within experimental error, V_m^E is zero indicating ideality in the mixing function. Since the Coulombic attraction between I^- and 4-mepyrH^+ must differ from the Coulombic attraction between Cl^- and 4-mepyrH^+ the apparent ideal behavior must be caused by compensating factors rather than uniformity of forces.

It is very likely that the reduction of molecular volume caused by hydrogen bonding is compensated for by expansion due to local relaxation (8). Therefore, as I^- is substituted for Cl^- the reduction in volume caused by ion pair formation between $>N-H^+$ and Cl^- is accompanied by just enough expansion, caused by local relaxation, for the excess partial molar volume to be zero.

Despite the fact that within experimental error V_m^E is zero, there is a distinct negative deviation from additivity in both the conductance and viscosity isotherms. Moreover, this deviation diminishes with increasing temperature. There is therefore a definite mixed univalent ion effect in the binary pyridinium salt system with all of the attributes of the mixed univalent cation effect in inorganic salts that were described by Moynihan (4). However, in the pyridinium melts it is the anion that is mixed and not the cation. Since the more mobile species is the anion (9, 10), and not the cation, as it is in most of the inorganic salts studied, we suggest that this effect is general and should be called the mixed mobile ion effect. Claes and Glibert have recently found what appears to be a very pronounced mixed univalent anion effect in $LiNO_3$ - Li(OH), $NaNO_3$ - Na(OH) and KNO_3 - K(OH) binary melts (11). However, the explanation for their results remains somewhat obscure because of the obvious difference in transport mechanism between the NO^-_3 ion and the OH^- ion.

In the pure 4-mepyrCl melt hydrogen bonding is an important factor, (12,13), but in the iodide melt hydrogen bonding does not occur (14). As I^- is substituted for Cl^-, complexes like

$$(\text{Me- PyrH--Cl--HPyr-Me})^+$$

will form, thus immobilizing the inherently more mobile Cl^- species and freeing the inherently less mobile I^- species. Complexes of this sort will continue to form until a mole fraction of 0.5 is reached and then any added 4-mepyrI will result in a reduction of the complex ion concentration. The conductance and viscosity should be at the minimum at a mole fraction of 0.5 which is close to the observed result. The reason why the viscosity of the melt also goes through a minimum (the fluidity goes through a maximum) is that there is a contracton of the ions along the >N-H-Cl-H-N< bond and a concommittant local expansion due to the positive charge being spread over a much greater volume than before (8). Hydrogen bonding in ionic systems tends to reduce viscosity whereas hydrogen bonding in molecular systems (water, ammonia, etc.) tends to increase viscosity.

Because the transport measurements give no specific information about the species present, we look to the HNMR spectra of the melts for help in this respect and these spectra corroborate our conjectures. If there is complex formation arising from hydrogen bonding between the $>N-H^+$ and Cl^- then the magnetic environment around the nitrogenic proton should reflect this hydrogen bonding. That it does reflect it is pointed out in in Fig. 4. Here the chemical shift deviates from linearity in a positive sense. That is, the nitrogenic proton is further down field (more acidic) and closer to the pure Cl- melt value. Again, at around a mole fraction of 0.5 the chemical shift begins to move upfield (proton becomes more shielded) more sharply until the pure I^- value is reached. The δ s of the ring protons and methyl groups showed no deviation from linearity.

There are many reasons why the mixed mobile species effect tends to vanish with increasing temperature, but the simplest way to summarize them is to say that the configurational entropy is greater, and the local relaxation times are shorter relative to the site to site jump times. Thus the system approaches a more "ideal" fluid state.

The estimated errors in this experiment are ± 0.2% in the density, ± 1% in the composition, ± 2% in the viscosity and HNMR spectra measurements yielding an overall accuracy of about ± 3%. Of some concern is the fact that we were unable to obtain a temperature dependent proton chemical shift which would correlate with the vanishing of the mixed mobile species effect. However, the temperature range available to us was only about 25°C and at the higher temperatures the iodide melt was beginning to decompose so that it may simply have been lost in experimental error.

CONCLUSION

Binary mixtures of molten pyridinium salts have been shown to exhibit a mixed univalent anion effect similar to the mixed univalent cation effect found in many molten inorganic salts, and we suggest it be called the mixed mobile species effect. Moreover, we have correlated th HNMR spectra with both viscosity and conductivity data to elucidate the effect of structure on transport properties of molten salts. Finally, we have shown that mixtures of molten pyridinium salts are viable systems for studying properties of molten salts in general.

LIST OF REFERENCES

1. J.H. Wilmshurst, J. Chem. Phys. 39, 1779 (1963).
2. D.S. Newman, R.M. Stevens, J. Electrochem. Soc. 131, 1275 (1984).
3. D.S. Newman, R.R. Rhinebarger, D. Siconolfi, O.A. Banjoko, J. Electrochem. Soc. 128, 2331 (1981).
4. C.T. Moynihan, J. Electrochem. Soc. 126, 2144 (1979).
5. M.S. Rozhdestavenskii, L.M. Brode, Zh. Prikl Khim (Leningrad) 10, 722 (1937).
6. A.I. Vogel, "A Textbook of Quantitative inoroganic Analysis", Longman's Green & Co., London (1951) p. 360-361.
7. D.S. Newman, D.P. Morgan, R.T. Tillack, J. Chem. Eng. Data, 21, 279 (1976).
8. D.S. Newman, P.D. Bikkani, "Proceedings of the Fourth International Symposium on Molten Salts", M. Blander, D.S. Newman, G. Mamantov, K. Johnson, Eds., The Electrochemical Society, 1984, p 206-216.
9. R.A. Carpio, L.A. King, R.E. Lindstrom, J.C. Nardi, C.L. Hussey, J. Electrochem. Soc. 126, 1644 (1979).
10. D.S. Newman, W. Rohr, D. Kirklin, H.D. Frame, J. Electrochem. Soc. 119, 797 (1972).
11. P. Claes, J. Glibert, J. Electrochem. Soc. 132, 857 (1985).
12. P.C. Rerat, Acta Cryst. 15, 427 (1962).
13. J.W. Shuppert, C.A. Angell, J. Chem. Phys. 67, 3050 (1977).
14. N. Goldstein, J.L. Ragle, J. Chem. Phys. 70, 5072 (1979).

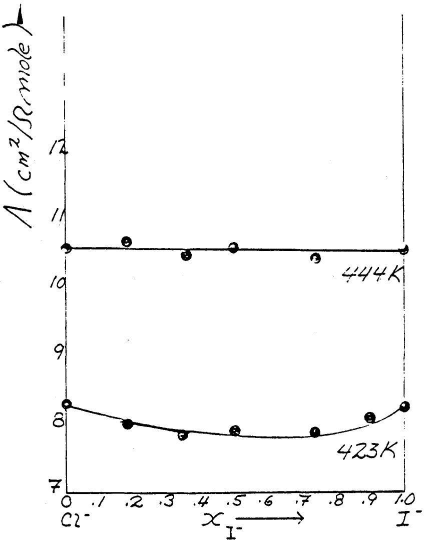

Fig. 1 Equivalent Conductance vs. Mole Fraction

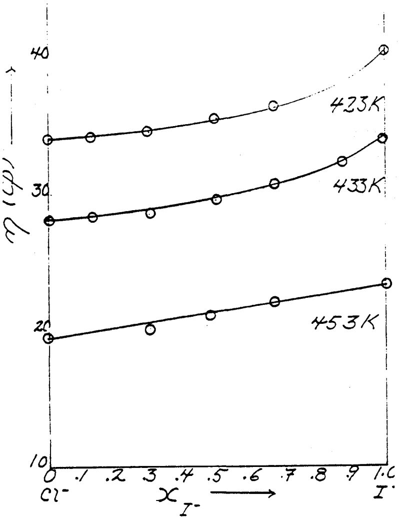

Fig. 2 Viscosity vs. Mole Fraction

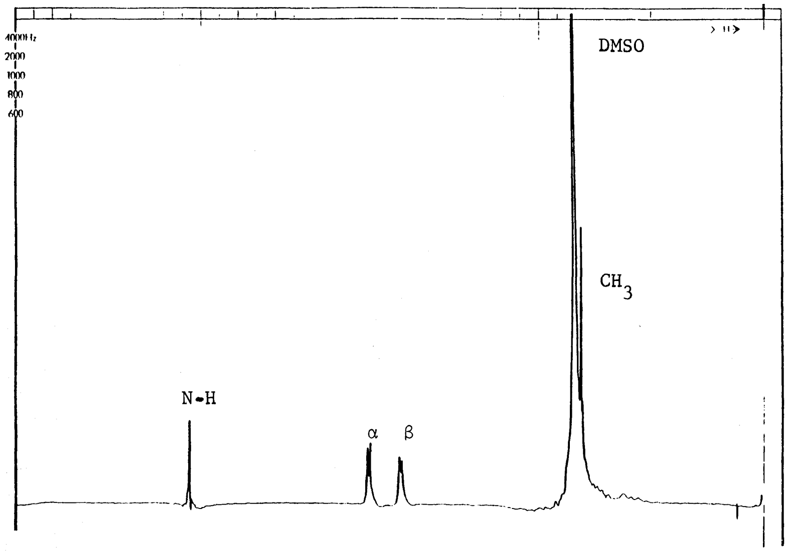

Fig. 3 HNMR Spectrum of a Binary Mixture of Molten Salts at 175°C

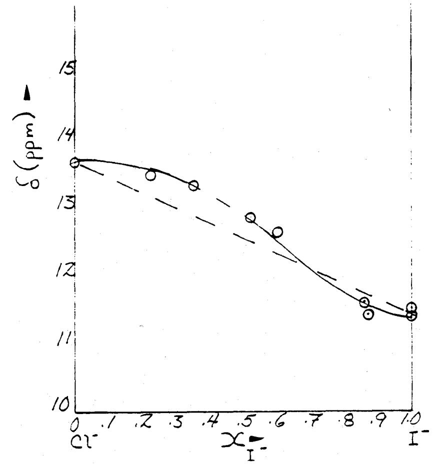

Fig. 4 N-H Chemical Shift vs. Composition at 175°C

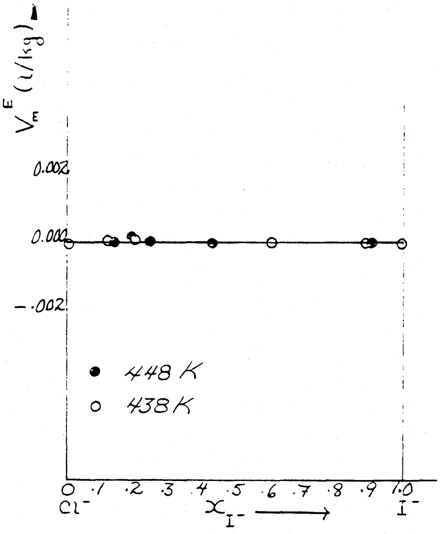

Fig. 5 V_m^E vs. Composition at Two Different Temperature

DOI: 10.1149/198601.0531PV

CONDUCTIVITY, DENSITY AND VISCOSITY OF MOLTEN HYDRATED SALT SYSTEMS: MIXTURES OF HYDRATED NITRATES OF THE ALUMINUM AND IRON, WITH CALCIUM, CADMIUM, MAGNESIUM, AND ZINC NITRATE HYDRATES

R. C. Sharma†, K. V. Ramana and H. C. Gaur
Centre of Advanced Study, Department of Chemistry
University of Delhi, Delhi-110007, India

ABSTRACT

Conductivity, density and viscosity of title systems were studied at temperatures in the range 270 to 365 K over a wide range of composition. Volumes of cerium-containing mixtures exhibited large negative deviation from additivity while those of iron- and aluminum-containing systems were nearly additive. Temperature-dependence of conductivity and viscosity was consistent with VTF equation. The results have been interpreted considering preferential hydration of trivalent cations and presence of co-ordinated and lattice water.

INTRODUCTION

The behaviour of molten hydrated salts of divalent cations have been explained considering the existence of weak field cations of the type $M(H_2O)_m^{2+}$ and anions. These solutions have been considered as hydrous melts since molten salt models have frequently been used to interpret the thermodynamic, transport and spectral behaviour. Several hydrated salts and mixtures show strong supercooling and glass-forming tendencies, enabling measurements well below the freezing point and thus over a wide range of temperature. The principle of additivity of volumes has generally been found to be applicable, at least to a first approximation. Conductivity and viscosity of the mixtures have been found to be dependent on the composition because of the difference in ion-ion and ion-water interactions.

In continuation of our studies in several hydrous melts and highly concentrated electrolyte solutions, results of density, conductivity, and viscosity of hydrated molten nitrates of aluminum and iron with calcium, cadmium, zinc, and magnesium nitrate hydrates are presented in this paper.

---

†Present Address: Delhi College of Engineering, K. Gate, Delhi-110006.

EXPERIMENTAL

All salts were of AnalaR (BDH) grade purity; water content of the salts, determined by volumetric titration with EDTA, were within ±0.01 of the stoichiometric value. Mixtures of varying composition were prepared individually by mixing calculated amounts of components, fusing in a stoppered glass vessel, filtering and maturing at 5-10° above the melting point for c 3 hrs.

The densimeter was essentially of the type used by Husband & McAuley (1,2), modified (3) to accommodate a wider range of temperatures. A Beckman conductivity bridge (Model RC-18A) based on Wien's bridge principle, provided with a CRT null detector and Wagner ground, operated at an a.c. frequency of 1 KHz, was used to measure the solution resistance. A decade capacitance (C_P) box was connected in parallel with a resistance (R_P) box in the measuring arm of the bridge, and the resistance in the ratio arms were matched. Considering the cell as a series combination of a resistance (R_S) and a capacitance (C_S), at the balance point one has:

$$R_S = R_P / \left(1 + (R_P C_P 2\pi f)^2\right)$$

where f is the frequency of the a.c. signal in Hz. A dip-capillary type conductivity cell was used. A three-limb Cannon-Ubbelhode-Flenske type viscometer used to measure viscosity was calibrated with triple distilled water, 20% and 40% sucrose and 98% glycerol solutions.

DISCUSSION

In these systems, the size of the common anion is large relative to other ions in the system; thus the common anion may be considered as the main space-filling species. Also, water of hydration is associated, almost fully, with the cation (4). Taking the analogy from concentrated aqueous electrolyte solutions, water may be differentiated as co-ordinated water forming the first hydration shell around the cation and the lattice water constituting the second, third, etc shells, possibly the formation of H-bonded dimers, trimers or polymers (clusters) of water molecules. The complexing nature of cations, and/or ion-ion interactions may lead to the formation of contact-ion-pairs (CIP) or solvent-separated ion-pairs (SSIP) in solution. Also, differences in cationic potentials may lead to hydration-dehydration equilibria of the type (5)

$$M_2(H_2O)_m^{3+} + M_1(H_2O)_n^{2+} \rightleftharpoons M_2(H_2O)_{m-x}^{3+} + M_1(H_2O)_{n+x}^{2+}$$

on addition of divalent nitrate hydrate* to the trivalent nitrate hydrate. In this lattice, water from the hydration sphere of the trivalent cation is accommodated as

---

*Subscripts 1 and 2 refer to divalent and trivalent cations respectively.

coordinated water if the available water of hydration of the latter is insufficient to complete the primary hydration shell or is taken up as lattice water of the latter. The various interactions affect the packing density and the transport behaviour of species in solution.

Volumetric behaviour of hydrated molten salts and mixtures may be discussed in terms of a reference state e.g., molten aluminum or iron(III) nitrate hydrate the implication being that at temperatures 5-50° away from the melting point and within the composition range, as used, the basic microscopic lattice structure of this component can still be considered to be predominant. The addition of the divalent metal nitrate hydrate perturbs or modifies the structure according to different interactions.

1. ($V - X_1$) isotherms

Typical results of the variations of molar volume (V) at 313.2, 333.2 and 353.2 K for $Al(NO_3)_2 \cdot 10H_2O$ - (Ca, Cd, Zn, Mg) $(NO_3)_2 \cdot 4,6\ H_2O$ (Fig. 1) show a nearly-linear decrease with increase in X. Strong polarization of NO_3^- ion towards hydrated Al^{3+} would lead to Al^{3+}-$(H_2O)_{n-x}$-NO_3^- interaction forming SSIP and consequent displacement of some lattice water from the hydration sphere of Al^{3+}. The water thus released would be accommodated in the (primary) hydration sphere of Ca^{2+}; also, NO_3^- would be attracted toward the positive part of dimeric water ($OH^- - H_3O^+$). Consequently, the packing density would increase and V would decrease with increasing X as was observed.

For nearly-ideal systems, partial molar volumes V_1 and V_2 could be evaluated by graphical extrapolation. Alternatively, V could be expressed as a linear function of the mole fraction of one of the components, (say 1) by

$$V = E + FX_1$$

from which, one has

$$E = \overline{V}_2 \text{ and } F = \overline{V}_1 - \overline{V}_2$$

Iron being a d-block element would, relative to Al, show stronger tendency to form CIP and also have stronger coordination bonds with water molecules. The difference in behaviour, not obvious in V-X plots, shows up in the partial volume parameters (Tables 1 and 2). Except for $Mg(NO_3)_2 \cdot 6H_2O$ -containing mixtures (vide infra), V_1 for other divalent metal nitrate hydrates in $Fe(NO_3)_3 \cdot 9H_2O$ - mixtures is 2-5% more than in $Al(NO_3)_3 \cdot 10H_2O$ mixtures.

2. $(\rho, V) - T$

At a given composition, both ρ and V varied linearly with T and could be least-square-fitted with an equation of the type

$$\rho(V) = A(A') + B(B') \ (T - 300)$$

where the parameters A, A′, B, B′ are constants, characteristic of the system and its composition. The fits enabled evaluation of expansion coefficient, $\alpha = (-1/\rho\ (d\rho/dT))$ which equals B, and molar thermal expansibility, V_E $(= (dV/dT)_X)$ which equals the parameter B′.

V_E and α are useful in interpreting structural changes with changes in composition and temperature. The molar volume of the mixture can be expressed as a sum of a van der Waals (V_O) volume and a free (V_f) volume due to an increase in temperature from a specified value:

$$V = V_O + V_f$$

For a given composition, variation of the volume with temperature is identical to that of the free volume, since V_O is not a function of temperature:

$$\frac{dV}{dT} = \frac{dV_f}{dT} = B'$$

V_f can also be expressed as:

$$V_f = V_O(\exp \int_{T_O}^{T} \alpha dT - 1)$$

where T_O is the temperature above which free volume is formed. If ΔT is the difference between temperature of study and T_O, one has:

$$V_f = V_O \exp[(\alpha\Delta T) - 1) \approx \alpha V_O \Delta T$$

and

$$\frac{dV_f}{dT} = V_E = V_O\alpha$$

Typical data of mixtures of $Al(NO_3)_3 \cdot 10H_2O$ with divalent metal nitrate hydrates (Fig. 2) show a decrease in V_E with X. Changes in α are relatively small; a decrease in V_E could be considered to arise largely due to a decrease in

V_O. The latter results from a decrease in the number of NO_3^- ions, the main space-filling species and also the number of water molecules per mole of the mixture. A slightly different trend for Zn-system (also Fig. 2) may be explained due to complexing nature of Zn^{2+} and the reported CIP $Zn^{2+} - NO_3^{--}$ formation, in concentrated zinc nitrate solutions. This would result in increase in V_O and hence a smaller decreasing trend in V_E.

According to the Born model of ion-solvent interaction, α has contributions both from configurational and virbrational factors. Molten hydrated salts in which the water of hydration is almost wholly associated with the cations, have low expansion coefficients. Addition of divalent cation to Al^{3+} -containing systems would decrease the electrostricting affect. This would increase free existence of dimers, trimers, etc of water increasing the configurational contribution to α, as observed.

A slightly higher slope for Zn-containing systems is consistent with the formation of CIP $Zn^{2+} - NO_3^-$ and consequent displacement of some of the coordinated water molecules of Zn^{2+} at lattice water. Increase in α with temperature in all cases results from a larger vibrational contribution of water molecules to α.

3. (κ, η) – X isotherms

Typical variations of κ for $Al(NO_3)_3 \cdot 10H_2O - Ca(NO_3)_2 \cdot 4H_2O$ system at 313.2, 333.2 and 353.2 K showed an initial decrease in κ up to $\underline{c} = 80$ mole of Ca^{2+}; on further addition of Ca^{2+}, κ is almost unaffected. This is consistent with strong Al^{3+} $(H_2O)_{n-x}$-NO_3^- interaction forming SSIP and the displacement of some lattice water from hydration sphere of Al^{3+} to new sites in the (primary) hydration sphere of Ca^{2+} forming species of type Ca^{2+} $(OH^- - H_3O^+)NO_3^-$. Both would result in a decrease in κ and an increase in η as observed. At higher concentration, a saturation in Ca^{2+}- $(OH^- - H_3O)NO_3^-$ interaction and also the reported formation of the CIP, Ca^{2+}-NO_3^- – (H_2O), would result in a decrease in κ and increase in η, as observed. It may be noted that formation of CIP does not contribute significantly to conductivity but affects the viscosity of the system much more.

In the $Fe(NO_3)_3 \cdot 9H_2O - Mg(NO_3)_2 \cdot 6H_2O$ system, a small decrease in κ and an increase in η are observed. It has been shown that Mg^{2+} does not form CIP to any significant extent but due to relatively higher cationic potential, would have strong tendency to form weak-field cation of the type $Mg(H_2O)_6^{2+}$. Addition of Mg^{2+} would change the ion-water interactions which are of smaller magnitude and hence a smaller variation in κ and η is shown.

4. (Λ, ϕ) – T data

Temperature variation of Λ and ϕ were non-Arrhenian, and could be satisfactorily expressed by the VTF equation (6-8)

$$y(\Lambda,\phi) = A_y \exp\left(\frac{-B_y}{T - T_{o,y}}\right)$$

where A_y and B_y are empirical parameters characteristic of the system purity and the transport property; and T_o is the temperature at which the transport property approaches a limiting value. Theoretical basis was provided by the free volume model (9) and the cooperative rearrangement (10) theory; T_o can be interpreted as the temperature above which free volume begins to form or at which the configurational entropy of the system is zero. Computer simulation of Λ, ϕ – T data was done to evaluate the parameters, A_y, B_y and T_o. Typical parameters for conductivity data for $Al(NO_3)_3 \cdot 10H_2O$ – $Zn(NO_3)_2 \cdot 6H_2O$ and viscosity data for $Fe(NO_3)_3 \cdot 9H_2O$ – $Ca(NO_3)_2 \cdot 4H_2O$ were evaluated.

T_o has been considered as a useful parameter for the observed changes in the total interaction energy of the system. Ionic systems in which principal interactions are ion-ion type have maximum value of T_o. On the other extreme are molecular liquids where principal interactions are of van der Waal type. Molten hydrated salts and highly concentrated aqueous electrolyte solutions have T_o in the intermediate range. In these, the interaction energy is determined by ion-ion, ion-water and water-water interactions. Since T_o depends on the total interaction energy, which is a funtion of X, a study of the variation of T_o with X has been corried out.

In $Al(NO_3)_3 \cdot 10H_2O$ – $Ca(NO_3)_2 \cdot 4H_2O$ system, T_o increases with X. It has been proposed earlier that addition of calcium nitrate results in increased interactions between Al^{3+} and NO_3^- decreasing Al^{3+}–H_2O interactions. Also Ca^{2+}–H_2O interaction decreases due to formation of dimeric water. The observed trend of increasing T_o with X is consistent with the predominance of ion-ion interactions. In the $Al(NO_3)_3 \cdot 10H_2O$ – $Mg(NO_3)_2 \cdot 6H_2O$ system, an almost constant T_o means that the change in magnitude of interactions is small since the predominant interactions are ion-water type. This is also supported by conductance-composition isotherms.

Hydrated ferric nitrate-containing systems do not show significant changes in T_o with X since, due to complexing nature of Fe^{3+}, change in magnitude of ion-ion interactions is small. It may be recalled that in discussing conductivity – composition isotherms, the main interactions considered were ion-water and water-water type, which do not influence the value of T_o significantly.

Volume dependence of the transport properties has also been fitted into Doolittle equation (11) which is similar to VTF equation

$$M = A'_M \exp\left(\frac{-B'}{V - V_{o,M}}\right)$$

where M is eitherΛ or ϕ and V_O is the instrinsic volume, which by analogy to VTF eqn is the molar volumes at T_O. Evaluated values of V_O are nearly the same from both conductivity and fluidity data.

ACKNOWLEDGMENTS

The authors thank the CAS for continued financial assistance. KVR thanks department of Atomic Energy for a junior research fellowship. HCG thanks Indian National Science Academy, Council of Scientific and Industrial Research Department of Education, Govt. of India and University of Delhi for International travel grant and the Electrochemical Society for hospitality.

REFERENCES*

1. L. J. B. Husband, J. Sci. Instr. ***35***, 300, 1958
2. W. J. McAuley, E. Rhodes, and A. R. Ubbelohde, Proc. Royal Soc. London, Series ***289***, 151, 1966
3. R. C. Sharma and H. C. Gaur, J. Chem. Eng. Data ***22***, 41, 1977
4. C. A. Angell, J. Electrochem. Soc. ***112***, 1224, 1965
5. S. K. Jain, J. Phys. Chem. ***82***, 1272, 1978
6. H. Vogel, Phys. Z. ***22***, 645, 1921
7. V. G. Tammann and W. Hesse, Z. Anorg. allg. Chem. ***156***, 245, 1926
8. G. S. Fulcher, J. Am. Ceram. Soc. ***8***, 339, 1925
9. M. H. Cohen and D. Turnbull, J. Chem. Phys. ***31***, 1164, 1959
10. G. Adam and J. H. Gibbs, J. Chem. Phys. ***43***, 139, 1965
11. A. K. Doolittle, J. Appl. Phys. ***22***, 1471, 1951

Editors note: These references were graciously provided by Prof. T. B. Tripp.

Table I. Partial Molar Volumes of Components of $Al(NO_3)_3.10\ H_2O + M(NO_3)_2.R\ H_2O$ Systems

$M(NO_3)_2.RH_2O$	Temp (K)	V_1 $cm^3\ mol^{-1}$	V_2 $cm^3\ mol^{-1}$	
$Ca(NO_3)_2.4H_2O$	313.2	252.53	134.59	(135.80)[a]
	333.2	254.47	135.80	
	353.2	256.79	136.90	
$Cd(NO_3)_2.4H_2O$	313.2	251.61	136.16	(136.70)[a]
	333.2	253.72	137.50	
	353.2	255.73	138.79	
$Zn(NO_3)_2.6H_2O$	313.2	253.44	157.33	(161.37)[b]
	333.2	255.12	159.23	
	353.2	257.78	161.07	
$Mg(NO_3)_2.6H_2O$	333.2	252.64	167.06	(166.88)[c]
	353.2	255.57	168.91	

a) Sharma, Jain, Gaur *J. Chem. Eng. Data*, 23 (1978) 2
b) Jain, Tamamushi *Can. J. Chem.*, 58 (1980) 1697
c) Jain, Jindal, Kulshreshta *J. Chem. Eng. Data* , 23 (1978) 36.

Table II. Partial Molar Volumes of Components for $Fe(NO_3)_2.9H_2O$ + $M(NO_3)_2.RH_2O$ System

$M(NO_3)_2.RH_2O$	Temp (K)	V_1 $cm^3\ mol^{-1}$	V_2 $cm^3\ mol^{-1}$	
$Ca(NO_3)_2.4H_2O$	313.2	241.37[d]	137.59	(135.80)[a]
	333.2	244.50	138.84	
	353.2	247.80	140.04	
$Cd(NO_3)_2.4H_2O$	313.2	240.82	137.10	(136.71)[a]
	333.2	243.97	138.39	
	353.2	247.24	139.68	
$Zn(NO_3)_2.6H_2O$	313.2	239.70	165.10	(161.37)[b]
	333.2	242.82	167.05	
	353.2	246.06	168.98	
$Mg(NO_3)_2.6H_2O$	313.2	241.82	152.56	
	333.2	244.42	160.43	(166.88)[c]
	353.2	247.69	161.91	

a) Sharma, Jain, Gaur J. Chem. Eng. Data, 23 (1978) 72
b) Jain, Tamamushi, Can. J. Chem., 58 (1980) 1697.
c) Jain, Jindal, Kulshrestha J. Chem. Eng. Data 23 (1978) 36
d) Gupta, Sharma, Gaur J. Chem. Eng. Data 26 (1981) 187

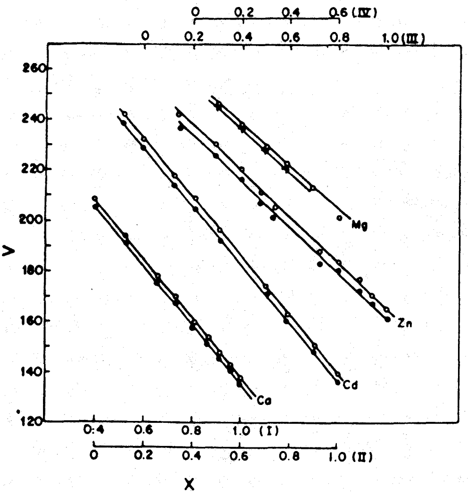

Fig. 1 Isotherms of molar volume (*V*) vs. mole fraction of divalent cation (X) for $Al(NO_3)_3 \cdot 10.03H_2O + M(NO_3)_2 \cdot RH_2O$ systems: ●, 313.2 K; X, 333.2 K; O, 353.2 K. Mole fraction axis scale: (I) for Ca, (II) for Cd, (III) for Zn, (IV) for Mg containing mixtures.

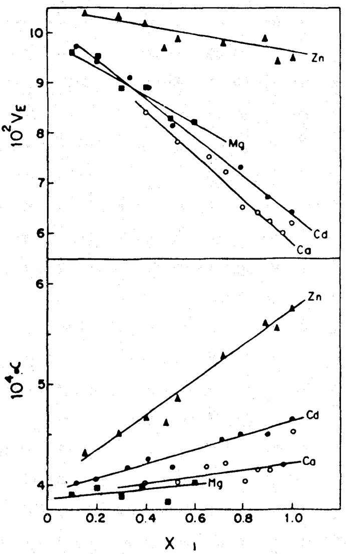

Fig. 2 Composition variation of thermal expansion coefficient (α) and molar expansivity (V_E) of $Al(NO_3)_3 \cdot 10.03H_2O + M(NO_3)_2 \cdot RH_2O$ Systems at 300 K.

DOI: 10.1149/198601.0541PV

Vapor Pressures of Hydrate Melts Containing Nitrate and Nitrite Salts

Terrance B. Tripp
NRC Inc.
45 Industrial Place
Newton, Ma. 02164

ABSTRACT

Vapor pressures of the systems $LiNO_3$-KNO_2-H_2O, .41$LiNO_3$-.41KNO_3-.18$NaNO_3$-H_2O, .41$LiNO_3$-.41KNO_3-.18$CsNO_3$-H_2O, .472$LiNO_3$-.472KNO_3-.056$Ca(NO_3)_2$-H_2O and .472$LiNO_3$-.472KNO_3-.056$Mg(NO_3)_2$-H_2O were measured over the temperature range 383.15 to 412.76 K. The water concentration was varied from approximately 0.05 to 1.4 mol H_2O/mol salt. The vapor pressure is a linear function of the water mole ratio R_H (mol H_2O/mol salt). Each system exhibits negative deviations from Raoult's Law in contrast to systems based on $AgNO_3$-$TlNO_3$ which do not have a strongly hydrated cation and show positive deviations from Raoult's Law. It appears that a requirement for linear dependence of the vapor pressure on water mole ratio and negative deviations from Raoult's Law is the presence of a strongly hydrate cation in the melt.

INTRODUCTION

Liquid solutions of electrolytes and water in which water is the solvent have received considerable experimental and theoretical attention during this century but only in the past twenty five years have systems where water is the solute been examined in any detail. The apparent limited interest in these hydrate melt solutions was probably due to 3 perceived lack of systems which exist in the molten state at reasonably low temperatures when water is the solute and the few recognized technological applications for hydrate melt systems. Progress toward a general model of solutions of electrolytes and water will come only after the determination of the physical properties of these systems over the entire range of concentration from pure water to fused salt and further it has been suggested that progress in the development of a general theory will more likely come from an extension of molten salt models (1).

Some progress has been made toward the understanding of hydrate melts over the past twenty years as a result of studies on systems containing primarily nitrate salts. Vapor pressures have been measured for a number of systems to temperature as low as 373 K, the densities of a variety of melts are now available along with an assortment of viscosity and conductivity data (1-17). The scope of work on hydrate melts has, however, remained relatively limited due in part to the perceived few systems available for study.

Recent work on an absorption cycle heat pump (18) lead to the discovery of several hydrate melt systems which exist at very low water concentrations to temperatures as low as 353 K. An absorption cycle heat pump utilizes a suitable hydrate melt to transfer energy from low to high temperatures and has the potential of achieving a considerable energy savings in, for example, industrial distillation processes.

This paper reports the results of a transpiration vapor pressure study of several newly identified hydrate melt systems containing alkali nitrates and nitrites which are doped in some cases with magnesium or calcium ions. The results are analyzed in light of previous work on hydrate melts and reveal the effect of preferential hydration on the vapor pressures and water activities of hydrate melts.

EXPERIMENTAL

Vapor pressures were measured by the differential transpiration method (1). Corrections were made for deviations of the nitrogen carrier gas water mixture from ideal behavior, the solubility of the carrier gas in the solution, and the Poynting effect. The uncertainty in the vapor pressures arising from the measurement of the drying tubes mass gain and the cell pressures is ±0.1%. The observed reproducibility of the vapor pressures over the course of hundreds of measurements is ±0.1%.

All chemicals were used as received except for drying. The sodium nitrite, sodium nitrate, and potassium nitrate were dried at 393 K for a minimum of 24 hours. The potassium nitrite was dried at 353 K for several hours, pulverized, and dried for 24 hours at 373 K. The lithium nitrate was dried at least 24 hours at 433 K. The calcium nitrate tetrahydrate was stored in a desiccator over magnesium perchlorate for several days and the magnesium nitrate hexahydrate was dried at 363 K for several days.

Melts were prepared by difference weighing of the appropriate quantity of each salt directly into the cell followed by the addition of sufficient water to make a solution of minimum water concentration. After a minimum of two vapor pressure measurements at a given water concentration, water was added to the cell using a weighed syringe to produce a new solution of known water content. A total of five water concentrations were studied with each melt and a minimum of two melts were used for each system under investigation.

RESULTS AND DISCUSSION

Vapor pressures for the system $LiNO_3$-KNO_2-H_2O at three temperatures and salt mole ratios, R_L, of 0.50, 0.60 and 0.70 mol Li^+/mol salt are summarized in Figure 1, results for the system $.41LiNO_3$-$.41KNO_3$-$.18NaNO_3$-H_2O at four temperatures are given in Figure 2, and the vapor pressures for the systems $.472LiNO_3$-$.472KNO_3$-$.056Ca(NO_3)_2$-H_2O, $.472LiNO_3$-$.472KNO_3$-$.056Mg(NO_3)_2$-H_2O, and $.41LiNO_3$-$.41KNO_3$-$.18CsNO_3$-H_2O are plotted in Figure 3. The water concentration is expressed as the water mole ratio R_H (mol H_2O/mol salt). Each system exhibits the Henry's Law linear dependence of the vapor pressure on the water mole ratio observed earlier (1, 3). The vapor pressures of the (Li,K,Na)NO_3-H_2O system are sufficiently low at 383 K to permit measurements well into the transition concentration region from where water is the solute to where it is the solvent. The onset of deviations from Henry's Law occur at a water concentration of approximately 0.9 mol H_2O/mol salt. For the $LiNO_3$-(K,Na)NO_2-H_2O system at this temperature, deviations from Henry's Law do not start until the water concentration is 1.4 mol H_2O/mol salt (5).

The vapor pressures for the systems containing calcium or magnesium ions, while having a linear dependence of vapor pressure on water mole ratio, extrapolate to a negative vapor pressure as the water mole ratio approaches zero. This behavior was also observed for the (Li,K)NO_3-H_2O system and the $LiNO_3$-KNO_2-H_2O system at salt mole ratios greater than 1.0 mole Li^+/mol salt.

The Henry's Law constants defined as

$$K_H = \lim_{R_H \rightarrow 0} (f_H / R_H)$$

where f_H is the fugacity and R_H is the activity of water are summarized in Figure 4 as a function of the reciprocal absolute temperature for the systems (Li,K,Na)NO_3-H_2O and $LiNO_3$-

KNO_2-H_2O. Results for the systems (Li,K)NO_3-H_2O (3) and $LiNO_3$-(K,Na)NO_2-H_2O (5) are included for comparison. The value of the enthalpy of vaporization of water from the melt as evaluated from the slope of the ln K_H vs. 1/T relationship is listed in Table I for each system. The enthalpy of vaporization of water at 408 K, the approximate center of the temperature range studied, is 9.6 kcal/mol (19).

TABLE I

The Enthalpy of Vaporization of Water
Hydrate Melt Systems

Hydrate Melt System	Temperature Range (Kelvin)	Enthalpy of Vaporization (kcal/mol)
$LiNO_3$-KNO_3-$NaNO_3$	383.15-412.76	10.3
$LiNO_3$-KNO_2-$NaNO_2$	383.15-422.66	10.4
$LiNO_3$-KNO_3 (R_L=.5)	391.91-422.66	10.5
$LiNO_3$-KNO_2 (R_L=.5)	383.15-402.66	10.6

Several studies involving hydrate melts have revealed a dependence of melt properties on the type of cations present in the solution. As examples, the vapor pressure of (Li,K)NO_3-H_2O melts decreases as the lithium ion to potassium ion mole ratio increases (1, 4), water activities for (Ag,Tl)NO_3 based melts exhibit positive deviations from Raoult's Law but the deviations become negative when cations like calcium and cadmium are introduced into the system (7, 8), and the molar conductivity of (Ca,Li,K)NO_3 melts decreases 40 percent when potassium ions are completely replaced by lithium ions (17). In each of the examples, the effect on properties can be attributed to the presence of a hydrated ion like lithium or calcium.

Further evidence of the hydrated cation effect is apparent from the results summarized in Figure 3. A comparison of the results for the (Li,K,Cs)NO_3-H_2O and (Li,K,Na)NO_3-H_2O systems reveals that the vapor pressure decreases at a fixed water concentration when the cesium ions are replaced by the smaller sodium ions. The two squares and two triangles plotted in Figure 3 represent calculated values of vapor pressure for the (Li,K)NO_3-H_2O system (1, 4) obtained by extrapolating the vapor pressures at fixed R_H values of 0.3 and 0.5 mol H_2O/mol salt to R_L values of 0.41 (squares) and 0.59

(triangles) mol Li^+/mol salt. These points represent systems in which conceptually the cesium or sodium ions have been replaced by potassium ions (R_L = 0.41) or lithium ions (R_L = 0.59). It is seen that the trend toward decreasing vapor pressure resulting from the replacement of a large cation by a smaller cation, as observed for the $(Li,K)NO_3$ system, holds for all combinations of alkali metal cations with the lithium ion producing the largest effect on the vapor pressure. This trend is consistent with the high charge density of small ions and their consequent greater ability to attract polar water molecules.

The decrease in vapor pressure is even greater when alkaline earth cations are introduced into the system; as shown in Figure 3 the addition of only 5.6 percent calcium ions into the melt composed of equimolar lithium and potassium nitrates produces a significant reduction in the vapor pressure and the introduction of the same quantity of magnesium ions lowers the vapor pressure approximately another twenty percent.

Figure 5 summarizes water activities as a function of the water mole fraction for a number of hydrate melt systems and shows that while most of the systems exhibit negative deviations from Raoult's Law, several deviate in the positive direction. Significantly, only the systems containing primarily $(Ag,Tl)NO_3$ and no strongly hydrated cation, deviate positively from Raoult's Law.

The vapor pressures as a function of water mole ratio for most of the hydrate melt systems considered in Figure 5 are plotted in Figure 6. An excellent correlation exists between the water mole fraction concentration dependence of the water activity and the water mole ratio concentration dependence of the vapor pressure; a system which exhibits negative deviation from Raoult's Law has a linear dependence of the vapor pressure on concentration, while a system which deviates positively from Raoult's Law does not have a linear relationship between water concentration and vapor pressure. Furthermore, it is apparent that in order for the vapor pressure to have a linear dependence on water mole ratio and negative deviations from Raoult's Law, the melt must contain one or more strongly hydrated cations like lithium, magnesium or calcium. By contrast, if the system does not contain any strongly hydrated cations the deviations from Raoult's Law will be positive and the vapor pressure will not vary linearly with the water mole ratio.

ACKNOWLEDGMENT

The author wishes to thank Donald Erickson, Energy Concepts Company, Annapolis, Maryland, for suggesting several of the systems studied in this work.

REFERENCES

1. Tripp, T. B. and Braunstein, J., J Phys. Chem., 73, 1984(1969).

2. Braunstein, H. and Braunstein, J., J. Chem. Thermodynamics, 3, 419(1971).

3. Tripp, T. B., J. Chem. Thermodynamics, 7, 263(1975).

4. Tripp, T. B., in "Molten Salts", The Electrochemical Soc. Inc., 1976, p. 560.

5. Tripp, T. B., in "Molten Salts", The Electrochemical Soc. Inc., 1984, p. 403

6. Trudelle, M-C, Abraham, M. and Sangster, J., Can. J. Chem., 55, 1711(1977).

7. Sangster, J., Abraham, M-C. and Abraham, M., J. Chem. Thermodynamics, 11, 619(1979).

8. Sangster, J., Abraham, M-C. and Abraham, M., Can. J. Chem., 56, 348(1978).

9. Abraham, M-C., Abraham, M. and Sangster, J., J. Sol. Chem., 8, 647(1979).

10. Abraham, M-C., Abraham, M. and Sangster, J., J. Chem. Eng. Data, 25, 331(1980).

11. Sacchetto, G. A., Bombi, G. G. and Macca, C., J. Chem. Thermodynamics, 13, 31(1981).

12. Jain, S. K., J. Chem. Eng. Data, 25, 36(1980).

13. Jain, S. K. and Tamamushi, R., Can. J. Chem., 58, 1697(1980).

14. Islm, N. and Dhawan, K., Ind. J. Chem., 20A, 958(1981).

15. Doan, T. H. and Sangster, J., *J. Chem. Eng. Data*, **26**, 141(1981).

16. Sharma, R. C. and Gaur, H. C., *Ind. J. Chem.*, **15A**, 84(1977).

17. Easteal, A. J., *Aust. J. Chem.*, **34**, 1853(1981).

18. Erickson, D. C. and Lutz, E. J., "Absorptive Recycle of Distillation Waste Heat", 4th Annual Industrial Energy Conservation Technology Conference, Houston, Texas, April, 1982.

19. National Engineering Laboratory Steam Tables 1964. Her Majesty's Stationary Office: Edinburgh, 1964.

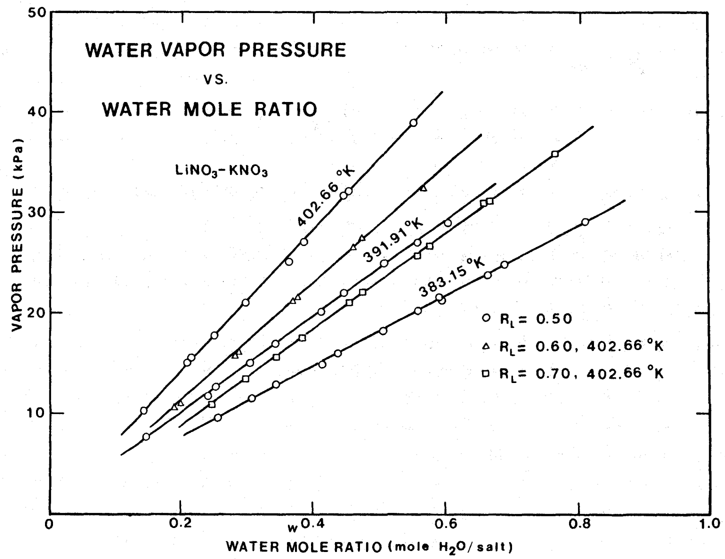

Figure 1. Vapor Pressures of the System $LiNO_3$-KNO_3-H_2O.

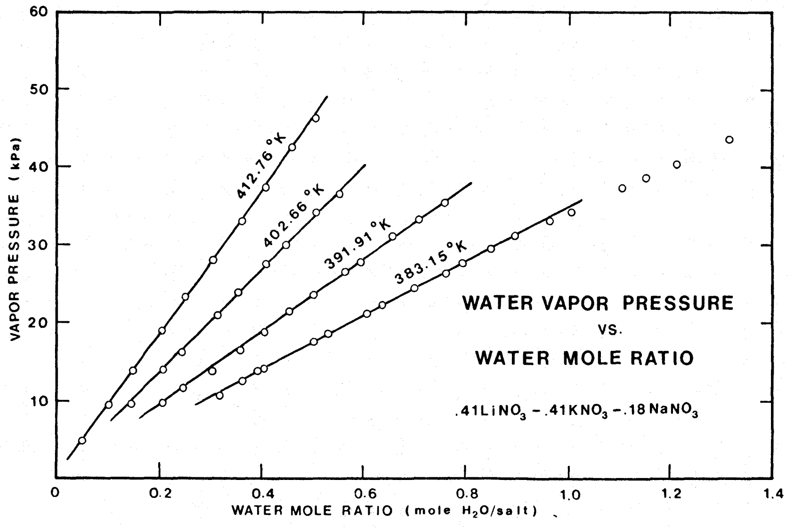

Figure 2. Vapor Pressures of the System .41$LiNO_3$-.41KNO_3-.18$NaNO_3$-H_2O.

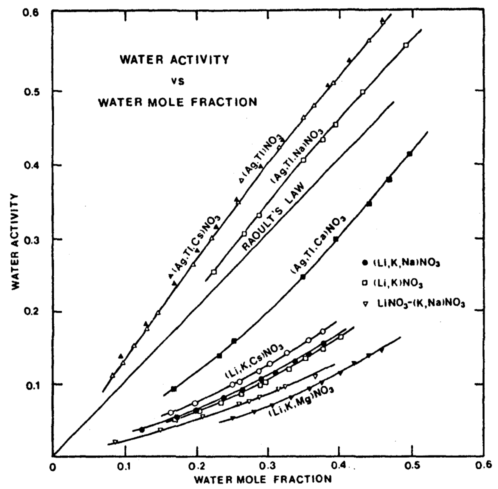

Figure 5. Water Activities vs. Water Mole Fraction for Hydrate Melt Systems. References: This Work, 1, 5-7,9, 10.

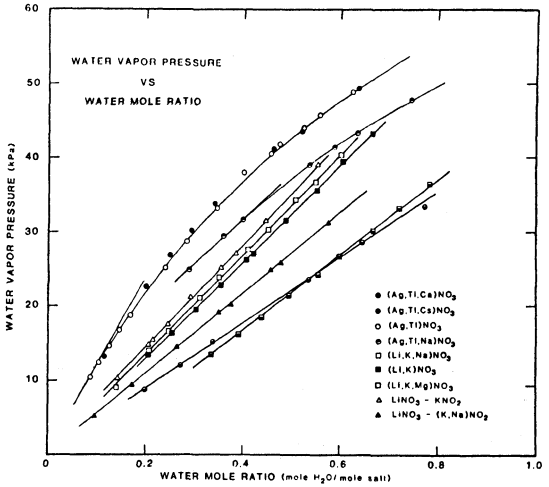

Figure 6. Vapor Pressures vs. Water Mole Ratio for Hydrate Melt Systems. References: This Work, 1, 5-7, 9, 10.

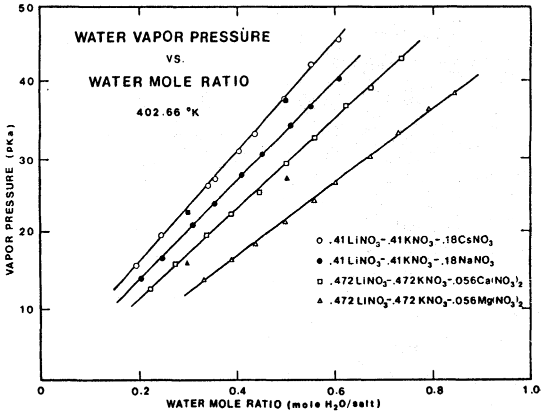

Figure 3. Vapor Pressures of the Systems $.41LiNO_3$-$.41KNO_3$-$.18CsNO_3$, $.472LiNO_3$-$.472KNO_3$-$.056Ca(NO_3)_2$-H_2O, and $.472LiNO_3$-$.472KNO_3$-$.056Mg(NO_3)_2$-H_2O at 402.66 K.

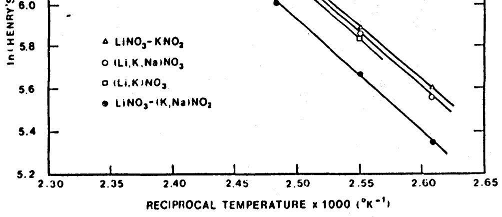

Figure 4. Henry's Law Constants vs. Reciprocal Absolute Temperature for Hydrate Melt Systems. References: This Work, 1, 5.

DOI: 10.1149/198601.0551PV

ELECTRODE POTENTIALS OF METAL CHLORIDES IN BINARY AND TERNARY FUSED SALT SOLUTIONS

WITH ALKALI CHLORIDES

P.J. Tumidajski and S.N. Flengas

Department of Metallurgy and Materials Science

University of Toronto
Toronto, Ontario
Canada M5S 1A4

ABSTRACT

The standard formal electrode potentials of several metals have been determined from 700-900°C in NaCl, KCl, CsCl or the equimolar mixtures of these salts using galvanic or redox cells with a silver-silver chloride reference electrode. The activity coefficients and other partial molar properties of these solutions were calculated as a function of temperature from the emf measurements.

INTRODUCTION

In a previous publication from this laboratory, the standard electrode potentials and the associated thermodynamic properties for the dilute solutions of $AlCl_3$ in binary and ternary fused salts were reported (1). For those experiments, the electrode potential in the solvents NaCl, KCl, CsCl or in the equimolar mixtures of these salts, was determined using a silver-silver chloride reference electrode. For the present investigation, this method was extended to the chlorides of cobalt, nickel, thorium, iron, chromium and copper.

The electrode potentials of the dilute solutions of metal chlorides in alkali chlorides have been the subject of several electrochemical studies. However, data for various solvent systems are incomplete, especially for the multicomponent systems. It is the purpose of the present investigation to establish the thermodynamic behaviour and the emf series of metals in different binary and ternary alkali chloride molten salt electrolytes from 700°C to 900°C. Also, the validity of theoretical expressions for the prediction of the thermodynamic properties of the ternary solutions from binary solution data was confirmed.

When a metal, M, has two stable valence states at high temperatures, namely M^{m+} and M^{n+} (where $n>m$), the electrode potentials to be determined are, respectively, E°_m and E°_n of the electrodes M/M^{m+} and M/M^{n+}, and the redox potential $E^\circ_{m,n}$ of the system M^{m+}/M^{n+}. The expression relating the three potentials is easily calculated using a thermodynamic cycle as,

$$nE^\circ_n - mE^\circ_m = (n-m)\,E^\circ_{m,n} \tag{1}$$

When any two of the three potentials are known, the unknown potential can be calculated. In general, in fused salts E°_n cannot be determined directly because of the reactivity of the metal with a solution containing the higher valence state chloride.

EXPERIMENTAL

The preparation and purification of the alkali chlorides has been described elsewhere (1). The metal chlories were anhydrous and better than 99.9% pure. The metal electrodes had a purity of greater than 99.9%. Two different types of electrochemical cells were used for determining electrode potentials.

(a) A cell for measuring metal electrode potentials.

This cell, similar to that reported earlier (1), can be described schematically as,

$$\underset{(-)}{\mathrm{M}}\;\Big|\;\underset{(X_2)}{\mathrm{MCl}_m - \mathrm{ACl}}\;\Big\|\;\underset{\text{diaphragm}}{\text{asbestos}}\;\Big\|\;\underset{(X_1)}{\mathrm{AgCl} - \mathrm{ACl}}\;\Big|\;\underset{(+)}{\mathrm{Ag}}$$

where, M was respectively cobalt, nickel, iron, chromium, copper or thorium. MCl_m was respectively $CoCl_2$, $NiCl_2$, $FeCl_2$, CuCl or $ThCl_4$. ACl represents the salt components NaCl, KCl, CsCl or the binary equimolar mixtures of these salts. The concentration of AgCl in alkali chloride is fixed at $X_1 = 0.05$. The spontaneous reaction for the Ag-M galvanic cell is,

$$\mathrm{M} + \underline{m\,\mathrm{AgCl}} \rightleftharpoons \underline{\mathrm{MCl}_m} + m\,\mathrm{Ag}$$

where the line under a salt species denotes a species in solution. The corresponding form of the Nernst equation for solutions dilute enough to obey Henry's law is written as,

$$E_{cell} = E^\circ_{f(cell)} - \frac{2.303\ RT}{m\ F} \log \frac{X_{MCl_m}}{X^m_{AgCl}} \tag{2}$$

where, X's are mole fractions and, the standard formal cell potential, $E^\circ_{f(cell)}$ is defined as,

$$E^\circ_{f(cell)} = E^\circ_{MCl_m} - E^\circ_{AgCl} - \frac{2.303\ RT}{m\ F} \log \frac{\gamma_{MCl_m}}{\gamma^m_{AgCl}} \tag{3}$$

For this expresssion, $E^{\circ}_{MCl_m}$ and E°_{AgCl} are the standard formation cell potentials of pure liquid MCl_m and AgCl. The values of $E^{\circ}_{MCl_m}$ and $E^{\circ}_{MCl_m}$ and E°_{AgCl} were obtained from the literature (2). F is the Faraday constant, given as 8.3144 J/K mol. The standard state in all cases was the pure liquid chloride at the temperature of the experiments.

(b) A cell for measuring redox potentials; this cell can be illustrated schematically as,

$$\begin{array}{c|c||c||c|c} \text{Ag} & \text{AgCl - ACl} & \text{asbestos} & MCl_m\ -\ MCl_n\ -\ ACl & \text{Pt} \\ (-) & (X_1) & \text{diaphragm} & (X_2)\qquad\quad (X_3)\quad & (+) \end{array}$$

where, MCl_m was, respectively, $FeCl_2$, $CrCl_2$ or CuCl at mole fraction X_2, and MCl_n was, respectively, $FeCl_3$, $CrCl_3$ or $CuCl_2$ at mole fraction X_3. ACl had the same meaning as described above. The cell reaction is,

$$Ag + \underline{MCl_n} = \underline{MCl_m} + AgCl$$

where n-m=1. For the redox cell, the corresponding form of the Nernst equation is,

$$E_{cell} = E^{\circ}_{r(cell)} - \frac{2.303\ RT}{F} \log \frac{X_{AgCl}\ X_{MCl_m}}{X_{MCl_n}} \qquad (4)$$

The standard formal redox cell potential is defined by:

$$E^{\circ}_{r(cell)} = E^{\circ}_{AgCl} - E^{\circ}_{MCl_m} - E^{\circ}_{MCl_n} - 2.303\ \ RT \log \frac{\gamma_{AgCl}\ \gamma_{MCl_m}}{\gamma_{MCl_n}} \qquad (5)$$

Formal formation potentials can also be defined by:

$$E^{\circ}_{f(MCl_m)} = E^{\circ}_{MCl_m} - \frac{2.303\ RT}{mF} \log\ \gamma_{MCl_m} \qquad (6)$$

Such formal formation potentials represent the free energy of formation of unit mole fraction of a hypothetical salt behaving thermodynamically as it would behave in an infinitely dilute state in a given solvent. Thus, for each solvent the formal potentials are a constant of the system from which emf series in fused salts may be tabulated.

The complete experimental apparatus and procedure have been described in detail elsewhere (1). Reversibility was confirmed by temperature cycling and by polarization tests. For the latter, 1 mA was passed through the cell, in each case the emf returned to the original value in less than one minute. Cell emf's were stable and reproducible to within 1 mV over a 24 h period. The adjustment for thermoelectric potentials was established by connecting the electrode tips in the absence of the electrolyte, and measuring the resulting emf at various temperatures.

RESULTS AND DISCUSSION

Tables 1 to 9 summarize the measured cell emf's which have been expressed as least squares lines of the form E = A T + B, where, E is the cell potential in volts, and T is the temperature in K. Cell emf's have been adjusted for thermoelectric effects. Melt compositions have been expressed in terms of the mole fractions of the metal chloride. Also, for the ternary solutions, the composition variable t has been defined as,

$$t = X_{CsCl}/(X_{CsCl} + X_{NaCl}) \tag{7a}$$

or

$$t = X_{CsCl}/(X_{CsCl} + X_{KCl}) \tag{7b}$$

for the CsCl ternary solutions, and as,

$$t= X_{KCl}/(X_{KCl} + X_{NaCl}) \tag{7c}$$

for the solutions containing only KCl and NaCl. The correlation coefficients in Tables 1 through 9 indicate that the plots of cell emf versus temperature are linear. Also, the estimate for the standard deviation of a cell potential for the regression of cell emf on temperature is smaller than 4 mV, for all cases.

A typical Nernst plot for the $ThCl_4$ system is given in Figure 1. For this metal chloride, the Nernst slope indicates a four electron transfer within a 99.9% confidence level. Thus, the tetravalent thorium ion is present in these melts, although it should be less stable for the NaCl solvents. For the $FeCl_2$, $NiCl_2$, $CoCl_2$, and $CrCl_2$ solutes the linear regression analysis for the Nernst plots gave correlation coefficients of almost unity in all cases. Within a 99.9% confidence level, there is a two electron transfer. For all the redox cells and for the CuCl galvanic cell, there is a one electron transfer reaction. The linear regression analysis for these Nernst plots also gave correlation coefficients of close to unit for every case. Since for all systems the Nernst relationship is obeyed, Henry's law is followed over a range of concentrations up to approximately 10^{-2} mole fraction.

Values of $E°_{f(cell)}$ and $E°_{r(cell)}$ determined graphically as well as the formal formation potentials of the higher valence state metal chlorides calculated from equation [1], are recorded in accordance with the IUPAC convention in Tables 10 a to 10c for three temperatures (3). The values have been adjusted to correspond to the chlorine gas reference electrode reported in a previous investigation (1). The results in the present study agree with values found in the literature (4-14). It can be seen that the magnitude of the formal potentials increase as CsCl is added, showing the pronounced effect of CsCl is creating thermodynamically stable solutions. In general, the magnitude of the formal potentials decrease as the temperature is increased which indicates a decrease in thermodynamic stability at the higher temperatures. Included in Tables 10a to 10c are values of the standard formal potentials in the ternary solutions as calculated from the previously derived expression (15-17),

$$E^\circ_{f(123)} = (1-t)\, E^\circ_{f(12)} + t\, E^\circ_{f(13)} \tag{8}$$

where, $E^\circ_{f(123)}$ is the standard formal potential in the ternary solution, and $E^\circ_{f(12)}$ and $E^\circ_{f(13)}$ are the standard formal potentials in the component binary systems. The t parameter was defined in equation (7). The experimental results for t = 1/2 are in agreement to approximately ± 6% of the predicted values.

Tables 11 to 13 summarize the thermodynamic properties. The thermodynamic properties for $CuCl_2$ were not calculated because the standard formation potential of liquid $CuCl_2$ is not available. Tables 11a to 11c list activity coefficients for three temperatures. The very low values of the activity coefficients when combined with exothermic enthalpies of mixing and negative excess entropies of mixing, to be discussed subsequently, are indicative of strong interactions in these solutions which are usually associated with the formation of complex species. With the exception of several NaCl solvents, the activity coefficients increase with temperature increase, indicating the dissociation of the complexes at higher temperatures. For a few NaCl solvents, the activity coefficients decrease as the temperature is increased which could be taken as due to clustering of the ionic species, rather than to any complex formation. Also included in Table 11 are the predicted values of the activity coefficients for the ternary solutions according to the equation given as (15-17),

$$\log \gamma_{123} = (1-t) \log \gamma_{12} + t \log \gamma_{13} \tag{9}$$

The partial molar enthalpies of mixing are summarized in Table 12. The solutions become increasingly exothermic as the radius of the alkali chloride changes from Na^+ to Cs^+. This is commonly explained on the basis of the competition for anions between the solute and solvent cations. Furthermore, the predicted values for the partial molar enthalpies of mixing in the ternary solutions, calculated from (15-17),

$$\overline{\Delta H}_{123} = (1-t)\, \overline{\Delta H}_{12} + t\, \overline{\Delta H}_{13} \tag{10}$$

are given in Table 12. The comparison between the measured and predicted value is better in the systems without NaCl where there is a minimum of extrapolation.

Table 13 lists the excess partial molar entropies of mixing. In general, the values are negative, and the magnitude increases in the order NaCl → KCl → CsCl. This indicates that part of the total entropy of mixing should be related to the change in frequency of the characteristic vibrations of the species in solution.

ACKNOWLEDGEMENT

Financial assistance by the Natural Sciences and Engineering Research Council of Canada to one of the authors (P.J.T.) in the form of Postgraduate Scholarship is gratefully acknowledge.

REFERENCES

1. P.J. Tumidajski and S.N. Flengas, Can. J. Chem. 63, 1080 (1985).
2. W.H. Hamer, M.S. Malmberg and B. Rubin, J. Electrochem. Soc. 103, 8 (1956).
3. T. Licht and A. de Bethune, J. Chem. Educ. 34, 443 (1957).
4. D.C. Hamby and A.B. Scott, J. Electrochem. Soc. 117, 319 (1970).
5. R. Combes, J. Vedel and B. Tremillon, J. Electroanal. Chem. 27, 174 (1970).
6. S.N. Flengas and T.R. Ingraham, Can. J. Chem. 35, 1139 (1957).
7. D.C. Hamby and A.B. Scott, J. Electrochem. Soc. 115, 704 (1968).
8. D.C. Hamby and A.R. Hohimer, J. Electrochem. Soc. 121, 104 (1974).
9. S.N. Flengas and T.R. Ingraham, Can. J. Chem. 35, 1254 (1957).
10. H. Kuhnl, M. Wittner and W. Simon, Electrochimica Acta 24, 55 (1979).
11. M.V. Smirnov, A.V. Pokrobskii and N.A. Loginov, Russ. J. Inor. Chem. 15, 1644 (1970).
12. S.N. Flengas and T.R. Ingraham, Can. J. Chem. 36, 1103 (1958).
13. M.V. Smirnov, A.V. Pokrovskii and N.A. Loginov, Zh. Prikl. Kh. 43, 2334 (1970).
14. R. Srinivasan and S.N. Flengas, Can. J. Chem. 42, 1315 (1964).
15. D.R. Sadoway and S.N. Flengas, J. Electrochem. Soc. 122, 515 (1975).
16. D.R. Sadoway and S.N. Flengas, in "Extractive Metallurgy of Retractory Metals", edited by H. Shohn, N. Carlson and J. Smith, AIME, Warrendale, Pa., pp. 315-339 (1981).

17. S.N. Flengas and D.R. Sadoway, in "Proceedings of the Third International Symposium on Molten Salts", edited by G. Mamantov, M. Blander and G.P. Smith, The Electrochemical Society, N.J., pp. 68-94 (1981).

Table 1. E_{cell} versus temperature for the $CoCl_2$ system

Solvent	X_{CoCl_2}	E = AT + B (V)		C Coeff.	Range (K)
		$A \times 10^4$	B		
NaCl	2.02×10^{-3}	-0.471	0.343	-0.999	1108-1178
	3.88×10^{-3}	-7.550	0.344	-0.999	1101-1166
	6.56×10^{-3}	-9.840	0.344	-0.999	1111-1186
	8.55×10^{-3}	-1.096	0.344	-0.999	1107-1181
KCl	3.55×10^{-3}	-1.272	0.426	-0.996	1081-1174
	5.63×10^{-3}	-1.504	0.430	-0.999	1091-1174
	7.61×10^{-3}	-1.627	0.429	-0.998	1100-1197
	1.03×10^{-2}	-1.753	0.428	-0.999	1075-1181
CsCl	6.11×10^{-3}	-1.804	0.497	-0.999	961-1118
	1.01×10^{-2}	-2.023	0.498	-0.999	965-1107
	1.31×10^{-2}	-2.137	0.498	-0.999	937-1104
	1.87×10^{-2}	-2.291	0.498	-0.999	941-1096
NaCl-KCl* (t=1/2)	1.72×10^{-3}	-1.207	0.453	-0.999	985-1101
	3.04×10^{-3}	-1.454	0.453	-0.999	957-1096
	5.20×10^{-3}	-1.678	0.452	-0.999	957-1109
	7.87×10^{-3}	-1.865	0.453	-0.999	946-1105
NaCl-CsCl* (t=1/2)	2.98×10^{-3}	-0.929	0.406	-0.999	966-1103
	7.35×10^{-3}	-1.320	0.406	-0.999	968-1102
	1.02×10^{-2}	-1.453	0.405	-0.999	969-1092
	1.26×10^{-2}	-1.545	0.405	-0.999	961-1105
KCl-CsCl* (t=1/2)	4.91×10^{-3}	-2.334	0.538	-0.999	990-1136
	8.11×10^{-3}	-2.550	0.538	-0.999	974-1109
	1.05×10^{-2}	-2.664	0.538	-0.999	960-1109
	1.43×10^{-2}	-2.800	0.539	-0.999	960-1102

*Equimolar.

Table 2. E_{cell} versus temperature for the $NiCl_2$ system

Solvent	X_{NiCl_2}	E = AT + B (V)		C Coeff.	Range (K)
		$A \times 10^4$	B		
NaCl	1.36×10^{-3}	-0.050	0.120	-0.972	1131-1189
	2.00×10^{-3}	-0.206	0.118	-0.999	1128-1185
	3.94×10^{-3}	-0.495	0.118	-0.999	1123-1186
	4.61×10^{-3}	-0.559	0.117	-0.998	1126-1191
KCl	2.00×10^{-3}	-0.041	0.106	-0.985	1078-1152
	3.43×10^{-3}	-0.256	0.104	-0.998	1068-1110
	5.23×10^{-3}	-0.440	0.104	-0.999	1048-1105
	6.78×10^{-3}	-0.565	0.106	-0.994	1077-1107
CsCl	5.25×10^{-3}	-1.016	0.170	-0.999	968-1100
	8.19×10^{-2}	-1.211	0.171	-0.999	937-1106
	1.19×10^{-2}	-1.374	0.172	-0.999	937-1094
	1.51×10^{-2}	-1.476	0.172	-0.999	940-1094
NaCl-KCl* (t=1/2)	1.27×10^{-3}	-1.801	0.335	-0.999	978-1093
	2.92×10^{-3}	-2.209	0.340	-0.997	973-1098
	4.46×10^{-3}	-2.353	0.336	-0.999	976-1101
	6.06×10^{-3}	-2.479	0.335	-0.998	970-1095
NaCl-CsCl* (t=1/2)	3.23×10^{-3}	-1.229	0.210	-0.999	953-1087
	6.96×10^{-3}	-1.555	0.209	-0.999	950-1087
	9.52×10^{-3}	-1.699	0.210	-0.999	954-1091
	1.27×10^{-2}	-1.817	0.209	-0.999	916-1091
KCl-CsCl* (t=1/2)	3.88×10^{-3}	-0.389	0.134	-0.998	947-1109
	7.60×10^{-3}	-0.680	0.134	-0.998	934-1109
	1.05×10^{-2}	-0.813	0.133	-0.999	934-1100
	1.32×10^{-2}	-0.917	0.134	-0.999	940-1100

*Equimolar.

Table 3. E_{cell} versus temperature for the $FeCl_2$ system

Solvent	X_{FeCl_2}	E = AT + B (V)		C Coeff.	Range (K)
		$A \times 10^4$	B		
CsCl	3.41×10^{-3}	-1.713	0.683	-0.992	969-1044
	8.46×10^{-3}	-2.105	0.683	-0.999	967-1070
	1.26×10^{-2}	-2.231	0.678	-0.997	958-1053
	1.68×10^{-2}	-2.400	0.683	-0.994	968-1051
NaCl-KCl*	2.79×10^{-3}	-1.279	0.614	-0.995	966-1029
	6.25×10^{-3}	-1.779	0.629	-0.998	953-1033
	9.18×10^{-3}	-1.849	0.619	-0.998	965-1036
	1.18×10^{-2}	-1.875	0.611	-0.998	957-1035
KCl-CsCl*	3.06×10^{-3}	-1.789	0.679	-0.997	974-1036
	6.25×10^{-3}	-2.119	0.682	-0.998	967-1036
	9.70×10^{-3}	-2.184	0.669	-0.999	962-1036
	1.26×10^{-2}	-2.438	0.684	-0.998	962-1031

*Equimolar.

Table 4. E_{cell} versus temperature for the $CrCl_2$ system

Solvent	X_{CrCl_2}	E = AT + B (V)		C Coeff.	Range (K)
		$A \times 10^4$	B		
NaCl	6.90×10^{-4}	1.234	0.660	0.999	1115-1172
	1.24×10^{-3}	1.356	0.619	0.999	1122-1173
	2.16×10^{-3}	1.035	0.630	0.999	1117-1175
	2.80×10^{-3}	1.105	0.609	0.999	1110-1166
KCl	7.01×10^{-4}	-2.695	1.076	-0.999	1082-1173
	1.21×10^{-3}	-1.552	0.925	-1.000	1086-1166
	1.72×10^{-3}	-1.611	0.914	-0.999	1092-1169
	2.29×10^{-3}	-2.234	0.970	-0.999	1084-1172
CsCl	1.65×10^{-3}	-3.459	1.071	-0.999	980-1114
	3.29×10^{-3}	-3.768	1.072	-0.999	980-1109
	5.03×10^{-3}	-3.949	1.072	-0.999	980-1107
	6.99×10^{-3}	-4.088	1.071	-0.999	981-1107
NaCl-KCl* (t=1/2)	6.67×10^{-4}	-1.152	0.929	-0.993	984-1122
	1.09×10^{-3}	-1.416	0.935	-0.998	984-1122
	1.76×10^{-3}	-1.691	0.940	-0.998	984-1131
	2.36×10^{-3}	-1.833	0.940	-0.998	978-1131
NaCl-CsCl* (t=1/2)	1.48×10^{-3}	-1.951	0.925	-0.998	1010-1132
	2.51×10^{-3}	-2.166	0.924	-0.999	977-1136
	3.38×10^{-3}	-2.269	0.921	-0.984	979-1118
	4.24×10^{-2}	-2.398	0.925	-0.999	978-1118
KCl-CsCl* (t=1/2)	9.76×10^{-4}	-2.758	1.016	-0.999	981-1105
	1.76×10^{-3}	-3.007	1.015	-0.999	978-1129
	2.83×10^{-3}	-3.217	1.016	-0.999	981-1118
	3.60×10^{-3}	-3.321	1.016	-0.999	979-1110

*Equimolar.

Table 5. E_{cell} versus temperature for the $CuCl_2$ system

Solvent	X_{CuCl}	E = AT + B (V)		C Coeff.	Range (K)
		$A \times 10^4$	B		
NaCl	1.01×10^{-3}	2.687	0.335	0.999	1090-1176
	1.93×10^{-3}	2.121	0.335	0.999	1087-1171
	2.84×10^{-3}	1.780	0.336	0.999	1082-1178
	3.68×10^{-3}	1.563	0.335	0.999	1084-1178
KCl	9.58×10^{-4}	2.228	0.432	0.999	1057-1156
	1.91×10^{-3}	1.623	0.433	0.999	1072-1181
	3.34×10^{-3}	1.150	0.432	0.999	1075-1173
	4.68×10^{-3}	0.858	0.432	0.998	1068-1181
CsCl	9.54×10^{-4}	1.642	0.511	0.998	962-1172
	1.91×10^{-3}	1.042	0.511	0.998	965-1175
	3.05×10^{-3}	0.633	0.512	0.997	986-1176
	4.94×10^{-3}	0.186	0.515	0.978	944-1181
NaCl-KCl* (t=1/2)	9.00×10^{-4}	1.036	0.548	0.999	983-1181
	1.80×10^{-3}	4.370	0.549	1.000	994-1177
	3.09×10^{-3}	-0.025	0.548	-0.999	954-1173
	4.24×10^{-3}	-0.301	0.549	-0.999	942-1175
NaCl-CsCl* (t=1/2)	9.25×10^{-4}	1.659	0.419	0.999	976-1175
	1.70×10^{-3}	1.140	0.418	0.999	966-1173
	2.77×10^{-3}	0.712	0.419	0.999	976-1173
	3.84×10^{-3}	0.432	0.419	0.999	964-1171
KCl-CsCl* (t=1/2)	1.02×10^{-3}	1.661	0.497	0.999	979-1174
	2.04×10^{-3}	1.068	0.496	0.999	980-1169
	3.05×10^{-3}	0.714	0.497	0.999	975-1174
	4.40×10^{-3}	0.395	0.497	0.985	976-1180

*Equimolar.

Table 6. E_{cell} versus temperature for the $ThCl_4$ system

Solvent	X_{ThCl_4}	E = AT + B (V)		C Coeff.	Range (K)
		A × 10^4	B		
NaCl	3.04×10^{-4}	1.371	1.248	0.999	1113-1177
	1.13×10^{-3}	1.090	1.247	0.999	1101-1177
	1.52×10^{-3}	1.038	1.246	0.995	1103-1175
	2.20×10^{-3}	0.961	1.246	0.997	1093-1175
KCl	7.75×10^{-4}	-2.230	1.750	-0.999	1100-1179
	1.53×10^{-3}	-2.387	1.752	-0.999	1071-1174
	2.12×10^{-3}	-2.455	1.751	-0.999	1072-1173
	2.70×10^{-3}	-2.510	1.752	-0.999	1067-1173
CsCl	2.64×10^{-3}	-5.981	2.207	-0.999	981-1087
	4.13×10^{-3}	-6.082	2.208	-0.999	972-1085
	5.52×10^{-3}	-6.144	2.208	-0.999	955-1080
	7.74×10^{-3}	-6.207	2.206	-0.999	960-1079
NaCl-KCl* (t=1/2)	6.73×10^{-4}	-4.007	1.936	-0.999	1009-1111
	8.22×10^{-4}	-4.064	1.937	-0.999	982-1092
	2.09×10^{-3}	-4.260	1.937	-0.999	982-1101
	2.88×10^{-3}	-4.324	1.936	-0.999	982-1101
	3.87×10^{-3}	-4.392	1.937	-0.999	981-1100
NaCl-CsCl* (t=1/2)	1.71×10^{-3}	-0.489	1.590	-0.999	953-1083
	4.18×10^{-3}	-0.663	1.588	-0.999	948-1079
	6.81×10^{-3}	-0.777	1.589	-0.999	950-1085
	8.85×10^{-3}	-0.836	1.589	-0.999	896-1085
KCl-CsCl* (t=1/2)	1.84×10^{-3}	-3.614	1.903	-0.999	961-1095
	3.68×10^{-3}	-3.769	1.904	-0.999	963-1092
	5.65×10^{-3}	-3.861	1.904	-0.998	963-1093
	8.35×10^{-3}	-3.944	1.903	-0.996	948-1093

*Equimolar.

Table 7. E_{cell} versus temperature for the $FeCl_2$-$FeCl_3$ system

Solvent	X_{FeCl_2}	X_{FeCl_3}	E = AT + B (V) A x 10^4	 B	C Coeff.	Range (K)
CsCl	3.46×10^{-3}	2.58×10^{-3}	1.010	0.666	0.997	955-1024
	3.45×10^{-3}	6.29×10^{-3}	1.897	0.655	0.997	950-1024
	3.44×10^{-3}	9.73×10^{-3}	2.344	0.649	0.999	950-1026
	3.43×10^{-3}	1.21×10^{-2}	2.430	0.659	0.998	960-1026
NaCl-KCl*	3.17×10^{-3}	4.33×10^{-3}	1.433	0.643	0.998	962-1026
	3.16×10^{-3}	8.73×10^{-3}	2.065	0.641	0.999	953-1031
	3.14×10^{-3}	1.31×10^{-2}	2.452	0.637	0.998	953-1021
	3.13×10^{-3}	1.53×10^{-2}	2.532	0.643	0.998	945-1017
KCl-CsCl*	3.57×10^{-3}	2.79×10^{-3}	0.425	0.714	0.969	953-1024
	3.56×10^{-3}	4.94×10^{-3}	1.208	0.685	0.997	948-1024
	3.55×10^{-3}	7.19×10^{-3}	1.409	0.697	0.996	948-1019
	3.53×10^{-3}	1.20×10^{-2}	1.937	0.689	0.998	950-1019

*Equimolar.

Table 8. E_{cell} versus temperature for the $CrCl_2$-$CrCl_3$ system

Solvent	X_{CrCl_2}	X_{CrCl_3}	E = AT + B (V)		C Coeff.	Range (K)
			A × 10^4	B		
NaCl	1.11×10^{-3}	1.72×10^{-3}	10.98	-0.491	0.999	1098-1181
	1.10×10^{-3}	3.51×10^{-3}	11.60	-0.492	0.999	1093-1180
	1.10×10^{-3}	5.13×10^{-3}	11.91	-0.490	0.999	1093-1184
	1.10×10^{-3}	6.95×10^{-3}	12.18	-0.491	0.999	1091-1182
	2.41×10^{-3}	6.94×10^{-3}	11.51	-0.491	0.999	1091-1187
KCl	6.75×10^{-4}	1.31×10^{-3}	6.286	-0.034	0.999	1097-1184
	6.72×10^{-4}	4.54×10^{-3}	7.374	-0.036	0.999	1089-1179
	6.71×10^{-4}	6.82×10^{-3}	7.731	-0.036	0.999	1088-1181
	6.69×10^{-4}	8.93×10^{-3}	7.958	-0.036	0.999	1083-1180
	$1.67 \quad 10^{-3}$	$8.92 \quad 10^{-3}$	7.169	-0.035	0.999	1076-1175
CsCl	2.21×10^{-3}	3.06×10^{-3}	3.618	0.178	0.999	996-1103
	2.20×10^{-3}	6.11×10^{-3}	4.220	0.178	0.999	976-1103
	2.19×10^{-3}	9.85×10^{-3}	4.619	0.180	0.999	983-1109
	2.18×10^{-3}	1.49×10^{-2}	5.000	0.177	0.999	983-1115
	3.74×10^{-3}	1.48×10^{-2}	4.531	0.178	0.999	979-1109
NaCl-KCl* (t=1/2)	9.68×10^{-4}	2.39×10^{-3}	10.83	-0.484	0.999	986-1126
	9.66×10^{-4}	4.03×10^{-3}	11.30	-0.485	0.999	985-1126
	9.65×10^{-4}	5.20×10^{-3}	11.52	-0.485	0.999	985-1130
	9.63×10^{-4}	7.80×10^{-3}	11.86	-0.484	0.999	978-1130
	2.40×10^{-3}	7.78×10^{-3}	11.08	-0.485	0.999	978-1135
NaCl-CsCl* (t=1/2)	7.80×10^{-4}	3.48×10^{-3}	8.189	-0.145	0.999	902-1098
	7.76×10^{-4}	8.65×10^{-3}	8.978	-0.145	0.999	917-1098
	7.73×10^{-4}	1.18×10^{-2}	9.248	-0.145	0.999	925-1131
	7.70×10^{-4}	1.56×10^{-2}	9.501	-0.146	0.999	923-1127
	3.36×10^{-3}	1.55×10^{-2}	8.223	-0.145	0.999	893-1127
KCl-CsCl* (t=1/2)	1.46×10^{-3}	4.22×10^{-3}	5.500	0.055	0.999	924-1118
	1.45×10^{-3}	8.34×10^{-3}	6.082	0.056	0.999	905-1086
	1.44×10^{-3}	1.34×10^{-2}	6.503	0.055	0.999	943-1086
	1.43×10^{-3}	1.70×10^{-2}	6.704	0.058	0.999	943-1120
	3.25×10^{-3}	1.70×10^{-2}	5.995	0.056	0.999	923-1120

*Equimolar.

Table 9. E_{cell} versus temperature for the CuCl-CuCl$_2$ systems

Solvent	X_{CuCl}	X_{CuCl_2}	E = AT + B (V)		C Coeff.	Range (K)
			A × 10^4	B		
NaCl	8.57×10^{-4}	4.86×10^{-4}	1.642	0.633	0.999	1096-1183
	8.56×10^{-4}	9.71×10^{-4}	2.260	0.631	0.999	1101-1174
	8.56×10^{-4}	1.50×10^{-3}	2.625	0.632	0.999	1092-1177
	8.55×10^{-4}	2.23×10^{-3}	2.977	0.631	0.999	1093-1179
KCl	8.84×10^{-4}	9.40×10^{-4}	-0.556	0.986	-0.999	1079-1171
	8.83×10^{-4}	1.73×10^{-3}	-0.031	0.986	-0.995	1071-1169
	8.82×10^{-4}	2.82×10^{-3}	0.394	0.985	0.999	1069-1165
	8.81×10^{-4}	3.68×10^{-3}	0.621	0.986	0.999	1068-1163
CsCl	1.48×10^{-3}	1.72×10^{-3}	-3.866	1.401	-1.000	988-1170
	1.48×10^{-3}	4.04×10^{-3}	-3.121	1.400	-1.000	985-1166
	1.48×10^{-3}	6.36×10^{-3}	-2.727	1.400	-0.999	990-1162
	1.47×10^{-3}	8.98×10^{-2}	-2.435	1.401	-0.998	987-1164
NaCl-KCl* (t=1/2)	4.03×10^{-4}	3.46×10^{-4}	4.048	0.440	0.999	985-1171
	4.03×10^{-4}	7.16×10^{-4}	4.678	0.439	0.999	984-1164
	4.02×10^{-4}	1.11×10^{-3}	5.053	0.440	0.999	998-1167
	4.02×10^{-4}	1.51×10^{-3}	5.318	0.439	0.999	989-1172
NaCl-CsCl* (t=1/2)	1.13×10^{-3}	1.25×10^{-3}	-0.840	1.014	-0.999	962-1099
	1.13×10^{-3}	2.60×10^{-3}	-0.205	1.014	-0.996	963-1105
	1.12×10^{-3}	4.05×10^{-3}	0.186	1.013	0.992	963-1103
	1.12×10^{-3}	5.49×10^{-3}	0.440	1.014	0.999	962-1103
KCl-CsCl* (t=1/2)	1.06×10^{-3}	1.33×10^{-3}	-2.096	1.197	-0.999	953-1095
	1.06×10^{-3}	2.80×10^{-3}	-1.459	1.197	-0.999	948-1102
	1.06×10^{-3}	4.25×10^{-3}	-1.094	1.197	-0.999	961-1099
	1.06×10^{-3}	5.69×10^{-3}	-0.832	1.196	-0.999	961-1100

*Equimolar.

Table 10a. Formal potentials at 1075 K

	E°_f (+ 0.003 V)								
	NaCl	KCl	CsCl	NaCl-KCl*		NaCl-CsCl*		KCl-CsCl*	
				Expt.	Calc.	Expt.	Calc.	Expt.	Calc.
$ThCl_4$	-2.265	-2.516	-2.653	-2.433	-2.391	-2.537	-2.459	-2.557	-2.585
$AlCl_3$**	-1.851	-1.872	-1.910			-1.871	-1.881	-1.894	-1.891
$CrCl_2$	-1.513	-1.615	-1.629	-1.560	-1.564	-1.560	-1.571	-1.586	-1.622
$FeCl_2$			-1.464			-1.352		-1.408	
$CrCl_3$	-1.145	-1.275	-1.316	-1.206	-1.210	-1.224	-1.231	-1.271	-1.296
$CoCl_2$	-1.062	-1.199	-1.295	-1.125	-1.131	-1.183	-1.179	-1.229	-1.247
CuCl	-1.041	-1.198	-1.270	-1.107	-1.120	-1.161	-1.156	-1.225	-1.234
$FeCl_3$			-1.118			-1.027		-1.074	
$NiCl_2$	-0.865	-0.984	-1.046	-0.929	-0.925	-0.956	-0.955	-1.023	-1.015
AgCl**	-0.779	-0.893	-0.950			-0.869	-0.865	-0.910	-0.922
$CuCl_2$	-0.618	-0.724	-0.763	-0.658	-0.671	-0.697	-0.691	-0.731	-0.744
$CrCl_2/CrCl_3$	-0.409	-0.591	-0.690	-0.500	-0.500	-0.550	-0.550	-0.639	-0.641
$FeCl_2/FeCl_3$			-0.426			-0.379		-0.407	
$CuCl/CuCl_2$	-0.194	-0.250	-0.256	-0.207	-0.222	-0.233	-0.225	-0.237	-0.253

*Equimolar

**Reference (1)

Table 10b. Formal potentials at 1100 K

	NaCl	KCl	CsCl	E°_f (+ 0.003 V) NaCl-KCl*		NaCl-CsCl*		KCl-CsCl*	
				Expt.	Calc.	Expt.	Calc.	Expt.	Calc.
$ThCl_4$	-2.259	-2.502	-2.632	-2.420	-2.381	-2.528	-2.446	-2.541	-2.567
$AlCl_3$**	-1.827	-1.849	-1.884			-1.845	-1.856	-1.868	-1.866
$CrCl_2$	-1.505	-1.600	-1.610	-1.549	-1.553	-1.544	-1.558	-1.568	-1.605
$FeCl_2$			-1.450			-1.338		-1.393	
$CrCl_3$	-1.129	-1.258	-1.299	-1.191	-1.194	-1.206	-1.214	-1.253	-1.279
$CoCl_2$	-1.049	-1.185	-1.281	-1.115	-1.117	-1.170	-1.165	-1.213	-1.233
CuCl	-1.028	-1.184	-1.256	-1.095	-1.106	-1.147	-1.142	-1.210	-1.220
$FeCl_3$			-1.106			-1.015		-1.063	
$NiCl_2$	-0.853	-0.972	-1.034	-0.917	-0.913	-0.946	-0.944	-1.012	-1.003
AgCl**	-0.768	-0.882	-0.940			-0.859	-0.854	-0.900	-0.911
$CuCl_2$	-0.606	-0.716	-0.759	-0.646	-0.661	-0.689	-0.683	-0.724	-0.738
$CrCl_2/CrCl_3$	-0.377	-0.572	-0.678	-0.474	-0.475	-0.525	-0.528	-0.623	-0.625
$FeCl_2/FeCl_3$			-0.419			-0.371		-0.402	
$CuCl/CuCl_2$	-0.184	-0.247	-0.262	-0.197	-0.216	-0.231	-0.223	-0.239	-0.255

*Equimolar

**Reference (1)

Table 10c. Formal potentials at 1125 K

				E°_f (+ 0.003 V)					
	NaCl	KCl	CsCl	NaCl-KCl*		NaCl-CsCl*		KCl-CsCl*	
				Expt.	Calc.	Expt.	Calc.	Expt.	Calc.
$ThCl_4$	-2.253	-2.487	-2.610	-2.406	-2.370	-2.520	-2.432	-2.524	-2.549
$AlCl_3$**	-1.803	-1.825	-1.858			-1.820	-1.831	-1.843	-1.842
$CrCl_2$	-1.496	-1.585	-1.591	-1.538	-1.541	-1.528	-1.544	-1.550	-1.588
$FeCl_2$			-1.436			-1.324		-1.379	
$CrCl_3$	-1.113	-1.241	-1.282	-1.175	-1.177	-1.188	-1.198	-1.236	-1.262
$CoCl_2$	-1.037	-1.171	-1.268	-1.105	-1.104	-1.157	-1.153	-1.198	-1.220
CuCl	-1.016	-1.170	-1.241	-1.082	-1.093	-1.134	-1.129	-1.195	-1.206
$FeCl_3$			-1.095			-1.003		-1.051	
$NiCl_2$	-0.841	-0.962	-1.022	-0.906	-0.902	-0.936	-0.932	-1.001	-0.992
AgCl**	-0.757	-0.871	-0.930			-0.848	-0.844	-0.889	-0.901
$CuCl_2$	-0.595	-0.707	-0.754	-0.635	-0.651	-0.681	-0.675	-0.717	-0.731
$CrCl_2/CrCl_3$	-0.346	-0.552	-0.666	-0.450	-0.449	-0.505	-0.506	-0.608	-0.609
$FeCl_2/FeCl_3$			-0.413			-0.364		-0.396	
$CuCl/CuCl_2$	-0.174	-0.244	-0.269	-0.187	-0.209	-0.229	-0.222	-0.240	-0.257

*Equimolar
**Reference (1)

Table 11a. Activity coefficients at 1075 K

	log γ								
	NaCl	KCl	CsCl	NaCl-KCl*		NaCl-CsCl*		KCl-CsCl*	
				Expt.	Calc.	Expt.	Calc.	Expt.	Calc.
$ThCl_4$	-0.065	-4.732	-7.323	-3.196	-2.399	-5.137	-3.694	-5.509	-6.028
$AlCl_3$**	-2.014	-2.319	-3.025			-2.375	-2.520	-2.722	-2.672
$CrCl_2$	-1.360	-2.318	-2.453	-1.803	-1.839	-1.812	-1.907	-2.053	-2.386
$FeCl_2$			-3.093			-2.047		-2.569	
$CrCl_3$	-0.230	-2.047	-2.637	-1.097	-1.139	-1.342	-1.434	-2.000	-2.342
$CoCl_2$	-1.831	-4.103	-4.033	-2.471	-2.967	-2.988	-2.932	-3.418	-4.068
CuCl	-0.562	-1.300	-1.647	-0.878	-0.931	-1.132	-1.105	-1.432	-1.474
$FeCl_3$			-5.041			-3.769		-4.434	
$NiCl_2$	-1.660	-2.794	-3.361	-2.299	-2.227	-2.529	-2.511	-3.150	-3.078
AgCl**	0.204	-0.329	-0.595			-0.218	-0.196	-0.410	-0.462

*Equimolar

**Reference (1)

Table 11b. Activity coefficients at 1100 K

	log γ								
	NaCl	KCl	CsCl	NaCl-KCl*		NaCl-CsCl*		KCl-CsCl*	
				Expt.	Calc.	Expt.	Calc.	Expt.	Calc.
$ThCl_4$	-0.247	-4.688	-7.025	-3.117	-2.468	-5.171	-3.636	-5.385	-5.857
$AlCl_3$**	-1.637	-1.929	-2.365			-1.861	-2.001	-2.170	-2.147
$CrCl_2$	-1.344	-2.227	-2.310	-1.752	-1.786	-1.711	-1.827	-1.926	-2.269
$FeCl_2$			-2.934			-1.920		-2.422	
$CrCl_3$	-0.240	-2.014	-2.561	-1.093	-1.127	-1.288	-1.401	-1.946	-2.288
$CoCl_2$	-1.771	-4.009	-3.900	-2.418	-2.890	-2.888	-2.836	-3.285	-3.955
CuCl	-0.522	-1.235	-1.563	-0.826	-0.879	-1.067	-1.043	-1.353	-1.399
$FeCl_3$			-4.878			-3.636		-4.286	
$NiCl_2$	-1.611	-2.701	-3.244	-2.228	-2.156	-2.454	-2.428	-3.025	-2.973
AgCl**	0.224	-0.298	-0.562			-0.191	-0.169	-0.381	-0.430

*Equimolar

**Reference (1)

Table 11c. Activity coefficients at 1125 K

	log γ								
	NaCl	KCl	CsCl	NaCl-KCl*		NaCl-CsCl*		KCl-CsCl*	
				Expt.	Calc.	Expt.	Calc.	Expt.	Calc.
$ThCl_4$	-0.427	-4.629	-6.733	-3.158	-2.528	-5.202	-3.580	-5.260	-5.681
$AlCl_3$**	-1.438	-1.726	-2.115			-1.633	-1.777	-1.934	-1.921
$CrCl_2$	-1.329	-2.128	-2.151	-1.699	-1.729	-1.604	-1.740	-1.790	-2.140
$FeCl_2$			-2.775			-1.793		-2.274	
$CrCl_3$	-0.249	-1.973	-2.504	-1.090	-1.111	-1.238	-1.377	-1.886	-2.239
$CoCl_2$	-1.711	-3.917	-3.743	-2.359	-2.814	-2.771	-2.727	-3.131	-3.830
CuCl	-0.481	-1.173	-1.493	-0.781	-0.827	-1.011	-0.987	-1.287	-1.333
$FeCl_3$			-4.716			-3.504		-4.138	
$NiCl_2$	-1.562	-2.651	-3.132	-2.158	-2.107	-2.383	-2.347	-2.913	-2.892
AgCl**	0.242	-0.269	-0.531			-0.165	-0.145	-0.354	-0.400

*Equimolar
**Reference (1)

Table 12. Partial molar enthalpies of mixing

				$\overline{\Delta H}$ (KJ/mol)					
	NaCl	KCl	CsCl	NaCl-KCl*		NaCl-CsCl*		KCl-CsCl*	
				Expt.	Calc.	Expt.	Calc.	Expt.	Calc.
$ThCl_4$	184	-50.7	-270	-15.5	66.7	24.6	-43.0	-106	-160
$AlCl_3$**	-179	-182	-227			-207	-203	-214	-205
$CoCl_2$	-60.6	-95.3	-119	-46.0	-78.0	-89.1	-89.8	-118	-107
$CrCl_2$	-15.6	-92.7	-128	-44.1	-54.2	-87.7	-71.8	-111	-110
$FeCl_2$			-125			-100		-115	
$NiCl_2$	-49.4	-66.2	-89.6	-55.6	-57.8	-55.3	-69.5	-87.8	-77.9
CuCl	-40.0	-58.8	-67.8	-42.5	-49.4	-53.3	-53.9	-63.8	-63.3
$FeCl_3$			-55.4			-45.2		-50.3	
$CrCl_3$	9.5	-34.2	-52.5	-29.3	-12.4	-37.7	-21.5	-45.8	-43.4
AgCl**	-17.6	-27.7	-28.9			-23.7	-23.3	-27.9	-28.3

*Equimolar

**Reference (1)

Table 13. Partial excess entropies of mixing

				$\overline{\Delta S}^{ex}$ (J/mol°K		
	NaCl	KCl	CsCl	NaCl-KCl*	NaCl-CsCl*	KCl-CsCl*
$ThCl_4$	172	43.7	-110	46.8	121	6.7
$AlCl_3$**	-130	-127	-159		-151	-150
$CoCl_2$	-21.1	-28.9	-33.9	4.5	-25.7	-44.3
$CrCl_2$	11.6	-41.6	-72.2	-6.5	-47.0	-64.1
$FeCl_2$			-56.4		-53.1	-57.8
$NiCl_2$	-13.9	-8.2	-19.1	-7.7	-3.0	-21.6
CuCl	-26.3	-29.8	-31.7	-22.8	-28.1	-32.2
$FeCl_3$			-9.5		-10.5	9.8
$CrCl_3$	13.2	7.4	1.4	18.3	-9.3	-4.3
AgCl**	-20.3	-19.5	-15.5		-17.9	-18.0

*Equimolar

**Reference (1)

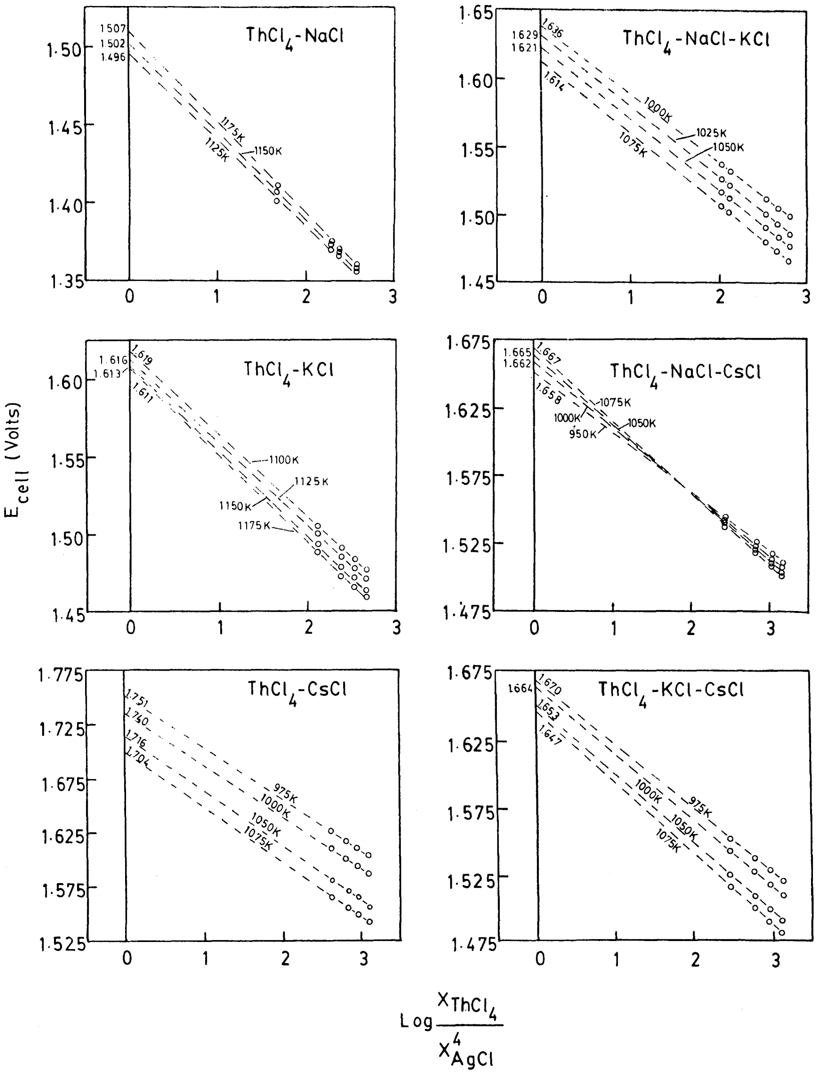

Figure 1. Nernst plot for the $ThCl_4$ systems.

DOI: 10.1149/198601.0576PV

PHASE STUDIES OF ZINC CHLORIDE CONTAINING MELTS

L G Macdonald, G S Perry, and S D Wilcox
AWRE Aldermaston, Reading, RG7 4 PR, UK

Liquidus diagrams of $ZnCl_2$-KCl-$CaCl_2$, $ZnCl_2$-KCl-LiCl, and $ZnCl_2$-CsCl-LiCl have been determined.
The $ZnCl_2$-KCl-LiCl system was found to have a miscibility gap as predicted. The phase diagram was compared with an unpublished calculated version and there was some agreement. The main discrepancy was attributed to the incorrect $ZnCl_2$-LiCl data being used in the calculated liquidus diagram. Immiscibility in the $ZnCl_2$-CsCl-LiCl system was not found.

1. INTRODUCTION

Over the past five years there has been a growing interest in the chemistry of zinc chloride melts in chemical processing and one important aspect of this is the need for reliable phase diagrams of the relevant systems. These include the binary and ternary salt systems, molten metals, and metal-salt systems encountered. We have concentrated on those systems containing $ZnCl_2$. In addition to gaining understanding of the phase relationships we have been particularly interested in those salt systems exhibiting a potential miscibility gap in the liquidus. Such a system is $ZnCl_2$-KCl-LiCl and this prompted a study of the CsCl system.

In this paper we report on the following ternary salt systems:-
$ZnCl_2$-KCl-$CaCl_2$
$ZnCl_2$-KCl-LiCl
$ZnCl_2$-CsCl-LiCl

2. EXPERIMENTAL

2.1 Starting Materials

All the salts (Table 1) were used without further purification, other than drying; care being taken to maintain dry conditions (nitrogen atmosphere containing <50 vpm water vapour) during their handling. The melting points of the compounds were determined and semi-quantitative analyses were carried out as checks on their purity.

2.2 Method

The method of thermal analysis (cooling curves) was used to determine liquidus and solidus temperatures (1).

All reagents and equipment were dried at 120°C. A 25g sample of the salt mixture under examination was weighed into a 20 mm diameter, open ended silica glass tube closed by a cap fitted with an alumina thermocouple sheath and a chromel-alumel thermocouple. The number of determinations ranged from 150 to 200 depending upon the complexity of the diagram.

The tube was supported in a furnace and the temperature raised above the melting point of the salt mixture. The power to the furnace was then reduced to control the cooling rate of the sample to about 2° per minute. Cooling curves were either recorded on a precision chart recorder or by a computer system to acquire the thermocouple data, which is automatically stored, interpreted, and later plotted. Where a pen chart recorder was used the thermal arrest was measured visually and temperatures are probably only accurate to about + or - 5°. Where data was handled by the computer (Apple IIe) then the results are believed to be rather better, + or - 1°.

3. DISCUSSION

3.1 $ZnCl_2$-KCl-$CaCl_2$

As there was no published data on this system the phase diagram was determined as well as being calculated by Chart et al. (4). The liquidus diagram in the temperature range 500-1000K is shown in Figure 1 where reasonable agreement was obtained between the measured and calculated diagrams. As anticipated the influence of the $CaCl_2$-KCl and $ZnCl_2$-KCl eutectics is very pronounced.
Three ternary eutectics were found at (mol%):-

(i) $ZnCl_2(26)$-KCl(72)-$CaCl_2(2)$
(ii) $ZnCl_2(50)$-KCl(48)-$CaCl_2(2)$
(iii) $ZnCl_2(67)$-KCl(27)-$CaCl_2(6)$

melting at 690K, 480K, and 495K respectively which agreed quite well with Chart's calculated values (690K, 490K, and 530K). No ternary compositions or compounds with melting points greater than the constituent salts were found.

3.2 $ZnCl_2$-KCl-LiCl

The $AlCl_3$-KCl-LiCl system has been extensively studied (5,6). It has a miscibility gap in the temperature range 623-1048K and the two liquid phases consist essentially of $KAlCl_4$ and LiCl. Immiscibility has also been reported in the two similar systems $AlCl_3$-KCl-NaCl and $FeCl_3$-KCl-LiCl. Both $ZnCl_2$ and $AlCl_3$ form the stable complex anion MCl_4 suggesting there may be a miscibility gap in $ZnCl_2$-KCl-LiCl, although likely to be less stable. Such a miscibility gap might be exploited as a molten salt extraction system.

When our determination of the liquidus diagram was almost complete our attention was drawn to an unpublished calculated diagram (Figure 2) by Skeaff, Bale, Pelton, and Thompson(7). The calculated diagram does not contain a miscibility gap, although there is a strong indication of its potential existence.

The $ZnCl_2$-KCl-LiCl liquidus-solidus diagram (Figure 3) was obtained using the methods described above. Two of the component binary phase diagrams LiCl-KCl (8) and $ZnCl_2$-KCl (1) are well known and data on the $ZnCl_2$-LiCl phase diagram has been extracted (9) from Evseeva and Bergman (10). However, during our study of the ternary we were unable to reconcile the $ZnCl_2$-LiCl-rich side with the published data (9). We therefore re-examined (11) the $ZnCl_2$-LiCl system and although there was much agreement with Evseeva and Bergman we found strong evidence for a compound in the $ZnCl_2$-rich part of the diagram (Figure 4). Since it is known Skeaff et al used the Evseeva and Bergman data this would undoubtedly have affected the calculation of the ternary system.

The $ZnCl_2$-KCl-LiCl liquidus diagram contained only two ternary eutectics: $ZnCl_2$(12)-KCl(65)-LiCl(23) and $ZnCl_2$(61)-KCl(34)-LiCl(5), melting at 600K and 465K. Our study also indicated there was immiscibility in the system.

In the LiCl-rich corner of the diagram the isotherms are widely spaced indicating little change in liquidus temperature over a wide composition range. The congruently melting compound, K_2ZnCl_4, has an influence on the liquidus in the KCl-rich corner but not to the same degree as the more stable Cs_2ZnCl_4 (see 3.3).

When we compared the diagram with that calculated by Skeaff et al there was reasonable agreement with the principal features in the KCl and LiCl-rich regions. But there was a major disagreement in the $ZnCl_2$-rich region which can be attributed to the $ZnCl_2$-LiCl phase diagram data (9) used to calculate the ternary.

Immiscibility in the system was examined at 900K by chemical analysis of the upper and lower layers of a number of compositions after quenching. The results showed a significant difference in composition between the layers but reproducibility was poor. The ternary $ZnCl_2$(12.6)-KCl(27.3)-LiCl(59.9) containing $CoCl_2$(0.1) was then studied in more detail and the results (Table 2) confirmed there was a difference between the two layers. The variations found arose from difficulties of sampling and volatilization of $ZnCl_2$ from the melt. The upper liquid phase was LiCl-rich, in contrast to $AlCl_3$-KCl-LiCl where the upper phase was almost exclusively the compound $KAlCl_4$. Tie lines in the miscibility gap of $AlCl_3$-KCl-LiCl system tended to converge on equimolar $AlCl_3$.KCl whereas in the $ZnCl_2$-KCl-LiCl ternary they converge on LiCl.

The distribution of various metal ions ($PrCl_3$, $CeCl_3$, $AlCl_3$, $SnCl_2$, $CuCl_2$, $CrCl_3$, and $NiCl_2$) between the two phases was studied but no consistent partitioning was observed although there was some evidence for the partition of $CoCl_2$ (see Table 2).

3.3 $ZnCl_2$-CsCl-LiCl

The liquidus diagram is shown in Figure 5, and covers the temperature range 500 to 850K.

Two ternary eutectics were verified at (mol%);
$ZnCl_2$(67)-CsCl(18)-LiCl(15), mp 472K, and
$ZnCl_2$(72)-CsCl(20)-LiCl(8), mp 487K.

The phase diagram shows solid and liquid phases co-exist over a wide temperature and composition range. The liquidus lines show how the stable compound, Cs_2ZnCl_4, influences the system in a more pronounced way than the corresponding less stable compound, K_2ZnCl_4, in the $ZnCl_2$-KCl-LiCl system described previously. Examination of the phase diagrams of the alkali halides and zinc chloride (8) shows increasing stability of M_2ZnCl_4 in the order M=Li to Cs (Figure 6) and a similar trend is found in the ZnF_2-MF series (12). But we were unable to find a miscibility gap in the system possibly due to compound formation in the LiCl-CsCl system which does not occur in LiCl-KCl.

4. Summary

The liquidus diagrams of three ternary salt systems $ZnCl_2$-KCl-$CaCl_2$, $ZnCl_2$-KCl-LiCl, and $ZnCl_2$-CsCl-LiCl have been determined. The first system contained three ternary eutectics and the liquidus diagram agreed quite well with the calculated version. The $ZnCl_2$-KCl-LiCl system contained two ternary eutectics and it was predicted to have a miscibility gap, by comparison with the corresponding $AlCl_3$ system. A miscibility gap was found at 900K in the system as predicted and partition of $CoCl_2$ was also demonstrated. The phase diagram was compared with an unpublished calculated version and there was some agreement. The main discrepancy was attributed to the incorrect $ZnCl_2$-LiCl data being used in the calculated liquidus diagram. However, immiscibility was not found in the $ZnCl_2$-CsCl-LiCl system.

5. Acknowledgment

The authors are pleased to acknowledge the assistance of D J Why with the experimental work.

REFERENCES

1. G. S. Perry, L. G. Macdonald, and S. Newstead, Thermochimica Acta,68,341(1983)
2. D. A. Craw and J. L. Rogers, J. Chem. Soc. 217(1956)
3. G. J. Janz, "Molten Salts Handbook", Academic Press (1967)
4. T. G. Chart, P. E. Potter, M. H. Rand, G. S. Perry, and S. Newstead, CALPHAD Conf. Argonne National Laboratory (1982)
5. H. Groethe and C. A. Piel, Z. Electrochem,54,219 (1950)
6. R. H. Moore, J. Chem. Eng. Data,8,164 (1963)
7. J. M. Skeaff, C. W. Bale, A. D. Pelton, and W. T. Thompson, CANMET Report No 79-23, Minister of Supply and Services, Canada (1980)
8. E. M. Levin, C. R. Robbins, and H. F. McMurdie, "Phase diagrams for Ceramists", Am.Ceram.Soc. (1964 and Suppl 1969)
9. N. K. Voskresenskaya, N. N. Evseeva, S. I. Berul, and I. P. Vereshchetina, "Handbook on the Fusibility of Anhydrous Salt Systems", p471, Moscow, Izdatel. Akad. Nauk. S.S.S.R. (1961)
10. N. N. Evseeva and A. G. Bergman, Zh. Obs. Khim., 21, 1767 (1951)
11. L. G. Macdonald, G. S. Perry, J. R. Smith, and S. D. Wilcox, Thermochimica Acta, in the press
12. J. E. Ricci, in "Molten Salt Chemistry", p239, M. Blander, Editor, Wiley and Sons, N.Y. (1964)

Table 1

Melting Points and Analysis of Salts

Material	Source	Melting Point (°C)		Main Impurities (ppm)
		Found	Reported (2,3)	
$ZnCl_2$	Alfa Chemicals (Ventron) Ultrapure	308	318	O (4000 ± 1000) Si (180 ± 20)
$CaCl_2$	Mallinckrodt (Food Quality)	759	782	O (7000 ± 2000) Na (100 ± 10) Mg (130 ± 20) Sr (120 ± 10)
KCl	BDH, (Analar)	771	772	No impurities > 100
LiCl	May & Baker (> 99%)	608	610	O (9000 ± 2000) Na (190 ± 20)
CsCl	Aldrich (> 99%)	630	645	O (4000 ± 1000) Na (2100 ± 200)

Table 2

Miscibility Gap : Analytical Results on the
LiCl (60 mol%) - KCl (27 mol%) - $ZnCl_2$ (13 mol%)
Composition with 0.1 mol% $CoCl_2$

Composition (mol%)								Distribution Coeff
Lower Layer				Upper Layer				
LiCl	KCl	$ZnCl_2$	$CoCl_2$	LiCl	KCl	$ZnCl_2$	$CoCl_2$	D
24.7	53.8	21.5	0.01	71.7	21.5	6.8	0.03	3.0
29.0	44.4	26.5	0.08	71.9	20.7	7.3	0.13	1.6
32.7	43.1	24.2	0.06	68.0	23.7	8.2	0.12	2.0
17.1	50.0	32.9	0.02	78.4	14.8	6.8	0.07	3.5
31.5	36.6	31.8	0.05	77.0	15.3	7.6	0.09	1.8
24.4	45.4	30.2	0.04	75.2	18.0	6.7	0.08	2.0
32.7	40.4	26.9	0.08	68.8	23.0	8.0	0.21	2.6
19.8	49.2	31.0	0.03	79.8	14.7	5.5	0.06	3.0

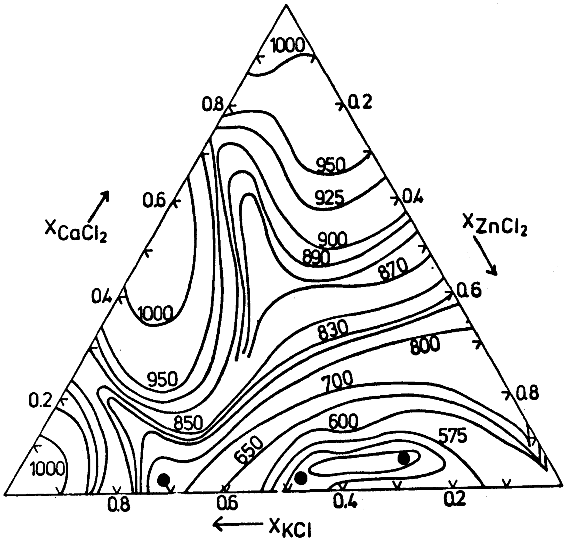

Figure 1
$ZnCl_2$-KCl-$CaCl_2$ Liquidus Diagram

Figure 2
$ZnCl_2$-KCl-LiCl Calculated Diagram (7)

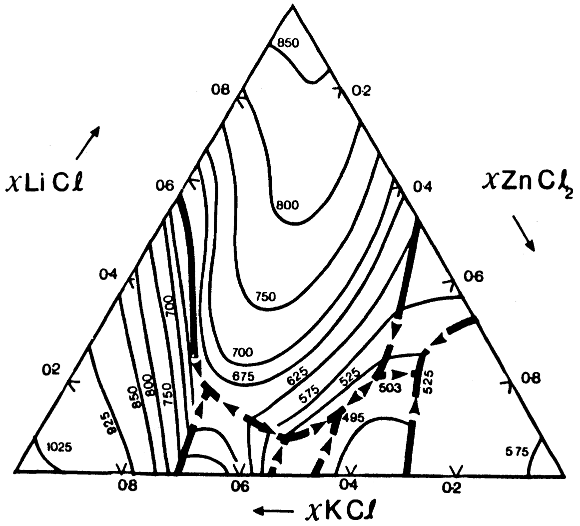

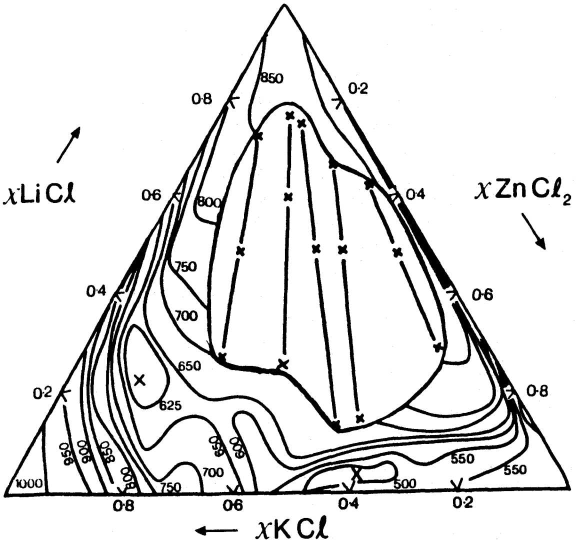

Figure 3

$ZnCl_2$-KCl-LiCl Liquidus Diagram

Figure 4

$ZnCl_2$-LiCl Phase Diagram

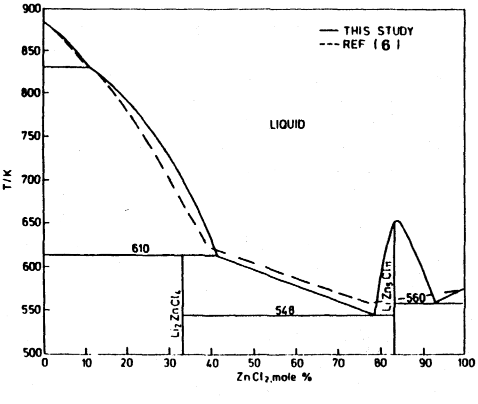

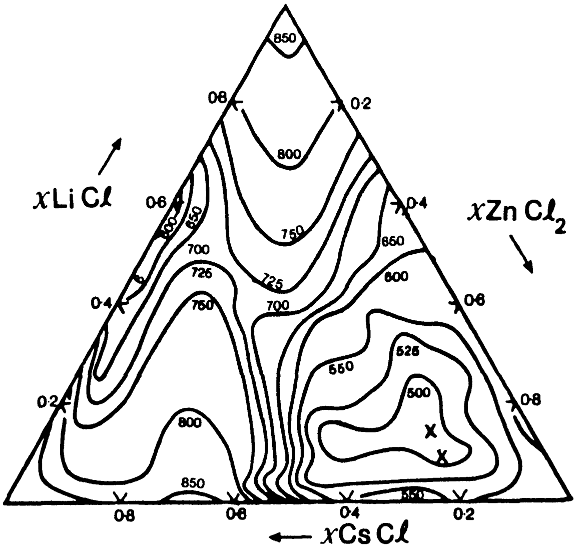

Figure 5

$ZnCl_2$-CsCl-LiCl Liquidus Diagram

Figure 6

Liquidus Curves of the $ZnCl_2$. 2MCl Compound

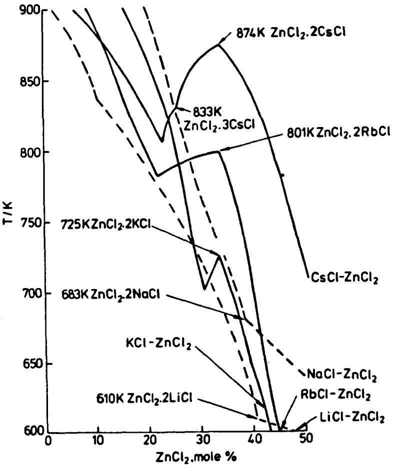

DOI: 10.1149/198601.0584PV

EFFECT OF OXIDE ADDITION ON THE OXYGEN REDUCTION REACTION IN MOLTEN CARBONATE

S. H. Lu*

and

J. R. Selman
Illinois Institute of Technology
Chicago, IL 60616

ABSTRACT

A detailed knowledge of the melt chemistry is essential for correct interpretation of electrode-kinetic measurements of oxygen reduction in molten carbonate, whatever the electrode material. The interaction of various species in Li-K eutectic carbonate melt at 650°C is investigated by adding small amounts of oxide, peroxide, or superoxide to the equilibrated melt and observing the response of the equilibrium potential. The effect of oxide addition on stationary polarization and on potential-step current transients is also investigated Chemical equilibria between oxygen and the various oxide species are established rapidly, whereas neutralization reactions involving CO_2 are remarkably slow.

Oxygen reacts at the cathode of a molten carbonate fuel cell not as molecular oxygen but as oxide, peroxide and superoxide ions [1-2]. The concentrations of these ions are not independent since they can interchange through chemical equilibria. Many phenomena observed in steady state polarization and potential scan measurements may be explained by the interactions among these and other species present in the melt. In particular, a clear understanding of the solution (melt) chemistry is essential for correct interpretation of kinetic results. A direct insight into such interactions can be achieved by suddenly increasing the oxide ion concentration in the melt and observing the effects on equilibrium potential, steady state current and potential step transient.

---

*Present address: Institute of Gas Technology, Chicago, IL 60616

This study focuses on the species which are stable in a Li/K carbonate eutectic melt. As suggested by Andersen [3], these species include cations (Li^+, K^+), anions (O^{2-}, O_2^{2-}, O_2^- and CO_3^{2-}), and dissolved gas molecules (O_2, CO_2). Species such as O^-, CO_2^-, $C_2O_4^{2-}$, etc., have been hypothesized occasionally [1,4,5] although they may be present as intermediate species, they will not be considered in this study.

There are three elementary chemical equilibria in molten carbonates, from which other reactions can be derived:

$$O_2^{2-} \rightleftharpoons O^{2-} + 1/2\ O_2 \qquad (1)$$

$$2\ O_2^- \rightleftharpoons O^{2-} + 3/2\ O_2 \qquad (2)$$

$$CO_3^{2-} \rightleftharpoons O^{2-} + CO_2 \qquad (3)$$

For example, formation of peroxide or superoxide ions results from a combination of reactions (1) or (2) with (3), respectively

$$1/2\ O_2 + CO_3^{2-} \rightleftharpoons CO_2 + O_2^{2-} \qquad (4)$$

$$3/2\ O_2 + CO_3^{2-} \rightleftharpoons CO_2 + 2\ O_2^- \qquad (5)$$

The disproportionation reaction between peroxide and superoxide ions is a combination of reactions (1) and (2)

$$O_2^{2-} + 2\ O_2^- \rightleftharpoons 2\ O^{2-} + 2\ O_2 \qquad (6)$$

Acid-Base Concept

In 1923 Bronsted proposed a general definition of acids and bases in aqueous solutions: an acid is a proton donor and a base is a proton acceptor. In 1939 Lux [6] extended the acid-base concept to oxide systems. The concept was further developed by Flood and Forland in 1947 [7]: an acid is an oxide ion acceptor and a base is an oxide ion donor. Their relationship can be expressed as

$$\text{Acid} + O^{2-} = \text{Conjugate Base} \qquad (7)$$

or

$$\text{Base} = \text{Conjugate Acid} + O^{2-} \qquad (8)$$

On this basis, peroxide, superoxide and carbonate ions are considered to be bases; whereas oxygen and CO_2 are acids. It is apparent that acids and bases are not defined unambiguously, for example, the superoxide ion is an acid with respect to the peroxide ion since

$$3\ O_2^{2-} \rightleftharpoons 2\ O^{2-} + 2\ O_2^{-} \qquad (9)$$

However, it behaves as a base when it donates an oxide ion to release oxygen in reaction (1).

Any reaction which involves the transfer of an oxide ion, such as the formation of peroxide (reaction 4) and superoxide (reaction 5) ions, can be formulated as an interchange of two acid-base conjugate pairs

$$\text{Acid 1} + \text{Base 2} = \text{Acid 2} + \text{Base 1} \qquad (10)$$

The basicity of the melt depends on the activity of O^{2-} ions and the partial pressure of CO_2. The function $p(O^{2-})$, corresponding to the concept of pH in the aqueous solution, may be used as a measure of the basicity since the mole fraction of CO_3^{2-} is very close to one, [8]

$$p(O^{2-}) = -\log a_{O^{2-}} \qquad p(CO_2) = -\log p_{CO_2}$$

$$p\ K_d = p(O^{2-}) + p(CO_2) \qquad (11)$$

where K_d is the dissociation constant of the carbonate ion

$$K_d = \frac{a_{O^{2-}} \cdot p_{CO_2}}{a_{CO_3^{2-}}} \qquad (12)$$

Since the equilibrium concentration of oxide ion is very low in molten carbonate melt, a small change in oxide concentration will affect the basicity of the melt drastically. Therefore alkali metal carbonate melts are melts with poor buffering capability.

Experimental

The apparatus and experimental procedures used in this work were similar to those described in a previous paper [9]. All measurements were carried out at a gold wire electrode (0.64 cm diameter) fitted snugly in an alumina capillary tube, so that the electrode was completely submerged in the melt, to avoid meniscus or film formation.

This is called the "working electrode" in the following discussion. A gold wire in equilibrium with a 33.3% O_2-66.7% CO_2 gas mixture inside an alumina tube served as the reference electrode. Its end was held against the bottom of the crucible. The binary carbonate eutectic mixture, 62 mol% Li_2CO_3 and 38 mol% K_2CO_3, was made up from Fisher ACS grade chemicals. Lithium oxide with assay higher than 95% was purchased from Alfa Products (Danvers, Mass.); no further purification was attempted. The reagents were carefully weighed and mixed in an electrolyte preparatory room with relative humidity less than five percent. A specially designed syringe was included in the gas feed-through flange so that a gas-tight glass chamber was formed, through which accurately weighed oxide pellets could be introduced into the cell via the gas exhaust tube. Li_2O pellets were formed by a pellet-press in the dry room and subjected to further drying, evacuation and equilibration with the feed gas ($0.7\ O_2 + 0.3\ CO_2$) for about 20 minutes before dropping them into the melt.

Effect on the Equilibrium Potential

Several heat effects are involved in the dissolution of solid oxides in the melt, including the sensible heat due to temperature change, the heat of fusion and the heat of mixing. In order to obtain a blank for subsequent experimental results, small amounts of carbonate mixtures with the same composition as the eutectic melt were added to the melt. Their effect on the equilibrium potential is shown in Figure 1. Dissolution of the electrolyte is quite fast and the maximum deviation of the equilibrium potential (at 15 to 60 sec) is about +4 mV. This potential displacement is small and approximately equal to the standard deviation of the potential measurements, therefore, it will be neglected in the following analysis.

To investigate the neutralization reaction and its effect on electrode potential, a small Li_2O pellet was added to the melt. The displacements of the equilibrium potential were recorded for a melt under stirred and unstirred conditions as shown in Figure 2. Under unstirred conditions, pellet addition disturbed the equilibrium potential but the mass transfer rate, and hence the potential response, were erratic. The poorly defined convection made a quantitative analysis of the response curve very difficult. In the stirred melt, an immediate displacement of the equilibrium potential was observed, the potential reached a minimum within a few minutes and then returned slowly to the initial value. The melt was well mixed, so it could be assumed that the concentrations of various species are uniform in the melt. During the relaxation of the equilibrium potential there was no potential difference between the potential of the working electrode and that of a much larger gold foil (which served as counter electrode in the measurements discussed below). This suggests that only a homogeneous chemical reaction is involved in the potential relaxation. Thus, the working electrode serves as a sensor which detects the concentration variation of oxide ions in the bulk melt.

The departure of the potential of the oxygen electrode from the equilibrium value depends on the local activity of oxide, as first suggested by Borucka [10]:

$$E_{O_2/CO_2} = E°_{O_2/CO_2} + \frac{RT}{2F} \ell n\ K_p + \frac{RT}{2F} \ell n\ [P_{O_2}^{1/2}/a_{ox}] \qquad (13)$$

where $E°(O_2,CO_2)$ is the standard O_2+CO_2 potential at gold, K_p is the dissociation constant of the carbonate ion in the melt, P_{O_2} is the partial pressure of oxygen, and a_{ox} is the local activity of oxide. Since feed gas is continually bubbled through the melt in the course of these measurements (at 80 to 100 ml/min, into 100 ml electrolyte) and the dissolution rate of the O_2+CO_2 gas mixture in the melt is very fast [10], the slow recovery of the equilibrium potential cannot be due to mass transfer limitation of CO_2.

Assuming a constant concentration of CO_2, the neutralization reaction behaves like a pseudo-first order reaction. The time variation of oxide concentration can be represented by

$$(O^{2-}) = (O^{2-})_o\ e^{-kt} - (O^{2-})_e \qquad (14)$$

where k is the rate constant of the recombination reaction; $(O^{2-})_e$ and $(O^{2-})_o$ refer to the equilibrium concentration and the initial concentration increment of oxide ion, respectively. The potential shift (ΔV) is related to the local activity of oxide by the equation

$$\Delta V = \frac{RT}{2F} \ell n\ [a_{ox}^{e}/a_{ox}] \qquad (15)$$

At the small concentrations of oxide in this experiment, it is a reasonable assumption that oxide activity equals oxide concentration. Combining Equations (13)-(15) the potential response is:

$$\ell n(e^{-\frac{2F}{RT}\Delta V} - 1) = -\ell n\,[\frac{(O^{2-})_e}{(O^{2-})_o}] - kt \qquad (16)$$

To test the validity of this expression, experimental data in Figure 2 were treated by this procedure; a fairly straight line was obtained as shown in Figure 3. From the slope of this plot, the rate constant, k, was found to be $5.17*10^{-3}$ sec^{-1} and the equilibrium concentration of oxide to be $4.61*10^{-10}$ mole/cm^3 for the particular feed gas composition (0.70 O_2 + 0.30 CO_2). This value is very close to that calculated from the equilibrium constant reported by Andersen [3], which is $4.22*10^{-10}$ mole/cm^3. Deviations of the experimental data from the straight line in the initial time period may be due to the limited solubility of Li_2O or the slowness of oxide dissolution in the melt.

Effect on the Steady State Current

The effect of a sudden increase in oxide ions on the electrode kinetics was examined by operating the cell under potentiostatic mode. A small pellet of Li_2O was added to the stirred melt when the steady state current had been reached at an overpotential of -50 mV. An immediate surge of anodic current was recorded; after reaching a maximum the current decayed slowly and returned to the original cathodic value, as shown in Figure 4. This response could be explained by the results in Figure 2: since addition of O^{2-} caused a displacement of the equilibrium potential in the negative direction, the controlled potential became positive relative to this new local "equilibrium potential" so that an anodic current resulted. As oxide ions reacted with CO_2, the equilibrium potential as well as the steady-state current returned slowly to their normal values, at almost the same pace.

Effect on the Potential Step Transient

The current reversal observed in the steady-state measurements confirms the conclusions reached from the equilibrium potential measurements. In order to observe the effect of added oxide on the kinetics of oxygen reduction, a transient technique is required which allows a direct comparison of reaction rate before and after oxide addition.

The potential step technique is preferable to other techniques, since it requires only the current variation during the initial time period (a few ms) when the kinetic effect is dominant. Another advantage is that the electrode potential is not seriously disturbed while applying a small potential perturbation to the working electrode. This was confirmed by the fact that the electrode potential returned to its slowly changing original value immediately after the step-response measurement.

Usually it takes about thirty minutes to let the electrode potential fully recover after oxide addition, so it is possible to carry out three or four potential step measurements during this period. A -50 mV potential step corresponding to the instant rest potential was applied to the working electrode and the resulting current transient from 0.3 to 1 ms was recorded. With the influence of the potential shift thus removed, the effect of oxide addition on electrode kinetics could be identified. The results are shown in Figure 5.

The electrode kinetics are clearly accelerated by oxide addition. These results are apparently contrary to the conclusions of Borucka [10], who stated that addition of Li_2O has no clear effect on oxygen reduction kinetics as determined from potential scan measurements. However, the enhanced kinetics observed in this work are understandable by considering the chemical equilibria in Equations (1) and (2). Rapid interaction of added O^{2-} with O_2 sparged into the melt generates excess peroxide and superoxide ions, which are responsible for the increase in current. The transient currents from potential step measurements decrease exponentially after the initial addition of oxide, and if measurements could be made at small time increments, a similar decay behavior of the steady-state current would be observed.

Conclusion

Oxygen reduction in Li/K carbonate melt, at a gold electrode, is a complex reaction. The neutralization of oxide ion has not been addressed earlier as a possibly rate-determining step. Its rate constant can be determined by an analysis of the potential relaxation curve upon oxide addition. A value of $5.17 * 10^{-3}$ sec^{-1} at 650°C is obtained. The local accumulation of oxide ions causes a negative shift of the electrode potential.

The electrode kinetics of oxygen reduction are accelerated by oxide addition to the melt. This can be explained by a rapid interaction of added O^{2-} with O_2 generating excess peroxide and superoxide ion.

ACKNOWLEDGMENT

This work was supported by the Electric Power Research Institute, Palo Alto, California, under Contract RP-1085-2, and carried out at the Institute of Gas Technology, Chicago, Illinois.

REFERENCES

[1] Appleby A. J. and Nicholson S., J. Electroanal. Chem., 83, 309 (1977).

[2] Appleby A. J. and Nicholson S., J. Electroanal. Chem., 112, 71 (1980).

[3] Andersen B. K., Ph.D. Thesis, Technical University of Denmark, Lyngby (1975).

[4] Borucka A. and Appleby A. J., J. Chem. Soc. (Far. Trans. 1) 73, 1420 (1977).

[5] Vogel W. M., Bregoli L. J. and Smith S. W., J. Electrochem. Soc. 127, 833 (1980).

[6] Lux H., Z. Elektrochem. 45, 303, (1939).

[7] Flood H. and Førland T., Acta Chem. Scand. 1, 781, (1947).

[8] Ingram M. D. and Janz G. J., Electrochim. Acta 10, 783 (1965).

[9] Lu S. H. and Selman J. R., J. Electrochem. Soc., 131, 2827 (1984).

[10] Borucka A., J. Electrochem. Soc., 124, 972 (1977).

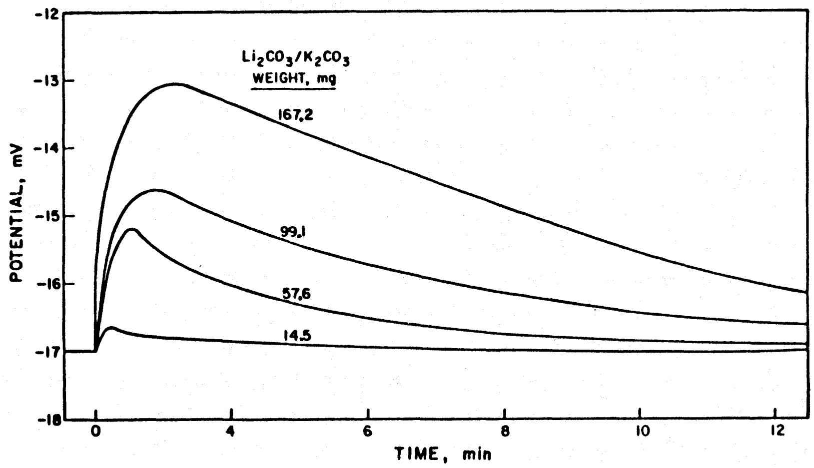

Figure 1. Effect of added eutectic mixture on the equilibrium potential at a gold electrode at 650°C

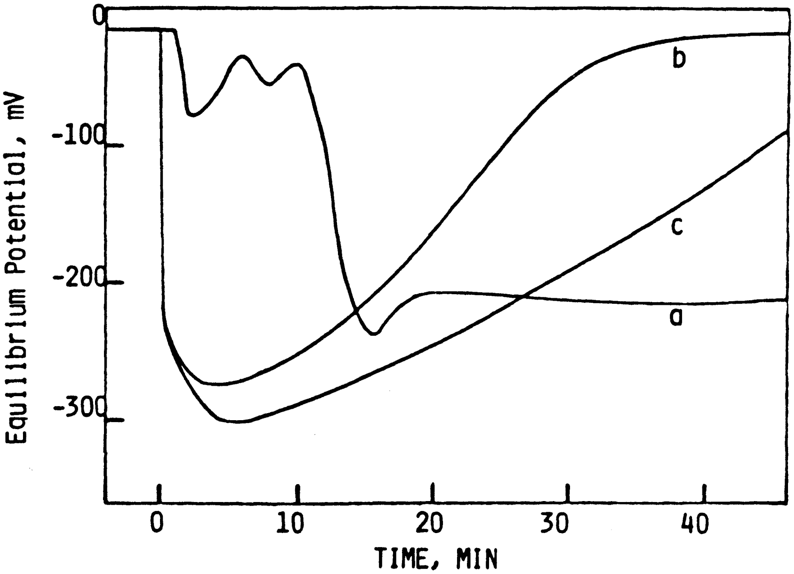

Figure 2. Effect of added Li_2O on the equilibrium potential at a gold electrode at 650°C. a. Unstirred melt, 28.0 mg b. Stirred melt, 26.2 mg c. Stirred melt, 95.3 mg

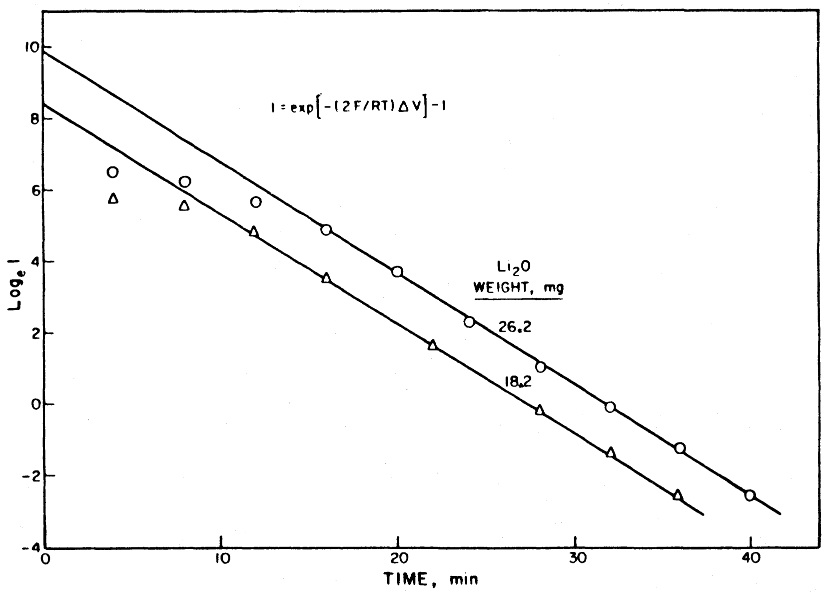

Figure 3. Determination of the rate constant of the oxide-CO_2 recombination reaction from potential relaxation curves (Li_2O addition) at 650°C

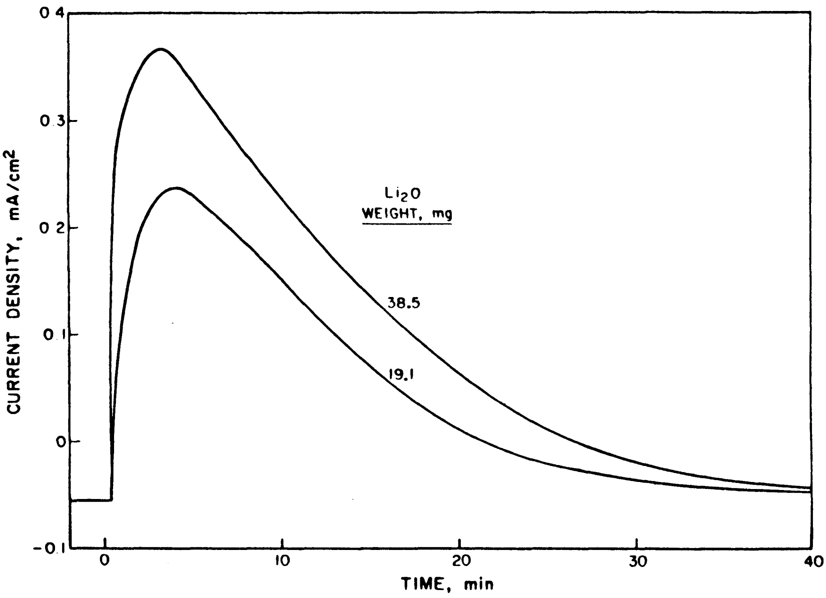

Figure 4. Effect of added Li_2O on the steady state current at -50 mV polarization (Gold Electrode at 650°C)

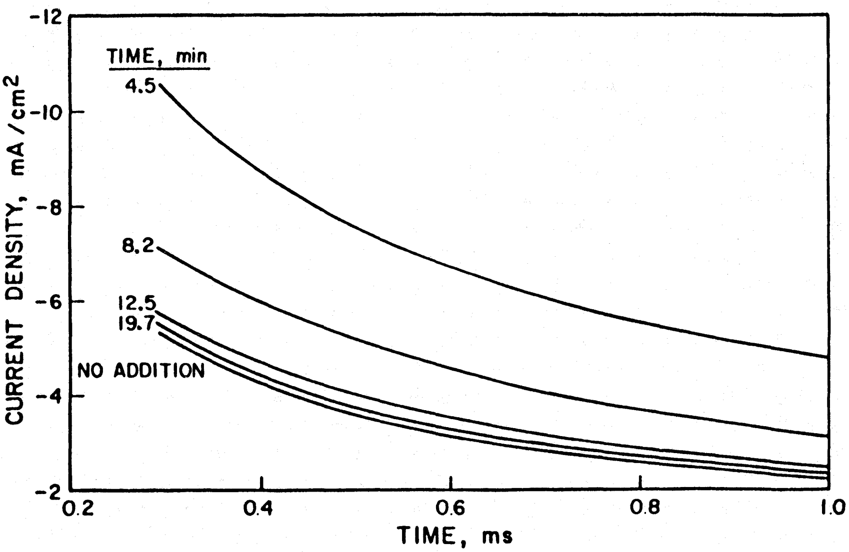

Figure 5. Effect of added Li_2O (18.2 mg) on potential step transients at a gold electrode at 650°C.

DOI: 10.1149/198601.0597PV

INFLUENCE OF PREPARATION CONDITIONS ON ELECTRONIC RESISTIVITY OF $LiFeO_2$ SYNTHESIZED IN MOLTEN CARBONATES

Nguyen Q. Minh, Gene H. Kucera and James L. Smith

Argonne National Laboratory
Chemical Technology Division
Argonne, Illinois 60439

ABSTRACT

$LiFeO_2$ has been synthesized in molten Li_2CO_3-K_2CO_3 eutectic at different temperatures and under different gas environments. The electronic resistivity of $LiFeO_2$ was found to be dependent on the partial pressure of CO_2 above the carbonate melt. A model for nonstoichiometric $LiFeO_2$ has been proposed to explain these experimental results. Dependence of resistivity on the synthesis temperature was also observed.

INTRODUCTION

The state-of-the-art molten carbonate fuel cell (MCFC) consists of a porous nickel anode (fuel electrode), a porous lithium-doped nickel oxide cathode (oxidant electrode), and a lithium aluminate matrix filled with lithium and potassium carbonates (62-70 mol % lithium carbonate) as the electrolyte. The cell is operated at temperatures of about 923 K and at pressures of 1 to 10 atm, with a humidified mixture of H_2 and CO as fuel gas and a mixture of O_2 and CO_2 containing water vapor as oxidant.

Nickel oxide has been used as the cathode material for MCFCs since 1959 (1). One important problem associated with the NiO cathode is its long-term instability. Nickel oxide dissolves at the cathode and precipitates as metallic nickel in the electrolyte owing to reducing conditions caused by the anode gas. The precipitation of nickel near the anode creates a nickel concentration gradient in the electrolyte which causes further NiO dissolution. This dissolution/precipitation phenomenon limits the life of the NiO; thus, the desired 40,000-h lifetime of the fuel cell for commercial applications will probably not be met under certain operating conditions. Development of alternative cathode materials to NiO has been attempted recently (2,3). In general, any cathode material for MCFCs should have the following characteristics: (i) stability in the fuel cell cathode environment, (ii) adequate electronic conductivity ($>0.1\ ohm^{-1}\cdot cm^{-1}$ at 923 K), (iii) low solubility in the electrolyte and no precipitation in the anode environment, and (iv) good catalytic activity for cathode reactions. $LiFeO_2$ is chemically stable, has low solubility, and does not precipitate in the anode environment (2,3). However, the resistivity of the material (in undoped form) under cathode conditions needs to be lowered before it can be used as electrode material.

There are few studies (4-9) reported in the literature on the structure and properties of $LiFeO_2$. The resistivity of $LiFeO_2$ prepared from Fe_2O_3 and Li_2CO_3 at 1023 K in air was investigated by Fayard (6). Fayard (6) reported that nonstoichiometric $LiFeO_2$ with lithium excess was formed by reaction of Fe_2O_3 with excess Li_2CO_3. In the present work, the influence of preparation conditions on the electronic resistivity of $LiFeO_2$ synthesized in molten Li_2CO_3-K_2CO_3 was investigated. The experimental results are presented and discussed.

EXPERIMENTAL

Samples of undoped $LiFeO_2$ were prepared by reacting Fe_2O_3 with Li_2CO_3 in excess Li_2CO_3-K_2CO_3 eutectic (62 mol % Li_2CO_3) for 60 h at several temperatures and under different gas atmospheres. After reaction, the products were washed with distilled water to remove the excess carbonate; they were then dried and pressed into pellets (about 2.85 cm diameter, 0.2 cm thick). The pellets were sintered in the synthesis gas (with the single exception described later) at 1323 K for 1 h. The electronic resistivity of the pellet was determined by the DC technique of van der Pauw (10). The materials were also characterized by X-ray diffraction, absorption spectrophotometry, chemical analysis, and Seebeck coefficient measurements. Chemical analysis for Fe^{4+} in $LiFeO_2$ was carried out by dissolution of $LiFeO_2$ in an excess of reducing material (As_2O_3) under a nitrogen atmosphere followed by titration of the remaining reductant with standard ceric sulphate solution.

RESULTS AND DISCUSSION

Figures 1 and 2 show the temperature dependence of the electronic resistivity of $LiFeO_2$ synthesized at 973 K in molten Li_2CO_3-K_2CO_3 under different mixtures of O_2 + CO_2 + N_2. No effect on resistivity could be detected for oxygen partial pressure of 0.15-0.7 atm and for partial pressure of $CO_2 > 0.005$ atm. Under these conditions, the resistivity of $LiFeO_2$ was about 300 ohm • cm at 923 K. On the other hand, Fig. 1 shows that synthesis with partial pressure of $CO_2 < 0.005$ atm produced $LiFeO_2$ with lower resistivity and that the resistivity decreased with decreasing CO_2 partial pressure. $LiFeO_2$ synthesized under air (partial pressure of $CO_2 = 0.0003$ atm) had a resistivity of 2-5 ohm•cm at 923 K.

The partial pressure of CO_2 will affect the activity of lithium oxide in the carbonate melt and, in that way, can affect the cation ratio (Li/Fe) of the lithium iron oxide synthesized in the melt. This effect is discussed by Schmalzried (11) and Smyth (12,13) for general ternary oxides. These authors point out that complete thermodynamic definition of a ternary oxide requires the specification of three variables (temperature, partial pressure of oxygen, and either binary oxide activity or ratio of the two cationic species). In the syntheses of $LiFeO_2$ in Li_2CO_3-K_2CO_3 eutectic, the activity of lithium oxide is determined by the gas composition, especially partial pressure of CO_2. Low partial pressure of CO_2 enhances the activity of lithium oxide, which tends to result in a more lithium-rich compound, i.e., a $LiFeO_2$ compound with a Li/Fe ratio > 1. The following possibilities of Li/Fe nonstoichiometry are recognized: (i) $Li_{1+x}Fe_{1-x}O_2$, $LiFe_{1-x}O_2$, and $Li_{1+x}FeO_2$. The model $Li_{1+x}Fe_{1-x}O_2$ was proposed by Fayard (6) and Anderson and Schieber (8) as the composition for nonstoichiometric $LiFeO_2$ prepared from Fe_2O_3 and Li_2CO_3 in air. It should be noted that while it is probable that the material has excess-oxygen nonstoichiometry, the discussion here will be focused on the effect of partial pressure of CO_2 and the consequent effect on resistivity via altering the Li/Fe cation ratio.

The activation energy of conduction of $LiFeO_2$ prepared in air is typically 0.4 eV, indicating a probable hopping mechanism. In this case, iron must exist in two valence states. In the first two defect structures given above for $LiFeO_2$ synthesized in low partial pressure of CO_2, the conductivity is due to the mixed valence states of Fe^{3+} and Fe^{4+} (p-type conduction); in the third structure, the mixed valences are Fe^{3+} and Fe^{2+} (n-type conduction). Chemical analysis of air-prepared $LiFeO_2$ indicates the presence of Fe^{4+} as the minor species. This result suggests that the nonstoichiometric composition of $LiFeO_2$ prepared under low CO_2 partial pressures is either $Li_{1+x}Fe_{1-x}O_2$ or $LiFe_{1-x}O_2$. Seebeck measurements on air-prepared samples, performed by H. Anderson of the University of Missouri-Rolla, show positive Seebeck coefficient (Fig. 3), indicating p-type conduction. While Fe^{4+} cannot presently be detected by absorption spectrophotometry, the method does indicate the absence of Fe^{2+} in those samples.

The presence of Fe^{4+} in $LiFeO_2$ synthesized under low partial pressure of CO_2 is consistent with the results of an experiment which studied the variation of the resistivity of air-prepared $LiFeO_2$ with cover gas. A plot of the resistivity versus time and cover gas for an air-prepared $LiFeO_2$ sample is given in Fig. 4. The improvement in conductivity under an oxygen atmosphere also indicates that conductivity is due to the presence of Fe^{4+}. If the conductivity were due to Fe^{2+}, increased partial pressure of oxygen would not be expected to improve the material conductivity. In addition, Fig. 4 shows a wide variation of equilibration times for different gases. This may be indicative of the relative defect concentration in the presence of the various gases.

A test was carried out to examine the proposed nonstoichiometric model for $LiFeO_2$. Figure 5 shows the resistivity of a $LiFeO_2$ sample synthesized under air and then sintered under high CO_2 partial pressure (0.3 atm). The data in Fig. 5 are consistent with the proposed model and can be explained as follows. The $LiFeO_2$ synthesized under air is a nonstoichiometric compound of the type $Li_{1+x}Fe_{1-x}O_2$ (or $LiFe_{1-x}O_2$). When the material is sintered under 30% CO_2-70% air, it tends toward a stoichiometric Li/Fe ratio:

$$Li_{1+x}Fe_{1-x}O_2 = (1-x)LiFeO_2 + xLi_2O + x/2O_2 \qquad [1]$$

$$Li_2O + CO_2 = Li_2CO_3 \quad . \qquad [2]$$

Because of this, the resistivity of the material is high in the lower temperature range of Fig. 5. However, because the resistivity measurements were carried out under air (partial pressure of CO_2 = 0.0003 atm), the reactions [1] and [2] are reversed, making the material nonstoichiometric at higher temperatures. Lower resistivity is thus observed. The resistivity of $LiFeO_2$ synthesized in high partial pressure of CO_2 is, on the other hand, not changed when measured in air; because resistivity measurements are carried out without the presence of Li_2CO_3, no lithium is available for incorporation to alter the Li/Fe ratio.

Although not enough information is available at present to determine whether the nonstoichiometric $LiFeO_2$ is $Li_{1+x}Fe_{1-x}O_2$ or $LiFe_{1-x}O_2$, the composition $Li_{1+x}Fe_{1-x}O_2$ appears to be more probable. The stoichiometric $LiFeO_2$ at 973 K has a disordered cubic structure, with lithium and iron distributed randomly on a single set of lattice sites. The composition $LiFe_{1-x}O_2$ is a representation of an iron vacancy. In the presence of excess Li_2CO_3 during synthesis, it is unlikely that the iron sites would remain vacant.

$LiFeO_2$ has also been synthesized in air at different temperatures. The resistivity of $LiFeO_2$ synthesized at 903-973 K decreases with increasing synthesis temperature (Fig. 6). For example, the resistivity at 923 K of $LiFeO_2$ synthesized at 903 K is about 120 ohm•cm, compared with about 72 ohm•cm for 923 K synthesis and about 3 ohm•cm for 973 K synthesis. At present, the type of nonstoichiometry (oxygen nonstoichiometry or Li/Fe nonstoichiometry) responsible for this phenomenon has not been investigated.

ACKNOWLEDGMENTS

This work was supported by the U.S. Department of Energy, Morgantown Energy Technology Center, Fuel Cell Projects Section under Contract W-31-109-ENG-38. Professor H. Anderson of the University of Missouri-Rolla provided input through discussions and Seebeck measurements. We would like to thank B. Tani for X-ray diffraction analysis, K. Jensen and A. Essling for chemical analysis. The support of Drs. J. P. Ackerman and R. D. Pierce is gratefully acknowledged.

REFERENCES

1. E. Gorin and H. L. Recht, Chem. Eng. Prog., 55, 51 (1959).
2. J. L. Smith, T. D. Kaun, N. Q. Minh, and R. D. Pierce, 1983 National Fuel Cell Seminar, p. 42, Orlando, Florida, November 13-16 (1983).
3. G. H. Kucera, N. Q. Minh, J. L. Smith, and F. C. Mrazek, 1985 Fuel Cell Seminar, p. 158, Tucson, Arizona, May 19-22 (1985).
4. F. Barblan, E. Brandenberger, and P. Niggli, Helv. Chim. Acta, 27, 88 (1944).
5. R. Collongues, C. R. Acad. Sci. Paris, 241, 1577 (1955).
6. M. Fayard, Ann. Chim. (Paris), 6, 1279 (1961).
7. D. E. Cox, G. Shirane, P. A. Flinn, S. L. Ruby and W. J. Takei, Phys. Rev., 132, 1547 (1963).
8. J. C. Anderson and M. Schieber, J. Phys. Chem. Solids, 25, 961 (1964).
9. G. Demoisson, N. Tannieres, C. Gleitzer, and J. Aubry, C.R. Acad. Sci. Paris Ser. C, 274, 1629 (1972).
10. L. J. van der Pauw, Philips Res. Rep., 13 (1), 1 (1958).
11. H. Schmalzried, Prog. Solid State Chem., 2, 265 (1965).
12. D. M. Smyth, J. Solid State Chem., 16, 73 (1976).
13. D. M. Smyth, J. Solid State Chem., 20, 359 (1977).

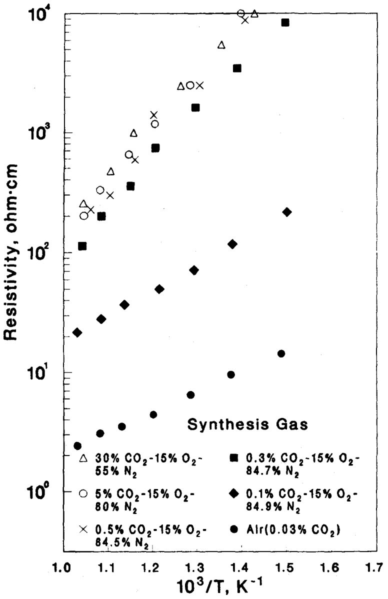

Fig. 1. Resistivities of $LiFeO_2$ Synthesized at 973 K under Different Partial Pressures of CO_2

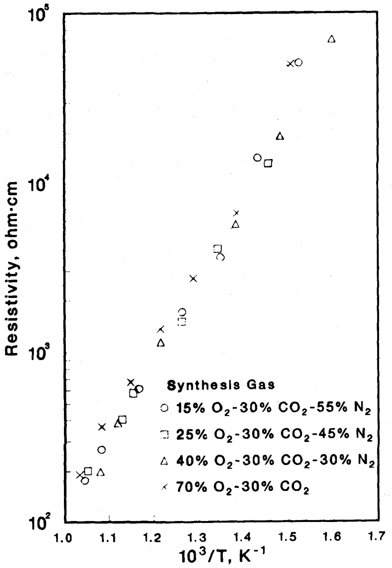

Fig. 2. Resistivity of $LiFeO_2$ Synthesized at 973 K under Different Partial Pressures of O_2

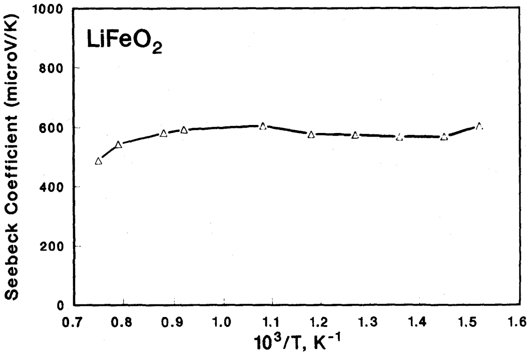

Fig. 3. Seebeck Coefficient of $LiFeO_2$ Synthesized at 973 K in Air

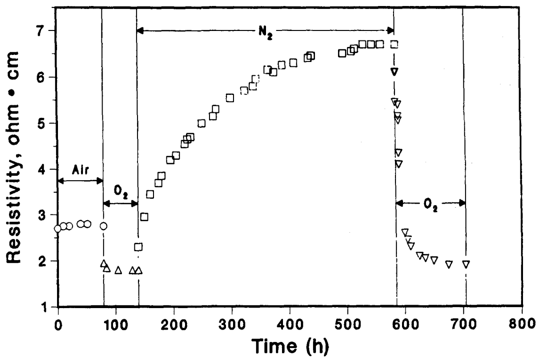

Fig. 4. Resistivity of $LiFeO_2$ Synthesized in Air as a Function of Time and Cover Gas

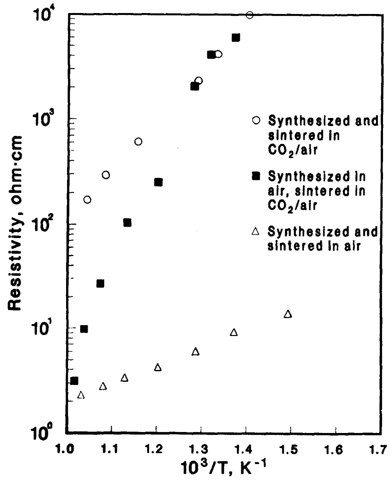

Fig. 5. Resistivity of $LiFeO_2$ Synthesized and Sintered under Different Gas Mixtures

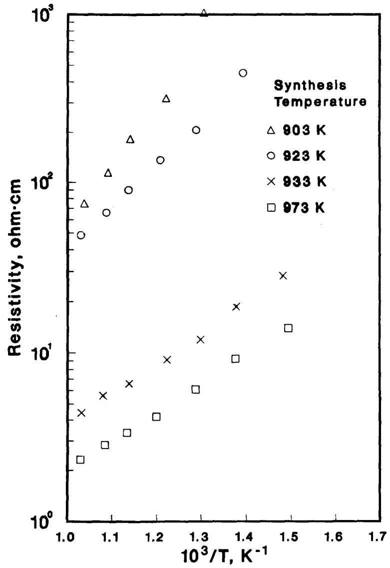

Fig. 6. Resistivity of $LiFeO_2$ Synthesized in Air at Different Temperatures

AUTHOR INDEX

SUBJECT INDEX